

C. M. González-Henríquez  
Juan Rodríguez-Hernández *Editors*

# Wrinkled Polymer Surfaces

Strategies, Methods and Applications



Springer

# Wrinkled Polymer Surfaces

C. M. González-Henríquez  
Juan Rodríguez-Hernández  
Editors

# Wrinkled Polymer Surfaces

Strategies, Methods and Applications

 Springer

*Editors*

C. M. González-Henríquez  
Department of Chemistry  
Universidad Tecnológica Metropolitana  
(UTEM)  
Santiago, RM - Santiago, Chile

Juan Rodríguez-Hernández  
Institute of Polymer Science  
and Technology (ICTP-CSIC)  
Madrid, Spain

Programa Institucional de Fomento a la  
Investigación  
Desarrollo e Innovación  
Universidad Tecnológica Metropolitana  
San Joaquín, Santiago, Chile

ISBN 978-3-030-05122-8      ISBN 978-3-030-05123-5 (eBook)  
<https://doi.org/10.1007/978-3-030-05123-5>

Library of Congress Control Number: 2018968444

© Springer Nature Switzerland AG 2019

This work is subject to copyright. All rights are reserved by the Publisher, whether the whole or part of the material is concerned, specifically the rights of translation, reprinting, reuse of illustrations, recitation, broadcasting, reproduction on microfilms or in any other physical way, and transmission or information storage and retrieval, electronic adaptation, computer software, or by similar or dissimilar methodology now known or hereafter developed.

The use of general descriptive names, registered names, trademarks, service marks, etc. in this publication does not imply, even in the absence of a specific statement, that such names are exempt from the relevant protective laws and regulations and therefore free for general use.

The publisher, the authors, and the editors are safe to assume that the advice and information in this book are believed to be true and accurate at the date of publication. Neither the publisher nor the authors or the editors give a warranty, express or implied, with respect to the material contained herein or for any errors or omissions that may have been made. The publisher remains neutral with regard to jurisdictional claims in published maps and institutional affiliations.

This Springer imprint is published by the registered company Springer Nature Switzerland AG  
The registered company address is: Gewerbestrasse 11, 6330 Cham, Switzerland

*J.R.H. would like to dedicate this book to his father. He was a source of inspiration and motivation to become a scientist. Thank you so much.*

*C.M.G.H. wants to dedicate this book to her beloved mother, Catalina, who was an example of perseverance, determination, and integrity.*

# Foreword

Inspired by nature, many materials scientists have focused their research efforts both on understanding the mechanisms involved in the unique properties of natural surfaces and trying to mimic their behavior from a synthetic point of view.

In this context, many of the strategies reported to reproduce the superior properties of surfaces in nature failed or resorted to intricate methodologies that require the use of expensive and sophisticated equipment. In this sense, many advances in the development of polymer surfaces have been associated with technological improvements. However, more recently, several alternative approaches have been developed in which the surface patterns originated are not the result of refined fabrication techniques but take advantage of the instabilities that can be produced in polymer surfaces.

Surface instabilities are sometimes intrinsic to thin films, but may also be induced. For instance, upon heating, applying an electric field, or upon exposure to aqueous solutions at different pH values, the surface may respond by altering the initially planar surface morphology. As a result, depending on the types of stimuli applied, the external conditions and material properties can be influenced to manifest a myriad of surface patterns. It is worth mentioning that some of these would be difficult, if not impossible, to obtain by conventional surface patterning techniques.

In this context, one of the most extensively explored surface patterns produced as a result of surface instabilities is the formation of surface wrinkles. Surface wrinkles have been obtained using different materials (hydrogels, elastomers, or thermoplastics), external stimulus (heating, swelling, mechanical stretching, etc.), and film structures (bilayer, gradient, and homogeneous films). In spite of the large amount of work carried out in this area, there are only a few collections and reviews of the recent advances in this area. Thus, the preparation of this book is motivated by two reasons: first, most reviews are several years old already, and as this is a research area that develops quickly, and so are out of date; second, there is a lack of a wide overview on the subject that would assist scientists, students, and engineers who

want to learn about wrinkle formation. We hope this volume will assist a wide variety of readers in acquiring relevant knowledge in this interesting and developing research area.

C. M. González-Henríquez  
Chemistry Department  
Universidad Tecnológica Metropolitana,  
Santiago, Chile

Juan Rodríguez-Hernández  
Department of Applied Macromolecular Chemistry  
Institute of Polymer Science and Technology,  
Madrid, Spain

# Preface

This volume, entitled *Wrinkled Polymer Surfaces: Strategies, Methods, and Applications* aims to cover topics ranging from the fundamental principles of wrinkle formation up to the final application of the materials developed. As a result, this book is divided into four main sections. The first part includes the basic principles of wrinkle formation and the most extended strategies for their fabrication. The goal of this part is to establish a basic understanding of the methodologies described in the book.

The second section is focused on describing novel approaches to forming wrinkled surfaces that have not been extensively explored, yet offer unique potentials. The methodologies selected for this volume include the fronta006C polymerization/vitrification, ion-beam bombardments, interfacial swelling on thermoplastic surfaces, and the use of direct laser interference patterning.

The third part involves chapters in which originality is the focus of the material employed. Thus, in addition to the typical elastomeric foundations (described in Part 1), this part covers the use of hydrogels with a homogeneous or a gradient structure that upon the appropriate stimulus form wrinkles. Besides hydrogels, this part includes illustrative examples of the formation of wrinkles in 2D materials, such as graphene, but also in 3D materials such as elastomeric Janus particles.

The fourth part is devoted to current and potential applications of wrinkled material surfaces. In view of the large potential of these surfaces for biomedical applications, an entire chapter is devoted to this application. Moreover, a second chapter includes other relevant applications, including the elaboration of conductive shrinkable devices, fabrication of electrochromic devices, and the elaboration of sensors and actuators, to name a few.

The final chapter aims to present both the advantages and limitations of wrinkled polymer surface science. Moreover, this chapter also discusses what, in our humble opinion, will be the next frontiers in this exciting research area.

Santiago, Chile  
Madrid, Spain

C. M. González-Henríquez  
Juan Rodríguez-Hernández

## Acknowledgments

The authors would like to thank their respective research organizations, the Spanish National Research Council (CSIC) and the Universidad Tecnológica Metropolitana (UTEM), for their support during the preparation of this volume. In addition, the authors acknowledge the financial support given by FONDECYT Grant Number 1170209 and VRAC Grant Number L216-04 of Universidad Tecnológica Metropolitana. Juan Rodríguez-Hernández acknowledges the financial support from Ministerio de Economía y Competitividad (MINECO) (Project MAT2016-78437-R, FEDER EU).

# Contents

## Part I Generalities on Surface Instabilities

- 1 Introduction to Surface Instabilities and Wrinkle Formation . . . . . 3**  
C. M. González-Henríquez, M. A. Sarabia Vallejos,  
and Juan Rodríguez-Hernández
- 2 Strategies for the Fabrication of Wrinkled Polymer Surfaces . . . . . 19**  
C. M. González-Henríquez, M. A. Sarabia Vallejos,  
and Juan Rodríguez-Hernández

## Part II Novel Approaches for Wrinkled Patterns Formation

- 3 Wrinkles Obtained by Frontal Polymerization/Vitrification . . . . . 63**  
C. M. González-Henríquez, M. A. Sarabia Vallejos,  
and Juan Rodríguez-Hernández
- 4 Control of Wrinkled Structures on Surface-Reformed  
Elastomers via Ion Beam Bombardment . . . . . 85**  
C. M. González-Henríquez, M. A. Sarabia Vallejos,  
and Juan Rodríguez-Hernández
- 5 Wrinkled Hydrogel Formation by Interfacial Swelling  
on Thermoplastic Surfaces . . . . . 109**  
Enrique Martínez, Alberto Gallardo, Ana Santos-Coquillat,  
Noelia Lujan, Helmut Reinecke, Adolfo del Campo,  
and Juan Rodríguez-Hernández
- 6 Laser-Induced Periodic Surface Structures (LIPSS)  
on Polymer Surfaces . . . . . 143**  
Esther Rebollar, Tiberio A. Ezquerro, and Aurora Nogales

<b>7</b>	<b>Design of Perfectly Ordered Periodic Structures on Polymers Using Direct Laser Interference Patterning</b> .....	157
	Andrés Fabián Lasagni, Sabri Alamri, Florian Rößler, Valentin Lang, and Bogdan Voisiat	
<b>Part III Materials Employed in Wrinkles Formation</b>		
<b>8</b>	<b>Micro- and Nano-patterned Hydrogels Fabricated by Taking Advantage of Surface Instabilities</b> .....	183
	C. M. González-Henríquez, M. A. Sarabia Vallejos, and Juan Rodríguez-Hernández	
<b>9</b>	<b>Wrinkling on Covalently Anchored Hydrogels</b> .....	205
	Chya-Yan Liaw, Jorge Pereyra, and Murat Guvendiren	
<b>10</b>	<b>Ripples and Wrinkles in Graphene: Beyond Continuum Mechanics</b> .....	229
	Hervé Elettro and Francisco Melo	
<b>11</b>	<b>Wrinkling Labyrinth Patterns on Elastomeric Janus Particles</b> ....	253
	Ana Catarina Trindade, Pedro Patrício, Paulo Ivo Teixeira, and Maria Helena Godinho	
<b>Part IV Applications</b>		
<b>12</b>	<b>Wrinkled Surfaces Designed for Biorelated Applications</b> .....	273
	C. M. González-Henríquez, M. A. Sarabia Vallejos, and Juan Rodríguez-Hernández	
<b>13</b>	<b>Tuning Surface Morphology of Polymer Films Through Bilayered Structures, Mechanical Forces, and External Stimuli</b> .....	291
	Ying Li and Shan Tang	
<b>14</b>	<b>Other Applications of Wrinkled Polymer Surfaces</b> .....	315
	C. M. González-Henríquez, M. A. Sarabia Vallejos, and Juan Rodríguez-Hernández	
<b>15</b>	<b>Summary and Future Outlooks</b> .....	345
	C. M. González-Henríquez, M. A. Sarabia Vallejos, and Juan Rodríguez-Hernández	
	<b>Index</b> .....	351

**Part I**  
**Generalities on Surface Instabilities**

# Chapter 1

## Introduction to Surface Instabilities and Wrinkle Formation



C. M. González-Henríquez, M. A. Sarabia Vallejos,  
and Juan Rodríguez-Hernández

### 1.1 Introduction to Surface Instabilities

The fabrication of functional and micro- and nanostructured polymer surfaces has been extensively explored during the last decades. The large effort carried out in the elaboration of these materials is justified by the wide variety of applications that largely depend on the surface properties of a particular material. For instance, both patterning and functionalization of polymer surfaces have been demonstrated to play a key role in the preparation of substrates for cell growth [1, 2] in the fabrication of microchips and microelectromechanical (MEM) devices [3, 4] or in the control of the interfacial adhesion/friction/lubrication [5] just to mention few of them.

The progresses carried out in the elaboration of functional and micro-/nanostructured polymer surfaces have been achieved using two alternative strategies. On the one hand, significant improvements have been accomplished by taking advantage of the technological advances in terms of fabrication facilities. These usually involve

---

C. M. González-Henríquez (✉)

Departamento de Química, Facultad de Ciencias Naturales, Matemáticas y del Medio Ambiente, Universidad Tecnológica Metropolitana, Santiago, Chile

Programa Institucional de Fomento a la Investigación, Desarrollo e Innovación, Universidad Tecnológica Metropolitana, San Joaquín, Santiago, Chile  
e-mail: [carmen.gonzalez@utem.cl](mailto:carmen.gonzalez@utem.cl)

M. A. Sarabia Vallejos

Escuela de Ingeniería, Departamento de Ingeniería Estructural y Geotecnia, Pontificia Universidad Católica de Chile, Santiago, Chile

Instituto de Ingeniería Biológica y Médica, Santiago, Chile

J. Rodríguez-Hernández (✉)

Departamento de Química Macromolecular Aplicada, Polymer Functionalization Group, Instituto de Ciencia y Tecnología de Polímeros-Consejo Superior de Investigaciones Científicas (ICTP-CSIC), Madrid, Spain  
e-mail: [jrodriguez@ictp.csic.es](mailto:jrodriguez@ictp.csic.es)

the development of novel fabrication techniques such as laser scanning [6], soft lithography [7–9], or laser ablation [10]. However, important advances have been also reached by adapting previously described techniques. This is, for instance, the case of hot embossing/molding [11–16] and also the micro-/nanoimprinting that can be today carried out in a continuous manner (roll-to-roll nanoimprinting) [17–20]. These novel or improved technological advances offered the scientist of novel fabrication facilities with enhanced resolution capabilities.

On the other hand, contrary to the abovementioned strategies that are directly associated to the use of sophisticated tools and are, therefore, expensive and time-consuming, diverse alternatives have been proposed for the preparation of micro-/nanostructured polymer surfaces. In particular, different methodologies have been reported more recently taking advantage of the surface instabilities induced in polymer surfaces to produce a wide variety of surface patterns.

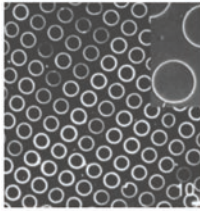
Today, it is widely admitted that surface instabilities on the polymer can be produced by two alternative routes. First, surface instabilities are spontaneously observed in confined systems at the small scale since these systems are inherently unstable. Alternatively, surface instabilities can be induced in metastable films by applying a particular external stimulus including a mechanical force that can be induced in metastable films applying an external stimulus. These external stimuli include the use of mechanical force (stretching or compression), applying an electric field or simply by heating the material. Upon removal of the force applied, the relaxation of the surface instabilities toward equilibrium produces the modification of the surface structure in order to minimize the surface energy. As a result, different surface morphologies with particular geometries and shapes with nano- and micrometer size moieties can be observed.

A large amount of scientific groups are currently using surface instabilities to pattern polymer surfaces mainly motivated by the cost reduction but also due to the wide variety of complex patterns that can be achieved. These complex surface features are challenging to fabricate by using other conventional patterning techniques. Moreover, depending on the methodology employed to produce the desired surface instability, a wide variety of intriguing morphologies have been described. As has been detailed in Chap. 2, surface instabilities currently employed for the fabrication of structured surfaces can be classified into three different groups including (see Fig. 1.1) [21]:

- (a) Those methodologies in which the structuration is driven by the thermodynamics: phase separation of polymer blends and block copolymers [22–25], dewetting [26–28], or template guided structuration [29–33]
- (b) Those that require an external field to induce the self-assembly and later the surface structuration: thermal gradient-induced surface patterning [34, 35], electrohydrodynamic patterning [36–41], reaction-diffusion surface patterns, [42] and growth processes, aggregation and crystal growth [43] and surface wrinkling [44]
- (c) Those in which the polymeric material is altered by a changing environment: water ion-induced nanostructuring [45, 46], nanobubble-assisted nanopatterning [47], and breath figs [48–52]

Whereas some of the instabilities on polymer films depicted in Fig. 1.1 are already widely known such as phase separation or film dewetting, others have been

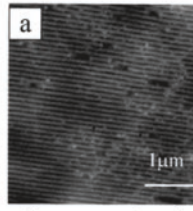
**a) Close to equilibrium: structuration driven by thermodynamics**



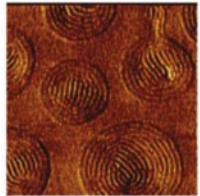
*Dewetting [53]*



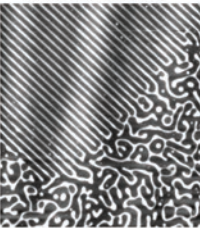
*Directing convection: evaporative self-organization. [54]*



*Phase separation of polymer blends and block copolymers. [55]*

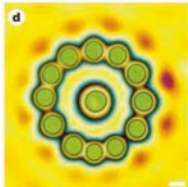


*Nanostructures obtained by surface segregation [56]*

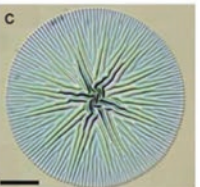


*Template guided structuration [57]*

**b) Far from equilibrium: Field-induced assembly**



*Electrohydrodynamic /Thermal-gradient induced surface patterning [58]*

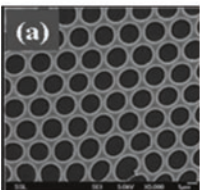


*Elastic Instability and Surface Wrinkling [59] (scale bar 10 μm).*

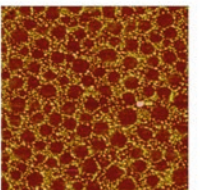


*Reaction-diffusion surface patterns. [60]*

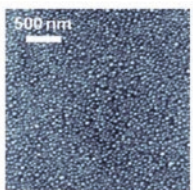
**c) Polymer material reconstruction in response to a changing environment**



*Breath Figures [61, 62]*



*Nanobubble assisted nanopatterning. [63]*



*Water-ions induced nanostructure. [46]*

**Fig. 1.1** Illustrative images of the surface patterns obtained by using different instability-based patterning approach: (a) structuration drove by surface/interfacial energy, (b) field-induced structuration, and (c) influence of water on hydrophobic polymer surfaces. Reproduced with permission from ref. [21]

only recently explored. The latter include the instabilities produced by using electric field-induced instabilities or thermal gradients. In spite of this, all these methodologies have been only recently employed for the fabrication of a myriad of polymer surface micro- and submicrometer size patterns. To provide a summarized overview of the different instability-based patterning techniques, Tables 1.1, 1.2, and 1.3 present the most relevant characteristics of each technique including the driving force that originates the instability, the pattern induced, the size of the surface features produced, and finally illustrative selected references from each methodology.

## 1.2 Wrinkling on Polymer Surfaces

Among the different patterning strategies based on surface instabilities, wrinkling instability has been the center of multiple studies as a self-organizing methodology to induce micro- and submicrometer-scale structures [44, 94]. As has been the case in other situations, nature provides unique inspiration to investigate and understand physical phenomena. Wrinkle formation is not an exception. Wrinkles appear in nature in many different forms. For instance, wrinkles appear when the skin is stretched or compressed using a mechanical force [94].

Moreover, mechanically induced surface instabilities are a central mechanism to control the development and progress of different surface patterns observed in nature [1]. Mechanically induced morphological changes are responsible for the proper functioning of different organs such as the intestine [5] or the mammalian brain [2–4]. Equally, as it is shown in Fig. 1.2, for the case of an apple, a date, and an apricot, an analogous mechanism causes the emergence of wrinkles in the course of the dehydration of fruits. Finally, as has been highlighted by Genzer and Groenewold [94], there are wrinkles with extremely large differences in length scales (more than ten orders of magnitude). For instance, mountains formed by compressive tectonic forces present wavelengths on the kilometer range. Wrinkles observed in both human or fruit skin (Fig. 1.2) obtained upon skin stretching/compression or drying respectively are in the mm length scale. Finally, synthetic systems can be prepared with wrinkles at the nanoscale. This is the case, for instance, in surface-treated elastomeric PDMS.

The formation of wrinkles at polymer surfaces is not new but rather an old observation made when using coatings. As a result, there are since the 1920s commercially available wrinkled coating. According to Genzer and Groenewold [94], pioneer workings in the formation of wrinkled coatings were done using China wood oil that was cured under atmospheric oxygen using a relatively high temperature (120–130 °C). Whereas the initial resulting coatings were somehow neglected, these materials finally lead to a new range of products known as wrinkle finishes coatings [118]. Another illustrative example of materials where the wrinkle formation was initially considered undesirable is the case of the marine and aerospace engineering during the World War II [94]. The fabrication of different elements, such as the wings, was carried out using cross-linked polymers foams having a rigid composite skin. This type of construction, known as “sandwich,” leads to buckling when a compressive external force surpasses a critical value. Buckling

**Table 1.1** Close to equilibrium: structuration driven by thermodynamics

Patterning method	Driving force	Pattern induced	Typical feature size	Observations	Selected references
Dewetting	Surface forces	Isotropic, random structures (well-defined mean length scale)	Submicron (down to ~ 100 nanometers)	Occur in molten ultrathin films or films with low elastic modulus. Nucleation can destabilize thicker films	[64–70]
Directing convection	Marangoni convection/ evaporation/self-assembly	Coffee rings, polygonal network structures, fingering instabilities, cracks, chevron patterns, etc.	Nm $\mu$ m size	Marangoni convection and stick-slip motion can determine the final patterns observed	[71–73]
Self-assembly and microphase separation	Phase separation of polymer blends and/or block copolymers	Random structures (polymer blends) and self-assembled nanostructures (block copolymers)	Nm to $\mu$ m	Phase separation influenced by the film thickness, temperature, and substrate	[69, 74–81]
Surface segregation	Surface/ interfacial energy	Layered segregation	Nm	Block copolymer segregation from blends afford nanostructured interfaces	[56, 82, 83]
Template-guided structuration	Surface-induced structure formation	Governed by the template: hexagonal, stripes, squares	Nm to $\mu$ m	Extensively employed in combination with block copolymers and blends Surface affinity assisted the self-assembly of block copolymers and blends	[29–33]

Reproduced with permission from ref. [21]

significantly affects and reduces the mechanical properties of the part. These two examples of wrinkle and buckling served as a starting point in the investigation of the forces and surface instabilities involved in the formation of these patterns.

Pioneer investigations about the wrinkle formation mechanism based exclusively on the experimental observations on cured wood oil lead to rather a controversial hypothesis. On the one hand, Auer et al. [119] reported that UV light was at the origin of the wrinkled formation. However, on the other hand, Merz et al. [120] demonstrated that wrinkles can be also formed without using UV light. At the same time, other groups evidenced that the environmental gases such as combustion product, the

**Table 1.2** Far from equilibrium: field-induced and dynamic control of surface structuration

Patterning method	Driving force	Pattern induced	Typical feature size	Observations	Selected references
Electrohydrodynamic	Electrical stress	Waves, holes, columns or channels	Submicrometer to $\mu\text{m}$	Morphology controlled by the film thickness, interelectrode distance, electrode patterning, applied field	[36–41]
Thermal gradient	External thermal gradient	Similar to electrohydrodynamic patterning	Submicrometer to $\mu\text{m}$	Morphology depends on film thickness, the gap between the plates, thermal gradient and temperature of the plates	[34, 35, 84–93]
Surface wrinkling, creasing, and folding	Mechanical stress	Controlled wrinkles	Down to $\mu\text{m}$	Wrinkle, creasing or folding orientation depends on the direction and magnitude of the applied stress	[94–105]
Reaction-diffusion	Reaction-diffusion dynamics	Hexagonal, striped, and mixed patterns	$\mu\text{m}$ to mm	Patterns obtained by reaction-diffusion competition [106, 107]	[108–110]

Reproduced with permission from ref. [21]

**Table 1.3** Waterborne methods

Patterning method	Driving force	Pattern induced	Typical feature size	Observations	Selected references
Breath figures	Condensation of water vapor	Porous films with variable surface distribution and pore sizes	Hundreds of nm up to ~20 $\mu\text{m}$	Water vapor condensation during solvent evaporation drives the formation of pores. Solvent, polymer concentration, temperature, and relative humidity play a key role in the pore formation	[61, 62, 111–113]
Water ion-induced nanostructuring	Instability due to the absorption of ions at the interface	Blobs eventually self-assembled	Few tens of nm	Depend on the amount of gas dissolved in the water and the ions in solution	[46, 114, 115]
Nanobubble-assisted nanopatterning	Nanobubble-assisted nanopatterning	Nanograins, net-like nanopatterns	Few tens of nm (below 50 nm in some cases)	Surface pattern obtained in seconds	[63, 116]

Reproduced with permission from ref. [21]

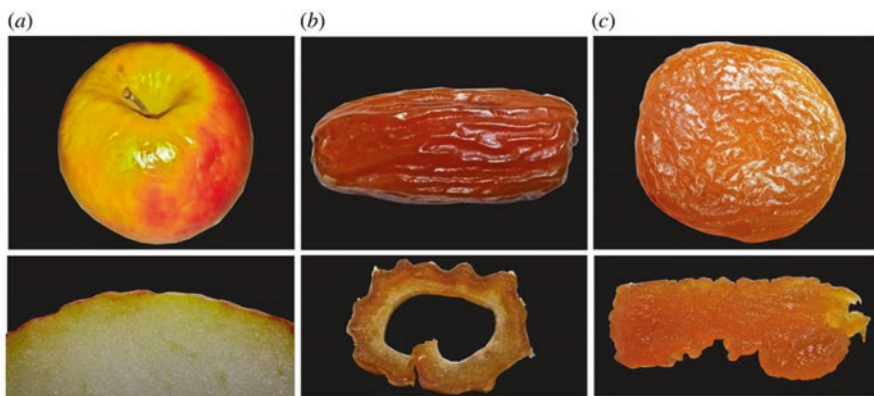


**Fig. 1.2** Wrinkling instabilities caused by dehydration in an apple (a), a date (b), and an apricot (c). Reproduced with permission from ref. [117]

water vapor during the drying process, or nitric acid gas appear to favor the wrinkling process [121]. A similar role was played by contamination products [122–124]. As has been mentioned, all these factors prevent or favor wrinkle formation to a limited extent. However, none of them are the main cause of this process. Later studies carried out by Burrell et al. [118] demonstrated that the formation of a stiff top layer of

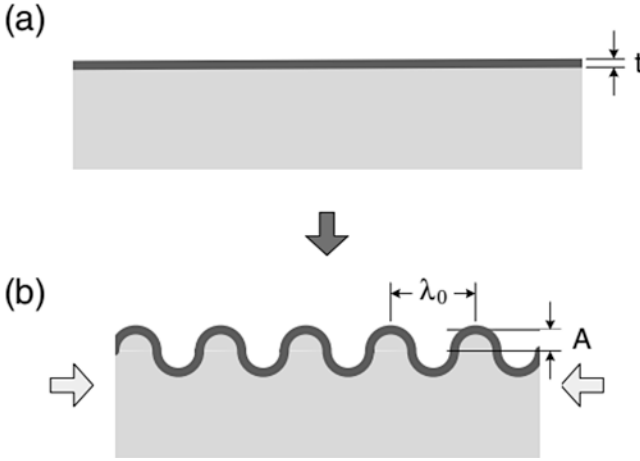


**Fig. 1.3** Illustration of the general mechanisms for the formation of wrinkles in bilayered systems comprising a rigid top layer on an elastic substrate. Reproduced with permission from ref. [125]

the material promotes wrinkle formation. In contrast to previous works that assumed that the surface layer expands faster than the layers beneath the surface, Burrell et al. proposed for the first time that shrinkage and not expansion is at the origin of wrinkle formation. This excellent work is the base of the widely accepted mechanism.

In effect, the general mechanism of wrinkle formation is illustrated in Fig. 1.3 for the case of a bilayer system composed of a rigid top layer on top of an elastic foundation. The first step involves the use of a mechanical stress force (originated by osmotic pressure, stretching, or heating just to mention a few of the available mechanisms). Then, the rigid layer is deposited on top of the polymer film. Finally, upon elimination of the applied stress, the initial shape of the elastic foundation is relaxed, and at the surface a wavy structure, i.e., “wrinkles,” is generated.

As will be thoroughly described in this book, without any doubt in these bilayer systems, the difference in the stiffness between the polymer surface (“skin”) and the elastic polymer foundation is critical to observe this kind of patterns.

From this generally accepted mechanism, several studies have been carried out to calculate basic parameters such as the minimal force required to form wrinkles or the characteristics of the wrinkles obtained including period and amplitude. First of all, taking into account that both the top layer and the elastic polymer foundation (bulk) have their own particular elastic modulus and Poisson’s ratio, the compressive force exerted on the skin can be calculated by using the following expression:

$$F = E_s \left[ \left( \frac{\pi}{\lambda} \right)^2 \frac{wh^3}{3(1-\nu_s^2)} + \frac{\lambda}{4\pi} \frac{E_f w}{(1-\nu_f^2)E_s} \right] \quad (1.1)$$

(where  $h$  is the thickness and  $w$  is the width of the skin layer;  $E_s$ ,  $\nu_s$ , and  $E_f$ ,  $\nu_f$  are the elastic moduli and the Poisson’s ratio of the skin and foundation, respectively; and  $\lambda$  is the sinusoidal deflection profile).

It is worth noting that, in the case when the load exceeds a critical value ( $F_c$ ), buckling in the skin will take place. From Eq. (1.1), the wavelength of the wrinkles can be calculated supposing that  $dF/d\lambda = 0$ . Using this assumption results in the following Eq. (1.2):

$$\lambda_c = 2\pi h \left[ \frac{(1-\nu_f^2)E_s}{3(1-\nu_s^2)E_f} \right]^{1/3} \quad (1.2)$$

Further studies proposed alternative methodologies to calculate the wrinkle wavelength [126–129]. In these studies, the authors evidenced that both amplitude and wavelength can be calculated taking into account an energy minimization ( $U$ ),  $U = U_B + U_S$  (energy due to bending ( $U_B$ ) and energy due to stretching along the wrinkles ( $U_S$ )). The use of this model permitted the calculation of the wrinkle parameters. In particular, in addition to the wrinkle periodicity, ( $\lambda$ ) permits to calculate the wrinkle amplitude ( $A$ ) as follows [128]:

$$\lambda \sim \left( \frac{B}{K} \right)^{1/4} \quad (1.3)$$

$$A \sim \left( \frac{\Delta}{w} \right)^{1/2} \lambda \quad (1.4)$$

For this expression, a thin sheet with a bending stiffness  $B$ , an effective elastic foundation of stiffness  $K$ , and an imposed compressive strain  $\Delta/W$  are considered.

In addition to bilayer systems, both homogeneous and also gradient substrates can produce surface wrinkling. In this case, surface instabilities are induced by film swelling (see Chaps. 4 and 5). Moreover, depending on the swelling extent, these systems can not only produce surface wrinkles but also form creases or even folding [94, 96, 130, 131]. More precisely, creases are generally observed in hydrogels supported onto a rigid substrate. In this situation, swelling limits the film, and the surface instability is produced [132, 133]. In addition, larger swelling is at the origin of eventual local delamination and the formation of buckled forms known as folded structures [134–138].

Wrinkling and a large number of alternatives to fabricate buckled structures involving surface treatments, swelling, or heating just to mention a few of them have been already described in the literature. Equally, the application of such structures has also been extensively investigated. For instance, recent examples on the use of microwrinkled surface for different applications include marine antifouling [139], responsive microfluidic channels [140], thin-film metrology [141–143], microlens arrays [140, 144], switchable wettability [105, 145, 146], flexible electronics [147, 148], tunable optical devices [140, 149, 150], dry adhesion [151], cell alignment [59, 152, 153], particle sorting [154], or the preparation of twisted nematic liquid crystal displays [155].

As will be thoroughly analyzed through this book, a large variety of strategies have been reported to induce buckling on polymer surfaces and finally produce wrinkled morphologies.

### 1.3 About this Book

The aim of this book is to present in a comprehensive manner the principles of wrinkle formation, the different strategies focusing on those reported recently, and of course the potential applications of such surface structures.

For this purpose, the book is divided into four sections. Part I is present the general principles of surface instabilities currently employed to fabricate micro- and nanostructured surfaces (Chap. 1) as well as to briefly present the different alternatives reported to fabricate wrinkled polymer surfaces (Chap. 2).

Part II involves a series of chapters of selected alternatives to produce wrinkled surfaces. These chapters have been selected based on the novelty of the strategies proposed. In this context, frontal polymerization/vitrification (Chap. 3), ion beam bombardment on elastic surfaces (Chap. 4), wrinkles prepared by interfacial diffusion (Chap. 5), and the use of lasers (Chaps. 6 and 7) are included in this section.

Wrinkles have been prepared using different polymeric materials including hydrogels, thermoplastics, elastomers, or even graphene-based materials. Part III covers recent examples of novel materials currently employed for the development of wrinkled surfaces. Thus, this section will describe the use of hydrogels anchored on solid substrates (Chaps. 8 and 9), wrinkles in graphene (Chap. 10), or elastomeric Janus particles (Chap. 11).

Part IV discussed in a systematic manner the most relevant applications of wrinkled polymer surfaces. Chapter 12 focuses on the bio-applications of these materials. Chapter 13 will describe the use of wrinkled surfaces for flexible electronics, and finally Chap. 14 attempts to summarize other applications in which the wrinkled surface morphology offers a clear advantage.

Finally, Chap. 15 recapitulates the most relevant aspects described in this book and provides an outlook about the future development in this particular area.

**Acknowledgments** The authors acknowledge financial support given by FONDECYT Grant N° 1170209. M.A. Sarabia acknowledges the financial support given by CONICYT through the doctoral program scholarship grant. J. Rodríguez-Hernández acknowledges financial support from Ministerio de Economía y Competitividad (MINECO) (Project MAT2016-78437-R, Fondos FEDER EU) and, finally, VRAC Grant Number L216-04 of Universidad Tecnológica Metropolitana.

### References

1. W. Tan, T.A. Desai, Microfluidic patterning of cells in extracellular matrix biopolymers: Effects of channel size, cell type, and matrix composition on pattern integrity. *Tissue Eng.* **9**(2), 255–267 (2003)
2. M.J. Dalby, M.O. Riehle, S.J. Yarwood, C.D.W. Wilkinson, A.S.G. Curtis, Nucleus alignment and cell signaling in fibroblasts: Response to a micro-grooved topography. *Exp. Cell Res.* **284**(2), 274–282 (2003)
3. S.Y. Chou, Nanoimprint lithography and lithographically induced self-assembly. *MRS Bull.* **26**(7), 512–517 (2001)
4. H.O. Jacobs, G.M. Whitesides, Submicrometer patterning of charge in thin-film electrets. *Science* **291**(5509), 1763–1766 (2001)
5. A.K. Geim, S.V. Dubonos, I.V. Grigorieva, K.S. Novoselov, A.A. Zhukov, S.Y. Shapoval, Microfabricated adhesive mimicking gecko foot-hair. *Nat. Mater.* **2**(7), 461–463 (2003)

6. O. Lyutakov, J. Tuma, I. Huttel, V. Prajzler, J. Siegel, V. Svorcik, Polymer surface patterning by laser scanning. *Appl. Phys. B Lasers Opt.* **110**(4), 539–549 (2013)
7. C. Acikgoz, M.A. Hempenius, J. Huskens, G.J. Vancso, Polymers in conventional and alternative lithography for the fabrication of nanostructures. *Eur. Polym. J.* **47**(11), 2033–2052 (2011)
8. R.S. Kane, S. Takayama, E. Ostuni, D.E. Ingber, G.M. Whitesides, Patterning proteins and cells using soft lithography. *Biomaterials* **20**(23–24), 2363–2376 (1999)
9. Y.N. Xia, G.M. Whitesides, Soft lithography. *Annu. Rev. Mater. Sci.* **28**, 153–184 (1998)
10. E. Rebollar, J.R. Vazquez de Aldana, I. Martin-Fabiani, M. Hernandez, D.R. Rueda, T.A. Ezquerro, C. Domingo, P. Moreno, M. Castillejo, Assessment of femtosecond laser induced periodic surface structures on polymer films. *Phys. Chem. Chem. Phys.* **15**(27), 11287–11298 (2013)
11. B. Farshchian, S.M. Hurst, J. Lee, S. Park, 3D molding of hierarchical micro- and nanostructures. *J. Micromech. Microeng.* **21**(3) (2011)
12. G. Shi, N. Lu, H. Xu, Y. Wang, S. Shi, H. Li, Y. Li, L. Chi, Fabrication of hierarchical structures by unconventional two-step imprinting. *J. Colloid Interface Sci.* **368**, 655–659 (2012)
13. S. Yang, D.L. Devoe, Microfluidic device fabrication by thermoplastic hot-embossing. *Methods Mol. Biol.* **949**, 115–123 (2013)
14. M.T. Eliason, J.L. Charest, B.A. Simmons, A.J. Garcia, W.P. King, Nanoimprint fabrication of polymer cell substrates with combined microscale and nanoscale topography. *J. Vac. Sci. Technol. B* **25**(4), L31–L34 (2007)
15. T.E. Kimerling, W.D. Liu, B.H. Kim, D.G. Yao, Rapid hot embossing of polymer microfeatures. *Microsyst. Technol. Micro Nanosyst. -Inf. Storage Process. Syst.* **12**(8), 730–735 (2006)
16. H.S. Lee, T.H. Kwon, J.H. Kim, S.S. Chang, Replication of nanostructures on microstructures by intermediate film mold inserted hot embossing process. *Microsyst. Technol. Micro Nanosyst. -Inf. Storage Process. Syst.* **14**(8), 1149–1155 (2008)
17. C.Y. Kuan, J.M. Chou, I.C. Leu, M.H. Hon, Sol-gel-derived ZnO coating with Nanopatterns fabricated by nanoimprinting. *J. Am. Ceram. Soc.* **91**(10), 3160–3166 (2008)
18. H. Lan, H. Liu, UV-nanoimprint lithography: Structure, materials and fabrication of flexible molds. *J. Nanosci. Nanotechnol.* **13**(5), 3145–3172 (2013)
19. L.J. Guo, Nanoimprint lithography: Methods and material requirements. *Adv. Mater.* **19**(4), 495–513 (2007)
20. S.A. Ruiz, C.S. Chen, Microcontact printing: A tool to pattern. *Soft Matter* **3**(2), 168–177 (2007)
21. J. Rodríguez-Hernández, C. Drummond, *Polymer Surfaces in Motion: Unconventional Patterning Methods* (Springer, Cham, 2015)
22. S. Reich, Y. Cohen, Phase separation of polymer blends in thin films. *J. Polym. Sci. Polym. Phys* **19**(8), 1255–1267 (1981)
23. A.E. Nesterov, Y.S. Lipatov, V.V. Horichko, O.T. Gritsenko, Filler effects on the compatibility and phase separation kinetics of poly(vinyl acetate)-poly(methyl methacrylate) mixtures. *Polymer* **33**(3), 619–622 (1992)
24. R.C. Ball, R.L.H. Essery, Spinodal decomposition and pattern formation near surfaces. *J. Phys. Condens. Matter* **2**(51), 10303–10320 (1990)
25. R.A.L. Jones, L.J. Norton, E.J. Kramer, F.S. Bates, P. Wiltzius, Surface-directed spinodal decomposition. *Phys. Rev. Lett.* **66**(10), 1326–1329 (1991)
26. R. Xie, A. Karim, J.F. Douglas, C.C. Han, R.A. Weiss, Spinodal dewetting of thin polymer films. *Phys. Rev. Lett.* **81**(6), 1251–1254 (1998)
27. A.M. Higgins, R.A.L. Jones, Anisotropic spinodal dewetting as a route to self-assembly of patterned surfaces. *Nature* **404**(6777), 476–478 (2000)
28. P. Muller-Buschbaum, Dewetting and pattern formation in thin polymer films as investigated in real and reciprocal space. *J. Phys. Condens. Matter* **15**(36), R1549–R1582 (2003)
29. A. Karim, J.F. Douglas, B.P. Lee, S.C. Glotzer, J.A. Rogers, R.J. Jackman, E.J. Amis, G.M. Whitesides, Phase separation of ultrathin polymer-blend films on patterned substrates. *Phys. Rev. E Stat. Phys. Plasmas Fluids Relat. Interdiscip. Topics* **57**(6), R6273–R6276 (1998)
30. B.D. Ermi, G. Nisato, J.F. Douglas, J.A. Rogers, A. Karim, Coupling between phase separation and surface deformation modes in self-organizing polymer blend films. *Phys. Rev. Lett.* **81**(18), 3900–3903 (1998)
31. G. Nisato, B.D. Ermi, J.F. Douglas, A. Karim, Excitation of surface deformation modes of a phase-separating polymer blend on a patterned substrate. *Macromolecules* **32**(7), 2356–2364 (1999)

32. D. Petera, M. Muthukumar, Effect of patterned surface on diblock-copolymer melts and polymer blends near the critical point. *J. Chem. Phys.* **107**(22), 9640–9644 (1997)
33. J.-W. Park, Y.-H. Cho, Surface-induced morphologies in thin films of a rod-coil diblock copolymer. *Langmuir* **22**(26), 10898–10903 (2006)
34. E. Schaffer, S. Harkema, R. Blossey, U. Steiner, Temperature-gradient-induced instability in polymer films. *Europhys. Lett.* **60**(2), 255–261 (2002)
35. E. Schaffer, S. Harkema, M. Roerdink, R. Blossey, U. Steiner, Thermomechanical lithography: Pattern replication using a temperature gradient driven instability. *Adv. Mater.* **15**(6), 514–517 (2003)
36. P. Deshpande, L.F. Pease, L. Chen, S.Y. Chou, W.B. Russel, Cylindrically symmetric electrohydrodynamic patterning. *Phys. Rev. E* **70**(4) (2004)
37. L.F. Pease, W.B. Russel, Electrostatically induced submicron patterning of thin perfect and leaky dielectric films: A generalized linear stability analysis. *J. Chem. Phys.* **118**(8), 3790–3803 (2003)
38. L.F. Pease, W.B. Russel, Limitations on length scales for electrostatically induced submicrometer pillars and holes. *Langmuir* **20**(3), 795–804 (2004)
39. L.F. Pease, W.B.R. III, Charge driven, electrohydrodynamic patterning of thin films. *J. Chem. Phys.* **125**(18) (2006)
40. N. Wu, L.F. Pease, W.B.R. III, Toward large-scale alignment of electrohydrodynamic patterning of thin polymer films. *Adv. Funct. Mater.* **16**(15), 1992–1999 (2006)
41. S. Herminghaus, Dynamical instability of thin liquid films between conducting media. *Phys. Rev. Lett.* **83**(12), 2359–2361 (1999)
42. G. Turk, *Generating Textures on Arbitrary Surfaces Using Reaction-Diffusion* (1991)
43. T.A. Witten, L.M. Sander, Diffusion-limited aggregation. *Phys. Rev. B* **27**(9), 5686–5697 (1983)
44. J. Rodríguez-Hernández, Wrinkled interfaces: Taking advantage of surface instabilities to pattern polymer surfaces. *Prog. Polym. Sci.* **42**, 1–41 (2015)
45. A. Agrawal, J. Park, D.Y. Ryu, P.T. Hammond, T.P. Russell, G.H. McKinley, Controlling the location and spatial extent of nanobubbles using hydrophobically nanopatterned surfaces. *Nano Lett.* **5**(9), 1751–1756 (2005)
46. I. Siretanu, J.P. Chapel, C. Drummond, Water-ions induced Nanostructuring of hydrophobic polymer surfaces. *ACS Nano* **5**(4), 2939–2947 (2011)
47. P. Janda, O. Frank, Z. Bastl, M. Klementova, H. Tarabkova, L. Kavan, Nanobubble-assisted formation of carbon nanostructures on basal plane highly ordered pyrolytic graphite exposed to aqueous media. *Nanotechnology* **21**(9) (2010)
48. J. Aitkek, Breath figures. *Nature* **86**, 516–517 (1911)
49. J. Aitkek, Breath figures. *Nature* **90**, 619–621 (1912)
50. J.W. Giltay, Breath figures. *Nature* **86**, 585–586 (1911)
51. L. Rayleigh, Breath figures. *Nature* **86**, 416–417 (1911)
52. L. Rayleigh, Breath figures. *Nature* **90**, 436–438 (1912)
53. G. Lu, W. Li, J.M. Yao, G. Zhang, B. Yang, J.C. Shen, Fabricating ordered two-dimensional arrays of polymer rings with submicrometer-sized features on patterned self-assembled monolayers by dewetting. *Adv. Mater.* **14**(15), 1049 (2002)
54. M. Byun, W. Han, B. Li, X. Xin, Z. Lin, An unconventional route to hierarchically ordered block copolymers on a gradient patterned surface through controlled evaporative self-assembly. *Angew. Chem. Int. Ed.* **52**(4), 1122–1127 (2013)
55. K. Fukunaga, H. Elbs, R. Magerle, G. Krausch, Large-scale alignment of ABC block copolymer microdomains via solvent vapor treatment. *Macromolecules* **33**(3), 947–953 (2000)
56. E. Ibarboure, A. Bousquet, G. Toquer, E. Papon, J. Rodriguez-Hernandez, Tunable hierarchical assembly on polymer surfaces: Combining microphase and macrophase separation in copolymer/homopolymer blends. *Langmuir* **24**(13), 6391–6394 (2008)
57. M. Boltau, S. Walheim, J. Mlynek, G. Krausch, U. Steiner, Surface-induced structure formation of polymer blends on patterned substrates. *Nature* **391**(6670), 877–879 (1998)
58. E. Schaffer, T. Thurn-Albrecht, T.P. Russell, U. Steiner, Electrically induced structure formation and pattern transfer. *Nature* **403**(6772), 874–877 (2000)
59. H. Vandeparre, S. Gabriele, F. Brau, C. Gay, K.K. Parker, P. Damman, Hierarchical wrinkling patterns. *Soft Matter* **6**(22), 5751–5756 (2010)

60. M. Guvendiren, S. Yang, J.A. Burdick, Swelling-induced surface patterns in hydrogels with gradient crosslinking density. *Adv. Funct. Mater.* **19**(19), 3038–3045 (2009)
61. A. Muñoz-Bonilla, M. Fernández-García, J. Rodríguez-Hernández, Towards hierarchically ordered functional porous polymeric surfaces prepared by the breath figures approach. *Prog. Polym. Sci.* **39**(3), 510–514 (2014)
62. P. Escale, L. Rubatat, L. Billon, M. Save, Recent advances in honeycomb-structured porous polymer films prepared via breath figures. *Eur. Polym. J.* **48**(6), 1001–1025 (2012)
63. H. Tarabkova, P. Janda, Nanobubble assisted nanopatterning utilized for ex situ identification of surface nanobubbles. *J. Phys. Condens. Matter* **25**(18) (2013)
64. L.V. Govor, G. Reiter, G.H. Bauer, J. Parisi, Treelike branched structures formed in dewetting thin films of a binary solution. *Appl. Phys. Lett.* **89**(13) (2006)
65. A. Sharma, G. Reiter, Morphological phase transitions in spontaneous dewetting of thin films on homogeneous and heterogeneous surfaces. *Phase Transit.* **75**(4–5), 377–399 (2002)
66. G. Reiter, Unstable thin polymer-films - rupture and dewetting processes. *Langmuir* **9**(5), 1344–1351 (1993)
67. A. Sharma, G. Reiter, Instability of thin polymer films on coated substrates: Rupture, dewetting, and drop formation. *J. Colloid Interface Sci.* **178**(2), 383–399 (1996)
68. S. Harkema, E. Schaffer, M.D. Morariu, U. Steiner, Pattern replication by confined dewetting. *Langmuir* **19**(23), 9714–9718 (2003)
69. P. Muller-Buschbaum, E. Bauer, O. Wunnicke, M. Stamm, The control of thin film morphology by the interplay of dewetting, phase separation and microphase separation. *J. Phys. Condens. Matter* **17**(9), S363–S386 (2005)
70. R. Mukherjee, A. Sharma, U. Steiner, *Surface Instability and Pattern Formation in Thin Polymer Films, Generating Micro- and Nanopatterns on Polymeric Materials* (Wiley), pp. 217–265
71. R.D. Deegan, O. Bakajin, T.F. Dupont, G. Huber, S.R. Nagel, T.A. Witten, Capillary flow as the cause of ring stains from dried liquid drops. *Nature* **389**(6653), 827–829 (1997)
72. V. Nguyen, K. Stebe, Patterning of small particles by a surfactant-enhanced Marangoni-Bénard instability. *Phys. Rev. Lett.* **88**(16), 164501 (2002)
73. E. Pauliac-Vaujour, A. Stannard, C. Martin, M. Blunt, I. Nottingher, P. Moriarty, I. Vancea, U. Thiele, Fingering Instabilities in Dewetting Nanofluids. *Phys. Rev. Lett.* **100**(17), 176102 (2008)
74. G. Reiter, G. Castelein, P. Hoerner, G. Riess, A. Blumen, J.U. Sommer, Nanometer-scale surface patterns with long-range order created by crystallization of diblock copolymers. *Phys. Rev. Lett.* **83**(19), 3844–3847 (1999)
75. W. Koehler, A. Krekhov, W. Zimmermann, Thermal diffusion in polymer blends: Criticality and pattern formation, in: A.H.E. Muller, H.W. Schmidt (Eds.). *Complex Macromol. Syst* **12010**, 145–198
76. R.A. Farrell, T.G. Fitzgerald, D. Borah, J.D. Holmes, M.A. Morris, Chemical interactions and their role in the microphase separation of block copolymer thin films. *Int. J. Mol. Sci.* **10**(9), 3671–3712 (2009)
77. H.-C. Kim, W.D. Hinsberg, Surface patterns from block copolymer self-assembly. *J. Vac. Sci. Technol. A* **26**(6), 1369–1382 (2008)
78. J.-U. Sommer, G. Reiter, The formation of ordered polymer structures at interfaces: A few intriguing aspects, in *Ordered Polymeric Nanostructures at Surfaces*, ed. by G.J. Vancso, G. Reiter (Springer, Berlin, 2006), pp. 1–36
79. V. Abetz, P.F.W. Simon, Phase behaviour and morphologies of block copolymers, in *Block Copolymers I*, ed. by V. Abetz (Springer, Berlin, 2005), pp. 125–212
80. R.A. Segalman, Patterning with block copolymer thin films. *Mater. Sci. Eng. R. Rep.* **48**(6), 191–226 (2005)
81. L. Xue, J. Zhang, Y. Han, Phase separation induced ordered patterns in thin polymer blend films. *Prog. Polym. Sci.* **37**(4), 564–594 (2012)
82. A. Bousquet, G. Pannier, E. Ibarboure, E. Papon, J. Rodríguez-Hernández, Control of the surface properties in polymer blends. *J. Adhes.* **83**(4), 335–349 (2007)
83. A. Bousquet, E. Ibarboure, F.J. Teran, L. Ruiz, M.T. Garay, J.M. Laza, J.L. Vilas, E. Papon, J. Rodríguez-Hernández, PH responsive surfaces with nanoscale topography. *J. Polym. Sci. A Polym. Chem.* **48**(14), 2982–2990 (2010)

84. E. Bormashenko, S. Balter, R. Pogreb, Y. Bormashenko, O. Gendelman, D. Aurbach, On the mechanism of patterning in rapidly evaporated polymer solutions: Is temperature-gradient-driven Marangoni instability responsible for the large-scale patterning? *J. Colloid Interface Sci.* **343**(2), 602–607 (2010)
85. M. Dietzel, S.M. Troian, Mechanism for spontaneous growth of nanopillar arrays in ultrathin films subject to a thermal gradient. *J. Appl. Phys.* **108**(7) (2010)
86. D.W. Janes, J.M. Katzenstein, K. Shanmuganathan, C.J. Ellison, Directing convection to pattern thin polymer films. *J. Polym. Sci. B Polym. Phys.* **51**(7), 535–545 (2013)
87. A. Voit, A. Krehov, W. Enge, L. Kramer, W. Kohler, Thermal patterning of a critical polymer blend. *Phys. Rev. Lett.* **94**(21) (2005)
88. L. Weh, Surface structures in thin polymer layers caused by coupling of diffusion-controlled Marangoni instability and local horizontal temperature gradient. *Macromol. Mater. Eng.* **290**(10), 976–986 (2005)
89. J. Peng, H.F. Wang, B.Y. Li, Y.C. Han, Pattern formation in a confined polymer film induced by a temperature gradient. *Polymer* **45**(23), 8013–8017 (2004)
90. M. Nedelcu, M.D. Morariu, S. Harkema, N.E. Voicu, U. Steiner, Pattern formation by temperature-gradient driven film instabilities in laterally confined geometries. *Soft Matter* **1**(1), 62–65 (2005)
91. T. Nmabu, Y. Yamuachi, T. Kushiro, S. Sakurai, Micro-convection, dissipative structure and pattern formation in polymer blend solutions under temperature gradients. *Faraday Discuss.* **128**, 285–298 (2005)
92. R. Verma, A. Sharma, I. Banerjee, K. Kargupta, Spinodal instability and pattern formation in thin liquid films confined between two plates. *J. Colloid Interface Sci.* **296**(1), 220–232 (2006)
93. T.M. Paronyan, E.M. Pigos, G. Chen, A.R. Harutyunyan, Formation of ripples in graphene as a result of interfacial instabilities. *ACS Nano* **5**(12), 9619–9627 (2011)
94. J. Genzer, J. Groenewold, Soft matter with hard skin: From skin wrinkles to templating and material characterization. *Soft Matter* **2**(4), 310–323 (2006)
95. B. Li, Y.-P. Cao, X.-Q. Feng, H. Gao, Mechanics of morphological instabilities and surface wrinkling in soft materials: A review. *Soft Matter* **8**(21), 5728–5745 (2012)
96. A. Schweikart, A. Fery, Controlled wrinkling as a novel method for the fabrication of patterned surfaces. *Microchim. Acta* **165**(3–4), 249–263 (2009)
97. Y. Ebata, A.B. Croll, A.J. Crosby, Wrinkling and strain localizations in polymer thin films. *Soft Matter* **8**(35), 9086–9091 (2012)
98. C.S. Davis, A.J. Crosby, Wrinkle morphologies with two distinct wavelengths. *J. Polym. Sci. B Polym. Phys.* **50**(17), 1225–1232 (2012)
99. E.P. Chan, E.J. Smith, R.C. Hayward, A.J. Crosby, Surface wrinkles for smart adhesion. *Adv. Mater.* **20**(4), 711 (2008)
100. E.P. Chan, A.J. Crosby, Spontaneous formation of stable aligned wrinkling patterns. *Soft Matter* **2**(4), 324–328 (2006)
101. H.S. Kim, A.J. Crosby, Solvent-responsive surface via wrinkling instability. *Adv. Mater.* **23**(36), 4188 (2011)
102. C. Harrison, C.M. Stafford, W.H. Zhang, A. Karim, Sinusoidal phase grating created by a tunably buckled surface. *Appl. Phys. Lett.* **85**(18), 4016–4018 (2004)
103. A. Chiche, C.M. Stafford, J.T. Cabral, Complex micropatterning of periodic structures on elastomeric surfaces. *Soft Matter* **4**(12), 2360–2364 (2008)
104. J.-H. Lee, H.W. Ro, R. Huang, P. Lemailet, T.A. Germer, C.L. Soles, C.M. Stafford, Anisotropic, hierarchical surface patterns via surface wrinkling of Nanopatterned polymer films. *Nano Lett.* **12**(11), 5995–5999 (2012)
105. J.Y. Chung, J.P. Youngblood, C.M. Stafford, Anisotropic wetting on tunable micro-wrinkled surfaces. *Soft Matter* **3**(9), 1163–1169 (2007)
106. A.M. Turing, The chemical basis of morphogenesis. *Philos. Trans. R. Soc. Lond. B Biol. Sci.* **237**(641), 37–72 (1952)
107. Q. Ouyang, H.L. Swinney, Transition from a uniform STATE to hexagonal and striped turing patterns. *Nature* **352**(6336), 610–612 (1991)

108. D. Walgraef, Reaction-diffusion approach to nanostructure formation and texture evolution in adsorbed monoatomic layers. *Int. J. Quantum Chem.* **98**(2), 248–260 (2004)
109. H. Katsuragi, Diffusion-induced spontaneous pattern formation on gelation surfaces. *Europhys. Lett.* **73**(5), 793–799 (2006)
110. B. Bozzini, D. Lacitignola, I. Sgura, A reaction-diffusion model of spatial pattern formation in electrodeposition, in *Isnd 2007: Proceedings of the 2007 International Symposium on Nonlinear Dynamics*, Pts 1–42008, ed. by J. He
111. M. Hernandez-Guerrero, M.H. Stenzel, Honeycomb structured polymer films via breath figures. *Polym. Chem.* **3**(3), 563–577 (2012)
112. U.H.F. Bunz, Breath figures as a dynamic templating method for polymers and nanomaterials. *Adv. Mater.* **18**(8), 973–989 (2006)
113. L. Heng, B. Wang, M. Li, Y. Zhang, L. Jiang, Advances in fabrication materials of honeycomb structure films by the breath-figure method. *Materials* **6**(2), 460–482 (2013)
114. I. Siretanu, J.P. Chapel, C. Drummond, Substrate remote control of polymer film surface mobility. *Macromolecules* **45**(2), 1001–1005 (2012)
115. T.A.L. Burgo, T.R.D. Ducati, K.R. Francisco, K.J. Clinckspoor, F. Galembeck, S.E. Galembeck, Triboelectricity: Macroscopic charge patterns formed by self-arraying ions on polymer surfaces. *Langmuir* **28**(19), 7407–7416 (2012)
116. S. Darwich, K. Mougín, L. Vidal, E. Gnecco, H. Haidara, Nanobubble and nanodroplet template growth of particle nanorings versus nanoholes in drying nanofluids and polymer films. *Nanoscale* **3**(3), 1211–1217 (2011)
117. S. Budday, S. Andres, B. Walter, P. Steinmann, E. Kuhl, Wrinkling instabilities in soft bilayered systems. *Philos. Trans. R. Soc. A* **375**(2093), 20160163 (2017)
118. H. Burrell, High polymer theory of the wrinkle phenomenon. *Ind. Eng. Chem.* **46**(10), 2233–2237 (1954)
119. L. Auer, The development of the gas coagulation theory as an example of dry fatty oils. *Kolloid-Zeitschrift* **40**(4), 334–338 (1926)
120. A. Eibner, O. Merz, H. Munzert, Zur Kenntnis der chinesischen Holzöle, *Chemische Umschau auf dem Gebiet der Fette, Oele, Wachse und Harze* **31**(15–16) 69–82 (1924)
121. W.W. Bauer, Some developments in controlling China wood oil varnishes. *Ind. Eng. Chem.* **18**, 1249–1251 (1926)
122. J. Hyman, T. Greenfield, Cause of “crystallization” of Tung oil vehicles. *Ind. Eng. Chem.* **28**, 238–241 (1936)
123. J. Marcusson, Die Polymerisation fetter Öle. Fünfte Mitteilung. *Angew. Chem.* **39**(15), 476–479 (1926)
124. H. Dannenberg, J.K. Wagers, T.F. Bradley, Frosting and gas-checking of conjugated drying oils. *Ind. Eng. Chem.* **42**(8), 1594–1599 (1950)
125. S. Yang, K. Khare, P.C. Lin, Harnessing surface wrinkle patterns in soft matter. *Adv. Funct. Mater.* **20**(16), 2550–2564 (2010)
126. J. Groenewold, Wrinkling of plates coupled with soft elastic media. *Physica A* **298**(1–2), 32–45 (2001)
127. E. Cerda, K. Ravi-Chandar, L. Mahadevan, Thin films – Wrinkling of an elastic sheet under tension. *Nature* **419**(6907), 579–580 (2002)
128. E. Cerda, L. Mahadevan, Geometry and physics of wrinkling. *Phys. Rev. Lett.* **90**(7) (2003)
129. N. Uchida, Orientational order in buckling elastic membranes. *Physica D Nonlinear Phenomena* **205**(1–4), 267–274 (2005)
130. C.-M. Chen, S. Yang, Wrinkling instabilities in polymer films and their applications. *Polym. Int.* **61**(7), 1041–1047 (2012)
131. S. McCormick, Materials science – Exploiting wrinkle formation. *Science* **317**(5838), 605–606 (2007)
132. F. Weiss, S. Cai, Y. Hu, M.K. Kang, R. Huang, Z. Suo, Creases and wrinkles on the surface of a swollen gel. *J. Appl. Phys.* **114**(7) (2013)
133. S. Cai, D. Chen, Z. Suo, R.C. Hayward, Creasing instability of elastomer films. *Soft Matter* **8**(5), 1301–1304 (2012)

134. S.S. Velankar, V. Lai, R.A. Vaia, Swelling-induced delamination causes folding of surface-tethered polymer gels. *ACS Appl. Mater. Interfaces* **4**(1), 24–29 (2012)
135. T. Bahners, L. Prager, S. Kriehn, J.S. Gutmann, Super-hydrophilic surfaces by photo-induced micro-folding. *Appl. Surf. Sci.* **259**, 847–852 (2012)
136. Y.-P. Cao, B. Li, X.-Q. Feng, Surface wrinkling and folding of core-shell soft cylinders. *Soft Matter* **8**(2), 556–562 (2012)
137. R. Schubert, T. Scherzer, M. Hinkefuss, B. Marquardt, J. Vogel, M.R. Buchmeiser, VUV-induced micro-folding of acrylate-based coatings. 1. Real-time methods for the determination of the micro-folding kinetics. *Surf. Coat. Technol.* **203**(13), 1844–1849 (2009)
138. D.P. Holmes, A.J. Crosby, Draping films: A wrinkle to fold Transition. *Phys. Rev. Lett.* **105**(3) (2010)
139. K. Efimenko, J. Finlay, M.E. Callow, J.A. Callow, J. Genzer, Development and testing of hierarchically wrinkled coatings for marine antifouling. *ACS Appl. Mater. Interfaces* **1**(5), 1031–1040 (2009)
140. H.S. Kim, A.J. Crosby, Solvent-responsive surface via wrinkling instability. *Adv. Mater.* **23**(36), 4188–4192 (2011)
141. C.M. Stafford, C. Harrison, K.L. Beers, A. Karim, E.J. Amis, M.R. VanLandingham, H.-C. Kim, W. Volksen, R.D. Miller, E.E. Simonyi, A buckling-based metrology for measuring the elastic moduli of polymeric thin films. *Nat. Mater.* **3**(8), 545 (2004)
142. J.Y. Chung, J.-H. Lee, K.L. Beers, C.M. Stafford, Stiffness, strength, and ductility of nanoscale thin films and membranes: A combined wrinkling–cracking methodology. *Nano Lett.* **11**(8), 3361–3365 (2011)
143. J.A. Howarter, C.M. Stafford, Instabilities as a measurement tool for soft materials. *Soft Matter* **6**(22), 5661–5666 (2010)
144. E.P. Chan, A.J. Crosby, Fabricating microlens arrays by surface wrinkling. *Adv. Mater.* **18**(24), 3238–3242 (2006)
145. P.-C. Lin, S. Yang, Mechanically switchable wetting on wrinkled elastomers with dual-scale roughness. *Soft Matter* **5**(5), 1011–1018 (2009)
146. T. Ohzono, H. Monobe, Morphological transformation of a liquid micropattern on dynamically tunable microwrinkles. *Langmuir* **26**(9), 6127–6132 (2010)
147. D.-Y. Khang, H. Jiang, Y. Huang, J.A. Rogers, A stretchable form of single-crystal silicon for high-performance electronics on rubber substrates. *Science* **311**(5758), 208–212 (2006)
148. D.-H. Kim, J.-H. Ahn, W.M. Choi, H.-S. Kim, T.-H. Kim, J. Song, Y.Y. Huang, Z. Liu, C. Lu, J.A. Rogers, Stretchable and foldable silicon integrated circuits. *Science* **320**(5875), 507–511 (2008)
149. W.H. Koo, S.M. Jeong, F. Araoka, K. Ishikawa, S. Nishimura, T. Toyooka, H. Takezoe, Light extraction from organic light-emitting diodes enhanced by spontaneously formed buckles. *Nat. Photonics* **4**(4), 222 (2010)
150. S.G. Lee, D.Y. Lee, H.S. Lim, D.H. Lee, S. Lee, K. Cho, Switchable transparency and wetting of elastomeric smart windows. *Adv. Mater.* **22**(44), 5013–5017 (2010)
151. E.P. Chan, E.J. Smith, R.C. Hayward, A.J. Crosby, Surface wrinkles for smart adhesion. *Adv. Mater.* **20**(4), 711–716 (2008)
152. X. Jiang, S. Takayama, X. Qian, E. Ostuni, H. Wu, N. Bowden, P. LeDuc, D.E. Ingber, G.M. Whitesides, Controlling mammalian cell spreading and cytoskeletal arrangement with conveniently fabricated continuous wavy features on poly (dimethylsiloxane). *Langmuir* **18**(8), 3273–3280 (2002)
153. M.T. Lam, S. Sim, X. Zhu, S. Takayama, The effect of continuous wavy micropatterns on silicone substrates on the alignment of skeletal muscle myoblasts and myotubes. *Biomaterials* **27**(24), 4340–4347 (2006)
154. K. Efimenko, M. Rackaitis, E. Manias, A. Vaziri, L. Mahadevan, J. Genzer, Nested self-similar wrinkling patterns in skins. *Nat. Mater.* **4**(4), 293 (2005)
155. Dynamics of surface memory effect in liquid crystal alignment on reconfigurable microwrinkles. *Appl. Phys. Lett.* **95**(1), 014101 (2009)

# Chapter 2

## Strategies for the Fabrication of Wrinkled Polymer Surfaces



C. M. González-Henríquez, M. A. Sarabia Vallejos,  
and Juan Rodríguez-Hernández

### 2.1 Introduction

A large amount of work has been carried out in the fabrication of different surface patterns based on surface instabilities. In particular, the wrinkled formation is one of the most extensively explored strategies to produce surface micro- and submicrometer scale structures. In order to organize the extensive literature reported in this area, we propose the classification of the different strategies first taking into account the film structure distinguishing three different situations: layered films, gradient, and homogeneous. Thus, this chapter is organized as follows. First, we will briefly describe the possible film structures to produce wrinkled structures. Second, we will, as a function of the film structure, discuss the different methodologies and the stimuli employed to induce buckling and thus produce wrinkled surface morphologies.

---

C. M. González-Henríquez

Departamento de Química, Facultad de Ciencias Naturales, Matemáticas y del Medio Ambiente, Universidad Tecnológica Metropolitana, Santiago, Chile

Programa Institucional de Fomento a la Investigación, Desarrollo e Innovación, Universidad Tecnológica Metropolitana, San Joaquín, Santiago, Chile

M. A. Sarabia Vallejos

Escuela de Ingeniería, Departamento de Ingeniería Estructural y Geotecnia, Pontificia Universidad Católica de Chile, Santiago, Chile

Instituto de Ingeniería Biológica y Médica, Santiago, Chile

J. Rodríguez-Hernández (✉)

Departamento de Química Macromolecular Aplicada, Polymer Functionalization Group, Instituto de Ciencia y Tecnología de Polímeros-Consejo Superior de Investigaciones Científicas (ICTP-CSIC), Madrid, Spain

e-mail: [jrodriguez@ictp.csic.es](mailto:jrodriguez@ictp.csic.es)

### 2.1.1 Films Structures of Wrinkled Surfaces

Wrinkle formation of polymer surfaces can be obtained using a large variety of different strategies [1–6] that can, otherwise, be divided and organized into three categories as a function of the structure of the precursor film. We can thus distinguish between (1) films formed by distinct layers (two or more), (2) homogeneous films, and (3) depth-wise gradient films formed by a gradual variation of the chemical/physical/mechanical properties from the surface to the bulk (Fig. 2.1).

Inside of each family, we will, in turn, subdivide into different groups taking into account the stimulus employed to induce wrinkle formation.

## 2.2 Layered Systems Composed of Layers with Dissimilar Mechanical Properties

Layered films are formed by two or more polymer or hybrid polymer/metal layers with, unlike mechanical properties. In order to describe the alternatives to obtain wrinkles from layered films, we will first describe the materials typically employed as substrates and as top layers including the methodologies used to achieve a rigid layer on the top of an elastic foundation. Then, we will classify the approaches reported to produce surface wrinkles based on the type of force applied to modify the form of the elastic foundation inducing the buckling of the rigid top layer.

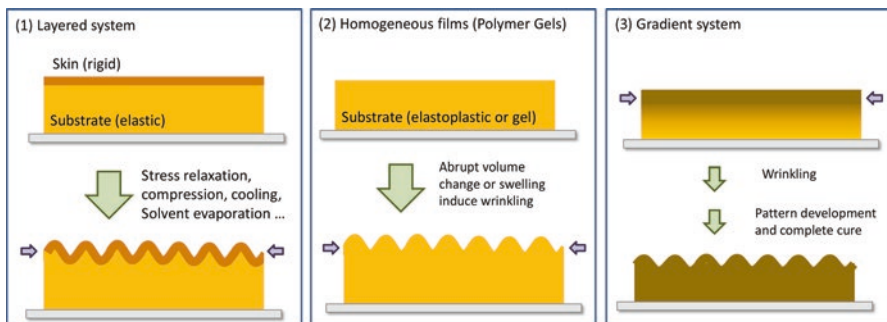


**Fig. 2.1** Film structures capable of forming wrinkles: (1) Layered film structure composed of an elastic substrate and a rigid skin. (2) homogeneous films (typically homogeneously cross-linked hydrogels), and (3) gradient film with variable mechanical properties as a function of the depth. (Reproduced with permission from ref. [7])

## 2.2.1 Bilayered Systems: Structure and Materials

### 2.2.1.1 Types of Substrates in Bilayered Systems

Whereas initial works have been mainly focused on the use of elastic substrates, typically PDMS, in view of enlarging the potential applications of wrinkled surfaces, other substrates have been equally proposed to produce wrinkled patterned structures. As a result, the substrate or film can be:

#### (a) Liquid substrates

Huang et al. [8] employed circular pieces of PS film detached from the substrate supported on deionized water. Later Vella [9] used the same system to explain the origin of the wrinkling of such membranes observed by Holmes et al. [10] employed a thin polymer film, either polydimethylsiloxane (PDMS) or polystyrene (PS), which is prepared via spin coating a polymer solution onto a clean silicon wafer. A circular film of radius  $L = 17.5$  mm is floated off the wafer onto the surface of the water. As depicted in Fig. 2.2, they found that the wrinkle wavelength is dictated by a balance of material properties and geometry, most directly the thickness of the

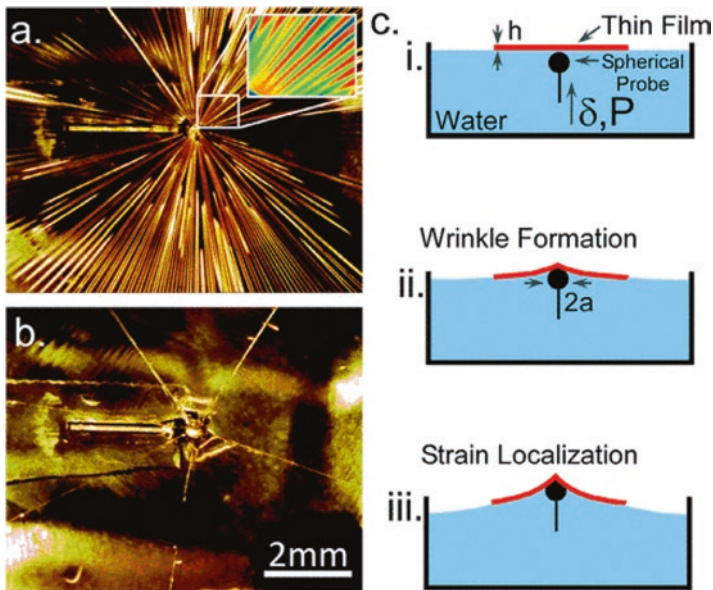


**Fig. 2.2** (a) Wrinkles on a thin film floating on water lifted by a spherical probe (inset: image via optical profilometry). (b) As the vertical displacement of the probe increases, the wrinkles localize into sharp folds. (c) Schematic of the experimental setup, where (i) depicts the axisymmetric thin film floating on water, (ii) the formation of wrinkles as the probe displaces the film vertically, and (iii) the critical displacement at which wrinkles collapse into folds. (Reproduced with permission from ref. [10])

draping film. At a critical strain, the stress in the film will localize, causing hundreds of wrinkles to collapse into several discrete folds.

Finally, another interesting example was reported by Pocivavsek et al. [11]. They employed a polyester of the top or either Millipore water or a soft gel. They explore the wrinkle formation and also the morphological transitions and found that a wrinkle-to-fold transition (Fig. 2.3A) takes place when the polyester sheet is lying on top of the water. However, the liquid substrate is not required for the transition to occur since (Fig. 2.3B) a similar evolution of the surface was observed with the polyester adhered to a soft gel. Moreover, smooth wrinkling (a in Fig. 2.3B) develops

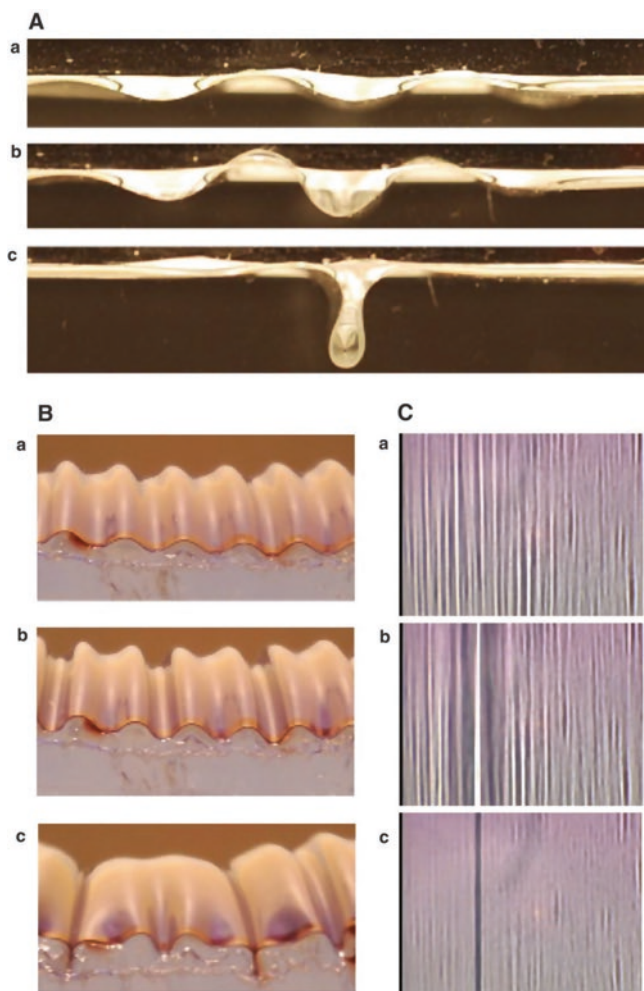


**Fig. 2.3** (A) Polyester film on water, (B) polyester film on gel substrate, and (C) trilayer of colloidal gold nanoparticles on water. (Reproduced with permission from ref. [11])

to unstable (b in Fig. 2.3B) and can potentially produce several folds relaxing the rest of the surface (c in Fig. 2.3B).

(b) *Viscous liquids as substrates*

Pioneer theoretical studies compared to experimental data about wrinkle formation on viscous liquids were carried out by Suo et al. [12, 13]. According to Suo et al., compressively stressed elastic films on finite-thickness viscous substrates may experience a buckling instability and, as a result, release stresses that may finally alter the planarity of the film. They carried out a linear stability analysis to assess the onset and maximally unstable mode of this buckling instability as a function of three main parameters, i.e., the thickness of the viscous layer, misfit strain, and viscosity. They found that the onset of the buckling instability of the film on a glass layer is the same as that retrieved in a compressively stressed free-standing film. However, the maximally unstable wavelength increases as the glass layer thickness increases.

More recently, Huang and coworkers [14] explored the buckling occurring on thin elastic films floating on a viscous liquid layer, in turn, supported on a pre-stretched rubber sheet (Fig. 2.4). Upon release of the stretching applied in the rubber, a viscous stress is induced in the liquid which, according to Huang et al., produced, in turn, a compressive stress in the elastic film and finally produced the buckling of the film. In contrast to previous studies on the wrinkling of floating films, the authors evidenced that the buckling process was dominated by viscous effects, whereas gravitational effects are negligible. The experimental work carried out using elastic polymer films and viscous polymer liquids evidenced trends that are qualitatively consistent with the predictions calculated using theoretical approaches. However, quantitatively, the experimentally measured wrinkle wavelengths were larger than predicted by the models.

(c) *Viscoelastic substrates*

Viscoelastic substrates and, in particular, polymers are probably the most explored type of substrates to produce surface wrinkling. Using these substrates, previous theoretical [15–17] and experimental [18–21] studies evidenced that under isothermal conditions, the time evolution of both the wrinkle amplitude and wavelength is directly connected to the viscoelastic response of the polymer film at the

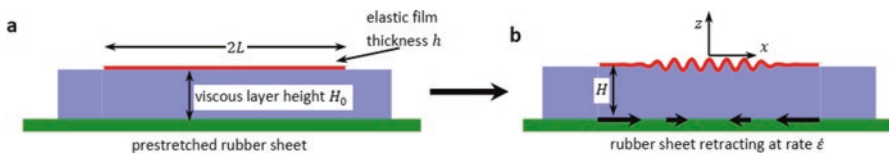


**Fig. 2.4** (a) Initially flat film floating on a fluid layer, covering a pre-stretched rubber sheet. (b) Film wrinkles when the rubber sheet is unstretched at a controlled rate. (Reproduced with permission from ref. [14])

annealing temperature. The annealing temperatures employed are typically near or slightly above the glass transition temperature of the polymer.

Chan et al. [22] employed the thermal-induced surface wrinkling to determine both the rubbery modulus and shear viscosity of polystyrene (PS) film depending on the annealing temperature. For this purpose, as depicted in Fig. 2.5, the authors employed surface laser-light scattering (SLS) to determine the wrinkled surface in real time. They monitored the changes in surface morphology as a function of annealing time at fixed annealing temperatures. Finally, the results obtained were compared to theoretical models that permitted the calculation of the viscoelastic properties of the PS thin film.

Im and Huang [16] reported a theoretical model to explain the wrinkle evolution in a bilayer thin film consisting of an elastic layer and a viscoelastic layer. They employed a thin-layer approximation for the viscoelastic layer. Moreover, the elastic layer subjected to a compressive residual stress was modeled by the nonlinear von Karman plate theory. The authors reported three stages of the wrinkle evolution and are identified as follows: the initial growth of the fastest-growing mode, intermediate growth with mode transition, and, finally, an equilibrium wrinkle state.

Finally, another illustrative example was reported by Hoo et al. [23]. As depicted in Fig. 2.6, they described the evolution of the wrinkle morphologies in a thin bilayer film of an elastic metal on a viscoelastic polymer. As explained by Hoo et al., a transition of initial island-like patterns (annealing time of several minutes) to a wrinkled structure occurs without a change in the wavelength. Moreover, the initially wrinkled structure is transformed into a mountainous topography in the late

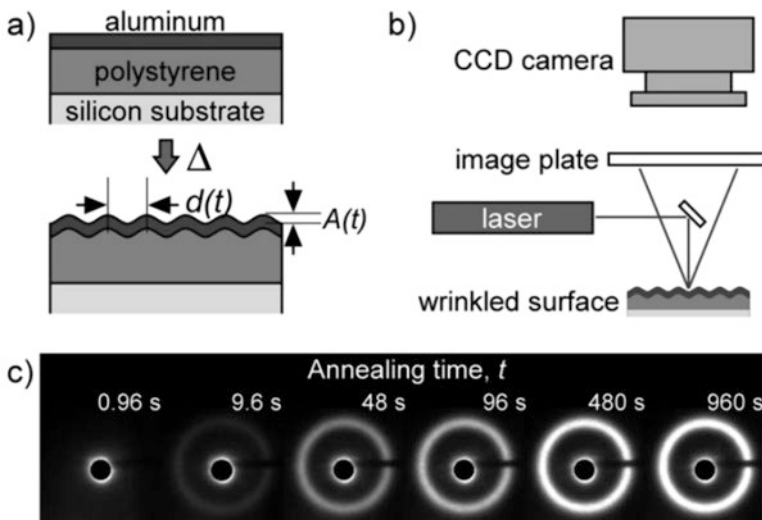


**Fig. 2.5** (a) Schematic of thermal wrinkling approach to measuring the rubbery modulus and viscosity of a confined PS thin film. (b) Schematic of the SLS experimental setup. (c) Representative time-evolved scattering patterning as captured by the SLS at 125 °C. (Reproduced with permission from ref. [22])

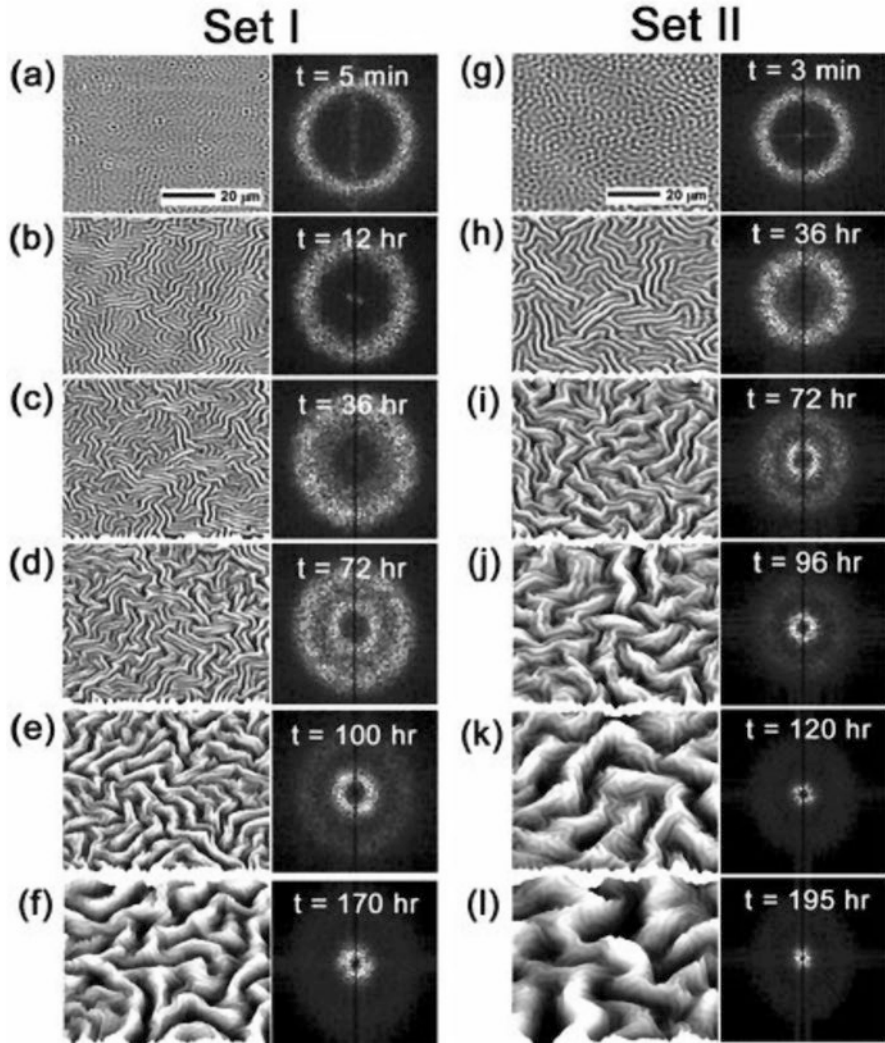


**Fig. 2.6** AFM images of the temporal evolution of stress-driven surface wavy patterns. Set I (a)–(f) is for smaller waves that result in a thin metal layer (40 nm) and a relatively thin polymer layer (350 nm), and set II (g)–(l) is for larger waves that result when the polymer layer is made thicker (580 nm). (a) Set I data after 3 min. (b) Set I data after 12 h. (c) Set I data after 36 h. (d) Set I data after 72 h. (e) Set I data after 100 h. (f) Set I data after 170 h. (g) Set II data after 3 min. (h) Set II data after 36 h. (i) Set II data after 72 h. (j) Set II data after 96 h. (k) Set II data after 120 h. (l) Set II data after 195 h. (Reproduced with permission from ref. [23])

stages that goes along with an increase in the length scale. This change in the wrinkle wavelength can be associated with the relaxation of the confined polymer that results in a transition from elastic- to viscous-like behavior, induces wave coarsening and macroscopic roughening [23].

(d) *Substrates capable of yielding or softening upon increasing temperature*

Examples of the use of substrates capable of yielding or softening are scarce neither from a theoretical nor from an experimental point of view. One of few examples was reported by Srinivasan et al. [24] who presented a theoretical analysis of the wrinkling processes where irreversible deformation occurs in the foundation. The proposed method was applicable to the analysis of foundations with elastic-damage response and to foundations with an elastoplastic response.

Another interesting example was recently reported by El Haitami et al. [25]. As depicted in Fig. 2.7, the bilayer model comprises a rubber chemically modified at the surface (micrometric depth) to increase the glass transition temperature above room temperature. To produce the surface wrinkles, the authors took advantage of the very slow glassy dynamics of the modified layer. The methodology employed to induce wrinkle formation is based on the difference in the glass transition temperature between the unmodified rubber  $T_{g,R}$  and that of the modified layer  $T_{g,layer}$  in which the system consists of a glassy layer on top of a rubber substrate. As a result, when the system is heated to above  $T_{g,layer}$  (step 1), the system is completely rubbery and can be easily stretched (step 2). In this situation, the modified layer can be

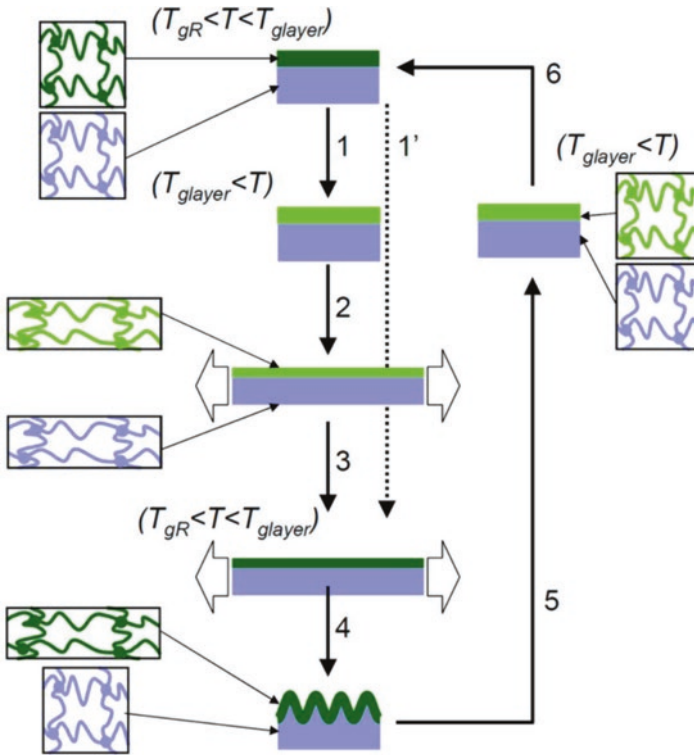


**Fig. 2.7** Schematic representation of the proposed wrinkling-unwrinkling approach. (Reproduced with permission from ref. [25])

frozen upon cooling between  $T_{g,R}$  and  $T_{g,layer}$  maintaining the deformation (step 3). Allowing the unmodified rubber substrate to recover elastically, stable wrinkles were produced (step 4). More interestingly, the wrinkles formed and stable at temperatures below the  $T_{g,layer}$  can be erased by heating the system again to above  $T_{g,layer}$  (step 5). Since no stretching is applied, the deformed network returns to thermodynamic equilibrium (step 6).

### 2.2.1.2 Top Layers

The different strategies proposed to obtain a rigid top layer can be grouped into two main approaches. On the one hand, either the substrate is exposed to physical or chemical treatments that change the surface mechanical properties of the substrate (i.e., oxidation of PDMS to produce rigid silica) or the substrate is coated with a rigid film coating (polymeric or metallic).

#### (a) *Formation of a rigid surface by surface treatments*

A stiff top layer has been achieved, for instance, by *direct oxidation* (UV-ozone or plasma treatments) of the polymer film using an elastic foundation such as PDMS [26–30]. Depending on the oxidation method and also the experimental conditions employed, nano- or microwrinkled surface structures have been obtained (from 150 nm to several hundreds of microns). However, the chemical composition is limited to particular oxides resulting in surface treatments. In addition, the different mechanical resistance of the layer deposited in comparison to the bulk may also introduce additional limitations in the lifetime of the wrinkles since folding and finally cracking can be observed on the surface formed.

Alternative surface treatments include the *reactive ion etching* that using fluorinated gases has been employed to treat polystyrene (PS). This approach permits upon heating the fabrication of wrinkles with precise wavelengths from micrometer down to few nanometers [31]. Finally, it is worth mentioning that *ultraviolet light* [32, 33] or *ion beam* [34] treatments of a pre-stretched substrate can also be employed to increase the stiffness of the skin layer.

#### (b) *Formation of a rigid top layer by metallic or polymeric thin film deposition*

The second group of strategies to create a bilayer system with layers having different mechanical properties involves the surface coating with a polymeric or even metallic thin layer. This coating is carried out either upon during thermal expansion or mechanical stretching/compression [35, 36]. Pioneer reports by Bowden et al. and Yoo et al. used the evaporation of aluminum that forms the rigid layer on a flexible substrate [35, 37–40]. For instance, the metal can be deposited on the thermally expanded PDMS layer (high temperature) that, upon cooling, will contract and generate a large stress that finally produced the surface wrinkles in the metallic layer. Other works carried out by Fu et al. and Vandeparre et al. resort to different metals such as gold [28] or titanium [41], respectively.

Not only metals but also polymers have been deposited as thin films on top of a substrate to form the bilayer skin or just employed to form the foundation. As has been already mentioned, it is crucial that the polymer employed has a clear difference in stiffness in comparison with the second component of the bilayer system. The most extended alternative involves the deposition of the film by transferring the polymeric films prepared on silicon wafers onto either a compressed or a pre-strained support or by spin coating [42]. Polymers employed for the fabrication of these bilayered structures include homopolymers, such as polystyrene [43] and polypyrrole [44]; more recently, other systems including the fabrication of plastic-rubber composites [45] or the elaboration of bilayers comprising a fluoropolymer ( $CF_x$ ) skin layer deposited on PDMS [46] soft skin have been equally reported.

Some authors substituted the polymer thin layer by polyelectrolyte multilayers (PEM) usually obtained by the layer-by-layer (LbL) methodology. LbL is carried out by alternating the deposition of positively and negatively charged polyelectrolytes from aqueous solution. This strategy allowed simultaneously to fabricate thin films with controlled composition and thickness [47–50]. For instance, an illustrative example was carried out by Lu et al. that reported the preparation of different multilayer films and found that poly(allylamine hydrochloride)–poly(sodium 4-styrene sulfonate) (PAH–PSS) formed particularly stable wrinkled multilayer films [51].

### 2.3 Classification of the Wrinkling Mechanisms as a Function of the Stimulus Employed to Induce Surface Buckling

As has been already anticipated in the previous section, wrinkling is usually achieved upon relaxation of a particular stress previously applied. While this is true, the nature of the stress applied to the foundation prior to surface modification can be significantly different:

#### (a) *Wrinkle formation in response to thermal variations.*

The principle of wrinkle formation due to thermal variations relies on the different expansion coefficients between the top layer and the foundation. More precisely, wrinkles are spontaneously formed due when the stress applied (created either upon heating or cooling) exceeds a critical value particular for each system as a result of the mismatch of thermal expansion coefficient between the substrate and the capping layer. During heating of the substrate, expansion occurs. In an expanded state, either the substrate is treated by using a physical process [22] or polymer/metal is deposited onto the substrate [35, 52]. Finally, upon cooling of the bilayered system, a compressive stress is created in the stiff surface layer that provokes the surface buckling and finally forms wrinkles that remain unaffected when the sample is cooled down [53]. Alternatively, other authors reported the wrinkle formation upon

heating. Illustrative examples of the latter have been reported by Bowden that reported the formation of wrinkled surfaces upon heating using bilayers composed of Al/polystyrene (PS) [26] or the system reported by Huntington based on polystyrene and treated with reactive ion etching [31].

While temperature is a key variable, there are many other variables that can affect the wrinkling such as experimental heating conditions and time, the molecular weight of the polymer, polymer film thickness, or even the cross-linking level of the polymer employed. For instance, in the same work, Yoo and Lee [21] explored the temporal evolution of an elastic wrinkling known as spinodal wrinkling (Fig. 2.8). The authors used a thick film (300–600 nm) of high molecular weight PS as substrate and an Al film (30–60 nm) as the top layer. The wrinkles were produced at 140 °C, which is around 25 °C higher than  $T_g$  of the PS. Two distinct transitions in the evolution of the wrinkling morphology can be observed in Fig. 2.8. On the one hand, the transition from an island-like pattern to a labyrinthine pattern is apparent in going from Fig. 2.8a–e. On the other hand, the second transition occurs at longer annealing times and is evidenced by the appearance of a second wave (Fig. 2.8f–h).

More interestingly, the same authors were able to present the different wrinkling regimes. The defined three types of wrinkling were defined by the thermomechanical behavior of the polymer, by strain saturation and bilayer pinning. The morphological diagram as a function of the molecular weight of the polymer employed, the film thickness as well as the processing temperature is depicted in Fig. 2.9. When a high molecular weight is employed (Fig. 2.9a), a remembered elastic response of polymer observed even above the glass transition temperature delivers an elastic contribution in the course of the wrinkle formation. This finally leads to various

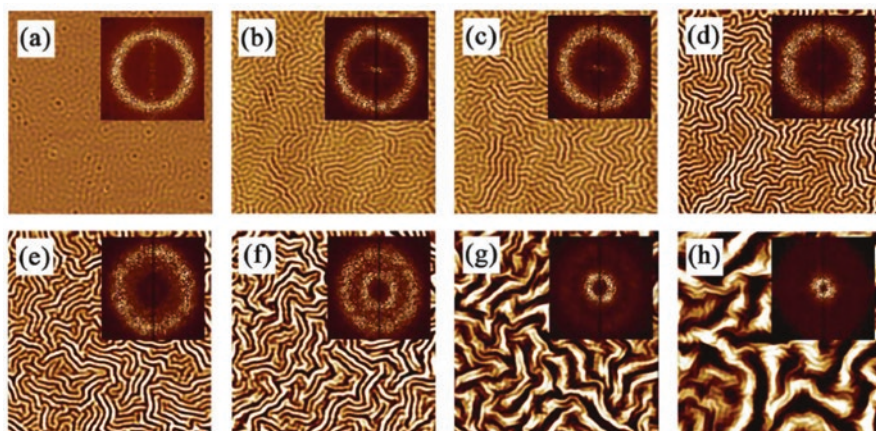


**Fig. 2.8** AFM images ( $80\ \mu\text{m} \times 80\ \mu\text{m}$ ) of the temporal evolution of wrinkled surfaces (40-nm-thick metal layer/350-nm-thick high molecular weight polymer layer/annealing at 140 °C). The insets depict the fast Fourier transform (FFT) images for given patterns: (a) after 3 min; (b) after 20 min; (c) after 3 h; (d) after 12 h; (e) after 36 h; (f) after 72 h; (g) after 100 h; (h) after 170 h. (Reproduced with permission from ref. [21])

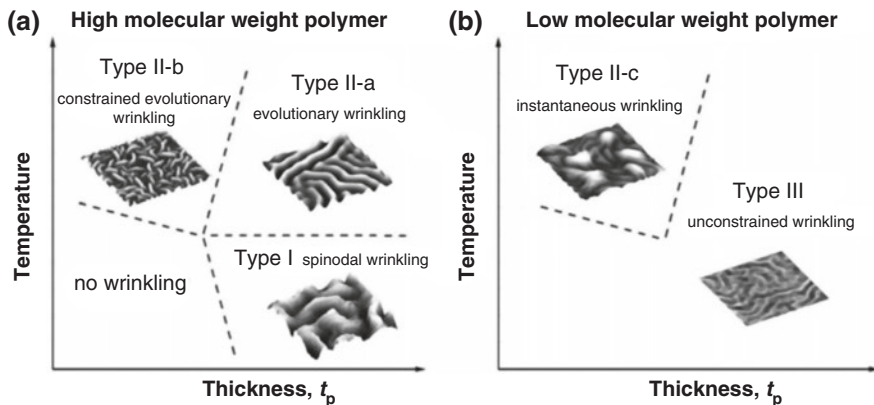


**Fig. 2.9** Illustrative wrinkled morphologies observed for the bilayer films as a function of the thickness and annealing temperature. Typical evolutionary characteristics are determined by elastic wrinkling (type I) or viscous wrinkling (types II and III). Insets are three-dimensional AFM images for the final morphology of each wrinkling regime. (a) High molecular weight polymer layer. (b) Low molecular weight polymer layer. (Reproduced with permission from ref. [21])

wrinkling morphologies. In the case of low molecular weight (Fig. 2.9b) polymers, the polymer substrate displays an entirely viscous behavior. This finally favors lower frequency mode and finally approaches an infinite wavelength wrinkle.

Thermal wrinkling on polymer/metal bilayer systems supported on a rigid substrate usually leads to random wrinkles on the surface caused by the compressive stress resulting from thermal annealing (Fig. 2.10a). However, the use of microstructured molds can modify the random organization and produce anisotropic wrinkling [20, 38, 54]. In order to induce the physical confinement effect, Yoo et al. [54, 55] employed a patterned polydimethylsiloxane (PDMS) mold which was placed on top of the metal/polymer bilayer surface prior to heating as depicted in Fig. 2.10. PDMS creates a solid conformal contact with the underlying metal surface, which provokes, in turn, that the edges of the line-and-space pattern act as nodes. As shown in Fig. 2.10b, the selected mold patterns are periodic squares with variable size and period. Interestingly, the resulting self-organized surface structure varied from a simple checkerboard to a more complicated pattern as the pattern period increased from 3 to 10  $\mu\text{m}$ . According to the authors, this is the result of the interactions of the wave generated in the wrinkles with the mold pattern wave or the pattern periodicity.

A similar concept was employed by Kwon et al. [38]. This group reported the preparation of a microstructured polystyrene (PS) layer fabricated by spin coating on a cleaned silicon substrate and then applying capillary force lithography. Thin aluminum films were deposited onto the microstructured PS layer. Finally, upon isothermal annealing, wrinkled structured were produced.

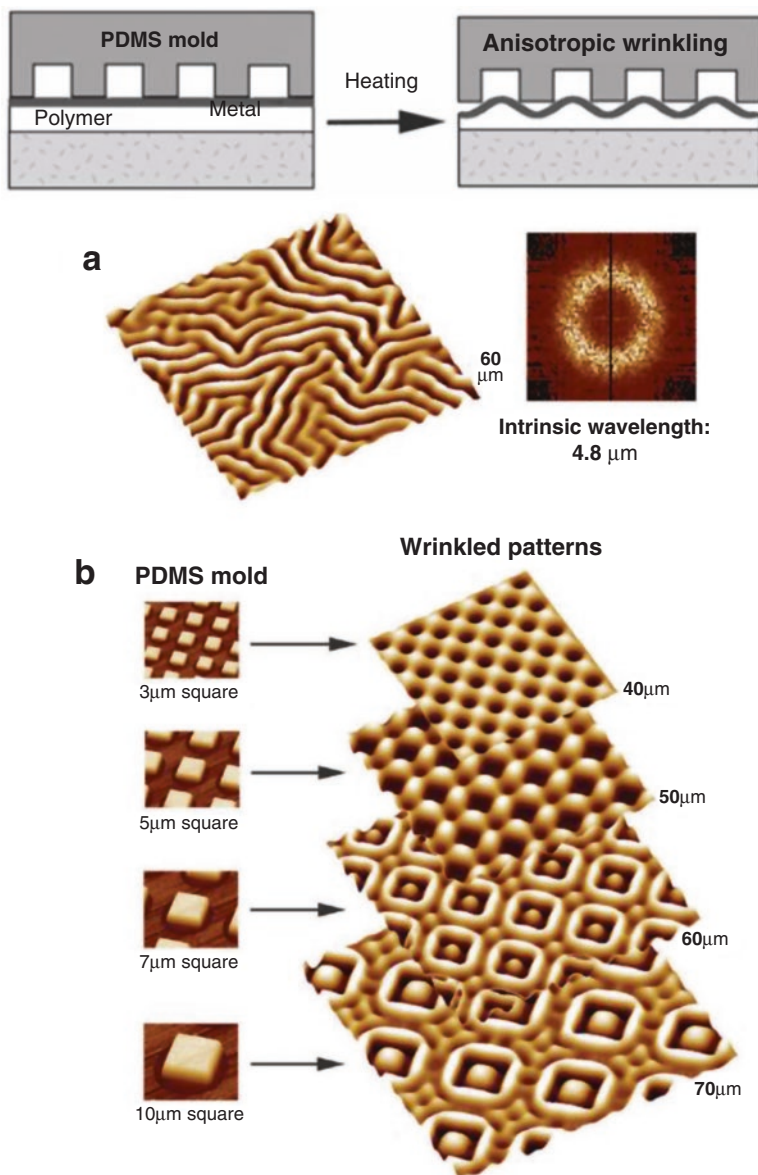


**Fig. 2.10** Top: Schematic diagram of the procedure involved in the self-organized anisotropic wrinkling. Down: (a) AFM micrographs of the isotropic wrinkles that result from the bilayer consisting of an 80-nm-thick metal layer ( $t_m$ ) and a 600-nm-thick polymer layer ( $t_p$ ). (b) AFM micrographs of self-organized wrinkle structures obtained through confinement-induced anisotropic wrinkling over the surface used in part a: (top to bottom) checkerboard pattern (3 μm period of the rectangular mold pattern), woven fabric array pattern (5 μm period), encircled dot array pattern (7 μm period), and encircled dot array separated by a tetrapod pattern (10 μm period). (Reproduced with permission from refs. [54, 55])

(b) *Wrinkles formed by mechanical stretching/compression.*

Wrinkles can be also produced by taking advantage of the elastic mechanical properties of a polymer substrate. In general, the strategy involves a uniaxial strain followed by film deposition. Finally, upon stress relaxation, wrinkles are formed at the surface of the elastic foundation. The out-of-plane deformation and thus the formation of the surface wrinkles is the direct consequence of the disparity in Young's modulus between the rigid top layer ( $E \sim \text{GPa}$ ) and the polymeric substrate ( $E \sim \text{MPa}$ ). Whereas the wrinkles created by temperature variations are typically random in nature, wrinkles obtained by mechanical stretching/compression are aligned orthogonally to the axis of the deformation. This feature together with the possibility to precisely control the wrinkles dimensions has made of this strategy one of the most extensively employed [56–61].

An illustrative example was reported by Efimenko et al. [62]. They demonstrated that the homogeneity of the buckle morphology depends on the strain removal rate. While the buckle period remains constant, stretched and UVO-modified specimens released at a fast rate (i.e., where the strain has been abruptly removed) usually present a larger number of defects (Fig. 2.11a). However, by decreasing the strain removal rate, the number of defects decreases accordingly. For instance, Fig. 2.11b and c depict optical microscopy images from samples whose strain removal rates

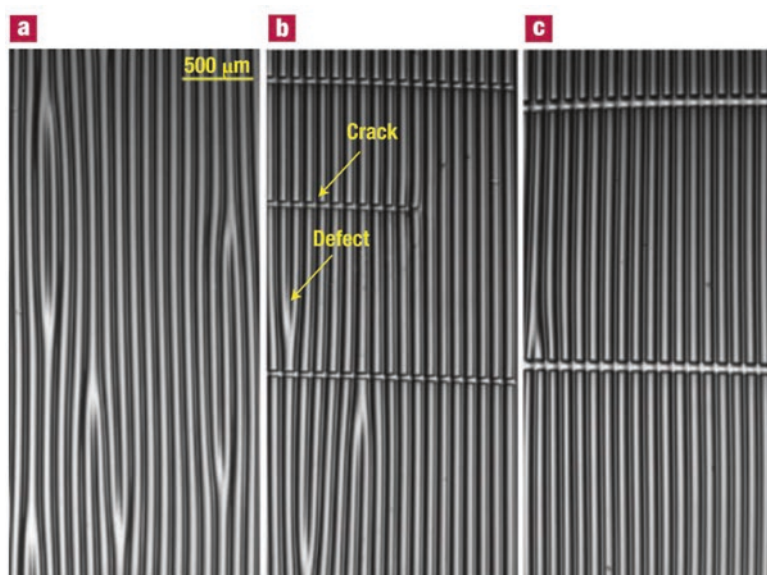


**Fig. 2.11** Optical microscopy images were taken in the transmission mode. Samples prepared by stretching PDMS sheets by  $\Delta = 50\%$ , exposing them to UVO for 60 min and releasing the strain: (a), instantaneously and (b, c) with the strain release rate of  $\sim 900$  (b) and  $\sim 58 \mu\text{m min}^{-1}$  (c). (Reproduced with permission from ref. [62])

were  $\sim 900 \mu\text{m min}^{-1}$  and present  $\sim 0.47$  defects per  $\text{mm}^2$  and  $\sim 58 \mu\text{m min}^{-1}$  with  $\sim 0.15$  defects per  $\text{mm}^2$ .

In contrast to the above-depicted methodology that resort to an initial pre-stretching step to produce the surface wrinkles, Ohzono and Shimomura explored the formation of ordered microwrinkled patterns by using a compressive strain [63, 64]. By using this strategy, complex wrinkle stripe patterns composed of convex and concave parts with an almost constant wavelength were ordered in the strain direction. Moreover, the wrinkles disappeared upon stress relaxation.

In general, either stretching or compression has been carried out in one single direction, thus leading to one-dimensional wrinkles. However, several other groups explored the possibility to stretch in different directions. An illustrative example of this alternative was reported by Chun and Yang [65]. The authors report the formation of various submicron wrinkle patterns and their transition from one-dimensional (1D) ripples to two-dimensional (2D) herringbone structures on polydimethylsiloxane films (Fig. 2.12). Using mechanical forces, they can separately control the amount and the timing of strain applied to the substrate on both planar directions either simultaneously or sequentially, which appears to be critical to guiding the pattern formation in real time. They demonstrate reversible transitions from flat to 1D ripple, to ripple with bifurcation, to ripple/herringbone mixed features, and to

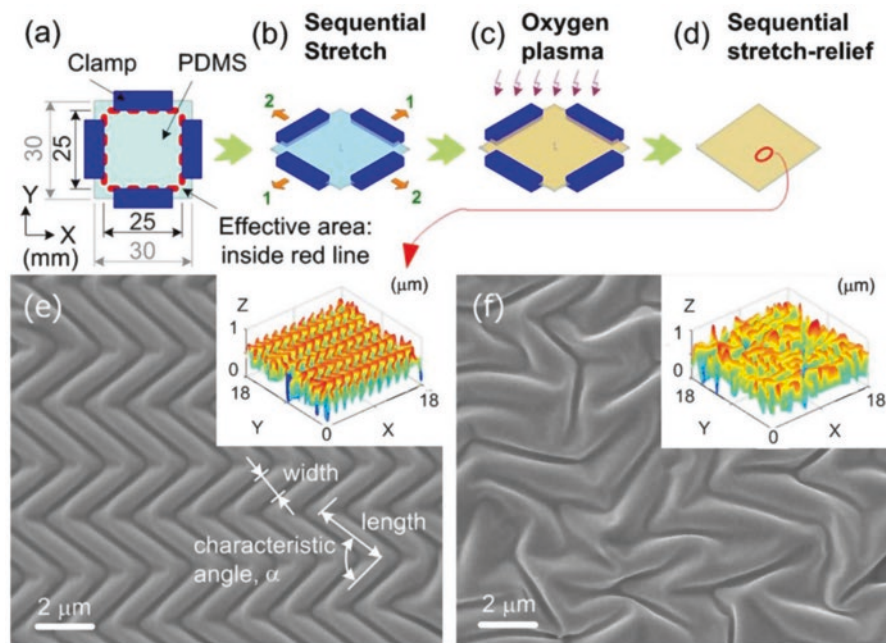
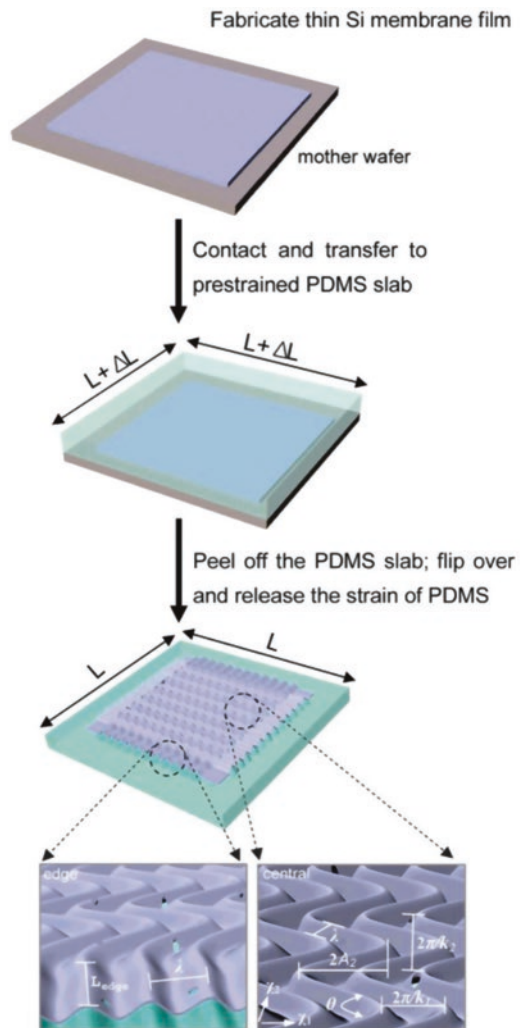


**Fig. 2.12** Color online Schematic fabrication process to generate wrinkle patterns (a–d). SEM and AFM images of surface patterns when stretching/release of PDMS film either sequentially (e) or simultaneously (f). (Reproduced with permission from ref. [65])

the well-controlled formation of a highly ordered zigzag-based 2D herringbone structures.

An alternative strategy to fabricate two-dimensionally buckled structures was reported by Choi et al. [66]. As illustrated in Fig. 2.13, the authors casting and curing prepolymers of polydimethylsiloxane (PDMS) against polished silicon wafers generated planar elastomeric substrates. Exposure to an ozone environment created by intense ultraviolet light for 5 min converted the hydrophobic PDMS surface to a hydrophilic state. Heating such an activated PDMS substrate at 70–180 °C induced anisotropic thermal expansion. Contacting this heated film with silicon-on-insulator (SOI) wafers followed by a peeling permitted to transfer the entire nanomembrane to the PDMS. Finally, the nanomembrane/PDMS structure was cooled to room tem-

**Fig. 2.13** Schematic illustration of steps for fabricating two-dimensional, “wavy” semiconductor nanomembranes on elastomeric supports. (Reproduced with permission from ref. [66])



perature (ca. 25 °C) to release the thermally induced pre-strain, thus leading to the spontaneous formation of two-dimensional (2D) wavy structures.

(c) *Swelling-induced wrinkles.*

Finally, wrinkle patterns can be also achieved by swelling usually induced by using a monomer solution but also solvents [23, 41, 67–75]. Upon immersion of the layered film using either a solvent vapor or a monomer mixture, regular wrinkles are formed. In this case, the final wrinkle characteristics, as well as the morphology, can be precisely controlled taking into account the solvent diffusion kinetics as well as the film characteristics including the geometry of the diffusion front or the cross-linking density [41].

For instance, Chan and Crosby [68] report a study in which a monomer diffusion is a basis to create microlens arrays and a variety of confined wrinkles. As depicted in Fig. 2.14, the authors employed a selective surface treatment (i.e., ultraviolet/ozone (UVO/O<sub>3</sub>) oxidation) of polydimethylsiloxane (PDMS) to obtain a stiff silica thin film on top of the PDMS. As a result of this surface treatment, the required elastic-moduli differences on the PDMS surface are obtained and allowed the authors to control and define the wrinkle formation. In this case, a monomer was employed to induce the surface swelling. The authors coated the surface with photopolymerizable n-butyl acrylate (nBA) and then covered the system with a glass superstrate. Whereas the acrylate monomer swelled entirely the PDMS, the surface wrinkles were only observed in the oxidized PDMS regions where the moduli mismatch existed. As a result, this surface modification permits the control over the spatial distribution of the wrinkle patterns. Interestingly, the wrinkle morphology

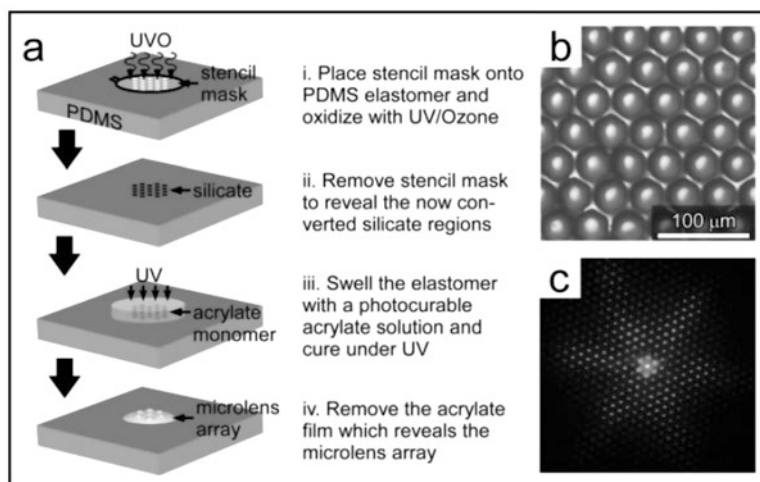


**Fig. 2.14** (a) General scheme for fabricating the microlens arrays on a planar PDMS surface based on Chan and Crosby surface-wrinkling approach. (b) Optical microscopy image of the microlens array fabricated using our wrinkling process. (c) The diffraction pattern of the microlens array illustrating uniformity of the array structure. (Reproduced with permission from ref. [68])

disappeared upon monomer evaporation but could be stabilized by photopolymerization of the nBA. Finally, we lifted away from the glass superstrate, which caused cohesive fracture of the polymerized poly(*n*-butyl acrylate) (PnBA) film and revealed the formation of the microlens (Fig. 2.14b).

As has been mentioned, the buckling process for microlens formation occurred as a result of the swelling of the moduli-mismatch oxidized PDMS regions. In a later contribution, [15] the authors demonstrated that the compressive stress can be finely tuned by changing the oxidation time and specific shape of the oxidized region. As a consequence, the control over the compressive stress state permitted both the creation of several forms of buckling structures and alignment of these wrinkle structures on both planar and nonplanar surfaces. Finally, the same authors [76] confirmed the capacity to fabricate reversible channels and microlens arrays by varying the area with local moduli mismatch as a function of the osmotic pressure (Fig. 2.15).

Another interesting example was reported by Vadeparre et al. [41, 73]. The authors described the preparation of bilayers following a two-step methodology. First, atactic polystyrene (PS) solutions in toluene were spin coated on bare silicon substrates to produce films with thicknesses around 0.25  $\mu\text{m}$ . Then, a 15-nm-thick titanium (Ti) layer was placed onto the polymer surface by thermal evaporation. Using this hybrid bilayer configuration, wrinkling was induced by immersing the

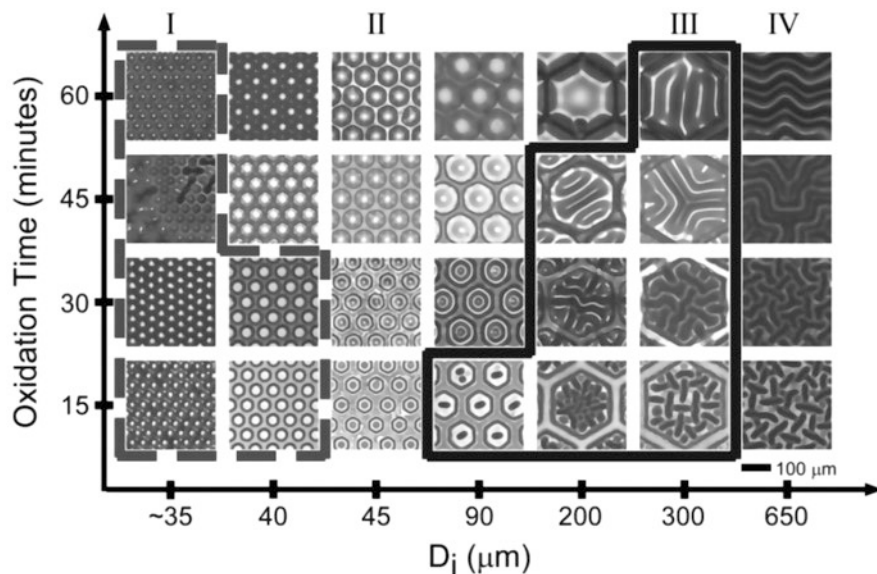


**Fig. 2.15** (a) Morphologies of the wrinkled structures observed varying simultaneously the oxidation time and size of the oxidized region. For a nearly semi-infinite case, the random 2D wrinkled patterns were formed (IV). At low levels of confinement, we again observed the formation of 2D isotropic wrinkles (III). However, as we further decreased  $D_i$ , lateral confinement played a significant role as the dimpled (II) and microlens (I) buckled structures were observed. (Reproduced with permission from ref. [68])

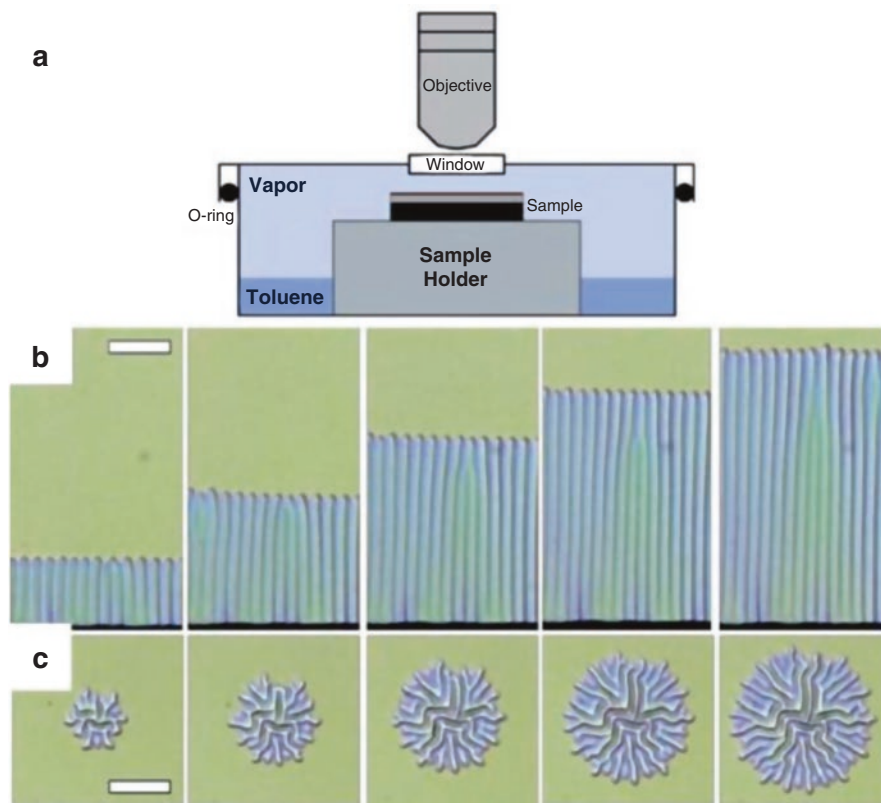


**Fig. 2.16** (a) A schematic representation of the experimental setup. From left to right: Successive optical micrographs of (b) the growth of parallel and (c) radial wrinkled domains obtained after immersion of a Ti/PS/SiO<sub>x</sub> trilayer in toluene vapors. The scale bar corresponds to 20  $\mu$ m. (Reproduced with permission from ref. [41])

films in toluene vapor at room temperature since toluene is a good solvent for PS that can swell the polymer layer by diffusion through the Ti membrane. The wrinkle formation was followed by optical microscopy (Fig. 2.16), and the authors evidenced the formation of the hierarchical structure of folds. Interestingly, due to the diffusion process, this pattern shifts advancing as it grows, closely following the wave front.

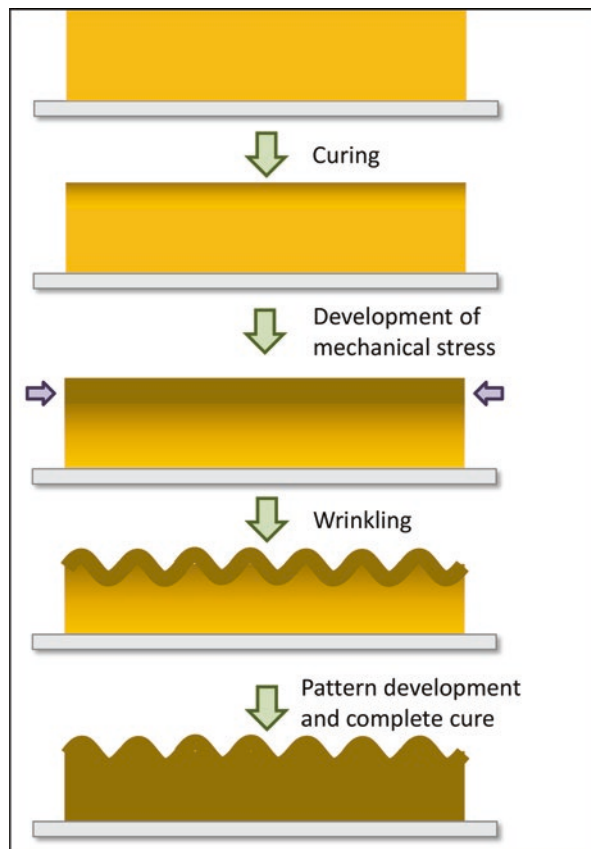
## 2.4 Depth-Wise Gradient Films

As an alternative to the use of bilayered films described in the previous section, wrinkle formation on films with modulus gradient has been proven to form a wide range of surface microstructures ranging from peanuts, lamellar, and wormlike

shapes, among others, as well as to control of the film structure over large areas [77, 78]. Gradual cross-linked films fabricated as precursors for wrinkle formation have been prepared using several diverse alternatives including photo and thermal polymerization [79–81], cross-linked via polymer infusion [82], or selective polymerization of the film surface. [79, 83–85].

Basu et al. [79] are at the origin of the generally accepted mechanism of wrinkle formation in these systems. They established a comprehensive theory of wrinkle formation in curing coating systems validated for different curing conditions (thermal and UV), for a wide range of chemistry and independently of the delivery (liquid and powder). Wrinkle formation in gradient cross-linked films is depicted in Fig. 2.17 according to the theory developed by Basu et al. In this mechanism, a uniform thick film is cured either thermally or by UV irradiation or both. The initially liquid coating develops a gradient in degree of cross-linking and therefore in their mechanical properties. The top layer cross-linked to a larger extent and behaves like a solid skin. Upon further cross-linking of the film, the stress produced by the bulk developed and stabilized the wrinkle formation [7].

**Fig. 2.17** Mechanism of wrinkle formation by gradient cross-linking polymerization. The cure occurs faster at the free surface, thus leading to the formation of a rigid layer. This layer will wrinkle as a consequence of the mechanical stress induced by the cross-linking of the bulk. (Figure adapted with permission from ref. [79])



As an alternative to the previously described one-step approach, other groups described recently strategies involving a two-step photocross-linking steps [86]. This approach, that requires two different irradiation steps, has been improved by Yang et al. [80] as well as Crosby et al. [81] that reduced the creation of wrinkled surface patterns to one-single step. In both strategies, a crucial aspect is the presence of oxygen diffusion in the top surface of the film which limits the polymerization in that particular region. Yang et al. [77] described the preparation of poly(hydroxyethyl methacrylate) (PHEMA) film from a partially polymerized HEMA embedded in a UV curable solution. For films with thicknesses above 20  $\mu\text{m}$ , the amount of oxygen diffused into the film is gradually reduced, thus forming a film with gradually increasing cross-linked density (Fig. 2.18). In addition, initiator and cross-linker concentration, precursor viscosity or exposure time, and intensity will allow the fine-tuning of the gradient formed. As a result, upon swelling, distinctive patterns were observed including random, lamellar, peanut, or hexagonal.

A similar principle was employed by Crosby et al. [81]. They prepared a mixture of monomers and cross-linkers. Then the samples were irradiated with UV light, while a controlled oxygen flow was applied on the top of the sample. Similar to the example described above, at the monomer/air interface, a thin layer is formed where the radicals are quenched by the oxygen and the monomers remained uncured. Below a certain depth, the radical generation is higher than the oxygen inhibition, and cross-linking occurs. As a consequence, a cross-linking gradient is observed, thus leading to the generation of perpendicular stresses that finally provoke the formation of the surface wrinkles.

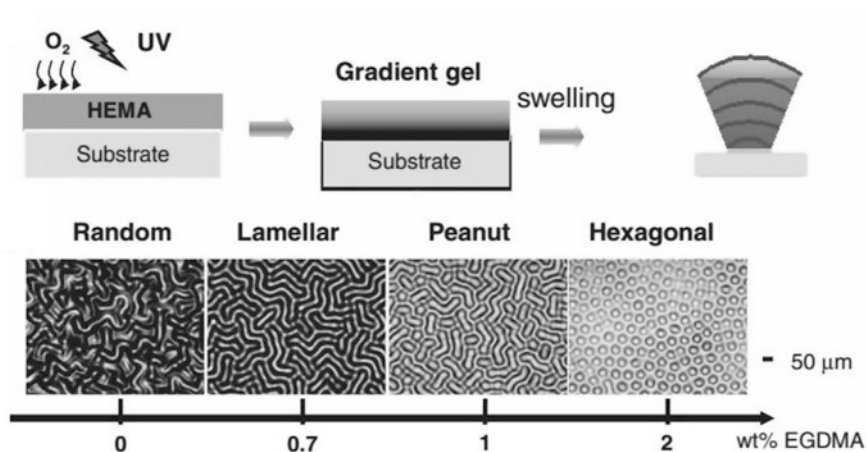


**Fig. 2.18** Above: Schematic illustration of the fabrication of PHEMA films with a modulus gradient and formation of wrinkling patterns upon swelling. Below: Optical images of patterns on the surfaces of water-swollen PHEMA films. The order of the patterns is determined by the concentration of cross-linker EGDMA [77]. (Figure reproduced from ref. [80])

## 2.5 Homogeneous Films

Homogeneous films include films formed by using an elastoplastic polymer or homogeneously cross-linked gels. A large number of studies have been reported since the pioneer systematic study on the pattern formation in homogeneously polymerized gels carried out by Tanaka group [87, 88]. Inspired by these studies, a large variety of both experimental and theoretical studies have been equally reported [89–92]. Here below we will attempt to describe the different alternatives reported to fabricate surface wrinkles as a function of the stimulus employed.

### 2.5.1 Wrinkle Formation by Solvent Swelling/Drying

Swelling a polymeric thin film with a preferred solvent or monomer solution [68, 70, 72, 77, 78, 81, 93] is also an extended strategy to produce surface wrinkles inhomogeneous films. In a typical situation, the swelling-induced surface patterns are originated as a result of the selective swelling of the top of the film since the bottom of the polymer films is constrained as a consequence of the rigid interface [88]. This gradual swelling from the top to the bottom generates an anisotropic osmotic pressure along the film thickness that leads to a compressive strain of the film (Fig. 2.19). In the case that the compressive strain overcomes a critical value, the film surface start to buckle and finally produce surface wrinkles. While different authors [87, 88] employed swelling as a stimulus to produce surface wrinkles, this strategy entails two major limitations. One of the major problems is the difficulty to prepare wrinkles since other morphologies such as folds or creases are rapidly formed when large strains are achieved. The second issue is related to the nonlinearity of the swelling process that makes it difficult to obtain large-ordered wrinkled surfaces.

In addition to swelling, hydrogel shrinking can also induce mechanical instabilities [94, 95]. Pioneer studies on the patterns generated upon shrinking were carried

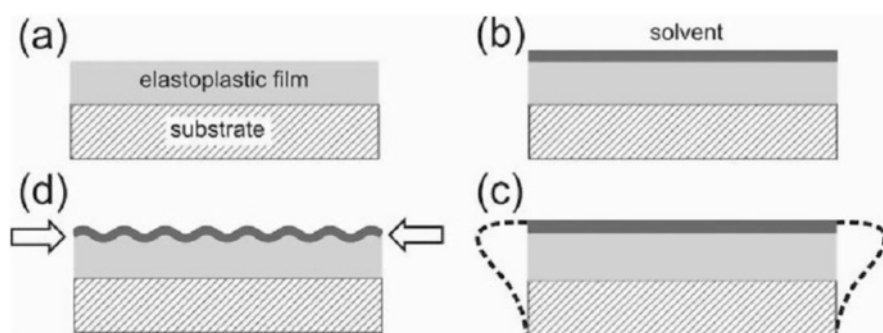


**Fig. 2.19** Wrinkling formation by controlled solvent swelling (a) of a viscoelastic (elastoplastic) polymer film onto a rigid substrate. Upon swelling (b), the free top layer is selectively expanded (c) leading to a compressive strain and therefore to buckling (d). (Reproduced with permission from reference [80])

out by Matsuo and Tanaka [96]. Their preliminary works attempt to establish the mechanism involved in the generation of surface patterns and also to classify the different patterns generated in the form of a diagram. Figure 2.20 represents the phase diagram including all the patterns observed as a function of the combination of acetone and the final hydrogel length. As can be observed, volume phase transition in the hydrogels provokes also mechanical instabilities through deswelling that finally produced different patterns including bamboo, bubbles, or tubes.

Mechanical instability induced by drying, instead of the swelling, has also been exploited for the formation of wrinkled morphologies. However, in comparison to swelling, there are only a few reports on wrinkling of gels induced by drying. One of these studies was reported by Pauchard et al. [97, 98] who reported the wrinkle formation upon film drying. In particular, they studied experimentally the situations under which drop surface buckling occurs and their dependence on the drying rate and contact angle. They used concentrated solutions of the hydrosoluble polysaccharide dextran and demonstrated that the large shape distortions that occur during the drying of sessile drops of polymer solution are shown to be related to a buckling instability. As the solvent evaporates, polymers accumulate near the vapor/drop interface and, depending on the experimental conditions, can form a glassy skin which bends as the volume it encloses decreases.

In addition to the effect on drying films, Rizzieri et al. [99] explored the formation of wrinkles in stretched drying gelatin films (Fig. 2.21). When a thin film of initially hydrated gelatin is allowed to dry from the surface, superficial changes in the structure of the material affect the local mechanical properties of the drying region. If the film is simultaneously subjected to large strain deformation (above 20%), a periodic pattern of wrinkles appears on the surface of the gelatin along with the length of the sample in the direction of the applied force. These wrinkles were uniformly distributed on the surface of the gelatin with a wavelength that is much smaller than the sample thickness, which changes with sample composition, aging time, and deformation rate.

More recently, Huraux et al. [94] described the wrinkling of poly(vinyl alcohol) gels (PVA gels) induced by drying. Drying of PVA gel cylinders is performed under controlled humidity and ventilation (Figs. 2.22 and 2.23). The gels are dried in a drying chamber under a flow and controlled humidity (16–90%) and a precise temperature. Huraux et al. show that the drying-induced morphology of the gel is due to the crossing of the glass transition while varying the solvent concentration. They demonstrated that drying can induce wrinkling by forming a glassy skin layer which is compressed by the shrinkage of the core/bulk.

### ***2.5.2 Wrinkles Produced Directly by Solvent Casting.***

In contrast to cross-linked systems, a recent approach has been reported in which the formation of wrinkles occurs upon solvent casting of a polymer on a substrate without applying external stress. Ramanathan et al. [3] employed an

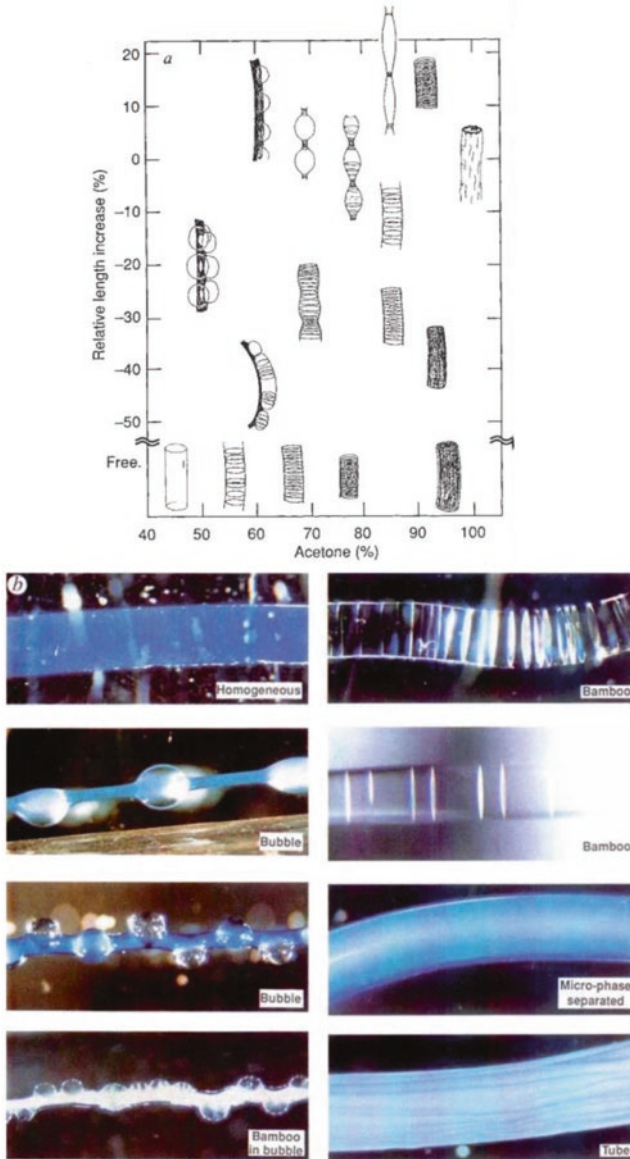


**Fig. 2.20** (a) “Phase diagram” showing the regions of acetone concentration and fixed final length of a gel at which different patterns of cylindrical acrylamide hydrogels are formed. A negative relative length increase indicates that the fixed length was shorter than the original relaxed length, whereas a positive value means that the gel was stretched before shrinking. (b) Photographs that best represent the various patterns; some are ionic gels. (Reproduced with permission from ref. [96])

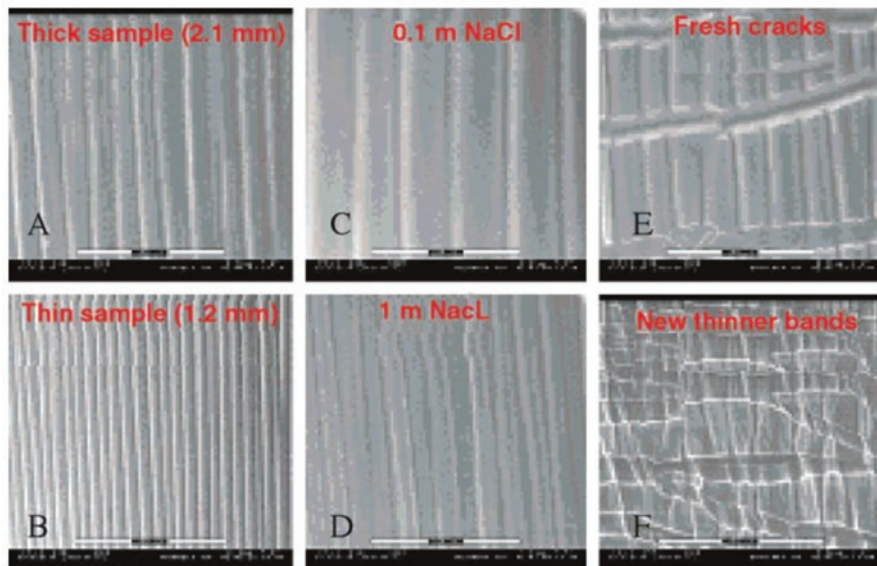


**Fig. 2.21** Variation of the wrinkling wavelength, with the sample thickness [(a) 2.1 mm and (b) 1.2 mm], with the amount of NaCl [(c) 0.1 M and (d) 1 M], and on the new thinner bands at the opening of the horizontal cracks (E,F). (Reproduced with permission from ref. [99])

azalactone-based functional polymer and demonstrated that wrinkles are formed in a particular direction depending on the mode of deposition (Fig. 2.24). Moreover, given the spontaneity and versatility of wrinkle formation, they extended the use of this strategy to nonplanar geometries including tubes, cones, and other 3D structures. Equally, the authors used this approach to guide the deposition of metal nanoparticles and quantum dots, creating a periodic, nanopatterned film.

### 2.5.3 *Wrinkles Produced by Marangoni Convection*

Ellison and coworkers [100, 101] and Kim et al. [102] investigated the use of the Marangoni effect to produce the fluid flow in response to gradients in surface energy and produce nanoscale surface patterns.

On the one hand, Ellison and coworkers took advantage of the fact that exposure of polystyrene (PS) to ultraviolet (UV) light undertakes partial dehydrogenation of the alkane polymer backbone which increases its surface energy (Fig. 2.25). Based on this idea, the authors exposed polystyrene films to UV light using a photomask to induce a patterned photochemical reaction producing regions in the film with differing surface energy. Upon heating the solid polymer film with the preprogrammed surface energy pattern to a liquid state, the polymer flows from the low surface energy unexposed regions to high surface energy exposed regions. This flow creates

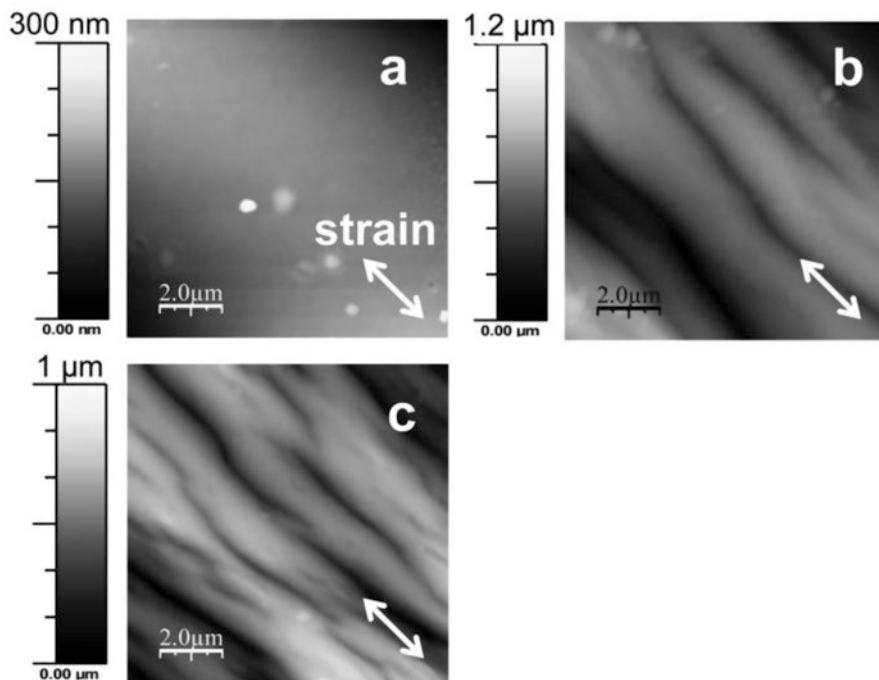


**Fig. 2.22** Surface morphology of PVA gels dried at a fixed length under different humidities ((a) 85%, (b) 45%, (c) 12%) measured by AFM

three-dimensional topography by the Marangoni effect, which describes convective mass transfer due to surface energy gradients. The topographical features can be permanently preserved by quenching the film below its glass to the liquid transition temperature. Their shape and organization are only limited by the pattern on the photomask. In particular, thermal annealing above the glass transition temperature induces the flow of polymer from unexposed to exposed regions. As a result, a sinusoidal film thickness variations of 120 nm using a 12.5  $\mu\text{m}$  half-pitch line and space mask.

The same group more recently [102] used the same Marangoni convection principle to generate microscale and nanoscale surface patterns using photosensitizers. In particular, the authors employed a near UV–visible light (NUV–vis) photosensitizer, 9,10-dibromo-anthracene (DBA) introduced into the thin films of poly(isobutyl methacrylate). As depicted in Fig. 2.26, upon light exposure through a photomask and heating above the glass transition, a flow of the film material into the exposed regions is observed.

Kim et al. [101] investigated the use of the Marangoni effect to produce the fluid flow in response to gradients in surface energy and produce nanoscale surface patterns. The procedure employed is depicted in Figs. 2.27 and 2.28. First, a poly(isobutyl methacrylate) (PiBMA) film containing 5 wt % 9,10-dibromo-

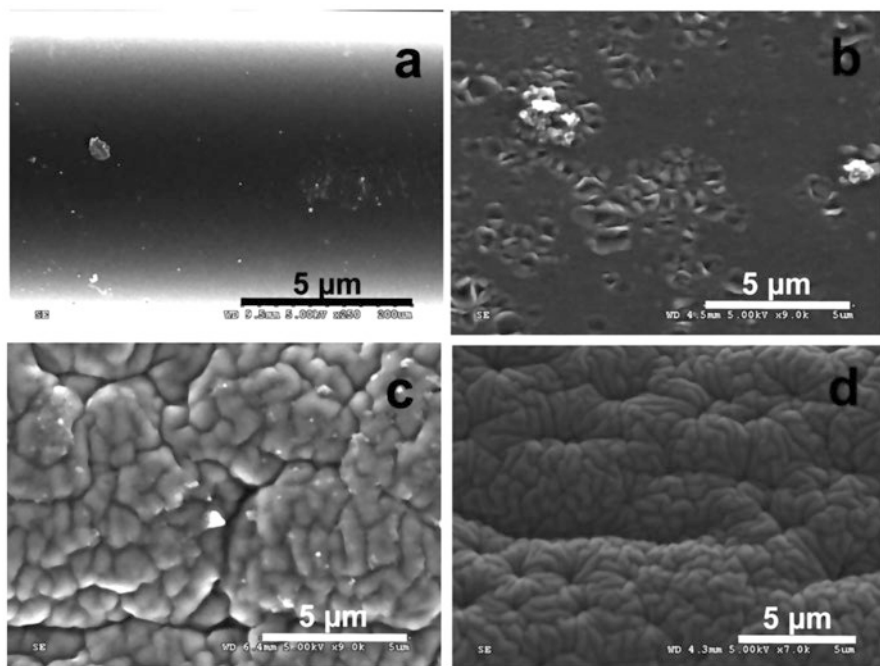


**Fig. 2.23** Surface morphology of PVA gels dried with a free extremity under different values of humidity ((a) 95%, (b) 66%, (c) 47%, and (d) 16%) observed by SEM

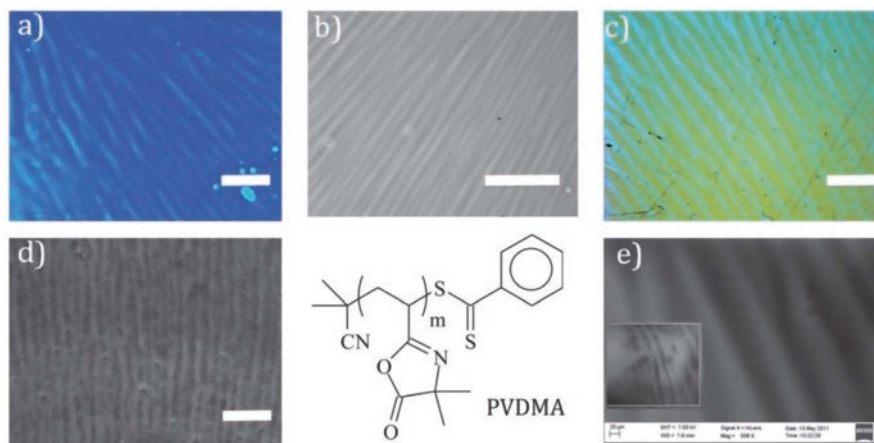


**Fig. 2.24** Optical micrographs of wrinkling patterns that are formed by spin casting a 1 wt% solution of PVDMA in  $\text{CHCl}_3$ . (a), (b), and (c) represent the PVDMA wrinkles (in reflectance mode) on a variety of substrates such as nitride ( $\text{Si}_3\text{N}_4$ ), oxide ( $\text{SiO}_x$ ), and noble metal (Au), respectively. (d) and (e) are a transmission optical micrograph (TOM) and a scanning electron micrograph (SEM) of PVDMA wrinkles, respectively. (Reproduced with permission from ref. [3])

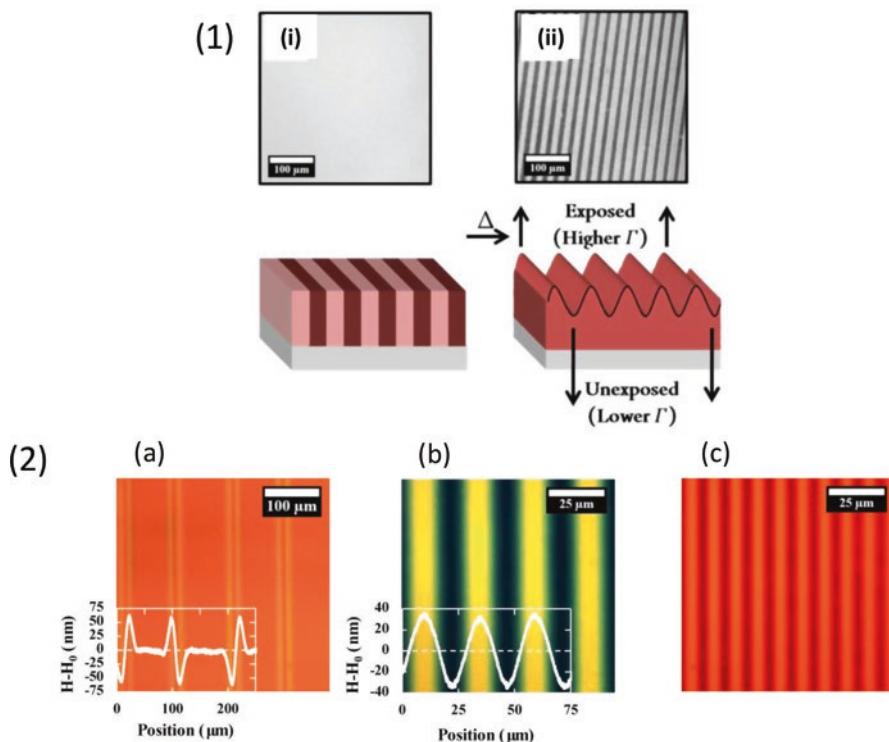


**Fig. 2.25** (1) Schematic illustration of the steps involved in feature formation in a PS thin film. (i) A bright-field micrograph of a glassy polymer film ( $\sim 150$ -nm-thick) after exposure to light through a photomask. No topography can be detected by atomic force microscopy after this stage. (ii) After heating the same film to  $110^\circ\text{C}$ , where the polymer becomes a liquid, the patterned surface energy drives formation of topographic features via the Marangoni effect. (2) Patterns created in  $\sim 150$ -nm-thick PS films with overlaid profilometry traces showing topography formed by using photomasks with different line spacing of (a)  $100\ \mu\text{m}$  chrome lines with a  $200\ \mu\text{m}$  pitch, (b)  $12.5\ \mu\text{m}$  chrome lines on a  $25\ \mu\text{m}$  pitch, and (c)  $5\ \mu\text{m}$  chrome lines on a  $10\ \mu\text{m}$  pitch. (Reproduced with permission from refs. [100, 101])

anthracene (DBA) was spin coated onto a silicon wafer. Then, a NUV-vis light exposure was applied through a photomask, and the DBA was photochemically oxidized in the exposed regions. Finally, upon thermal annealing above the  $T_g$  and due to the Marangoni effect, polymer flows into the exposed regions from the unexposed regions. This results in a film with a smoothly varying thickness profile reflective of the photomask pattern.

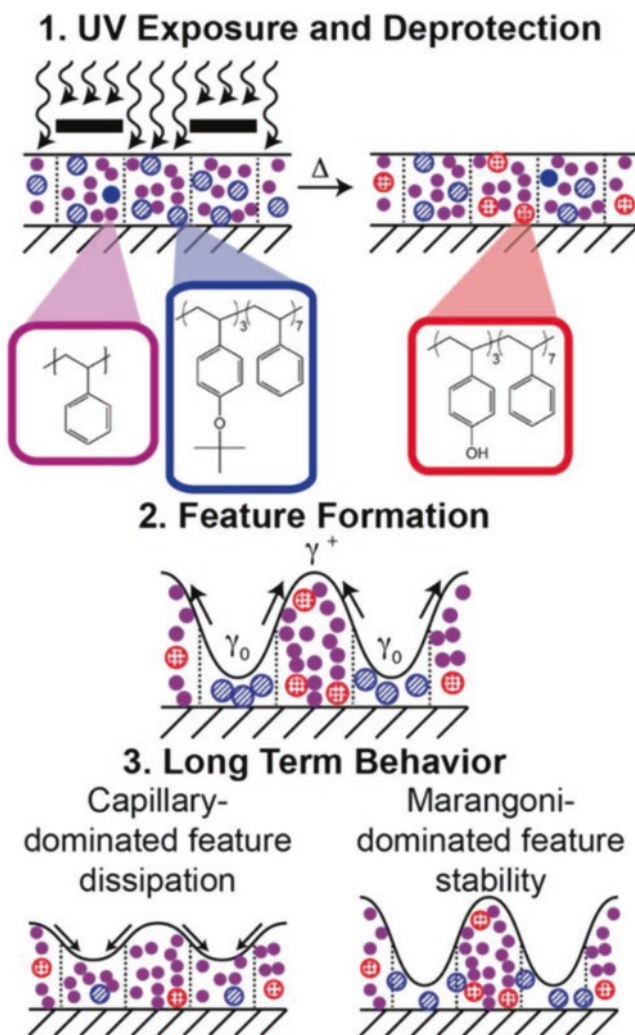


**Fig. 2.26** Polymer patterning methodology. (1) Schematic of the polymer blend which is composed of a low molecular weight PS (solid purple) and a high molecular weight copolymer, P(tBOS-ran-S) (blue hashed circles). Spatial control of the surface energy gradient is achieved by exposing films through a photomask, and the subsequent annealing of these films leads to a photochemical transformation of P(tBOS-ran-S) into P(HOST-ran-S) (red dotted circles) with the aid of a photoacid generator. (2) With extended annealing time, polymer flows from regions of low to high surface energy, and (3) the long-term behavior (dissipation or stability of topography) is determined by whether capillary or Marangoni forces dominate, respectively. (Reproduced with permission from ref. [102])

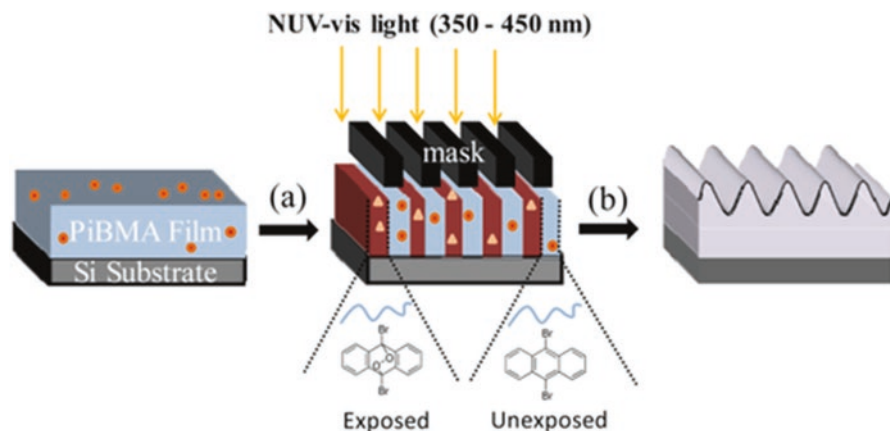


**Fig. 2.27** Patterning schematic of (a) NUV-vis light exposure in an ambient air atmosphere and (b) subsequent thermal annealing. Exposed regions (higher surface energy) rise, while the unexposed regions (lower surface energy) sink upon thermal annealing. (Reproduced with permission from ref. [101])

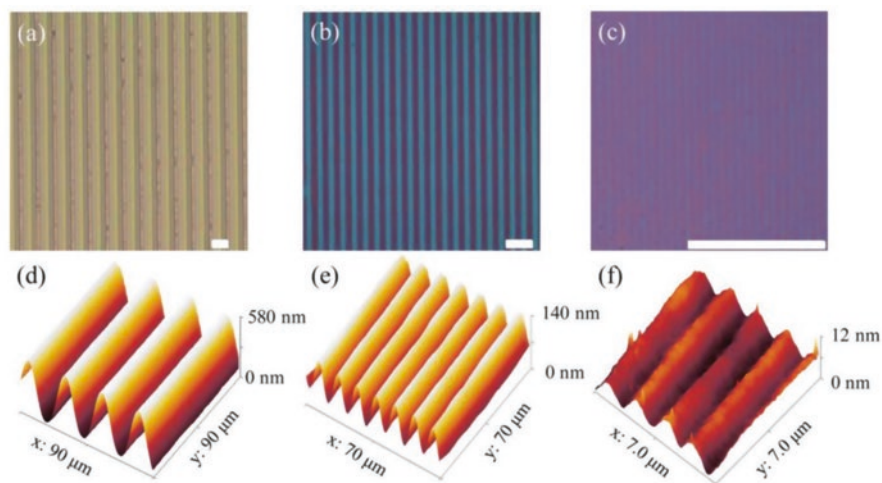


**Fig. 2.28** Optical micrographs of the patterned samples using (a) 12.5  $\mu\text{m}$ , (b) 5  $\mu\text{m}$ , and (c) 800 nm half-pitch “line and space” masks. All scale bars indicate 25  $\mu\text{m}$ . AFM images of the corresponding patterned samples are shown below. Initial film thicknesses were 300 nm. All samples were exposed to light for 15 min. (Reproduced with permission from ref. [101])

### 2.5.4 Film Wrinkling under Capillary Forces

Examples of wrinkling of films under capillary forces are rather rare in spite that very often thin films are dipped in fluid environments. As a result, thin films are usually exposed to different deformations and surface tensions. An illustrative example of wrinkling under capillary forces was reported by Huang et al. [8]. They studied films based on high molecular weight polystyrene with a high aspect ratio (the ratio of the

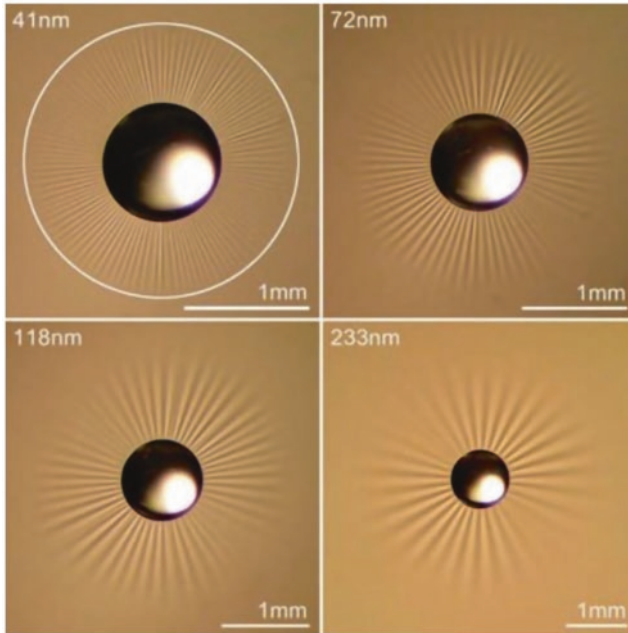


**Fig. 2.29** Four PS films of diameter  $D = 22.8$  mm and of varying thicknesses floating on the surface of water, each wrinkled by water drops of radius  $a \approx 0.5$  mm and mass  $m \approx 0.2$  mg. As the film is made thicker, the number of wrinkles  $N$  decreases (there are 111, 68, 49, and 31 wrinkles in these images), and the length of wrinkles  $L$  increases. (Reproduced with permission from ref. [8])

diameter  $D$  to thickness  $h$  is  $D/h \sim 5 \times 10^5$ ) spin coated onto glass substrates (Fig. 2.29). The film thickness  $h$  was varied from 31 to 233 nm. Because PS is hydrophobic, the film floated to the surface of the water where it was stretched flat by the surface tension of the air-water interface at its perimeter. Wrinkles were induced in the stretched, floating film by placing a drop of water in the center of the film by placing a solid disk in the center of the film. Later, Vella et al. [9] described a physically based model for the deformation of a floating elastic membrane caused by the presence of a liquid drop that explains the wrinkle formation observed by Huang et al. [8]. The authors started using the equations of membrane theory modified to account for surface energies to evidence that the presence of a liquid drop causes an azimuthal compression over a finite region determining the extent of the wrinkled region.

### 2.5.5 Direct Laser Interference Patterning (DLIP)

Direct laser interference patterning (DLIP) permits through the selective surface ablation the design of a wide range of surface patterns in polymers in a single-step process. In particular, DLIP is an alternative methodology for the direct fabrication of periodic arrays [103]. As depicted in Fig. 2.30, this method involves the irradiation of the sample surface with two or more coherent laser beams, thus producing a

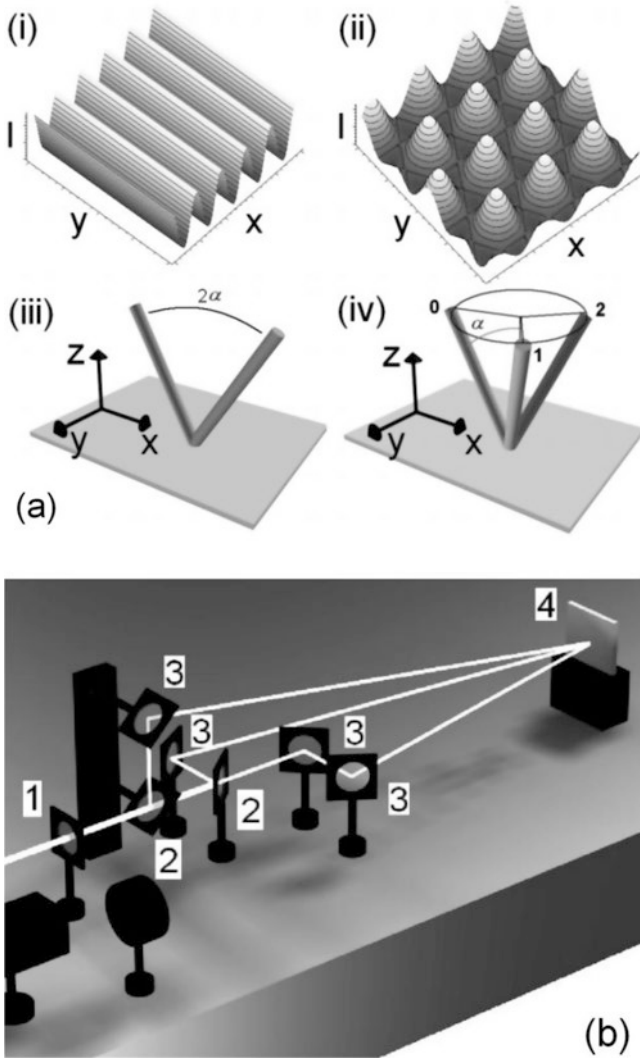


**Fig. 2.30** (a) Two- and three-laser beam interference patterns: (i) Line-type pattern with corresponding two-laser beam (iii) configuration; (ii) dot-type pattern with corresponding three-laser beam; (iii) symmetrical configuration. (b) Experimental setup for three-laser beam interference experiments: (1) Lens; (2) mirror; (3) beam splitter; (4) sample. (Reproduced with permission from ref. [105])

periodic distribution of laser intensity due to the phenomenon of interference [104]. This methodology requires the use of high-power lasers, and by the interaction of these lasers with the surface of different materials, these can be directly modified leading to periodic arrays with features in the micro-/nanoscale on macroscopic areas [105]. In comparison to other alternative lithographic methods, DLIP has a distinctive advantage since no additional process steps are required (i.e., etching, development of photoresist) [106].

As will be thoroughly described in Chap. 7, a wide variety of polymeric materials can be microstructured using this methodology. For instance, polymer typically employed for the fabrication of different biomedical devices such as poly(etherimide) (PEI) is used in harmonic scalpels, poly(imide) (PI) is used in off-pump coronary artery bypass devices, polycarbonate (PC) is used in electrophysiology catheters or poly(ether ether ketone) (PEEK) resists sterilization by radiation or heat treatment, and it has been used to produce kidney dialysis machine components [105]. This methodology permits also the surface microstructuring of conductive polymers that usually present limited solubility such as PANI [107, 108] or fabricate linear structures in PEDOT-PSS films with ns-lasers [109] and also form complex surface patterns using copolymers such as polystyrene-polymethyl methacrylate copolymers [110].

### 2.5.6 *Laser-Induced Periodic Surface Structures (LIPSS)*

In addition to DLIP, an alternative approach has been reported in which the polymer surface is illuminated by using a pulsed laser source with gentle fluences. This pulsed irradiation allows for the formation of different period structures, and the methodology is known as laser-induced periodic surface structures (LIPSS) [111–114]. An abundant diversity of experimental work has been reported during the last years on LIPSS, and as a result, different theoretical approaches have been developed [115, 116]. In spite of the large number of works devoted to the use of LIPSS, only a few of them focus on the structuration of polymers with femtosecond lasers.

Pioneer experiments carried out by Baudach et al. [117] reported the formation of microstructures by ablation on polyimide (PI) with femtosecond laser pulses. The same group extended this work to other polymeric materials such as polycarbonate (PC), polyethylene terephthalate (PET), polytetrafluoroethylene (PTFE), and polymethylmethacrylate (PMMA) [118]. In these preliminary works assumed, the authors assumed that ablation was at the origin of the microstructuring. However, as mentioned by Forster et al. [119], ablation can potentially alter not only the chemical but also the physical properties of the polymer. These can include the altered optical absorption and, in particular, for PI, increased electrical conductivity due to carbonization of the surface.

In order to avoid ablation, Forster et al. [119] applied ultrashort laser pulses tailored on a picosecond time scale to study the influence of different pulse durations (150 fs–5 ps) and double pulses (with time delays between 300 fs and 11 ps) on the formation of ripples on PI, taking into account the nonlinearity of interaction but also the dynamics of phase transitions. Interestingly, according to their findings, the process of ripple formation is correlated to material properties as, e.g., the electron-phonon relaxation time. In this case, the amount of material removed from the surface is negligible, so the formation of ripples is mainly due to a self-organization process.

By using the simplest configuration, LIPSS generally forms ripples at the surface, and the periodicity corresponds approximately to the wavelength of the laser radiation employed. The pattern formation has been attributed to the interference

between the incident and scattered light or excited surface waves [120]. More precisely, the interference between incident linearly polarized light and the surface-scattered wave generated during the pulse leads to a periodic modulation of the absorbed light intensity and, consequently to a modulated surface roughening which enhances the development of the structures [121].

As an illustrative example (see Chap. 6 for more information about this method), Rebollar et al. [121] employed three different polymers, i.e., poly(ethylene terephthalate) (PET), poly(trimethylene terephthalate) (PTT), and polycarbonate bisphenol A (PC), to study the laser parameters in order to form homogeneous patterned surfaces. Figure 2.31 shows illustrative AFM height images of PET, PTT, and PC irradiated at 265 nm with 5000 pulses at different fluences ranging from 1.1 to  $1.6 \text{ mJ/cm}^2$ . Whereas for low fluences ( $F < 1 \text{ mJ/cm}^2$ ), no morphological changes

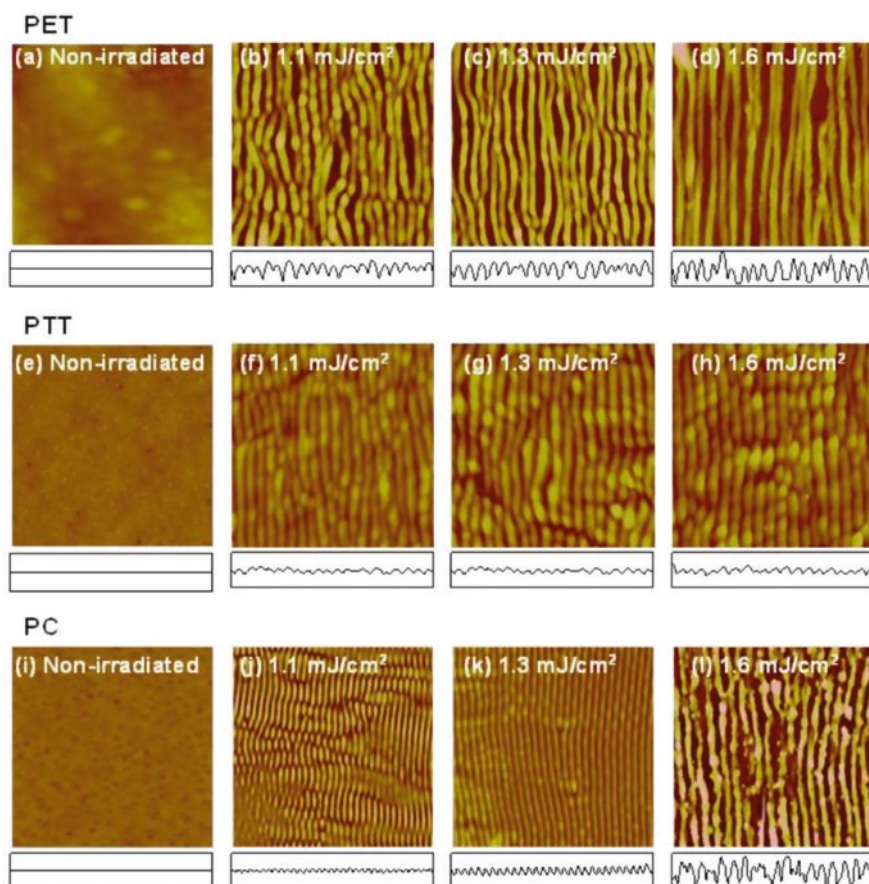


**Fig. 2.31** AFM height images ( $5 \times 5 \mu\text{m}^2$ ) of PET, PTT, and PC irradiated at 265 nm with 5000 pulses at the indicated fluences. Images of as-spun polymers are shown as a reference. The height profile along a  $5 \mu\text{m}$  line perpendicular to the ripples is shown below every image (height scale: 250 nm). (Reproduced with permission from ref. [121])

were observed at the polymer surface increasing the fluence above  $1 \text{ mJ/cm}^2$ , structures start to be formed and develop the form of parallel and well-defined ripples. Moreover, upon further increase of the fluence at approximately  $1.6\text{--}1.9 \text{ mJ/cm}^2$ , LIPSS start to distort indicating that an optimum range of irradiation intensity is required to obtain well-defined surface structures.

## 2.6 Conclusions

This chapter attempt to briefly describe, in an organized manner, the different alternatives reported producing micro- and nano-wrinkled surface structures. A wide variety of strategies have been reported that are classified as a function of the film structure, i.e., layered films, depth-wise gradient films, and homogeneous films.

Swelling, temperature, mechanical stretching, or even the irradiation with light or lasers are at the origin of the creation of surface instabilities that finally lead to the formation of wrinkles with variable sizes (from nano- to micrometer scale) and eventually particular orientations (random, parallel, or following the morphologies of pre-patterned substrates).

The large number of existing methodologies that finally offers alternatives to produce micropatterned substrates with controlled morphology as well as with variable chemical composition with potential for multiple applications as will be thoroughly described in Chaps. 12, 13, and 14.

**Acknowledgments** The authors acknowledge financial support given by FONDECYT grant N° 1170209. M.A. Sarabia acknowledges the financial support given by CONICYT through the doctoral program scholarship grant. J. Rodriguez-Hernandez acknowledges financial support from Ministerio de Economía y Competitividad (MINECO) (Project MAT2016-78437-R, FEDER EU). Finally, this study was funded by VRAC grant number L216-04 of Universidad Tecnológica Metropolitana.

## References

1. P. Gruner, M. Arlt, T. Fuhrmann-Lieker, Surface wrinkling induced by photofluidization of low molecular azo glasses. *ChemPhysChem* **14**(2), 424–430 (2013)
2. N. Lambrecht, T. Pardoën, S. Yunus, Giant stretchability of thin gold films on rough elastomeric substrates. *Acta Mater.* **61**(2), 540–547 (2013)
3. M. Ramanathan, B.S. Lokitz, J.M. Messman, C.M. Stafford, S.M. Kilbey II, Spontaneous wrinkling in azlactone-based functional polymer thin films in 2D and 3D geometries for guided nanopatterning. *J. Mater. Chem. C* **1**(11), 2097–2101 (2013)
4. Z. Wu, N. Bouklas, R. Huang, Swell-induced surface instability of hydrogel layers with material properties varying in thickness direction. *Int. J. Solids Struct.* **50**(3–4), 578–587 (2013)
5. Z. Chen, Y.Y. Kim, S. Krishnaswamy, Anisotropic wrinkle formation on shape memory polymer substrates. *J. Appl. Phys.* **112**(12) (2012)

6. Y.-C. Chen, A.J. Crosby, Wrinkling of inhomogeneously strained thin polymer films. *Soft Matter* **9**(1), 43–47 (2013)
7. J. Rodríguez-Hernández, Wrinkled interfaces: Taking advantage of surface instabilities to pattern polymer surfaces. *Prog. Polym. Sci.* **42**, 1–41 (2015)
8. J. Huang, M. Juskiewicz, W.H. De Jeu, E. Cerda, T. Emrick, N. Menon, T.P. Russell, Capillary wrinkling of floating thin polymer films. *Science* **317**(5838), 650–653 (2007)
9. D. Vella, M. Adda-Bedia, E. Cerda, Capillary wrinkling of elastic membranes. *Soft Matter* **6**(22), 5778–5782 (2010)
10. D.P. Holmes, A.J. Crosby, Draping films: A wrinkle to fold transition. *Phys. Rev. Lett.* **105**(3), 038303 (2010)
11. L. Pocivavsek, R. Dellsy, A. Kern, S. Johnson, B. Lin, K.Y.C. Lee, E. Cerda, Stress and fold localization in thin elastic membranes. *Science* **320**(5878), 912–916 (2008)
12. N. Sridhar, D. Srolovitz, Z. Suo, Kinetics of buckling of a compressed film on a viscous substrate. *Appl. Phys. Lett.* **78**(17), 2482–2484 (2001)
13. R. Huang, Z. Suo, Wrinkling of a compressed elastic film on a viscous layer. *J. Appl. Phys.* **91**(3), 1135–1142 (2002)
14. S. Chatterjee, C. McDonald, J. Niu, S.S. Velankar, P. Wang, R. Huang, Wrinkling and folding of thin films by viscous stress. *Soft Matter* **11**(9), 1814–1827 (2015)
15. R. Huang, Kinetic wrinkling of an elastic film on a viscoelastic substrate. *J. Mech. Phys. Solids* **53**(1), 63–89 (2005)
16. S. Im, R. Huang, Evolution of wrinkles in elastic-viscoelastic bilayer thin films. *J. Appl. Mech.* **72**(6), 955–961 (2005)
17. R. Huang, S.H. Im, Dynamics of wrinkle growth and coarsening in stressed thin films. *Phys. Rev. E* **74**(2), 026214 (2006)
18. K. Dalnoki-Veress, J. Forrest, J. Dutcher, Mechanical confinement effects on the phase separation morphology of polymer blend thin films. *Phys. Rev. E* **57**(5), 5811 (1998)
19. P.J. Yoo, K.Y. Suh, S.Y. Park, H.H. Lee, Physical self-assembly of microstructures by anisotropic buckling. *Adv. Mater.* **14**(19), 1383–1387 (2002)
20. T. Okayasu, H.L. Zhang, D.G. Bucknall, G.A.D. Briggs, Spontaneous formation of ordered lateral patterns in polymer thin-film structures. *Adv. Funct. Mater.* **14**(11), 1081–1088 (2004)
21. P.J. Yoo, H.H. Lee, Morphological diagram for metal/polymer bilayer wrinkling: Influence of thermomechanical properties of polymer layer. *Macromolecules* **38**(7), 2820–2831 (2005)
22. E.P. Chan, K.A. Page, S.H. Im, D.L. Patton, R. Huang, C.M. Stafford, Viscoelastic properties of confined polymer films measured via thermal wrinkling. *Soft Matter* **5**(23), 4638–4641 (2009)
23. P.J. Yoo, H.H. Lee, Evolution of a stress-driven pattern in thin bilayer films: Spinodal wrinkling. *Phys. Rev. Lett.* **91**(15), 154502 (2003)
24. K. Srinivasan, G. Subbarayan, T. Siegmund, Wrinkling on irreversibly deforming foundations. *Thin Solid Films* **520**(17), 5671–5682 (2012)
25. A. El Haitami, F. Bretagnol, P. Assuid, G. Petitet, S. Cantournet, L. Corté, Erasable and reversible wrinkling of halogenated rubber surfaces. *Langmuir* **29**(50), 15664–15672 (2013)
26. N. Bowden, W.T.S. Huck, K.E. Paul, G.M. Whitesides, The controlled formation of ordered, sinusoidal structures by plasma oxidation of an elastomeric polymer. *Appl. Phys. Lett.* **75**(17), 2557–2559 (1999)
27. D.B.H. Chua, H.T. Ng, S.F.Y. Li, Spontaneous formation of complex and ordered structures on oxygen-plasma-treated elastomeric polydimethylsiloxane. *Appl. Phys. Lett.* **76**(6), 721–723 (2000)
28. C.-C. Fu, A. Grimes, M. Long, C.G.L. Ferri, B.D. Rich, S. Ghosh, S. Ghosh, L.P. Lee, A. Gopinathan, M. Khine, Tunable Nanowrinkles on shape memory polymer sheets. *Adv. Mater.* **21**(44), 4472 (2009)
29. X.M. Zhao, Y.N. Xia, O.J.A. Schueller, D. Qin, G.M. Whitesides, Fabrication of microstructures using shrinkable polystyrene films. *Sens. Actuators A Phys.* **65**(2–3), 209–217 (1998)

30. Y. Zhao, W.M. Huang, Y.Q. Fu, Formation of micro/nano-scale wrinkling patterns atop shape memory polymers. *J. Micromech. Microeng.* **21**(6) (2011)
31. M.D. Huntington, C.J. Engel, A.J. Hryn, T.W. Odom, Polymer Nanowrinkles with continuously tunable wavelengths. *ACS Appl. Mater. Interfaces* **5**(13), 6438–6442 (2013)
32. P. Kim, M. Abkarian, H.A. Stone, Hierarchical folding of elastic membranes under biaxial compressive stress. *Nat. Mater.* **10**(12), 952–957 (2011)
33. A. Verma, A. Sharma, G.U. Kulkarni, Ultrafast large-area micropattern generation in nonabsorbing polymer thin films by pulsed laser diffraction. *Small* **7**(6), 758–765 (2011)
34. M.-W. Moon, S.H. Lee, J.-Y. Sun, K.H. Oh, A. Vaziri, J.W. Hutchinson, Wrinkled hard skins on polymers created by focused ion beam. *Proc. Natl. Acad. Sci. U. S. A.* **104**(4), 1130–1133 (2007)
35. N. Bowden, S. Brittain, A.G. Evans, J.W. Hutchinson, G.M. Whitesides, Spontaneous formation of ordered structures in thin films of metals supported on an elastomeric polymer. *Nature* **393**(6681), 146–149 (1998)
36. W.T.S. Huck, N. Bowden, P. Onck, T. Pardoan, J.W. Hutchinson, G.M. Whitesides, Ordering of spontaneously formed buckles on planar surfaces. *Langmuir* **16**(7), 3497–3501 (2000)
37. P.J. Yoo, K.Y. Suh, H. Kang, H.H. Lee, Polymer elasticity-driven wrinkling and coarsening in high temperature buckling of metal-capped polymer thin films. *Phys. Rev. Lett.* **93**(3) (2004)
38. S.J. Kwon, P.J. Yoo, H.H. Lee, Wave interactions in buckling: Self-organization of a metal surface on a structured polymer layer. *Appl. Phys. Lett.* **84**(22), 4487–4489 (2004)
39. P.J. Yoo, S.Y. Park, S.J. Kwon, K.Y. Suh, H.H. Lee, Microshaping metal surfaces by wave-directed self-organization. *Appl. Phys. Lett.* **83**(21), 4444–4446 (2003)
40. P.J. Yoo, H.H. Lee, Evolution of a stress-driven pattern in thin bilayer films: Spinodal wrinkling. *Phys. Rev. Lett.* **91**(15) (2003)
41. H. Vandeparre, S. Gabriele, F. Brau, C. Gay, K.K. Parker, P. Damman, Hierarchical wrinkling patterns. *Soft Matter* **6**(22), 5751–5756 (2010)
42. C.M. Stafford, B.D. Vogt, C. Harrison, D. Julthongpiput, R. Huang, Elastic moduli of ultrathin amorphous polymer films. *Macromolecules* **39**(15), 5095–5099 (2006)
43. K.Y. Suh, S.M. Seo, P.J. Yoo, H.H. Lee, Formation of regular nanoscale undulations on a thin polymer film imprinted by a soft mold. *J. Chem. Phys.* **124**(2) (2006)
44. M. Watanabe, H. Shirai, T. Hirai, Wrinkled polypyrrole electrode for electroactive polymer actuators. *J. Appl. Phys.* **92**(8), 4631–4637 (2002)
45. J. Yang, S. Damle, S. Maiti, S.S. Velankar, Stretching-induced wrinkling in plastic–rubber composites. *Soft Matter* **13**(4), 776–787 (2017)
46. D. Rhee, W.K. Lee, T.W. Odom, Crack-free, soft wrinkles enable switchable anisotropic wetting. *Angew. Chem. Int. Ed.* **56**(23), 6523–6527 (2017)
47. T. Boudou, T. Crouzier, K. Ren, G. Blin, C. Picart, Multiple functionalities of polyelectrolyte multilayer films: New biomedical applications. *Adv. Mater.* **22**(4), 441–467 (2010)
48. Y. Wang, A.S. Angelatos, F. Caruso, Template synthesis of nanostructured materials via layer-by-layer assembly. *Chem. Mater.* **20**(3), 848–858 (2008)
49. Z. Tang, Y. Wang, P. Podsiadlo, N.A. Kotov, Biomedical applications of layer-by-layer assembly: From biomimetics to tissue engineering. *Adv. Mater.* **18**(24), 3203–3224 (2006)
50. P.T. Hammond, Form and function in multilayer assembly: New applications at the nanoscale. *Adv. Mater.* **16**(15), 1271–1293 (2004)
51. C. Lu, H. Mohwald, A. Fery, A lithography-free method for directed colloidal crystal assembly based on wrinkling. *Soft Matter* **3**(12), 1530–1536 (2007)
52. J. Kim, H.H. Lee, Wave formation by heating in thin metal film on an elastomer. *J. Polym. Sci. B Polym. Phys.* **39**(11), 1122–1128 (2001)
53. T. Okayasu, H.L. Zhang, D.G. Bucknal, G. Andrew, D. Briggs, Spontaneous formation of ordered lateral patterns in polymer thin-film structures. *Adv. Funct. Mater.* **14**(11), 1081–1088 (2004)
54. P.J. Yoo, Invited paper: Fabrication of complexly patterned wavy structures using self-organized anisotropic wrinkling. *Electron. Mater. Lett.* **7**(1), 17–23 (2011)

55. P.J. Yoo, H.H. Lee, Complex pattern formation by adhesion-controlled anisotropic wrinkling. *Langmuir* **24**(13), 6897–6902 (2008)
56. C. Jiang, S. Singamaneni, E. Merrick, V.V. Tsukruk, Complex buckling instability patterns of nanomembranes with encapsulated gold nanoparticle arrays. *Nano Lett.* **6**(10), 2254–2259 (2006)
57. T.R. Hendricks, I. Lee, Wrinkle-free nanomechanical film: Control and prevention of polymer film buckling. *Nano Lett.* **7**(2), 372–379 (2006)
58. D. Mertz, J. Hemmerlé, J. Mutterer, S. Ollivier, J.-C. Voegel, P. Schaaf, P. Lavalley, Mechanically responding Nanovalves based on polyelectrolyte multilayers. *Nano Lett.* **7**(3), 657–662 (2007)
59. C.M. Stafford, C. Harrison, K.L. Beers, A. Karim, E.J. Amis, M.R. Vanlandingham, H.C. Kim, W. Volksen, R.D. Miller, E.E. Simonyi, A buckling-based metrology for measuring the elastic moduli of polymeric thin films. *Nat. Mater.* **3**(8), 545–550 (2004)
60. A.J. Nolte, M.F. Rubner, R.E. Cohen, Determining the young's modulus of polyelectrolyte multilayer films via stress-induced mechanical buckling instabilities. *Macromolecules* **38**(13), 5367–5370 (2005)
61. R.C. Hedden, H. Saxena, C. Cohen, Mechanical properties and swelling behavior of end-linked poly(diethylsiloxane) networks. *Macromolecules* **33**(23), 8676–8684 (2000)
62. K. Efimenko, M. Rackaitis, E. Manias, A. Vaziri, L. Mahadevan, J. Genzer, Nested self-similar wrinkling patterns in skins. *Nat. Mater.* **4**(4), 293 (2005)
63. T. Ohzono, M. Shimomura, Ordering of microwrinkle patterns by compressive strain. *Phys. Rev. B* **69**(13), 132202 (2004)
64. T. Ohzono, M. Shimomura, Geometry-dependent stripe rearrangement processes induced by strain on preordered microwrinkle patterns. *Langmuir* **21**(16), 7230–7237 (2005)
65. P.-C. Lin, S. Yang, Spontaneous formation of one-dimensional ripples in transit to highly ordered two-dimensional herringbone structures through sequential and unequal biaxial mechanical stretching. *Appl. Phys. Lett.* **90**(24), 241903 (2007)
66. W.M. Choi, J. Song, D.-Y. Khang, H. Jiang, Y.Y. Huang, J.A. Rogers, Biaxially stretchable “wavy” silicon nanomembranes. *Nano Lett.* **7**(6), 1655–1663 (2007)
67. H.S. Kim, A.J. Crosby, Solvent-responsive surface via wrinkling instability. *Adv. Mater.* **23**(36), 4188 (2011)
68. E.P. Chan, A.J. Crosby, Fabricating microlens arrays by surface wrinkling. *Adv. Mater.* **18**(24), 3238–3242 (2006)
69. J.Y. Chung, J.-H. Lee, K.L. Beers, C.M. Stafford, Stiffness, strength, and ductility of nanoscale thin films and membranes: A combined wrinkling–cracking methodology. *Nano Lett.* **11**(8), 3361–3365 (2011)
70. J.Y. Chung, A.J. Nolte, C.M. Stafford, Diffusion-controlled, self-organized growth of symmetric wrinkling patterns. *Adv. Mater.* **21**(13), 1358–1362 (2009)
71. E.P. Chan, E.J. Smith, R.C. Hayward, A.J. Crosby, Surface wrinkles for smart adhesion. *Adv. Mater.* **20**(4), 711–716 (2008)
72. D. Breid, A.J. Crosby, Surface wrinkling behavior of finite circular plates. *Soft Matter* **5**(2), 425–431 (2009)
73. H. Vandeparre, P. Damman, Wrinkling of stimuloresponsive surfaces: Mechanical instability coupled to diffusion. *Phys. Rev. Lett.* **101**(12), 124301 (2008)
74. H. Vandeparre, J. Léopoldès, C. Poulard, S. Desprez, G. Derue, C. Gay, P. Damman, Slippery or sticky boundary conditions: Control of wrinkling in metal-capped thin polymer films by selective adhesion to substrates. *Phys. Rev. Lett.* **99**(18), 188302 (2007)
75. S.K. Basu, A.V. McCormick, L.E. Scriven, Stress generation by solvent absorption and wrinkling of a cross-linked coating atop a viscous or elastic base. *Langmuir* **22**(13), 5916–5924 (2006)
76. H.S. Kim, A.J. Crosby, Solvent-responsive surface via wrinkling instability. *Adv. Mater.* **23**(36), 4188–4192 (2011)

77. M. Guvendiren, S. Yang, J.A. Burdick, Swelling-induced surface patterns in hydrogels with gradient crosslinking density. *Adv. Funct. Mater.* **19**(19), 3038–3045 (2009)
78. M. Guvendiren, J.A. Burdick, S. Yang, Kinetic study of swelling-induced surface pattern formation and ordering in hydrogel films with depth-wise crosslinking gradient. *Soft Matter* **6**(9), 2044–2049 (2010)
79. S. Basu, L.E. Scriven, L.F. Francis, A.V. McCormick, Mechanism of wrinkle formation in curing coatings. *Prog. Org. Coat.* **53**(1), 1–16 (2005)
80. S. Yang, K. Khare, P.-C. Lin, Harnessing surface wrinkle patterns in soft matter. *Adv. Funct. Mater.* **20**(16), 2550–2564 (2010)
81. D. Chandra, A.J. Crosby, Self-wrinkling of UV-cured polymer films. *Adv. Mater.* **23**(30), 3441–3445 (2011)
82. Y. Li, J.J. Peterson, S.B. Jhaveri, K.R. Carter, Patterned polymer films via reactive Silane infusion-induced wrinkling. *Langmuir* **29**(14), 4632–4639 (2013)
83. S. Basu, L.E. Scriven, L.F. Francis, A.V. McCormick, V. Reichert, Wrinkling of epoxy powder coatings. *J. Appl. Polym. Sci.* **98**(1), 116–129 (2005)
84. J.M. Torres, C.M. Stafford, B.D. Vogt, Photoinitiator surface segregation induced instabilities from polymerization of a liquid coating on a rigid substrate. *Soft Matter* **8**(19), 5225–5232 (2012)
85. Y. Gan, X. Jiang, J. Yin, Self-wrinkling patterned surface of photocuring coating induced by the fluorinated POSS containing thiol groups (F-POSS-SH) as the reactive Nanoadditive. *Macromolecules* **45**(18), 7520–7526 (2012)
86. R. Schubert, T. Scherzer, M. Hinkefuss, B. Marquardt, J. Vogel, M.R. Buchmeiser, VUV-induced micro-folding of acrylate-based coatings. I. Real-time methods for the determination of the micro-folding kinetics. *Surf. Coat. Technol.* **203**(13), 1844–1849 (2009)
87. T. Tanaka, S.T. Sun, Y. Hirokawa, S. Katayama, J. Kucera, Y. Hirose, T. Amiya, Mechanical instability of gels at the phase-transition. *Nature* **325**(6107), 796–798 (1987)
88. E.S. Matsuo, T. Tanaka, Patterns in shrinking gels. *Nature* **358**(6386), 482–485 (1992)
89. T. Mizoue, Y. Aoki, M. Tokita, H. Honjo, H.J. Barraza, H. Katsuragi, Control of polymer gel surface pattern formation and its three dimensional measurement method. *J. Polym. Eng.* **30**(9), 523–534 (2010)
90. T. Mizoue, M. Tokita, H. Honjo, H.J. Barraza, H. Katsuragi, The effective surface roughness scaling of the gelation surface pattern formation, in *Gels: Structures, Properties, and Functions: Fundamentals and Applications*, ed. by M. Tokita, K. Nishinari (Springer, Berlin, 2009), pp. 63–67
91. M. Tokita, S. Suzuki, K. Miyamoto, T. Komai, Confocal laser scanning microscope imaging of a pattern in shrinking gel. *J. Phys. Soc. Jpn.* **68**(2), 330–333 (1999)
92. M. Tokita, K. Miyamoto, T. Komai, Polymer network dynamics in shrinking patterns of gels. *J. Chem. Phys.* **113**(4), 1647–1650 (2000)
93. E.P. Chan, E.J. Smith, R.C. Hayward, A.J. Crosby, Surface wrinkles for smart adhesion. *Adv. Mater.* **20**(4), 711 (2008)
94. K. Huraux, T. Narita, B. Bresson, C. Frétygny, F. Lequeux, Wrinkling of a nanometric glassy skin/crust induced by drying in poly (vinyl alcohol) gels. *Soft Matter* **8**(31), 8075–8081 (2012)
95. B. Li, Y.-P. Cao, X.-Q. Feng, H. Gao, Mechanics of morphological instabilities and surface wrinkling in soft materials: A review. *Soft Matter* **8**(21), 5728–5745 (2012)
96. E.S. Matsuo, T. Tanaka, Patterns in shrinking gels. *Nature* **358**(6386), 482 (1992)
97. L. Pauchard, C. Allain, Stable and unstable surface evolution during the drying of a polymer solution drop. *Phys. Rev. E* **68**(5), 052801 (2003)
98. L. Pauchard, C. Allain, Buckling instability induced by polymer solution drying. *Europhys. Lett.* **62**(6), 897–903 (2003)
99. R. Rizzieri, L. Mahadevan, A. Vaziri, A. Donald, Superficial wrinkles in stretched, drying gelatin films. *Langmuir* **22**(8), 3622–3626 (2006)

100. J.M. Katzenstein, D.W. Janes, J.D. Cushen, N.B. Hira, D.L. McGuffin, N.A. Prisco, C.J. Ellison, Patterning by photochemically directing the Marangoni effect. *ACS Macro Lett.* **1**(10), 1150–1154 (2012)
101. A.R. Jones, C.B. Kim, S.X. Zhou, H. Ha, R. Katsumata, G. Blachut, R.T. Bonnacaze, C.J. Ellison, Generating large thermally stable Marangoni-driven topography in polymer films by stabilizing the surface energy gradient. *Macromolecules* **50**(11), 4588–4596 (2017)
102. B.K. Chae, D.W. Janes, D.L. McGuffin, C.J. Ellison, Surface energy gradient driven convection for generating nanoscale and microscale patterned polymer films using photosensitizers. *J. Polym. Sci. B Polym. Phys.* **52**(18), 1195–1202 (2014)
103. A. Lasagni, C. Holzapfel, F. Mücklich, Periodic pattern formation of intermetallic phases with long range order by laser interference metallurgy. *Adv. Eng. Mater.* **7**(6), 487–492 (2005)
104. F. Mücklich, A. Lasagni, C. Daniel, Laser interference metallurgy—Periodic surface patterning and formation of intermetallics. *Intermetallics* **13**(3–4), 437–442 (2005)
105. A.F. Lasagni, D.F. Acevedo, C.A. Barbero, F. Mücklich, One-step production of organized surface architectures on polymeric materials by direct laser interference patterning. *Adv. Eng. Mater.* **9**(1–2), 99–103 (2007)
106. F. Yu, P. Li, H. Shen, S. Mathur, C.-M. Lehr, U. Bakowsky, F. Mücklich, Laser interference lithography as a new and efficient technique for micropatterning of biopolymer surface. *Biomaterials* **26**(15), 2307–2312 (2005)
107. D.A. Acevedo, A.F. Lasagni, C.A. Barbero, F. Mücklich, Simple fabrication method of conductive polymeric arrays by using direct laser interference micro-/Nanopatterning. *Adv. Mater.* **19**(9), 1272–1275 (2007)
108. A. Lasagni, D. Acevedo, C. Barbero, F. Mücklich, Advanced design of conductive polymeric arrays with controlled electrical resistance using direct laser interference patterning. *Appl. Phys. A* **91**(3), 369–373 (2008)
109. A.F. Lasagni, J.L. Hendricks, C.M. Shaw, D. Yuan, D.C. Martín, S. Das, Direct laser interference patterning of poly (3, 4-ethylene dioxythiophene)-poly (styrene sulfonate)(PEDOT-PSS) thin films. *Appl. Surf. Sci.* **255**(22), 9186–9192 (2009)
110. A. Lasagni, D. Acevedo, C. Barbero, F. Mücklich, Direct patterning of polystyrene–polymethyl methacrylate copolymer by means of laser interference lithography using UV laser irradiation. *Polym. Eng. Sci.* **48**(12), 2367–2372 (2008)
111. E. Rebollar, S. Pérez, J.J. Hernández, I. Martín-Fabiani, D.R. Rueda, T.A. Ezquerro, M. Castillejo, Assessment and formation mechanism of laser-induced periodic surface structures on polymer spin-coated films in real and reciprocal space. *Langmuir* **27**(9), 5596–5606 (2011)
112. E. Rebollar, D.R. Rueda, I. Martín-Fabiani, Á. Rodríguez-Rodríguez, M.-C. García-Gutiérrez, G. Portale, M. Castillejo, T.A. Ezquerro, In situ monitoring of laser-induced periodic surface structures formation on polymer films by grazing incidence small-angle X-ray scattering. *Langmuir* **31**(13), 3973–3981 (2015)
113. Á. Rodríguez-Rodríguez, E. Rebollar, M. Soccio, T.A. Ezquerro, D.R. Rueda, J.V. Garcia-Ramos, M. Castillejo, M.-C. Garcia-Gutierrez, Laser-induced periodic surface structures on conjugated polymers: Poly(3-hexylthiophene). *Macromolecules* **48**(12), 4024–4031 (2015)
114. I. Michaljaníčová, P. Slepíčka, S. Rimpelová, N. Slepíčková Kasálková, V. Švorčík, Regular pattern formation on surface of aromatic polymers and its cytocompatibility. *Appl. Surf. Sci.* **370**, 131–141 (2016)
115. Z. Guosheng, P. Fauchet, A. Siegman, Growth of spontaneous periodic surface structures on solids during laser illumination. *Phys. Rev. B* **26**(10), 5366 (1982)
116. A. Barborica, I. Mihailescu, V. Teodorescu, Dynamical evolution of the surface microrelief under multiple-pulse-laser irradiation: An analysis based on surface-scattered waves. *Phys. Rev. B* **49**(12), 8385 (1994)
117. S. Baudach, J. Bonse, W. Kautek, Ablation experiments on polyimide with femtosecond laser pulses. *Appl. Phys. A* **69**(1), S395–S398 (1999)

118. S. Baudach, J. Krüger, W. Kautek, Femtosecond laser processing of soft materials. *Rev. Laser Eng.* **29**(11), 705–709 (2001)
119. M. Forster, W. Kautek, N. Faure, E. Audouard, R. Stoian, Periodic nanoscale structures on polyimide surfaces generated by temporally tailored femtosecond laser pulses. *Phys. Chem. Chem. Phys.* **13**(9), 4155–4158 (2011)
120. W. Biegel, *D. Bliuerle Laser Processing and Chemistry* (Springer, Berlin/Heidelberg/New York, 1996). ISBN: 3-540-60541-X, DM 128, 00. *Berichte der Bunsengesellschaft für physikalische Chemie* **101**(6), 984–984 (1997)
121. E. Rebollar, J.R.V. de Aldana, I. Martín-Fabiani, M. Hernández, D.R. Rueda, T.A. Ezquerro, C. Domingo, P. Moreno, M. Castillo, Assessment of femtosecond laser induced periodic surface structures on polymer films. *Phys. Chem. Chem. Phys.* **15**(27), 11287–11298 (2013)

**Part II**  
**Novel Approaches for Wrinkled Patterns**  
**Formation**

# Chapter 3

## Wrinkles Obtained by Frontal Polymerization/Vitrification



C. M. González-Henríquez, M. A. Sarabia Vallejos,  
and Juan Rodríguez-Hernández

### 3.1 Introduction

Frontal vitrification or frontal polymerization (FP) is a methodology in which the polymerization occurs in only one direction in a localized and specific reaction zone, thus generating the so-called polymerization front which moves through the material until it is completely polymerized. The first record of FP method in the literature was reported by Chechilo et al. [1] in the year 1972, which studied an adiabatic system of methyl methacrylate (MMA) subjected to high pressure. Under these conditions, a self-propagating synthesis at high temperature was discovered, which was later coined as FP. There are three main types of FP according to Pojman [2]. The first one and, by far, the most widely used in the last years is photofrontal polymerization [3–5]. In this methodology, the polymerization front is continuously propagated in a unidirectional radiation flux; usually, a UV lamp is used as radiation source. The second methodology is known as isothermal frontal polymerization [6, 7]; this method is based on the gelification capacity of some

---

C. M. González-Henríquez

Departamento de Química, Facultad de Ciencias Naturales, Matemáticas y del Medio Ambiente, Universidad Tecnológica Metropolitana, Santiago, Chile

Programa Institucional de Fomento a la Investigación, Desarrollo e Innovación, Universidad Tecnológica Metropolitana, Santiago, Chile

M. A. Sarabia Vallejos (✉)

Escuela de Ingeniería, Departamento de Ingeniería Estructural y Geotecnia, Pontificia Universidad Católica de Chile, Santiago, Chile

Instituto de Ingeniería Biológica y Médica, Santiago, Chile

e-mail: [masarabi@uc.cl](mailto:masarabi@uc.cl)

J. Rodríguez-Hernández

Polymer Functionalization Group. Instituto de Ciencia y Tecnología de Polímeros-Consejo Superior de Investigaciones Científicas (ICTP-CSIC), Departamento de Química Macromolecular Aplicada, Madrid, Spain

materials with the finality to create localized reaction zones which propagate slowly through the polymer. The third type of FP is the so-called thermal frontal polymerization [8], which results from a combination of thermal transport and Arrhenius reaction rate dependence; this type of polymerization generates an exothermic reaction. There also exists a fourth one, which is not considered in the article of Pojman, which is called as plasma-ignited frontal polymerization [9]. This kind of methodology is commonly used in several applications related to the generation of wrinkled patterns by taking advantage of surface instabilities.

There are also other types of frontal polymerizations which do not correspond to any of the other types mentioned before, like the so-called radical induced cationic frontal polymerization [10]; this methodology is based on a complex synthetic process which involves a cationic free radical reaction that forms a high reactive superacid in the monomer that subsequently polymerizes in an exothermic reaction. The resulting heat induces a thermopolymerization in the unreacted zone of the material, generating a second radical which cleaves the photoinitiator forming another superacid, like the previously mentioned, that starts the exothermic reaction in the adjacent region (polymerization front). Other research groups, for example, Crivello et al. [11], mix two of the methodologies mentioned by Pojman in order to develop a dual photo- and thermally initiated frontal polymerizations. The same group of Crivello et al. [12, 13] design a photoactivated cationic ring-opening FP; the application of this method has a deep impact on various molecular (structural and experimental) parameters, which permit to create adhesives that can be photoactivated and then used for the rapid bonding of opaque substrates.

Most of the studies reported in the literature use photofrontal or plasma-ignited frontal polymerization for generating wrinkled patterns by taking advantage of surface instabilities [14], so these two methodologies will be fully explained next.

### ***3.1.1 Photofrontal Polymerization***

In general, this type of polymerization uses a continuous radiation input, which, as was mentioned before, is usually UV light [15]. In most of the cases, it is necessary to add a photoinitiator to the mixture in order to trigger the polymerization reaction. The front propagation rate depends on several reaction parameters such as the photoinitiator concentration, radiation dose applied, or physical properties of the compounds (monomers) used, among others. Photofrontal polymerization is a versatile synthesis method which has been used in numerous research fields, including prosthetic materials [16], adhesive applications [17], microfluidics [18], etc.

This methodology has been used for various decades; one of the first academic articles which report a similar protocol was published by the group of Koike and Ohtsuka et al. [19, 20] in the year 1984. In these studies, they fabricate a light-focusing plastic rod through two-step copolymerization and photopolymerization processes by using different monomer mixtures based on MMA and vinyl bromide (VB) with other components. The most interesting aspect of these articles is that,

besides they were one of the first to report this methodology, the physicochemical process involved in the polymerization is deeply characterized and some important findings of the front propagation kinetics are clarified. In the year 2013, Yang et al. [15] reported a photo-triggered method to generate an FP process by a redox reaction of thermally sensitive monomers. This novel approach integrates a photocaged superbases (QA-DBU) with a peroxide initiator (dibenzoyl peroxide, BPO); the mixture of these two components generates an effectively actuate redox FP in a diffusion-controlled manner inside the material. By changing the front velocity and the concentration of the superbases, it is possible to control the temperature of the polymerization front. Compared with conventional free radical initiators, redox ones possess lower activation energy, short induction period, and high initiating capability. According to this, the thermally sensitive polymer synthesized through this novel methodology exhibits enhanced fluorescence emission intensity compared to that synthesized with conventional thermal FP. In this case, a mixture of trimethylolpropane triacrylate (TMPTA), 1,6-hexanediol diacrylate (HDDA), tri(propylene glycol) diacrylate (TPGDA), and isobornyl acrylate (IBOA) was synthesized by using this novel approach; a fluorescent brightener was also added to the mixture in order to characterize their fluorescence capacity. In Fig. 3.1 (left) is depicted a schematic representation of the methodology proposed by Yang et al. At the right are depicted some results which demonstrate the improvement on fluorescence capability generated by using this method on thermosensitive polymers.

In general, an analytical expression for the front speed of the localized traveling wave can be determined with the next equation, reported by Terrones and Pearlstein in the year 2001 [21], which is an approximation obtained from a model of free radical photopolymerization with a photobleaching initiator:

$$\text{Frontspeed} = \frac{\phi I_0}{C_{A,0}}$$

where  $\phi$ ,  $I_0$ , and  $C_{A,0}$  are the quantum yield of the photoinitiator, incident intensity, and photoinitiator concentration, respectively.

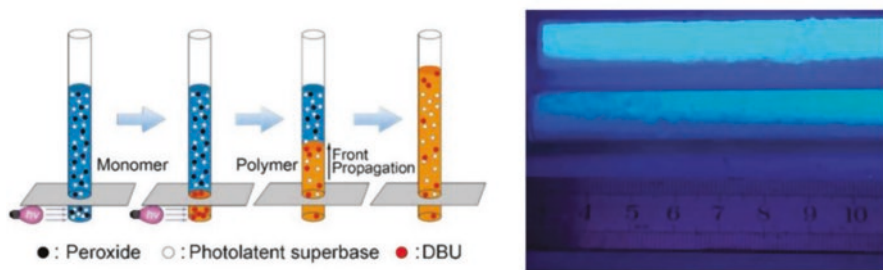


**Fig. 3.1** (Left) Schematic representation of the photo-triggered ascending redox FP. (Right) Photographs of fluorescent polymer composites prepared with redox and conventional FP methodologies. (Reproduced with permission from Ref. [15])

UV-triggered frontal polymerization is not the only way to produce photofrontal polymerization; there also exist other types of radiation sources that are used to polymerize materials like the methodology called IR laser-ignited frontal polymerization [22, 23]. In the article of Chen et al. [22], the synthesis of a hydrogel based on *poly*(N-methylolacrylamide-*co*-N-vinylcaprolactam) and *poly*(NMA-*co*-VCL) was produced via IR laser-ignited FP. The swelling capacity of the hydrogels synthesized through this methodology was higher than the produced via conventional thermal FP. In this case, the temperature of the polymerization front was also characterized, and it was found that it has an important effect on propagation velocity. More interestingly, the frontal reaction can be triggered via long-range IR laser irradiation. The experiments show that FP reactions can be triggered from 15 m away, but in theory, it could be from longer distances. The hydrogels polymerized through this procedure also show a change in its structure compared with those produced via thermal FP. Attenuated total reflectance FT-IR (ATR FT-IR) shows a new absorption peak at  $842\text{ cm}^{-1}$  in the case of laser-ignited FP, a band which is characteristic of the hydroxymethyl group self-cross-linking reaction. This process can be explained via the fact that IR laser induces hydroxyl ( $-\text{OH}$ ) groups oxidation into carbonyl or carboxyl groups during the FP process.

### 3.1.2 Plasma-Ignited Frontal Polymerization

The first group which synthesizes polymers via FP by using plasma as initiation stimulus was the group of Chen et al. in the year 2010 [24]; this method takes advantage on the electron energy of the plasma to trigger the reaction. They were responsible for coining this method as plasma-ignited frontal polymerization. In this article, hydrogels based on N-vinylpyrrolidone (NVP) and N-methylolacrylamide (NMA) were synthesized by igniting the upper part of the mixture with air plasma. Two photographs are shown in Fig. 3.2 which explain the procedure involved in plasma-ignited FP. It is important to mention that air plasma is only necessary to initiate the reaction, and then the polymerization propagates through the material without external energy application. In the left part of Fig. 3.2 is shown the exact moment of plasma activation, and then, in the right section of Fig. 3.2 is depicted the polymerization front generated by this method. In comparison with traditional FP methods, plasma-ignited FP is furthermore time-saving and convenient.

In later studies, the group of Chen et al. performs several experiments related to plasma-ignited FP. Some of these studies are, for example, the creation of amphiphilic gels based on 2-hydroxypropyl acrylate (HPA) and vinyl versatate (VeoVa 10) with enhanced physicochemical properties for industrial wastewater treatment applications [25] and the synthesis of white light-emitting polymers based on cadmium sulfide (CdS), 2-hydroxyethyl acrylate (HEA), and N-vinylcarbazole (NVK) which could be used for quantum dot (QD) or light-emitting diode (LED) applications. In a recent article, the group of Chen et al. [26] reports an ease synthesis of superabsorbent polyampholytic hydrogels based on N-vinylimidazole (VI) and



**Fig. 3.2** Setup of plasma-ignited FP; the photographs show two different moments of the methodology, (left) initiation via air plasma and (right) polymerization front propagation. (Reproduced with permission from Ref. [24])

methacrylic acid (MAA). CdS nanocrystals were included in the polymer matrix, generating fluorescent hydrogels with potential applications in biosensing or other related topics. The main advantage of this methodology is the reaction time required to obtain a fully polymerized material. Instead of conventional FP methods, plasma-ignited FP just takes a few minutes for finishing the polymerization.

### 3.2 Examples of Wrinkled Patterns Generated by FP

According to Rodríguez-Hernández [14], the generation of surface-wrinkled patterns can be achieved via three different methodologies: (1) by creating a layered system, (2) by using homogeneous films, or (3) by taking advantage of gradient systems (Fig. 3.3). The third case is intimately related to FP processes because it is possible to generate a polymerization gradient instead of a defined polymerization front in the material via the variation of synthesis parameters, like initiators or monomer nature, among others.

According to this, it is possible to generate a polymerization gradient from the top to the bottom of the film via FP methods and, thus, produce surface instabilities caused by the interaction of a rigid top film (fully polymerized material) and a soft foundation (less or non-polymerized material). These “layers” present slight differences in their mechanical or thermal behavior but enough to depict different performances under certain controlled conditions. Subsequently, the wrinkled pattern generation could be triggered via an external stimulus like mechanical strain/release, swelling/deswelling, thermal exposure, etc. Several methodologies which use frontal polymerization to create wrinkled patterns on surfaces are reported in the literature; some remarkable examples are depicted next.

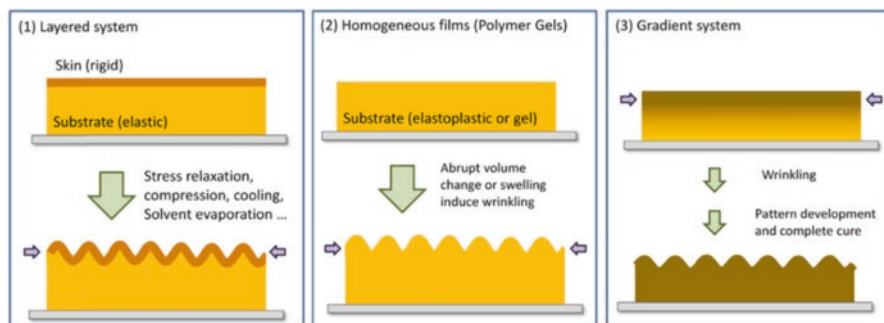


**Fig. 3.3** Schematic description of the three main methods used to generate wrinkled patterns through surface instabilities. (Reproduced with permission from Ref. [14])

### 3.2.1 Via Photofrontal Polymerization

An interesting example is reported by the group of Kloxin et al. in the year 2013 [4]. They employ a two-stage polymerization strategy in which firstly an elastomer is synthesized using a stoichiometric imbalance of tetra-thiol and diacrylate monomers forming a polymer network with an excess of acrylate functional groups. The second photopolymerization was carried out via UV exposure, which increases cross-link density in the material. This second step is restricted to the elastomer surface, thus generating variable polymerization degrees in the different strata of the film due to the sequential reaction produced acrylate groups present in the material. The polymerization front advance is controlled with the insertion of a photoabsorber to the reaction mixture (Tinuvin 328); this compound is in charge of confining the photopolymerization of the acrylate pendant groups to a thin layer (skin) on the top of the film. This process finally creates a polymerization gradient in the material through a controlled photofrontal mechanism. Prior to photopolymerization, the material was stretched until a predetermined strain (20%). After finalizing the UV exposure, the strain is released, thus triggering the wrinkled pattern formation. In this article, the UV dosing time was varied from 5 to 40 s, showing an increment in wrinkle pattern wavelength and amplitude. In Fig. 3.4 are depicted some illustrations which schematically explain the procedure proposed by Kloxin et al.

In parallel, the approach exhibited by Kloxin et al., of using photofrontal polymerization to form wrinkles, enables an interesting application which is the spatioselective control of the wrinkle generation, i.e., this methodology permits them to create well-defined boundaries for wrinkle confinement by using photomasks during UV exposure. Figure 3.5 shows some of the intricate patterns which can be produced via this methodology.

There are several examples in the literature on the last years of studies which use UV gradient photopolymerization methods with the finality to generate wrinkled patterns. As an example, in the year 2014, Jiang et al. [27], by using a mixture of acrylate cross-linkers and hydrophobic copolymers, fabricated a liquid resin film

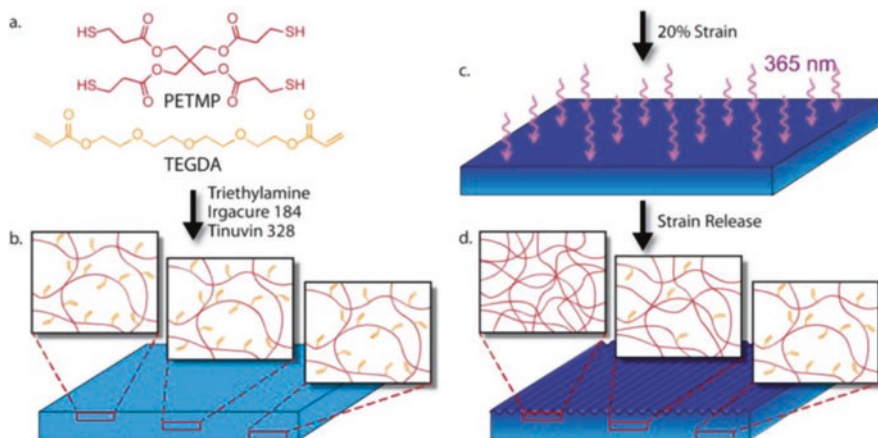


**Fig. 3.4** Illustrations which schematically explain the procedure of gradient photofrontal polymerization generation. (a–b) A mixture of tetra-thiol and diacrylate monomers produces an excess of acrylate groups, (c) which upon strain and UV exposure (d) generate a photopolymerization gradient in the material. (Reproduced with permission from Ref. [4])

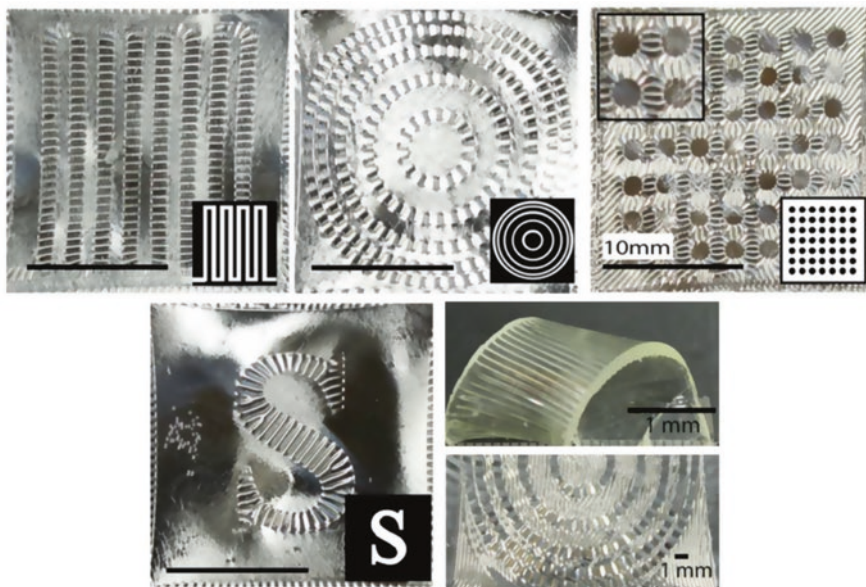


**Fig. 3.5** Photolithography of different patterns using UV masks. All samples were irradiated for 20 s at 80 W/m [2]. (Reproduced with permission from Ref. [4])

which can spontaneously produce a thin layer of fluorinated compounds (fluorinated poly(methyl methacrylate), PMMA-F, and fluorinated poly(butyl acrylate), PBA-F) on the top due to the interface energy between the acrylate monomer and air. Then, the film was photofrontal polymerized, causing a gradient of compressive stresses, resulting in wrinkling pattern generation. Figure 3.6 (top) shows a schematic description of the aftermentioned methodology. By tuning the content of hydrophobic copolymer in the reaction mixture, a series of submicron wrinkling patterns were successfully fabricated. Contact angles were also measured for the wrinkling patterns, showing an increase from  $70^\circ$  to  $135^\circ$  with the addition of fluorinated copolymers. The surface also depicts a self-healing capacity, which was tested by exposing the surface to  $\text{Ar}^+$  sputtering damage. This process decreases the contact angle to  $64^\circ$ , showing an important damage to the fluorinated chains on the surface. After damage, the sample was exposed to a thermal treatment which generates a self-replenishing mechanism in the fluorinated chains, thus increasing the contact angle to  $110^\circ$ . Figure 3.6 (bottom) shows some photographs of the contact angle and a schematic illustration of the proposed mechanism of self-healing.

Crosby and Chandra reported a one-pot approach to fabricate wrinkled patterns by using photofrontal polymerization in the year 2011 [28]. In this article, a UV-curable composite, formed by a mixture of 2-phenoxyethyl acrylate,

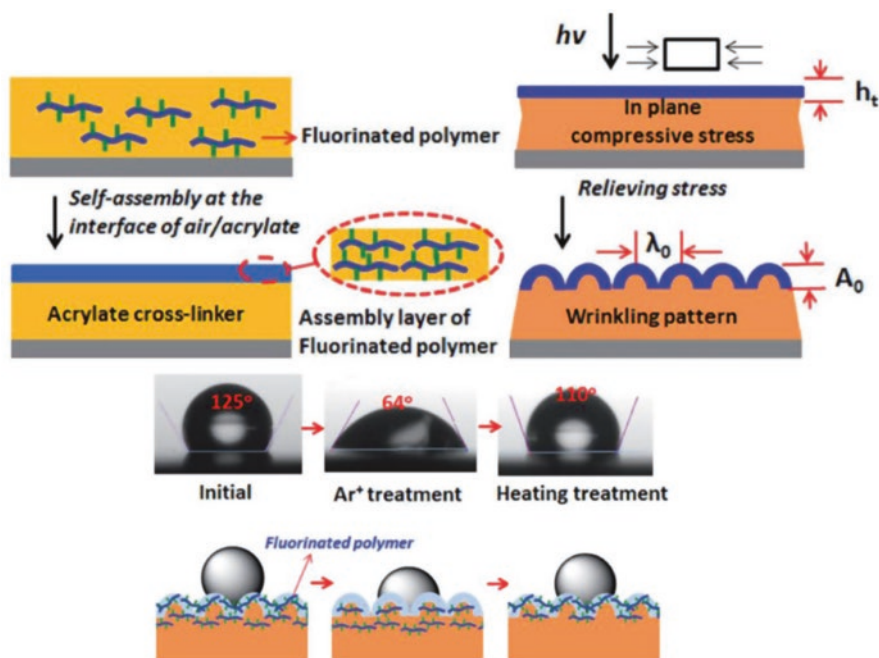


**Fig. 3.6** (Top) Schematic description of the wrinkling formation protocol exposed by Jiang et al. (Bottom) Contact angles which show the self-healing capacity of the material and proposed mechanism of self-replenishing. (Reproduced with permission from Ref. [27])

1,6-hexanediol diacrylate (cross-linker), and Irgacure 184 (photoinitiator), was used to create an uncured liquid layer. Then, induced by oxygen inhibition, the film was photofrontal polymerized, but, due to quenching of free radicals by oxygen presence, a thin liquid layer of uncured monomers was formed on the surface. Finally, after 20 min, this uncured layer is swelled by the underlying polymerized film, thus generating spontaneously wrinkled patterns on the surface. This wrinkling formation mechanism, mediated by photofrontal polymerization, is different from other previously reported because normally it requires two steps to form wrinkles; in this case, only one step is required. Figure 3.7 shows a schematic description of the procedure (left). At the right, a micrograph of the wrinkled pattern is depicted along with a 3D optical profilometer image of the same sector.

Other studies, like those performed by Nagano and Seki et al. [29], use photoresponsive polymers to create wrinkled patterns via photofrontal polymerization. In this article, azobenzene-based polymer layers were transferred to a thick elastomeric substrate (polydimethylsiloxane, PDMS) and then compressed to form wrinkled patterns. UV irradiation was performed on selected sectors, producing unwrinkling due to their photoresponsive behavior of poly(azobenzene) (PAz) which changes their stiffness to a value similar to PDMS. Figure 3.8a shows two micrographs in which the photoresponsive behavior of the film is demonstrated. By taking advantage of this characteristic, the photoresponsive films were UV irradiated

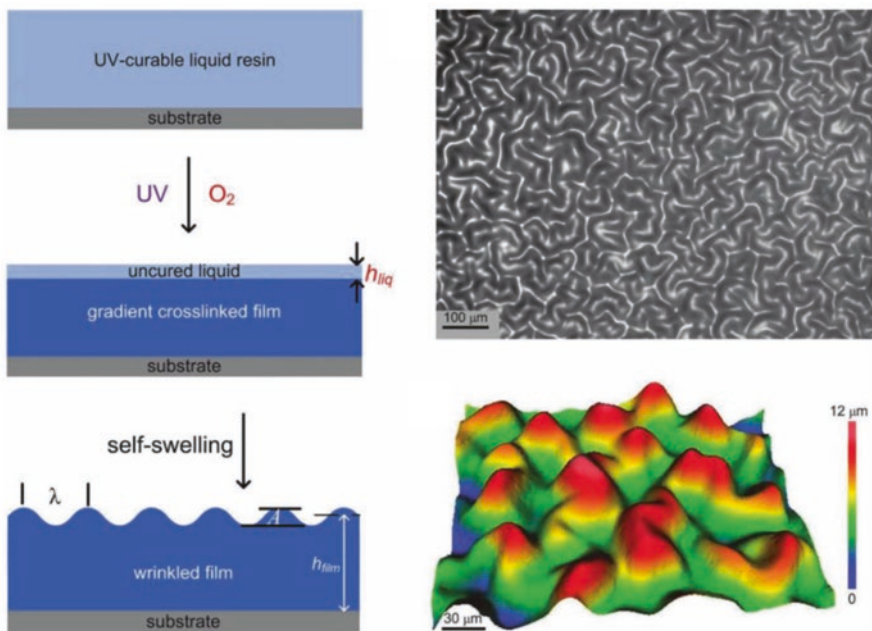


**Fig. 3.7** (Left) Schematic description of the one-step protocol proposed by Crosby and Chandra. (Right) Micrograph and profilometer image of the wrinkled surface obtained through this methodology. (Reproduced with permission from Ref. [28])

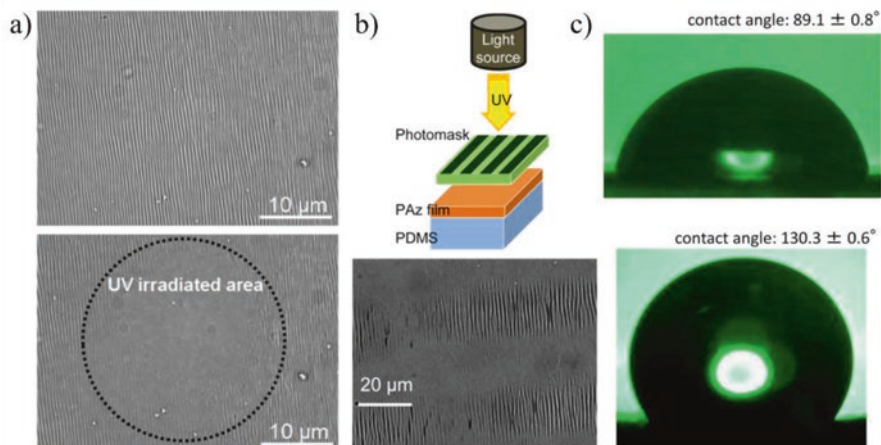


**Fig. 3.8** (a) Microscopy images of sectors before and after UV irradiation, showing their photo-responsive characteristic of Paz. (b) Schematic description of the photomasking procedure. (c) Contact angle images of the wrinkled and unwrinkled surfaces. (Reproduced with permission from Ref. [29])

by using a photomask to selectively create wrinkled or unwrinkled patterns on the surface (Fig. 3.8b). Contact angle was measured in these sectors showing important variations before and after compression, which generates the wrinkled pattern generation (Fig. 3.8c).

More recent examples demonstrate that chemical structure of UV liquid resin used to form the layers influences wrinkled pattern structure. Park et al. [30], in the year 2017, synthesize liquid prepolymer solution based on 2,3,5,6-tetrafluorostyrene and different backbone structures. Films were prepared by spin-coating these solutions on silicon oxide-coated glasses, which were then photofrontal polymerized in order to generate wrinkled patterns. In this article, it was showed that chemical structure produces important changes in wrinkled patterns' amplitude and wavelength. Figure 3.9 shows the different patterns formed according to the prepolymer solution used to create the films.

Another interesting example is reported by Rodríguez-Hernández and Nogales et al. in the year 2016 [31], which modify the surface of PDMS layers to form wrinkled patterns by using ultraviolet ozone (UVO) radiation. A mercury lamp, which emits radiation in 185 and 254 nm, generates simultaneously O atoms when O<sub>2</sub> is dissociated, via 185 nm radiation, and O<sub>3</sub> through association of O<sub>2</sub> and O mediated by radiation at 254 nm. The 254 nm radiation is absorbed by most hydrocarbons and also by ozone. This continuous generation of O<sub>3</sub> can be applied to chemically modify the surface of polymeric materials, like PDMS, which upon UVO exposure forms a layer of stiff silica on the top of the material. The photofrontal polymerization process is performed in a substrate stretched state; once the UVO irradiation concludes, the PDMS is released, and wrinkled patterns are spontaneously formed on the surface. In this article, the chemical modification that

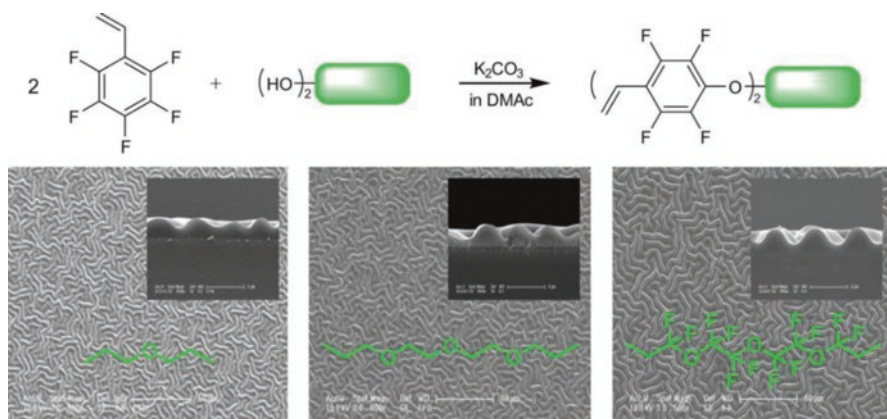


**Fig. 3.9** SEM micrographs of wrinkled patterns formed via photofrontal polymerization method using polymer solutions based on 2,3,5,6-tetrafluorostyrene and different backbone structures. (Reproduced with permission from Ref. [30])

produces UVO exposure on the surface, as well as the effect which generates this variation in wrinkled pattern dimension, was deeply studied. The scientific advance which produces this study relies on the fact that it demonstrated the formation of a 4- $\mu\text{m}$ -thick modified layer, a gradient polymerization front, instead of a thin stiff polymerized layer as was reported in previous works (20–200 nm). Also, local mechanical characterization of the surface was performed; the results show important differences in the mechanical performance when exposed or unexposed UVO sectors were analyzed. Figure 3.10 (top) shows contact angle measurements performed to PDMS surface at different UVO exposure times, showing an important decrease with time increase. On the bottom, an AFM micrograph of a photomask surface is showed (left); in parallel, the local elastic modulus is also depicted in the image at the right.

As it was mentioned in the previous section, UV is not the only way to generate photofrontal polymerization. Accordingly, other methods of photofrontal polymerization are used to create wrinkled patterns. As an example, Zhao et al. [32] reported a study in which a spatially controllable wrinkled pattern was produced by using a focused  $\text{CO}_2$  laser (with a spot size of 127  $\mu\text{m}$ ) over PDMS substrates. This method provides the possibility of creating micropatterns in large areas, without the necessity of incurring in much high costs. Wrinkled micropatterns with wavelengths ranging between 50 and 300  $\mu\text{m}$  were obtained in few minutes using this methodology. To reduce surface cracking, a typical problem in large-area micropatterning, the laser path was created in order to separate neighboring laser exposure areas with intercalated non-exposure gaps. In Fig. 3.11 (top) is depicted a schematic diagram of the process developed in this article. In the middle, some photographs of wrinkled patterns at different laser scan widths are shown. As is possible to observe, wrinkle wavelength tends to increase with laser scan width (Fig. 3.11, bottom).

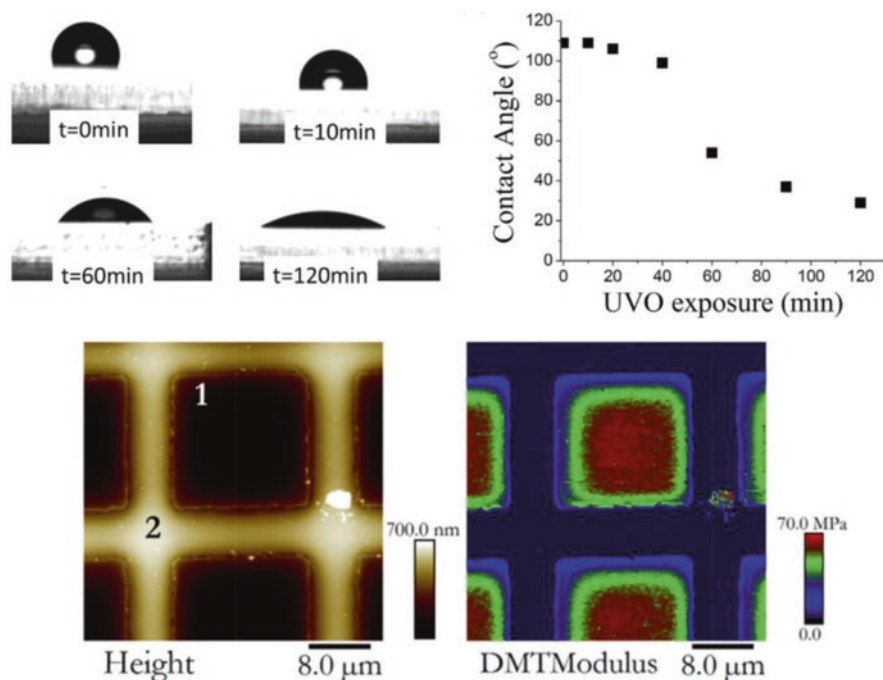


**Fig. 3.10** (Top) Contact angle measurements against UVO exposure time. (Bottom) AFM and DMT microographies which permit to compare topography and local mechanical properties (elastic modulus) in UVO-exposed or UVO-unexposed zones. (Reproduced with permission from Ref. [31])

### 3.2.2 *Via Thermo-/Photofrontal Polymerizations*

There also exist some recently reported methodologies which mix photofrontal polymerization with thermal treatments in order to create wrinkled hierarchical patterns. For example, Ellison et al. in the year 2015 [33] describe the formation of coatings with patterned features by using a photofrontal polymerization method mediated by a mask. This method does not take advantage of surface instabilities; instead, it uses differential polymerization states to form patterns via photomasking. Poly(isobutyl methacrylate) (PiBMA) was used as the main component for film formation through spin-coating technique over silicon wafers. Then, the films were exposed to UV irradiation (365 nm) for photomasking the surface by reducing a fraction of benzophenone groups present in the mixture. Then, the films were heated above its glass transition temperature, inducing melt-state flowing (Fig. 3.12, right). The final cross-linking step of the surface was performed by using UVB/UVC irradiation (260 nm) which produce that benzophenone groups graft to polymer chains, promoting polymerization by covalently linking the PiBMA chains. In some samples, no UVB/UVC exposure was performed, thus showing an uncross-linked flowable state after a second annealing cycle (Fig. 3.12, left).

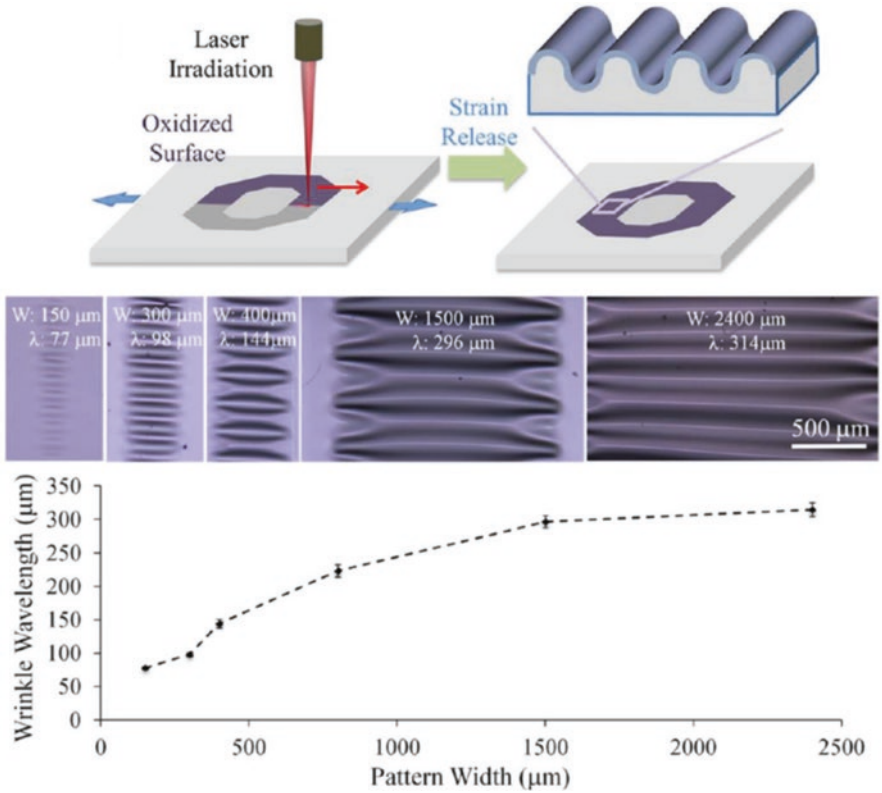


**Fig. 3.11** (Top) Schematic description of CO<sub>2</sub> laser oxidation method proposed to form wrinkles in PDMS surface. (Middle) Photographs of wrinkled patterns formed via this methodology by changing laser scan width. (Bottom) A graph which shows the effect of pattern width on wrinkle wavelength. (Reproduced with permission from Ref. [32])

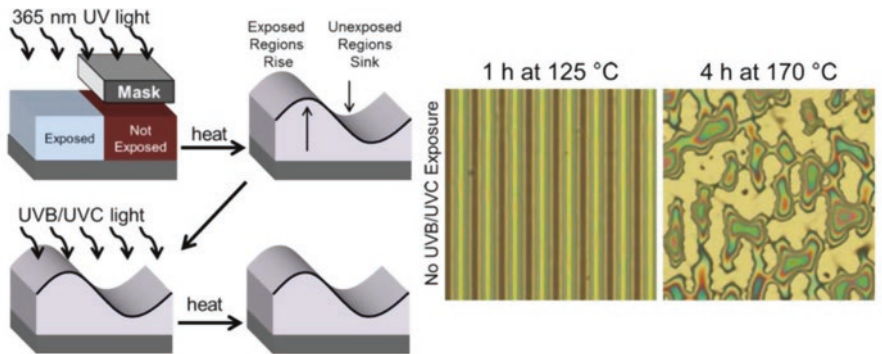


**Fig. 3.12** (Right) Schematic description of procedure proposed by Ellison et al. to form patterns. (Left) Micrographs of an uncross-linked sample before and after the second annealing process. (Reproduced with permission from Ref. [33])

Following a similar method, Jiang et al. [34] can accomplish the fabrication of light/thermo-reversible wrinkled patterns by depositing mixtures of anthracene-containing copolymer (PAN) and n-butyl acrylate (BA) films by spin-coating technique over PDMS substrates. The bilayered systems were exposed to UV irradiation for generating a photofrontal polymerization gradient in the material. Then, a heating process was performed in order to generate the wrinkled patterns. Via sequential UV (at 254 or 365 nm) and thermal exposure, wrinkled or unwrinkled patterns could be generated. A schematic map of wrinkling/unwrinkling processes triggered by UV or thermal stimulus is depicted in Fig. 3.13. The wrinkling patterns also show self-healing capacity upon UV/thermal processes. Smart devices and surfaces with dynamically tunable morphology is a novel topic nowadays; accordingly, Jiang et al. test these tunable wrinkled patterns as smart Braille characters obtaining remarkable results.

Recently, Kloxin et al. [35] fabricate films of thiol-ene-based polymers via blade casting method, which, upon rapid UV exposure (90 s) and low strain application (4%), was able to generate controllable wrinkled patterns in their surface (Fig. 3.14, right). The photofrontal polymerized films were deposited on glass or silicon substrates and then were transferred to an elastomer substrate to be stretched. The excess of thiols in the elastomer and excess of enes in the film allow covalent attachment of the film to the elastomeric substrate. The films were then heated to evaporate solvents. Photomasks were used to generate intricate patterns on the surface. Finally, by coating and photopatterning in sequence, spatial wrinkle wavelength control could be accomplished (Fig. 3.14, left). The novelty of this work relies on the short time of UV exposure needed to form wrinkles on thiol-ene polymers, a material that has the characteristic of being compatible with a variety of functional monomers – charged monomers, mechanophores, and light-responsive moieties, among others.

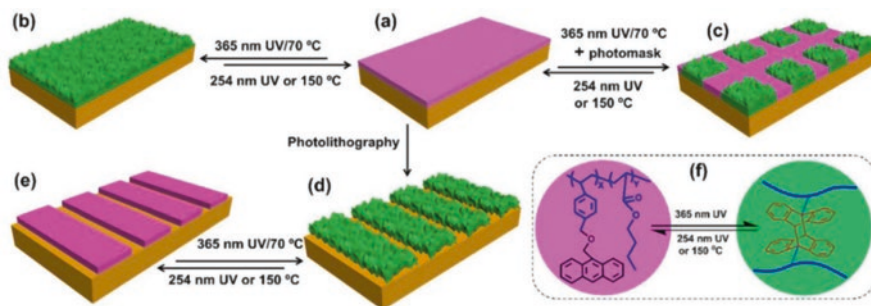


**Fig. 3.13** Strategy proposed to generating light/thermo-reversible wrinkled patterns. (a–c) Reversible processes performed with or without a photomask to selectively generate wrinkled patterns. (d–e) Similar patterns could be developed via photolithography. (f) Chemical structures of PAN which illustrate the dynamic photo-dimerization reaction. (Reproduced with permission from Ref. [34])

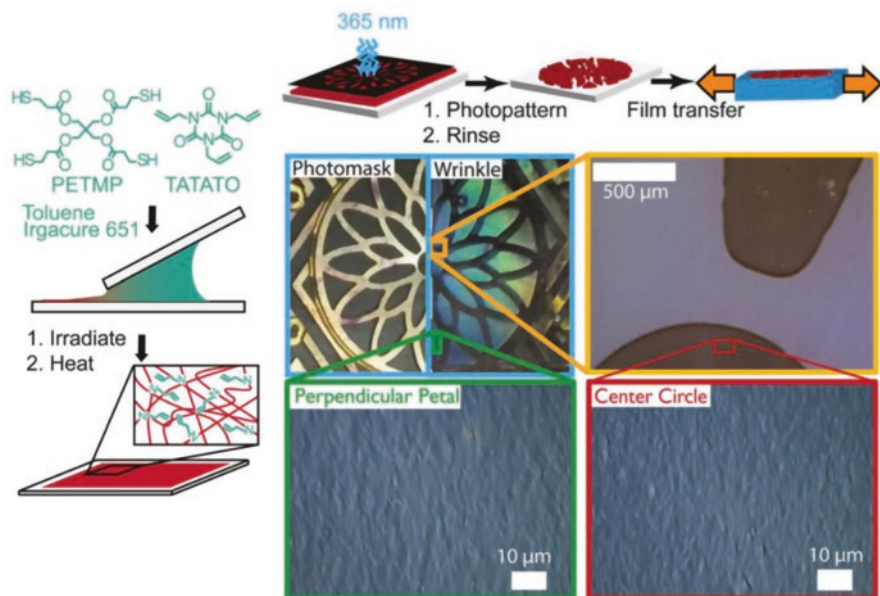


**Fig. 3.14** (Right) Chemical structures of the compounds used to create the film; also, a scheme of blade casting method is shown. (Left) Photopatterning and transferring methods are shown schematically, and micrographs of the obtained wrinkled pattern are depicted. (Reproduced with permission from Ref. [35])

### 3.2.3 Via Plasma-Ignited Frontal Polymerization

The group of Cabral et al. [9, 36] is one of the worldwide experts in the formation of wrinkled patterns via plasma-ignited FP; in fact, they were one of the first to coin the term frontal vitrification to this process. By using air plasma, they were able to generate a glassy film which is gradually formed on the surface of PDMS (substrate) by substituting hydrogen and methyl groups with hydroxyl groups and oxide links. This thin glassy film densifies into a rigid top layer, whose thickness depends on plasma dose. During plasma exposure, the layer was strained, and upon finalization, it was released thus forming permanently wrinkled patterns on the surface (Fig. 3.15, top). In these articles, the effect of plasma frequency (kHz or MHz), oxygen content (from pure  $O_2$  to air), pressure (0.5–1.5 mbar), as well as plasma exposure time and power is quantified in terms of the resulting glassy skin thickness. Layer thicknesses were estimated from the models and measured with X-ray reflectometry. Also, the minimum thickness of the rigid top layer necessary to form a wrinkled pattern was determined via mechanical models. Three frontal polymerization regimes were clearly identified during the early stage of plasma exposure, which is coined as induction, formation, and propagation. In Fig. 3.15 (bottom), a micrograph of the wrinkled pattern obtained after strain release is depicted.

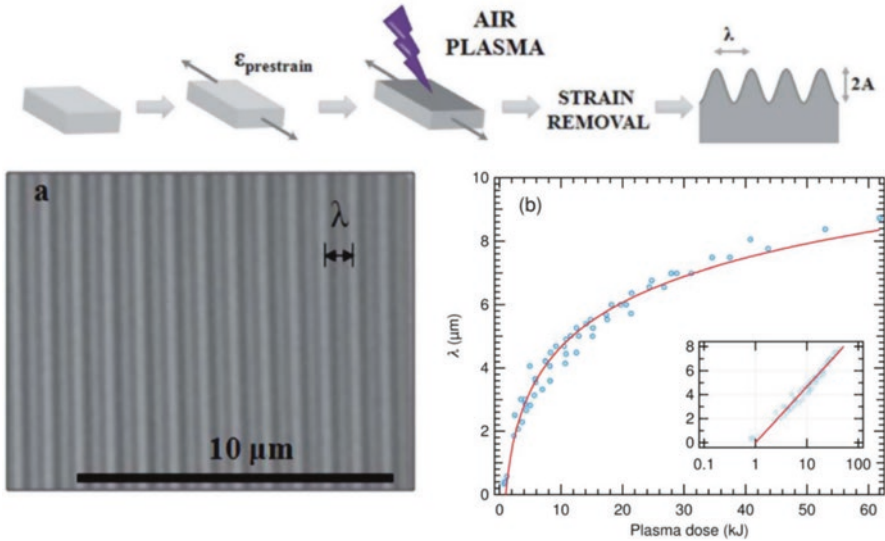


**Fig. 3.15** (Top) Schematic description of the methodology performed by Cabral et al. (Bottom) Microscopy image of a wrinkled pattern formed through this methodology and a graph which shows the dependence of wrinkled pattern wavelength with plasma dose. (Reproduced with permission from Refs. [9, 36])

Similarly, Cao and Lu et al. [37] create controlled wrinkled patterns by using a spatioselective method of FP via  $O_2$  plasma exposure on PDMS substrates with Cu grids as masks. By changing the order of stretching and plasma exposure steps, it was possible to create different types of wrinkled patterns. In Fig. 3.16 is depicted a schematic description of the different paths with interleaved steps of  $O_2$  plasma exposure or stretching. The results of this study clarify the processes needed to fabricate hierarchically wrinkled patterns with a well-defined wavelength, amplitude, organization, orientation, and location using such strategies. Also, it opens the way to clever and new combinations of mechanical stretching and selective exposure to create intricate patterns.

Air or oxygen plasma is not the only way to produce wrinkled patterns on surfaces. Argon plasma is commonly used to this end. For example, Carpick et al. [38], in the year 2009, create controllable wrinkled patterns by using plasma-ignited FP in pre-stretched PDMS substrates. The wrinkled pattern morphologies generated on the surface are in agreement with theoretical predictions performed based on the interplay between PDMS bulks and their nanoscale cross-linked top layer. Figure 3.17 shows some of the wrinkled patterns obtained after 30 s of Ar plasma exposure on PDMS substrates of variable thicknesses. Hasebe et al. [39] also used Ar plasma to trigger wrinkled pattern formation on PDMS substrates coated with a diamond-like carbon (DLC) thin film. They were able to form highly ordered wrinkled patterns of DLC on stripe-patterned PDMS substrates; interestingly, the wrinkle direction is perpendicular to the steps of the ridges in the substrate. Those

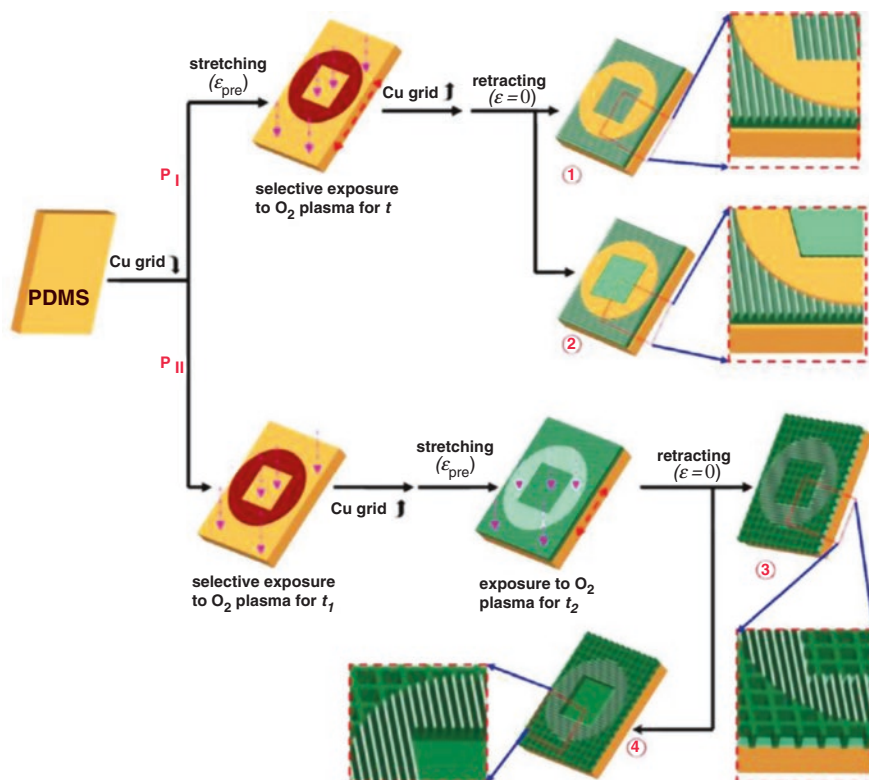


**Fig. 3.16** Schematic description of the different paths followed by Cao and Lu et al. in which interleaved steps of  $O_2$  plasma exposure or mechanical stretching are performed. (Reproduced with permission from Ref. [37])

substrates were previously treated with Ar plasma; wrinkled film dimensions (amplitude and wavelength) exhibited slight variations according to the duration of plasma treatment.

Vaziri and Moon [40], in the year 2009, were able to create wrinkled patterns via a multi-step plasma treatment. This method allowed them to fabricate one-dimensional, two-dimensional, or nested hierarchical wrinkling patterns. As it was mentioned before and corroborated in this article, wavelength and amplitude of the wrinkled pattern could be easily controlled by plasma exposure time or stretching rate. Also, uniaxial and biaxial stretchings were performed on the PDMS substrates, forming interesting wrinkled architectures (Fig. 3.18, left). Subsequent steps of plasma exposure and stretch could be performed in order to create nested hierarchical architectures (Fig. 3.18, right). This methodology for surface engineering of polymers has far-ranging applications, such as tissue engineering, regenerative medicine, microfluidics, lab-on-chip devices, shape-shifting materials, stretchable electronics, and devising tunable surface adhesion for robotics, among others.

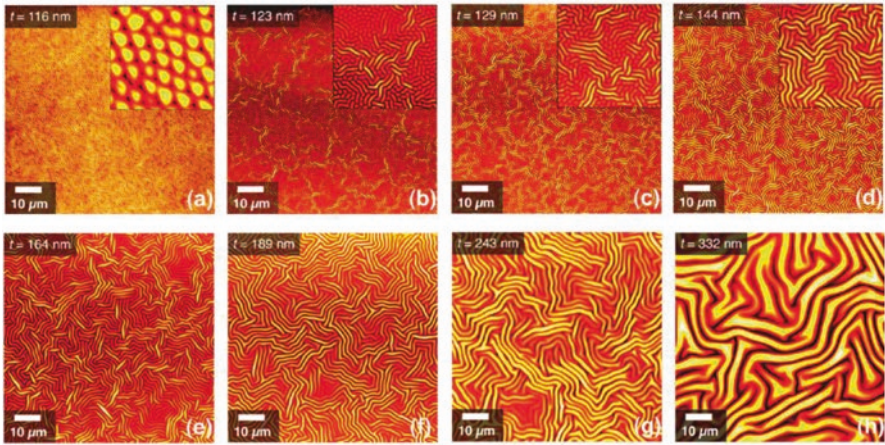


Fig. 3.17 AFM micrographs of wrinkled patterns formed through Ar plasma treatment (30 s) on PDMS substrates of variable thicknesses. (Reproduced with permission from Ref. [38])

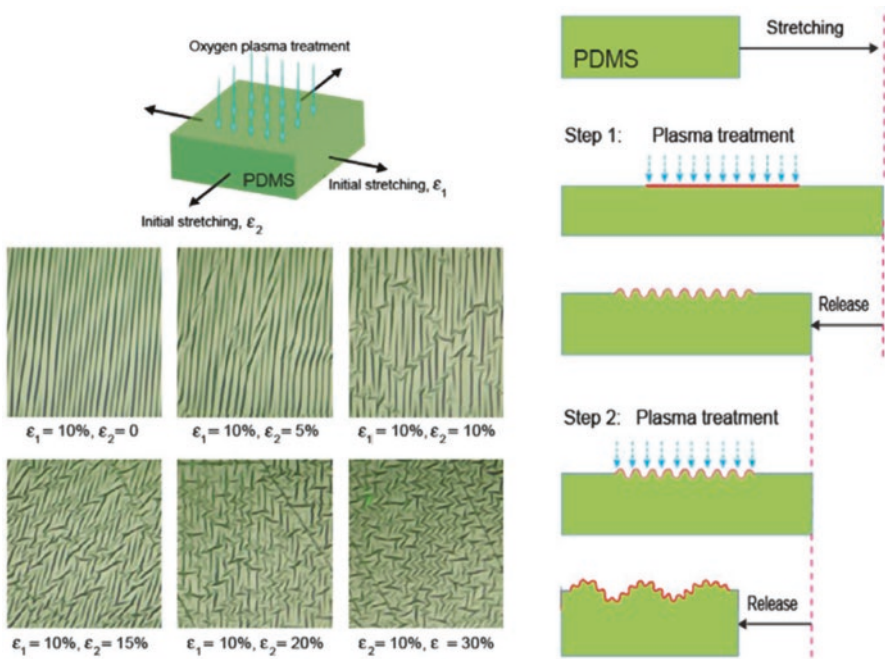
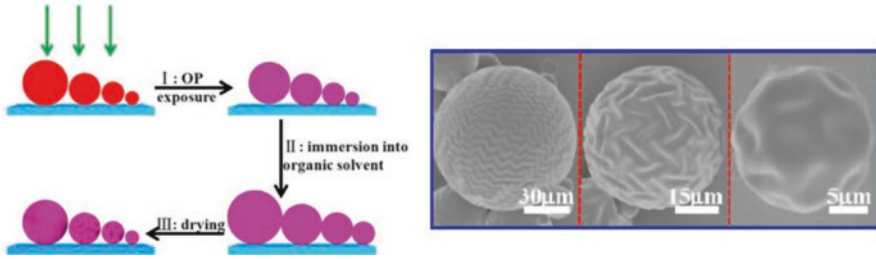


Fig. 3.18 (Left) Wrinkled patterns formed by changing the biaxial stretching conditions. (Right) Schematic representation which illustrates the methodology performed to obtain nested hierarchical wrinkled patterns. (Reproduced with permission from Ref. [40])



**Fig. 3.19** (Left) Schematic description of the protocol proposed by Lu et al. (Right) SEM micrographs of PDMS microspheres with different sizes which show variable wrinkled patterns' dimensions and distributions. (Reproduced with permission from Ref. [41])

The group of Lu et al. generates wrinkled patterns over PDMS microspheres by using a combination of  $O_2$  plasma exposure and solvent treatment [41]. Firstly, the synthesized PDMS microspheres were exposed to plasma, creating an oxidized  $SiO_x$  layer on the sphere surface and leaving the core in the same state. A subsequent solvent swelling and evaporation processes induce the spontaneous formation spherical wrinkles (Fig. 3.19, left), which have the property of being curvature- and overstress-sensitive. The results show that there exists a power-law dependence of the wrinkling wavelength with the microsphere dimensions (Fig. 3.19, right). Also, solvent nature has a strong influence on wrinkled pattern morphology mediated via swelling ratio of PDMS.

### 3.2.4 *Via a Mixture of Plasma-Ignited and Photofrontal Polymerizations*

Recently, the group of Cabral et al. [5], in the year 2017, generates wrinkled patterns with dimensions under 100 nm by fabricating tri-layered systems with excellent interfacial properties. This was accomplished via a double frontal oxidation process over PDMS layers by mixing photofrontal with plasma-ignited frontal polymerization. X-ray and neutron reflectivity (XRR and NR) scans were carried out on the PDMS samples in order to obtain UVO and air plasma-oxidized layer thicknesses. Also, independent studies of UVO and air plasma exposure are reported on the article, but neither shows wrinkled patterns with considerably smaller dimensions.

As is visualized in Fig. 3.20 (top), the PDMS layers were first strained, and then a UVO surface treatment was performed; subsequently, maintaining the strain of the substrate layer, an air plasma exposure was carried out. Then, when the PDMS layer was released, a small wrinkled pattern could be observed, smaller than the cases of bare UVO and air plasma exposure, showing that by mixing two different frontal polymerization processes, it is possible to reduce the surface topography pattern, reaching sub-100 nm ranges in some cases (Fig. 3.20, bottom).

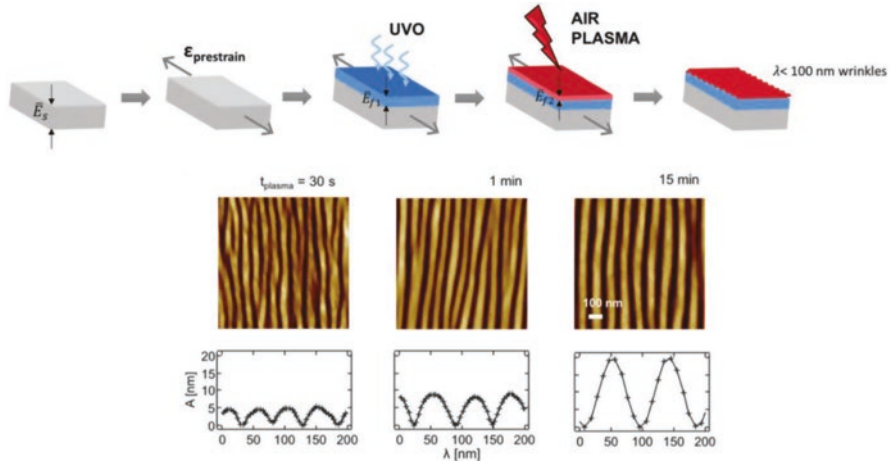


**Fig. 3.20** (Top) Schematic illustration of two-step FP processes via UVO radiation and air plasma exposure. (Bottom) AFM micrographs of sub-100 nm wrinkled patterns obtained through this methodology by varying the plasma exposure time and maintaining the UVO time (60 min). (Reproduced with permission from Ref. [5])

### 3.3 Conclusion

Frontal polymerization (FP) is based on a particular type of methodology in which the polymerization is carried out controllably in only one direction. This methodology has shown to be remarkably simple, fast, and low-cost method to produce polymers with variable types of chemical structures. Four types of FP methods are mentioned in the chapter, but only two of these are fully explained because they are the most used to generate wrinkled patterns, photofrontal polymerization, and plasma-ignited frontal polymerization. By using these types of FP, a polymerization gradient could be created in the material. The interface between the polymerized layer and the unpolymerized one generates mechanical interactions which lead to stress mismatch, thus creating surface instabilities. These instabilities, under particular stimuli, like releasing of mechanical strain, could trigger the formation of wrinkled patterns in the surface. Several methods to form wrinkled patterns by using FP are listed in this chapter. The last advances of these methodologies were able to generate wrinkled patterns with dimensions considerably small, opening the path to new types of applications in the fields of optics, photonics, nano-fluidic devices, as well as template formation and contact printing in nanoscales, among others.

**Acknowledgments** The authors acknowledge financial support given by FONDECYT Grant No. 1170209. M.A. Sarabia acknowledges the financial support given by CONICYT through the doctoral program Scholarship Grant. J. Rodríguez-Hernández acknowledges financial support from Ministerio de Economía y Competitividad (MINECO) (Project MAT2016-78437-R, FEDER EU). Finally, this study was funded by VRAC Grant Number L216-04 of Universidad Tecnológica Metropolitana.

## References

1. N.M. Chechilo, R.J. Khvilivitskii, N.S. Enikolopyan, Phenomenon of polymerization reaction spreading. *Dokl. Akad. Nauk SSSR* **204**, 1180 (1972)
2. J.A. Pojman, *Frontal Polymerization*, vol 4 (Elsevier B.V, Amsterdam, 2012)
3. C. Nason, T. Roper, C. Hoyle, et al., UV-induced frontal polymerization of multifunctional (Meth)acrylates. *Macromolecules* **38**, 5506–5512 (2005)
4. S.J. Ma, S.J. Mannino, N.J. Wagner, et al., Photodirected formation and control of wrinkles on a Thiol–ene elastomer. *ACS Macro Lett.* **2**, 474–477 (2013)
5. M. Nania, F. Foglia, O.K. Matar, et al., Sub-100 nm wrinkling of polydimethylsiloxane by double frontal oxidation. *Nanoscale* **9**, 2030–2037 (2017)
6. J.A. Pojman, V.M. Ilyashenko, A.M. Khan, Free-radical frontal polymerization: Self-propagating thermal reaction waves. *J. Chem. Soc. Faraday Trans.* **92**, 2825 (1996)
7. Y.A. Chekanov, J.A. Pojman, Preparation of functionally gradient materials via frontal polymerization. *J. Appl. Polym. Sci.* **78**, 2398–2404 (2000)
8. C. Nason, J.A. Pojman, C. Hoyle, The effect of a trithiol and inorganic fillers on the photo-induced thermal frontal polymerization of a triacrylate. *J. Polym. Sci. Part A Polym. Chem.* **46**, 8091–8096 (2008)
9. M. Nania, O.K. Matar, J.T. Cabral, Frontal vitrification of PDMS using air plasma and consequences for surface wrinkling. *Soft Matter* **11**, 3067–3075 (2015)
10. D. Bomze, P. Knaack, R. Liska, Successful radical induced cationic frontal polymerization of epoxy-based monomers by C–C labile compounds. *Polym. Chem.* **6**, 8161–8167 (2015)
11. J.V. Crivello, U. Bulut, Dual photo- and thermally initiated cationic polymerization of epoxy monomers. *J. Polym. Sci. Part A Polym. Chem.* **44**, 6750–6764 (2006)
12. J.V. Crivello, B. Falk, M.R. Zonca, Photoinduced cationic ring-opening frontal polymerizations of oxetanes and oxiranes. *J. Polym. Sci. Part A Polym. Chem.* **42**, 1630–1646 (2004)
13. J.V. Crivello, Hybrid free radical/cationic frontal photopolymerizations. *J. Polym. Sci. Part A Polym. Chem.* **45**, 4331–4340 (2007)
14. J. Rodríguez-Hernández, Wrinkled interfaces: Taking advantage of surface instabilities to pattern polymer surfaces. *Prog. Polym. Sci.* **42**, 1–41 (2015)
15. M. He, X. Huang, Z. Zeng, et al., Photo-triggered redox frontal polymerization: A new tool for synthesizing thermally sensitive materials. *J. Polym. Sci. Part A Polym. Chem.* **51**, 4515–4521 (2013)
16. C. Decker, The use of UV irradiation in polymerization. *Polym. Int.* **45**, 133–141 (1998)
17. C. Decker, Light-induced crosslinking polymerization. *Polym. Int.* **51**, 1141–1150 (2002)
18. J.T. Cabral, S.D. Hudson, C. Harrison, et al., Frontal photopolymerization for microfluidic applications. *Langmuir* **20**, 10020–10029 (2004)
19. Y. Ohtsuka, Y. Koike, Studies on the light-focusing plastic rod 16: Mechanism of gradient-index formation in photocopolymerization of multiple monomer systems. *Appl. Opt.* **23**, 1774 (1984)
20. Y. Koike, H. Hatanaka, Y. Ohtsuka, Studies on the light-focusing plastic rod 17: Plastic GRIN rod Lens prepared by photocopolymerization of a ternary monomer system. *Appl. Opt.* **23**, 1779 (1984)
21. G. Terrones, A.J. Pearlstein, Effects of optical attenuation and consumption of a photobleaching initiator on local initiation rates in photopolymerizations. *Macromolecules* **34**, 3195–3204 (2001)
22. Z.-F. Zhou, C. Yu, X.-Q. Wang, et al., Facile access to poly(NMA-Co-VCL) hydrogels via long range laser ignited frontal polymerization. *J. Mater. Chem. A* **1**, 7326 (2013)
23. W.Q. Tang, L.H. Mao, Z.F. Zhou, et al., Facile synthesis of 4-vinylpyridine-based hydrogels via laser-ignited frontal polymerization and their performance on ion removal. *Colloid Polym. Sci.* **292**, 2529–2537 (2014)
24. J. Zhou, H. Shao, J. Tu, et al., Available plasma-ignited frontal polymerization approach toward facile fabrication of functional polymer hydrogels. *Chem. Mater.* **22**, 5653–5659 (2010)

25. C. Yu, J. Zhou, C.F. Wang, et al., Rapid synthesis of poly(HPA-Co-VeoVa 10) amphiphilic gels toward removal of toxic solvents via plasma-ignited frontal polymerization. *J. Polym. Sci. Part A Polym. Chem.* **49**, 5217–5226 (2011)
26. H. Shao, C.F. Wang, S. Chen, et al., Fast fabrication of superabsorbent polyampholytic nanocomposite hydrogels via plasma-ignited frontal polymerization. *J. Polym. Sci. Part A Polym. Chem.* **52**, 912–920 (2014)
27. Y. Gan, J. Yin, X. Jiang, Self-wrinkling induced by the photopolymerization and self-assembly of fluorinated polymer at air/liquid interface. *J. Mater. Chem. A* **2**, 18574–18582 (2014)
28. D. Chandra, A.J. Crosby, Self-wrinkling of UV-cured polymer films. *Adv. Mater.* **23**, 3441–3445 (2011)
29. T. Takeshima, W.Y. Liao, Y. Nagashima, et al., Photoresponsive surface wrinkle morphologies in liquid crystalline polymer films. *Macromolecules* **48**, 6378–6384 (2015)
30. S.K. Park, Y.-J. Kwark, S. Nam, et al., A variation in wrinkle structures of UV-cured films with chemical structures of prepolymers. *Mater. Lett.* **199**, 105–109 (2017)
31. A. del Campo, A. Nogales, T.A. Ezquerro, et al., Modification of poly(dimethylsiloxane) as a basis for surface wrinkle formation: Chemical and mechanical characterization. *Polymer (Guildf)*. **98**, 327–335 (2016)
32. L. Qi, C. Ruck, G. Szychalski, et al., Writing wrinkles on poly(dimethylsiloxane) (PDMS) by surface oxidation with a CO<sub>2</sub> laser engraver. *ACS Appl. Mater. Interfaces* **10**, 4295–4304 (2018)
33. J.M. Katzenstein, C.B. Kim, N.A. Prisco, et al., A photochemical approach to directing flow and stabilizing topography in polymer films. *Macromolecules* **47**, 6804–6812 (2014)
34. H. Hou, F. Li, Z. Su, et al., Light-reversible hierarchical patterns by dynamic photo-dimerization induced wrinkles. *J. Mater. Chem. C* **5**, 8765–8773 (2017)
35. S.J. Ma, N.J. Wagner, C.J. Kloxin, Rapid and controlled photo-induced thiol–ene wrinkle formation via flowcoating. *Mater. Horizons*, 5:514–520 (2018)
36. F.A. Bayley, J.L. Liao, P.N. Stavrinou, et al., Wavefront kinetics of plasma oxidation of polydimethylsiloxane: Limits for sub- $\mu\text{m}$  wrinkling. *Soft Matter* **10**, 1155–1166 (2014)
37. Y. Yang, X. Han, W. Ding, et al., Controlled free edge effects in surface wrinkling via combination of external straining and selective O<sub>2</sub> plasma exposure. *Langmuir* **29**, 7170–7177 (2013)
38. H.T. Evensen, H. Jiang, K.W. Gotrik, et al., Transformations in wrinkle patterns: Cooperation between nanoscale cross-linked surface layers and the submicrometer bulk in wafer-spun, plasma-treated polydimethylsiloxane. *Nano Lett.* **9**, 2884–2890 (2009)
39. S. Nagashima, T. Hasebe, D. Tsuya, et al., Controlled formation of wrinkled diamond-like carbon (DLC) film on grooved poly(dimethylsiloxane) substrate. *Diam. Relat. Mater.* **22**, 48–51 (2012)
40. M.-W. Moon, A. Vaziri, Surface modification of polymers using a multi-step plasma treatment. *Scr. Mater.* **60**, 44–47 (2009)
41. Q. Li, X. Han, J. Hou, et al., Patterning poly(dimethylsiloxane) microspheres via combination of oxygen plasma exposure and solvent treatment. *J. Phys. Chem. B* **119**, 13450–13461 (2015)

# Chapter 4

## Control of Wrinkled Structures on Surface-Reformed Elastomers via Ion Beam Bombardment



C. M. González-Henríquez, M. A. Sarabia Vallejos,  
and Juan Rodríguez-Hernández

### 4.1 Introduction

Ion beam (IB) bombardment corresponds to a technique which has been highly used in the last years with the finality of generating micro- and nano-patterned surfaces. This methodology presents several advantages over currently used techniques, for example, it is possible to develop patterns with very small feature sizes (less than 20 nm) [1], to generate high aspect ratio features (width/height), and to fabricate three-dimensional patterned devices [2] with a focus depth up to 500  $\mu\text{m}$  [3]. Additionally, the interaction between ions and material's electrons does not result in any significant deviation of proton trajectory, unlike electron beam. In contrast to techniques which involve photons, IB can induce structural modifications in the material, producing mechanical and chemical changes at the surface. Those changes can be performed by, for example, varying ion species and tuning the acceleration energy or ion fluence, among others. Due to their advantages, IB

---

C. M. González-Henríquez (✉)

Departamento de Química, Facultad de Ciencias Naturales, Matemáticas y del Medio Ambiente, Universidad Tecnológica Metropolitana, Santiago, Chile

Programa Institucional de Fomento a la Investigación, Desarrollo e Innovación, Universidad Tecnológica Metropolitana, Santiago, Chile

e-mail: [carmen.gonzalez@utem.cl](mailto:carmen.gonzalez@utem.cl)

M. A. Sarabia Vallejos

Departamento de Ingeniería Estructural y Geotecnia, Pontificia Universidad Católica de Chile, Escuela de Ingeniería, Santiago, Chile

Instituto de Ingeniería Biológica y Médica, Santiago, Chile

J. Rodríguez-Hernández (✉)

Departamento de Química Macromolecular Aplicada, Polymer Functionalization Group, Instituto de Ciencia y Tecnología de Polímeros-Consejo Superior de Investigaciones Científicas (ICTP-CSIC), Madrid, Spain

e-mail: [jrodriguez@ictp.csic.es](mailto:jrodriguez@ictp.csic.es)

has been used to generate micro-patterns with tunable and controllable characteristics for several years.

In parallel, there is another technique, called focused ion beam (FIB), in which the IB is focused into a specific spot. In this case, the beam is moved by using electrostatic or magnetic fields across the material surface with the finality to create the desired pattern. The advantage of this technique, compared to IB, is related to its flexibility. A variation in the pattern can be performed by the control software and not by changing masks as in the IB technique, making possible to generate intricate and complex patterns on the surface. Both methodologies are widely used to fabricate patterns with micro- and nanoscale features, producing surface instabilities induced by the collisions of ions with molecules in the material.

There is a particular interest in using modifiable and cheap materials for IB patterning, and some polymers arise as biocompatible and/or biodegradable materials suitable for this task. There exist several polymeric materials used to generate micro-patterns via IB technology, but, by far, poly(dimethylsiloxane) (PDMS) is the most widely used due to its interesting properties. PDMS is an elastomer that has optical transparency, low autofluorescence [4], moldability with a submicron resolution [5], and high oxygen permeability [6]. According to their biocompatibility, it has been widely used as biomaterial [7] for applications including microfluidics, cell culture substrates, and flexible electronic and medical devices, among others. When this polymer is bombarded via IB, an oxidation at the surface is produced, forming a silica-like top layer that interacts with the inner PDMS, leading, in some cases, to the formation of complex wrinkled structures through surface instabilities generated by layer stress mismatch inside the material [8].

The main focus of this chapter is to present a broad overview of IB and FIB techniques used for fabricating nano- and micro-patterns. These methodologies can control the orientation of wrinkled patterns and also their dimensions such as width and height of undulations. According to this, the aspect ratio of wrinkled patterns can be modified by varying the temperature, deposition time, ion beam voltages, electric fluence, beam incidence angle, and metal ion implantation, among others. Different examples and applications also are mentioned in the next chapter.

## 4.2 Wrinkling Background

Basic theory for wrinkling instability of stiff skin or film layers on soft substrates under compression has been studied comprehensively in the last years [9, 10]. A metal film, with nanometric thickness, could be deposited at an elevated temperature on a thick elastomeric substrate. When this system is cooled, the large mismatch between the thermal expansion of the metal and the elastomer produces a biaxial compression in the film, generating highly ordered patterns with distinctive features. On the right hand in Fig. 4.1, a buckled pattern arises when the substrate surface has a series of flat depression running linearly in the vertical direction. Due to the local deformation of the substrate, the in-plane film stress is seemingly relaxed

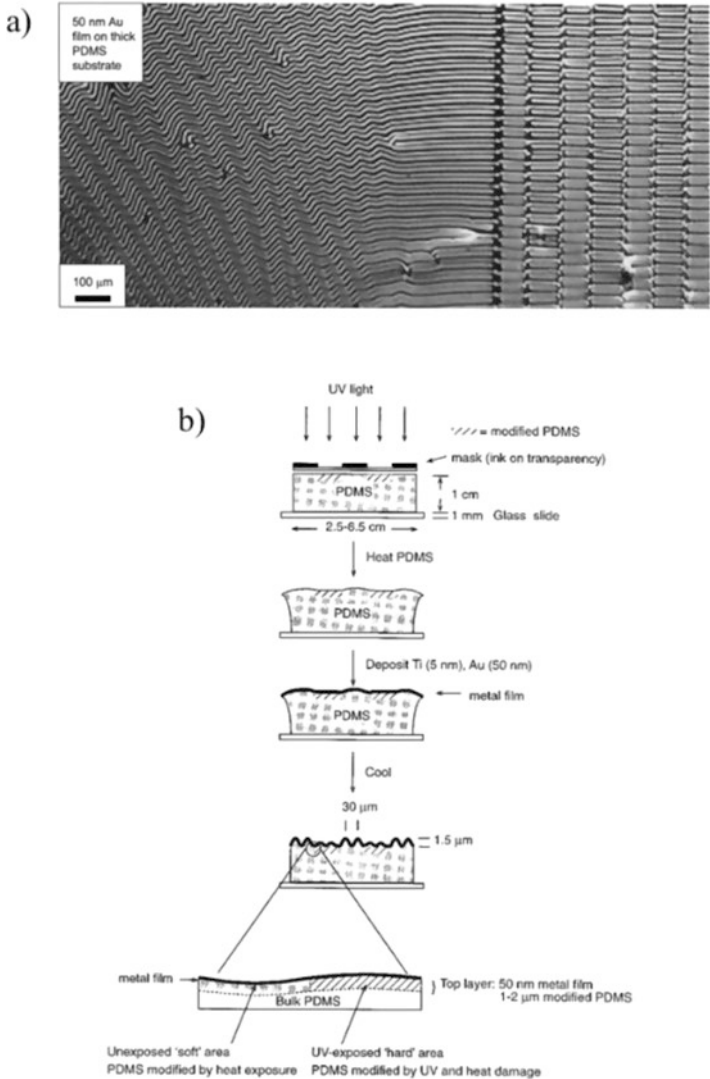


**Fig. 4.1** (a) Buckling patterns formed on a thick elastomer (PDMS) substrate. (b) Schematic procedure used to obtain aligned buckles on patterned PDMS. (Reproduced with permission from Ref. [11])

in the edge normal direction, resulting in a buckle alignment. On the other hand, it is possible to observe a transition from parallel undulations (in the left center of the figure) to herringbone patterns, which appears whenever there exists a sufficiently large patch of a smooth substrate and when the system has been cooled below the buckling onset. In this segment it is possible to observe irregularities in the herringbone pattern, including local distortion, most likely due to the imperfections in

either the film or the substrate. In Fig. 4.1b is showed schematically the method used to generate a semi-regular pattern of buckles over PDMS.

Wrinkling pattern geometries, like wavelength/width ( $\lambda$ ) or amplitude/height ( $A$ ), are determined by the intrinsic properties of the films [10, 12]. Additionally, the onset strain is obtained by the ratio of the layer elastic modulus ( $\bar{E}_f / \bar{E}_s$ ), where the subscripts  $f$  and  $s$  refer to the top-layer film and substrate, respectively, and  $t$  is film thickness.

$$\frac{\lambda}{t} = \alpha^3 \sqrt{\frac{\bar{E}_f}{\bar{E}_s}} \quad \frac{A}{t} = \sqrt{\left(\frac{\varepsilon}{\varepsilon_c}\right)^2 - 1} \quad \varepsilon_c = -\frac{1}{4} \left(\frac{3\bar{E}_s}{\bar{E}_f}\right)^{2/3}$$

A typical form of surface mechanical instabilities occurs once the compressive strain ( $\varepsilon$ ) in the top layer exceeds the critical strain ( $\varepsilon_c$ ), which results from minimizing the total energy stored in the films. In the equations,  $\alpha$  is about 4.36 for the case of plane strain condition. Note that wavelength would increase by increasing the thickness of the film and the ratio of elastic modulus.

### 4.3 Ion Beam Deposition

Ion beam deposition technique offers interesting possibilities for the preparation of metastable quasi-amorphous films owing to a high local activation and rapid quenching on an atomic scale [13]. The fundamental physics of the interaction between incident particles and target atoms provides the underlying science for ion beam analysis. These particle interactions (which include scattering, inner-shell ionization, and nuclear reaction) depend on several parameters, like ion velocity, ion energy, ion and atom size, atomic number/mass, and the distance between ion and material surface (Fig. 4.2). Particularly, the IB method is carried out by using an ion accelerator which imparts enough energy to the ions for penetrating into the bulk [14]. These ions modify the chemical composition of the surface as deeply as their penetration depth allows them [8], producing changes in the oxidized state of certain molecules at the surface. And, as it was mentioned before, PDMS is the most widely used material as a support, due to its biocompatibility and mechanical flexibility, which allow it to be used in different applications including microfluidics [15], tunable optics [16], stretchable electronics [17], lithography-free nano-/micro-patterning [18], and stretchable hydrophobic substrates [19].

Chan and Crosby proposed a methodology to generate aligned surface wrinkled patterns over PDMS. Their orientation was controlled through the manipulation of moduli-mismatch regions by alternating oxidized and non-oxidized striped regions of the elastomers [20]. Subsequently, the group of Crosby, in the year 2007 [21], design and test an alternative for simple patterning; this methodology was used to generate various surface topographies.

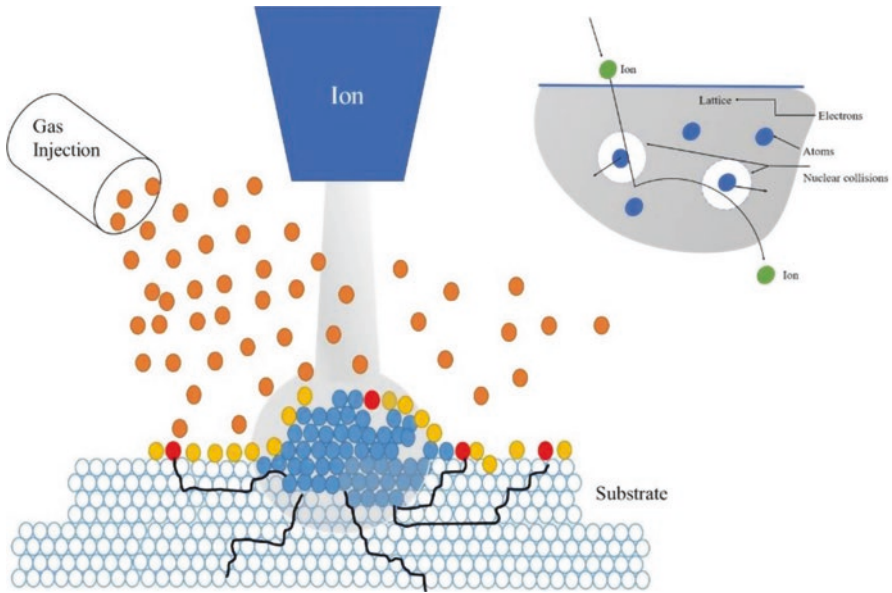


Fig. 4.2 Scheme of IB technique on a crystal lattice

On the other hand, ion milling has been widely used as a common etching process, such as the FIB system, which is popular in scientific instruments for analytical techniques or thin film characterization methodologies. An improvement from sputter in plasma etching is reactive ion etching (RIE), which is conducted by chemically active ions and radicals to increase the etching depth or to improve the sputtering rate. The main steps in the RIE process are (1) formation of plasma and reactive particles, (2) arrival of reactive particles which etched the surface, (3) surface adsorption and chemical reaction of the reactive particle, and (4) remotion of the volatile product molecule from the reactor. Reproduced with permission from Ref. [22]

## 4.4 Ion Beam-Induced Surface Patterns on Polymers via IB

### 4.4.1 Aspect Ratio on Wrinkled Patterns

#### 4.4.1.1 Temperature Variations

Park et al. [8] were able to control the amplitude and wavelength of wrinkled structures by adjusting PDMS annealing temperature. As the temperature increases, the amplitude and wavelength of the wrinkled patterns formed by IB changed from 604.35 to 69.01 nm and from 3.07 to 0.80  $\mu\text{m}$ , respectively. However, their stiffness was not changed (as confirmed by XPS analysis and AFM-force spectroscopy

measurements), but the storage modulus of the substrate increases. This behavior is related to the fact that increased stiffness of annealed PDMS substrates at higher temperature might restrict the ion penetration depth, thereby controlling the wrinkle dimensions. As shown in Fig. 4.3, the wrinkle wave numbers tended to increase as the annealing temperature was increased (Fig. 4.3b, top). In the 2D FFT (Fig. 4.3c, top), the size of the white circular distribution increased with PDMS annealing temperature, indicating that the wrinkle wavelength decreased as the annealing temperature increased, consistent with the results of the wave number analysis. However, the O/Si ratios were almost identical among all IB-irradiated samples regardless of the annealing temperature, strongly suggesting that the formation of the silica-like skin layer has no connection with the annealing temperature. To determine the cause of the variations in wrinkle size, the mechanical properties were studied by using an indentation experiment via AFM force-distance spectroscopy. Theoretically, the formation of a stiff skin layer breaks the material's symmetry, thereby inducing surface undulations (wrinkle patterns). This effect is explained in Fig. 4.3, bottom. The inner layers are characterized by its stretching energy; increased stretching energy causes wrinkle wavelength to increase. In contrast, the outer layers are characterized by its bending energy; increased bending energy causes wrinkle wavelength to decrease [23]. Additionally, Park et al. studied the surface modification of ferroelectric polymers films based on poly(vinylidene fluoride-trifluoroethylene) films, which affect the uniform liquid crystal alignment (twisted nematic) [24].

#### 4.4.1.2 Deposition Time

Ahmed et al. [25] created buckle patterns with a high aspect ratio via the deposition of amorphous carbon films employing glancing angle deposition (GLAD) on a PDMS substrate. The carbon film deposition was performed at three different incident angles (0, 45, and 75 °) under approximately equi-biaxial compressive stress; the created wrinkles were semi-herringbone or semi-labyrinth shapes, depending on the incidence angle. At angles of 0° and 45°, the aspect ratios are relatively independent of the deposition time (30 s–50 min). In contrast, the aspect ratio of the patterns created with an incident angle of 75° increases by increasing the deposition time. Figure 4.4a (bottom) showed SEM images of four different patterns created on pre-patterned PDMS surface. Figure 4.4b, c (bottom) shows the measured wavelength and amplitude of patterns after 10 and 30 min of carbon deposition on a pre-patterned polymeric surface. Thus, for 10 and 30 min, the thickness of the deposited carbon films is 100–150 nm and 500–600 nm, respectively, leading to an aspect ratio in the range of 1/5 to 1/2.5 and 1, respectively. Summarizing, the amplitude of the patterns was varied between several nm to submicron size, by changing the carbon deposition time, allowing to create patterned polymeric substrates for a variety of applications.

Another interesting case study was performed by Herzog et al. [26], which described the formation of wrinkled patterns on PMMA microbeads that had been

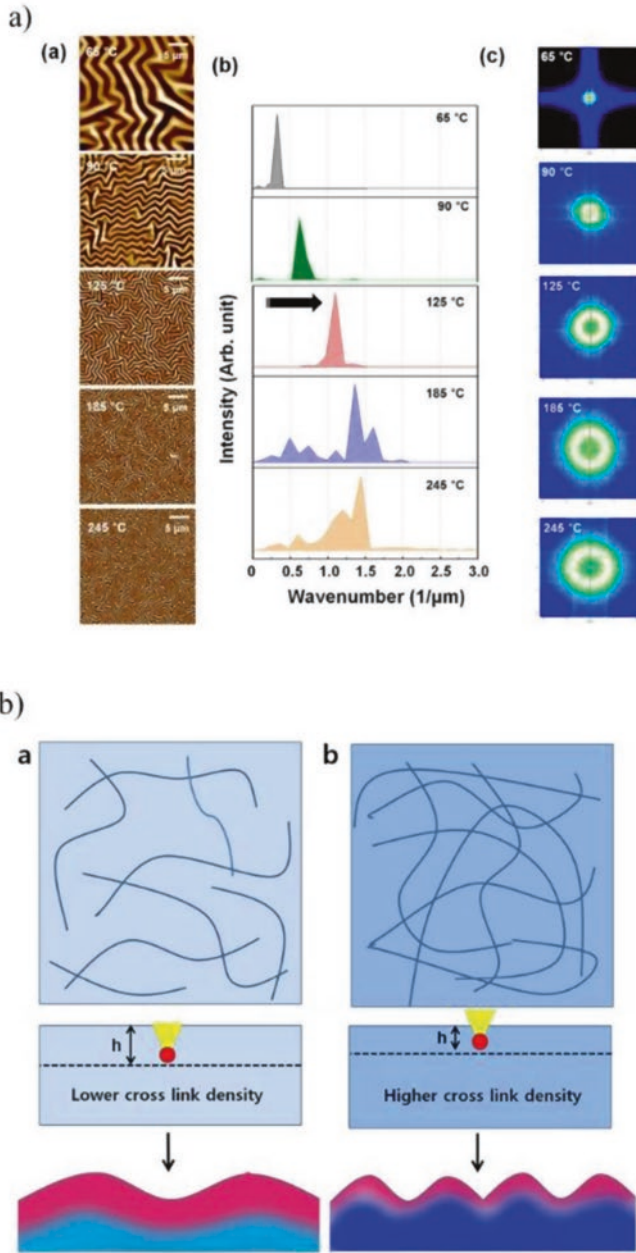


**Fig. 4.3** Top: (a) AFM images and (b) wave number distributions from these images. (c) 2D FFT patterns of wrinkled structures formed on PDMS films annealed at various temperatures. Bottom: Schematic diagram illustrating the proposed mechanism of PDMS annealing at higher temperatures prior to IB irradiation. (a) PDMS annealed at low temperature. (b) PDMS annealed at high temperature. (Reproduced with permission from Ref. [8])

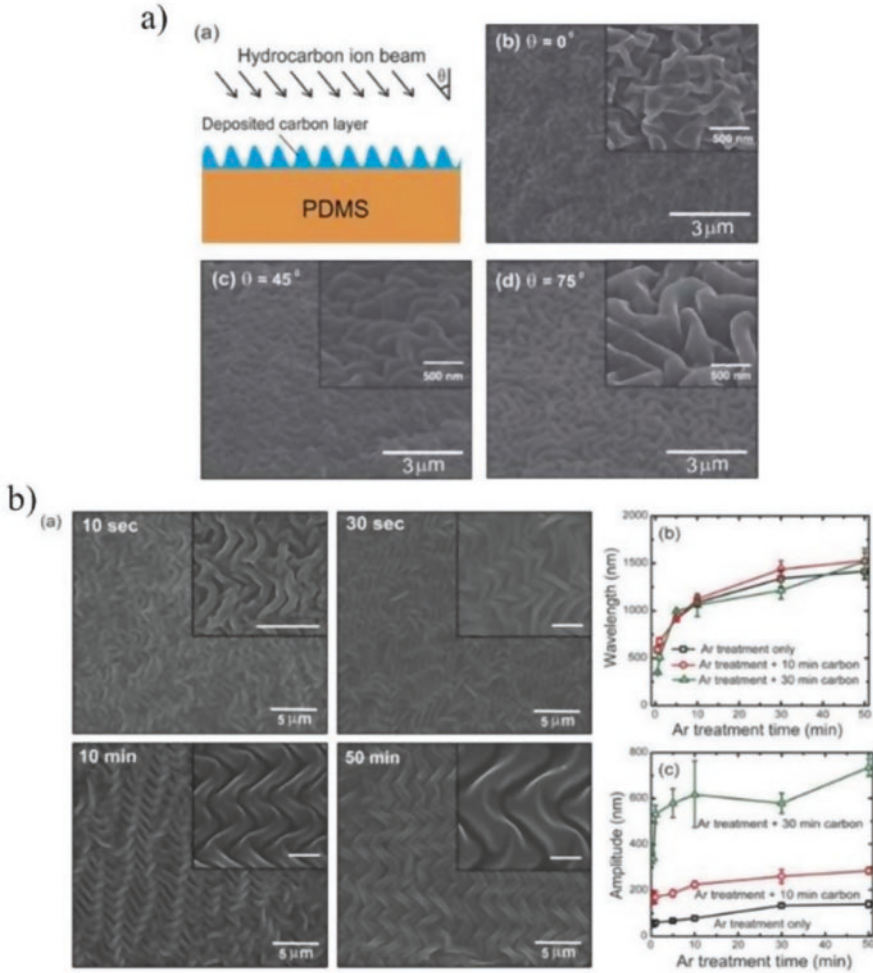


**Fig. 4.4** Top: (a) Schematic illustration of the experiments. (b–d) SEM images of the PDMS surface after 50 min carbon film deposition at different incident angles ( $0^\circ$ ,  $45^\circ$ , and  $75^\circ$ ). Bottom: (e) SEM images of the PDMS surface, pre-patterned by  $\text{Ar}^+$  at different treatment times (10s, 30s, 10 min, and 50 min) and then subjected to 10 min carbon films deposition at  $75^\circ$  incident angles. (Reproduced with permission from Ref. [25])

metal-sputtered for 100 s, whose acceleration voltage of the *e-beam* was 12 kV (penetration depth  $\sim 1 \mu\text{m}$ , Fig. 4.5a). The wrinkle formation appears immediately when the irradiation started. The sputtering time was between 50 and 300 s (Fig. 4.5b), and the absolute thickness of the metal layer was 5 nm and 25 nm, respectively. A slight dependence of wrinkle width and periodicity upon sputtering was observed. In order to elucidate the effect of the thickness of the soft polymer layer, it is produced core-shell particles of polystyrene/PMMA. Thus, Fig. 4.5c shows that a thin PMMA layer on top of a polystyrene core leads to a shorter wave-

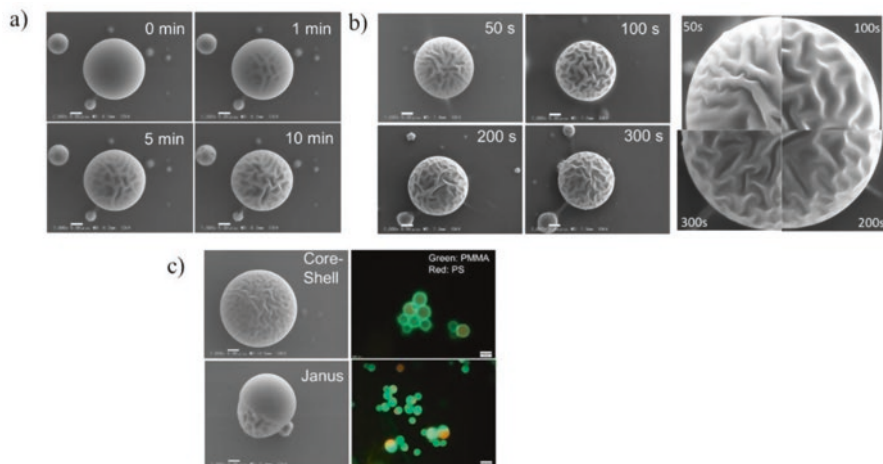


**Fig. 4.5** (a) Temporal development of the wrinkled structures during the irradiation with 12 keV. (b) Dependence of the wrinkled structure upon the metal layer thickness. (c) Wrinkle patterns for core-shell and Janus particles. (Reproduced with permission from Ref. [26])

length of the wrinkled structure. Additionally, Janus-type particles show a surface structure in which the PMMA hemisphere shows the usual, large wrinkle wavelength and the polystyrene hemisphere is wrinkle-free.

The stiff skin formed in the initial period of ion beam processing on PDMS surface is simultaneously compressed under ion bombardments to give rise highly non-linear wrinkle patterns [27]. Aiming to induce wrinkles and in order to control the strain and morphological evolution during ion beam deposition, acetylene ( $C_2H_2$ ) has been deposited on PDMS in 30 s–30 min to form a stiff thin film of amorphous carbon [28]. The wrinkle formation is explained by the induced strain and the mismatching strain in amorphous carbon film. However, even when IB was used, the chemical interaction and collisions between ion particles would occur, leading to ion scattering and inducing the bombardment and strains in different directions.

#### 4.4.1.3 Different Ion Beam Voltages

The group of Ahmed et al. [28] reported the evolution of the two-dimensional self-assembled folding thin amorphous carbon film, which was deposited over PDMS with an acetylene ( $C_2H_2$ ) precursor gas using the IB system. During deposition of amorphous carbon by IB technique with high energy, compliant PDMS substrates allowed lateral growth of the films, resulting in an insignificant film stress and a large increase in the mismatch strain of the film. As the deposition duration increased (from 30 s to 30 min), the configuration of the wrinkled film transformed into two different nonlinear modes, i.e., semi-periodically distributed ridges and asymmetrically localized folds. Besides, the thickness of the deposited films was changed

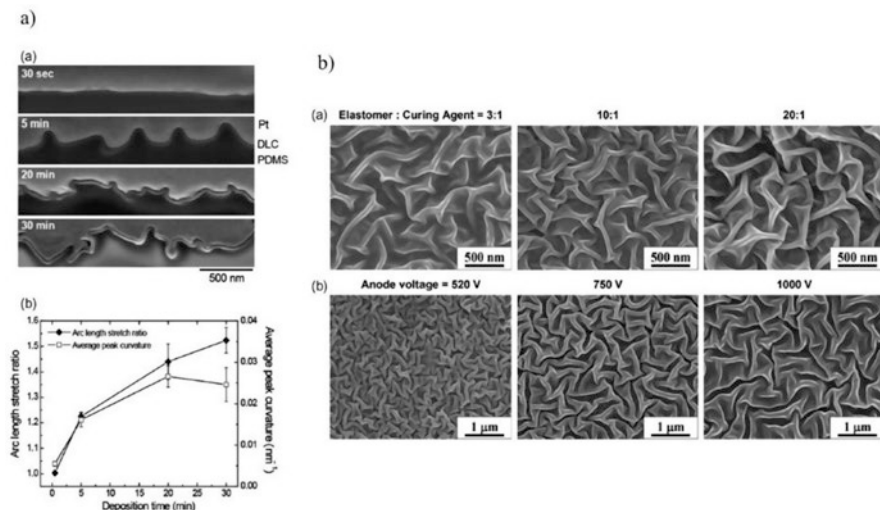


**Fig. 4.6** Left: (a) FIB cross-sectional image of an amorphous carbon film on PDMS with different deposition times. (b) Variation of the arc length stretch ratio and average peak curvature with deposition time. Right: SEM images of (a) three different stretch ratios for PDMS at 520 V and substrate bias voltage of  $-200$  V. (b) Different ion beam voltages at substrate bias voltage of  $-200$  V. (Reproduced with permission from Ref. 28)

from a few nm to 10 nm (Fig. 4.6a, left). The stretch strain of the amorphous film was measured as 50% for a 30 min deposition, which is much larger than 1–2% observed in the amorphous carbon films deposited on stiff substrates such as Si. The average curvature at the peak of the individual patterns also increases and saturated at  $0.025 \text{ nm}^{-1}$  (Fig. 4.6b, right). The authors considered that several factors such as substrate compliance or ion beam energy or power may govern the folding behavior of the deposited thin film. First of all, to check the compliance effect of the deposited thin film, the compliance of PDMS was varied by changing the mixing ratio of elastomer over curing agent (3:1, 10:1, and 20:1). The folding appears to have smaller average amplitude and the characteristic wavelength than those for higher mixing ratio. The effect of IB energy also was studied by increasing the voltage from 520 V to 1000 V during 5 min. The average wavelength of the fold pattern also increases from 148 nm to 347 nm, respectively.

#### 4.4.1.4 Incidence Angle

Jeong et al. [29] studied the effect of the IB incidence angle on wrinkle morphology. By changing it, their group was able to control the orientation of the structure and their dimensions (wavelength and amplitude). Moreover, it was demonstrated that the wrinkled pattern direction affects the LC nematic phase alignment of the material. PDMS sample was exposed to Ar<sup>+</sup> IB for 2 min with five different incident

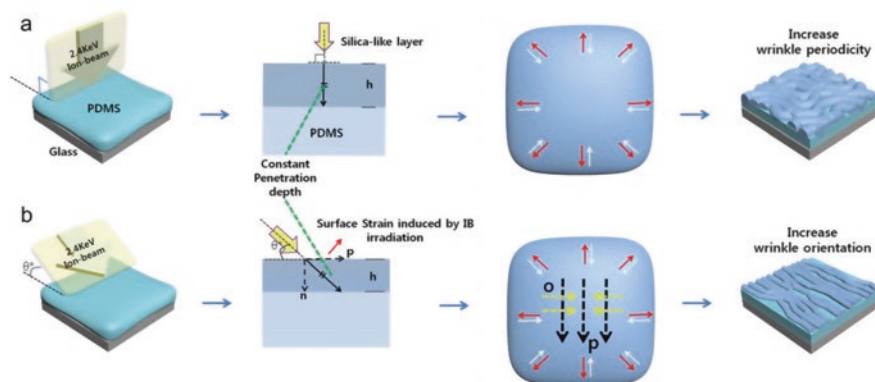


**Fig. 4.7** Schematic description about the fabrication of wrinkled structures using IB with various incidence angles (Reproduced with permission from Ref. [29])

angles (15, 30, 45, 60, and 90° separately). Additionally, the exposure time was changed from 30 s to 4 min with incidence angles of 15° and 90° to effectively test the skin modulus using the aspect ratio of the wrinkle obtained from each condition. The O/Si ratio at an incidence angle of 90° exhibited a fully oxidized PDMS.

Figure 4.7 illustrates the mechanism for controlling the wrinkle wavelength and their orientation. When the PDMS was irradiated by IB with an incidence angle of 90°, it develops isotropic compressive stress on the surface because of the lack of the directional order, thereby forming a random pattern (Fig. 4.7a). On the other hand, when IB has an incidence angle, the incident IB was spanned by two dotted arrows, namely, normal direction  $n$  and parallel direction  $p$ , which were perpendicular to each other, as shown in Fig. 4.7b. According to this, the normal penetration depth of an incident IB could be varied along with the incidence angle. Thus, the O/Si ratio increased with the incidence angle (increase in the penetration depth along the  $n$  direction), and therefore the thickness of the silica-like stiff skin layer increased.

#### 4.4.1.5 Metal Ion Implantation

Winton et al. [30] study the effect of different metal ion implantations (Fe, Co, Ni, and Ta), which were carried out at room temperature using a metal vapor vacuum arc ion source. The ion acceleration voltage and the beam current were kept fixed at 45 kV and 8 mA, respectively. Several implantation times were used from 5 s to 20 min to determine the effect of controlling the dose on the sigmoidal-like buckling behavior. Eu, Mg, Ni, and Ti were also implanted at both high and low doses. He RBS (He Rutherford backscattering spectrometry), AFM, optical microscope, and TEM were used to study the surface morphology of the samples. In this study was demonstrated that the diffusion time is influenced by both the thickness of the

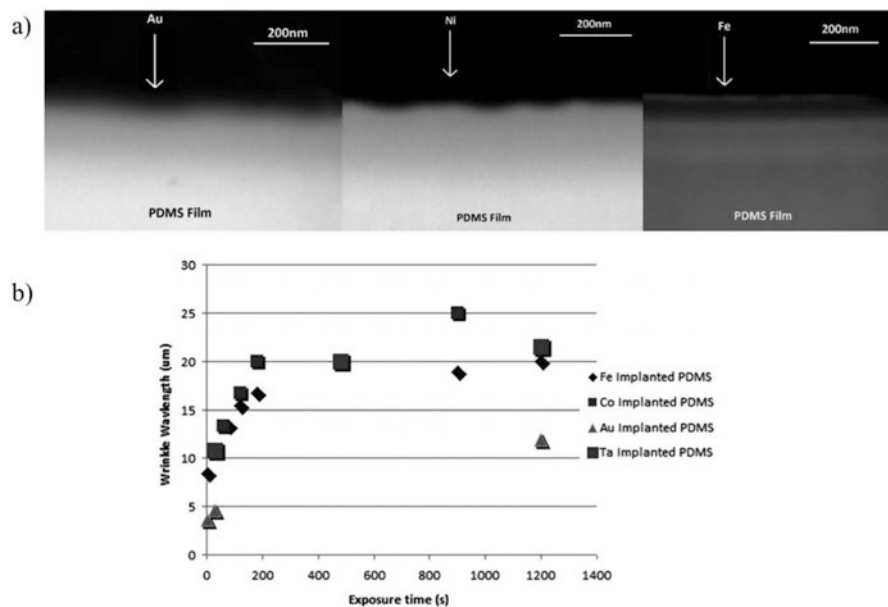


**Fig. 4.8** (a) Cross-sectional TEM images of PDMS irradiated with Ni, Fe, and Au for 20 min; the black region is metal coating grown on the surface. (b) Dependence of the wrinkle wavelength on the implanted metallic ion. (Reproduced with permission from Ref. [30])

surface layer and the thickness of the metal-rich layer acting as a diffusion barrier [31]. This explains why the Au-implanted surface formed wrinkles within seconds, followed by Fe, Ni, and Co (Fig. 4.8a). All the implanted ions behaved similarly with dose, with the wavelength of the wrinkles rapidly increasing with increasing dose until a critical dose at which the increases in wavelength started leveling off in a sigmoidal-like behavior, as seen in Fig. 4.8b.

#### 4.4.2 Configuring the Wrinkle Pattern by Using Templates

Hasan et al. [32] developed a multi-walled carbon nanotubes/PDMS (MWCNT/PDMS) piezoresistive tactile sensor. In this article, it was showed that the height increase of the surface conformations is another aspect of improving the performance of piezoresistive tactile sensors. Thus, low-energy Ar<sup>+</sup> IB treatment was carried out to generate stiff straight and curved-shaped micropillars. The effects of this methodology were investigated via resistance measurements and FE-SEM images in terms of the electrical properties of the MWCNT/PDMS film. Besides, shape changes of the micropillars and tactile sensing of MWCNT/PDMS micropillar were tested under normal pressure and shear stress.

The tactile sensor consists of two MWCNT/PDMS films with curve micropillar surface texture interlocked with each other. Figure 4.9a (left) illustrates the five steps necessary for the fabrication of the MWCNT/PDMS film with micropillars. To generate a curvature or an inclination degree of the pillars, the incident angle of the Ar<sup>+</sup> ion beam was varied from 0°, 30°, 60°, and 80°, respectively. When a shear pressure is applied along the interlocking direction, the resistance of the tactile sensor will be decreased due to the tight and strong contact between the interlocked curved micropillars, whereas the resistance of the sensor will be increased upon application of a shear force against the interlocking direction. A decrease in the resistance of the device according to the tilting angle (0°–80°) is related to the methodology employed (Fig. 4.9b, right). The IB irradiation on PDMS cannot form a graphite-like carbonized structure due to the presence of high level of silicon, a result which was demonstrated via XPS.

By analyzing the characteristics of a localized irradiation-induced wrinkle, Jeong et al. [33] achieved to control the orientation of wrinkle pattern by altering the width of the mask pattern, from 800 to 250 μm. Additionally, the authors examine the coverage of different wrinkle patterns in detail by changing the IB intensity from 800 to 2000 eV, exhibiting an increase in the wrinkle wavelength as a function of the intensity. It should be mentioned that for the formation of wrinkled structure, the IB power intensity needs to be larger than a critical wrinkle-formation threshold (≥800 eV). Figure 4.10b (right) shows a localized IB irradiation-induced wrinkle-formation mechanism that involves different wrinkle patterns at separated regions, where the red and blue lines represent the direction of expansion and contraction, respectively. Besides, localized IB irradiation-induced inhomogeneity of wrinkle patterns was confirmed by observing a pseudo-compressive strain, whose morphology was investigated by optical microscopy (OM) and AFM. Surface inhomogeneity is affected by the distance from the edge. As the distance from the center increases, the relaxation direction converges by applying an anisotropic strain along the pattern (Region A–C; Fig. 4.10, bottom). At the center, the stress is released in all directions, thereby inducing a random labyrinth structure equally distributed 2D FFT graphs (Region A). At area B, four separate sections can be observed, indicating a perpendicularly alternating pattern. Finally, the opposing sides of 2D FFT indicate an anisotropic pattern (Region C). The localized irradiation leads to a relatively different compressive stress on the surface, inducing a different orientation of the wrinkle pattern which is consistent with the morphological characteristics. This study on the inhomogeneity of a wrinkle pattern using a localized treatment can be potentially applied to nano/microfabrication, the arrangement of nanomaterials, and flexible electron devices.

Another interesting case is studied by Rahmawan et al. [34], who presented an alternative method for creating 3D dual-scale superhydrophobic surface structures by depositing a thin layer of diamond-like carbon (DLC) coating with high compressive stress on a pre-patterned PDMS substrate (1–10, contain micropillars 4 μm in diameter and 5 μm in height) in order to explore the effect of microscale roughness on hydrophobicity (Fig. 4.11a, b, top). The thin DLC film contains residual compressive stress, which can directly produce nanoscale wrinkled patterns as shown in

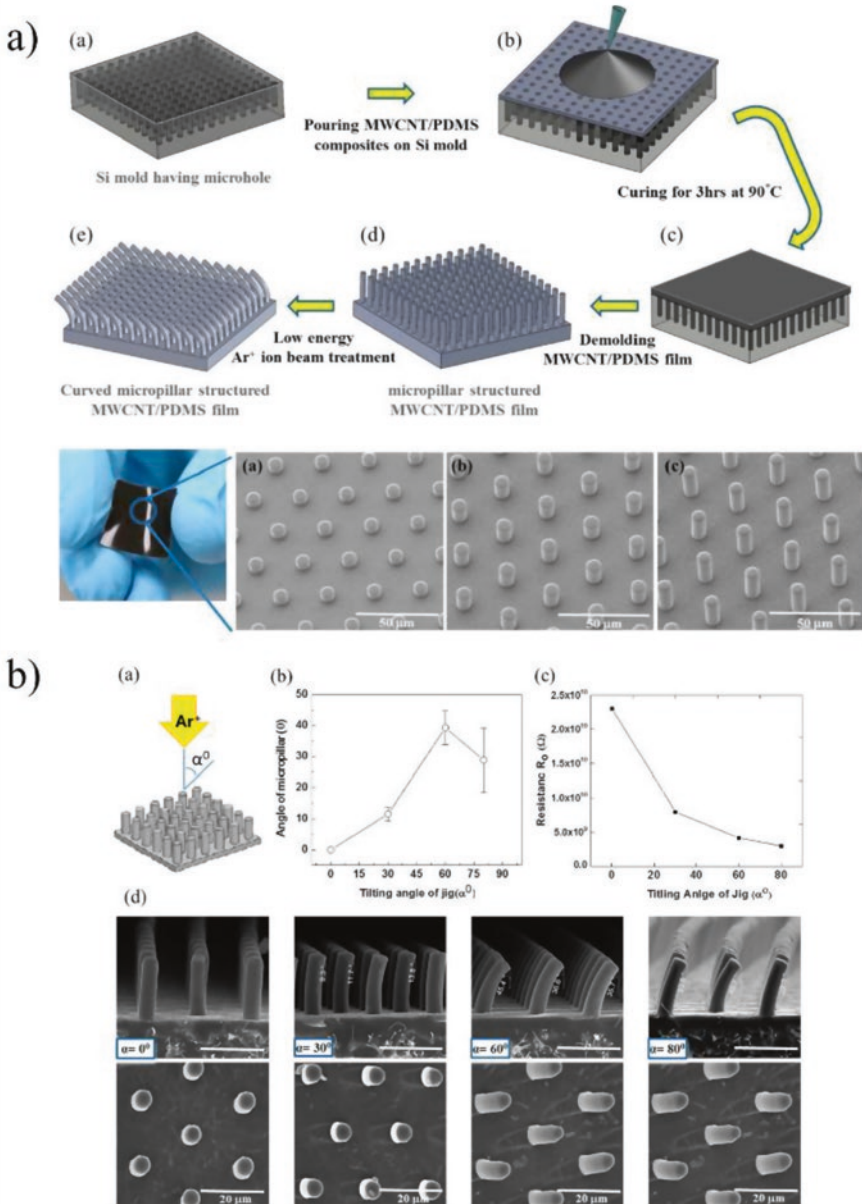


**Fig. 4.9** Top: (a–e) Schematic diagrams of the fabrication process for the micropillar structured MWCNT/PDMS films and FE-SEM images of the obtained surfaces. Bottom: (a) Schematic of ion beam irradiation. (b) Angles of curved micropillars according to the incident angles of ion beam irradiation. (c) Initial resistances of the curved micropillar structured MWCNT/PDMS films according to the incident angles of ion beam irradiation. (d) FE-SEM images of the micropillars according to the incident angles of ion beam 0°, 30°, 60°, and 80° in side view (upper images) and top view (bottom images). (Reproduced with permission from Ref. [32])

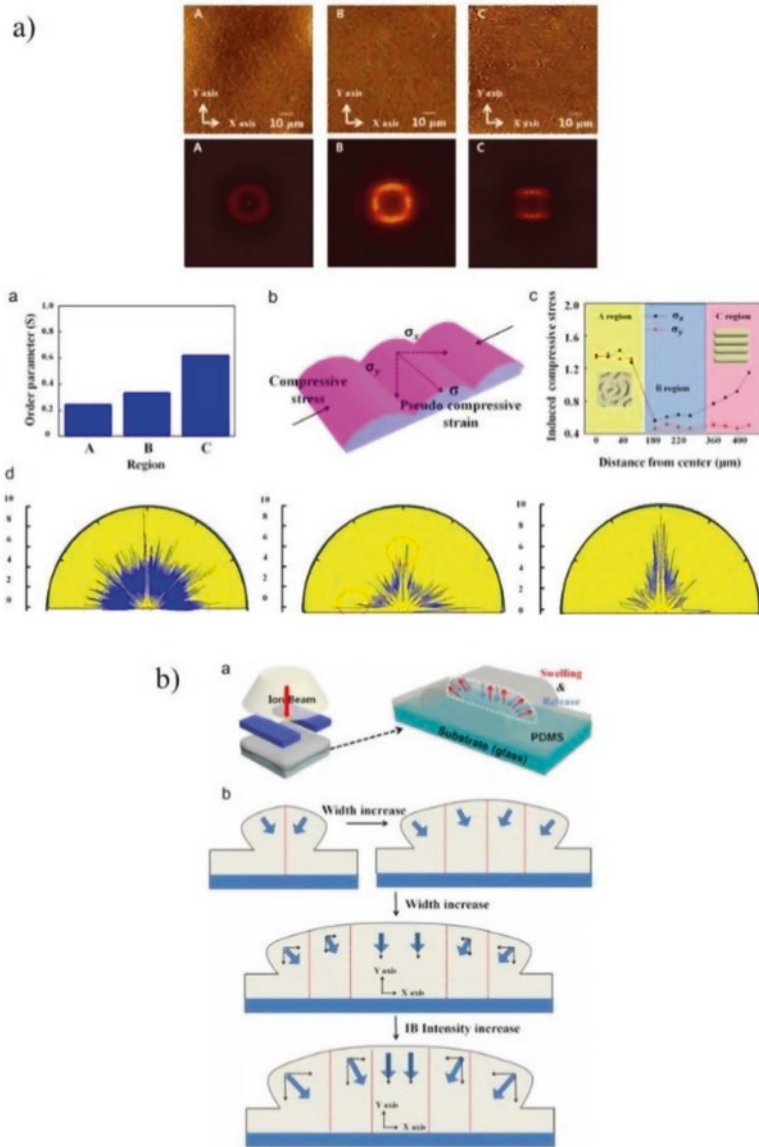


**Fig. 4.10** Top: (up) AFM and 2D-FFT images of different masked regions, (a–d) parameter order plot, scheme of the pseudo-compressive strain, and the polar coordinates of the wrinkles. Bottom: Schematic diagram of the mechanism proposed for inhomogeneous wrinkle formation. (Reproduced with permission from Ref. [33])

Fig. 4.11c–g. Here, hexamethyldisiloxane (HMDSO) was selected as a precursor gas for the DLC film because of its ability to decompose SiO<sub>x</sub> incorporated in DLC thin film with hydrophobic nature during film deposition. According to this procedure, the wavelength and amplitude of these nanoscale wrinkles can be controlled

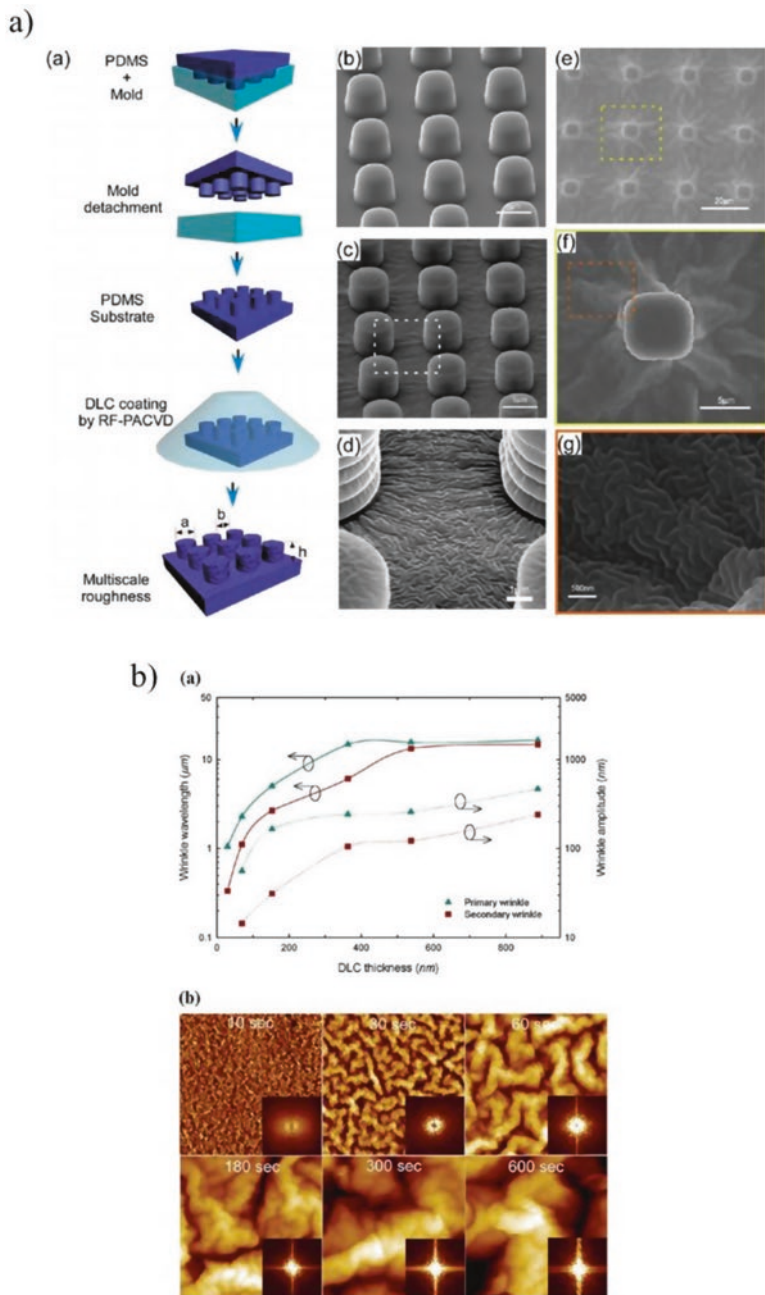


**Fig. 4.11** Top: (a) Two-step method for the fabrication of surface with 3D dual-scale surface structure method. (b) PDMS surface with microscale pillar structures after step 1. (c) SEM images after deposition of DLC for 10s. (d) Magnified images of the multiscale 3D hierarchical structures. (e) SEM images after deposition of DLC for 1 min. (f and g) Magnified images of the multiscale 3D hierarchical structures. Bottom: (a) Effect of DLC thickness on wavelength and amplitude of hierarchical wrinkle pattern with primary (long) and secondary (short) wavelengths. (b) AFM images of wrinkle morphology on PDMS substrate with FFT images in the inset. (Reproduced with permission from Ref. [34])

by changing the thickness of the DLC coating on the pre-patterned PDMS pillar array. Figure 4.11b bottom shows the formation and evolution of the wrinkled surface with two wavy modes as a function of film thickness. The primary (large) wavy patterns grow linearly with DLC thickness, while the secondary (small) wavy pattern shows a retarded growth on top of the primary mode wrinkle, forming a hierarchical wrinkle pattern. Finally, the experimental results show that superhydrophobicity can be achieved on the 3D hierarchical surface structure with a low microstructure spacing ratio. Static contact angle (CA) was over  $160^\circ$ , at larger microstructure spacing ratios, and a transition to a Wenzel<sup>(m)</sup>–Cassie<sup>(n)</sup> state develops a wetting angle of approximately  $130^\circ$ , where m and n denote micro- and nanoscale roughness, respectively.

On the other hand, Bae et al. [35] construct microstructures with periodic and ordered directionalities but with random architecture, like mazes (orthogonal, sigma, and theta shape). Highly regular maze structures, consisting of several tessellations with customized designs, were fabricated by precisely controlling wrinkling with the ridge-guiding structure, analogous to the creases in origami. Experimentally, these were fabricated by groove array with a checkerboard pattern on the particle surface by blocking UV light using 1 pixel by pixel black dots in the photomask. Then, each ridge decision point was randomly transformed to either an ending, a bend, a straight line, or a bifurcation type during the wrinkling (Fig. 4.12b, top). Figure 4.12c (top) shows that the guiding structures itself could both show a specific pattern, revealing that the final structure was spontaneously organized through the wrinkling process rather than through direct lithography patterning (Fig. 4.12d, top). Figure 4.12a bottom shows the degree of ridge confinement along one axis by changing the dimensions of the orthogonal groove array. On the other hand, Fig. 4.12b (bottom) shows the confinement of the pattern wavelength based on the guiding structure dimensions.

The liquid crystal alignment with certain orientation and conformation with a specific pretilt angle has been performed through of a polyimide (PI) layer using a conventional technique [36]. According to this, Jeon et al. [37] demonstrated self-alignment of positive liquid crystals (LCs) using a PDMS film through a long and narrow mask pattern used to produce a wrinkled structure. The formation of this pattern (non-contact mode) helped to align the LC molecules homogeneously. Above the critical wrinkle-formation threshold, the amplitude and wavelength of the wrinkles increased as the IB power increased. Because of the narrow width of the mask pattern used in this study, well-aligned wrinkles formed along the widthwise direction of the mask. The relative difference in stress that caused the wrinkled structure to form in a parallel alignment is analogous to the strain induced on a substrate by stretching and therefore an anisotropy along the lengthwise direction of the mask (Fig. 4.13f–h, top). In addition, the non-treated region between the wrinkled walls was observed to have a smooth, flat surface. Forming a wrinkled wall caused the application of a transversal stress to the non-treated region between the treated regions (Fig. 4.13, bottom).

Other interesting examples were performed by Oh et al., which fabricated a nanostructured superhydrophobic silk, using IB treatment of oxygen etching and

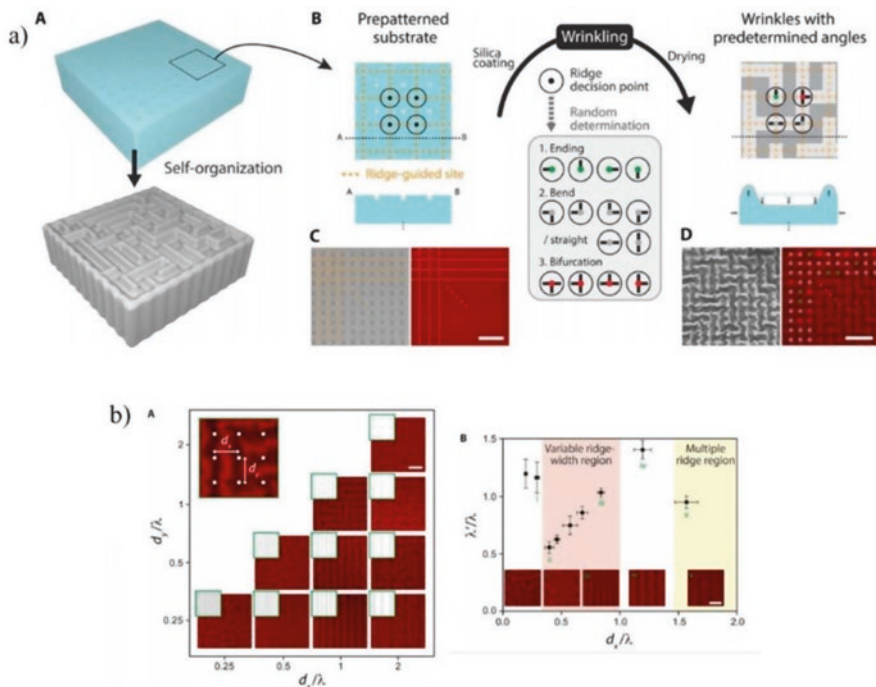


**Fig. 4.12** Top: (a) Schematic illustration of the self-organization of maze-like structures and their fabrication process using ridge-guiding structures. Bottom: Confinement of (a) ridge straightness and (b) pattern wavelength based on the guiding structure dimensions. (Reproduced with permission from Ref. [35])

subsequently hydrophobic deposition [38]. These structures were characterized by the static contact angle ( $170^\circ$ ), the shedding angle (less than  $5^\circ$ ), and the water repellency for various liquids. Chemical analysis and mechanical properties were performed before and after the IB treatment by XPS technique and universal testing machine, respectively. This technique presents a two-step manufacturing process: nanostructure using  $O_2$  gas as an ion source to produce oxygen ions and a subsequent deposition of low-energy materials through of a mixture of  $C_2H_2$  and  $CF_4$  gases. This process can create superhydrophobicity on one side of the silk fabric, while the other side of the silk fabric remains intact (asymmetric wettability).

#### 4.4.3 Energy Dependence: Fluence of the Ion Beam

Moon et al. [39] report a controlled creation of nanoscale wrinkled patterns on PDMS by changing the acceleration voltage (5–30 KeV) and fluency of the ion beam ( $10^{12}$ – $10^{18}$  ions  $cm^{-2}$ ).  $Ga^+$  focused ion beam (FIB) controls the movement of

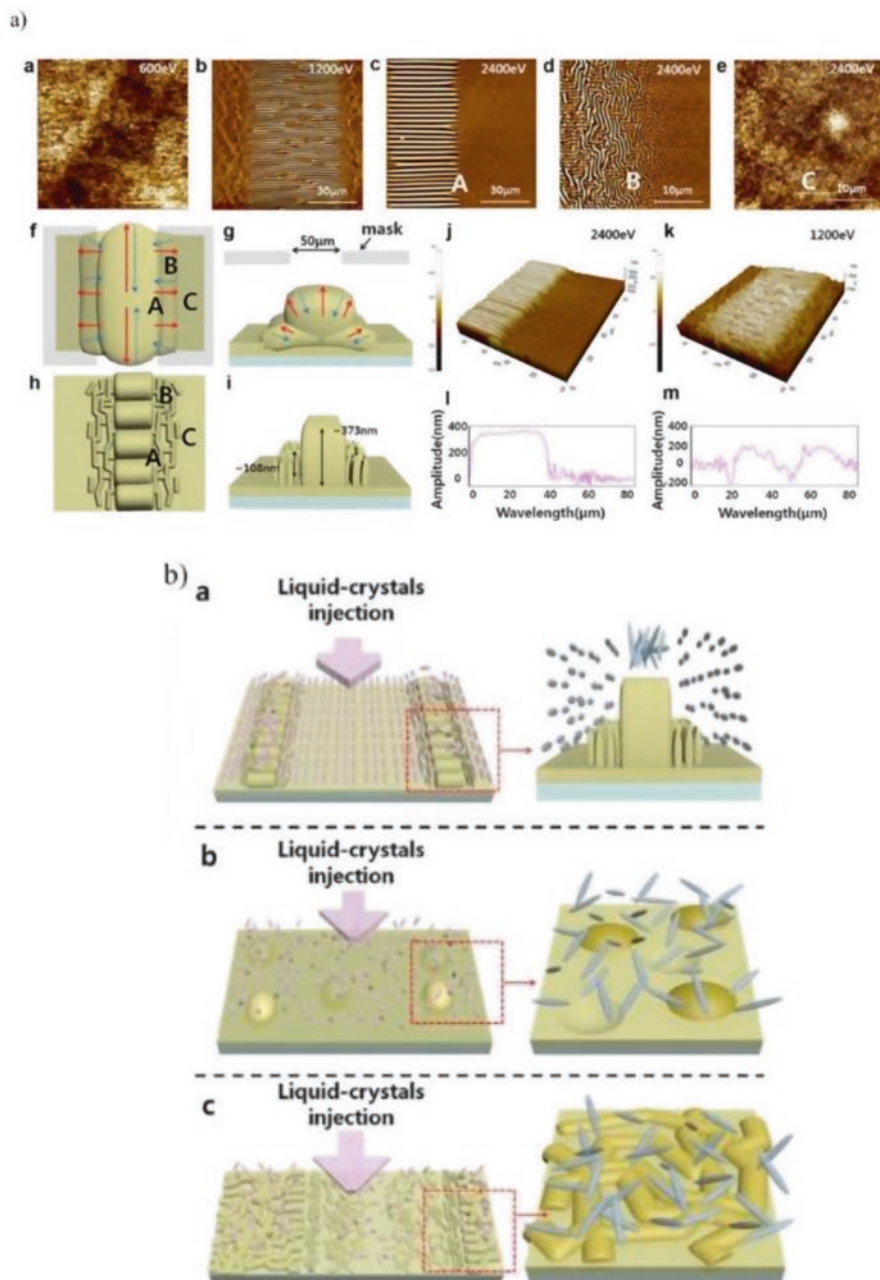


**Fig. 4.13** Top: AFM images of narrow-patterned PDMS films fabricated at IB powers of (a) 600 eV, (b) 1200 eV, (c–e) 2400 eV. (f–i) Schematic description of the formation mechanism. (j–k) 3D AFM images. (l–m) Crossline profiles. Bottom: Schematic description of liquid crystal injection. (Reproduced with permission from Ref. [37])

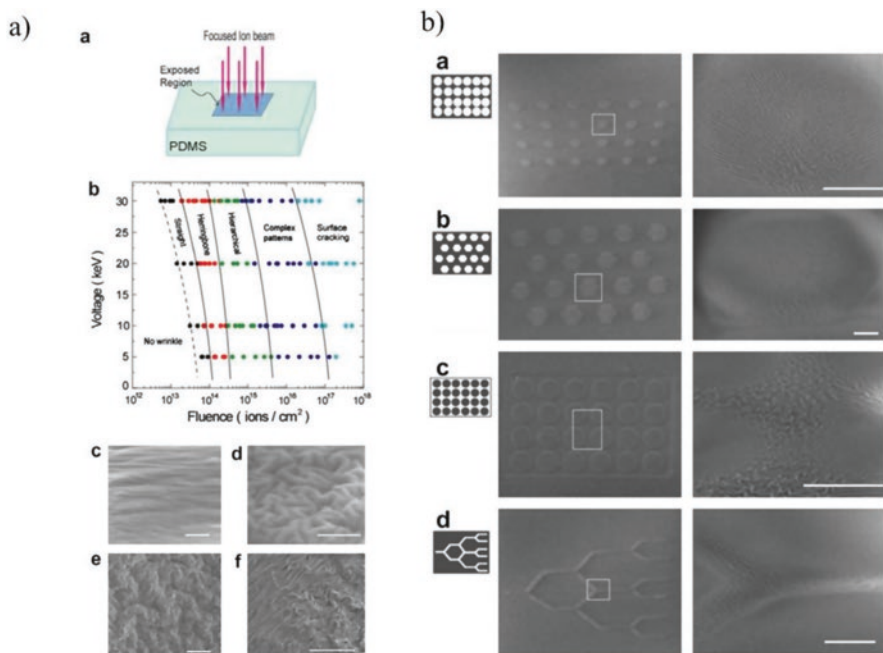


**Fig. 4.14** Left: (a) A schematic description of the FIB on PDMS experiment. (b) Wrinkle morphology as a function of FIB acceleration voltage and ion beam fluence. (c–f) SEM images of the wrinkling patterns at different acceleration voltages and fluencies. Right: (a–d) SEM images of patterns formed with FIB using different patterned shapes. (Reproduced with permission from Ref. [39])

the ion beam on the surface of PDMS, resulting in the formation of a stiff skin on the substrate, which has a chemical composition resembling amorphous silica. In Fig. 4.14a (left) is showed an illustrative scheme of the experiments, and in Fig. 4.14b is observed the critical value of ion fluence associated with the onset of the appearance for a given wrinkle pattern. At very high fluence, complex patterns and cracking of the surface were observed, denoted by the “surface cracking.” Figure 4.14c–f (left) shows SEM images of the induced patterns, at each acceleration voltage. Straight and one-dimensional buckles appear at low ion beam fluence, while at higher ion fluence, more complex patterns are created, including herringbone and double-scale morphologies with two or more distinct wavelengths (Fig. 4.14b, right). In Fig. 4.14b (a–d, right) is shown the bitmap files of the exposure patterns, using a virtual mask in the FIB system and using a low energy ion beam of acceleration voltage 10 keV; wrinkling patterns with wavelength  $\sim 120$  nm and amplitude of 5–30 nm were created in the exposed region of the substrate.

Liu et al. [40] studied the nano-/microscale patterns with controlled stiffness by modifying the ion fluence, acceleration voltage, and ion incidence angle. In Fig. 4.15a, it is possible to observe a scheme of the PDMS, focused Ga<sup>+</sup> ion beam,

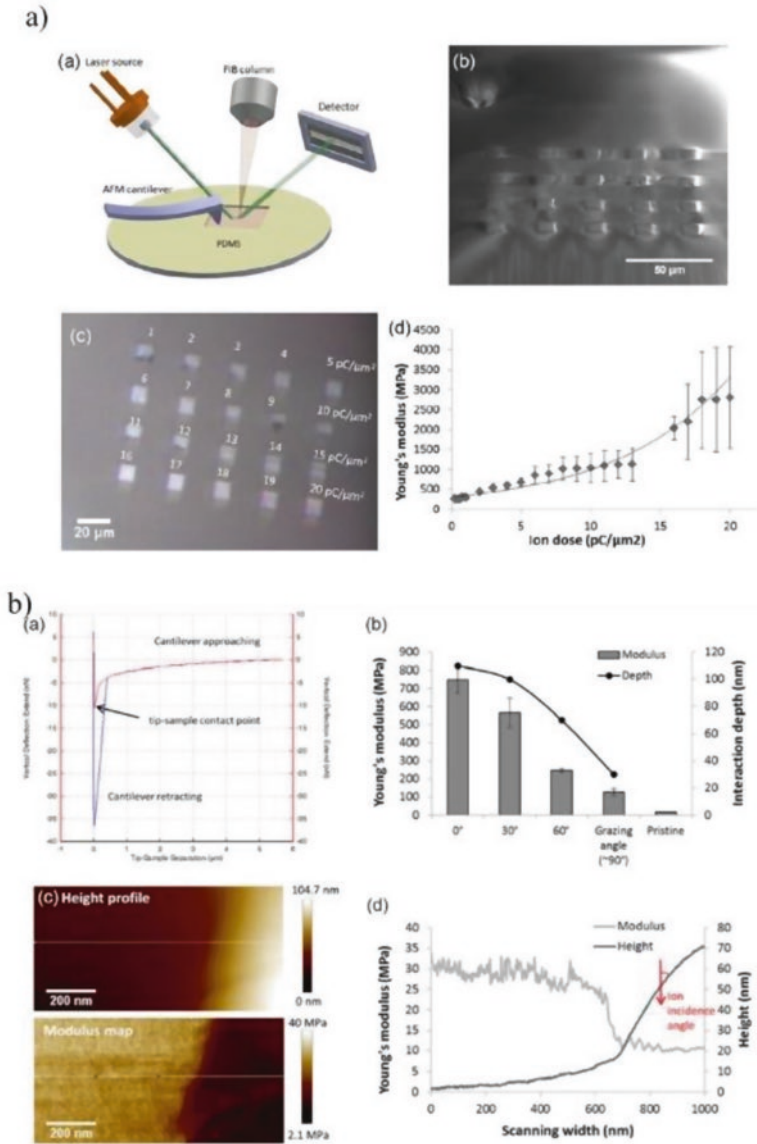


**Fig. 4.15** Top: (a) Schematic illustration of the experimental setup including FIB milling on a PDMS surface. (b–c) Milled patterns without gold coating imaged with SEM. (d) The resultant modulus of PDMS increases with ion fluence. Bottom: (a) An example of the force-distance curve. (b) The modulus and ion penetration depth at increasing ion incidence angles. (c) The height profile (top) and modulus map (bottom) near the edge. (d) Comparison of topography and modulus. (Reproduced with permission from Ref. [40])

AFM, and Raman spectrometer (laser 532 nm). The charging effect during the FIB milling was reduced by gold coating at the surrounding area. The sample stage was tilted to  $52^\circ$  to maintain the ion incident angle at  $0^\circ$  to study the effect of ion fluence on the modulus. Figure 4.15b, c (top) shows the corresponding optical images of the FIB patterns, whose numeral results are observed in Fig. 4.15d (top). The results of nanoindentation by AFM revealed that Young's modulus increased exponentially with the increase of ion fluence from 200 MPa to 2GPa because higher ion dose does not only increase the cross-linking density but also promote the formation of metal-PDMS nanocomposites; both mechanisms induced by ion implantations contributed to elevate the Young's modulus (Fig. 4.15, bottom). The stiffening was found to be less significant with irradiation at higher ion incident angle and lower accelerating voltage, implying minimal changes on the surface hydrophobicity. Raman spectroscopy results also confirmed that disordering caused by cross-linking and hydrogen release occurred on the PDMS surface. By modeling and experimenting on PDMS-Si<sub>3</sub>N<sub>4</sub> bilayer structures, the volume reduction ratios of PDMS with the ion beam and electron beam irradiation were estimated. The proposed site-specific modulating method and understanding of detailed governing mechanisms will allow tuning the PDMS surface with great accuracy and flexibility toward future applications in tissue engineering and microfabrication. Similar studies and conclusions were obtained by Kim et al., in the year 2014 for hydrogels [41].

## 4.5 Conclusions

The IB or FIB methodology is based on the alteration of the chemical and/or mechanical composition sample surface. Their application will considerably affect the micromorphology of the sample. The pattern obtained can be modified and controlled by different factors such as temperature variations, deposition time, variable ion beam voltages, and ion implantation, together with the ion fluence and area exposure. The capabilities of the technique are also extended by adopting the maskless patterning via FIB system, which allows the creation of self-assembled wrinkling patterns within desired intricate surfaces. These techniques were tested for different applications where it is necessary to control the alignment of wrinkled patterns. The methodology described in this chapter could be potentially applied from medicine (tissue engineering, biosensor, and microfluidic devices) to engineering fields (flexible electron devices), involving the nano- and micro-fabrication, among other remarkable usages.

**Acknowledgments** The authors acknowledge financial support given by FONDECYT Grant N° 1170209. M.A. Sarabia acknowledges the financial support given by CONICYT through the doctoral program Scholarship Grant. J. Rodríguez-Hernández acknowledges financial support from Ministerio de Economía y Competitividad (MINECO) (Project MAT2016-78437-R, FEDER EU) and finally VRAC Grant Number L216-04 of Universidad Tecnológica Metropolitana.

## References

1. G. Grime, Ion beam patterning, in *Nanolithography and Patterning Techniques in Microelectronics*, ed. by D. Bucknall (Ed), (Woodhead Publishing Limited/CRC Press LLC, 2015), pp. 184–217
2. K. Ansari, J.A. van Kan, A.A. Bettiol, et al., Fabrication of high aspect ratio 100nm metallic stamps for nanoimprint lithography using proton beam writing. *Appl. Phys. Lett.* **85**, 476–478 (2004)
3. A.A. Tseng, Recent developments in nanofabrication using ion projection lithography. *Small* **1**, 594–608 (2005)
4. A. Piruska, I. Nikcevic, S.H. Lee, et al., The autofluorescence of plastic materials and chips measured under laser irradiation. *Lab Chip* **5**, 1348–1354 (2005)
5. F. Hua, Y. Sun, A. Gaur, et al., Polymer imprint lithography with molecular-scale resolution. *Nano Lett.* **4**, 2467–2471 (2004)
6. S.G. Charati, S.A. Stern, Diffusion of gases in silicone polymers: Molecular dynamics simulations. *Macromolecules* **31**, 5529–5535 (1998)
7. M.-C. Bélanger, Y. Marois, Hemocompatibility, biocompatibility, inflammatory and in vivo studies of primary reference materials low-density polyethylene and polydimethylsiloxane: A review. *J. Biomed. Mater. Res.* **58**, 467–477 (2001)
8. H.-G. Park, H.-C. Jeong, Y.H. Jung, et al., Control of the wrinkle structure on surface-reformed Poly(Dimethylsiloxane) via ion-beam bombardment. *Sci. Rep.* **5**(1–8), 12356 (2015)
9. X. Chen, J.W. Hutchinson, Herringbone buckling patterns of compressed thin films on compliant substrates. *J. Appl. Mech.* **71**, 597–603 (2004)
10. G.M. Whitesides, N. Bowden, S. Brittain, et al., Spontaneous formation of ordered structures in thin films of metals supported on an elastomeric polymer. *Nature* **393**, 146–149 (1998)
11. W.T.S. Huck, N. Bowden, P. Onck, et al., Ordering of spontaneously formed buckles on planar surfaces. *Langmuir* **16**, 3497–3501 (2000)
12. H. Hou, F. Li, Z. Su, et al., Light-reversible hierarchical patterns by dynamic photo-dimerization induced wrinkles. *J. Mater. Chem. C* **5**, 8765–8773 (2017)
13. C. Weissmantel, K. Bewilogua, D. Dietrich, et al., Structure and properties of quasi-amorphous films prepared by ion beam techniques. *Thin Solid Films* **72**, 19–32 (1980)
14. B.I. Prenitzer, C.A. Urbanik-Shannon, L.A. Giannuzzi, et al., The correlation between ion beam/material interactions and practical FIB specimen preparation. *Microsc. Microanal.* **9**, 216–236 (2003)
15. Z. Isiksacan, M.T. Guler, B. Aydogdu, et al., Rapid fabrication of microfluidic PDMS devices from reusable PDMS molds using laser ablation. *J. Micromech. Microeng.* **26**(1–8), 035008 (2016)
16. E.-H. Ko, H.-J. Kim, S.-M. Lee, et al., Stretchable Ag electrodes with mechanically tunable optical transmittance on wavy-patterned PDMS substrates. *Sci. Rep.* **7**(1–12), 46739 (2017)
17. D. Park, S.J. Shin, T.S. Oh, Stretchable characteristics of thin Au film on polydimethylsiloxane substrate with parylene intermediate layer for stretchable electronic packaging. *J. Electron. Mater.* **47**, 9–17 (2018)
18. C. Wu, T.G. Lin, Z. Zhan, et al., Fabrication of all-transparent polymer-based and encapsulated nanofluidic devices using nano-indentation lithography. *Microsyst. Nanoeng.* **3**, 16084 (2017)
19. H.-S. Liu, B.-C. Pan, G.-S. Liou, Highly transparent AgNW/PDMS stretchable electrodes for elastomeric electrochromic devices. *Nanoscale* **9**, 2633–2639 (2017)
20. E.P. Chan, A.J. Crosby, Spontaneous formation of stable aligned wrinkling patterns. *Soft Matter* **2**, 324–328 (2006)
21. D.P. Holmes, M. Ursiny, A.J. Crosby, Crumpled surface structures. *Soft Matter* **4**, 82–85 (2008)
22. J.W. Coburn, H.F. Winters, Plasma etching—A discussion of mechanisms. *J. Vac. Sci. Technol.* **16**, 391–403 (1979)

23. E. Cerda, L. Mahadevan, Geometry and physics of wrinkling. *Phys. Rev. Lett.* **90**, 074302 (2003)
24. H.-G. Park, Y.S. Park, K.Y. Park, et al., Homogeneous liquid crystal alignment on Poly(Vinylidene Fluoride-Trifluoroethylene) films subjected to ion-beam irradiation. *Liq. Cryst.* **42**, 1262–1268 (2015)
25. S.F. Ahmed, G.-H. Rho, K.-R. Lee, et al., High aspect ratio wrinkles on a soft polymer. *Soft Matter* **6**, 5709–5714 (2010)
26. A. Herzog, K. Uchiya, O. Karthaus, Pollen-like particles can be prepared by exposure of polymer microparticles to an electron beam. *Matters (Zürich)* **2016**, 1–4
27. M.-W. Moon, S.H. Lee, J.-Y. Sun, et al., Wrinkled hard skins on polymers created by focused ion beam. *Proc. Natl. Acad. Sci.* **104**, 1130–1133 (2007)
28. S. Faruque Ahmed, S. Nagashima, J.Y. Lee, et al., Self-assembled folding of a biaxially compressed film on a compliant substrate. *Carbon N. Y.* **76**, 105–112 (2014)
29. H.-C. Jeong, H.-G. Park, Y.H. Jung, et al., Tailoring the orientation and periodicity of wrinkles using ion-beam bombardment. *Langmuir* **32**, 7138–7143 (2016)
30. B. Winton, M. Ionescu, S.X. Dou, The control of time-dependent buckling patterns in thin confined elastomer film. *J. Mater. Res.* **25**, 1929–1935 (2010)
31. D.T. Eddington, J.P. Puccinelli, D.J. Beebe, Thermal aging and reduced hydrophobic recovery of polydimethylsiloxane. *Sensors Actuators B Chem.* **114**, 170–172 (2006)
32. S. Hasan, Y. Jung, S. Kim, et al., A sensitivity enhanced MWCNT/PDMS tactile sensor using micropillars and low energy Ar<sup>+</sup> ion beam treatment. *Sensors* **16**(1–10), 93 (2016)
33. H.-C. Jeong, H.-G. Park, J.H. Lee, et al., Localized ion-beam irradiation-induced wrinkle patterns. *ACS Appl. Mater. Interfaces* **7**, 23216–23222 (2015)
34. Y. Rahmawan, M.-W. Moon, K.-S. Kim, et al., Wrinkled, dual-scale structures of diamond-like carbon (DLC) for superhydrophobicity. *Langmuir* **26**, 484–491 (2010)
35. H.J. Bae, S. Bae, J. Yoon, et al., Self-organization of maze-like structures via guided wrinkling. *Sci. Adv.* **3**(1–6), e1700071 (2017)
36. S.-C. Jeng, S.-J. Hwang, Controlling the alignment of polyimide for liquid crystal devices, in *High Performance Polymers - Polyimides Based - From Chemistry to Applications*, (InTech, 2012), pp. 87–104
37. H.-C. Jeong, H.-G. Park, J.H. Lee, et al., Homogeneous self-aligned liquid crystals on wrinkled-wall Poly(Dimethylsiloxane) via localised ion-beam irradiation. *Sci. Rep.* **5**, 8641 (2015)
38. J.-H. Oh, T.-J. Ko, M.-W. Moon, et al., Nanostructured superhydrophobic silk fabric fabricated using the ion beam method. *RSC Adv.* **4**, 38966–38973 (2014)
39. M.-W. Moon, S.H. Lee, J.-Y. Sun, et al., Controlled formation of nanoscale wrinkling patterns on polymers using focused ion beam. *Scr. Mater.* **57**, 747–750 (2007)
40. B. Liu, J. Fu, Modulating surface stiffness of polydimethylsiloxane (PDMS) with kiloelectron-volt ion patterning. *J. Micromech. Microeng.* **25**(1–9), 065006 (2015)
41. Y. Kim, A.Y. Abuefilat, S.P. Hoo, et al., Tuning the surface properties of hydrogel at the nanoscale with focused ion irradiation. *Soft Matter* **10**, 8448–8456 (2014)

# Chapter 5

## Wrinkled Hydrogel Formation by Interfacial Swelling on Thermoplastic Surfaces



Enrique Martinez, Alberto Gallardo, Ana Santos-Coquillat, Noelia Lujan, Helmut Reinecke, Adolfo del Campo, and Juan Rodríguez-Hernandez

### 5.1 Wrinkling: Some Basic Concepts

In the most extended case, wrinkling formation in a typical film is shown in Fig. 5.1a obtained upon initial mechanical stress (by heating, mechanical stretching, or even osmotic pressure) and deposition of a rigid layer on top of a polymer film followed by removal of the stress applied. In this situation, the film foundation is allowed to relax, and due to the difference in the stiffness between the polymer surface (“skin”) and the foundation, a wavy structure known as “wrinkles” is formed.

In addition to surface wrinkles, creases and even folds are also common structures observed in hydrogel polymer films [1–4]. On the one hand, creases can be formed at the free hydrogel surface film upon swelling (Fig. 5.1b). Creases usually appear in gels placed on a rigid support; thus swelling constrains the film and produces the instability [5, 6]. Weiss et al. [5] calculated the critical situations for the

---

E. Martinez

Instituto de Ciencia y Tecnología de Polímeros (ICTP), Consejo Superior de Investigaciones Científicas (CSIC), Madrid, Spain

Tissue Engineering Group; Instituto de Estudios Biofuncionales, Associated Unit to the ICTP-CSIC Polymer Functionalization Group, Universidad Complutense de Madrid, Madrid, Spain

A. Gallardo (✉) · N. Lujan · H. Reinecke · J. Rodríguez-Hernandez (✉)

Instituto de Ciencia y Tecnología de Polímeros (ICTP), Consejo Superior de Investigaciones Científicas (CSIC), Madrid, Spain

e-mail: [gallardo@ictp.csic.es](mailto:gallardo@ictp.csic.es); [jrodriguez@ictp.csic.es](mailto:jrodriguez@ictp.csic.es)

A. Santos-Coquillat

Tissue Engineering Group; Instituto de Estudios Biofuncionales, Associated Unit to the ICTP-CSIC Polymer Functionalization Group, Universidad Complutense de Madrid, Madrid, Spain

A. del Campo

Instituto de Cerámica y Vidrio (ICV-CSIC), Madrid, Spain

© Springer Nature Switzerland AG 2019

C. M. González-Henríquez, J. Rodríguez-Hernández (eds.), *Wrinkled Polymer Surfaces*, [https://doi.org/10.1007/978-3-030-05123-5\\_5](https://doi.org/10.1007/978-3-030-05123-5_5)

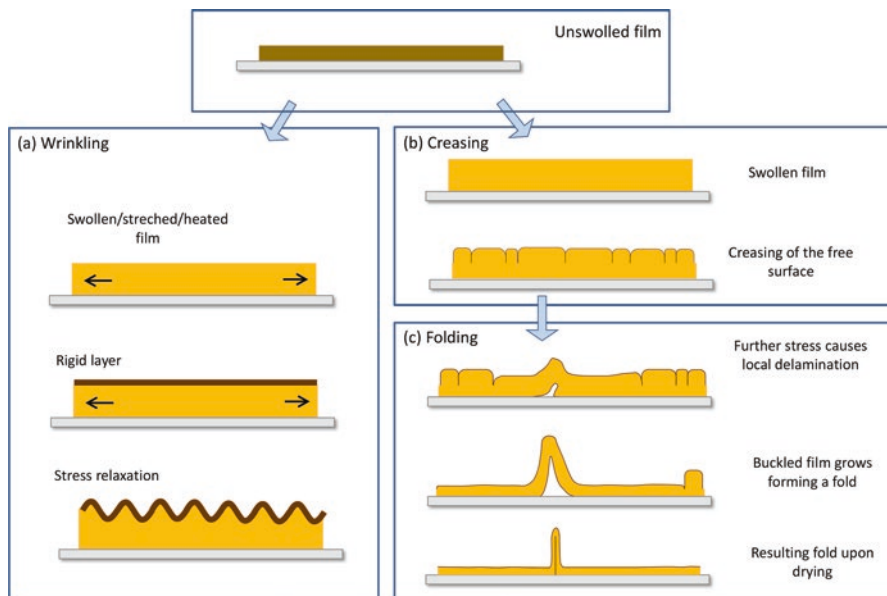


**Fig. 5.1** Schematic illustration of surface structures produced on supported hydrogels: (a) wrinkles are usually observed upon relaxation of a stress in a bilayer system composed of a rigid skin and an elastic foundation; (b) creases and (c) folds appear usually in gel films during swelling. Initially, creases are observed, while larger solvent swelling produces delamination and the formation of folds [7]. (Reproduced with permission from Ref. [12])

beginning of wrinkle and crease formation in a swollen gel attached to a rigid substrate. The authors estimated theoretically that the critical swelling ratio required for the formation of creases is considerably lower than that of wrinkles which also resulted in good agreement with experimental observations. In addition to creases, upon larger swelling, the hydrogel film can buckle, and due to the large stress induced at the surface, local delamination may finally produce folded structures [7–10]. According to Crosby et al. [11], at a critical strain, the stress in the film will localize, causing wrinkles to collapse into several discrete folds.

Today, a large variety of different strategies have been reported up to date to induce wrinkle formation requiring all that a residual stress goes beyond a certain value. The residual stress can be induced by either using external forces mechanical stretching/compression [13–18], by heating the film [19–23], by solvent swelling [24–28], or by capillarity [29, 30] just to mention few of them.

As a result, wrinkles with variable characteristics, i.e., wavelength ( $\lambda$ ) and amplitude ( $A$ ), can be obtained depending not only on the residual stress but also on the intrinsic properties of the films.

## 5.2 Approaches for the Preparation of Wrinkled Hydrogels on Solid Supports

Hydrogels can be defined as cross-linked polymeric materials forming insoluble three-dimensional (3D) structures that, similar to living tissues, are able to retain a large amount of water and biological fluids when in their swollen state [31–33]. Hydration and osmotic as well as capillary forces are involved in the interaction between polymeric chains and either biological fluids or water. The result of these forces provokes the swelling of the cross-linked networks up to a certain equilibrium [34]. These conditions in the equilibrium, which depend on the relative magnitude of the forces and the chain extension induced, govern the inherent hydrogel properties including diffusion characteristics, internal transport, and also its mechanical properties [35].

Hydrogels are currently employed in a myriad of different applications based on the ever-growing amount of functional monomers, and macromeres widen its applicability [36, 37] including biomedical implants, tissue engineering, regenerative medicines, cell encapsulation, diagnostics, biosensor, and biomedical microelectromechanical devices [33, 37, 38]. Equally, hydrogel able to respond to external stimuli has been also explored for such applications as wound dressing contact lenses and controlled drug delivery or for the preparation of artificial muscles [37, 39].

In addition to the chemical design, the surface structural characteristics of the hydrogels [40–45] play a key role in view of their use for other purposes such as surface coatings [46] and chemical actuators [47] or even for lubrication [48]. For instance, microstructured hydrogels have a crucial influence on cell spreading and proliferation as well as differentiation [49, 50]. Today it is widely admitted that the singular location of the cells within a hydrogel surface pattern influences the localized cytoskeletal tension and may, finally, trigger or not cell differentiation. Also, in other recent application areas such as the development of soft actuation devices, the development of structural hydrogels is of high interest [47]. These structural hydrogels facilitate a fast stimuli response of the fabricated devices, which are typically formed by bilayer patterned hydrogels [51]. Finally, it is worth mentioning that recent reports evidenced that the precise structural (from macro- to the nanoscale) design of hydrogels can efficiently change the interfacial properties such as the lubrication [48].

In spite of the potential applications and the advantages of structural hydrogels mentioned above, their fabrication remains a challenge, and the literature in this context is scarce. A huge effort is currently being doing in the fabrication of structured hydrogels with variable patterns and geometries depending on the targeted application. The variety of patterned hydrogels in size features varied from nanoscale to microscale and even to the macroscale [40].

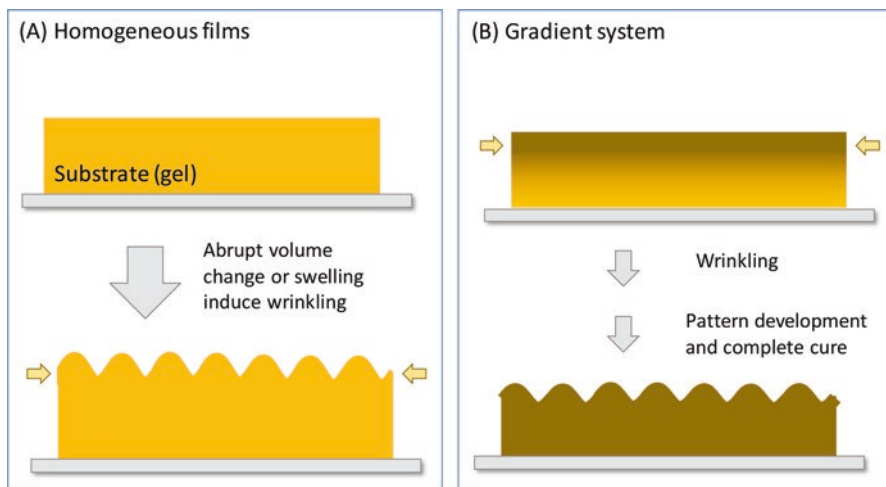


**Fig. 5.2** Film structures capable of forming wrinkles: (a) homogeneous films (typically homogeneously cross-linked hydrogels) and (b) gradient film with variable mechanical properties as a function of the depth. (Adapted from Ref. [12])

In this context, the surface structuration of hydrogel by surface wrinkling is an interesting alternative. The formation of wrinkle hydrogel surfaces has been achieved using mainly two different film configurations [52–57] based on the construction of the precursor film: (A) homogeneous films and (B) films formed by a gradual variation of the mechanical properties from the surface to the bulk (Fig. 5.2). Here below we will analyze some recent examples reported in the literature in which either homogeneous or gradient film structures have been employed for the preparation of wrinkled surfaces.

#### (A) Gradient film with variable mechanical properties as a function of the depth

Substrate-attached homogeneous hydrogel films produce buckling typically by swelling. As the swelling is limited by the rigid substrate, they can only expand along the direction normal to the substrate. As a result, the anisotropic swelling and in-plane compressive stress are generated within the gel. Finally, as depicted in Fig. 5.3, when a certain level of stress is achieved, the free surface of the gel will locally buckle and even fold forming different surface patterns [58–60]. Unfortunately, in general, the patterns produced on swollen hydrogel films are rather heterogeneous, thus preventing their use for a particular application.

The use of film structures with a gradient top layer and a uniform bottom layer has been fabricated to induce surface wrinkling while significantly improving the regularity of the surface pattern generated. An interesting alternative to fabricating these hydrogel structures was reported by Guvendiren et al. [62]. Their investigations were based on the idea that a certain level of dissolved oxygen can consume radicals and therefore prevent the photopolymerization and cross-linking of poly-

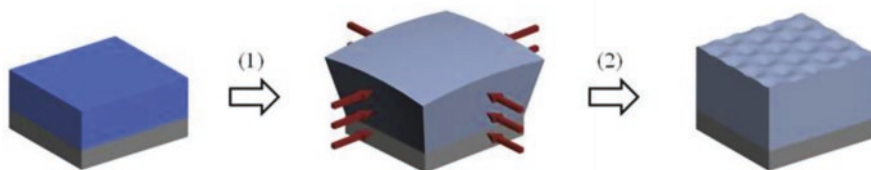


**Fig. 5.3** Schematic representation of swelling-induced wrinkling of a substrate-attached hydrogel film. Upon anisotropic swelling, equibiaxial compressive stress is produced within the film. In a second step, the surface tends to buckle if the stress produced upon swelling overcomes a critical threshold. (Reproduced with permission from Ref. [61])

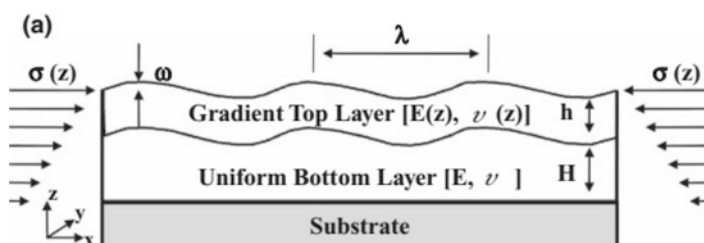


**Fig. 5.4** Schematic illustration of gradient hydrogel film, which is composed of two layers: bottom layer with uniform mechanical properties and a thinner top layer with gradient modulus due to oxygen inhibition during photocross-linking. ( $\lambda$  is the characteristic wavelength,  $\nu$  is the Poisson's ratio,  $E$  is Young's modulus,  $\sigma$  is the stress). (Reproduced with permission from Ref. [62])

mers. The authors prepared PHEMA films thicker than  $20\ \mu\text{m}$ , in which the consumed oxygen could not be replaced fast enough to limit cross-linking and the amount of diffused oxygen gradually decreased along the film depth. As a result, controlling both film thickness and cross-linker concentration (in turn related to the  $\text{O}_2$  diffusion in the hydrogel film during the UV irradiation step of PHEMA films), the authors were able to form films with a modulus gradient with depth. In addition, the cross-linking gradient profile with depth can be equally modulated by the concentrations of initiator, precursor viscosity, exposure time, and intensity. As a result, as depicted in Fig. 5.4, the top surface layer (in contact with air) had a lower cross-linking density and modulus, which gradually increased with film depth and remain constant below after a critical depth for oxygen diffusion has been reached.

More interestingly, by varying the gradient obtained, Guvendiren and coworkers prepared a series of surface wrinkling patterns that presented morphological changes upon swelling. As depicted in Fig. 5.5, the PHEMA films were prepared from a photosensitive solution composed, in this case, of partially polymerized PHEMA, a photoinitiator, and a cross-linker (ethylene glycol dimethacrylate, EGDMA). The structures observed varied from the highly ordered hexagonal pattern to peanut-shaped, lamellar, and, finally, random worm-like structures depending on the wt% of EGDMA introduced in the photosensitive mixture (Fig. 5.5) [62].

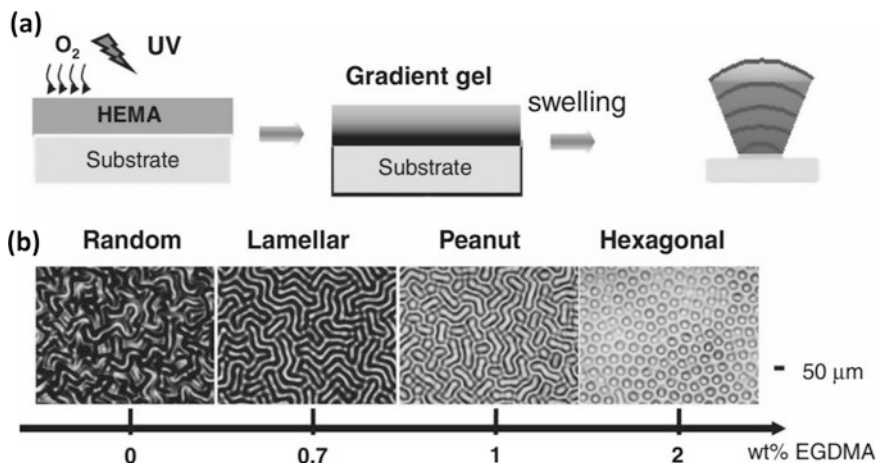


**Fig. 5.5** (a) Schematic illustration of the fabrication of PHEMA films with a modulus gradient and formation of wrinkling patterns upon swelling. (b) Optical images of patterns on the surfaces of DI-water-swollen PHEMA films. The patterns observed are directly related to the concentration of cross-linker EGDMA introduced in the photosensitive mixture [62]

More recently, Gonzalez-Henriquez et al. [63] reported a strategy that permits the spontaneous formation of corrugated patterns using a two-step procedure involving an initial thermal pre-polymerization followed by UV exposure. In contrast to previously described approaches that required either functionalization of the solid substrate to covalently anchor the hydrogel, the authors reported a strategy to produce micrometer-sized wrinkles that do not require sophisticated surface modification steps to produce surfaces with micrometer-sized structures. The approach proposed is illustrated in Fig. 5.6. The initial photosensitive mixture comprises a linear monomer (HEMA), a divalent cross-linking agent (PEGDA), and two initiators APS and Irgacure 2959, which permits an initial thermal and subsequently photoinitiations, respectively. The first polymerization step was carried out at 50 °C and limited in duration to 5 min in order to limit the reaction conversion and therefore produce nano- and micro-gels (Fig. 5.6b) upon deposition onto a solid substrate (Fig. 5.6c) either by spin coating or electrospraying. The films were exposed to UV light to complete the polymerization fixing the film structure. As illustrated in Fig. 5.6c–e, the UV photopolymerization produced flat films that could change their surface structure reversibly upon drying and swelling cycles. Interestingly, the wrinkle pattern could be varied by changing the molecular weight of the cross-linking agent employed. An increase of the molecular weight of the cross-linking agent has associated an increase of the wrinkled wavelength and amplitude.

### (B) Homogeneously cross-linked hydrogels

As has been mentioned above, in general, homogeneously cross-linked hydrogels lead to rather heterogeneous wrinkled surfaces. However, several strategies have been reported in order to avoid this limitation. For instance, Guvendiren et al.

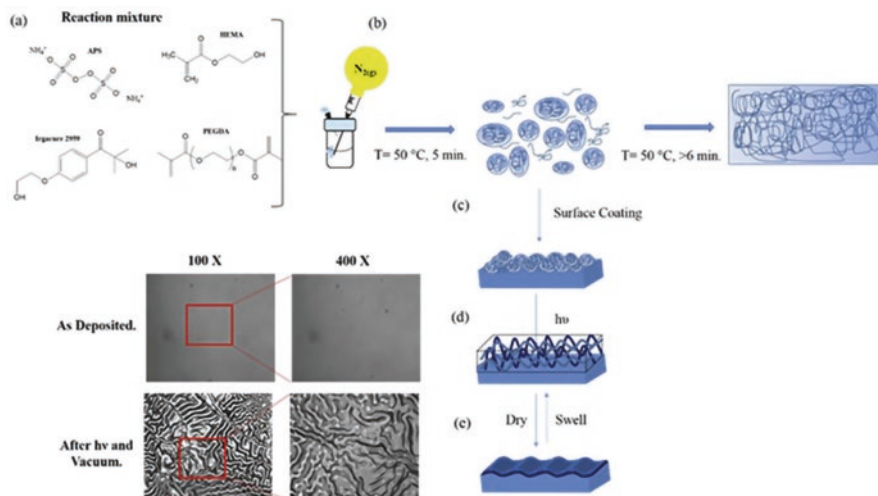


**Fig. 5.6** Schematic approach of the strategy employed to fabricate reversible wrinkled planar surfaces. The fabrication involves consecutive thermal and photopolymerization steps. Upon drying under vacuum, the films exhibit the formation of wrinkles. (Reproduced with permission from Ref. [63])

[64] reported the use of wrinkled PDMS molds to fabricate via a replica molding process a series of gels with uniform mechanics but alter surface wrinkle size and shape (Fig. 5.7).

Instead of using consecutive thermal and UV light treatments or the two-stage UV-curing procedure reported by Guvendiren et al. [65], Gu et al. [61] recently reported an alternative strategy that involves exclusively one-step UV curing of HEMA liquid. This methodology overcomes important limitations of two-stage procedures. On the one hand, first thermal and UV curing are difficult to maintain constantly, and this could have a significant influence on the properties of the final film. Moreover, in view of the eventual mass production, in two-stage procedures, a limited amount of prepolymer solution is usually prepared, thus limiting their scale-up. Gu et al. develop a straightforward methodology for the synthesis of wrinkled PHEMA films.

The strategy (depicted in Fig. 5.8) involves the use of a prepolymer solution (monomer, cross-linker, and photoinitiator) UV-irradiated first for 20 s. The lamp was then switched off, and the sample was allowed to stand for 5 h. Then the solution was UV-irradiated for an additional 180 s. In this way, PHEMA films with a smooth surface were successfully obtained that upon swelling in water develop different wrinkling morphologies.

Finally, Tang et al. [66] reported the fabrication of hydrogels supported on dielectric elastomers (Fig. 5.9) and analyzed the formation of voltage-induced wrinkles. An aligned wrinkle pattern was obtained in the hydrogel upon a direct current voltage. Interestingly, when the current was removed, the wrinkles disappeared. The

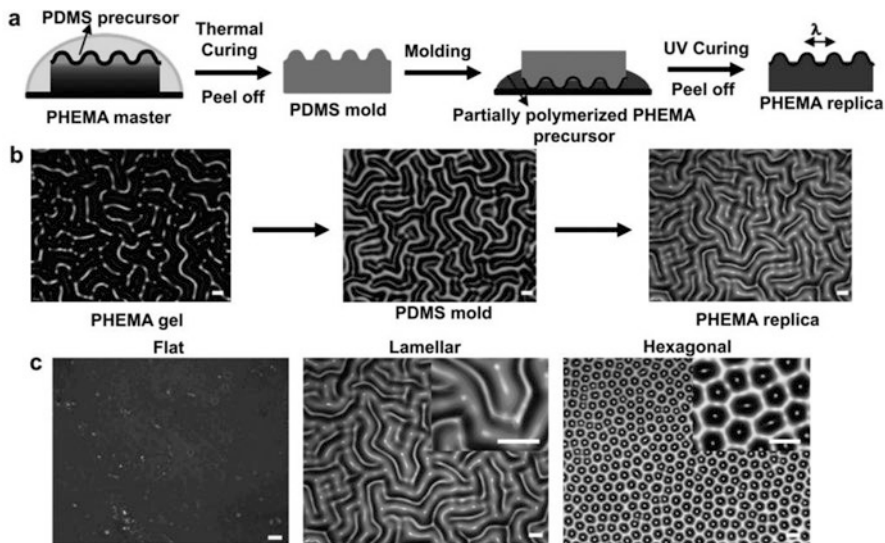


**Fig. 5.7** (a) Schematic of the patterned hydrogel fabrication process. (b) Optical microscopy images of the original, gradient-PHEMA gel with swelling surface patterns, PDMS mold, and PHEMA replica. (c) PHEMA gels containing 1 wt% EGDMA with uniform mechanical properties ( $w150$  kPa) but different surface topography: flat, lamellar, and hexagonal. Scale bars are 50  $\mu$ m. (Reproduced with permission from Ref. [64])

morphology and nonlinear mechanics of the electro-wrinkling deformation were characterized and analyzed. The optical property of the wrinkle in hydrogel was investigated, demonstrating a tunable blurring effect in optics. The electro-wrinkling performance offers a potential application with soft and tunable optical property in hydrogel-based actuators.

### 5.3 Cell Behavior on Microwrinkled Surfaces

While it is widely accepted that cells and in particular stem cells are responsive to both extrinsic and intrinsic cues, only a few studies were reported up to date about the use of microwrinkled surfaces for cell culture purposes. Herein, we briefly compiled some illustrative examples of the potential applications of the microwrinkled surface for cell culture purposes.

#### 5.3.1 Cell Morphology on Wrinkled Surfaces

One of the pioneer works was reported by Guvendiren et al. [64] that explored the use of wrinkled hydrogel surfaces to analyze the cell morphology and the differentiation process. For their tests they prepared both lamellar and hexagonal patterns

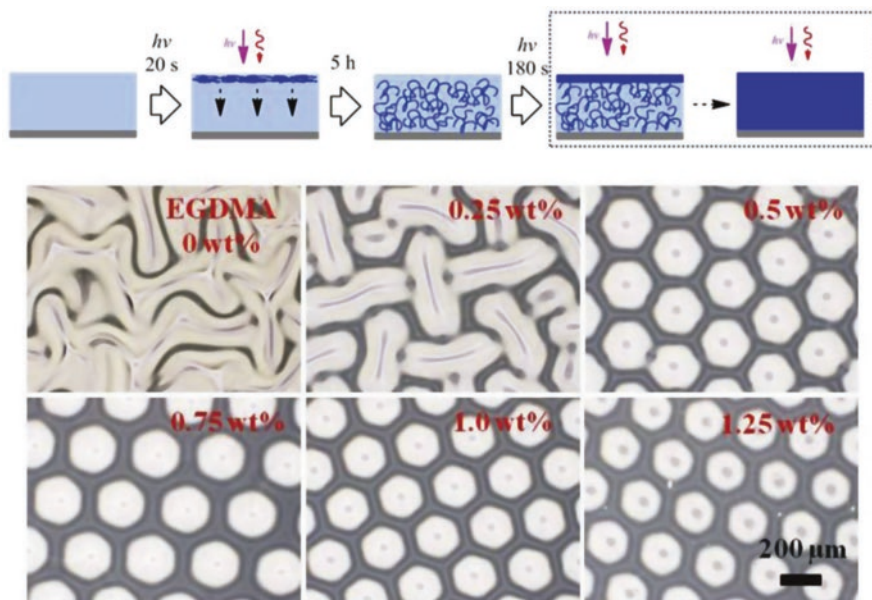


**Fig. 5.8** Top: synthesis of PHEMA hydrogel films. The prepolymer solution (monomer HEMA + cross-linker EGDMA + photoinitiator Darocur 1173) was cured directly by 180 s UV irradiation. Bottom: wrinkling patterns developed on the PHEMA films with various contents of cross-linker EDGMA as indicated. (Reproduced with permission from Ref. [61])

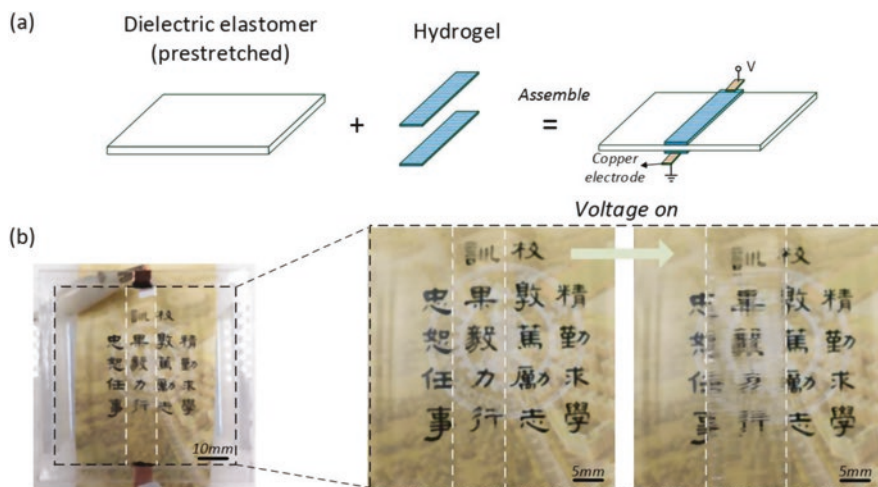


**Fig. 5.9** Hydrogels are attached to the pre-stretched dielectric elastomer, consisting of a soft and fully transparent tri-layer laminate. After applying voltage, the hydrogel deforms and wrinkles. (a) The fabrication process of the actuator. (b) Blurring effect in optics. The white dash box showing the area which is covered with hydrogel. (Reproduced with permission from Ref. [66])

with  $\lambda = 50$  or  $100 \mu\text{m}$  (amplitude  $\sim 20 \mu\text{m}$ ) and used a flat hydrogel for comparative purposes (Fig. 5.10). The authors employed human mesenchymal stem cells (hMSCs) and found that they attach and spread randomly onto the flat hydrogels: around 80% of the cells had an aspect ratio (AR) between 1 and 4, whereas the remaining 20% had AR between 4 and 16. In addition, the cell area varied randomly from  $1 \times 10^3$  to  $7 \times 10^3 \mu\text{m}^2$ .

However, when the cells were seeded on the wrinkled hydrogel surfaces, hMSCs were able to recognize the pattern geometry, but these were largely determined by the pattern size, and the stem cell morphology was influenced by the location of the cell relative to the pattern. Thus, in the case of lamellar patterns with  $\lambda \sim 50 \mu\text{m}$ , most of the cells spread randomly and were not able to recognize the surface pattern. However, for  $\lambda \sim 100 \mu\text{m}$ , most of the cells were able to align along the microwrinkled patterns. In addition, these cells displayed an extensive range of spreading of  $2\text{--}6 \times 10^3 \mu\text{m}^2$ . Finally, when cells were cultured on hexagonal patterns with  $\lambda \sim 50 \mu\text{m}$ , most of the cells attached inside the patterns constrained by the groove and remained rounded. When the pattern size was increased to  $\lambda \sim 100 \mu\text{m}$ , the majority of the cells were found to be inside the patterns with a low aspect ratio (AR = 1–2). These results show that the morphology and size of the hydrogel surface wrinkle control the attached stem cell shape and spreading.

## 5.4 Differentiation on Microstructured Wrinkled Hydrogels

As has been already described in the literature, the shape of the cell when in contact with a particular surface is directly related to the differentiation process. As a result, elongated or cuboidal cells facilitate calcium deposition during bone remodeling in osteocytes [67, 68]. Equally, round cells (circular with low spreading) permit for optimal lipid storage in adipocytes [69, 70].

Guvendiren et al. selected lamellar patterns with  $\lambda \sim 100 \mu\text{m}$ , where they previously detected aligned cells with a high aspect ratio in order to induce osteogenesis, and hexagonal patterns with  $\lambda \sim 50 \mu\text{m}$ , in which round cells were observed to induce adipogenesis. In order to carry out the experiment, hMSCs were allowed to attach and spread for 1 day in growth media, and they were later incubated for 14 days in 1:1 adipogenic/osteogenic mixed media. As a result, differentiation was found to be upregulated. More precisely,  $\sim 91\%$  of the cells stained for alkaline phosphatase for lamellar patterns, followed by  $\sim 74\%$  for flat gels and  $\sim 61\%$  for hexagonal patterns. Likewise, adipogenic differentiation was found to be upregulated such that  $\sim 39\%$  of the cells stained positive for oil droplets for hexagonal patterns, followed by  $\sim 26\%$  for flat gels and  $\sim 9\%$  for lamellar patterns. More interestingly the authors found that the cell position in and out whether the cell adheres inside or outside of the grooves plays a key role in the differentiation process (Fig. 5.11). For lamellar patterns, osteogenic differentiation was upregulated ( $\sim 98\%$  of the cells) for cells that were outside the patterns, in contrast to only a 20% variance in favor of osteogenic differentiation for cells inside the patterns. For hexagonal patterns, nearly all of the

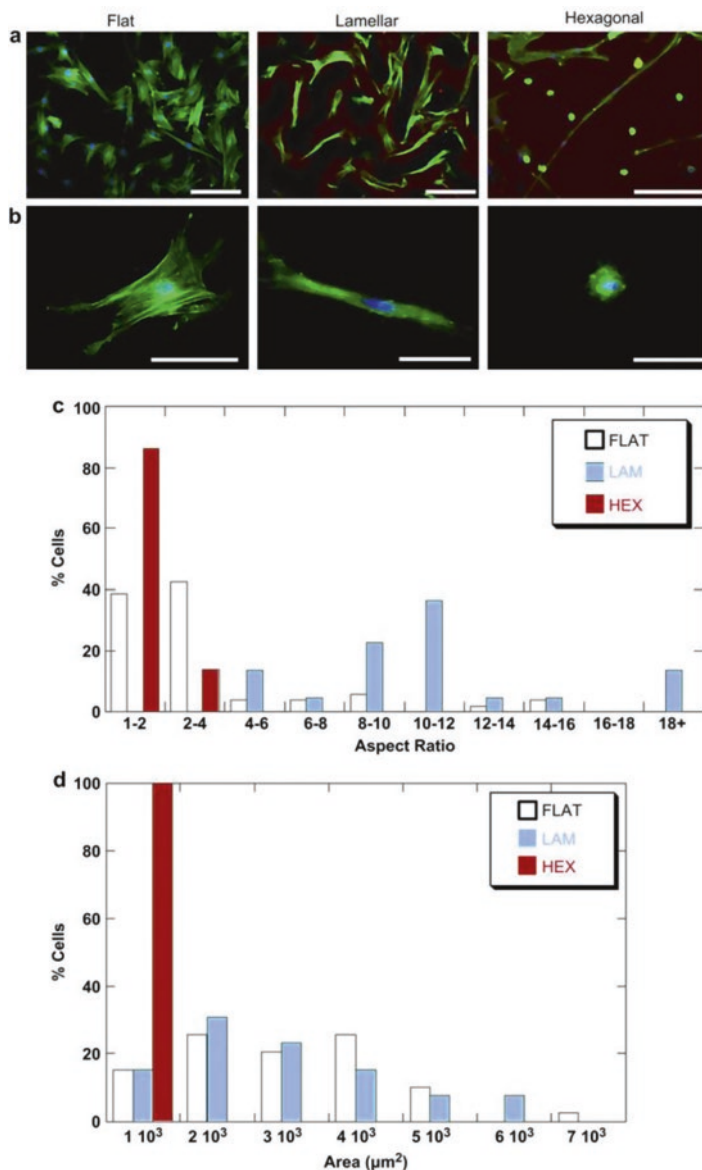


**Fig. 5.10** Fluorescent microscopy images of hMSCs seeded on flat (FLAT), lamellar (LAM), and hexagonal (HEX) hydrogel patterns (staining: blue, nuclei; green, actin; and red, hydrogel) and cultured for 24 h (a–b). Images showing typical stem cell morphology and spreading: random for flat, spread and elongated for lamellar, and rounded with small area for hexagonal patterns. Stem cell aspect ratio (c) and spreading (d) for flat, lamellar, and hexagonal hydrogels. Scale bars are 100  $\mu\text{m}$  for the top panel and 25  $\mu\text{m}$  for the bottom panel. (Reproduced with permission from Ref. [64])

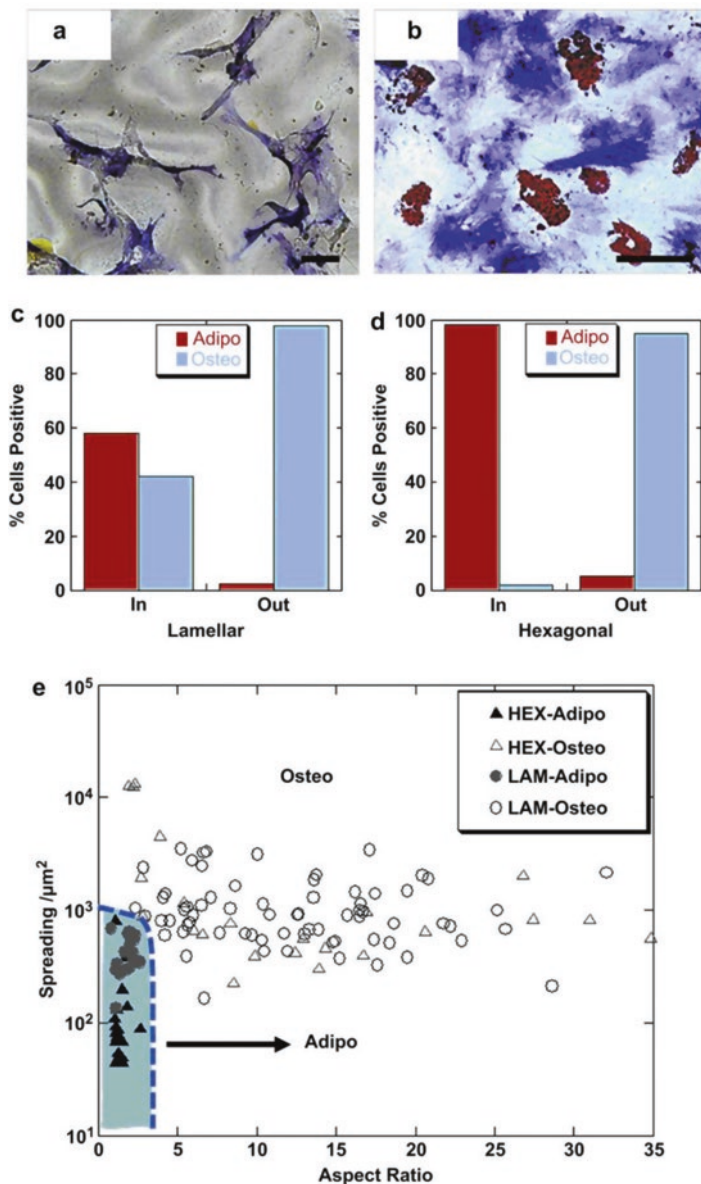


**Fig. 5.11** Optical microscopy images of hMSCs seeded on flat hydrogels and hydrogels with (a) lamellar and (b) hexagonal patterns and cultured for 14 days in mixed media. Cells were stained for alkaline phosphatase (blue) and oil droplets (red) to indicate osteogenesis and adipogenesis, respectively. Scale bars are 50  $\mu\text{m}$ . Staining results showing % cells that were stained positive for oil droplets (adipo) and alkaline phosphatase (osteo) for lamellar and hexagonal patterns. Cells that were in the pattern grooves are denoted by “in” and on the patterns by “out.” (e) Spreading versus aspect ratio for overall cell population on lamellar and hexagonal patterns. (Reproduced with permission from Ref. [64])

cells (~98%) inside the grooves stayed rounded with low AR and differentiated toward an adipogenic phenotype, whereas the majority of the cells (~95%) that were outside the patterns differentiated toward an osteogenic phenotype.

## 5.5 Formation of Three-Dimensional Multicellular Spheroids

Three-dimensional (3D) multicellular spheroids (MCSs) mimic the structure and function of real tissue much better than the conventional 2D cell monolayers. MCSs have been fabricated using different from various types of cells, including hepatocyte [71, 72], human embryonic stem cells (hESCs) [73], HepG2 [74–76], embryonic stem (ES) cells [77–81], human umbilical vein endothelial cells (HUVECs) [82], pancreatic islet cells [83, 84], human and murine pluripotent stem cells [85], etc.

However, their application was severely hindered by difficulties in their generation. An ideal method for MCS fabrication should produce spheroids with narrow size distribution and allow for control over their size. As a result, these structures have been fabricated using microfabrication techniques, such as micromolding [74], soft lithography [75, 78], and contact-lithographic process [83]. It is, however, desirable to find a simple, cheap, and scalable method for the fabrication of such structures. In this context, wrinkled surfaces and in particular those presenting hexagonal features have been proposed for this application.

Zhao et al. [86] reported the use of patterned nonadhesive poly(2-hydroxyethyl methacrylate) hydrogel films to guide the self-assembly of cells. The films were fabricated directly in the wells of cell culture plates. They were patterned spontaneously by swelling in water, without the use of any template or specialized facilities. This group followed the strategy reported previously by Guvendiren et al. [65]. More precisely, they introduced vinyl groups at the glass surface by immersing the slides in a 1.0 wt % ethanolic solution of 3-(trimethoxysilyl)propyl methacrylate. In parallel, they prepared a prepolymer solution comprising HEMA and Darocur 1173, and the photosensitive mixture was irradiated with a UV lamp for 190 s to obtain a viscous, partially polymerized solution. Finally, additional Darocur 1173 and cross-linker EGDMA were added to form the photocurable precursor solution. The precursor solution was coated onto the glass slides and irradiated for 4 min to obtain the PHEMA-based hydrogel films. Upon optimization of the film thickness and the amount of cross-linking agent, the authors prepared wrinkled surfaces with hexagonal features.

When cell suspension is added to the hexagonal wrinkled hydrogels, the cells settle down by gravity to the bottom. Because of the presence of the wrinkling pattern composed of uniformed microcaves, the cells accumulate to the center of the microcaves and gradually self-assemble into MCSs. Using this method, monodisperse MCSs were generated, and the size of the spheroids could be straightforwardly controlled.

wardly controlled by the number of cells seeded. In addition, the cells cultured as 2D monolayer were immunohistochemically examined. As it is shown in Fig. 5.12, the cells in 2D monolayer presented a spread-out structure with an extended cytoplasm. On the contrary, cells in the 3D spheroids (Fig. 5.12 below) presented clustered, rounded morphologies. Interestingly, the actin filaments can be clearly identified at the edges of cells with a cortical distribution.

Also, Gu et al. [61] reported the fabrication of multicellular spheroids. To produce the spheroids, the authors fabricated highly ordered hexagonal arrays in PHEMA films (Fig. 5.13a). Following the strategy reported by Zhao et al. [86], cell suspensions were then added on top of the hexagonal arrays. Under the influence of gravity, the cells settled down and accumulated in the microcaves in several minutes. These cells gradually aggregated into cellular spheroids because PHEMA is nonadhesive for them [87], and a relatively weak cell-substrate interaction facilitates the formation of multicellular aggregates [75, 83] (Fig. 5.13b–c). Thanks to the high regularity of the patterns, the number of cells accumulated in each microcave is almost the same. Therefore, the resulting spheroids displayed a narrow size distribution. In addition, the cells in the spheroids exhibit a high viability.

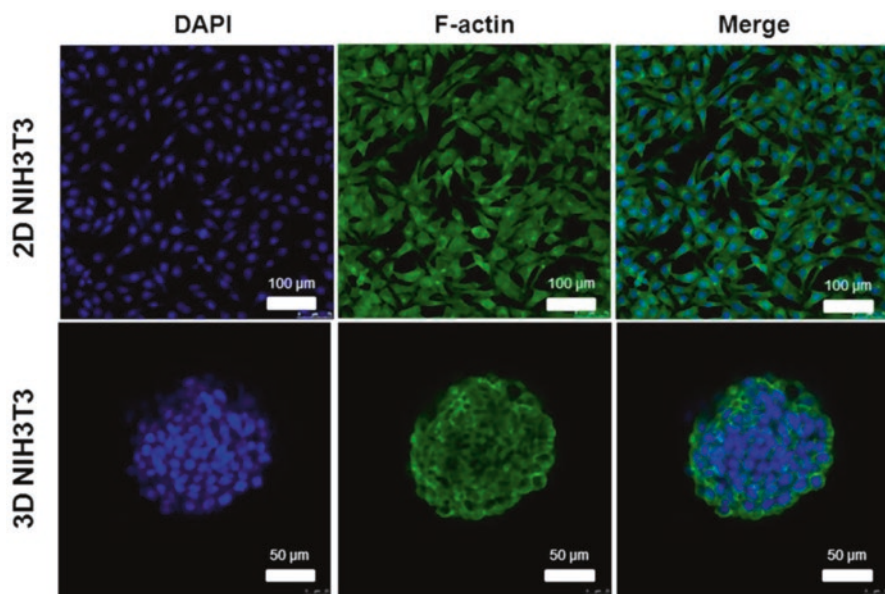


**Fig. 5.12** Fluorescence confocal images of immunohistochemically stained NIH3T3 2D monolayers (top) and 3D multicellular spheroids (bottom). The blue color is related to the cell nuclei staining and the green color to the F-actin. (Reproduced with permission from Ref. [86])

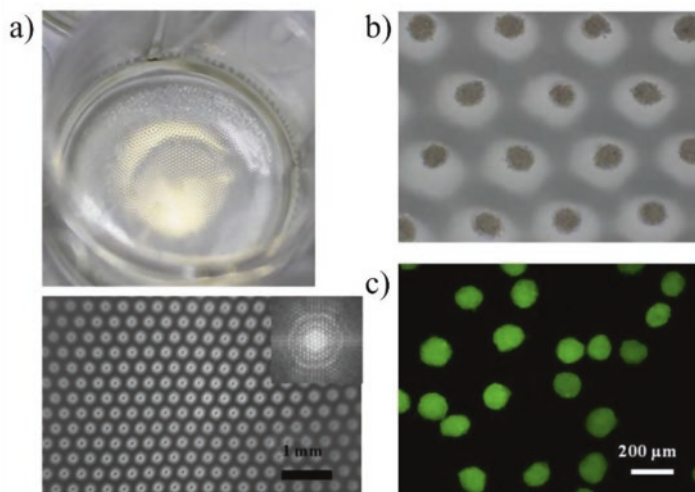


**Fig. 5.13** (a) Above: optical image of a PHEMA film fabricated on the bottom of a 12-well plate with wrinkling patterns. Below: zoom image of the wrinkling pattern with an FFT inset. (b) Photography of the multicellular spheroids generated on the microstructured PHEMA films. (c) Fluorescence image of the multicellular spheroids. (Reproduced with permission from Ref. [61])

## 5.6 Fabrication of Supported Wrinkled Hydrogel Substrates on Thermoplastic Polymers

In addition to the methodologies depicted in Sect. 5.2, our group has proposed an alternative to fabricate wrinkled hydrogel surfaces on thermoplastic polymers. As will be depicted, the supported hydrogels are based on vinylpyrrolidone (VP), a monomer largely known for their antifouling properties and their use as support for cell culture and subsequent transplant. More precisely, a vinylpyrrolidone (VP)-based photopolymerizable formulation has described that permits, in a single step, to fabricate robust pseudo-double network (pseudo-DN) hydrogels with high swelling capabilities (90 weight % of water). More interestingly, these hydrogels exhibited a unique performance as cell culture supports [88]. However, two still remaining issues required further consideration. On the one hand, nonsupported hydrogels were difficult to handle, and those hydrogels did not exhibit any surface pattern.

In order to improve these two limitations, we designed a strategy that involves the use of thermoplastics as supports in order to anchor the hydrogel and the formation of interfacial instabilities to introduce micro structuration. The strategy is schematically shown in Fig. 5.14. The photosensitive solution containing the photoinitiator, VP, and the cross-linking agents was confined between a transparent

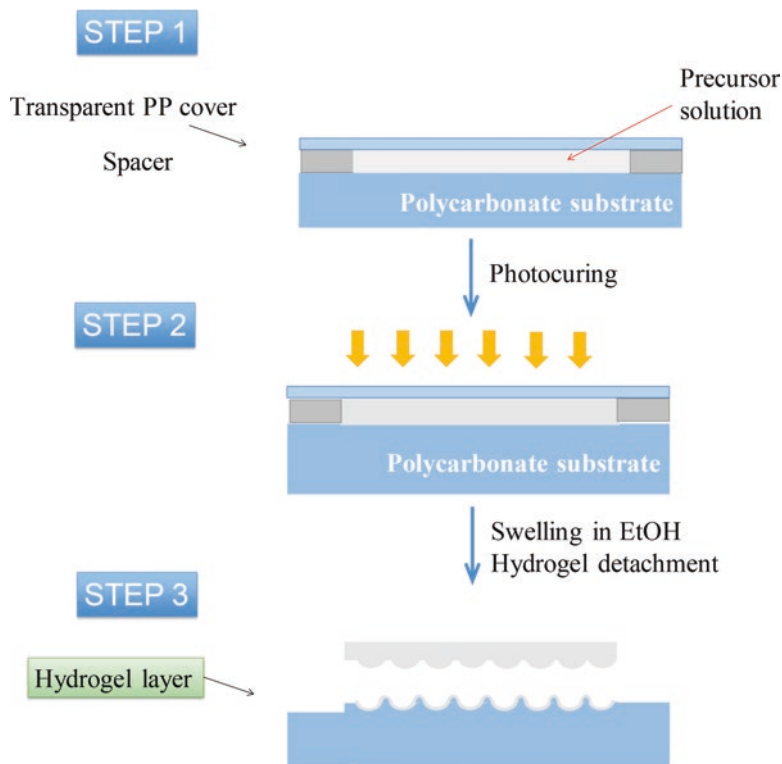


**Fig. 5.14** Setup for the fabrication of PC surfaces modified with VP-based hydrogels

polypropylene cover and a substrate of polycarbonate. The hydrogel thickness was controlled using a spacer. The photosensitive mixture remains in contact with the substrate during a period of time (that requires to be controlled) and is then irradiated with UV-vis during 30 min to assure complete monomer conversion. Finally, the polypropylene cover is removed, and the hydrogel formed was submerged in an EtOH solution [89]. In this situation, as depicted in Fig. 5.15, two different alternatives were observed. On the one hand, some photosensitive mixtures clearly detached from the surface and, interestingly, produced both a wrinkled hydrogel surface and a wrinkled thermoplastic counterpart. On the other hand, using other photosensitive mixtures, the hydrogel remains anchored at the surface. To the best of our knowledge and taking into account the explanation reported by Yuk et al. [90], the hydrogel detachment can be directly associated with the interfacial (hydrogel/substrate) tension originated upon swelling in water. These are related to the number of anchoring points between the PC substrate and the hydrogel. This number of anchoring points is strongly related to the cross-linking degree. As a result, an

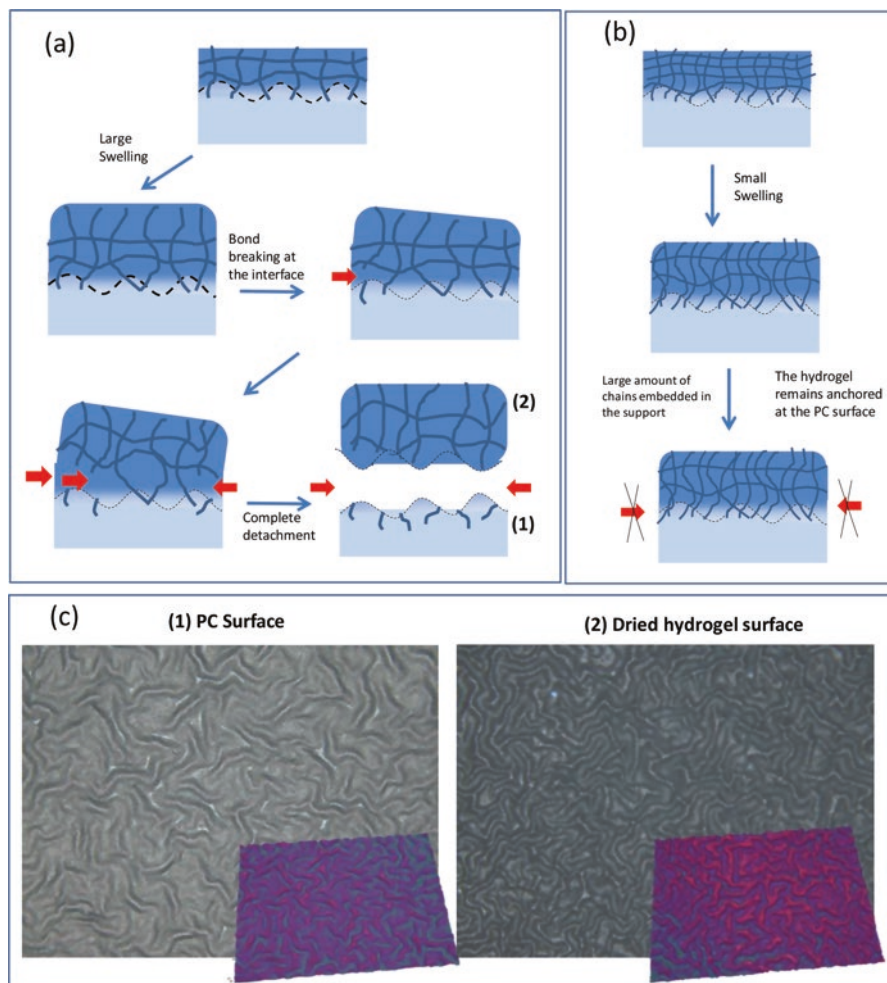


**Fig. 5.15** Schematic illustration of the alternatives observed upon hydrogel formation on top of a thermoplastic: (a) hydrogels are completely removed leaving a wrinkled PC substrate. (b) Hydrogels remain partially/totally anchored to the surface. (c) 3D optical profiler image of a PC wrinkled surfaces (left) and the surface of the detached hydrogel (right). (Reproduced with permission from Ref. [89])

increase in the amount of cross-linking agent employed leads to either a partial detachment or a complete anchoring of the hydrogel to the PC substrate (depending on the contact time). On the contrary, a reduction of the cross-linking concentration leads to a complete detachment of the hydrogel from the PC, thus leaving a wrinkled surface. Thus, it appears to exist a critical cross-linking degree. Below this critical value, swelling induces the bond breaking at the interface, and the hydrogel detaches.

On the contrary, above this value, the large amount of anchoring points together with a lower swelling enables the hydrogel to remain anchored.

## 5.7 Variation of the Wrinkle Characteristics: Period and Amplitude

One of the most interesting aspects of this strategy is that the wrinkle characteristics (including both period and amplitude) can be, at least to some extent, varied. Among others, two parameters play a key role on the final wrinkle characteristics, i.e., the contact time between the photosensitive mixture and the thermoplastic before the UV-vis irradiation step and the solvents (amount and type of solvent) employed in the photosensitive mixture.

On the one hand, the influence of contact time was investigated by varying the lag time (between 0 and 30 min) between the contact established and the beginning of the UV light irradiation. As observed in Fig. 5.16, the surface topography pro-

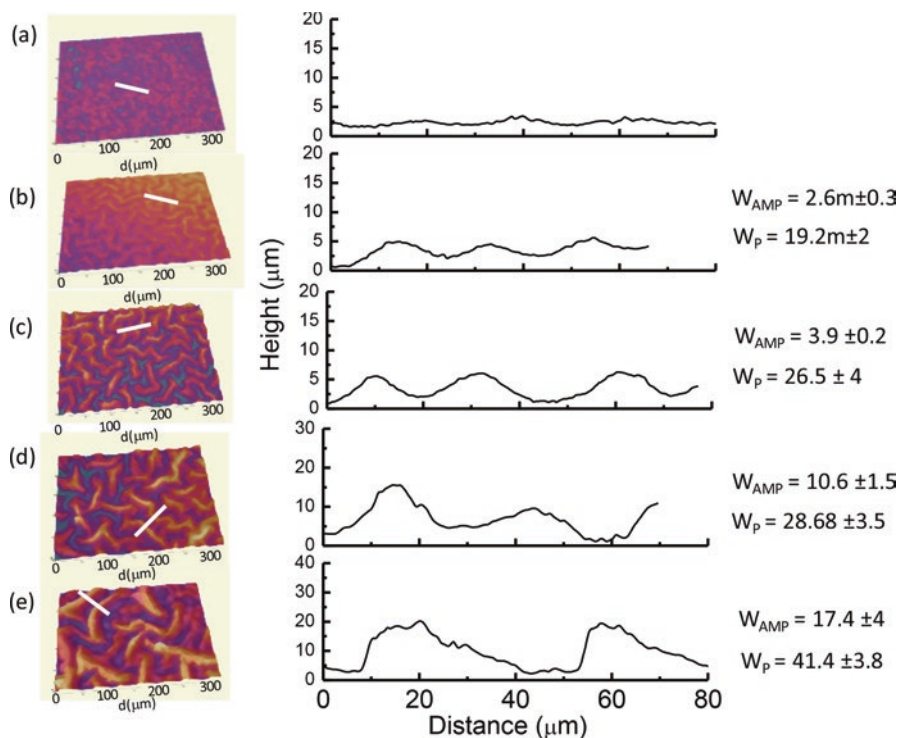


**Fig. 5.16** Optical profilometer images of the PC surface topography upon hydrogel detachment. Wrinkles with variable period and amplitude were formed depending on the contact time between the photosensitive mixture and the PC substrate previous to the photopolymerization step: (a) 0 min, (b) 5 min, (c) 10 min, (d) 20 min, and (e) 30 min.  $W_{AMP}$  wrinkle amplitude,  $W_P$  wrinkle period. (Reproduced with permission from Ref. [89])

**Table 5.1** Photosensitive precursor solutions employed using a mixture of water and ethanol

Name		HYD_1	HYD_2	HYD_3	HYD_4
Cross-linker (mol %)		2.0	2.0	2.0	2.0
Solvent (ml)	EtOH	–	–	0.245	0.490
	Water	0.735	1.000	0.490	0.245

The contact times used prior to the photopolymerization were 0, 5, 10, 20, and 30 min

gressively varies from a flat surface morphology to a wrinkled surface by increasing the contact time between the photosensitive mixture and the PC substrate. Contact times below 5 min produced a rather small increase on the surface roughness (Fig. 5.16a). On the opposite, an increase on the surface roughness together with the formation of wrinkled morphologies is observed with contact times of 5 min and larger. Wrinkles with periods around  $\sim 20$   $\mu\text{m}$  and amplitudes below 3  $\mu\text{m}$  were observed for 5 min contact time (Fig. 5.16b). However, the wrinkle characteristics gradually increased with the contact time. Therefore, for 20 and 30 min, wrinkles with periods from 19  $\mu\text{m}$  to 40  $\mu\text{m}$  and amplitudes comprised between 2.6  $\mu\text{m}$  and 17  $\mu\text{m}$  were measured.

As has been mentioned, an alternative to modifying the wrinkle characteristics is the use of a different solvent or even the use of solvent mixtures. To understand the role of the solvent on the wrinkle formation, several samples (Table 5.1) were prepared using either water or a mixture of ethanol/water. The optical profiler images of the surfaces prepared using these solvents or mixtures are shown in Fig. 5.17. In all cases, as has been mentioned above, the wrinkle dimensions (amplitude and period) clearly varied depending on the contact time for all the samples. However, significant differences were observed depending on the solvent. By using the **HYD\_2** solution with a larger amount of water and therefore with a higher monomer dilution, the size of the wrinkles detected is visibly smaller than those observed using **HYD\_1**. On the contrary, the introduction of ethanol in the photosensitive mixture produced larger wrinkle. In addition, an increase of the relative amount of ethanol/water in the solvent mixture produced wrinkles with larger periods and amplitudes in comparison to those prepared either with water or with a lower amount of ethanol in water. As a result, the combination of contact time together with the possibility to change the solvent permitted us to obtain a rather large variety wrinkles with periods ranging between 10 and 100  $\mu\text{m}$  and amplitudes from 1 to 20  $\mu\text{m}$ .

## 5.8 Composition at the Interface: Contact Angle Measurements and Confocal Raman

While it was proven that the interface between the hydrogel and the thermoplastic is significantly altered during the contact and UV-vis irradiation step, it remains unclear whether the wrinkled interface remaining after hydrogel detachment is exclusively formed by thermoplastic or contains part of the hydrogel. In order to address this aspect, first, both static and dynamic contact angle measurements were carried out

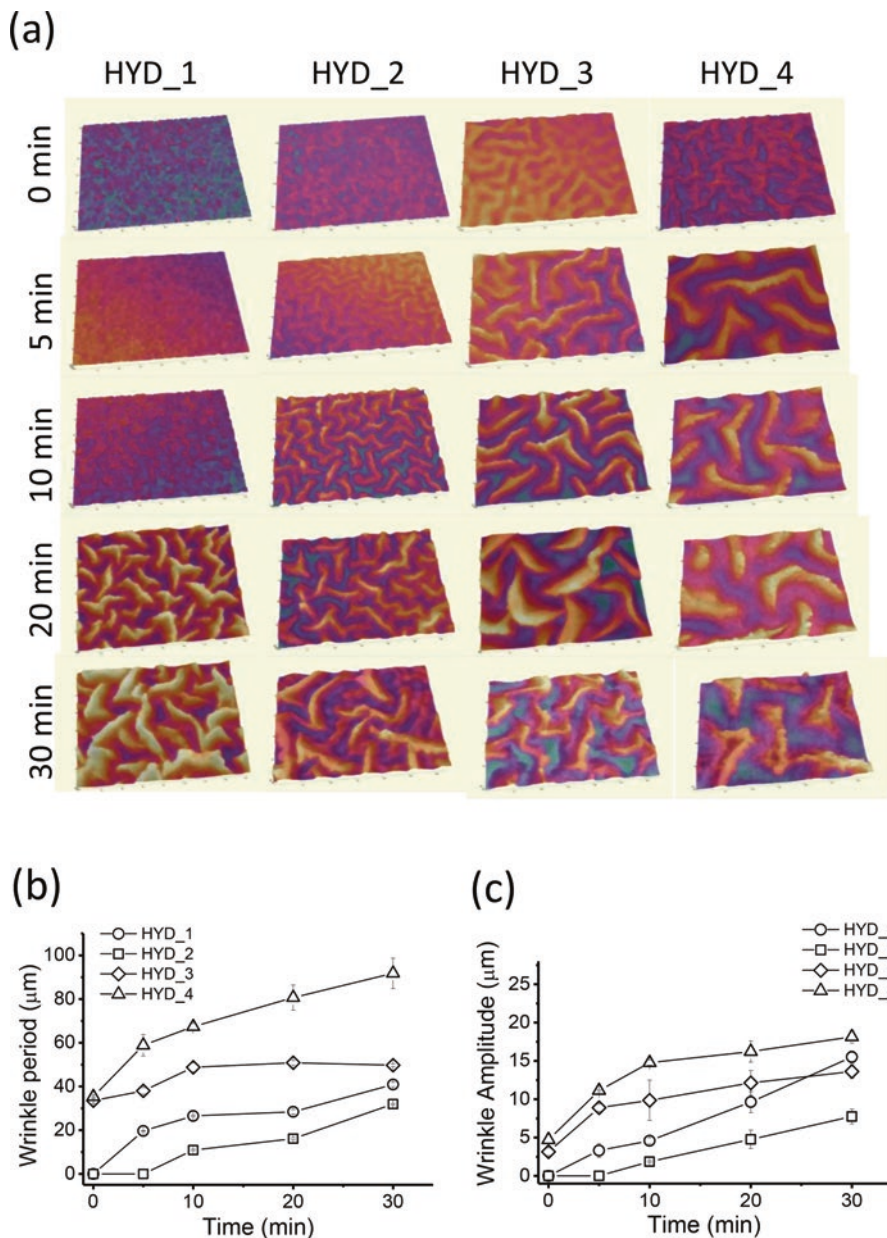


**Fig. 5.17** (a) Optical profilometer images of the different wrinkled surfaces prepared using either water or a mixture ethanol/water (image size,  $350\ \mu\text{m} \times 250\ \mu\text{m}$ ). Variation of the wrinkle period (b) and amplitude (c) respective for the different exposition times of the monomer solution to the PC substrate and for the different solvents employed. (Reproduced with permission from Ref. [89])

on both pristine and wrinkled PC surfaces obtained upon hydrogel detachment. Static contact angle evidenced that the treated surfaces are more hydrophilic than the pristine PC. More interestingly, dynamic measurements (advancing and receding angle measurements) evidenced additional differences. The precursor substrate exhibits, independently of the cycle, advancing angles of around  $90\text{--}93^\circ$  and receding contact angle values of  $15\text{--}18^\circ$ . On the contrary, in the case of PC surfaces treated, significant differences were observed between the first and the rest of the advancing/receding cycles. During the first advancing/receding cycle, the first advancing water contact angle measured was around  $82^\circ$  but was significantly reduced for the following cycles at around  $10\text{--}12^\circ$ . This clearly indicates that upon the first wetting, the treated surfaces are able to accommodate the humidity and remain wetted during the next cycles. These results constitute a preliminary evidence indicating that part of the hydrogel should remain anchored at the PC surface.

Contact angle experiments clearly demonstrated the creation of a hydrophilic surface layer. However, those experiments do not deliver any details neither about the surface chemical composition of the wrinkled surfaces nor about the depth profile of the treatment. In contrast to the contact angle, confocal Raman is an excellent technique to obtain additional information about these two aspects. After analyzing the Raman spectra of the hydrogel and the PC separately, it was possible to identify signals of each material. In particular, the signal found at  $1675\text{ cm}^{-1}$  corresponds to the C=O groups of the PVP-based hydrogel, whereas the carbonyl functional groups present in the PC provide a Raman signal at  $1613\text{ cm}^{-1}$  [91, 92]. As depicted in Fig. 5.18, the comparison between the Raman spectrum observed for the PC substrate and the spectra recorded for the hydrogel, the formation of a top layer in which the chemical composition is a mixture of PC- and VP-based hydrogel, can be clearly observed [93]. Moreover, a further interesting feature of confocal Raman microspectroscopy is related to the possibility to obtain depth profiles that show the variation of the chemical composition from the surface to the PC bulk. As a result, an increase of the contact time of the photopolymerizable solution on the substrate before the UV-vis irradiation step leads to an increase of the wrinkle characteristics and also to an increase of the hydrogel layer thickness observed at the wrinkled surface.

The surface obtained using this approach clearly evidenced the formation of surface instabilities in the form of wrinkles that can only come from the fact that monomers are able to diffuse into the PC. These analyses are consistent with the initial hypothesis of monomer penetration into the outer layers of the PC and formation of wrinkles because of a surface deformation caused by the gradient swelling, similar to that described by Guvendiren et al. [65]. As contact time increases, the monomer mixture penetrates deeper into the PC, swelling occurs to a larger extent, and surface instabilities appeared. Photopolymerization forms the VP-based network (actually the integrated hydrogel/PC outer layers form a semi-interpenetrated structure) and “freezes” the surface deformation. The detachment of the hydrogel, finally, reveals the wrinkles at the interface. According to the observations described above using the 3D optical profiler, the wrinkle size increases as the modified layer increases as well. Thus the process of wrinkle formation is directly related to the extent of swelling.

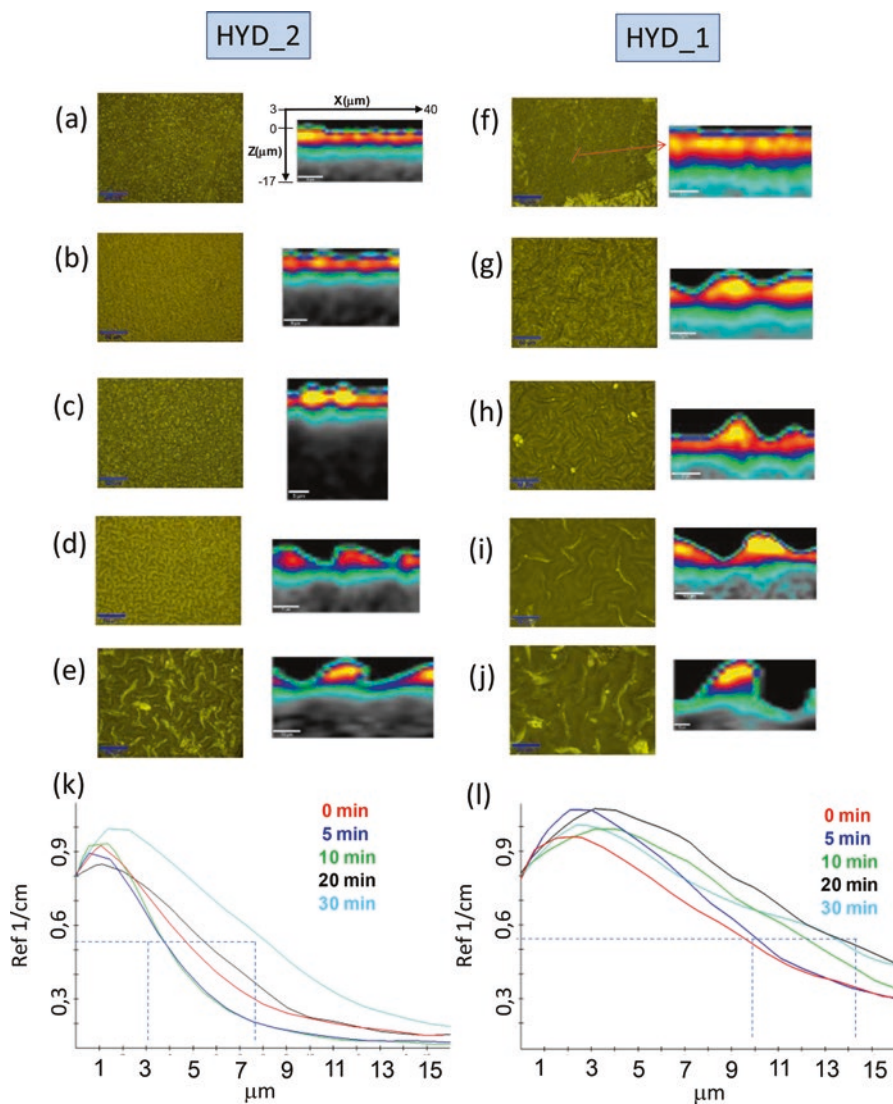


**Fig. 5.18** Above: optical images and the corresponding cross-sectional profiles for a series of wrinkled surfaces prepared using the HYD\_1 (a–e) and HYD\_2 (f–j). The cross-sectional profiles were obtained by the representation of the intensity ratio between the signals at  $1676\text{ cm}^{-1}$  observed in the hydrogel and the band at  $1615\text{ cm}^{-1}$  assigned to the PC. Below: evolution of the intensity of the signal depicted above as a function of the depth for **HYD\_2** (k) and **HYD\_1** (l). (Reproduced with permission from Ref. [89])

## 5.9 Preparation of Wrinkles with a Variable Chemical Composition

One of the major limitations of the approaches depicted in Sect. 5.2 is that all of them refer to a particular hydrogel and they usually do not involve any modification to vary the chemical composition of the wrinkled surface. The strategy reported herein allowed us to change the photosensitive formulation introducing alternative monomers and thus enabling to finely tune the composition of the resulting hydrogel [94]. In Fig. 5.19 are shown illustrative 3D optical profiler images for the series

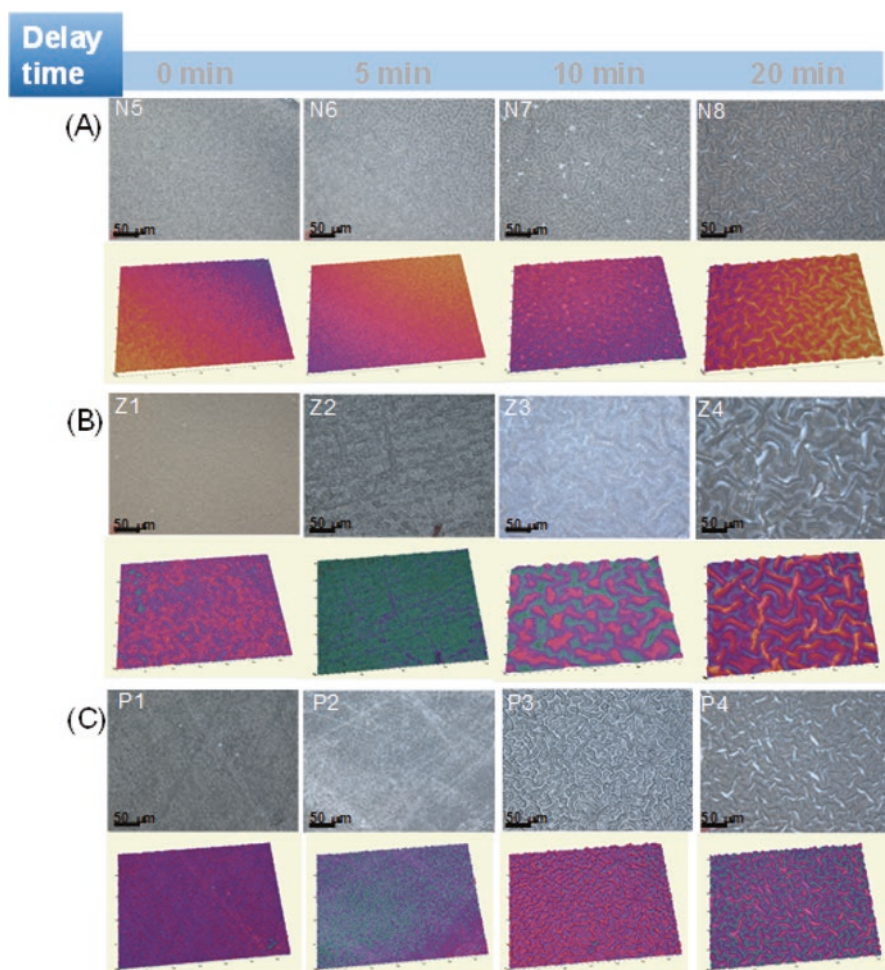


**Fig. 5.19** Profilometer images of wrinkled hydrogel/PC surfaces prepared using different monomers in the photosensitive mixture and varying the delay time between 0 and 20 min. (a) Wrinkled surfaces prepared using photosensitive mixtures that only contain  $M-SO_3^-$  (N5-N8). (b) Wrinkled surfaces prepared using an equimolecular amount of  $M-SO_3^-$  and  $M-N^+$  (samples Z1-Z4). (c) Wrinkled surfaces prepared by incorporating  $M-N^+$  in the photosensitive mixture (samples P1-P4)

prepared using [2-(methacryloyloxy)ethyl]trimethylammonium chloride solution ( $M-N^+$ ) (P-series), potassium sulfopropyl methacrylate ( $M-SO_3^-$ ) (N-series), or an equimolecular amount of both (Z-series). As depicted in Fig. 5.19, a general trend, already found for the previous experiments, was confirmed where the size of the wrinkles formed is directly related to the contact time. In spite of this, also important differences were found depending on the monomer or monomer mixture employed. According to the results depicted in Fig. 5.19, the mixture comprising equimolecular amounts of the two positively and negatively charged monomers produced the largest wrinkles with periods up to 80  $\mu\text{m}$  and amplitudes up to 17  $\mu\text{m}$ . In comparison, wrinkles obtained using photosensitive mixtures that contain either the positively charged or the negatively charged monomer produced smaller wrinkles. On the one hand, using the  $M-SO_3^-$  as a monomer in the photosensitive mixture produced wrinkles with periods of up to 25  $\mu\text{m}$  and amplitudes up to 8  $\mu\text{m}$  in period for the largest contact time. On the other hand, using  $M-N^+$  wrinkles below 60  $\mu\text{m}$  and amplitudes below 15  $\mu\text{m}$  were produced after 20 min of contact time.

## 5.10 Biological Evaluation of VP-Based Hydrogel Wrinkled Surfaces

The effect of surface charge in cell activity over VP-based hydrogel wrinkled surfaces is a key aspect to be firstly analyzed, and for this purpose, endothelial C166-GFP cell line was used as a biocompatibility model. This adherent cell line proliferates forming a monolayer and expresses cell-to-cell and cell-to-extracellular matrix junctions over the biomaterial's surface. As shown in previous work [88], flat VP-based hydrogels have been validated due to their good biological behavior, allowing cell adhesion and monolayer formation over their surfaces. Nevertheless, a delay in early cell adhesion over hydrogel was detected (first 24–48 h) with respect to treated culture plates (TCP), showing that cell-to-surface recognition and posterior cell extension are affected over this kind of supports. Consequently, cell proliferation started later, even though confluent monolayers were equally achieved.

Thereby, wrinkled hydrogel/PC surfaces with similar average wrinkle sizes ranging between 65 and 70  $\mu\text{m}$  and presenting different surface charge were biologically evaluated. These supports were prepared using negative (N)  $M-SO_3^-$  monomers, positive (P)  $M-N^+$  groups, or an equimolecular amount of  $M-SO_3^-$  and  $M-N^+$  to obtain neutralized (Z) surfaces. After 72 h from endothelial C166-GFP cell seeding, small groups of cells were detected over all samples, with no clear differences between them in terms of cell proliferation (Fig. 5.20a). As it was expected, the delay in cell adhesion triggered a tendency of a rounded shape, with a minor group of cells with an extended phenotype over hydrogel surfaces. It is worth mentioning that cell distribution allowed the location of cell clusters proliferating into the wrinkles.

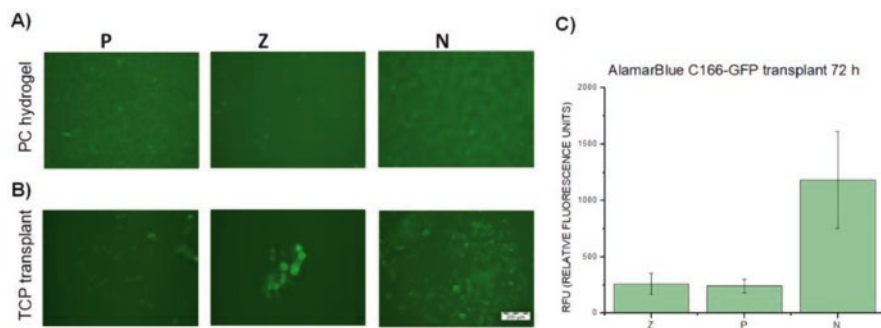


**Fig. 5.20** (a) Fluorescence images of the PC-hydrogel substrates (positive  $M-N^+$ , P; equimolecular amount of  $M-SO_3^-$  and  $M-N^+$ , Z; negative  $M-SO_3^-$ , N) upon 3 days of endothelial C166-GFP cell culture growth. (b) Fluorescence images of the cell transplants on TCP at 72 h after transplantation process. (c) Metabolic activity analysis of transplanted cultures. (Reproduced with permission from Ref. [94])

An additional and advantageous characteristic of VP-based hydrogels is their capacity of spontaneous cell culture detachment from these supports, allowing cell harvesting in a gentle manner. As it has been described, cell sheets were spontaneously transplanted onto TCP surfaces avoiding harmful agents (trypsin, EDTA, or methods such as cell scrapping) [88, 95]. Maintenance of extracellular matrix and cell junctions can improve transplant activity and allow its use in cell therapy for regenerative purposes. Moreover, it has already been described that the implantation of specific cell sheets accelerates the healing process in several models [96], such as skin injuries, damaged cardiac tissue, or bone fractures.

For this goal, wrinkled VP-PC supports were analyzed also as cell harvesting platforms. Cultured samples were turned down and located into a different TCP well, permitting endothelial cell contact with polystyrene surface. Once the culture adhered to the new TCP well, transplants were allowed to proliferate over the new substrate during 72 h, and micrographs were taken (Fig. 5.20b). It could be depicted that cell transplants from wrinkled and negative-charged surfaces (N) presented higher confluence levels than transplants from positive (P) or neutralized (Z) surfaces. This fact was confirmed through mitochondrial metabolic activity analysis using Alamar Blue assay (Fig. 5.20c), where transplants from N surfaces showed an increase in fluorescence levels of fourfold more than transplants from P or Z surfaces.

These results turned out to be of great interest, as they differed with respect to nonsupported VP hydrogel biological behavior. As it has been described in a previous work [95], not only negative but also positive or neutralized flat hydrogels allowed high cell proliferation and transplantation rates. This finding could suggest a main role to be played by surface topography, as microwrinkled P and Z VP-PC supports did not behave as well as their flat counterparts in these evaluated biological terms. In order to achieve a better understanding of the wrinkling effect in cell culture activity and transplantation, negative-charged surfaces with different wrinkle periods were tested.

## 5.11 Biological Evaluation of Negative-Charged Surfaces with Different Wrinkle Periods

As described previously, surface topography and micro structuration can affect several cell processes, such as adhesion, proliferation, or differentiation. However, very few significant efforts have been made in order to study the influence of surface topography in eukaryotic cell detachment. With this objective, negative-charged wrinkled VP-PC surfaces with a range of wrinkle periods (N-large, 50–70  $\mu\text{m}$ ; N-intermediate, 30–50  $\mu\text{m}$ ; N-small, 7–17  $\mu\text{m}$ ) were tested using three different cell lines. Besides endothelial C166-GFP model, which can reach a 40–50  $\mu\text{m}$  diameter, both MC3T3 preosteoblasts and RAW264.7 macrophages were also evaluated. These murine cell lines show a diameter of 70  $\mu\text{m}$  and 7–10  $\mu\text{m}$ , respectively.

Related to cell adhesion and proliferation over negative VP-PC wrinkled surfaces, all samples allowed these biological processes for the three cell lines tested, but several differences were identified (Fig. 5.21). N-intermediate supports (48  $\mu\text{m}$ ) showed elongated and well-adhered preosteoblasts, whereas endothelial and macrophagic cultures proliferated in small cell clusters over the entire surface, including the depth areas of the samples. In addition, N-large samples (near 40  $\mu\text{m}$ ) behaved

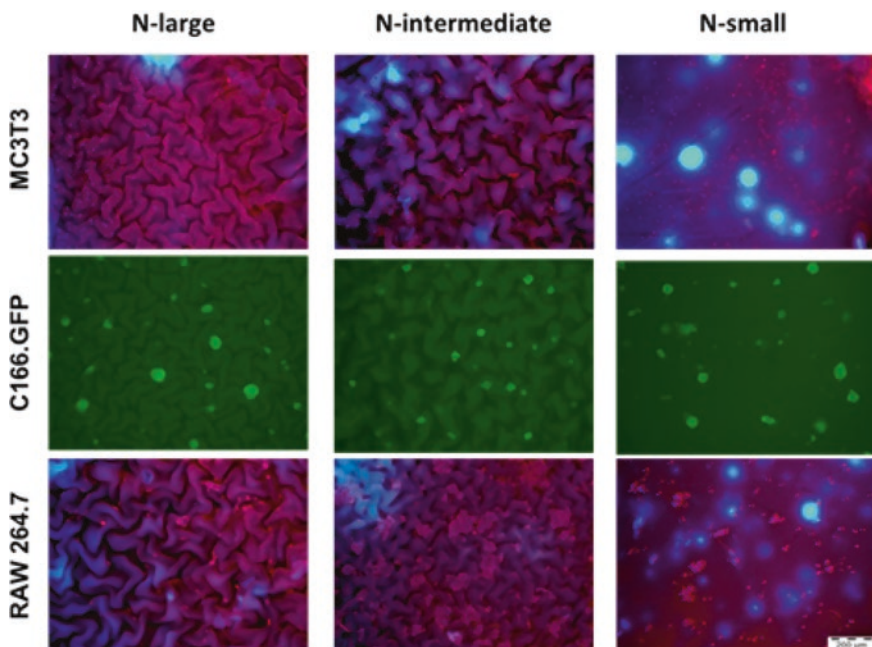


**Fig. 5.21** Cell adhesion and proliferation over negative-charged wrinkled surfaces (N-large, 50–70  $\mu\text{m}$ ; N-intermediate, 30–50  $\mu\text{m}$ ; N-small, 7–17  $\mu\text{m}$ ) 96 h after seeding. First and third line: actin (red)/Hoechst (blue) staining (merge). Second line: GFP autofluorescence. (Reproduced with permission from Ref. [94])

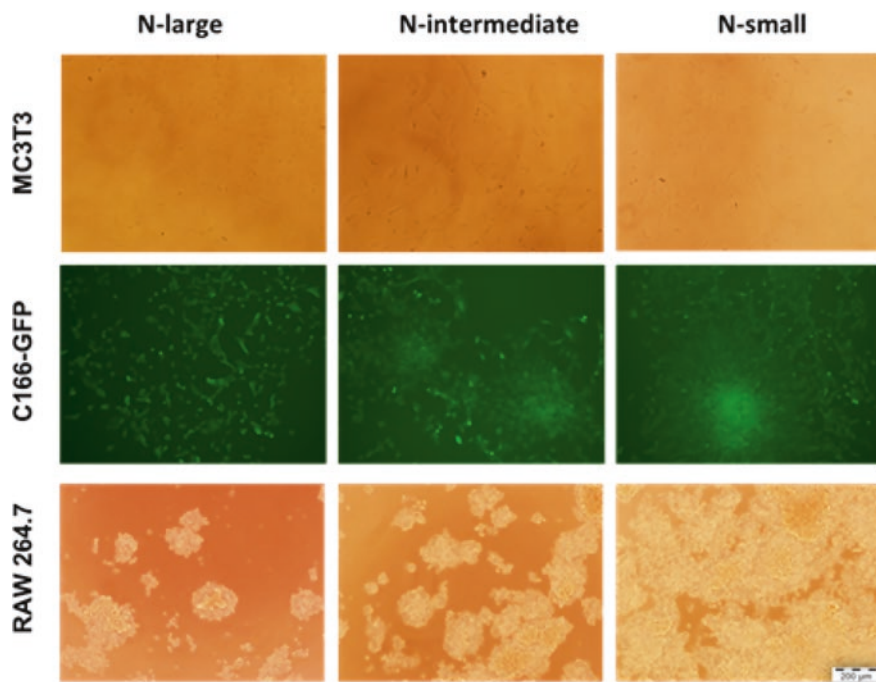


**Fig. 5.22** Cell transplants from PC-hydrogel support (72 h since transplantation process). (Reproduced with permission from Ref. [94])

similarly, allowing cell interaction inside the wrinkles. Finally, N-small wrinkled surfaces (7  $\mu\text{m}$ ) also behave properly, supporting cell activity for the three cell lines tested and showing a reduced interaction with surface features. A significant fact was found with the endothelial C166-GFP culture, which presented a rounded morphology with cluster growth over all tested samples. In contrast, these endothelial cells are characterized for a stretched and well-adhered morphology over standard TCP cultures.

Following the same procedure, VP-PC wrinkled platforms supporting endothelial, preosteoblastic, and macrophagic cultures have been evaluated in terms of cell transplantation to a new TCP well. Thus, all wrinkled surfaces allowed transplantation of the three cell lines tested (Fig. 5.22) but with several differences related to both wrinkle amplitude and specific cell type. First, osteoblastic cultures did not achieve a homogenous transplantation from any of the evaluated supports, finding isolated groups with a poor metabolic activity (Fig. 5.23). However, small and rounded endothelial clusters were transplanted to the new PS surface from all wrinkled supports and especially from platforms with small and medium wrinkle periods. These endothelial clusters adhered to TCP well and begun to proliferate following a radial pattern (Fig. 5.22). Finally, large macrophagic transplants were found from VP-PC platforms with small and medium wrinkle periods, presenting

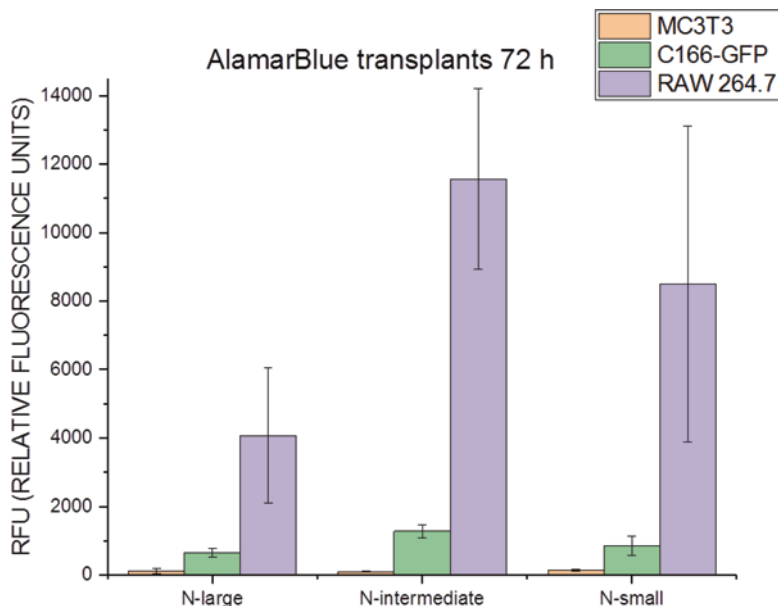


**Fig. 5.23** Metabolic activity (Alamar Blue) of cell transplants (72 h since transplantation process). (Reproduced with permission from Ref. [94])

the highest metabolic activity measures. In summary, these results presented a scenario where surface charge and topography can be tailored in VP-PC platforms to optimize cell harvesting, a situation that can be potentially interesting for cell sheet engineering and regenerative medicine therapies.

## 5.12 Conclusion

The fabrication of wrinkled surfaces decorated with VP-based hydrogels has been described. A selected mixture of monomer/cross-linking agents when in contact with PC diffuses and swells the polymer surface. As a result, upon hydrogel swelling either in EtOH or water, a controlled hydrogel detachment takes place, leaving a thin hydrogel layer at the PC surface. This thin hydrogel layer is produced by partial diffusion and, as a result, swelling of the PC surface by the hydrogel precursor. The diffusion observed has two simultaneous consequences. Firstly, the surface chemical composition of the PC is altered, and a surface with a larger hydrophilicity is obtained. Secondly, diffusion and swelling of the PC surface induce surface instabilities that finally result in the formation of wrinkled surfaces. Interestingly, by modifying the composition of the precursor solution as well as the contact time, a reasonable control over the wrinkle characteristics (period and amplitude) is obtained.

This fabrication strategy in which thermoplastic supports can be modified with hydrogels is currently being evaluated for different applications including the fabrication of platforms with reduced friction and their use as cell culture templates. The interest of the complementary wrinkling on the detached hydrogel, i.e., its influence on in vitro cell response, will be faced in the next future.

**Acknowledgments** The authors gratefully acknowledge support from the Consejo Superior de Investigaciones Científicas (CSIC). Equally, this work was financially supported by the Ministerio de Economía y Competitividad (MINECO) through MAT2013-47902-C2-1-R, MAT2013-42957-R, and MAT2016-78437-R, FEDER-EU.

## References

1. C.-M. Chen, S. Yang, Wrinkling instabilities in polymer films and their applications. *Polym. Int.* **61**(7), 1041–1047 (2012)
2. A. Schweikart, A. Fery, Controlled wrinkling as a novel method for the fabrication of patterned surfaces. *Microchim. Acta* **165**(3–4), 249–263 (2009)
3. J. Genzer, J. Groenewold, Soft matter with hard skin: From skin wrinkles to templating and material characterization. *Soft Matter* **2**(4), 310–323 (2006)
4. S. McCormick, Materials science – Exploiting wrinkle formation. *Science* **317**(5838), 605–606 (2007)
5. F. Weiss, S. Cai, Y. Hu, M.K. Kang, R. Huang, Z. Suo, Creases and wrinkles on the surface of a swollen gel. *J. Appl. Phys.* **114**(7), 073507 (2013)
6. S. Cai, D. Chen, Z. Suo, R.C. Hayward, Creasing instability of elastomer films. *Soft Matter* **8**(5), 1301–1304 (2012)
7. S.S. Velankar, V. Lai, R.A. Vaia, Swelling-induced delamination causes folding of surface-tethered polymer gels. *ACS Appl. Mater. Interfaces* **4**(1), 24–29 (2012)
8. T. Bahners, L. Prager, S. Kriehn, J.S. Gutmann, Super-hydrophilic surfaces by photo-induced micro-folding. *Appl. Surf. Sci.* **259**, 847–852 (2012)
9. Y.-P. Cao, B. Li, X.-Q. Feng, Surface wrinkling and folding of core-shell soft cylinders. *Soft Matter* **8**(2), 556–562 (2012)
10. R. Schubert, T. Scherzer, M. Hinkefuss, B. Marquardt, J. Vogel, M.R. Buchmeiser, VUV-induced micro-folding of acrylate-based coatings. 1. Real-time methods for the determination of the micro-folding kinetics. *Surf. Coat. Technol.* **203**(13), 1844–1849 (2009)
11. D.P. Holmes, A.J. Crosby, Draping films: A wrinkle to fold transition. *Phys. Rev. Lett.* **105**(3), 038303 (2010)
12. J. Rodríguez-Hernández, Wrinkled interfaces: Taking advantage of surface instabilities to pattern polymer surfaces. *Prog. Polym. Sci.* **42**, 1–41 (2015)
13. K. Efimenko, M. Rackaitis, E. Manias, A. Vaziri, L. Mahadevan, J. Genzer, Nested self-similar wrinkling patterns in skins. *Nat. Mater.* **4**(4), 293 (2005)
14. T. Ohzono, M. Shimomura, Ordering of microwrinkle patterns by compressive strain. *Phys. Rev. B* **69**(13), 132202 (2004)
15. T. Ohzono, M. Shimomura, Geometry-dependent stripe rearrangement processes induced by strain on preordered microwrinkle patterns. *Langmuir* **21**(16), 7230–7237 (2005)
16. W.M. Choi, J. Song, D.-Y. Khang, H. Jiang, Y.Y. Huang, J.A. Rogers, Biaxially stretchable “wavy” silicon nanomembranes. *Nano Lett.* **7**(6), 1655–1663 (2007)
17. H. Jiang, D.-Y. Khang, J. Song, Y. Sun, Y. Huang, J.A. Rogers, Finite deformation mechanics in buckled thin films on compliant supports. *Proc. Natl. Acad. Sci.* **104**(40), 15607–15612 (2007)

18. N. Uchida, T. Ohzono, Orientational ordering of buckling-induced microwrinkles on soft substrates. *Soft Matter* **6**(22), 5729–5735 (2010)
19. P.J. Yoo, Fabrication of complexly patterned wavy structures using self-organized anisotropic wrinkling. *Electron. Mater. Lett.* **7**(1), 17–23 (2011)
20. N. Bowden, S. Brittain, A.G. Evans, J.W. Hutchinson, G.M. Whitesides, Spontaneous formation of ordered structures in thin films of metals supported on an elastomeric polymer. *Nature* **393**(6681), 146 (1998)
21. J. Kim, H.H. Lee, Wave formation by heating in thin metal film on an elastomer. *J. Polym. Sci. B Polym. Phys.* **39**(11), 1122–1128 (2001)
22. P.J. Yoo, H.H. Lee, Complex pattern formation by adhesion-controlled anisotropic wrinkling. *Langmuir* **24**(13), 6897–6902 (2008)
23. T. Okayasu, H.L. Zhang, D.G. Bucknall, G.A.D. Briggs, Spontaneous formation of ordered lateral patterns in polymer thin-film structures. *Adv. Funct. Mater.* **14**(11), 1081–1088 (2004)
24. J.Y. Chung, A.J. Nolte, C.M. Stafford, Diffusion-controlled, self-organized growth of symmetric wrinkling patterns. *Adv. Mater.* **21**(13), 1358–1362 (2009)
25. H. Vandeparre, S. Gabriele, F. Brau, C. Gay, K.K. Parker, P. Damman, Hierarchical wrinkling patterns. *Soft Matter* **6**(22), 5751–5756 (2010)
26. S.K. Basu, A.V. McCormick, L. Scriven, Stress generation by solvent absorption and wrinkling of a cross-linked coating atop a viscous or elastic base. *Langmuir* **22**(13), 5916–5924 (2006)
27. D. Breid, A.J. Crosby, Surface wrinkling behavior of finite circular plates. *Soft Matter* **5**(2), 425–431 (2009)
28. M. Guvendiren, J.A. Burdick, S. Yang, Kinetic study of swelling-induced surface pattern formation and ordering in hydrogel films with depth-wise crosslinking gradient. *Soft Matter* **6**(9), 2044–2049 (2010)
29. J. Huang, M. Juskiewicz, W.H. De Jeu, E. Cerda, T. Emrick, N. Menon, T.P. Russell, Capillary wrinkling of floating thin polymer films. *Science* **317**(5838), 650–653 (2007)
30. D. Vella, M. Adda-Bedia, E. Cerda, Capillary wrinkling of elastic membranes. *Soft Matter* **6**(22), 5778–5782 (2010)
31. O. Wichterle, D. Lim, Hydrophilic gels for biological use. *Nature* **185**(4706), 117 (1960)
32. F. Ullah, M.B.H. Othman, F. Javed, Z. Ahmad, H.M. Akil, Classification, processing and application of hydrogels: A review. *Mater. Sci. Eng. C* **57**, 414–433 (2015)
33. K. Varaprasad, G.M. Raghavendra, T. Jayaramudu, M.M. Yallapu, R. Sadiku, A mini review on hydrogels classification and recent developments in miscellaneous applications. *Mater. Sci. Eng. C* **79**, 958–971 (2017)
34. W. Roorda, H. Bodde, A. De Boer, H. Junginger, Synthetic hydrogels as drug delivery systems. *Pharm. Weekbl.* **8**(3), 165–189 (1986)
35. S.J. Buwalda, K.W. Boere, P.J. Dijkstra, J. Feijen, T. Vermonden, W.E. Hennink, Hydrogels in a historical perspective: From simple networks to smart materials. *J. Control. Release* **190**, 254–273 (2014)
36. E.M. Ahmed, Hydrogel: Preparation, characterization, and applications: A review. *J. Adv. Res.* **6**(2), 105–121 (2015)
37. W.A. Laftah, S. Hashim, A.N. Ibrahim, Polymer hydrogels: A review. *Polym.-Plast. Technol. Eng.* **50**(14), 1475–1486 (2011)
38. G.M. Raghavendra, K. Varaprasad, T. Jayaramudu, *Biomaterials: Design, Development and Biomedical Applications, Nanotechnology Applications for Tissue Engineering*. (Elsevier, Oxford, 2015), pp. 21–44
39. K. Sharma, B. Kaith, V. Kumar, S. Kalia, V. Kumar, H. Swart, Water retention and dye adsorption behavior of Gg-cl-poly (acrylic acid-aniline) based conductive hydrogels. *Geoderma* **232**, 45–55 (2014)
40. S. Ma, B. Yu, X. Pei, F. Zhou, Structural hydrogels. *Polymer* **98**, 516–535 (2016)
41. B.R. Saunders, B. Vincent, Microgel particles as model colloids: Theory, properties and applications. *Adv. Colloid Interf. Sci.* **80**(1), 1–25 (1999)

42. P. Bradna, P. Stern, O. Quadrat, J. Snuparek, Thickening effect of dispersions of ethyl acrylate-methacrylic acid copolymer prepared by different polymerization routes. *Colloid Polym. Sci.* **273**(4), 324–330 (1995)
43. L.A. Lyon, Z. Meng, N. Singh, C.D. Sorrell, A.S. John, Thermoresponsive microgel-based materials. *Chem. Soc. Rev.* **38**(4), 865–874 (2009)
44. C.M. Nolan, M.J. Serpe, L.A. Lyon, Thermally modulated insulin release from microgel thin films. *Biomacromolecules* **5**(5), 1940–1946 (2004)
45. J. Kim, M.J. Serpe, L.A. Lyon, Hydrogel microparticles as dynamically tunable microlenses. *J. Am. Chem. Soc.* **126**(31), 9512–9513 (2004)
46. K. Ishii, Synthesis of microgels and their application to coatings. *Colloids Surf. A Physicochem. Eng. Asp.* **153**(1–3), 591–595 (1999)
47. L. Ionov, Biomimetic hydrogel-based actuating systems. *Adv. Funct. Mater.* **23**(36), 4555–4570 (2013)
48. S. Ma, M. Scaraggi, D. Wang, X. Wang, Y. Liang, W. Liu, D. Dini, F. Zhou, Nanoporous substrate-infiltrated hydrogels: A bioinspired regenerable surface for high load bearing and tunable friction. *Adv. Funct. Mater.* **25**(47), 7366–7374 (2015)
49. L. Binan, A. Aji, G. De Crescenzo, M. Jolicoeur, Approaches for neural tissue regeneration. *Stem Cell Rev. Rep.* **10**(1), 44–59 (2014)
50. A.E. Haggerty, M. Oudega, Biomaterials for spinal cord repair. *Neurosci. Bull.* **29**(4), 445–459 (2013)
51. N. Bassik, B.T. Abebe, K.E. Laffin, D.H. Gracias, Photolithographically patterned smart hydrogel based bilayer actuators. *Polymer* **51**(26), 6093–6098 (2010)
52. P. Gruner, M. Arlt, T. Fuhrmann-Lieker, Surface wrinkling induced by photofluidization of low molecular azo glasses. *ChemPhysChem* **14**(2), 424–430 (2013)
53. N. Lambrecht, T. Pardoën, S. Yunus, Giant stretchability of thin gold films on rough elastomeric substrates. *Acta Mater.* **61**(2), 540–547 (2013)
54. M. Ramanathan, B.S. Lokitz, J.M. Messman, C.M. Stafford, S.M. Kilbey II, Spontaneous wrinkling in azlactone-based functional polymer thin films in 2D and 3D geometries for guided nanopatterning. *J. Mater. Chem. C* **1**(11), 2097–2101 (2013)
55. Z. Wu, N. Bouklas, R. Huang, Swell-induced surface instability of hydrogel layers with material properties varying in thickness direction. *Int. J. Solids Struct.* **50**(3–4), 578–587 (2013)
56. Z. Chen, Y.Y. Kim, S. Krishnaswamy, Anisotropic wrinkle formation on shape memory polymer substrates. *J. Appl. Phys.* **112**(12), 124319 (2012)
57. Y.-C. Chen, A.J. Crosby, Wrinkling of inhomogeneously strained thin polymer films. *Soft Matter* **9**(1), 43–47 (2013)
58. J. Dervaux, M.B. Amar, Mechanical instabilities of gels. *Annu. Rev. Condens. Matter Phys.* **3**(1), 311–332 (2012)
59. C.M. Chen, S. Yang, Wrinkling instabilities in polymer films and their applications. *Polym. Int.* **61**(7), 1041–1047 (2012)
60. B. Li, Y.-P. Cao, X.-Q. Feng, H. Gao, Mechanics of morphological instabilities and surface wrinkling in soft materials: A review. *Soft Matter* **8**(21), 5728–5745 (2012)
61. J. Gu, X. Li, H. Ma, Y. Guan, Y. Zhang, One-step synthesis of PHEMA hydrogel films capable of generating highly ordered wrinkling patterns. *Polymer* **110**, 114–123 (2017)
62. M. Guvendiren, S. Yang, J.A. Burdick, Swelling-induced surface patterns in hydrogels with gradient crosslinking density. *Adv. Funct. Mater.* **19**(19), 3038–3045 (2009)
63. C.M. González-Henríquez, D.H. Sagredo-Oyarce, M.A. Sarabia-Vallejos, J. Rodríguez-Hernández, Fabrication of micro and sub-micrometer wrinkled hydrogel surfaces through thermal and photocrosslinking processes. *Polymer* **101**, 24–33 (2016)
64. M. Guvendiren, J.A. Burdick, The control of stem cell morphology and differentiation by hydrogel surface wrinkles. *Biomaterials* **31**(25), 6511–6518 (2010)
65. M. Guvendiren, S. Yang, J.A. Burdick, Swelling-induced surface patterns in hydrogels with gradient crosslinking density. *Adv. Funct. Mater.* **19**(19), 3038–3045 (2009)

66. C. Tang, B. Li, C. Zou, L. Liu, H. Chen, Voltage-induced wrinkle performance in a hydrogel by dielectric elastomer actuation. *Polymer* **10**(7), 697 (2018)
67. A. Parfitt, Age-related structural changes in trabecular and cortical bone: Cellular mechanisms and biomechanical consequences. *Calcif. Tissue Int.* **36**(1), S123–S128 (1984)
68. V.I. Sikavitsas, J.S. Temenoff, A.G. Mikos, Biomaterials and bone mechanotransduction. *Biomaterials* **22**(19), 2581–2593 (2001)
69. F. Gregoir, C. Smas, H. Sul, Understanding adipocyte differentiation. *Physiol. Rev.* **78**, 783–809 (1998)
70. A.E. Grigoriadis, J. Heersche, J.E. Aubin, Differentiation of muscle, fat, cartilage, and bone from progenitor cells present in a bone-derived clonal cell population: Effect of dexamethasone. *J. Cell Biol.* **106**(6), 2139–2151 (1988)
71. J. Fukuda, Y. Sakai, K. Nakazawa, Novel hepatocyte culture system developed using micro-fabrication and collagen/polyethylene glycol microcontact printing. *Biomaterials* **27**(7), 1061–1070 (2006)
72. S.F. Wong, D.Y. No, Y.Y. Choi, D.S. Kim, B.G. Chung, S.-H. Lee, Concave microwell based size-controllable hepatosphere as a three-dimensional liver tissue model. *Biomaterials* **32**(32), 8087–8096 (2011)
73. J.C. Mohr, J.J. de Pablo, S.P. Palecek, 3-D microwell culture of human embryonic stem cells. *Biomaterials* **27**(36), 6032–6042 (2006)
74. J. Fukuda, A. Khademhosseini, Y. Yeo, X. Yang, J. Yeh, G. Eng, J. Blumling, C.-F. Wang, D.S. Kohane, R. Langer, Micromolding of photocrosslinkable chitosan hydrogel for spheroid microarray and co-cultures. *Biomaterials* **27**(30), 5259–5267 (2006)
75. H. Tekin, M. Anaya, M.D. Brigham, C. Nauman, R. Langer, A. Khademhosseini, Stimuli-responsive microwells for formation and retrieval of cell aggregates. *Lab Chip* **10**(18), 2411–2418 (2010)
76. K.H. Lee, D.Y. No, S.-H. Kim, J.H. Ryoo, S.F. Wong, S.-H. Lee, Diffusion-mediated in situ alginate encapsulation of cell spheroids using microscale concave well and nanoporous membrane. *Lab Chip* **11**(6), 1168–1173 (2011)
77. Y.-S. Hwang, B.G. Chung, D. Ortmann, N. Hattori, H.-C. Moeller, A. Khademhosseini, Microwell-mediated control of embryoid body size regulates embryonic stem cell fate via differential expression of WNT5a and WNT11. *Proc. Natl. Acad. Sci.* **106**(40), 16978–16983 (2009)
78. J.M. Karp, J. Yeh, G. Eng, J. Fukuda, J. Blumling, K.-Y. Suh, J. Cheng, A. Mahdavi, J. Borenstein, R. Langer, A. Khademhosseini, Controlling size, shape and homogeneity of embryoid bodies using poly(ethylene glycol) microwells. *Lab Chip* **7**(6), 786–794 (2007)
79. J. Park, C.H. Cho, N. Parashurama, Y. Li, F. Berthiaume, M. Toner, A.W. Tilles, M.L. Yarmush, Microfabrication-based modulation of embryonic stem cell differentiation. *Lab Chip* **7**(8), 1018–1028 (2007)
80. M.D. Ungrin, C. Joshi, A. Nica, C. Bauwens, P.W. Zandstra, Reproducible, ultra high-throughput formation of multicellular organization from single cell suspension-derived human embryonic stem cell aggregates. *PLoS One* **3**(2), e1565 (2008)
81. H.-C. Moeller, M.K. Mian, S. Shrivastava, B.G. Chung, A. Khademhosseini, A microwell array system for stem cell culture. *Biomaterials* **29**(6), 752–763 (2008)
82. A.P. Napolitano, P. Chai, D.M. Dean, J.R. Morgan, Dynamics of the self-assembly of complex cellular aggregates on micromolded nonadhesive hydrogels. *Tissue Eng.* **13**(8), 2087–2094 (2007)
83. A.B. Bernard, C.-C. Lin, K.S. Anseth, A microwell cell culture platform for the aggregation of pancreatic  $\beta$ -cells. *Tissue Eng. Part C Methods* **18**(8), 583–592 (2012)
84. B.R. Lee, J.W. Hwang, Y.Y. Choi, S.F. Wong, Y.H. Hwang, D.Y. Lee, S.-H. Lee, In situ formation and collagen-alginate composite encapsulation of pancreatic islet spheroids. *Biomaterials* **33**(3), 837–845 (2012)
85. J. Dahlmann, G. Kensah, H. Kempf, D. Skvorc, A. Gawol, D.A. Elliott, G. Dräger, R. Zweigerdt, U. Martin, I. Gruh, The use of agarose microwells for scalable embryoid body formation and

- cardiac differentiation of human and murine pluripotent stem cells. *Biomaterials* **34**(10), 2463–2471 (2013)
86. Z. Zhao, J. Gu, Y. Zhao, Y. Guan, X. Zhu, Y. Zhang, Hydrogel thin film with swelling-induced wrinkling patterns for high-throughput generation of multicellular spheroids. *Biomacromolecules* **15**(9), 3306–3312 (2014)
  87. A. Ivascu, M. Kubbies, Rapid generation of single-tumor spheroids for high-throughput cell function and toxicity analysis. *J. Biomol. Screen.* **11**(8), 922–932 (2006)
  88. I. Aranaz, E. Martínez-Campos, M.E. Nash, M.G. Tardajos, H. Reinecke, C. Elvira, V. Ramos, J.L. Lopez-Lacomba, A. Gallardo, Pseudo-double network hydrogels with unique properties as supports for cell manipulation. *J. Mater. Chem. B* **2**(24), 3839–3848 (2014)
  89. A. Gallardo, N. Lujan, H. Reinecke, C. García, A.D. Campo, J. Rodríguez-Hernandez, Chemical and topographical modification of polycarbonate surfaces through diffusion/photocuring processes of hydrogel precursors based on vinylpyrrolidone. *Langmuir* **33**(7), 1614–1622 (2017)
  90. H. Yuk, T. Zhang, S. Lin, G.A. Parada, X. Zhao, Tough bonding of hydrogels to diverse non-porous surfaces. *Nat. Mater.* **15**(2), 190–196 (2016)
  91. X. Zhu, P. Lu, W. Chen, J. Dong, Studies of UV crosslinked poly(N-vinylpyrrolidone) hydrogels by FTIR, Raman and solid-state NMR spectroscopies. *Polymer* **51**(14), 3054–3063 (2010)
  92. M. Luo, Y. Hong, W. Yao, C. Huang, Q. Xu, Q. Wu, Facile removal of polyvinylpyrrolidone (PVP) adsorbates from Pt alloy nanoparticles. *J. Mater. Chem. A* **3**(6), 2770–2775 (2015)
  93. K. Bruckmoser, K. Resch, T. Kisslinger, T. Lucyshyn, Measurement of interdiffusion in polymeric materials by applying Raman spectroscopy. *Polym. Test.* **46**, 122–133 (2015)
  94. E. Martínez-Campos, A. Gallardo, N. Lujan, A. Santos-Coquillat, H. Reinecke, A.D. Campo, J. Rodríguez-Hernandez, Wrinkled hydrogel surfaces with modulated surface chemistry and topography: Evaluation as supports for cell growth and transplant. Submitted to *ACS Appl. Biomater.* (2018)
  95. A. Gallardo, E. Martínez-Campos, C. García, A.L. Cortajarena, J. Rodríguez-Hernández, Hydrogels with modulated ionic load for mammalian cell harvesting with reduced bacterial adhesion. *Biomacromolecules* **18**(5), 1521–1531 (2017)
  96. K. Nagase, M. Yamato, H. Kanazawa, T. Okano, Poly (N-isopropylacrylamide)-based thermo-responsive surfaces provide new types of biomedical applications. *Biomaterials* **153**, 27–48 (2018)

# Chapter 6

## Laser-Induced Periodic Surface Structures (LIPSS) on Polymer Surfaces



Esther Rebollar, Tiberio A. Ezquerro, and Aurora Nogales

### 6.1 Introduction

Under the influence of external conditions, instabilities may appear in viscous liquids in general and in particular in polymer surfaces. The instabilities are the response of the system to the loss of equilibrium. Sometimes, these instabilities produce regular dissipative structures whose shape and geometrical characteristics depend on the nature of the different physical mechanisms that lead to restoring equilibrium. Examples of these dissipative structures can be found in a variety of systems, from the oceanic waves, the disintegration of liquid jets into droplets of wrinkles in the skin [1]. In polymer processing, originally instabilities were considered as an uncontrollable problem that may spoil a given manufacturing product, for example, the sharkskin effect in extruding polyethylene [2]. However, when the instabilities are produced in a controlled way, they can be seen as an opportunity to obtain periodically structured surfaces in polymers, with modified properties of technological importance, like friction, adhesion, or wetting. Examples of this can be found in wrinkles due to thermal stress, osmotic pressure, and mechanical stress applied on bilayer and gradient polymer films. These effects present potential applications in several fields such as optical components, templates to create ordered surface arrays, responsive microfluidic channels, thin-film metrology, tunable wetting and directed assembly of liquid crystal molecules, flexible electronics, particle sorting, and flexible electronics, among others [3, 4]. Another example is the formation of ordered pores ensembles in polymer surfaces when evaporating a polymer solution in a controlled humidity atmosphere. The exploitation of this effect is

---

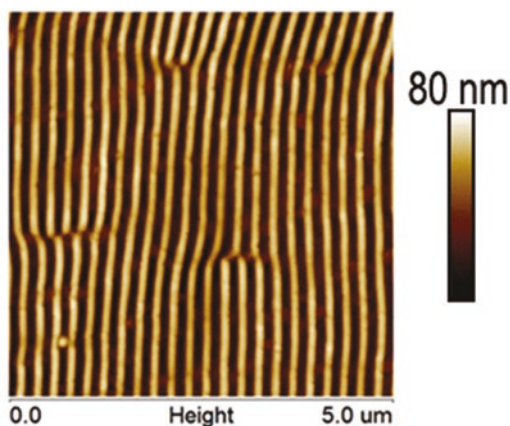
E. Rebollar  
Instituto de Química Física Rocasolano, Madrid, Spain

T. A. Ezquerro · A. Nogales (✉)  
Instituto de Estructura de la Materia, Madrid, Spain  
e-mail: [aurora.nogales@csic.es](mailto:aurora.nogales@csic.es)

known as the breath figure technique that has been used, for example, to fabricate antibacterial substrates [5]. In general, the instabilities are produced by the presence of an external stimulus that takes the polymer surface out of equilibrium. Examples of this are temperature gradients and evaporation of solvents, among others. Electric fields have been observed to produce also instabilities in polymer melts, which give rise to dissipative structures that can be tuned through the intensity and shape of the applied electric field. By this method, upon cooling, these dissipative structures can be frozen out in the cooled polymer melt [6]. This technique, referred to as electrohydrodynamic lithography [7], can produce ordered surface structures as small as a 100 nm. One of the difficulties of this lithographic technique is the request of cooling down the polymer melt fast enough so that the ordered structures are retained in the solid polymer. Laser techniques have been also explored in order to create surface instabilities leading to structure formation. Indirect laser interference writing [8], for example, a beam of an ultrafast laser, is tightly focused into the volume of a transparent, photosensitive material, initiating its polymerization by nonlinear absorption within the focal volume. This technique is restricted to photosensitive materials, although its lithography power is not directly related to surface instabilities. Another example of laser techniques to obtain lithographic patterning directly on polymer surfaces is direct laser interference lithography, described in Chap. 7 of this book. With this technique, the laser either ablates or modifies the material directly. Thus, depending on the nature of the interaction light material, the underlying mechanism will be photochemical, photothermal, or a combination of both. In a different approach, repeated illumination of a polymer surface by a pulsed laser source with tender fluences, laser-induced periodic surface structures (LIPSS) have been observed [9–12]. Figure 6.1 shows an example of these structures in polystyrene (PS) as observed by atomic force microscopy (AFM). LIPSS is parallel to the polarization of the laser.

By the combination of the electric field associated with the laser beam and the heating of the polymer surface during a short period of time, which typically is in the range of nanosecond, when the irradiating with nanosecond laser pulses of are

**Fig. 6.1** AFM topography from a LIPSS pattern in a 130-nm-thick polystyrene film deposited on silicon, obtained upon irradiation at 266 nm at a fluence of 10 mJ/cm<sup>2</sup> and 4800 pulses. (Courtesy of Dr. Jing Cui)



used, periodic dissipative structures appear. In this chapter, a description of the experimental setup required for obtaining LIPSS is presented. Afterward, the necessary conditions to obtain LIPSS in polymer surfaces are discussed, and finally, LIPSS in different polymers are reviewed.

## 6.2 Setup Required for LIPSS Formation

To obtain LIPSS, the polymer surface is exposed to a given number of pulses of a linearly polarized laser beam within a narrow fluence range well below the ablation threshold [13–15]. It is important to note that ripple formation is originated from a self-organization process and not caused by ablation, since the amount of material removed during laser irradiation is negligible [16]. Figure 6.2 displays the schematic of LIPSS formed on a film. For LIPSS formed with nanosecond laser pulses, two main stages can be considered: (1) interference at the surface and (2) surface response to it. The interference between the incident and reflected/refracted laser light with the scattered light near the surface results in LIPSS with a characteristic size in the order of magnitude of the wavelength of the laser beam [17].

The period of the obtained ripples ( $L$ ) is related to the laser wavelength ( $\lambda$ ) and to the angle of incidence of the radiation. The spacing of the structures can be described by the following expression [18]:

$$L = \frac{\lambda}{n - \sin \theta} \quad (6.1)$$

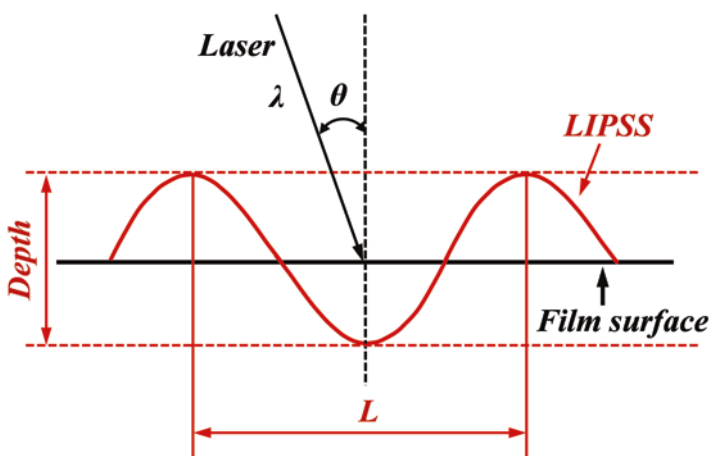


Fig. 6.2 Schematic illustration of the surface corrugation of LIPSS formed on a film

where  $n$  is the effective refractive index of the material and  $\theta$  the incidence angle of the laser beam with respect to the normal to the sample plane.

The features of LIPSS might be affected by the polymer properties, which are dependent not only on the chemical composition but also on the polymer structural state, either amorphous or semicrystalline.

A scheme of a typical experimental setup used for obtaining LIPSS in polymer thin films is shown in Fig. 6.3. In this case a linearly polarized laser beam of a Q-switched Nd:YAG laser (Lotis TII LS-2131 M, pulse duration  $\tau = 8$  ns full-width half-maximum) is shined at a repetition rate of 10 Hz on a thin polymer film deposited on a silicon wafer. The fluence of irradiation is determined by measuring the laser energy in front of the sample with a Joulemeter and by calculating the area of the irradiated spots after delimitating the beam with an iris of known diameter. Irradiation is performed at normal incidence.

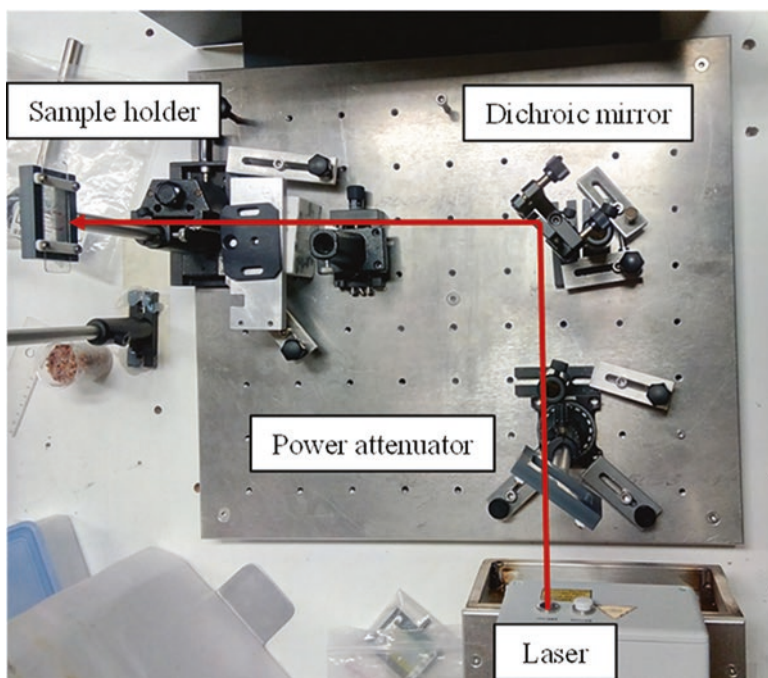


Fig. 6.3 Experimental setup for LIPSS formation

### 6.3 Conditions for LIPSS Formation in Polymer Surfaces

When a polymer film is exposed to laser light, the film surface scatters light due to its roughness and these scattered waves interfere with the incident laser beam resulting in a modulated distribution of the energy on the surface [9]. This energy may induce a modulated change in temperature, depending, mainly, on whether the radiation is efficiently absorbed by the polymer. The magnitude that provides information on this absorption process is the linear absorption coefficient of the polymer at the wavelength of laser irradiation. If the polymer absorbs the energy of the laser pulse, the temperature of the outermost polymer layer may increase, and eventually, a softening of this layer is produced, allowing the diffusion of the polymeric chains [19].

In general, the increase of temperature of a single pulse is not very dramatic. The temperature increase produced by the laser pulse can be estimated by solving the one-dimensional heat transfer equation, considering the laser as the only heat source on the polymer surface. The temperature at a given time  $t$  taken from the start of the laser pulse, and at a given depth  $x$  below the polymer surface, can be estimated as [9, 13]:

$$\frac{\partial^2 T(x,t)}{\partial x^2} - a^2 \frac{\partial T(x,t)}{\partial t} = -\frac{\alpha}{\kappa} P(t) e^{-\alpha x} F_0 \quad (6.2)$$

where  $a^2 = \frac{\rho c}{\kappa}$  being  $\rho$  the density of the polymer,  $c$  its specific heat at constant pressure,  $\kappa$  its thermal conductivity, and  $\alpha$  the absorption coefficient.  $F_0$  is the incident fluence, and  $P(t)$  is a function which describes the temporal shape of the laser pulse which is considered as a modified Gaussian beam:

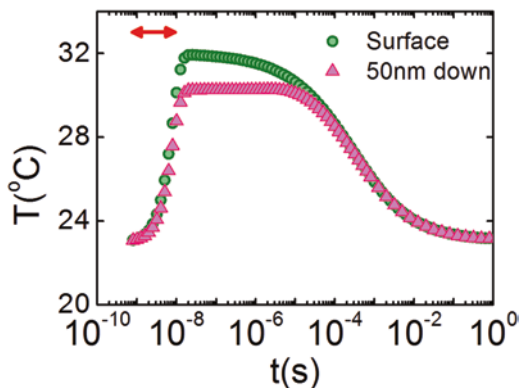
$$P(t) = \frac{2t}{\tau^2} \exp\left[-(t/\tau)^2\right] \quad (6.3)$$

where the  $t$  factor ensures that intensity vanishes at  $t = 0$  and  $\tau$  is the pulse duration.

Figure 6.4 shows the dependence of the temperature with the elapsed time from the beginning of a single pulse in PS, for two different depths along the thickness of the film.

The result shows that, once the first pulse reaches the film, the temperature of the surface increases since the laser energy absorbed by PS is transformed into heat. As the pulse finishes, the surface of the sample starts to cool down due to the dissipation of heat into the cooler surrounding bulk material. In this case, the highest temperature achieved at the polymer surface by the initial single pulse is estimated to be around 32 °C, far below the  $T_g$  of PS, which is 106 °C. Although at first glance it seems that the temperature for long times is similar to the initial temperature, a small positive offset is still present at the time the next pulse arrives (0.1 s later, in this case, considering a repetition rate of 10 Hz). Accumulation of laser pulses on the irradiated spot induces subsequent cycles of heating and cooling. Assuming that

**Fig. 6.4** Calculated time dependence of the surface temperature of PS after irradiation with the first pulse (red arrow) at 266 nm at a fluence of  $10 \text{ mJ/cm}^2$  at the indicated depths



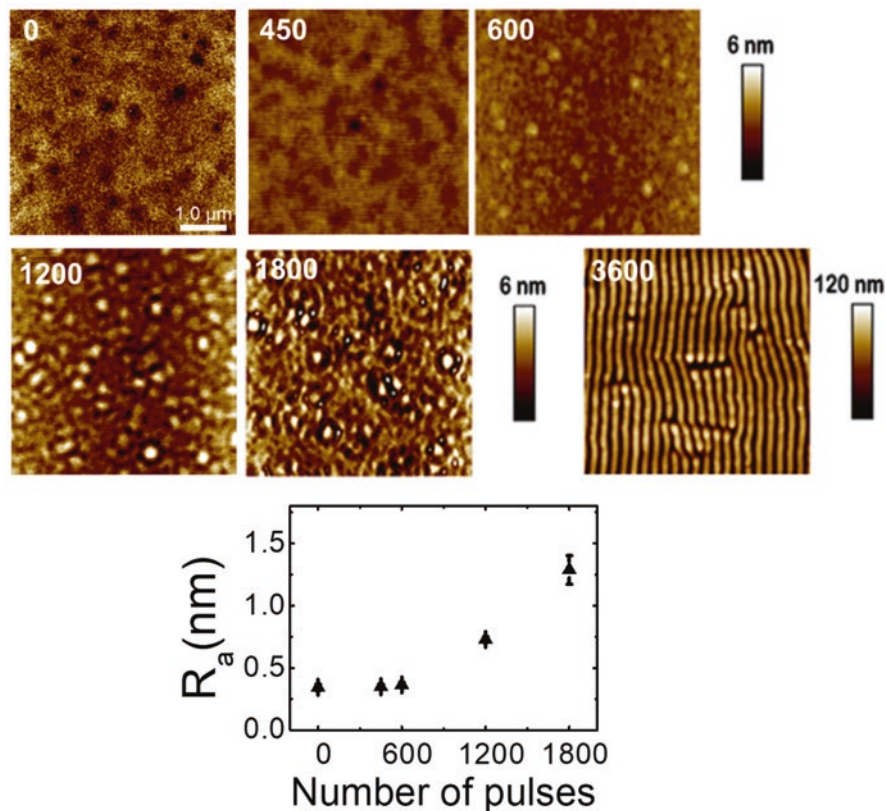
none of the physical magnitudes of the polymer change with temperature, one can estimate that each pulse will heat the sample and that the surface will be at a slightly higher temperature than the previous one after the arrival of the next laser pulse. A minimum number of pulses are, therefore, necessary to ensure that the surface temperature overcomes the  $T_g$ . This result suggests that the generation of LIPSS in polymers requires a minimum number of pulses to observe a modification of the surface roughness, prior to the generation of ordered structures in line with published reports [9–12].

Figure 6.5 shows a sequence AFM image on a PS film irradiated by different amount of pulses of a 266 nm laser with a fluence of  $10 \text{ mJ/cm}^2$  leading finally to the formation of LIPSS.

This result suggests that the increase on roughness observed in Fig. 6.4 (right panel) during the incubation regime before LIPSS formation occurs when the temperature has increased above the  $T_g$  of PS. After a laser pulse induces local heating, the material cools down (Fig. 6.4). Frozen surface inhomogeneities generate a roughness increment (Fig. 6.5). These inhomogeneities generated by a pulse are expected to be enhanced as the next pulse reaches a rougher surface than before. This effect facilitates a feedback mechanism needed for LIPSS formation [20]. It should be contemplated that here the temperature calculation is simplified and the temperature dependence of the polymer physical parameters was not considered. Additionally, the possible changes in the thermal properties of the surface during the transformations caused by the previous laser pulses (i.e., incubation effects) were also neglected. Nevertheless, considering only the thermal effects induced by every laser pulse and the repetitive heating/cooling cycles, the calculation can explain LIPSS formation and supports the presence of the feedback mechanism.

It has been shown that the period, quality, and height of the LIPSS formed depend on the thickness of the polymer film, in the case of supported polymers [21]. Figure 6.6 shows the obtained LIPSS on PS films of different thickness supported on silicon under similar irradiation conditions as those shown in Fig. 6.5.

As illustrated, LIPSS is not well formed in the thinnest film. Csete et al. [22] reported that there is a critical thickness below which line shape structures cannot



**Fig. 6.5** Sequence of AFM images on a PS-supported surface irradiated with fixed fluence and wavelength with different numbers of pulses as labeled. The increase of roughness prior to the formation of LIPSS is observed in the bottom panel

be formed in supported films. Therefore, another aspect to consider, in view of the dependence of the temperature with the depth, as shown in Fig. 6.4, is that the LIPSS formation may depend on the thickness of the polymer film. Thus, in the case of thin films (below 100 nm thick for most polymers), the substrate has an impact on the development of LIPSS on the polymer surface. In Fig. 6.7 AFM images of LIPSS obtained from a similar thickness, PS film on different substrates are shown. As observed, the formed nanostructures on the polymer surface depend on the underlying substrate. Although linear ripples are formed on the film with thickness around 120 nm, the morphology of them is different. While the polymer on silicon forms rather continuous and homogeneous ripples (Fig. 6.7a), LIPSS induced in the polymer on quartz (Fig. 6.7c), although well-defined, appear disturbed in several places. Also, the period of the formed structures is smaller in the case of a quartz substrate than in the case of the silicon substrate. Although weaker, a similar trend is observed for the thicker films [21].

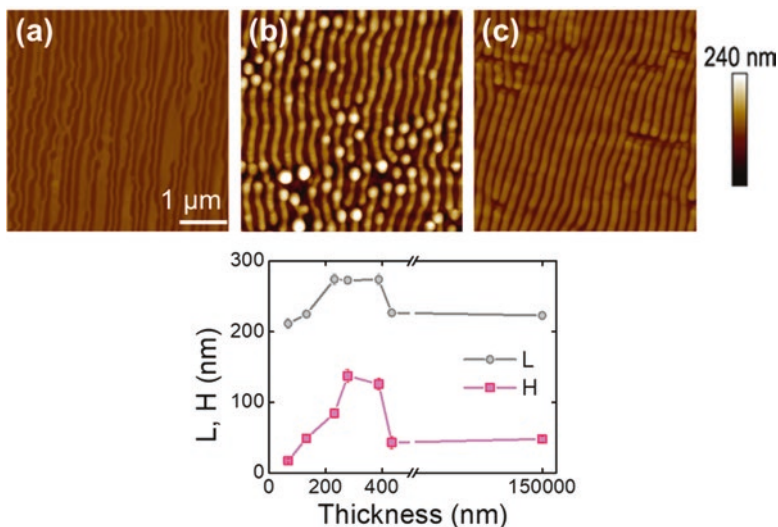
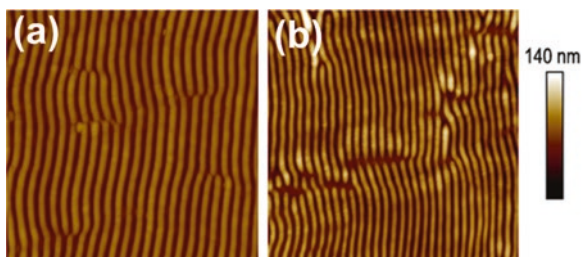


**Fig. 6.6** AFM height images ( $5 \mu\text{m} \times 5 \mu\text{m}$ ) of PS films with different thicknesses irradiated at a fluence of  $10 \text{ mJ/cm}^2$  and a number of pulses of 4800: (a) 67 nm, (b) 231 nm, and (c) 434 nm. (Bottom) Period length ( $L$ ) and (h) the LIPSS height ( $H$ ) as a function of the film thickness for PS film at a fluence of  $10 \text{ mJ/cm}^2$  and a number of pulses of 4800. Lines are plotted to guide the eyes

**Fig. 6.7** AFM height images ( $5 \mu\text{m} \times 5 \mu\text{m}$ ) of a 120-nm-thick PS film deposited on two different substrates. (left) Silicon, (right) quartz



To understand this effect, one should consider that, when a laser pulse reaches the polymer surface, the radiation can be reflected, scattered, and/or absorbed. The fraction which is absorbed by the polymer transforms into heat, while the rest of the energy, if the film is thin enough, eventually may reach the underlying substrate and be dissipated by it. The amount of energy at a given depth  $x$  from the surface can be determined by the Beer-Lambert law:

$$A = \log \frac{I_0}{I} = \log \frac{1}{T} = \alpha l \quad (6.4)$$

where  $\alpha$  is the absorption coefficient at a given wavelength and  $l$  is the film thickness.

In the case of PS, considering an absorption coefficient of  $1.6 \times 10^5 \text{ m}^{-1}$  at 266 nm [21] means that for a 430-nm-thick sample, 93% of the incident energy is transmitted and it will reach the substrate. Thus, the thermal properties of the substrate can be relevant. The differences observed in the morphology of the LIPSS formed on PS films with different thicknesses and deposited onto different substrates may be explained on the basis of the substrate physical properties, in particular to their thermal and optical properties. For a single pulse, the temperature increase at the substrate surface due to the transmitted light through the PS film can be estimated by using the values of the corresponding physical properties listed in Table 6.1 as:

$$\Delta T = \frac{F\alpha}{c\rho} \quad (6.5)$$

where  $F$  is the fluence. Considering the high amount of energy transmitted through the polymer film and reaching the substrate, the estimated temperature increase can be calculated using the value of incoming fluence, and the estimated temperatures obtained are listed in Table 6.1.

After the fast increase of temperature, the heat is dissipated depending on the thermal conductivity of the substrate. The thermal diffusion time,  $t_d$ , is given by [9, 29]:

$$t_d = \frac{1}{D\alpha^2} \quad (6.6)$$

where  $D$  is thermal diffusivity of the material expressed by  $D = \frac{\kappa}{c\rho}$ . The calculated parameters are listed in Table 6.1.

It is interesting to observe the differences in the calculated increase of the substrate temperature under the same illumination conditions. The increase in the temperature of the silicon substrate is significantly higher than that obtained in the case of the quartz substrate. Nevertheless, the calculations for the thermal diffusion time indicate that the heat is dissipated in length scales shorter than the arrival of next pulse, but the presence of this heat bath may alter the calculations shown in Fig. 6.4,

**Table 6.1** Linear absorption coefficient ( $\alpha$ ) at 266 nm, specific heat ( $c$ ), density ( $\rho$ ), thermal conductivity ( $\kappa$ ), and refractive index at 266 nm ( $n$ ) of silicon and quartz. Temperature increase ( $\Delta T$ ), thermal diffusivity ( $D$ ), and thermal diffusion time ( $t_d$ ) of the substrates

	Silicon	Quartz
$\alpha$ ( $\text{m}^{-1}$ )	$1.97 \cdot 10^8$ [23, 24]	3 [25]
$c$ ( $\text{J kg}^{-1} \text{K}^{-1}$ )	703 [26]	710 [27]
$\rho$ ( $\text{kg m}^{-3}$ )	2330 [26]	2649 [27]
$k$ ( $\text{W m}^{-1} \text{K}^{-1}$ )	163.3 [26]	10.7 [27]
$n$	1.9 [23]	$\sim 1.5$ [28]
$\Delta T$ (K)	$1.2 \times 10^3$	$1.6 \times 10^{-5}$
$D$ ( $\text{m}^2/\text{s}$ )	$9.97 \times 10^{-5}$	$5.7 \times 10^{-6}$
$t_d$ (ns)	$2.6 \times 10^{-4}$	–

and the rise in temperature of the polymer at the arrival of the next pulse is probably higher in the case of silicon substrates than in the case of quartz silicon.

## 6.4 Examples of LIPSS on Functional Polymers, Blends, and Composites

Along the past years, a variety of LIPSS structures obtained by pulsed nanosecond lasers have been presented. Lazare [30] and Csete et al. [13] reported the creation of LIPSS on polyethylene terephthalate (PET). Later, the benefits of having a groovy surface structure were exploited for improving cell adhesion and spreading [31–34] and for the fabrication of substrates for surface-enhanced Raman spectroscopy [35, 36]. It has been demonstrated in the literature that LIPSS can be obtained in polymers, provided they absorb the light in the irradiation wavelength [11, 37–40]. Later on, LIPSS have been reported in semiconducting polymers interesting for applications in photovoltaics [11, 37] and in polymer blends, where a synergistic effect has been observed, obtaining best quality LIPSS in the blend than in the individual components [37, 41]. LIPSS can be also obtained in polymers reinforced with carbon-based additives, in particular, expanded graphite (EG) and single-wall carbon nanotubes (SWCNT) [42, 43]. The obtained LIPSS in these cases were very similar to those obtained in the bare polymer, although they required more pulses to obtain similar LIPSS. This is due to the higher thermal conductivity and diffusivity of the composites, which make the feedback mechanism less efficient since the temperature reached will be lower in the case of the nanocomposite. An example of this effect is shown in Fig. 6.8.

As mentioned before, the possibility of generating LIPSS in a polymer surface depends mainly on the polymer absorbing efficiently the laser light. However, there have been attempts to obtain LIPSS even in non-absorbing systems. A two-step method, involving LIPSS creation on stainless steel and subsequent replication of the structures onto biomaterials using the steel LIPSS as a mold, has been used by Hendrikson et al. [44] for stem cell biology and applications in the regenerative

**Fig. 6.8** AFM height images ( $5\ \mu\text{m} \times 5\ \mu\text{m}$ ) of PET and PET/EG 0.4 wt.% surfaces after irradiation at 266 nm and a laser fluence of  $8\ \text{mJ}/\text{cm}^2$  at the indicated number of pulses

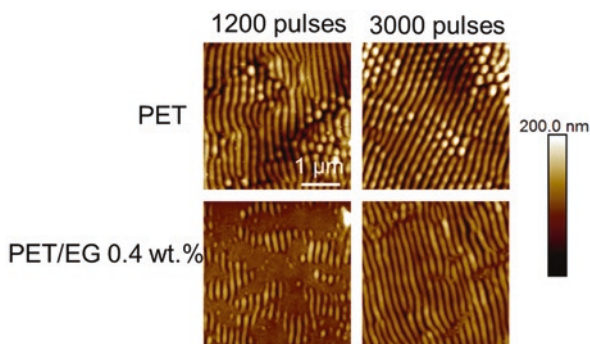
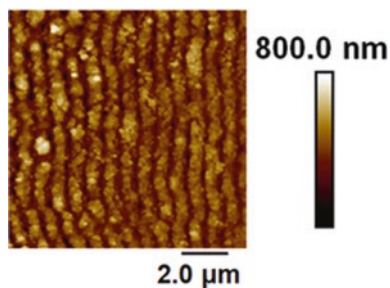


**Fig. 6.9** AFM height images ( $10\ \mu\text{m} \times 10\ \mu\text{m}$ ) of PET after irradiation at 795 nm with 50,000 pulses of 120 fs and a fluence of  $87\ \text{mJ}/\text{cm}^2$



medicine. The synergistic effect of combining two materials that respond differently to the formation of LIPSS has been used by Martinez Tong et al. [45] to obtain LIPSS in a non-absorbing ferroelectric polymer by irradiating a bilayer formed by a substrate of absorbing polymer. The obtained ferroelectric LIPSS can be used to store information via their ferroelectric properties, and due to the ripple structure, the information storage density increases by an order of magnitude compared to that of the unstructured bilayer.

A different approach for generating LIPSS at a wavelength at which the polymers has a low linear absorption coefficient consists of the use of femtosecond laser pulses. Upon irradiation with this type of lasers, multiphoton absorption and ionization processes mediate the coupling of laser light with the polymer due to the large intensities involved [16, 46, 47]. This fact makes possible to obtain LIPSS at wavelengths in the IR region where most of the polymers are transparent. Thus, by using femtosecond laser pulses, it is possible to tune and control the morphology and size of the periodic structures in a wider range. In Fig. 6.9 the AFM image of PET irradiated at 795 nm with fs is shown. LIPSS obtained have a period close to 800 nm.

In conclusion, wrinkled surfaces can be obtained through the control of surface instabilities produced by repeated irradiation of polymer surfaces by pulsed lasers. The periodic rippled topography is directly related to the wavelength of the laser. The actors like the substrate, the absorption of polymer, and the thermal conductivity and diffusivity are key on tuning the obtaining periodic structures.

**Acknowledgments** This work has been supported by the Spanish Ministry of Economy and Competitiveness under the projects MAT2014-59187-R, MAT2015-66443-C02-1-R, and CTQ2016-75880-P. E.R. thanks MINECO for the tenure of a Ramón y Cajal contract (No. RYC-2011-08069).

## References

1. A.Y. Malkin, Surface instabilities. *Colloid J.* **70**(6), 673–689 (2008)
2. M.M. Denn, Extrusion instabilities and wall slip. *Annu. Rev. Fluid Mech.* **33**(1), 265–287 (2001)
3. C.-M. Chen, S. Yang, Wrinkling instabilities in polymer films and their applications. *Polym. Int.* **61**(7), 1041–1047 (2012)

4. J. Rodríguez-Hernández, Wrinkled interfaces: Taking advantage of surface instabilities to pattern polymer surfaces. *Prog. Polym. Sci.* **42**, 1–41 (2015)
5. N. Vargas-Alfredo et al., Highly efficient antibacterial surfaces based on bacterial/cell size selective microporous supports. *ACS Appl. Mater. Interfaces* **9**(51), 44270–44280 (2017)
6. E. Schäffer et al., Electrically induced structure formation and pattern transfer. *Nature* **403**, 874 (2000)
7. N. Wu, W.B. Russel, Micro- and nano-patterns created via electrohydrodynamic instabilities. *Nano Today* **4**(2), 180–192 (2009)
8. M. Malinauskas et al., Ultrafast laser nanostructuring of photopolymers: A decade of advances. *Phys. Rep.* **533**(1), 1–31 (2013)
9. E. Rebollar et al., Assessment and formation mechanism of laser-induced periodic surface structures on polymer spin-coated films in real and reciprocal space. *Langmuir* **27**(9), 5596–5606 (2011)
10. E. Rebollar et al., In situ monitoring of laser-induced periodic surface structures formation on polymer films by grazing incidence small-angle X-ray scattering. *Langmuir* **31**(13), 3973–3981 (2015)
11. Á. Rodríguez-Rodríguez et al., Laser-induced periodic surface structures on conjugated polymers: Poly(3-hexylthiophene). *Macromolecules* **48**(12), 4024–4031 (2015)
12. I. Michaljaníčová et al., Regular pattern formation on surface of aromatic polymers and its cytocompatibility. *Appl. Surf. Sci.* **370**, 131–141 (2016)
13. M. Csete, Z. Bor, Laser-induced periodic surface structure formation on polyethylene-terephthalate. *Appl. Surf. Sci.* **133**(1), 5–16 (1998)
14. M. Csete et al., The role of original surface roughness in laser-induced periodic surface structure formation process on poly-carbonate films. *Thin Solid Films* **453–454**, 114–120 (2004)
15. M. Csete et al., Attenuated total reflection measurements on poly-carbonate surfaces structured by laser illumination. *Appl. Surf. Sci.* **208–209**, 474–480 (2003)
16. E. Rebollar et al., Ultraviolet and infrared femtosecond laser induced periodic surface structures on thin polymer films. *Appl. Phys. Lett.* **100**(4), 041106 (2012)
17. Z. Guosheng, P.M. Fauchet, A.E. Siegman, Growth of spontaneous periodic surface structures on solids during laser illumination. *Phys. Rev. B* **26**(10), 5366–5381 (1982)
18. D.W. Bäuerle, *Laser Processing and Chemistry* (Springer, Berlin/Heidelberg, 2011)
19. M. Li et al., Effects of post-thermal treatment on preparation of surface microstructures induced by polarized laser on polyimide film. *Mater. Chem. Phys.* **77**(3), 895–898 (2003)
20. C.M. Mate, M.F. Toney, K.A. Leach, Roughness of thin perfluoropolyether lubricant films: Influence on disk drive technology. *IEEE Trans. Magn.* **37**(4), 1821–1823 (2001)
21. J. Cui et al., Influence of substrate and film thickness on polymer LIPSS formation. *Appl. Surf. Sci.* **394**, 125–131 (2017)
22. P. Slepíčka et al., Angle dependent laser nanopatterning of poly(ethylene terephthalate) surfaces. *Appl. Surf. Sci.* **257**(14), 6021–6025 (2011)
23. M.A. Green, Self-consistent optical parameters of intrinsic silicon at 300K including temperature coefficients. *Sol. Energy Mater. Sol. Cells* **92**(11), 1305–1310 (2008)
24. F.A. Lasagni et al., Fabrication and characterization in the micro-nano range. *Adv. Struct. Mater.* **10**, 361–377 (2011)
25. E.C. Beder, C.D. Bass, W.L. Shackelford, Transmissivity and absorption of fused quartz between 0.22  $\mu$  and 3.5  $\mu$  from room temperature to 1500° C. *Appl. Opt.* **10**(10), 2263–2268 (1971)
26. P. Crystran Ltd, U., Silicon (Si). <https://www.crystran.co.uk/optical-materials/silicon-si>
27. P. Crystran Ltd, U., Quartz Crystal (SiO<sub>2</sub>). <https://www.crystran.co.uk/optical-materials/quartz-crystal-sio2>
28. I.H. Malitson, Interspecimen comparison of the refractive index of fused silica\*,†. *J. Opt. Soc. Am.* **55**(10), 1205–1209 (1965)
29. A. Vogel, V. Venugopalan, Mechanisms of pulsed laser ablation of biological tissues. *Chem. Rev.* **103**(2), 577–644 (2003)

30. S. Lazare et al., New surface modifications of polymer films with the excimer laser radiation, in *Ninth International Symposium on Gas Flow and Chemical Lasers*, (SPIE, Bellingham, 1993)
31. E. Rebollar et al., Physicochemical modifications accompanying UV laser induced surface structures on poly(ethylene terephthalate) and their effect on adhesion of mesenchymal cells. *Phys. Chem. Chem. Phys.* **16**(33), 17551–17559 (2014)
32. E. Rebollar et al., Proliferation of aligned mammalian cells on laser-nanostructured polystyrene. *Biomaterials* **29**(12), 1796–1806 (2008)
33. G. Mayer et al., Physico-chemical and biological evaluation of excimer laser irradiated polyethylene terephthalate (pet) surfaces. *Biomaterials* **27**(4), 553–566 (2006)
34. X. Wang et al., Cell directional migration and oriented division on three-dimensional laser-induced periodic surface structures on polystyrene. *Biomaterials* **29**(13), 2049–2059 (2008)
35. E. Rebollar et al., Gold coatings on polymer laser induced periodic surface structures: Assessment as substrates for surface-enhanced Raman scattering. *Phys. Chem. Chem. Phys.* **14**(45), 15699–15705 (2012)
36. E. Rebollar et al., Laser-induced surface structures on gold-coated polymers: Influence of morphology on surface-enhanced Raman scattering enhancement. *J. Appl. Polym. Sci.* **132**(45), 42770 (2015)
37. J. Cui et al., Laser-induced periodic surface structures on P3HT and on its photovoltaic blend with PC71BM. *ACS Appl. Mater. Interfaces* **8**(46), 31894–31901 (2016)
38. S. Pérez et al., Laser-induced periodic surface structuring of biopolymers. *Appl. Phys. A* **110**(3), 683–690 (2013)
39. I. Martín-Fabiani et al., Laser-induced periodic surface structures nanofabricated on poly(trimethylene terephthalate) spin-coated films. *Langmuir* **28**(20), 7938–7945 (2012)
40. M. Csete, O. Marti, Z. Bor, Laser-induced periodic surface structures on different polycarbonate films. *Appl. Phys. A* **73**(4), 521–526 (2001)
41. Á. Rodríguez-Rodríguez et al., Patterning conjugated polymers by laser: Synergy of nanostructure formation in the all-polymer heterojunction P3HT/PCDTBT. *Langmuir* **34**(1), 115–125 (2018)
42. R.I. Rodríguez-Beltrán et al., Laser induced periodic surface structures on polymer nanocomposites with carbon nanoadditives. *Appl. Phys. A* **123**(11), 717 (2017)
43. R.I. Rodríguez-Beltrán et al., Laser induced periodic surface structures formation by nanosecond laser irradiation of poly (ethylene terephthalate) reinforced with expanded graphite. *Appl. Surf. Sci.* **436**, 1193–1199 (2018)
44. W. Hendrikson et al., Mold-based application of Laser-Induced Periodic Surface Structures (LIPSS) on biomaterials for nanoscale patterning. *Macromol. Biosci.* **16**(1), 43–49 (2015)
45. D.E. Martínez-Tong et al., Laser fabrication of polymer ferroelectric nanostructures for non-volatile organic memory devices. *ACS Appl. Mater. Interfaces* **7**(35), 19611–19618 (2015)
46. E. Rebollar et al., Assessment of femtosecond laser induced periodic surface structures on polymer films. *Phys. Chem. Chem. Phys.* **15**(27), 11287–11298 (2013)
47. M. Forster et al., Periodic nanoscale structures on polyimide surfaces generated by temporally tailored femtosecond laser pulses. *Phys. Chem. Chem. Phys.* **13**(9), 4155–4158 (2011)

# Chapter 7

## Design of Perfectly Ordered Periodic Structures on Polymers Using Direct Laser Interference Patterning



Andrés Fabián Lasagni, Sabri Alamri, Florian Rößler, Valentin Lang, and Bogdan Voisiat

### 7.1 Introduction to Interference Patterning Methods

Surfaces with controlled topographic characteristics can provide enhanced properties in comparison to surfaces with a random roughness [1]. Several examples of ordered topographies can be found on the surfaces of different plants and animals, resulting from several 1000 years of evolution. In this way, nature has shown to be the best technologist to overcome any survival challenge by using bottom-up approaches of patterning.

Laser-based technologies can provide the required technological and economical aspects to reproduce such surfaces using a top-down approach [2]. One technology capable of producing periodic surface structures is laser interference lithography (LIL) [3, 4]. In LIL, the standing wave pattern existing at the intersection of two or more laser beams is used to expose a photosensitive layer such as a resist in a parallel manner. In the case of a negative resist, the positions corresponding to the intensity maxima of the interference pattern are photopolymerized, and after development, a periodic variation of the surface topography results.

LIL has important advantages compared to other serial lithographic methods such as electron beam lithography (EBL) or ion beam lithography (IBL) including a higher efficiency and a wider workspace. Other advantages include low cost and high throughput, no contamination on the surface as the material is polymerized and not ablated, the capability to fabricate patterns in large areas (up to hundreds of mm

---

A. F. Lasagni (✉) · S. Alamri · V. Lang  
Institute for Manufacturing Technology, Technische Universität Dresden, Dresden, Germany  
Fraunhofer Institute for Werkstoff- und Strahltechnik IWS, Dresden, Germany  
e-mail: [andres\\_fabian.lasagni@tu-dresden.de](mailto:andres_fabian.lasagni@tu-dresden.de)

F. Rößler · B. Voisiat  
Institute for Manufacturing Technology, Technische Universität Dresden, Dresden, Germany

in diameter), as well as software-controlled reconfigurable patterns (with different periods, feature sizes, and pattern shapes) [4].

If laser systems with sufficient pulse energy are utilized, the irradiated materials can be directly processed. Hence, the method has been called, in this case, direct laser interference patterning (DLIP) [5–10].

Similar to laser-based fabrication methods, the laser radiation can be used to facilitate various metallurgical processes, such as melting, recrystallization, or crystallization of amorphous materials.

The most important requirement to produce a periodic structure using DLIP is that the material to be processed must absorb the energy of the laser at the selected wavelength. The laser must provide also sufficient pulse energy (from tens of  $\mu\text{J}$  to some J) to be capable of ablating or modifying the material directly. Depending on the nature of the interaction of the laser light with the used materials, the microstructuring process can be based on mechanisms of photothermal or photochemical nature as well as a combination of both (photophysical ablation) [11, 12].

In this chapter, different aspects of the DLIP method for the treatment of polymers will be introduced. In the first part of the chapter, the main parameters used to control and obtain interference patterns are introduced. After that, several examples of pattern fabrication are discussed showing the potential of the method. The examples include the fabrication of single-scaled and multiple-scaled patterns as well as the structuring of polymer-polymer foil's interfaces. Finally, a general model for the simulation of the process is given.

## 7.2 Principle of Interference

Interference of electromagnetic waves appears when at least two coherent beams, propagating at a certain angle to each other, interact. In general case, the intensity profile in the interference area can be expressed by the formula [13]:

$$I(\vec{\mathbf{r}}) \propto \left( \sum_{i=1}^N \vec{\mathbf{E}}(\vec{\mathbf{r}}, t) \right)^2, \quad (7.1)$$

where  $\vec{\mathbf{r}}$  is the coordinate vector,  $i$  is the index of interfering beams,  $N$  is the number of the beams,  $\vec{\mathbf{E}}$  is the electrical field of  $i$ -th beam,  $t$  is time, and brackets denote averaging in time at least for one period of radiation. The electrical field of  $i$  wave can be expressed as follows:

$$\vec{\mathbf{E}}_i = \vec{\mathbf{E}}_{0i} \cos(\vec{\mathbf{k}} \cdot \vec{\mathbf{r}} - \omega t + \varphi_i), \quad (7.2)$$

where  $\vec{\mathbf{E}}_i$  is the electrical field amplitude of  $i$  wave,  $|\vec{\mathbf{k}}| = 2\pi / \lambda$  is the wave vector of  $i$ -th wave,  $\lambda$  is the wavelength of radiation,  $\omega$  is the angular frequency of

radiation, and  $\varphi_i$  is the phase of  $i$ -th wave. If the wavelength of all the beams is the same, Eqs. (7.1) and (7.2) can be simplified as follows [14]:

$$I(\vec{r}) \propto \sum_{i=1}^N |\vec{E}_{0i}|^2 + 2 \sum_{j<i}^N \sum_{i=1}^N \vec{E}_{0i} \cdot \vec{E}_{0j} \cos\left(\left(\vec{k}_i - \vec{k}_j\right) \vec{r} + \varphi_i - \varphi_j\right) \quad (7.3)$$

Periodical intensity field is formed, and the period depends on the incident angle between the beams and wavelength. The shape of the pattern is affected by the number of beams, phase difference between them, and polarization direction.

Different beam distributions and corresponding intensity profiles are shown in Fig. 7.1. Each beam has the same angle with the optical axis ( $\theta = \text{const.}$ ) and is distributed symmetrically around it ( $\varphi = \text{const.}$ ).

The interference pattern formed by two beams is a one-dimensional grating with the period  $\Lambda_2 = \lambda/2 \sin \theta$ . The three and six beams superposition produce the same periodic structures consisting of the intensity maxima placed in the triangular lattice but with the different periods (distances between the closest maxima)  $\Lambda_3 = 2\lambda/3 \sin \theta$  and  $\Lambda_6 = 2\lambda / \sqrt{3} \sin \theta$ . The four beam superposition results in periodic structures consisting of the intensity maxima placed in the square lattice configuration with a period  $\Lambda_4 = \lambda/3 \sin \theta$  [13].

Other complex interference patterns can be obtained by varying the phase and/or polarization of the beams. When the phases of the beams are varied for two- or three-beam configurations, the shape of the interference patterns remain the same, while the patterns move in the direction of the beam that phase changes.

For four and six beams, the situation is totally different. In the case of four beams (Fig. 7.2a–d), the intensity distribution gradually changes to chessboard-like pattern when the phase of one beam is increased to  $180^\circ$  or phases of two beams are equally

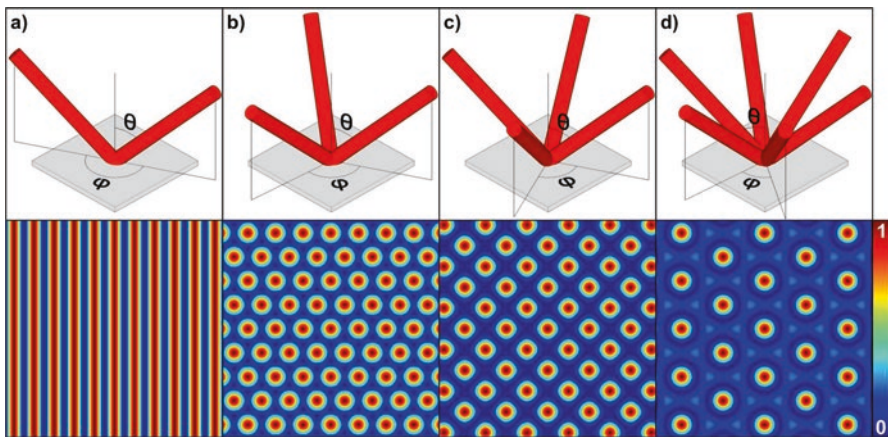


**Fig. 7.1** Two (a), three (b), four (c), and five (d) symmetrically distributed (top) beams interference intensity distributions (bottom)

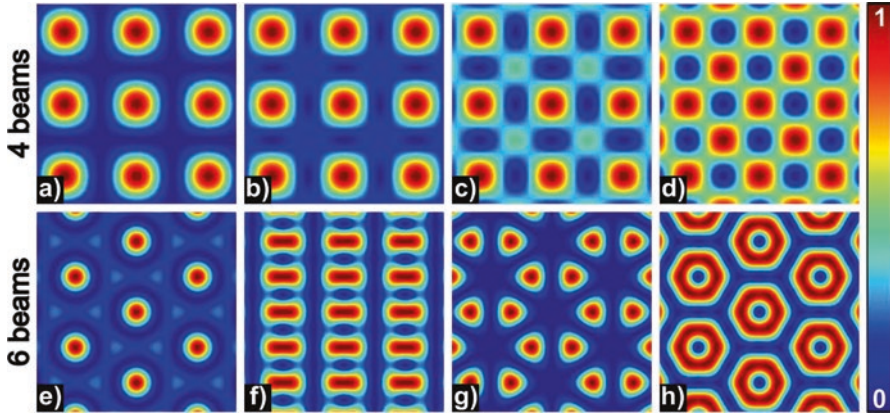


**Fig. 7.2** Intensity distribution of four (top) and six (bottom) beams interference when the phases of the 4 beam is: (a)  $-0^\circ, 0^\circ, 0^\circ, 0^\circ$ ; (b)  $-90^\circ, 0^\circ, 0^\circ, 0^\circ$ ; (c)  $-120^\circ, 0^\circ, 0^\circ, 0^\circ$ ; (d)  $-180^\circ, 0^\circ, 0^\circ, 0^\circ$ ; and 6 beams: (e)  $-0^\circ, 0^\circ, 0^\circ, 0^\circ, 0^\circ, 0^\circ$ ; (f)  $-180^\circ, 0^\circ, 0^\circ, 0^\circ, 0^\circ, 0^\circ$ ; (g)  $-90^\circ, 0^\circ, 90^\circ, 0^\circ, 0^\circ, 0^\circ$ ; (h)  $-0^\circ, 60^\circ, 120^\circ, 180^\circ, 240^\circ, 300^\circ$

increased to  $90^\circ$ . In the case of six beams (Fig. 7.2e–h), the intensity shape dependence on beam phases is stronger and produces more distinct patterns.

When the polarization of the beams is varied and the phase remains constant, the shape of the intensity pattern can be changed not only for four or six beams interference configurations but also when three beams are superposed.

In the case of two beams, the angle between polarization vectors controls only the contrast of the interference pattern. For a three-beam configuration (Fig. 7.3a–d), it is, for instance, possible to achieve inverted profiles (see Fig. 7.3a, b). In addition, periodic structures with smaller spatial periods can be obtained without changing the beam intersection angle also by rotating the polarization of the beams (see for example Figs. 7.3 and 7.4b for four and six beam setups, respectively).

Also, control of the polarization direction allows creating very complex structures, especially for the six-beam configuration. For example, a circle-shaped intensity distribution can be obtained using the polarization vectors directions depicted in Fig. 7.4d, e. Other many complex geometries are shown also in Figs. 7.3 and 7.4.

### 7.3 Single-Scale Interference Patterning

Using two- and three-beam configurations, poly(imide) (PI), poly(etheretherketone) (PEEK), polycarbonate (PC), and poly(etherimide) (PEI) polymers were treated using 266 and 355 nm laser wavelengths [15]. The spatial period was  $6.2 \mu\text{m}$ . The evolution of the structure depth as a function of the laser fluence for line-like patterns for the abovementioned polymers is shown in Fig. 7.5. In the case of PC, at 266 nm the laser fluence required to initiate the structuring process was  $60 \text{ mJ/cm}^2$ ,

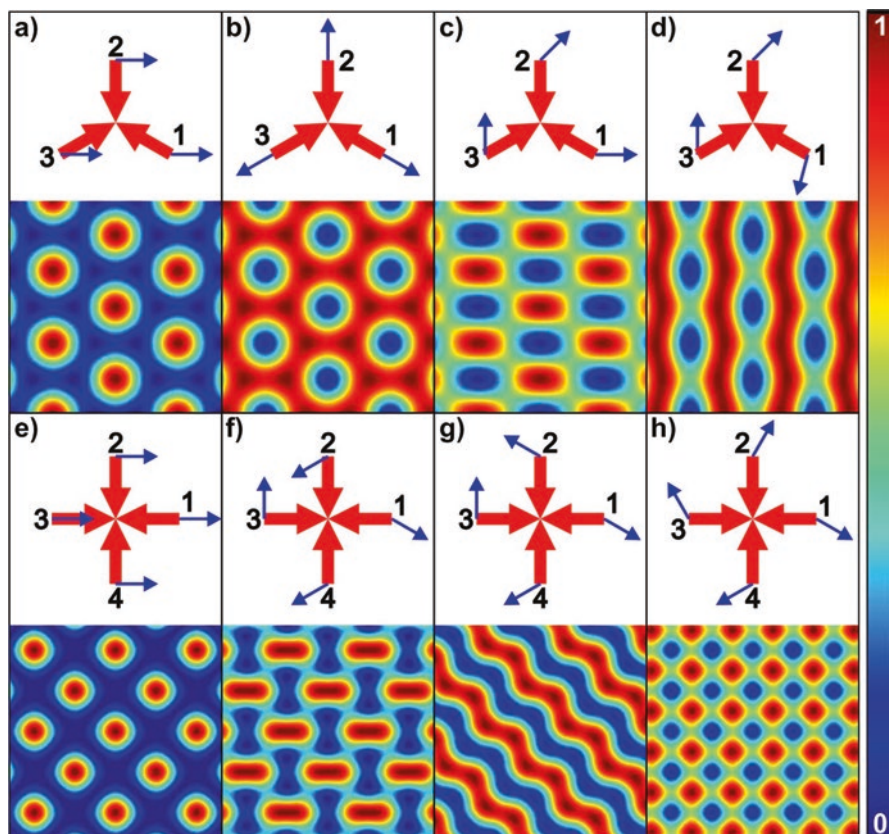


**Fig. 7.3** Top view of laser beams (red arrows) and polarization vectors (blue arrows) distribution and corresponding interference intensity profiles. The polarization vector angles: (a)  $-0^\circ, 0^\circ, 0^\circ$ ; (b)  $-330^\circ, 90^\circ, 210^\circ$ ; (c)  $-0^\circ, 45^\circ, 90^\circ$ ; (d)  $-45^\circ, 150^\circ, 255^\circ$ ; (e)  $-0^\circ, 0^\circ, 0^\circ, 0^\circ$ ; (f)  $-330^\circ, 210^\circ, 90^\circ, 210^\circ$ ; (g)  $-330^\circ, 150^\circ, 90^\circ, 210^\circ$ ; (h)  $-330^\circ, 60^\circ, 120^\circ, 210^\circ$

while at 355 nm, this value was  $\sim 1500$  mJ/cm<sup>2</sup>. In comparison, in PI, PEEK, and PEI, these laser fluences were quite similar at both wavelengths. The absorption coefficient of PC is about 100 times higher at 266 than at 355 nm, while absorbance of PI, PEI, and PEEK do not differ very much. Therefore, these threshold laser fluences can be directly related to the absorption coefficient of the polymers.

The same can be explained by means of the cutoff wavelength of the studied polymers. PI, PEI, and PEEK present absorption cutoff at wavelengths higher than ca. 350 nm, while the cutoff wavelength of PC is given at about 300 nm [16–20]. Thus, since laser ablation takes place only when the laser radiation is absorbed, a maximal absorbance at a defined wavelength is necessary.

As can be observed also in Fig. 7.5, the structure depth increases linearly with the laser fluence until a certain value is reached. Above this value, the structure depth still increases with the laser fluence but with a lower slope.

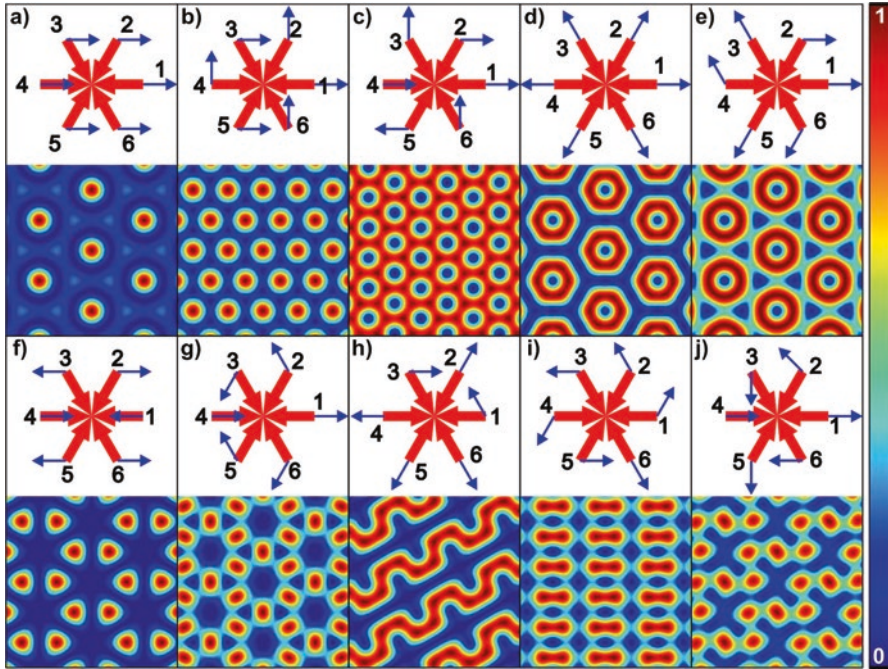


**Fig. 7.4** Top view of laser beams (red arrows) and polarization vectors (blue arrows) distribution and corresponding interference intensity profiles. The polarization vector angles: (a)  $-0^\circ, 0^\circ, 0^\circ, 0^\circ, 0^\circ, 0^\circ$ ; (b)  $-0^\circ, 90^\circ, 0^\circ, 0^\circ, 90^\circ, 0^\circ$ ; (c)  $-0^\circ, 0^\circ, 90^\circ, 0^\circ, 180^\circ, 90^\circ$ ; (d)  $-0^\circ, 60^\circ, 120^\circ, 180^\circ, 240^\circ, 300^\circ$ ; (e)  $-0^\circ, 0^\circ, 120^\circ, 120^\circ, 240^\circ, 240^\circ$ ; (f)  $-0^\circ, 180^\circ, 0^\circ, 180^\circ, 0^\circ, 180^\circ$ ; (g)  $-0^\circ, 120^\circ, 240^\circ, 0^\circ, 120^\circ, 240^\circ$ ; (h)  $-120^\circ, 60^\circ, 0^\circ, 180^\circ, 240^\circ, 300^\circ$ ; (i)  $-600^\circ, 120^\circ, 180^\circ, 240^\circ, 0^\circ, 300^\circ$ ; (j)  $-0^\circ, 135^\circ, 270^\circ, 0^\circ, 270^\circ, 180^\circ$

In Fig. 7.6, the topographies of typical structures obtained by two- and three-beam interference patterning as a function of laser fluence in PI are shown. For the two-beam case, the period of the micropatterns was  $6.2 \mu\text{m}$ , and the width of the ablated lines varies from  $3.3$  to  $6.2 \mu\text{m}$  for  $312$  and  $1023 \text{ mJ/cm}^2$ , respectively. For low laser fluences ( $300 \text{ mJ/cm}^2$ ), the profile of the micropatterns can be described by a sinusoidal-trapezoidal shape (Fig. 7.6a). For medium values of the laser fluence ( $600 \text{ mJ/cm}^2$ ), a sinusoidal profile is obtained (Fig. 7.6b), while for high laser fluences ( $1000 \text{ mJ/cm}^2$ ) a U-shaped profile is observed (Fig. 7.6c).

These geometries can be explained as follows. Laser ablation occurs when a certain laser intensity threshold value is exceeded. The intensity distribution of the interference pattern is described by a trigonometric function. At low fluences, only a very small area of the polymer can be ablated at the interference maxima positions (Fig. 7.6a) producing a sine-trapezoidal profile. As the laser fluence increases, a larger portion of the interference pattern surpasses the threshold energy needed to ablate the polymer resulting in wider ablated regions with a sinusoidal shape (Fig. 7.6b). For high laser fluences, the polymer is ablated nearly everywhere but with different ablation ratios obtaining a U-shaped profile (Fig. 7.6c).

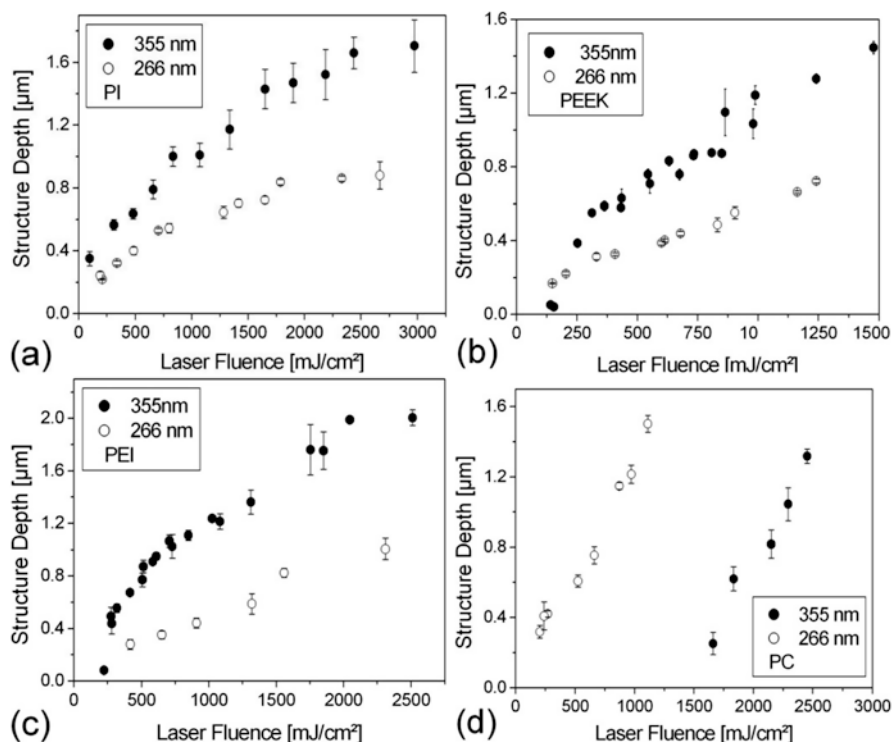


**Fig. 7.5** Structure depth as a function of the laser fluence for (a) PI, (b) PEEK, (c) PEI, and (d) PC irradiated with laser radiation of 266 and 355 nm of wavelength. Line-type interference pattern. In all cases, the period was 6.2 μm. (Reproduced with permission from Ref. [15])

Similar results were observed when the polymeric samples were irradiated with a three-beam interference pattern (Fig. 7.6d, e). In this case, the used spatial period was 7.2 μm. The diameter of the ablated circular regions changed from 3.6 to 7.2 μm from 99 to 854 mJ/cm² of laser fluence, respectively. Due to the geometry of the interference pattern, the micro-cavities collapse at a laser fluence of ~ 850 mJ/cm² forming a star-shaped periodic pattern (Fig. 7.6e). Each of the six triangles of the star-shaped pattern corresponds to the region of the unmodified material.

## 7.4 Multiple-Scale Interference Patterning

### 7.4.1 Single-Pulse Strategy

Direct laser interference patterning was used to create post-like patterns on the surface of PET substrates. To fabricate the three-level hierarchical micropatterns, the following procedure was applied (see Fig. 7.7).

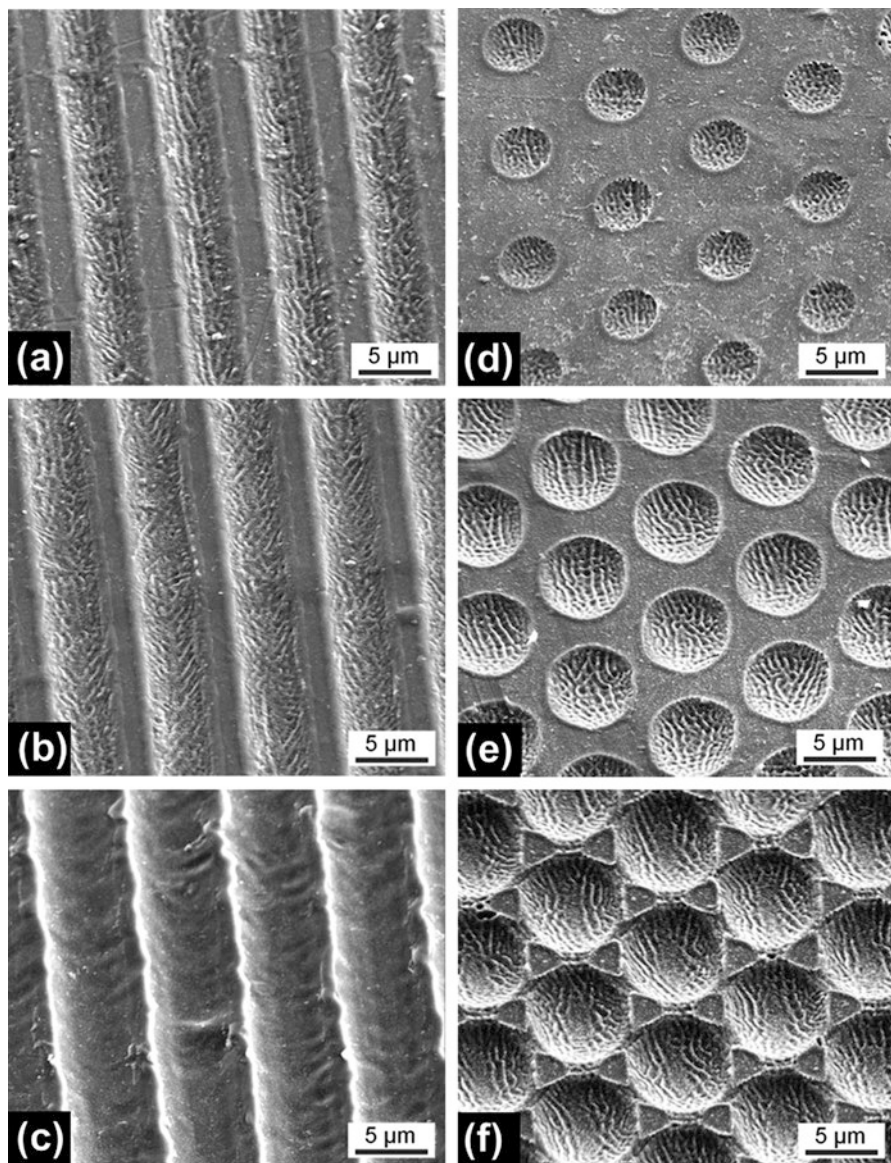


**Fig. 7.6** Evolution of the micropattern profiles in PI as a function of the laser fluence (wavelength: 355 nm) for two (a–c) and three-beam (d–f) setups. (a) Sinusoidal-trapezoidal profile (312 mJ/cm<sup>2</sup>); (b) sinusoidal profile (676 mJ/cm<sup>2</sup>); (c) U-shaped profile (1023 mJ/cm<sup>2</sup>); dot-like patterns produced with (d) 99 mJ/cm<sup>2</sup>; (e) 277 mJ/cm<sup>2</sup>; and (f) 854 mJ/cm<sup>2</sup>. (Reproduced with permission from Ref. [15])

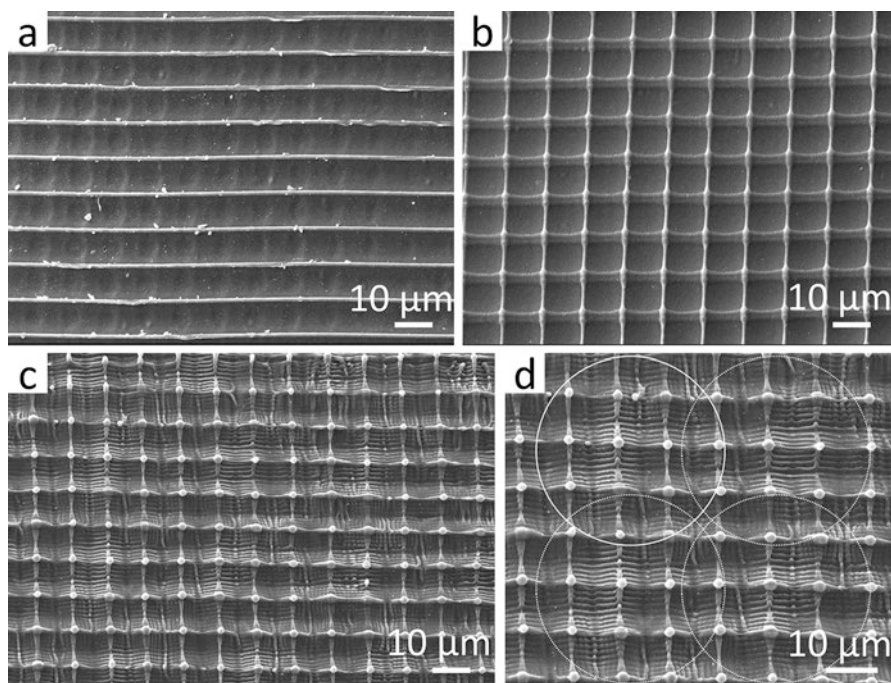


**Fig. 7.7** SEM images of structured PET. (a) Line-like pattern ( $\Lambda = 10 \mu\text{m}$ ) obtained using a two-beam interference setup with a single laser pulse. (b) The post-like pattern is produced after  $90^\circ$  rotation of the sample (second level), (c) post-like pattern ( $\Lambda = 1 \mu\text{m}$ ,  $90^\circ$  rotation) produced on the previous pre-patterned surface (third level). In (d) also the position of the holographic pixels containing the small periodic surface pattern can be observed. The pixels are approximately  $50 \mu\text{m}$  in diameter (white circles) and are separated by  $35 \mu\text{m}$  (first level). (Reproduced with permission from Ref. [21])

Firstly, the  $10 \mu\text{m}$  line-like patterns were produced (Fig. 7.7a) using a single irradiation process with a two-beam interference pattern. Secondly, the  $10 \mu\text{m}$  post-like pattern (Fig. 7.7b) is achieved by a second irradiation after rotating the PET substrate by an angle of  $90^\circ$ . The smaller periodic patterns ( $1\text{--}2 \mu\text{m}$ ) are consecutively processed at the same surface areas to obtain the multi-scale structures (Fig. 7.7c). In the last case, the laser beams are focused on the material surface, and an interference pattern within a pixel of approximately  $50 \mu\text{m}$  in diameter is obtained. Thereby, the small-scale structure is only fabricated within the holographic pixels, and the structure depth decreases close to the pixel edges due to the Gaussian distribution of the laser beam intensity. Therefore, an additional structure dimension, corresponding to the pixel diameter as well as the distance between two individual pixels ( $\sim 35 \mu\text{m}$ ), is achieved together with the small-scale features (Fig. 7.7d). In this way, a three-level hierarchy was obtained consisting of: (i) the  $10 \mu\text{m}$  post-like patterns (second level) and (ii) the  $1 \mu\text{m}$  post-like patterns (third level) and the ablated regions corresponding to the pixel used to produce the  $1 \mu\text{m}$  posts, with a distance of  $35 \mu\text{m}$  (first level).

The soft topology of the patterns can be explained by the nature of the interaction of the laser light with the PET substrate. In this case, the laser-photon energy is mainly transferred to the material by a photothermal process [22, 23]. Thereby, the material is softened or molten and evaporated at the positions of the intensity maxima due to high temperature. High pressure provoked by the ablation products occurs during the laser pulse. Thus, the softened (or molten) material is pushed toward the intensity minima where it resolidifies [24, 25]. This behavior is reflected by the sinusoidal-like morphology on patterned PET surfaces.

In order to determine the optical properties of the processed PET transparent polymers, an analysis of the diffraction characteristic of the treated materials was realized using a red laser at 633 nm wavelength. The results were compared with simulated diffraction patterns obtained from a numerical calculation. The patterned PET film can be considered as an optical phase shifting grating due to a different light transmission time resulting from the surface topography. Afterward, the electrical field of light in the diffraction pattern can be calculated by a Fourier transform (FT) from the phase-shifted electrical field after the grating [26, 27]. Since hierarchical structures are the superposition of multiple single-scale patterns with a certain depth ( $d$ ) and period ( $\Lambda$ ), they can be mathematically expressed using Eq. (7.4):

$$z(x,y) = z_0 - \sum_{n=1}^N z_n (d_n, \Lambda_n) \quad (7.4)$$

Since the surface topography influences the phase shift and not the amplitude, the surface shape  $z(x, y)$  is located in the exponent within the FT. Finally, the diffraction pattern of the hierarchical structure can be calculated using Eq. (7.5), which describes the Fourier transform (FT) of the hierarchical surface as convolution (\*) of the individual Fourier transforms of the ( $N$ ) single patterns, based on the convolution theorem [27].

$$FT \left( \prod_{n=1}^N e^{z(d_n, \Lambda_n)} \right) = FT \left( e^{z(d_1, \Lambda_1)} \right) * \dots * FT \left( e^{z(d_N, \Lambda_N)} \right) \quad (7.5)$$

Simulated and measured diffraction patterns from a surface pattern with the 10  $\mu\text{m}$  post-like structure covered with a 1  $\mu\text{m}$  post-like pattern are shown in Fig. 7.8. The calculated diffraction patterns do not include the additional geometry provided by holographic pixels ( $\sim 35 \mu\text{m}$ ).

As it can be observed, these patterns are very complex since they result from the convolution of all diffraction patterns obtained from each level of pattern hierarchy [21]. This means that the diffraction pattern produced by the 10  $\mu\text{m}$  structure is repeated at every order of the 1  $\mu\text{m}$  diffraction pattern.

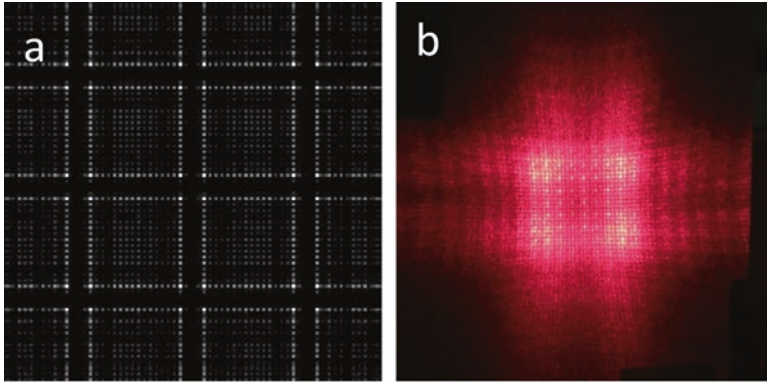


**Fig. 7.8** Simulated (a) and measured (b) diffraction pattern from hierarchical microstructures 1 on 10  $\mu\text{m}$ . (Reproduced with permission from Ref. [21])

### 7.4.2 Multiple-Pulse Strategy

A possible processing strategy in DLIP is to employ a pixel-wise structuring, that means making use of slightly focalized interfering beams and irradiating areas with an interference area with dimensions ranging from tens to a few hundreds of  $\mu\text{m}$  [28–30]. It has been also demonstrated that under specific conditions, polymers can be structured by DLIP obtaining unusual ablation profiles [28]. This is the case of transparent polycarbonate which, for low spatial periods and high laser fluence, shows a high amount of unselectively ablated material in the upper part of the treated DLIP pixel volume. If this phenomenon is controlled, it is also possible to obtain hierarchical structures as it will be shown [31].

Preliminary investigations aiming to explore the behavior of PC under high pulse overlap structuring has been carried out irradiating polycarbonate sheets with a UV (266 nm) laser, a spatial period of 2.0  $\mu\text{m}$ , and a pulse overlap varying from 90% to 99.57%. The results were analyzed monitoring how the nonstructured depth changes with the pulse overlap, with the aim to investigate the saturation depth of the method. The large-periodicity depth increases linearly with the number of laser pulses up to approximately 200 pulses, corresponding to 22  $\mu\text{m}$  in depth. On the other hand, the height of the upper interference-generated structures remains constant after 100 pulses, reaching the value of about 1.2  $\mu\text{m}$ , due to saturation effects associated with the plasma formation during the ablation process [31].

An example of the structures produced with this method is presented in Fig. 7.9a, where 194 pulses with a fluence of 1.63  $\text{J}/\text{cm}^2$  were employed. As it can be noticed, the upper part of the structures consists of DLIP line-like structures which, due to the high overlap, has a strong modulation of the depth, in the horizontal direction (perpendicular to the pattern). The shape of these structures resembles the multi-level structure of the rice leaf, in which the grooves act as a major role in the anisotropic spreading of the water droplet along the lines.

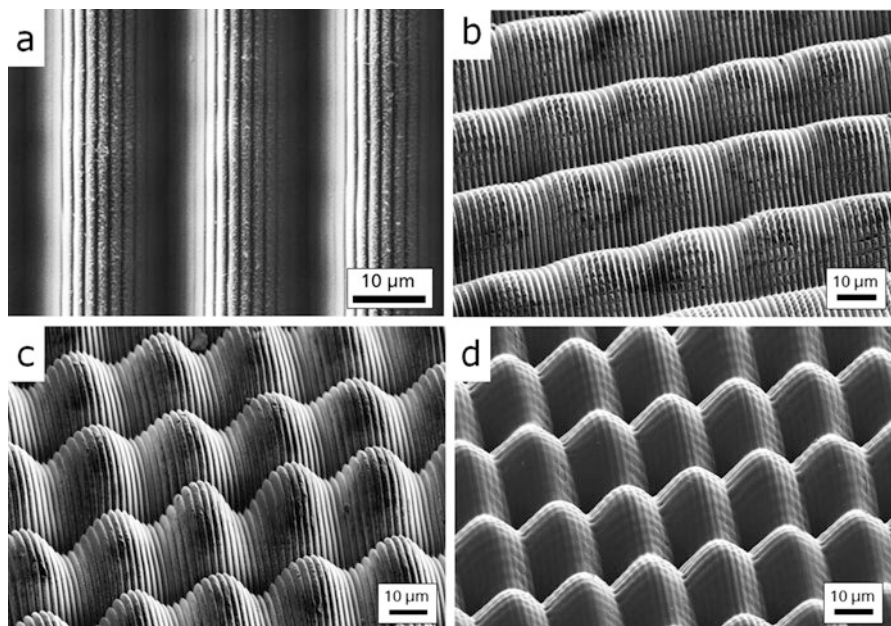


**Fig. 7.9** (a) Top-view SEM image of the hierarchical line-like on line-like structures parallel oriented, (b) line-like on line-like structures perpendicularly oriented, (c) line-like structures on pillars, and (d) pillar-like on pillar-like structures. (Reproduced with permission from Ref. [31])

If a second irradiation is performed after the first structuring, rotating by  $90^\circ$  the sample, pillar-like structures with rectangular symmetry can be obtained and its dual-scale geometry can be varied through the laser fluence of the second process. An example of the results for a double-irradiation DLIP is presented in Fig. 7.9b, c, where the first structuring process has been carried out with  $1.48 \text{ J/cm}^2$  and a structure period of  $2 \mu\text{m}$ , with an overlap variation corresponding to 90 pulses per pixel. The same parameters have been employed after a  $90^\circ$  rotation but using a fluence of  $0.51 \text{ mJ/cm}^2$  (Fig. 7.9b): the result is a hierarchical structure with lines on line-like structures perpendicularly orientated. In this case, second irradiation has erased the first DLIP lines, but the large-period lines have not been strongly affected. Figure 7.9c shows instead hierarchical structures consisting of lines on pillar-like structures, obtained with a second irradiation fluence of  $1.63 \text{ mJ/cm}^2$ . In this case, the second irradiation has not only erased the first DLIP structures, but also ablated the large-periodicity structures, leaving pillars in the lower hierarchy level.

Although the fabrication of hierarchical structures was possible, it is worth mentioning that through the double-irradiation method, it is not possible to create well-balanced structures (DLIP pillars on large pillars) within two irradiation steps. Another strategy to fabricate balanced hierarchical structures consists of performing the structuring process with a pulse-based method. This consists in moving the sample using the translational stages to a certain position and then irradiating it with a

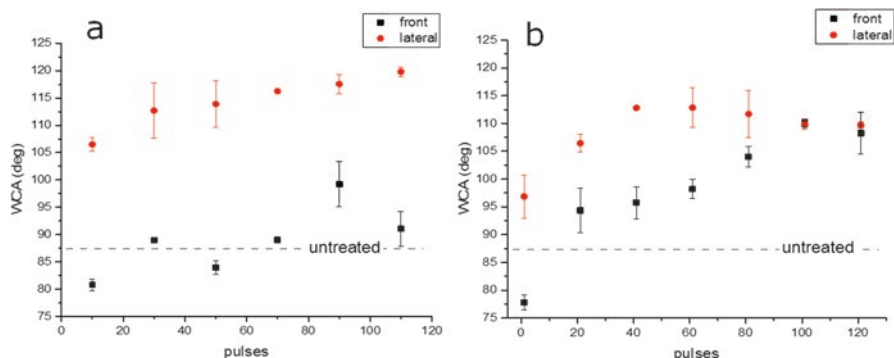


**Fig. 7.10** Water contact angle response measured in orthogonal directions for the different pulse overlap conditions, for anisotropic line-like on pillars structures (a) and isotropic pillars on pillars structures (b). (Reproduced with permission from Ref. [31])

certain number of laser pulses. After that, the sample is moved in x and y to a new position and this procedure is repeated until the surface is totally treated. Since the structuring of polycarbonate presents a Gaussian unselective ablation for every pulse, for a high number of pulses, this method can produce an alternation of valleys and heights in both directions and hierarchical structures can be fabricated in a single-step process. Choosing correctly the pixel distance and the number of pulses, hierarchical structures consisting of line-like structures on the top of pillars can be fabricated in a single-step process, similar to the ones presented in Fig. 7.9c. Consequently, a second structuring process can be performed by irradiating orthogonally to the first DLIP lines with a low-overlap scan-based process, which can selectively ablate only this pattern, creating balanced pillars on the top of large pillars (Fig. 7.9d).

The change in the topography, structure geometry, and orientation resulted in having an effect on the wettability response of the treated polycarbonate samples. For this purpose, the water contact angle (WCA) has been measured in orthogonal directions, corresponding to the direction parallel (front) and perpendicular (lateral) to the DLIP lines of the structures. The results, correlated with the pulse overlap of the structures, are presented in Fig. 7.10, reporting the results for the structures presented in Fig. 7.9c, d.

As it can be seen, in the case of anisotropic structures (Fig. 7.10a), the WCA in both directions increases with the number of pulses, since the structure depth increases as well. However, a strong difference ( $\sim 20^\circ$ ) can be appreciated between the WCA values measured in the front and lateral direction: this can be ascribed to the strong anisotropy of the structures realized with this method. On the other hand, when the structures are sufficiently balanced in both directions, the hydrophobicity increases with the structure depth and the WCA values are comparable in both directions (Fig. 7.10b).

As a result of the different high-rate irradiation processes, the structuring has made possible to change the polycarbonate wettability, increasing the static contact

angle from  $87.8^\circ \pm 0.4^\circ$  to  $117.6^\circ \pm 1.8^\circ$ , without a significant changing of the surface chemistry [31]. Moreover, due to the different structure geometries obtained, different wetting regimes and preferential wetting directions were possible.

## 7.5 High-Throughput Processing of Polycarbonate

High-throughput interference patterning has been achieved recently, by developing new DLIP optical heads and strategies [29]. This can be performed, for instance, using a q-switched high power Nd:YAG laser (up to 180 W) emitting 1064 nm wavelength and pulses of 8 ns duration (EdgeWave). In this case, the typical intensity distribution of the output beam is top-hat in one direction and Gaussian in the perpendicular one. The initial beam geometry is rectangular with an edge length of  $\sim 5.0$  mm. Using a telescope (Fig. 7.11), the beam diameter can be controlled which is necessary to combine the laser with the DLIP optics. Then, the shaped laser beam is split into two beams by the DLIP optical head (developed at Fraunhofer IWS, Dresden) which are overlapped and focused with a cylindrical lens on the workpiece.

Using this configuration, polycarbonate (PC) foils doped with a black IR absorber were treated. Three different speeds were used for the translational stage:  $v = 0.25$ , 0.50 and 1.00 m/s. The pulse frequency was set to 5 kHz, resulting in a pulse energy of 31 mJ at 155 W power. The angle between the laser beams was set to  $2.73^\circ$  obtaining a spatial period of  $\Lambda = 22.2 \mu\text{m}$ . Due to the strategy utilized to shape the

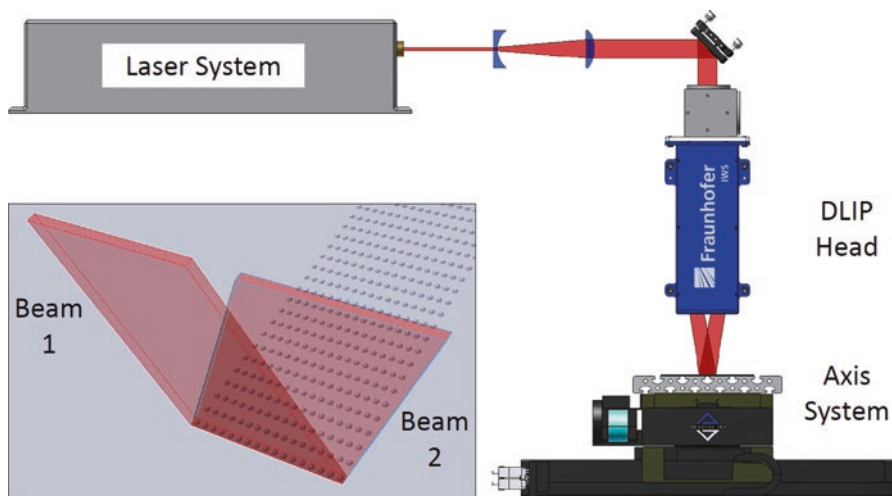


**Fig. 7.11** Schematic drawing of the two-beam laser interference setup for high-speed laser patterning. (Reproduced with permission from Ref. [29])

beams, a long-stretched spot ( $\sim 15$  mm by  $\sim 20$   $\mu\text{m}$ ) containing the interference pattern was obtained.

The sample movement was set to be perpendicular to the line-shaped beams. Thus, the pattern periodicity is on the one hand determined by the DLIP spatial period and on the other direction by the distance between to laser pulses ( $\Delta M$ ) which is defined by the axis speed and the pulse frequency.

Exemplary confocal microscopic images of the treated polycarbonate material are shown in Fig. 7.12a–c. According to the used axis speeds (1.00 m/s, 0.50 m/s, and 0.25 m/s), spatial spacing ( $\Delta M$ ) between the laser spots of 200  $\mu\text{m}$ , 100  $\mu\text{m}$ , and 50  $\mu\text{m}$  was obtained. For the used polycarbonate foils doped with a black IR absorber, it was found that local swelling of the irradiated material took place at the interference maxima positions. For the used laser conditions (laser fluence: 1.2 J/cm<sup>2</sup>), the structure height was approximately 4  $\mu\text{m}$ .

Finally, the fabrication throughput was calculated for different used conditions. Fig. 7.13 shows the attained processing speeds of the realized DLIP attempt at laser repetition rates of 5 kHz and 10 kHz. For a repetition rate of 5 kHz and a line spot length of 15 mm, structuring speeds of 0.25, 0.45, and 0.90 m<sup>2</sup>/min were obtained for axis speeds of 0.25, 0.50, and 1.00 m/s, respectively. For 10 kHz repetition frequency with a line spot of 12 mm, fabrication speeds of 0.18, 0.36, and 0.72 m<sup>2</sup>/min were achieved for the same axis speeds.

The reason for the maximum processing speed of 0.90 m<sup>2</sup>/min being achieved at 5 kHz and not at 10 kHz (0.72 m<sup>2</sup>/min) is due to the higher available pulse energy at 5 kHz, thus enabling a larger line-like spot and accordingly a larger treated area per unit of time.

The process parameters (repetition rate and axis speed) do not only have an influence on the structuring speed but also on the density of features per unit of area (see Fig. 7.13). Increasing the speed of the axis and keeping the laser power constant results in a larger distance between the laser-treated line-like areas. If higher repetition rates are used, a higher number of features per unit of area can be produced. For example,  $1.8 \times 10^9$  features per m<sup>2</sup> can be produced at 10 kHz repetition rate (at 0.18 m<sup>2</sup>/min) compared to  $0.91 \times 10^9$  features per m<sup>2</sup> at 5 kHz (at 0.23 m<sup>2</sup>/min). The abovementioned feature densities were calculated for a spatial period of 22 mm. At 5 kHz, for a surface processing speed of 0.90 m<sup>2</sup>/min, the number of produced features per m<sup>2</sup> reduces to  $0.23 \times 10^9$  (Fig. 7.13).

Figure 7.13 also compares typical processing speeds and the feature density of patterns produced with conventional DLW. While conventional laser processing generates only one feature for every single pulse, DLIP allows the simultaneous fabrication of several thousands of features utilizing one single laser pulse. In this study, 682 features were produced with a single laser pulse using DLIP (line length: 15 mm, spatial period: 22  $\mu\text{m}$ ). Typical processing speeds for DLW are shown in Fig. 7.13 for a 300 kHz laser system. To obtain a feature density per m<sup>2</sup> of  $0.9 \times 10^9$ , a maximum processing speed of only 0.04 m<sup>2</sup>/min can be achieved using DLW. These speeds are about 10 and 6.25 times slower, compared to high-speed DLIP at 10 and 5 kHz, respectively.

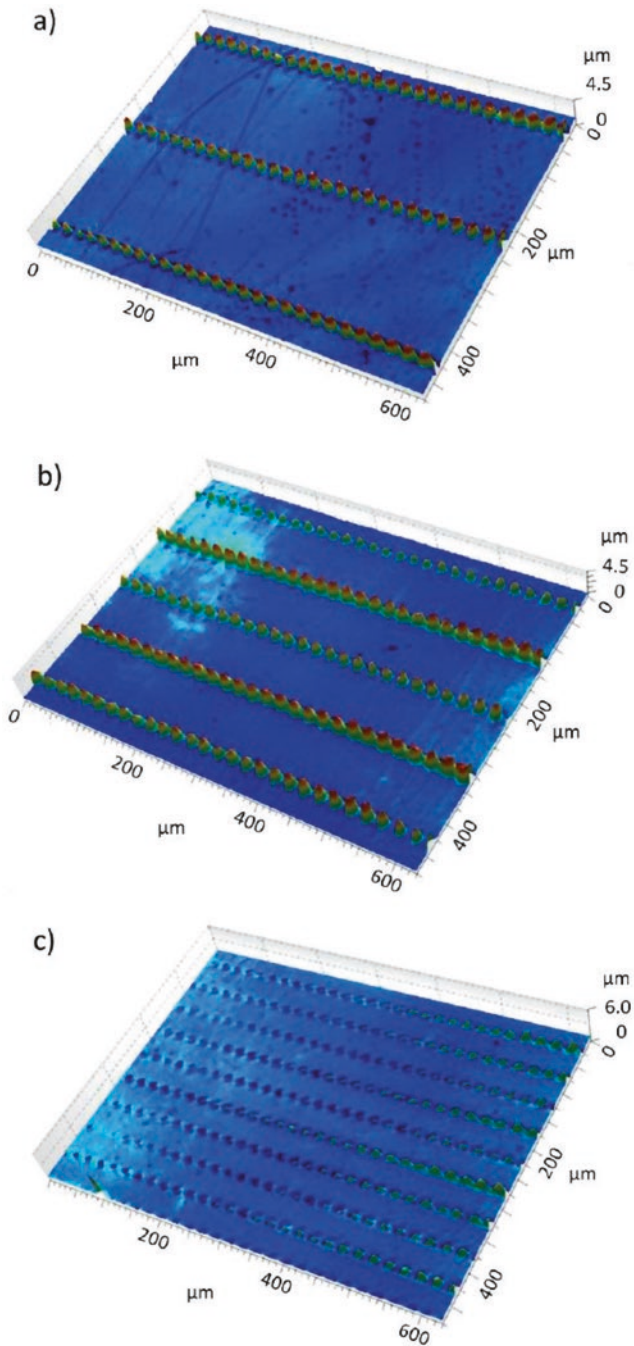


**Fig. 7.12** DLIP patterned PC with various axis speed  $v$ : (a)  $v = 1.00$  m/s, (b)  $v = 0.50$  m/s, and (c)  $v = 0.25$  m/s. The pulse frequency was 5 kHz and the laser fluence was  $1.2$  J/cm $^2$ . (Reproduced with permission from Ref. [29])

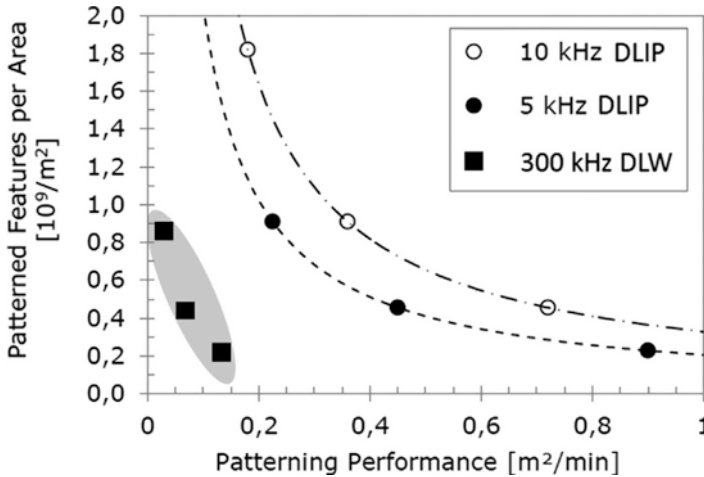


**Fig. 7.13** Comparison of patterning performance attained with DLIP to conventional direct laser writing (DLW). (Reproduced with permission from Ref. [29])

## 7.6 In-Volume Interference Patterning

In-volume structures were fabricated inside a PMMA/PC foil, consisting of a UV laser light (263 nm) transmitting PMMA layer on a UV absorbing PC layer. Two-beam laser interference was used to obtain a line-like intensity distribution at the interface of both layers, by irradiating the substrate from the PMMA side. Using this process, a well-defined characteristic rainbow color (or holographic color) was observed after the treatment. Thus, a periodic pattern is indicated. A cross-section polisher was used to prepare a PMMA/PC film for investigations inside the material (Fig. 7.14).

The cut was performed perpendicularly to the used line-like interference distribution. It is possible to observe a periodic arrangement of microstructures which are visible as round-shaped small cavities at the interior of the treated foil. The shape of the produced cavities can be observed with a higher detail in the inset. This image also permits to recognize a separation distance of approximately 1.0  $\mu\text{m}$ , the distance that is in good agreement with the spatial period of the interference pattern. The width of the cavities is around 500 nm, while their height is approximately 350 nm. From an additional EDX line scan of this cross-section, it is known that the cavities are at the interface of both layers but slightly located at the side of the absorbing PC layer [32].

The temperature distribution at the cross-section was calculated using a FEM Model at 3.5 ns and 80 ns after the pulse time ( $t_p$ ). The results are shown in Fig. 7.15a, b for the abovementioned pulse durations, respectively.

From Fig. 7.15, two important characteristics can be observed. Firstly, the positions corresponding to the highest temperatures are below the PMMA/PC interface (denoted by the continuous black line). Secondly, the temperature distribution in the cross-section plane is round-shaped at the maxima, similar to the cavity shape (see

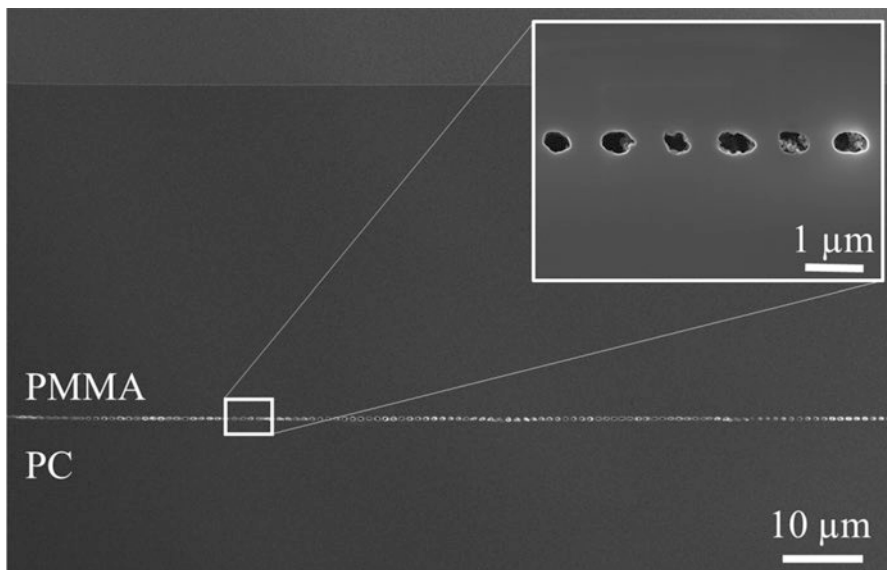


**Fig. 7.14** Argon ion-polished cross-section of a treated multilayer PMMA/PC film (SEM image). The pattern is visible as round-shaped cavities. The used spatial period was  $1.0\ \mu\text{m}$ , and the structures were produced with a single laser pulse at  $600\ \text{mJ}/\text{cm}^2$ . (Reproduced with permission from Ref. [32])

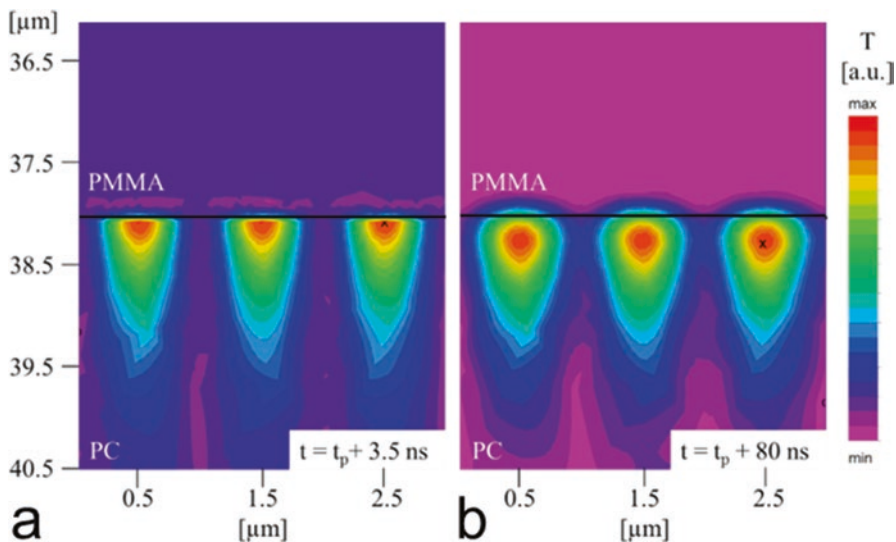


**Fig. 7.15** Temperature distribution at the PMMA/PC interface simulated with FEM at a time (a)  $3.5\ \text{ns}$  and (b)  $80\ \text{ns}$  after the temporal pulse intensity peak ( $t_p$ ). (Reproduced with permission from Ref. [32])

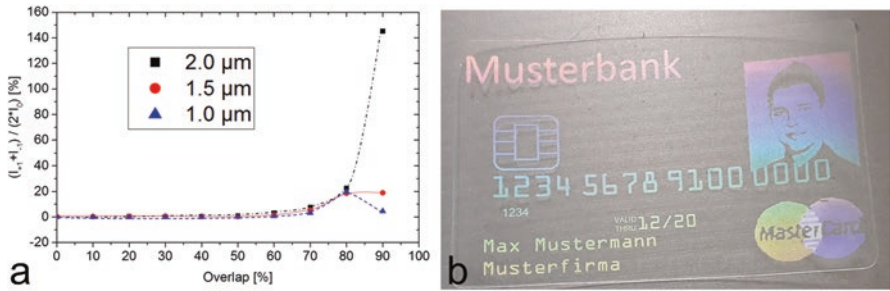


**Fig. 7.16** (a) Normalized diffraction efficiency as a function of overlap (0–90%) and period, (b) decorative example of a patterned credit card. (Reproduced with permission from Ref. [32])

Fig. 7.14). This behavior results from the heat transfer mechanism, where the heat is transferred almost symmetrically in all directions resulting in a round-shaped temperature distribution. The position of the zones with the highest temperatures varied as a function of time and moves from 50 nm below the interface after 3.5 ns to  $\sim 300$  nm below the interface after 80 ns. Clearly, this effect can be only explained by the flow of heat toward the PMMA layer, which has a very similar heat conductivity compared to PC.

Afterward, the diffraction efficiency of the PMMA/PC foils was optimized for decorative applications. Figure 7.16 shows the results of the optical characterization.

The quality of the produced periodic surface patterns was quantitatively characterized by measuring the average intensity of the first diffraction orders  $(I_{+1} + I_{-1})/2$  normalized to the zero-order intensity  $I_0$ . Thus, patterns with high diffraction efficiency show a more intense rainbow color and thus better performance for decorative applications (Fig. 7.16a). As it can be seen, the normalized diffraction efficiency for all three evaluated periods remains close to zero until an overlap of 50%. An additional increase of the pulse-to-pulse overlap up to 80% also permits to improve the diffraction efficiency for all spatial periods. Clearly, an increase of the overlap produces better-defined structures and thus the normalized diffraction efficiency is improved. Further increasing the overlap up to 90% leads to an ambivalent behavior. While the normalized diffraction efficiency of the 2.0  $\mu\text{m}$  structure increase further to 145.2%, the 1.5  $\mu\text{m}$  structure stays on almost the same level at 18.8%, and the 1.0  $\mu\text{m}$  structure shows a reduction of the efficiency to 4.5%. This behavior results from delamination of both layers caused by the high energy input at the high overlap [32]. This is coupled with a high amount of molten and vaporized material that is produced at the interface zone. Differently, the 2.0  $\mu\text{m}$  periodic structure was not damaged since the distance between the interference maxima is larger allowing the material at the minima positions to be less affected by the laser treatment and thus reducing the detachment between both layers.

Finally, Fig. 7.16b demonstrates an application example of the in-volume DLIP concept simulating a transparent credit card, including all usual information as well as an additional image of the cardholder for individualization. The individual spots

have a diameter of  $32\ \mu\text{m}$ , which corresponds to a resolution  $\sim 800\ \text{dpi}$ . As an advantage over surface structures, the interface pattern is protected against scratches, fingerprints, and wear. Thus, the lifetime can be prolonged.

## 7.7 Modeling of DLIP Process in Polymers

Several advances in polymer structuring through DLIP have been made, showing several possibilities to obtain different structures and properties. Although the geometry and characteristic pitch of an interference pattern can be perfectly controlled by the beams' delivery system, identical experimental conditions applied to different polymers can result in totally different topologies [33, 34].

Due to previous investigations of polymer materials treated through DLIP showing unusual structuring behavior, pigmented and transparent polycarbonate (PC) substrates were chosen to conduct an experiment with the aim to systematically analyze the structuring behavior [29].

UV laser interference irradiation on transparent polycarbonate with spatial periods  $\Lambda$  ranging from  $0.57$  to  $2.13\ \mu\text{m}$  and laser fluences up to  $0.64\ \text{J}/\text{cm}^2$  revealed that well-defined line-like patterns, which perfectly match the periodic intensity distribution, are obtained only for a small range of laser fluences and large spatial periods (Fig. 7.17a) [28]. For high laser fluences and small spatial periods, the upper part of the structured features appears erased, leading to a partially structured volume (Fig. 7.17b).

A possible explanation of this structuring mechanism can be related to the plasma formation and expansion during the ablation process. Since the plasma is ignited in the interference maxima positions, the untreated material in the interference minima could be affected by the plasma expansion and unselectively ablated, especially for

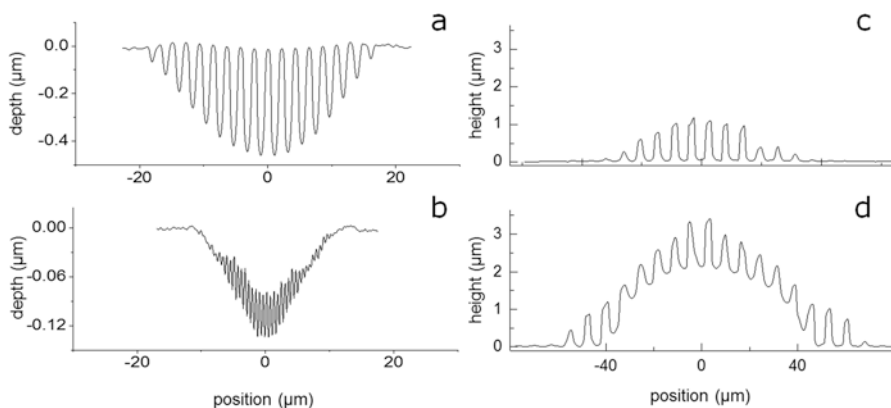


**Fig. 7.17** Confocal microscope profiles showing periodic line-like structures produced on the transparent PC treated with 3 ns single pulses at 263 nm laser wavelength; in (a) the influence of the laser fluence on the pattern morphology is shown, while in (b) the spatial period is varied at constant laser fluence. (Reproduced with permission from Ref. [28])

high expansion pressures. Moreover, since the expansion pressure depends on the ablation rate and is independent on the interference period, the unselective ablation becomes highly effective for small interference periods and high laser fluences [28].

Adding a dopant to the polymer matrix to change its optical properties can result in a completely different structuring process. PC substrates doped with a black dye were used to quantitatively investigate the swelling process under interference patterns for IR radiation at 1053 nm [28]. In this case, the laser fluence was varied between 0.55 J/cm<sup>2</sup> and 1.29 J/cm<sup>2</sup> and the structure period from 2.31 μm to 7.13 μm, revealing swelled structures instead of ablated pixels. Similarly, to the ablation case, it was found that only for low laser fluences and especially for large spatial periods the polymer was only swelled at the interference maxima positions (see for example Fig. 7.17c, d obtained for a fluence of 0.86 J/cm<sup>2</sup> and 1.29 J/cm<sup>2</sup>, respectively). Focused-ion-beam cuts performed onto the treated black-doped polycarbonate revealed the presence of pores in the swelled regions, corresponding to the position of the interference maxima [28]. The reason for the swelling process has been then attributed to the absorption of IR photons by the black dye, which dissociates into gaseous by-products producing pores and thus increasing the local volume [35].

After determining the different structuring mechanisms on polymer materials using DLIP, a model for predicting the three-dimensional geometry as a function of the laser wavelength, spatial period, and laser fluence was developed. Based on the assumption that only photochemical processes take place during the DLIP irradiation, the Lambert-Beer law has been modified in order to include the following structuring processes: (i) interference periodic ablation; (ii) Gaussian nonperiodic ablation; (iii) interference periodic swelling; and (iv) Gaussian nonperiodic swelling.

The model takes into account the four mechanisms associating to each of them a structure depth (with positive values for the ablation case and negative values for the swelling process):

$$d(x) = d_i(x) + d_G(x) + d_s(x) + d_{GS}(x) \quad (7.6)$$

where  $d_i$  is the depth of the periodic modulation corresponding to the interference ablation,  $d_G$  is the depth of the upper nonperiodic ablated region (Gaussian-like),  $d_s$  is the height of the swelled features due to the interference pattern, and  $d_{GS}$  is the height of the lower nonperiodic swelled region (Gaussian-like). Moreover, to be consistent with the Lambert-Beer law, each term must be expressed in the logarithmic form:

$$\begin{aligned} d(x) = & k_i(\Lambda) \cdot \ln\left(\frac{F(x,\theta)}{F_{th}}\right) + k_G(\Lambda) \cdot \ln\left(\frac{F(x,0)}{F_{th}}\right) \\ & + k_s(\Lambda) \cdot \ln\left(\frac{F(x,\theta)}{F_{th}^S}\right) + k_{GS}(\Lambda) \cdot \ln\left(\frac{F(x,0)}{F_{th}^S}\right) \end{aligned} \quad (7.7)$$

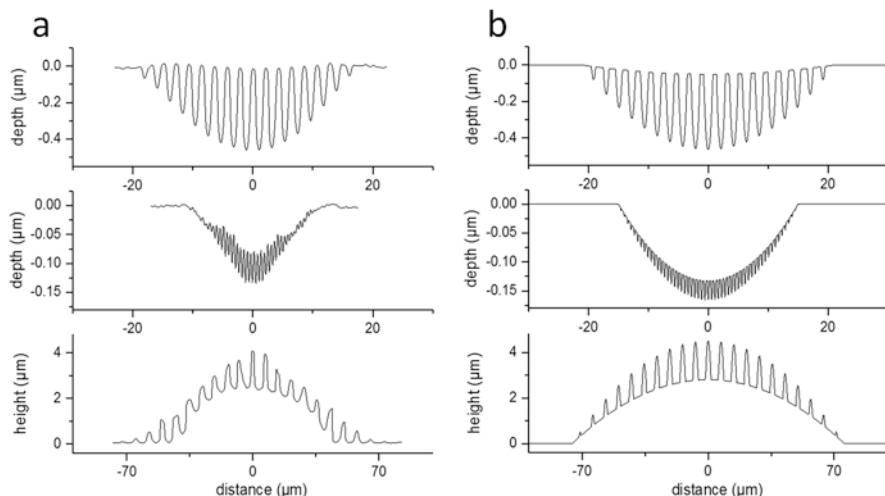


**Fig. 7.18** Comparison between (a) experimental and (b) calculated profiles for different structuring conditions: complete periodic-modulated ablation (Lexan SLX,  $\lambda = 263$  nm,  $\Lambda = 2.13$   $\mu\text{m}$ ,  $E_p = 2$   $\mu\text{J}$ ), predominant Gaussian-modulated ablation mechanism (Lexan SLX,  $\lambda = 263$  nm,  $\Lambda = 0.56$   $\mu\text{m}$ ,  $E_p = 0.37$   $\mu\text{J}$ ), and combined periodic and Gaussian-modulated swelling (Lexan FR25A,  $\lambda = 1053$  nm,  $\Lambda = 7.31$   $\mu\text{m}$ ,  $E_p = 0.24$  mJ). (Reproduced with permission from Ref. [28])

where  $F$  is the Gaussian-modulated fluence of the interference distribution,  $F_{th}$  is the ablation threshold,  $F_{th}^S$  is the swelling threshold, and  $k$  [ $\mu\text{m}$ ] are the rate coefficients for each of the four structuring mechanism, calculated as a function of the spatial period  $\Lambda$  [ $\mu\text{m}$ ]. The ablation coefficients  $k_I$  and  $k_G$  are related to the interference structuring ablation and the nonperiodic Gaussian-like ablation, respectively, while the swelling coefficients  $k_S$  and  $k_{GS}$  refers to the upper periodic swelled modulation and the nonperiodic Gaussian-like lower swelled region. These coefficients represent the speed rate of the process and can be calculated from a fitting procedure based on structuring experiments as a function of the spatial period.

The structuring coefficients  $k$  can be retrieved by fitting the ablation curves of the polymers with different structuring conditions (period and wavelength). Thus, applying Eq. 7.7 the surface topography of the irradiated material can be calculated and compared with the experimental observations. This comparison is reported in the following, showing three different structuring behaviors (Fig. 7.18a) and their calculated profiles (Fig. 7.18b). Furthermore, this model can be applied to describe the DLIP structuring process of any polymer substrate and to design more complex structures, even employing the combination of ablated and swelled structures.

**Acknowledgments** The work of S.A. was supported by the Laser4Fun project ([www.laser4fun.eu](http://www.laser4fun.eu)), funded from the European Union's Horizon 2020 research and innovation programme under the Marie Skłodowska-Curie grant agreement No. 675063. The work of A. L. is also supported by the German Research Foundation (DFG) under Excellence Initiative program by the German federal and state governments to promote top-level research at German universities.

## References

1. E. Favret, N. Fuentes, *Functional Properties of Bio-Inspired Surfaces: Characterization and Technological Applications* (World Scientific Publishing Co. Pte. Ltd, Singapore, 2009)
2. A.F. Lasagni, T. Kunze, M. Bieda, D. Günther, A. Gärtner, et al., Large area micro-/nano-structuring using direct laser interference patterning. *Proc. SPIE* **9735**, 973515 (2016)
3. A. Lasagni, B.S. F; Menéndez-Ormaza, Two- and three-dimensional micro- and sub-micrometer periodic structures using two-beam laser interference lithography. *Adv. Eng. Mater.* **12**, 54–60 (2010)
4. J.H. Seo, J.H. Park, Z. Ma, J. Choi, B.-K. Ju, Nanopatterning by laser interference lithography: Applications to optical devices. *J. Nanosci. Nanotechnol.* **14**, 1521–1532 (2014)
5. A. Lasagni, F. Mücklich, Structuring of metallic bi- and tri-nano-layer films by laser interference irradiation: Control of the structure depth. *Appl. Surf. Sci.* **247**, 32–37 (2005)
6. A.F. Lasagni, F. Mücklich, Study of the multilayer metallic films topography modified by laser interference irradiation. *Appl. Surf. Sci.* **240**, 214–221 (2005)
7. F. Yu, F. Muecklich, P. Li, H. Shen, S. Mathur, C. Lehr, U. Bakowsky, In vitro cell response to a polymer surface micropatterned by laser interference lithography. *Biomacromolecules* **6**, 1160–1167 (2005)
8. A. Rosenkranz, L. Reinert, C. Gachot, F. Mücklich, Alignment and wear debris effects between laser-patterned steel surfaces under dry sliding conditions. *Wear* **318**, 49–61 (2014)
9. A. Aktag, S. Michalski, L. Yue, R.D. Kirby, S.H. Liou, Formation of an anisotropy lattice in Co/Pt multilayers by direct laser interference patterning. *J. Appl. Phys.* **99**, 093901 (2006)
10. L. Guo, H.-B. Jiang, R.-Q. Shao, Y.-L. Zhang, S.-Y. Xie, J.-N. Wang, X.-B. Li, F. Jiang, Q.-D. Chen, T. Zhang, H.-B. Sun, Two-beam-laser interference mediated reduction, patterning and nanostructuring of graphene oxide for the production of a flexible humidity sensing device. *Carbon* **50**, 1667–1673 (2012)
11. M. Bieda, C. Schmädicke, T. Roch, A.F. Lasagni, Ultra-low friction on 100Cr6-steel surfaces after direct laser interference patterning. *Adv. Eng. Mater.* **17**, 102–108 (2015)
12. A.F. Lasagni, C. Gachot, K.E. Trinh, M. Hans, A. Rosenkranz, et al., Direct laser interference patterning, 20 years of development: From the basics to industrial applications, in *Proceedings of SPIE* 2017, 10092, 1009211-1-11
13. H. Misawa, S. Juodkakis, *3D Laser Microfabrication. Principles and Applications* (WILEY-VCH Verlag GmbH & Co. KGaA, Weinheim, 2006)
14. E. Hecht, *Optics* (Addison-Wesley, San Francisco, 2002)
15. A.F. Lasagni, D.F. Acevedo, C.A. Barbero, F. Mücklich, One-step production of organized surface architectures on polymeric materials by direct laser interference patterning. *Adv. Eng. Mater.* **9**(1–2), 99–103 (2007)
16. D. Bäuerle, *Laser Processing and Chemistry*, 2nd edn. (Springer, Berlin, 1996)
17. T. Lippert, J.T. Dickinson, S.C. Langford, H. Furutani, H. Fukumura, H. Masuhara, T. Kunz, A. Wokaun, Photopolymers designed for laser ablation–photochemical ablation mechanism. *Appl. Surf. Sci.* **117**, 127–129 (1998)
18. R.C. Progelhof, J. Franey, T.W. Haas, Absorption coefficient of unpigmented poly (methyl methacrylate), polystyrene, polycarbonate, and poly (4-methylpentene-1) sheets. *J. Appl. Polym. Sci.* **15**, 1803 (1971)
19. S.B. Babu, G.C. D’Cuoto, F.D. Egitto, Excimer laser induced ablation of polyetheretherketone, polyimide, and polytetrafluoroethylene. *J. Appl. Phys.* **72**, 692 (1992)
20. Y. Feng, J. Gottmann, E.W. Kreutz, Structuring of poly ether ether ketone by ArF excimer laser radiation in different atmospheres. *Appl. Surf. Sci.* **211**, 68 (2003)
21. F. Rößler, D. Günther, A.F. Lasagni, Fabrication of hierarchical micro patterns on PET substrates using direct laser interference patterning. *Adv. Eng. Mater.* **18**(10), 1755–1762 (2016)
22. H. Watanabe, M. Yamamoto, Laser ablation of poly (ethylene terephthalate). *J. Appl. Polym. Sci.* **64**(6), 1203–1209 (1997)

23. R. Srinivasan, B. Braren, Ultraviolet laser ablation of organic polymers. *Chem. Rev.* **89**(6), 1303–1316 (1989)
24. T. Bahners, E. Schollmeyer, Morphological changes of the surface structure of polymers due to excimer laser radiation: A synergetic effect. *J. Appl. Phys.* **66**(4), 1884–1886 (1989)
25. A.F. Lasagni, D. Langheinrich, S. Eckhardt, Direct fabrication of periodic patterns on polymers using laser interference. *Plastic Research Online*, 1–2 (2012)
26. G. Fowles, *Introduction to Modern Optics*, 2nd edn. (Holt, Rinehart and Winston, New York, 1975)
27. J.W. Goodman, *Introduction to Fourier Optics* (Roberts & Co., Englewood, 2005)
28. S. Alamri, A.F. Lasagni, Development of a general model for direct laser interference patterning of polymers. *Opt. Express* **25**(9), 9603–9616 (2017)
29. V. Lang, T. Roch, A.F. Lasagni, High-speed surface structuring of polycarbonate using direct laser interference patterning: Toward  $1 \text{ m}^2 \text{ min}^{-1}$  fabrication speed barrier. *Adv. Eng. Mater.* **18**, 1342–1348 (2016)
30. T. Kunze, C. Zwahr, B. Krupop, S. Alamri, F. Rößler, A.F. Lasagni, Development of a scanner-based direct laser interference patterning optical head: New surface structuring opportunities. *Proc. SPIE* **10092**, 1009214 (2017)
31. S. Alamri, A.I. Aguilar-Morales, A.F. Lasagni, Controlling the wettability of polycarbonate substrates by producing hierarchical structures using direct laser interference patterning. *Eur. Polym. J.* **99**, 27–37 (2018)
32. F. Rößler, K. Günther, A.F. Lasagni, In-volume structuring of a bilayered polymer foil using direct laser interference patterning. *Appl. Surf. Sci.* **440**, 1166–1171 (2018)
33. A.F. Lasagni, D.F. Acevedo, C.A. Barbero, F. Mücklich, Direct patterning of polystyrene–polymethyl methacrylate copolymer by means of laser interference lithography using UV laser irradiation. *Polym. Eng. Sci.* **48**, 2367–2372 (2008)
34. M.F. Broglia, D.F. Acevedo, D. Langheinrich, H.R. Perez-Hernandez, C.A. Barbero, A.F. Lasagni, Rapid fabrication of periodic patterns on Poly (styrene-co-acrylonitrile) surfaces using direct laser interference patterning. *Int. J. Polym. Sci.* **2015**, 721035 (2015)
35. F. Beinhorn, J. Ihlemann, K. Luther, J. Troe, Micro-lens arrays generated by UV laser irradiation of doped PMMA. *Appl. Phys. A Mater. Sci. Process.* **68**, 709–713 (1999)

**Part III**  
**Materials Employed in Wrinkles**  
**Formation**

# Chapter 8

## Micro- and Nano-patterned Hydrogels Fabricated by Taking Advantage of Surface Instabilities



C. M. González-Henríquez, M. A. Sarabia Vallejos,  
and Juan Rodríguez-Hernández

### 8.1 Background

Hydrogels are a particular kind of polymers formed by highly interconnected three-dimensional arrangement. This network is created by repetitive crosslinked units of different polymeric chains with variable chemistry and properties. Hydrogels have the capacity to absorb and retain large amounts of solvents, which allow them to increase their volume several times when are exposed to aqueous environments. This characteristic confers it a soft consistency, comparable to those observed in living tissues [1], making them good candidates to be considered for biomedical applications due to their high water absorbance and retention properties and enhancing their biocompatibility [2]. There are several applications for this kind of materials, particularly for treatment or replacement of tissues, or even whole organs, healing of chronic and traumatic wounds, surface coatings for implants, drug delivery, and, also, cell encapsulation and tissue engineering applications [3–7].

---

C. M. González-Henríquez

Departamento de Química, Facultad de Ciencias Naturales, Matemáticas y del Medio Ambiente, Universidad Tecnológica Metropolitana, Santiago, Chile

Programa Institucional de Fomento a la Investigación, Desarrollo e Innovación, Universidad Tecnológica Metropolitana, Santiago, Chile

M. A. Sarabia Vallejos (✉)

Departamento de Ingeniería Estructural y Geotecnia, Pontificia Universidad Católica de Chile, Escuela de Ingeniería, Santiago, Chile

Instituto de Ingeniería Biológica y Médica, Santiago, Chile

e-mail: [masarabi@uc.cl](mailto:masarabi@uc.cl)

J. Rodríguez-Hernández

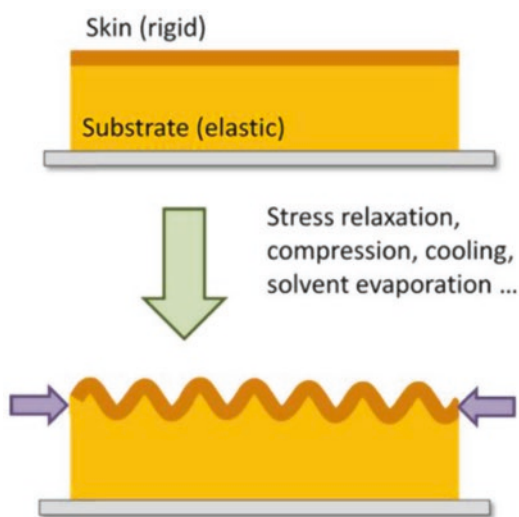
Departamento de Química Macromolecular Aplicada, Polymer Functionalization Group. Instituto de Ciencia y Tecnología de Polímeros-Consejo Superior de Investigaciones Científicas (ICTP-CSIC), Madrid, Spain

Most recent approaches are attempting to finely tune both hydrogel's biological and physical attributes, thus inducing specific interactions or responses when these are found in presence of cellular systems [6]. Other studies are particularly interested in mimicking some biological environments, for example, the group of Zhao et al. [8] fabricated artificial mucosa scaffolds using hydrogels as a base material. In order to replicate the structures which present mucosa in their surface (folded patterns), like respiratory, gastrointestinal, or urogenital tracts, they relax pre-stretched hydrogel substrates. This process generates compressive strains on the film, which undergoes mechanical surface instabilities (SIs), evolving into controlled morphological micro-patterns [9].

There exist several ways to produce micro-patterns on soft materials; in fact, buckling is a very common process in nature, for example, wrinkles appear when the skin is deformed by any form of mechanical force, like muscle contraction. This happens because the skin is a multilayer system (epidermis, dermis, and hypodermis) with different mechanical properties, which, under the external stimulus, generates a strain mismatch in the material interface, thus producing micro-patterned surfaces in the material due to the competition between destabilizing and stabilizing forces (metastable system) [9]. Particularly, most of the processes used to generate wrinkled patterns on hydrogels are based on bilayered systems; Fig. 8.1 shows a simple schematic description of this process.

Although the wrinkle formation is a very common process and it is possible to observe it repetitively on a large number of natural surfaces, the physical and chemical basis that sustains this effect is still not fully understood. In fact, there is a large number of research groups that are still studying the mechanics behind the process [10, 11], which indicate us that this topic is still open and, thus, is possible to generate scientific advances in this particular field.

**Fig. 8.1** Schematic representation of the wrinkling process in a bilayered system (rigid skin layer and elastic substrate foundation). (Reproduced with permission from Ref. [9])



The aim of this chapter is to introduce the reader to different methodologies to produce wrinkled patterns on hydrogels. Also, some of the most common and innovative applications will be reviewed in the last section.

## 8.2 Methodologies to Form Micro- and Nano-patterns on Hydrogels

Some research groups are interested in generating highly controlled micro- and nano-patterned topographies on polymer surfaces; in these cases, they use sophisticated methods such as laser ablation, micro-molding, wet etching, photo-/ion-/viscoelastic lithography or micro-/nano-indentation printing, among others [12]. For example, Zhang et al. [13] use stereo-lithography principles to create micro-patterns over poly(acrylic acid) (PAA) hydrogel substrate. When the UV light interacts with the photoinitiator present in the monomeric mixture, polymerizes the sector exposed to the radiation, thus making possible to generate controllable micro-patterns on the surface of the hydrogel. These micro-patterns were tested as optical lines at different conditions (wavelength and surrounding media pH) showing variable response according to the external stimulus applied to the system. Another interesting example of highly controlled micro-patterns on soft materials is reported by Lee et al. [14], which describe a simple and cost-effective approach to fabricate honeycomb microarchitectures by using natural collagen–Matrigel material, which resembles the extracellular matrix. These devices were tested for culture hepatocytes and epithelial cells with the finality of mimicking a 3-D liver model. This article uses an innovative method to generate the pattern, coined as “viscoelastic lithography,” a process which relies on the surface tension of the viscoelastic materials and the vacuum pressure. The shapes and dimensions of the self-organized micro-honeycombs could be readily controlled by changing the distance between the base mold or by altering the vacuum pressure. Figure 8.2a shows a schematic description of how this lithography method is performed. Figure 8.2b is possible to observe SEM micrographs (top and cross section) of the micro-honeycomb patterns obtained using this methodology.

The group of Ghosh et al. [15–18] generates micro-patterned surfaces on soft polymers, particularly over hydrogel films, by applying a nano-indentation procedure. Normal mechanical force is generated with a specialized AFM tip over different kinds of substrates; by using this method, it was possible to create and control the defect dimensions produced by the tip indentation. In their studies, the group of Ghosh et al. tests different indentation parameters, such as separation between indentation center, force applied, indentation depth, and substrate mechanical characteristics, among others. They also perform his studies on bilayered materials, like silicon wafer with a poly(methyl methacrylate) (PMMA) layer on top, epoxy resin as substrate with PMMA on top, etc., showing that the Young modulus of the top soft layer and the rigid foundation are fundamental for the type of indentation defect produced on surface.

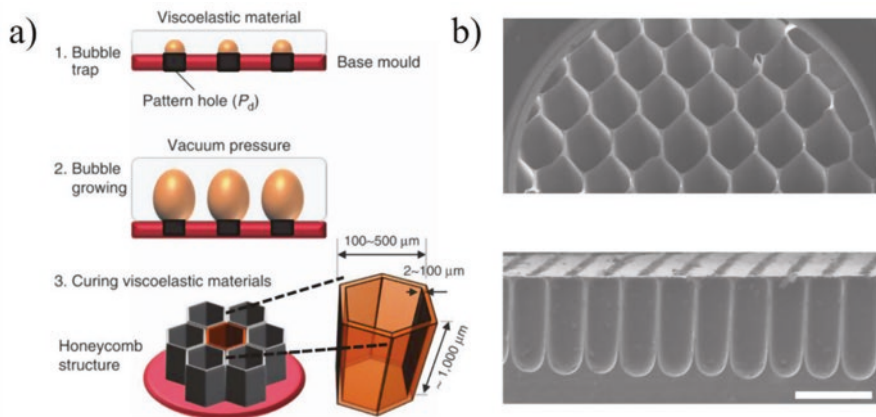


**Fig. 8.2** (a) Schematic description of the viscoelastic lithography method. (b) SEM micrographs (top and cross section) of the honeycomb patterns. (Reproduced with permission from Ref. [14])

Another common, and relatively simple, technique to produce micro-patterns is the breath figure method, which is based on the formation of microstructures generated by the condensation of water droplets from humid air onto the surface of an evaporating polymer solution, where the water droplets do not coalesce due to Marangoni thermal stresses [19]. The film attains the structure of hexagonally arrayed pores upon complete evaporation of the solvent and the water droplets, thus forming the called honeycomb pattern, characteristic of the breath figure methodology. Arora et al. [20] generate this kind of honeycomb pattern on poly(ethylene glycol) (PEG) and poly(lactic-co-glycolic acid) (PLGA) films. The inverse replica of this patterns was then transferred to poly(2-hydroxyethyl methacrylate) (PHEMA) substrates via direct contact. These surfaces were tested as superoleophobicity devices, which change their contact behavior according to inverse-honeycomb micro-pattern dimensions.

### 8.3 Taking Advantage of SIs

In this reviewing chapter, we will be more focused on the generation of micro-patterns over hydrogels using simple, cheap, and affordable methods, by slightly sacrificing control and reproducibility on pattern dimensions, structure, and distribution. The most common and easy method to generate wrinkled patterns on soft substrates is to take advantage of SIs.

### 8.3.1 *SIs Generated by Swelling/Drying Processes*

There are several methods to form wrinkled patterns which involve the use of hydrogels by using this methodology, for example, Gallardo et al. [21] group uses photopolymerizable vinylic hydrogels as a medium to produce wrinkled patterns on poly(carbonate) (PC) substrates by following a simple process (1), contacting with a photopolymerizable vinylic solution (2), solution UV curing, and (3) detachment of the formed polymer network, upon swelling in ethanol. This process allows to slightly change the dimensions of the patterns by varying some simple parameters in the process like contact time, monomeric concentration, photopolymerization degree, and type of solvent used. Figure 8.3a shows some of the surface patterns obtained via this method and also a schematic description of the process. Gallardo et al., by using confocal Raman spectroscopy, demonstrate that some part of the monomeric solution diffuses on the PC substrate, thus producing SIs; some of these results are shown in Fig. 8.3b. Finally, in Fig. 8.3c is possible to observe the PC surface topography (obtained by profilometry) by varying solvent used and contact time.

Izawa [22] reports another innovative method to generate wrinkled patterns in soft polymer surfaces by using a lignification-mimetic reaction with posterior drying. Via the immersion in methanol/phenolic acid solution, a top skin layer is synthesized on a chitosan substrate. Then, via a subsequent surface reaction with horseradish peroxidase, the wood lignification process is mimicked. Upon drying, the micron-scale wrinkled pattern is spontaneously formed on top, as a result of the inhomogeneous shrinkage of the top layer compared to the foundation. The dimensions of the wrinkled pattern can be varied by changing some parameters like the molecular structure of the components or immersion temperature. Figure 8.4 shows some of the results obtained by changing the chemical structure of the material (a, b, and c) and the immersion temperature (30, 40, 50, and 60 °C from left). In all cases, the wrinkle dimensions gradually decrease with temperature increase.

The group of Zhang et al. [23] recently develop a simple and affordable one-step method based on UV curing and swelling of liquid HEMA which always results in the formation of a corrugated surface. They also demonstrate that the insertion of a previously polymerized network (ethylene glycol dimethacrylate, EGDMA) to the solution could prevent wrinkle formation on top, and by varying the composition between HEMA and EGDMA, it was possible to change the surface morphology of the pattern, resulting in random wormlike, peanut, and honeycomb patterns. Figure 8.5 shows some of the patterns formed by varying the composition between HEMA and EGDMA.

### 8.3.2 *SIs Generated by Electrophoresis on Hydrogels*

Another interesting and innovative method to generate wrinkled patterns on hydrogels by taking advantage of SIs, or interface instabilities in this case, is the report by the group of Asoh et al. [24] which use electrophoresis to form wrinkled structures between

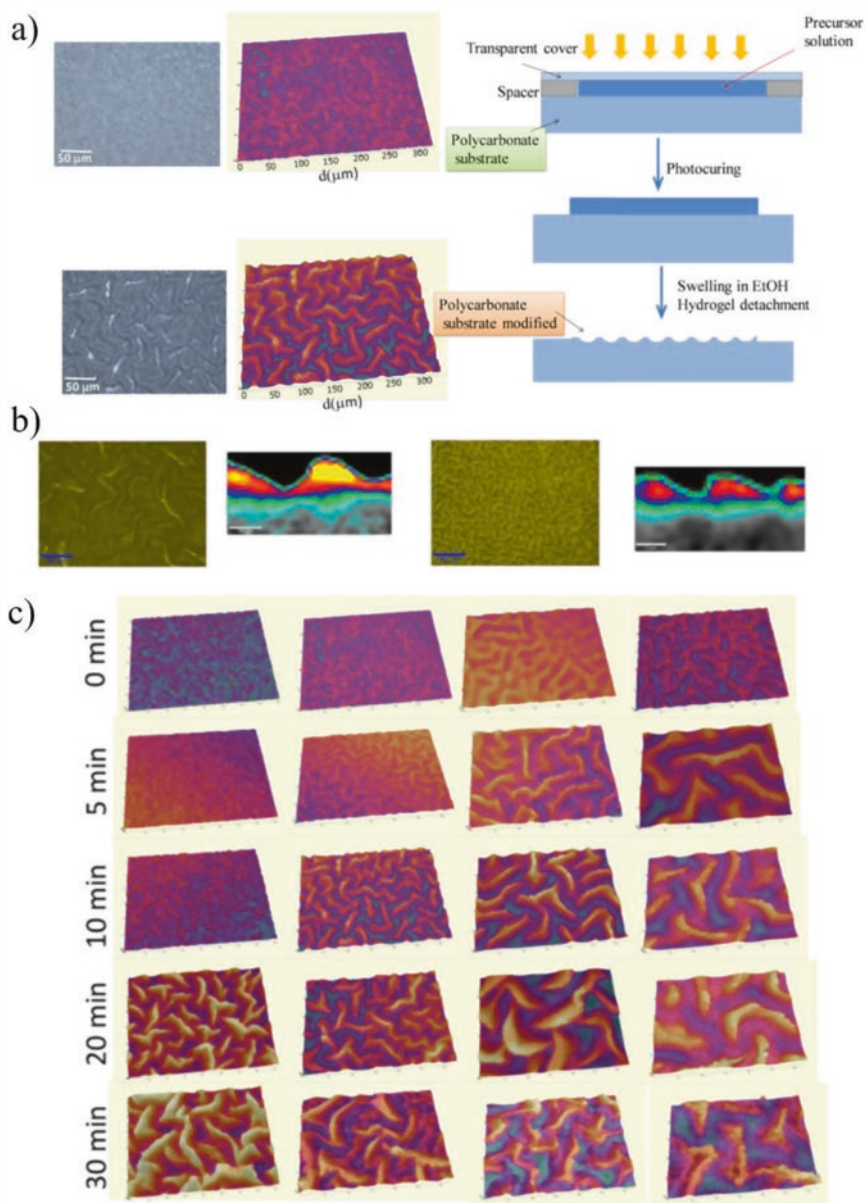


**Fig. 8.3** (a) Schematic description and some images of the swelling-induced wrinkled patterns formed. (b) Raman confocal cross sections of the wrinkled patterns. (c) Surface profilometry of the samples using different formation parameters (solvent type and contact time). (Reproduced with permission from Ref. [21])

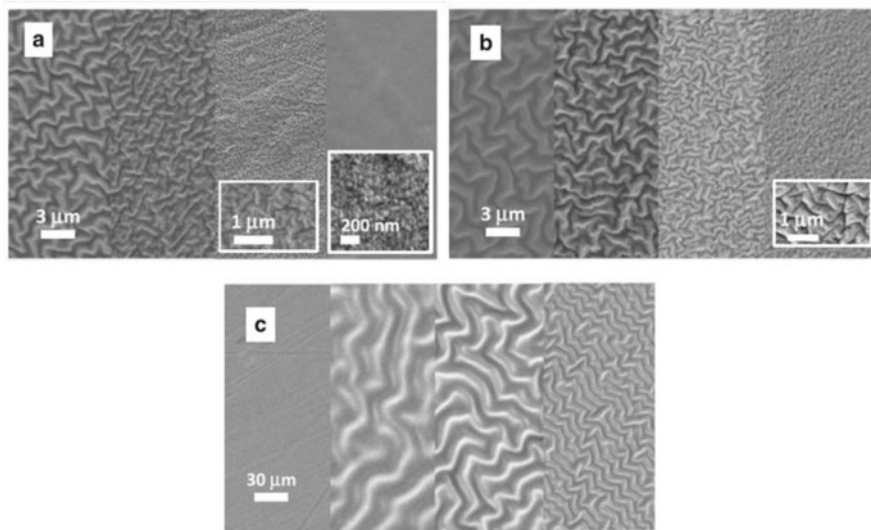


**Fig. 8.4** SEM plane-view images of the wrinkled films obtained using (a) p-coumaric acid (CO), (b) ferulic acid (FE), and (c) caffeic acid (CA)–methanol solutions, for immersion treatment temperatures at 30, 40, 50, or 60 °C. (Reproduced with permission from Ref. [22])

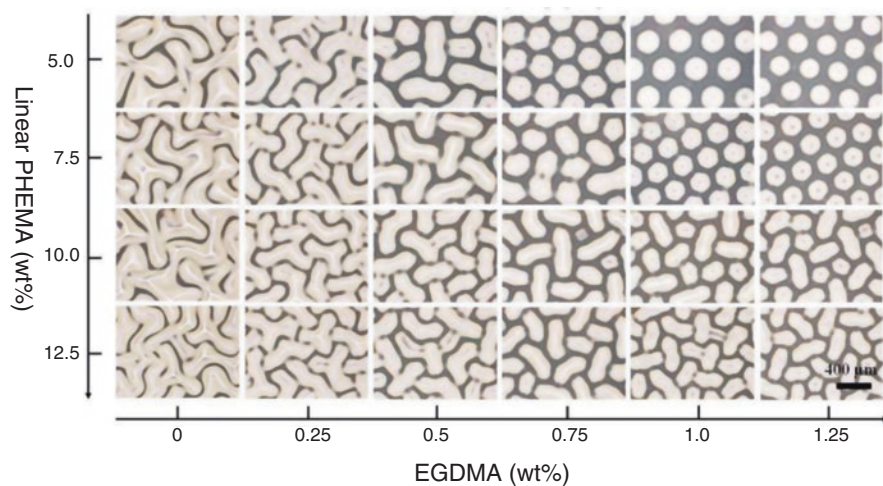


**Fig. 8.5** One-step swelling-induced wrinkled patterns containing PHEMA and EGDMA at different concentrations. Patterns from random wormlike to honeycombs are observed. (Reproduced with permission from Ref. [23])

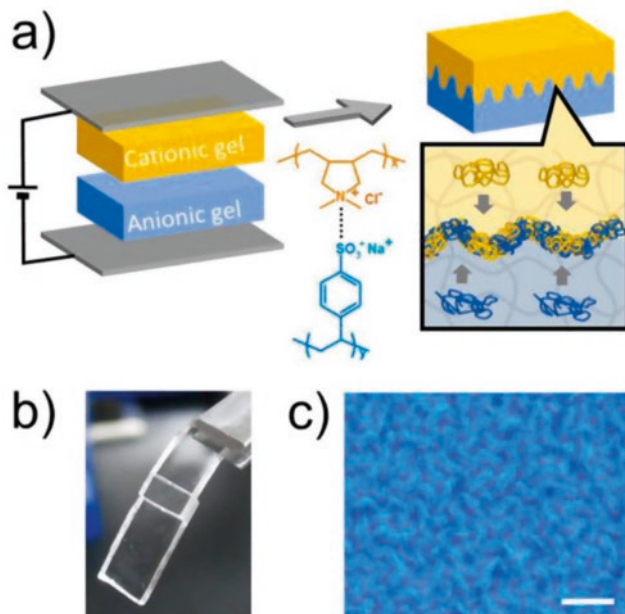


**Fig. 8.6** (a) Schematic representation which explains the wrinkled formation process in the interface of the semi-IPNs via electrophoresis. (b) Photograph of the transparent hydrogel and (c) phase-contrast micrograph of the semi-IPNs interface in which it is possible to observe the micro-wrinkled pattern. (Reproduced with permission from Ref. [24])

cationic and anionic semi-interpenetrated polymer networks (semi-IPNs). The preparation of cationic and anionic hydrogels was carried out by copolymerization of *N,N*-dimethylacrylamide (DMAAm) and *N,N'*-methylene bis(acrylamide) (MBAAm) in presence of sodium poly(styrene sulfonate) (PSS) or poly(diallyldimethylammonium chloride) (PDDA) by using either an anionic or cationic initiator. Figure 8.6a shows a schematic description of the methodology used to generate wrinkles by electrophoresis on semi-IPNs. Also, images of the transparent polymer and wrinkled formed in the interface are depicted in Fig. 8.6b, c, respectively.

The group of Asoh et al. uses these semi-IPN materials to study the adhesion mechanisms of this rugged interfaces. In Fig. 8.7a is depicted the experimental setup used for measuring the interface adhesion (lap shear test) of the semi-IPNs. Figure 8.7b, c shows two graphs which explain the mechanical behavior of this system. In the first one (Fig. 8.7b), it is possible to observe the difference in adhesion strength when semi-IPNs are used instead of the copolymer without the electrophoresis step. In the second plot (Fig. 8.7c), the tendency of adhesion strength is compared with the wrinkled wavelength pattern generated in the interface between the semi-IPNs. According to these results, it is possible to conclude that lower wrinkled pattern dimensions generate higher adhesion between the copolymer layers.

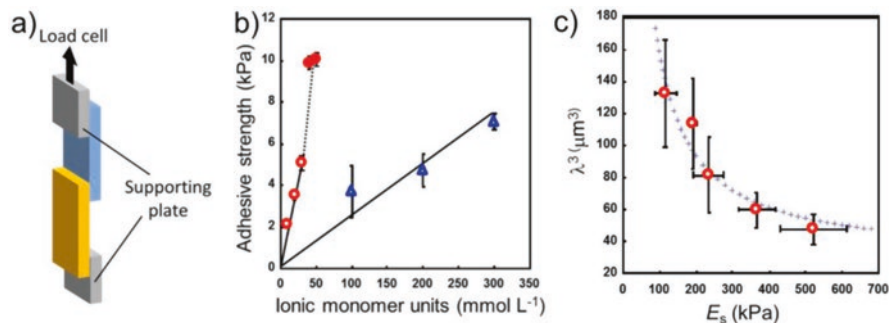


**Fig. 8.7** (a) Schematic illustration of the experimental procedure for lap shear tests. (b) Adhesive strength of semi-IPNs (circle) and copolymer (triangle) materials versus monomeric units of the cationic/anionic polymer. (c) Wrinkling interface wavelength against Young's modulus of the gels. (Reproduced with permission from Ref. [24])

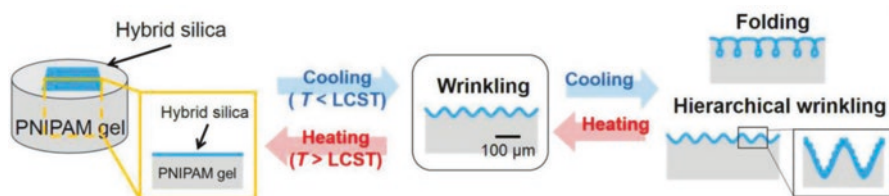


**Fig. 8.8** Schematic explication of the strategy used to create thermoresponsive microstructures on bilayered materials of hybrid silica and PNIPAM. The microstructures are reversibly switchable by subsequent heating/cooling processes. (Reproduced with permission from Ref. [25])

### 8.3.3 SIs Generated by Subsequent Cooling and Heating Steps

The group of Takahashi et al. [25] reports an interesting method to form submillimeter wrinkled patterns by using bilayered systems of thermoresponsive materials, poly(N-isopropylacrylamide) (PNIPAM) and hybrid silica. PNIPAM possesses the property of changing their shape at lower critical solution temperature, and thereby wrinkled patterns appear and disappear as a function of the environmental temperature. Large deformation could be achieved by taking advantage of this thermoresponsive property of the PNIPAM, making possible to obtain different structures such as folds and nested wrinkling structures by following subsequent heating/cooling processes. Figure 8.8 shows a schematic description of the process reported in this article. Also, some optical microscopy images of the wrinkled surfaces at different temperatures (cooling process) are shown in Fig. 8.9.

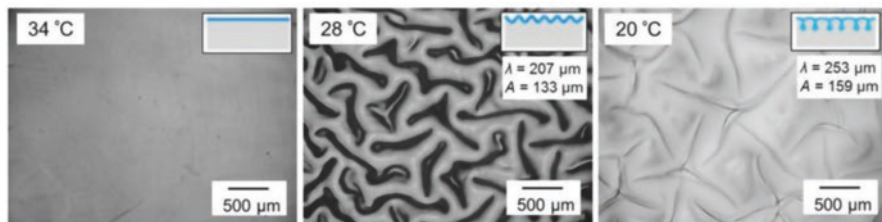


**Fig. 8.9** Optical microscope images of surface microstructures at different temperatures. (Reproduced with permission from Ref. [25])

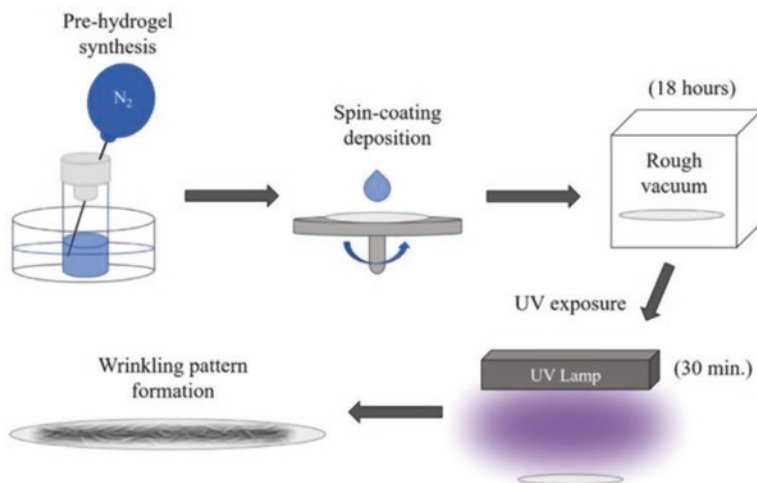


**Fig. 8.10** Schematic description of the process performed to form wrinkled patterns using subsequent heating and UV exposure processes. (Reproduced with permission from Ref. [27])

### 8.3.4 *SIs Generated on Hydrogels by Subsequent Heating and UV Exposure Steps*

Spontaneous wrinkled patterns can be also formed on hydrogel surfaces by using subsequent steps of heating and UV exposure steps on HEMA-poly(ethylene glycol) diacrylate (PEGDA) hydrogels. Interestingly, the group of Gonzalez et al. [26] uses a preheating step to increase the polymerization degree of the material with the finality of obtaining an appropriate viscosity to achieve a correct hydrogel layer deposition. Once the film is formed, it is exposed to UV and deswelling processes to generate the wrinkled pattern on the surface (Fig. 8.10). In this article, Gonzalez

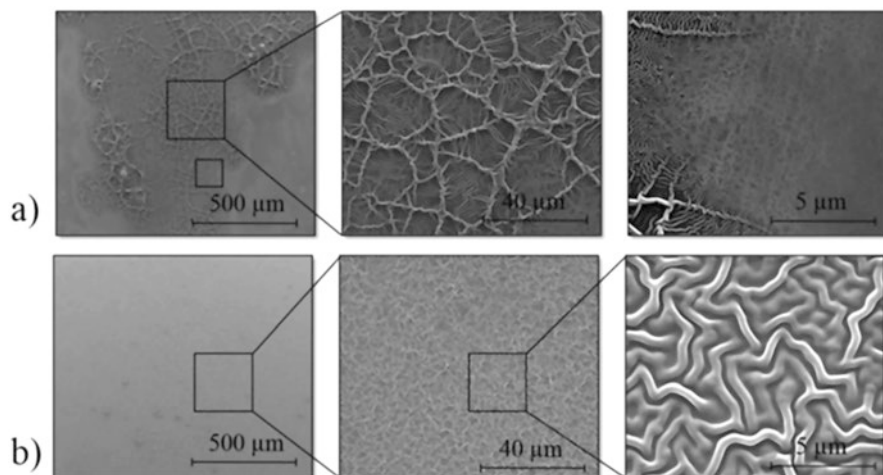


**Fig. 8.11** FE-SEM micrographs of HEMA-PEGDA hydrogel deposited by (a) electro-spray technique and (b) spin-coating method. (Reproduced with permission from Ref. [26])

et al. firstly study the effect generated by the deposition method, by using electro-spray and spin-coating methods. Their results show that, as was expected, the spin-coating method generates a homogeneous and high coverage film, while electrospinning generates drops of material deposited over the surface. Figure 8.11 shows some of the results obtained by using the different methodologies.

Secondly, they study the effect that produces the molecular weight ( $M_n$ ) of the cross-linking agent (PEGDA) on wrinkle dimensions. Thus, three different  $M_n$  were tested (250, 575, and 700 g/mol). As is possible to observe in Fig. 8.12, the wrinkle width (and also height) depends on the molecular weight of the PEGDA used in the synthesis, which increases with the  $M_n$  of the cross-linking agent. This could be related to the packing degree of the polymeric network obtained with each cross-linking agent.

In other studies of the same group, the formation of a chemically different thin layer (more polymerized) in the top of the film was demonstrated by using confocal Raman spectroscopy. To achieve this, the signal intensities of the C=O and the C=C bonds were compared during a cross-sectional scan of the wrinkled pattern. Figure 8.13 shows some of the results obtained. The red color indicates a higher presence of the C=O bond. A decrease of C=O linkage of PEGDA means that the cross-linking agent is more polymerized on the top of the surface.

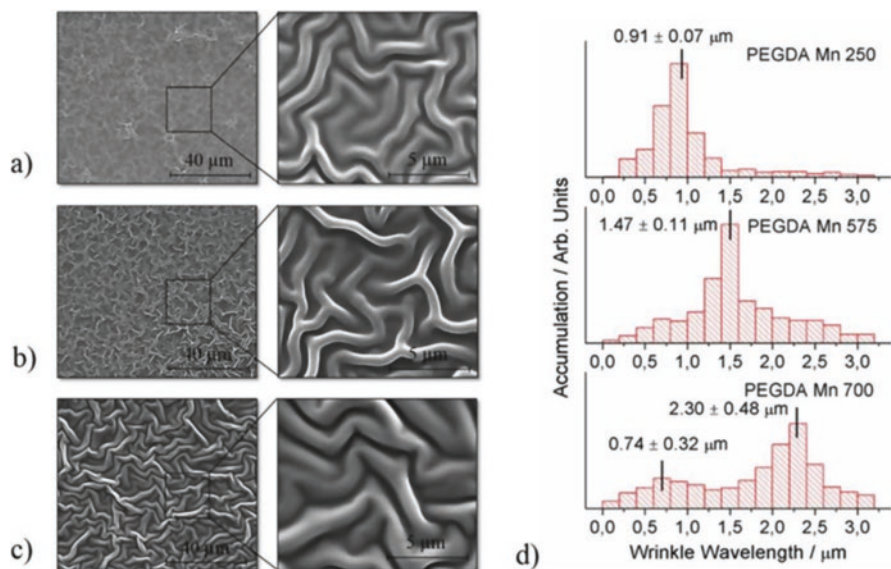


**Fig. 8.12** FE-SEM micrographies of HEMA-PEGDA hydrogel layers using different cross-linking agent molecular weight (Mn): (a) 250, (b) 575, and (c) 700 g/mol. (d) Distributions of the wrinkle width for each case. (Reproduced with permission from Ref. [26])

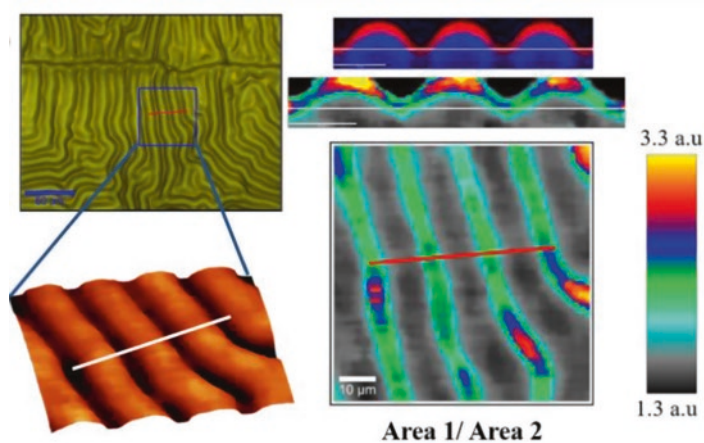


**Fig. 8.13** Optical (top-left), 3-D AFM profile images (bottom-left) as well as confocal Raman analysis (right: cross section on top and 2-D analysis at the bottom) for the wrinkled patterns. (Unpublished data)

## 8.4 Applications of Hydrogel Wrinkled Patterns Generated by SIs

There are several examples, in different fields, in which hydrogels that present wrinkled patterns are applied with a specific purpose. As a matter of fact, the group of Gonzalez et al. [27] reported the formation of pH-sensitive wrinkled patterns by using a similar methodology than explained before (by using subsequent heating and UV exposure steps). In this case, HEMA:PEGDA hydrogels were mixed with N,N-diethylaminoethyl methacrylate (DEAEMA) monomer, which has pH-sensitive capacities. In this study, the amount of each monomer (HEMA or DEAEMA) was varied with the finality to change the surface morphology and the chemistry response of the wrinkled patterns formed on top after the UV and vacuum exposure processes. In order to test the pH-sensitiveness of the final hydrogel, the static contact angle was measured by using different buffers (pH 5.4, 7.4, and 8.3). The obtained results, depicted in Fig. 8.14, indicate that the contact angle increases with the pH independent of the concentration of monomers used, but at higher DEAEMA concentration, the contact angle of the hydrogel surface increases considerably.

The same group, Gonzalez et al., recently fabricates a different kind of hydrogel surfaces with pH-sensitiveness by using a similar methodology and slightly different monomer, N,N-dimethylaminoethyl methacrylate (DMAEMA), which presents in addition to pH response, thermosensitive behavior. In this case, the contact angle

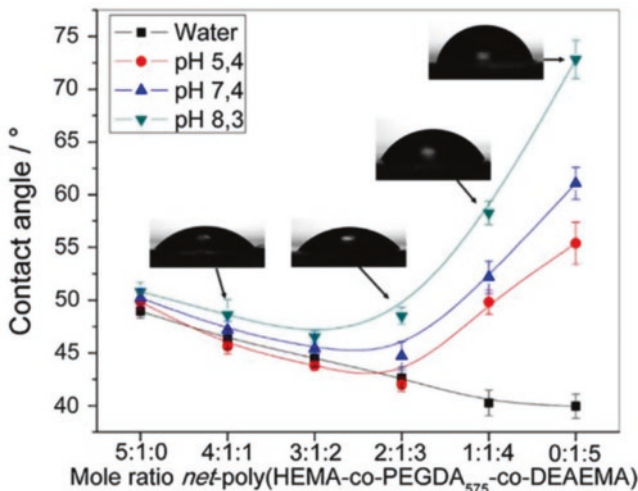


**Fig. 8.14** Contact angle variations measured by using different buffers as aqueous media over the hydrogel films with variable HEMA-DEAEMA compositions. (Reproduced with permission from Ref. [27])

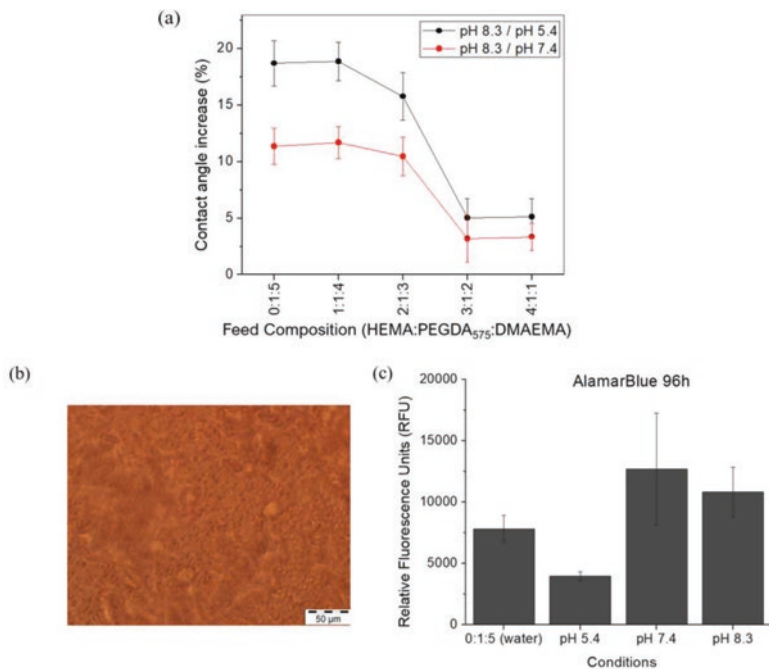


**Fig. 8.15** (a) Percentage increase of static contact angle for the samples HEMA:PEGDA<sub>575</sub>:DMAEMA at different pH. (b) Detailed magnification in vertical microscopy of the cells adhered over the grooves of a particular sample. (c) Metabolic activity values (AlamarBlue) at 96 h after cell culture. (Unpublished data)

was also measured in wrinkled pattern surface (Fig. 8.15a), showing a clear dependence on pH as well as DMAEMA monomer concentration in the mixture. As this material presents temperature responsiveness, cellular proliferation and biocompatibility tests were carried out at physiological conditions (37 °C and pH 7.4) showing better results (higher cellular proliferation after 96 h of culturing) than obtained in water (neutral environment), acidic (pH 5.4), or basic conditions (pH 8.3). Some of the results obtained are depicted in Fig. 8.15b, c.

Similarly, these hydrogels, based on HEMA, can be used to generate selective antibiofouling surfaces which could allow cell proliferation while avoiding bacterial colonization. Particularly, in this study, the group of Gonzalez et al. manipulates the hydrophobic/hydrophilic balance of the composite by including different amounts of fluorinated radical groups in the chemical structure of the hydrogel. This was achieved by gradually adding 2,2,2-trifluoroethyl methacrylate (TFMA), a hydrophobic monomer, in the reaction mixture. The results show that the inclusion of fluorinated radical groups not only affects the biofouling response of the surface but also the mechanical properties of the materials and, therefore, the wrinkle dimensions of the patterns formed on top. The synergy between these two processes, the change in the chemical and morphological properties of the hydrogels,

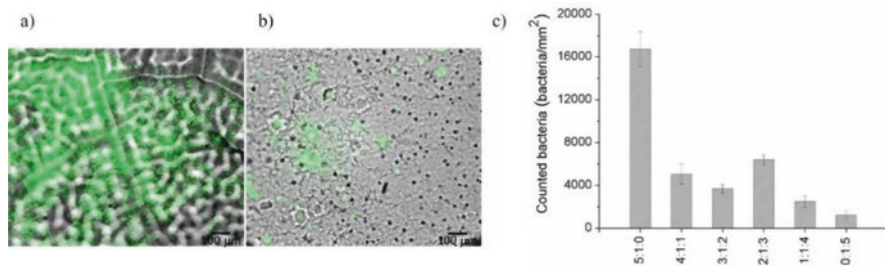


**Fig. 8.16** Bacterial adhesion test on the micro-wrinkled surfaces. (a, b) Merged bright-field and green fluorescence optical microscopy images of surfaces with a variable amount of TFMA. (c) Amount of bacteria adhered to the surfaces as a function of the molar amount of TFMA. (Unpublished data)

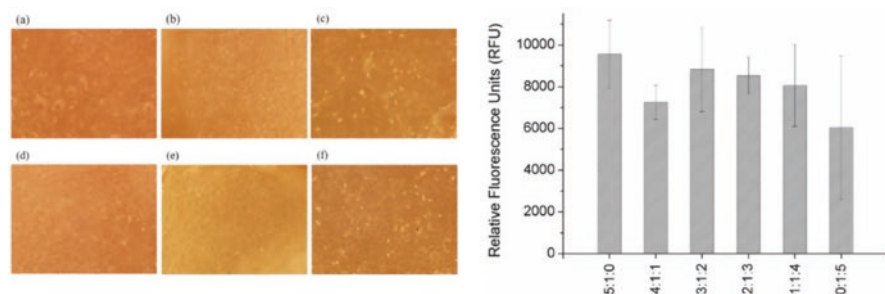


**Fig. 8.17** (a–f) Optical microscopy images of C166-GFP endothelial cells adhered on the wrinkled surfaces after 96 h of culture. **Right:** Metabolic activity of endothelial cells (AlamarBlue assay) at 96 h. (Unpublished data)

could generate the observed decrease in bacterial growth, while the cellular proliferation maintains almost the same trend in the same period. Figures 8.16 and 8.17 show some of the results obtained in this study; the first figure shows the response of the surfaces against bacterial colonization, and, as is possible to observe the sample with lower TFMA amount, Fig. 8.16a shows higher bacterial concentration after 96 h, opposite behavior than the exposed by the sample in Fig. 8.16b, which shows minimal bacterial concentration after the same period. In Fig. 8.16c the bacterial presence was quantified via fluorescence methods, demonstrating a clear decrease trend when TFMA concentration in the mixture increased. Figure 8.17 shows the response of these samples when mammalian cells are cultured on their surface. As is possible to observe in the micrographs depicted in Fig. 8.17a–f, in all the cases, a well-formed monolayer of epithelial cells is detected after 96 h of incubation. The autofluorescence property of these cells allows quantifying the number of cells in each case. As is possible to observe in Fig. 8.17 (right), although the cell concentration tends to decrease with TFMA amount increase in the reaction mixture, the decrease is not so important as in the case of the bacteria, showing that there exists

a trend of avoiding bacteria colonization while allowing cellular proliferation on top (anti-biofouling tendency) after 96 h of culturing. This behavior could be caused by a synergistic response between the chemistry and topography changes occurred when TFMA amount in the reaction mixture is varied. The cells, which are much bigger than the wrinkle size, could be grown on pattern top without being affected by their topography but slightly altered by the surface hydrophobicity increase due to TFMA increase. On the other hand, bacteria size is similar or lower than wrinkle dimensions, which implies that in this case the surface pattern effectively affects bacterial growth, as does the surface hydrophobicity increase.

The group of Gonzalez et al. [28] in the year 2015 reports a novel methodology to produce wrinkled hydrogel films by using the electrospinning technique to deposit the hydrogel films, which were then exposed to vacuum and UV to form the wrinkled patterns on top. To achieve the proper viscosity for electrospinning deposition, the reaction mixtures need to be previously heated to form a pre-hydrogel composite. By varying the electrospinning deposition parameters, it was possible to create flat or wrinkled surfaces according to the voltage used. Then these surfaces were used as support for artificial phospholipid bilayers. These biomimetic artificial bilayers were deposited on top of hydrogel films by following the methodology of Langmuir-Blodgett. According to the results, it was possible to demonstrate that the samples which present smooth micro-wrinkled patterns (deposited with 20 kV) have the higher water absorbance and retention. These last mentioned layers possess the capacity to stabilize the phospholipid bilayer for longer periods and after several heating cycles, permitting to serve as a base for biocompatible biosensors. FE-SEM micrographs of the hydrogel wrinkled surfaces obtained at different deposition voltages are shown in Fig. 8.18.

Similar results were obtained by the same group in the year 2016, but in this case, the spin-coating technique was used as the deposition method, and the cross-linking agent nature was changed [29]. It was demonstrated that when acrylamide (AAM) and di(ethylene glycol) dimethacrylate (DEGDMA) were used as cross-linking agents, flat surfaces were obtained after the vacuum and UV exposure steps. On the other hand, when PEGDA was used, wrinkled surfaces are obtained. Gonzalez and Sarabia [30], in the year 2015, were capable of demonstrating that similar results can be achieved by using the electrospray deposition method. Hydrogel films which have AAM or DEGDMA as a cross-linking agent were unable to generate wrinkled surfaces, while HEMA:PEGDA effectively can. In general, hydrogel film works as a “lubricant cushion” which maintains the tethered bilayer stabilized under rough external stimulus due to their capability in absorbing and retaining the humidity.

Other research groups use micro-patterned hydrogel surfaces to create cells with particular shapes. One of the most renowned is the group of Guvendiren et al. [31–33] which, by using PHEMA hydrogel wrinkled surfaces, were able to change the morphology of stem cells grown on the top of the patterns and able to induce cellular differentiation according to their shape (random, spheroid, or lamellar).

A similar approach was reported recently by Paul et al. [34], in which micron-sized aligned and unaligned wavy patterns can be imprinted in soft, cell-adhesive

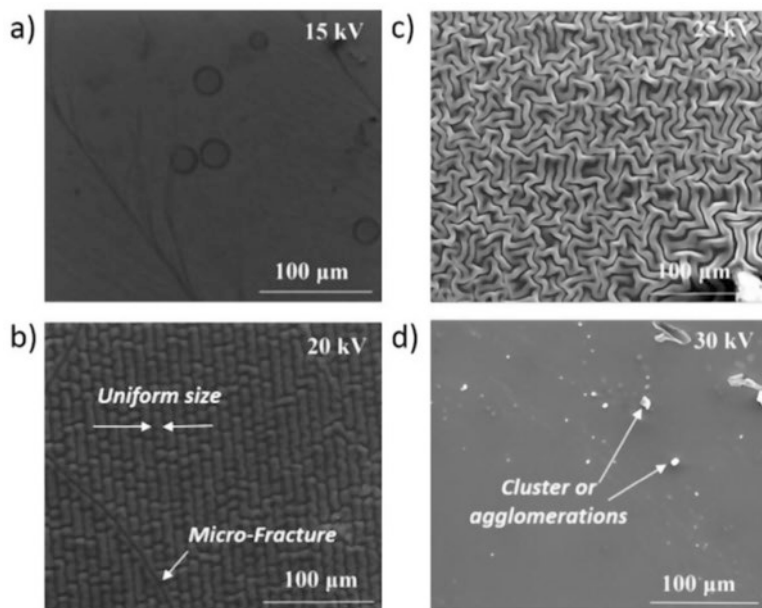


**Fig. 8.18** FE-SEM micrographs of HEMA:PEGDA hydrogel films at different deposition voltages: (a) 15 kV, (b) 20 kV, (c) 25 kV, and (d) 30 kV. (Reproduced with permission from Ref. [28])

hydrogels for a wide range of periodicities, widths, and amplitudes by micro-molding with PDMS. The stem cells migrated over the patterned surfaces during the first 24 h after seeding and showed active interaction with the scaffold via cytoplasmic projections. As it was predicted by Guvendiren et al., the cells tend to create a randomly oriented structure when “2-D” patterns are used, while tending to align in one particular direction on “1-D” patterns. Figure 8.19 shows some of the results obtained by Paul et al. [34].

Some research groups were also interested in using the micro-patterned hydrogel surfaces for creating spheroid multicellular particles. One of the first was the group of Zhang et al. [35], in the year 2014, which use PHEMA water-swollen wrinkled substrates to guide the formation of multicellular spheroid structures with narrow distributions. When cell suspension is added on the PHEMA wrinkled substrates, the cells settle down by gravity to the bottom of the grooves. The cells tend to accumulate in the center of the microcaves and gradually self-assemble into multicellular spheroid structures. After 48 h, it is possible to detect multicellular structures of similar sizes on the bottom of the microcaves, while, on flat surfaces, cell agglomerations of variable sizes can be detected. The size of the spheroids can be altered by means of variation of surface morphology as well as cell concentration. Recently, Lim et al. [36] developed a different method to culture human salivary gland cells on micro-patterned hydrogel surfaces based on PEG composites mixed with

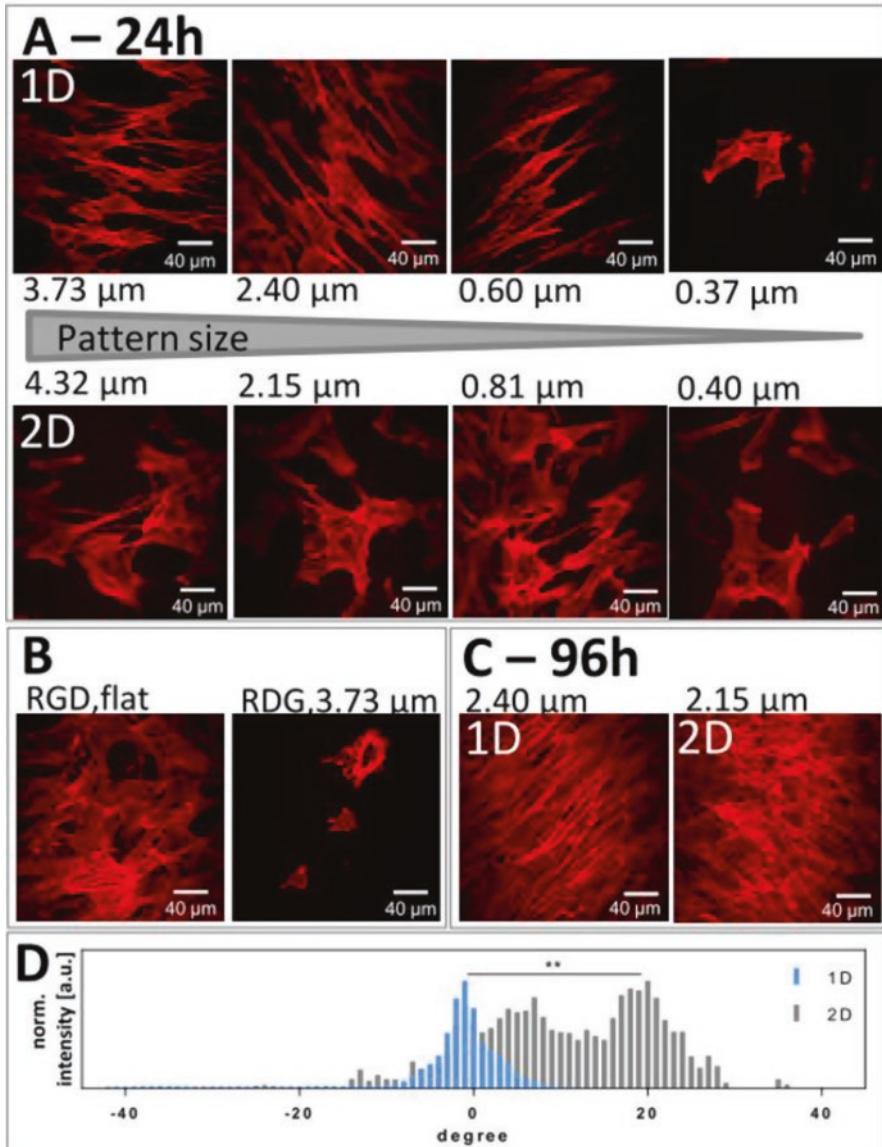


**Fig. 8.19** (a) Actin cytoskeletal filaments of cells 24 h after seeding on aligned “1-D” waves (top) and unaligned “2-D” waves (bottom). (b) Cells also adhere to unpatterned substrates but with minimal. (c) Cells become confluent after 96 h. (d) Normalized angle distribution of actin filaments. (Reproduced with permission from Ref. [34])

poly(caprolactone) (PCL) nanofibrous microwells for inducing self-assembly of multicellular spheroid structures. A schematic illustration of the methodology used in this article is shown in Fig. 8.20. By using this methodology, it was possible to establish a bioengineering 3-D culture system to promote robust, functional, and reproducible acinar-like organoids.

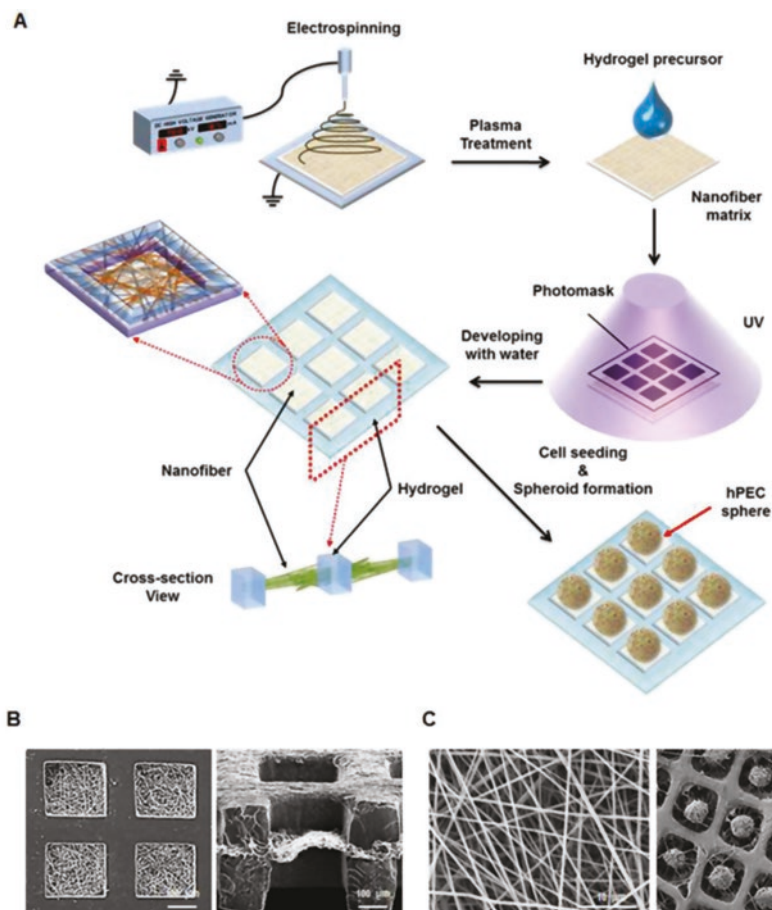


**Fig. 8.20** (a) Schematic illustration of PCL nanofibrous scaffolds with PEG wall micro-patterning. SEM micrographs of (b) electrospun PCL microwells and (c) salivary gland cells forming spheroids within the PCL microwells after 3 days. (Reproduced with permission from Ref. [36])

Another interesting example was the recent report by Levkin et al. [37] which develop an innovative method based on superhydrophobic-hydrophilic arrays to create well-defined-shaped micro-hydrogel particles with cells inside. Figure 8.21 (left) shows some of the micro-hydrogel shapes which could be formed by using this methodology (circular, triangular, hexagonal, quadrangular, heart-shaped, and fiber-like arrays). In Fig. 8.21 (right) are observed bright-field and fluorescence images of freestanding hydrogels with encapsulated cells. They demonstrated the feasibility of this new method to fabricate free-standing hydrogel particles with defined geometries and sizes while maintaining control of the elastic modulus and the composition of the hydrogel. This technology was also used to form magnetic hydrogel particles, incorporating live cells which can be employed for modular tissue engineering applications due to the possibility to manipulate both single particles and particle assemblies using external magnetic fields.

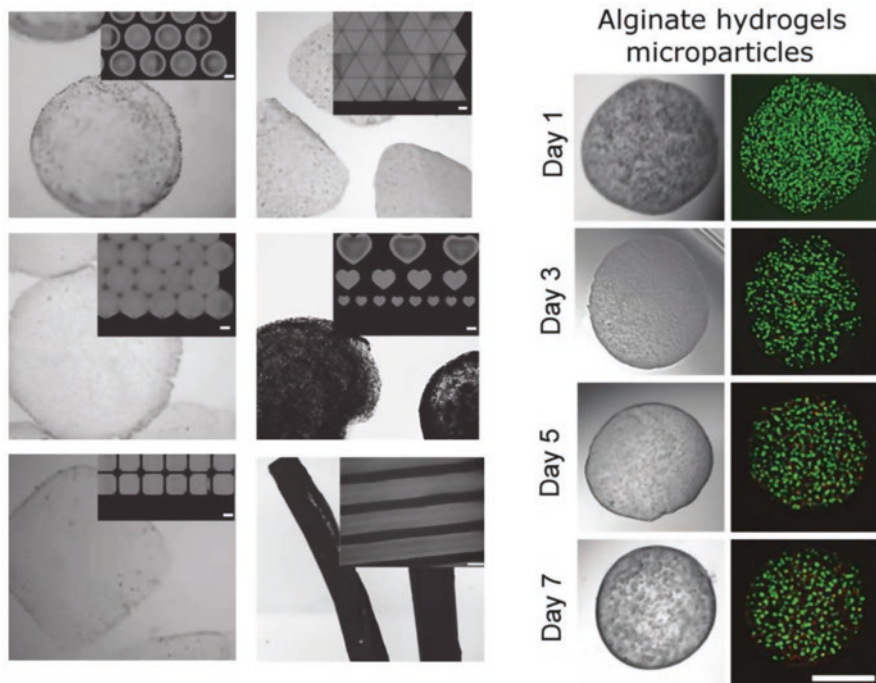


**Fig. 8.21** (left) Optical micrographs of some micro-hydrogel shapes (circular, triangular, hexagonal, quadrangular, heart-shaped, and fiber-like shapes). (right) Representative bright-field and fluorescence images of freestanding hydrogels with encapsulated cells after 7 days of culture. Live cells are visualized as green, and dead cells are stained with red. (Reproduced with permission from Ref. [37])

## 8.5 Conclusion and Remarks

This reviewing chapter is mainly focused on the formation of micro-patterned structures by taking advantage of surface instabilities. This methodology is an easy, economically affordable, and scalable procedure which generates spontaneously wrinkled patterns in a wide range of sizes when the surface is exposed to different external stimulus like mechanical stretching, temperature, pH, swelling/deswelling, or electrical impulses, among others. The control of pattern morphology and distribution is a key feature that can be tuned by changing some deposition or formation parameters. Using this methodology, it is possible to obtain large homogenous micro-patterned surfaces on biocompatible or responsive hydrogels which can be used in different application fields like tissue regeneration, antibiofouling, cell scaffold, multicellular spheroid generation, soft actuators, and robots, among others. In this chapter, some interesting examples of this application are reviewed, and also different methodologies to form wrinkled patterns on hydrogel surfaces are mentioned. Hydrogels, as a material, present several advantages over another kind of

polymers due to their malleability, easy synthesis, and biocompatibility; this characteristic makes them good candidates for future and affordable biomedical and another kind of applications.

**Acknowledgments** The authors acknowledge financial support given by FONDECYT Grant N° 1170209. M.A. Sarabia acknowledges the financial support given by CONICYT through the doctoral program Scholarship Grant. J. Rodríguez-Hernández acknowledges financial support from Ministerio de Economía y Competitividad (MINECO) (Project MAT2016-78437-R, FEDER-EU) and finally VRAC Grant Number L216-04 of Universidad Tecnológica Metropolitana.

## References

1. M. Malmsten, Antimicrobial and antiviral hydrogels. *Soft Matter* **7**, 8725 (2011)
2. C.M. Gonzalez-Henriquez, M.A. Sarabia-Vallejos, J. Rodríguez-Hernández, Advances in the fabrication of antimicrobial hydrogels for biomedical applications. *Materials (Basel)* **10**, 232 (2017)
3. M.W. Tibbitt, K.S. Anseth, Hydrogels as extracellular matrix mimics for 3D cell culture. *Biotechnol. Bioeng.* **103**, 655–663 (2009)
4. N.A. Peppas, J.Z. Hilt, A. Khademhosseini, et al., Hydrogels in biology and medicine: From molecular principles to Bionanotechnology. *Adv. Mater.* **18**, 1345–1360 (2006)
5. A.S. Veiga, J.P. Schneider, Antimicrobial hydrogels for the treatment of infection. *Biopolymers* **100**, 637–644 (2013)
6. D. Seliktar, Designing cell-compatible hydrogels for biomedical applications. *Science* **336**, 1124–1128 (2012)
7. R. Censi, P. Di Martino, T. Vermonden, et al., Hydrogels for protein delivery in tissue engineering. *J. Control. Release* **161**, 680–692 (2012)
8. H.F. Chan, R. Zhao, G.A. Parada, et al., Folding artificial mucosa with cell-laden hydrogels guided by mechanics models. *Proc. Natl. Acad. Sci.* **115**, 7503–7508 (2018)
9. J. Rodríguez-Hernández, Wrinkled interfaces: Taking advantage of surface instabilities to pattern polymer surfaces. *Prog. Polym. Sci.* **42**, 1–41 (2015)
10. X. Huang, B. Li, W. Hong, et al., Effects of tension-compression asymmetry on the surface wrinkling of film-substrate systems. *J. Mech. Phys. Solids* **94**, 88–104 (2016)
11. Z. Zhou, Y. Li, T.F. Guo, et al., Surface instability of bilayer hydrogel subjected to both compression and solvent absorption. *Polymers (Basel)*, **8**, 1–15 (2018)
12. K. Subramani, Fabrication of hydrogel micropatterns by soft photolithography, in *Emerging Nanotechnologies for Manufacturing*, (Elsevier, Oxford, 2015), pp. 279–293
13. M.J. Yin, M. Yao, S. Gao, et al., Rapid 3D patterning of Poly(Acrylic Acid) ionic hydrogel for miniature PH sensors. *Adv. Mater.* **28**, 1394–1399 (2016)
14. G.S. Jeong, D.Y. No, J. Lee, et al., Viscoelastic lithography for fabricating self-organizing soft micro-honeycomb structures with ultra-high aspect ratios. *Nat. Commun.* **7**, 1–9 (2016)
15. G. Mallikarjunachari, P. Ghosh, Nanomechanical study of polymer-polymer thin film interface under applied service conditions. *J. Appl. Polym. Sci.* **133**, 1–13 (2016)
16. A. Rath, S. Mathesan, P. Ghosh, Nanomechanical characterization and molecular mechanism study of nanoparticle reinforced and cross-linked Chitosan biopolymer. *J. Mech. Behav. Biomed. Mater.* **55**, 42–52 (2015)
17. G. Mallikarjunachari, P. Ghosh, Analysis of strength and response of polymer nano thin film interfaces applying nanoindentation and nanoscratch techniques. *Polym. (United Kingdom)* **90**, 53–66 (2016)
18. G. Mallikarjunachari, P. Ghosh, Application of nanomechanical response of wrinkled thin films in surface feature generation. *Eur. Polym. J.* **89**, 524–538 (2017)

19. F. Girard, M. Antoni, K. Sefiane, On the effect of marangoni flow on evaporation rates of heated water drops. *Langmuir* **24**, 9207–9210 (2008)
20. J.S. Arora, J.C. Cremaldi, M.K. Holleran, et al., Hydrogel inverse replicas of breath figures exhibit superoleophobicity due to patterned surface roughness. *Langmuir* **32**, 1009–1017 (2016)
21. A. Gallardo, N. Luján, H. Reinecke, et al., Chemical and topographical modification of polycarbonate surfaces through diffusion/photocuring processes of hydrogel precursors based on Vinylpyrrolidone. *Langmuir* 2017, acs.langmuir.6b04143.
22. H. Izawa, Preparation of biobased wrinkled surfaces via lignification-mimetic reactions and drying: A new approach for developing surface wrinkling. *Polym. J.* **49**, 759–765 (2017)
23. J. Gu, X. Li, H. Ma, et al., One-step synthesis of PHEMA hydrogel films capable of generating highly ordered wrinkling patterns. *Polymer (Guildf)*. **110**, 114–123 (2017)
24. M. Kato, Y. Tsuboi, A. Kikuchi, et al., Hydrogel adhesion with wrinkle formation by spatial control of polymer networks. *J. Phys. Chem. B* **120**, 5042–5046 (2016)
25. Y. Tokudome, H. Kuniwaki, K. Suzuki, et al., Thermoresponsive wrinkles on hydrogels for soft actuators. *Adv. Mater. Interfaces* **3**, 1–5 (2016)
26. C.M. Gonzalez-Henriquez, D.H. Sagredo-Oyarce, M.A. Sarabia-Vallejos, et al., Fabrication of micro and sub-micrometer wrinkled hydrogel surfaces through thermal and photocrosslinking processes. *Polymer (Guildf)*. **101**, 24–33 (2016)
27. C.M. González-Henríquez, P.A. Alfaro-Cerda, D.F. Veliz-Silva, et al., Micro-wrinkled hydrogel patterned surfaces using PH-sensitive monomers. *Appl. Surf. Sci.* **457**, 902–913 (2018)
28. C.M. González-Henríquez, G.D.C. Pizarro, M.A. Sarabia-Vallejos, et al., Thin and ordered hydrogel films deposited through electrospinning technique; a simple and efficient support for organic bilayers. *Biochim. Biophys. Acta Biomembr.* **1848**, 2126–2137 (2015)
29. C.M. Gonzalez-Henriquez, G. Pizarro, C. del, E.N. Córdova-Alarcón, et al., Artificial biomembranes stabilized over spin coated hydrogel scaffolds. Crosslinking agent nature induces wrinkled or flat surfaces on the hydrogel. *Chem. Phys. Lipids* **196**, 13–23 (2016)
30. C.M. Gonzalez-Henriquez, M.A. Sarabia-Vallejos, Electrospinning deposition of hydrogel fibers used as Scaffold for biomembranes. Thermal stability of DPPC corroborated by Ellipsometry. *Chem. Phys. Lipids* **190**, 51–60 (2015)
31. M. Guvendiren, J.A. Burdick, The control of stem cell morphology and differentiation by hydrogel surface wrinkles. *Biomaterials* **31**, 6511–6518 (2010)
32. P. Viswanathan, M. Guvendiren, W. Chua, et al., Mimicking the topography of the epidermal-dermal interface with Elastomer substrates. *Integr. Biol. (Camb)*. **8**, 21–29 (2016)
33. M. Guvendiren, J.A. Burdick, Stem cell response to spatially and temporally displayed and reversible surface topography. *Adv. Healthc. Mater.* **2**, 155–164 (2013)
34. A. Paul, M. Stührenberg, S. Chen, et al., Micro- and nano-patterned Elastin-like polypeptide hydrogels for stem cell culture. *Soft Matter* **13**, 5665–5675 (2017)
35. Z. Zhao, J. Gu, Y. Zhao, et al., Hydrogel thin film with swelling-induced wrinkling patterns for high-throughput generation of multicellular spheroids. *Biomacromolecules* **15**, 3306–3312 (2014)
36. H.S. Shin, Y.M. Kook, H.J. Hong, et al., Functional spheroid organization of human salivary gland cells cultured on hydrogel-micropatterned nanofibrous microwells. *Acta Biomater.* **45**, 121 (2016)
37. A.I. Neto, K. Demir, A.A. Popova, et al., Fabrication of hydrogel particles of defined shapes using superhydrophobic-hydrophilic micropatterns. *Adv. Mater.* **28**, 7613–7619 (2016)

# Chapter 9

## Wrinkling on Covalently Anchored Hydrogels



Chya-Yan Liaw, Jorge Pereyra, and Murat Guvendiren

### 9.1 Introduction

Surface patterns are commonly observed in nature and the human body, such as mucosal folds on the intestinal wall which facilitate rapid exchange of mass, nutrient, and waste [1]; wrinkles on the human skin [2]; folds in the human brain to increase surface area [3], and buckling protrusions on tumor surfaces which are believed to promote tumor invasion [4–5]. While patterns in nature provide important functions, surface instabilities on hydrogels have generally been considered as undesirable defects that need to be avoided. Until recently, increasing theoretical and experimental studies have been reported to predict and control the formation of surface patterns enabling the use of surface instabilities for a wide range of applications including sensors, optical devices, micro-/nano-fabrication tools, and bioengineering [6].

Hydrogels are three-dimensional networks of polymers that are capable of absorbing and retaining large amounts of water. The physical and chemical properties of hydrogels closely mimic natural living tissues; therefore, the formation of surface patterns on hydrogels has numerous potential applications in tissue engineering, biosensing, and drug delivery applications.

The use of surface patterns in soft hydrogels was reported as far back as the mid-nineteenth century in the fine art reproduction process known as “colloTYPE printing” [7]. In the process, the printing plate was coated with a light-sensitive dichromated gelatin film and exposed to light under a photographic negative. Gelatin hardened selectively, producing surface patterns and wrinkles, upon swelling. Wrinkles varied in their ink/water absorption capacity, which gives rise to a delicate continuous-tone effect [8]. A similar phenomenon was later reported by

---

C.-Y. Liaw · J. Pereyra · M. Guvendiren (✉)  
Otto H. York Department of Chemical and Materials Engineering,  
New Jersey Institute of Technology, Newark, NJ, USA  
e-mail: [muratg@njit.edu](mailto:muratg@njit.edu)

Tanaka et al. by swelling polyacrylamide hydrogels in water [9]. Following these observations, many experimental and theoretical studies have been carried out to further exploit the surface instabilities in hydrogels.

In this chapter, we focus on the formation of surface instabilities in confined hydrogels. We first classify the types and mechanisms of the instability patterns. A detailed review on commonly used hydrogel systems to generate surface instabilities is given. Finally, a brief overview of the applications and challenges associated with the use of hydrogel instability patterns is given.

## 9.2 Types and Mechanisms of Hydrogel Surface Instabilities

Surface patterns in hydrogels are usually induced by lateral confinement of the hydrogel while undergoing large volume changes mainly due to swelling. They hydrogels can be classified into three main systems according to the generation of the confinement: (1) uniform and soft hydrogel attached on a stiff substrate [10–13], (2) stiff hydrogel layer on top of a compliant foundation [14], and (3) hydrogel with depth-wise cross-linking gradients [15–18] (Fig. 9.1). In the first system, a homogeneously cross-linked hydrogel is bonded to a stiff substrate. This system also includes polyelectrolyte multilayers (PEM) prepared by layer-by-layer (LBL) deposition. In the second system, a bilayer configuration consists of a rigid hydrogel layer on top of a compliant support. The support layer can be the same hydrogel or a different polymer/hydrogel. In the third system, a hydrogel film with a depth-wise gradient in cross-linking (or mechanical properties) is prepared on a substrate. The modulus gradient can be generated due to oxygen inhibition during UV curing process [18] or the infusion of reactive chemicals [15] into the hydrogel.

The possible mechanisms of pattern formation are depicted in Figs. 9.2 and 9.3. The general principle of the formation of surface instability involves lateral confinement in combination with an in-plane compressive strain  $\varepsilon_M$  (or mismatch strain) in the hydrogel film. The compressive strain  $\varepsilon_M$  can be caused by either volume expansion of the surface layer (Fig. 9.2a, path A) or shrinkage of the bottom layer (Fig. 9.2b, path B). When the compressive strain exceeds a critical value, the surface becomes unstable and spontaneously forms surface waves. In path A, the top layer

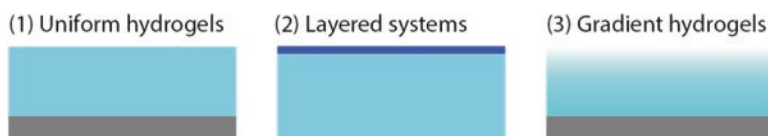


**Fig. 9.1** Three types of film structure systems widely used in generating surface instability patterns: (1) uniform hydrogels with homogeneous cross-linking fixed on a rigid substrate, (2) layered film structures consist of a stiff hydrogel on a compliant hydrogel, (3) hydrogels with a gradual change of physical properties (e.g., modulus or polymer concentrations) and/or chemical compositions along the film thickness

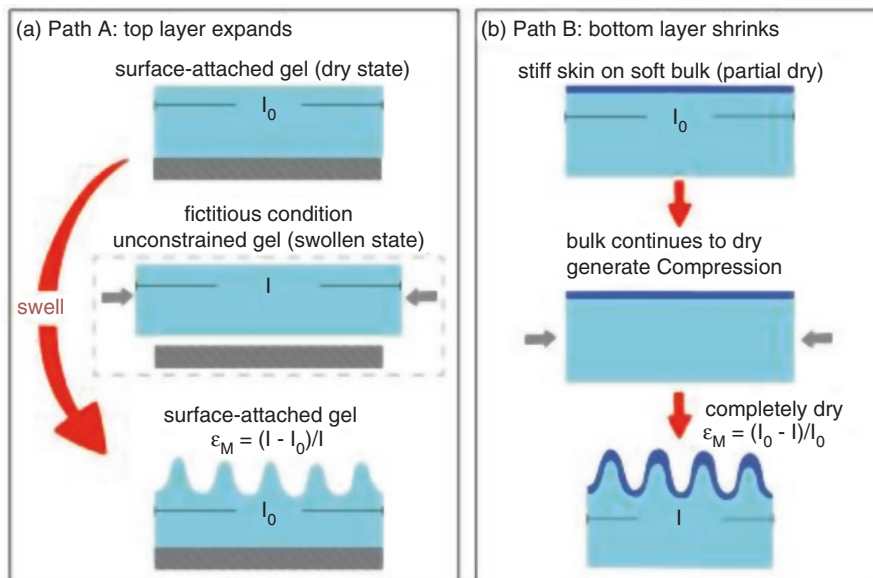


**Fig. 9.2** Schematic diagram showing the mechanism of the development of surface instability patterns in hydrogels due to mismatched strain. The mismatched strain can arise from (a) volume expansion of the top layer or (b) shrinkage of the bottom layer. Note that the image in the dashed box shows a fictitious step which helps to better understand. The real deformation steps are guided by the red arrows

with an initial length  $l_0$  is able to swell more than the bottom layer when subjected to an external stimulus, such as solvent diffusion or temperature change creating an anisotropic swelling. Let us first consider swelling of an unconstrained gel (shown in the dashed box). It can swell isotropically and reach its stress-free state with a final length of  $l$ . However, in the real situation, the gel is anchored on the substrate, which prohibits it from fully expanding to an equilibrium state. Therefore, the top layer is experiencing an equibiaxial compressive strain, which is equal to  $(l - l_0)/l$ . Note that the first two systems shown in Fig. 9.1 form surface instabilities normally through path A. For system 1, a uniform soft gel layer (as shown in blue in Fig. 9.2a) is bonded to a stiff substrate (as shown in gray), such as glass slides or silicon wafers. In the case of system 2, a stiff, swelling layer (blue) is placed on top of a soft non-swelling thick foundation (gray). The two layers in system 2 are usually composed of the same hydrogel but with different swelling and mechanical properties. In contrast, there are only a few reports showing surface instability of hydrogels induced through path B, and most of the observations are during drying/shrinking of hydrogels.

When compared to surface patterns produced in uniform hydrogel films, the wrinkles prepared in depth-wise gradient films (system 3) are much smoother. The gradients in physical and mechanical properties across the thickness of the hydrogels have been reported in two opposite directions. In the first case (Fig. 9.3a),

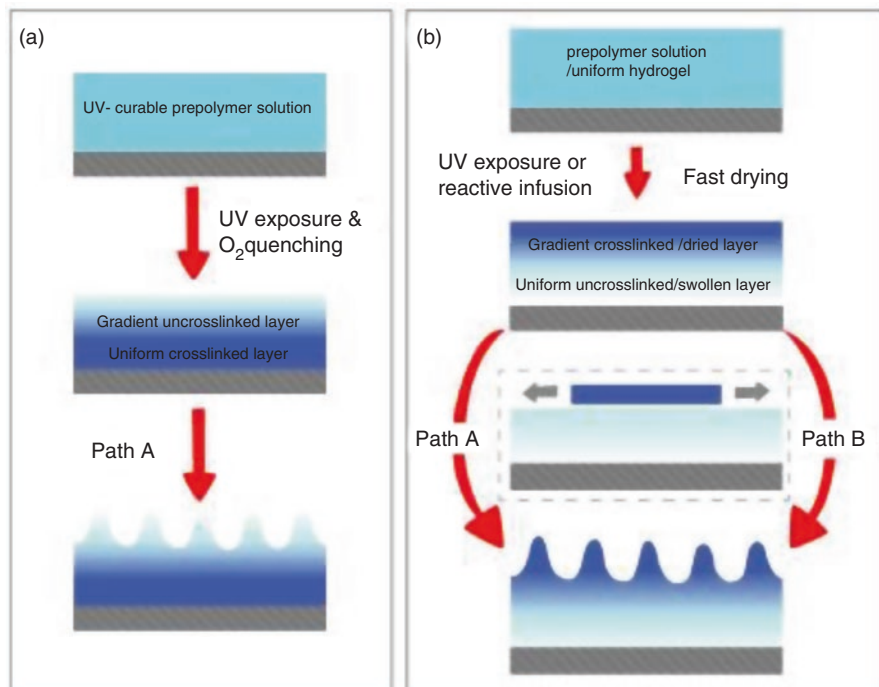


**Fig. 9.3** Schematic illustrations showing the strategies to develop depth-wise gradient in hydrogels. (a) An uncross-linked gradient top layer and a uniform cross-linked bottom layer. (b) A cross-linked or drier gradient top layer and a uniform uncross-linked or swollen bottom layer. The image shown in the dashed box indicates an intermediate state of the film at which the film is under tension

a modulus gradient with a soft top layer that gradually stiffened with depth was developed. Normally, the hydrogel films are prepared by depositing a UV-curable prepolymer solution and exposing the film to UV in the presence of oxygen. Due to the quenching of free radicals by oxygen, which inhibits cross-linking toward the top layer, a modulus gradient was developed. Subsequent immersion of the film in a “good solvent,” i.e., polymer is soluble in this solvent, induces anisotropic swelling of the film and, thus, produces biaxial compressive stress within the film, as described in path A. In the second case (Fig. 9.3b), a stiff skin layer forms at the surface above a soft foundation at the early stage of curing (path A) or drying (path B). In the case of the cure-induced gradient, the cured stiff skin layer is created by infusing reactive cross-linkers into the hydrogel film or by exposing the hydrogel film to a light with low penetration depth. Alternatively, fast-drying hydrogel at low humidity also experiences partial dehydration, which leads to the formation of a glassy skin layer. It should be noted that at this stage, the outer layer is drier or with higher cross-linking density and thus contracts more than the bulk. In other words, the skin layer is subject to a tensile stress (as shown in the dashed box) [19–20]. When the hydrogel film is immersed in a solvent, the compressive stress exerted by

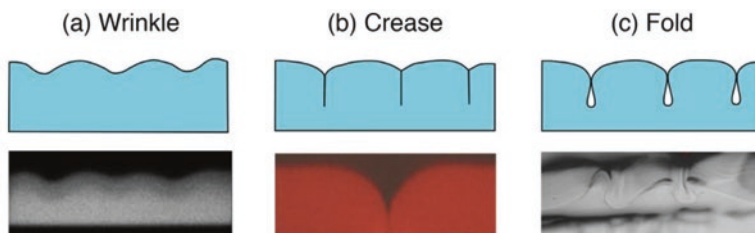


**Fig. 9.4** Schematics (top row) and optical images (bottom row) showing the three most common types of surface instabilities found in constrained hydrogels. The optical images show the cross section of (a) polyHEMA [17], (b) polyNIPAM [25], (c) polyNIPAM [14] hydrogels

the substrate progressively increases and finally overcomes the opposing tensile stress (path A). The explanation is similar to the mechanism first proposed by Basu et al. for acrylate coatings during the UV curing process [20]. Whereas in the drying hydrogel system, the contraction of the bulk due to subsequent drying results in the generation of compressive stress in the skin layer, which also leads to the formation of surface instability (path B). This phenomenon is similar to the poly(dimethylsiloxane) system in which a mechanically stretched poly(dimethylsiloxane) (PDMS) is exposed to UV/ozone radiation, thus creating a stiff oxidized surface layer, followed by strain release [21].

Considering the three main hydrogel systems described above, various modes of surface instabilities, including wrinkling, creasing, folding, period doubling, and ridging, were reported both experimentally and theoretically (Fig. 9.4). Wrinkles represent uniform and sinusoidal deformations. Creases are nonlinear deformations forming sharp self-contacting indentations with localized large strains [22–23]. Other instability modes such as folds and ridges also represent localized strains and are typically evolved from wrinkles. When the mismatch stress between the film and substrate is low and the applied strain is far beyond the onset of wrinkles, wrinkles double their period and form folds. In contrast, when the strain mismatch is high, wrinkles evolve into ridges, which form spaced-out and large aspect ratio peaks. The patterns arising from the surface instabilities can be either irreversible or reversible. Irreversible patterns are present after they are induced and can no longer be erased, while reversible patterns show the reversible formation of patterns when materials subject to cycles of the loading-unloading processes, such as swelling/drying or heating/cooling. The reversibility of the patterns is mainly dependent on the film thickness, the cross-linking degree, and the gradient, as well as the modulus of the substrate [24].

Wang and Zhao developed a general three-dimensional phase diagram using a plane-strain finite element model to define the conditions for each type of the surface instabilities with respect to three dimensionless parameters (Fig. 9.5). This phase diagram is originally designed for uniform layered hydrogels (system 1 and 2). For this system, the dimensionless parameters are film to substrate modulus ratio ( $E_f/E_s$ ), mismatch strain within the film  $\varepsilon_M$ , and normalized adhesion energy ( $\Gamma/E_s t$ ), where  $\Gamma$  is the adhesion energy per unit area between the film and substrate, and  $t$  is

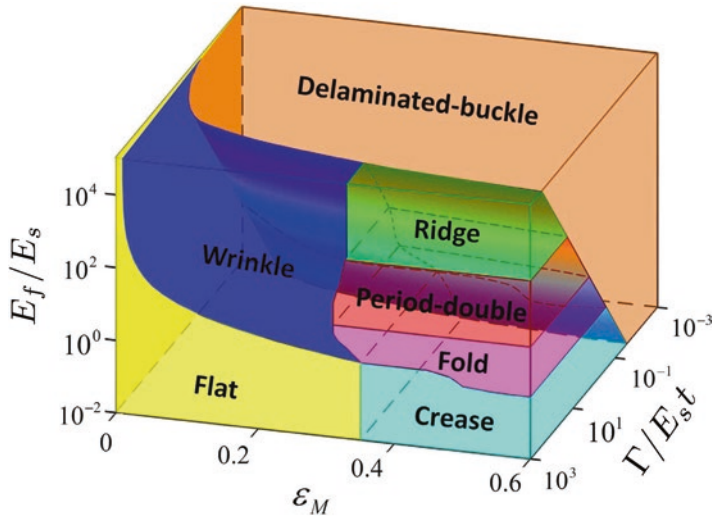


**Fig. 9.5** Numerically simulated phase diagram showing various types of surface instabilities determined by three dimensionless parameters: mismatch strain  $\epsilon_M$ , modulus ratio of the film and substrate  $E_f/E_s$ , and the normalized adhesion energy  $\Gamma/E_s t$  ( $t$  is the film thickness). (Reproduced with permission from Ref. [34])

the film thickness). The moduli of hydrogels are generally measured using an atomic force microscope or a tensile tester [16, 18, 26]. The mismatch strain within the hydrogel film can be measured by determining the linear expansion of unconstrained hydrogels with identical composition as the constrained counterpart [11]. The adhesion energy between the hydrogel and the substrate can be enhanced by treating the substrate with adhesion promoters (e.g., trimethoxysilane) [11, 17–18]. For well-bonded systems, hydrogels with  $E_f/E_s$  in the range of  $10^0$ – $10^4$  generally develop wrinkles when the mismatch strain is small ( $\epsilon_M = 0.05$ – $0.25$ ). A great example can be found in natural mucosal tissues, where surface wrinkling and folding are crucial for the biological function. Mucosae consist of a stiff and collagenous mucosal layer and a soft, loosely connected elastin and collagen submucosal layer constrained on a much stiffer muscular layer. Volumetric growth in the mucosal layer could lead to the formation of surface wrinkling or transform into folds or period double when mismatch strains become larger ( $\epsilon_M > 0.3$ ) [27]. Other biological tissues [28] and engineered hydrogels [14, 29] also show similar layered structures and wrinkling/folding phenomena. Unlike wrinkles and folds, creases are generally developed in uniform hydrogel films without hard skin [5, 9, 11]. Biot’s classical linear perturbation analysis failed to capture the critical condition for the onset of creases. Until recently, Hohlfeld and Mahadevan simulated the onset of creases numerically and found that a critical strain value  $\epsilon_M \approx 0.35$  [30], which does not depend on the modulus and thickness of the material. Many experimental studies showed remarkable agreement with this value [11, 31]. For instance, Trujillo et al. reported that the onset of creasing in swelling polyacrylamide-based hydrogels occurred at a critical strain equal to 0.33 [11].

It is worthwhile mentioning that it is not easy to directly measure the compressive strain  $\epsilon_M$  in the case of surface-attached hydrogels. For example, to calculate the compressive strain in constrained hydrogels, Trujillo et al. measured the linear extent of swelling for unconstrained hydrogels. However, they mentioned that it was difficult to handle the unsupported films due to the fragility of the films. The swelling ratio  $\alpha_c$ , defined as the ratio of the film thickness in a swollen state and in a dry state, is commonly used as an alternative method to determine the onset of surface instability. The range of the reported critical values is wide [32]. For example, Trujillo et al. reported a critical swelling ratio for the onset of creases of about 2 for the polyacrylamide hydrogel system [11], while Dervaux et al. found a low instability threshold of roughly 1.5 for their ring polyacrylamide model [5]. On the other hand, Guvendiren et al. found that  $\alpha_c$  is about 1.12 for the onset of wrinkling of the polyHEMA system [16]. Recently, Han et al. showed that  $\alpha_c$  of surface wrinkling observed for a model system of layer-by-layer PVP/PAA hydrogel was higher than 2 [33].

### 9.3 Commonly Used Hydrogel Systems for Surface Patterning

The formation of surface instability morphologies on a hydrogel surface is the result of a large change in osmotic pressure within the gel. The osmotic pressure can be varied by changing a variety of factors, such as solvent composition, temperature, pH of the solvent, ionic strength, etc. Here, we classify the external stimuli into three major types: (1) solvent, (2) temperature, and (3) others (such as electric field and light).

#### 9.3.1 Solvent-Induced Systems

##### 9.3.1.1 Polyacrylamide(pAAM)-Based

Polyacrylamide-based hydrogels are widely used as a model system for investigating surface instability since their mechanical and swelling properties can be easily tuned by controlling the chemical composition. The pAAM hydrogels are generally prepared by copolymerizing acrylamide monomers with anionic monomers, such as sodium acrylate (SA) in the presence of bifunctional cross-linkers (bisacrylamide), and chemically attached on a rigid substrate. The osmotic pressure and degree of swelling within the pAAM/SA gels can be varied by adjusting the amount of sodium acrylate monomers, and the film modulus is varied by changing the concentration of monomers and cross-linkers. Pioneering works by Tanaka et al. have demonstrated the kinetic evolution of surface patterns of an ionized acrylamide gel in a petri dish swelled in water. They suggested that the critical osmotic pressure for the onset of

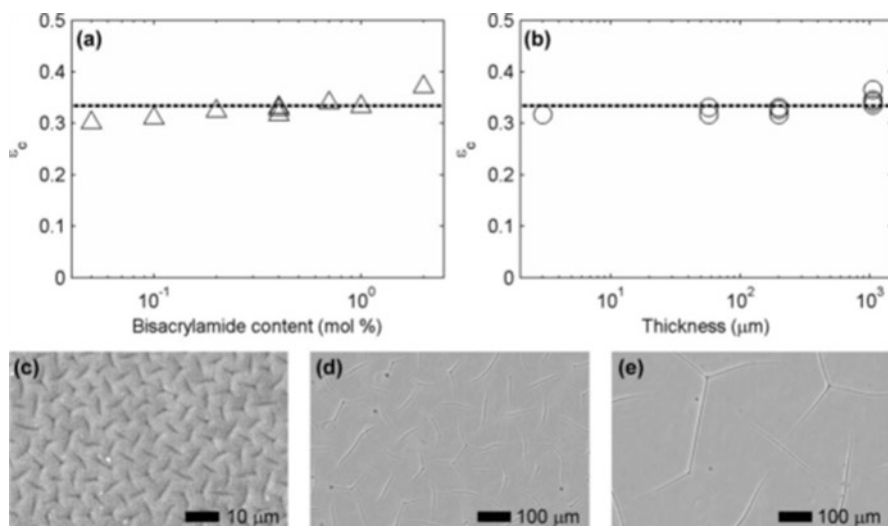


**Fig. 9.6** The critical strain for the onset of creasing as a function of the (a) concentration of cross-linkers (at a constant thickness of 200  $\mu\text{m}$ ) and (b) gel thickness at a constant degree of cross-linking (0.4 mol % bisacrylamide). In both cases, the critical strain varies only slightly, which is in good agreement with the prediction of Biot, as shown by the dashed lines. (c–e) Optical images of crease structures as a function of the initial film thickness of (c) 3  $\mu\text{m}$ , (d) 40  $\mu\text{m}$ , (e) 160  $\mu\text{m}$ . (Reproduced with permission from Ref. [11])

surface instability depends on Young's modulus of the gel but independent of the gel thickness [9]. Later, Trujillo et al. used polyacrylamide copolymer hydrogels as a model system to investigate the critical condition for the onset of creasing (Fig. 9.6) [11]. They found that the critical strain was  $\varepsilon_M \approx 0.33$  (0.30–0.37) and the swelling ratio was  $\alpha_c \approx 1.5$ –2. These values only varied slightly as the film modulus changed from 0.6 to 24 kPa and were independent of the investigated gel thickness (3  $\mu\text{m}$ –1 mm). The value of  $\varepsilon_M$  agrees well with the theoretical predictions proposed by Biot for rubber under equibiaxial compression using linear perturbation analysis [35]. In addition, results obtained from a prior experimental study of rubber with moduli on the order of 1 MPa swelled in n-decane showed an almost identical value of  $\varepsilon_M$  [36], indicating that this critical strain value is nearly universal for swell-induced surface instability in confined polymer layers.  $\varepsilon_M$  may increase when scaling down the film thickness as the capillary force and elasticity become comparable. A follow-up study by the same research group attempted to elucidate the effect of creased soft substrate on stem cell behavior [37]. The results showed that neural stem cells can sense the surface creases and formed neurite branches along the creases, while the cells on the smooth pAAM substrate uniformly attached and differentiated.

Other interesting instability behaviors have been found when arranging layers of pAAm/SA hydrogels with dissimilar swelling and mechanical properties.

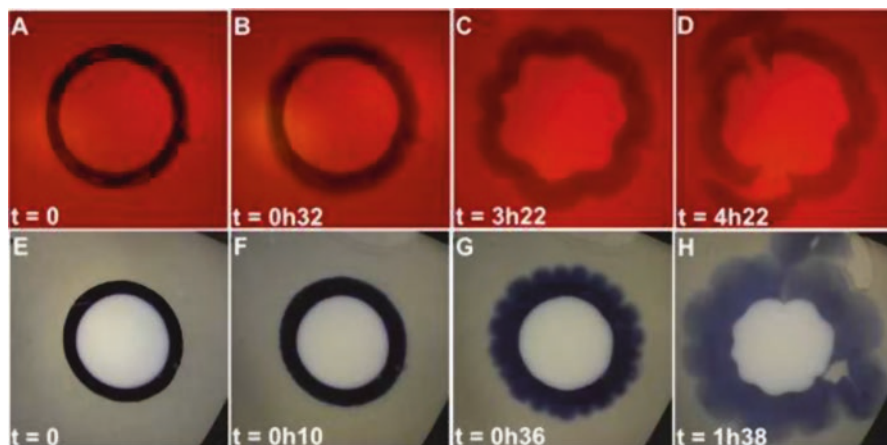


**Fig. 9.7** Evolution of two systems composed of two parts: a neutral hydrogel in the center (diameter  $A$ , elastic modulus  $\mu_I$ ) and a swelling hydrogel layer (thickness  $H$ , elastic modulus  $\mu_{II}$ ). Both systems have a similar initial ratio of  $H/A \sim 0.26\text{--}0.27$  but with different ratio of elastic modulus. (**A–D**)  $\mu_I \lesssim \mu_{II}$ , a buckling pattern appears in the ring and at the inner interface; (**E–H**)  $\mu_I \gtrsim \mu_{II}$ , only the ring forms sharp creases. (Reproduced with permission from Ref. [5])

Folding was demonstrated by chemically bonding two layers of pAAM/SA gels with a stiff and swelling layer on top of a soft and non-swelling layer [29]. In the study, a numerical model for predicting equilibrium folding configurations was proposed, in which the surface instability was represented by a set of self-avoiding rods on a Winkler foundation. The calculated results showed that the amplitude and wavelength of the surface oscillations exhibited a linear dependence of the film thickness and the numerical equilibrium configurations show closer proximity with experimental results than the classical buckling analysis. Other arrangements have been reported including strip geometry, in which two gels were connected by their edges [38]; and the corona geometry, in which a thin corona of the soft gel was attached to a disk of stiff gel [5]. For example, Dervaux et al. designed an artificial tumor model using two layers of pAAM/SA arranged in a corona geometry (Fig. 9.7) [5]. Various patterns were observed in the swelling layer or at the free boundary by changing the ratio of the modulus and thickness between the corona and center region. This study shed light on the correlation between cell geometry, mechanical properties, and their morphological evolution and metastasis potential.

Pattern formation and evolution have also been investigated during the shrinking process. In contrast to the swelling pattern, the shrinking patterns are metastable, have short lifetimes, and are less studied [39]. Li et al. investigated the shrinking patterns of pAAM/SA in acetone/water mixture [39]. When the concentration of acetone (a bad solvent for pAAm) increased, patterns including hexagons, grains, and bubbles were observed due to the formation of a dense surface during the shrinking process.

### 9.3.1.2 Poly(Hydroxyethyl Methacrylate) (polyHEMA)

PolyHEMA hydrogels have found extensive uses in biomedical field, such as soft contact lenses [40], bone implants [41], and drug delivery system [42–43] because they are highly biocompatible, transparent, and resistant to heat and acid/alkaline hydrolysis [44]. The ability to generate patterned structures in this widely used hydrogel would enable remarkable progress in their applications. The procedure to develop wrinkled patterns in polyHEMA films with a modulus gradient along the film thickness was first reported by Guvendiren et al. using a two-step UV curing process [18]. The procedure involved the irradiation with UV light to a solution composed of HEMA monomers and photoinitiators (Darocur 1173) that was then followed by the second round of UV exposure in the presence of air after adding additional photoinitiator and cross-linker (ethylene glycol dimethacrylate, EGDMA). Due to oxygen diffusion during the UV cross-linking process, a modulus gradient along depth was created. Upon swelling, various instability patterns including random worms, lamellae, peanuts, and long-range ordered hexagonal patterns were observed by varying concentrations of cross-linker, and the wrinkle wavelengths were found to be dependent only on the initial film thickness. In addition, they found that as the cross-linker concentration was increased, the modulus gradient increased and hence the critical osmotic pressure to induce wrinkles. Therefore, the critical osmotic pressure and the resulted patterns can be easily tuned by the modulus gradient. A second publication by the same research group examined the kinetics of the wrinkle evolution at the early stage and at the equilibration states in water (Fig. 9.8) [16]. They found that the characteristic wavelength of the patterns increased with the square root of time at early stages and reached an equilibrium plateau. The swelling ratio  $\alpha_c$  for the onset of wrinkling was reported as  $\sim 1.12$ , which was independent of the investigated EGDMA concentration but decreased with increasing film thickness. In contrast, the swelling ratio at the equilibrium state  $\alpha_c$  decreased significantly, from 2.55 to 1.2, with increasing cross-linker concentration (from 0 to 3 wt.%). Another study from the same research group examined the transition of wrinkling to creasing instability by manipulating solvent quality [17]. In a good solvent, such as alcohol and alcohol/water mixture, the network was highly swollen. The resulting large volume change induced surface instability from wrinkling to creasing (Fig. 9.8). By changing the ratio of ethanol and water, reversible switching between wrinkling and creasing was obtained. In addition, they found that the swelling ratio for the onset of creasing depended on cross-linker concentration:  $\alpha_c \approx 2$  and 1.3 for gels with 1 and 3 wt% EGDMA, respectively.

The polyHEMA-wrinkled patterns have been used for experiments involving cell culture. Wrinkling of lamellar and hexagonal patterns was used by Guvendiren et al. for the study of stem cell response to surface topography [45]. By culturing human mesenchymal stem cell (hMSCs) on hydrogels with uniform mechanics using a replica molding technique, they showed that hMSCs exhibited high aspect ratios and differentiated into an osteogenic lineage on lamellar wrinkles, while hMSCs cultured on hexagonal patterns led to rounded shape with low spreading and differentiated toward an adipogenic phenotype (Fig. 9.9). Moreover, Zhao and coworkers showed that the patterned nonadhesive polyHEMA hydrogel films

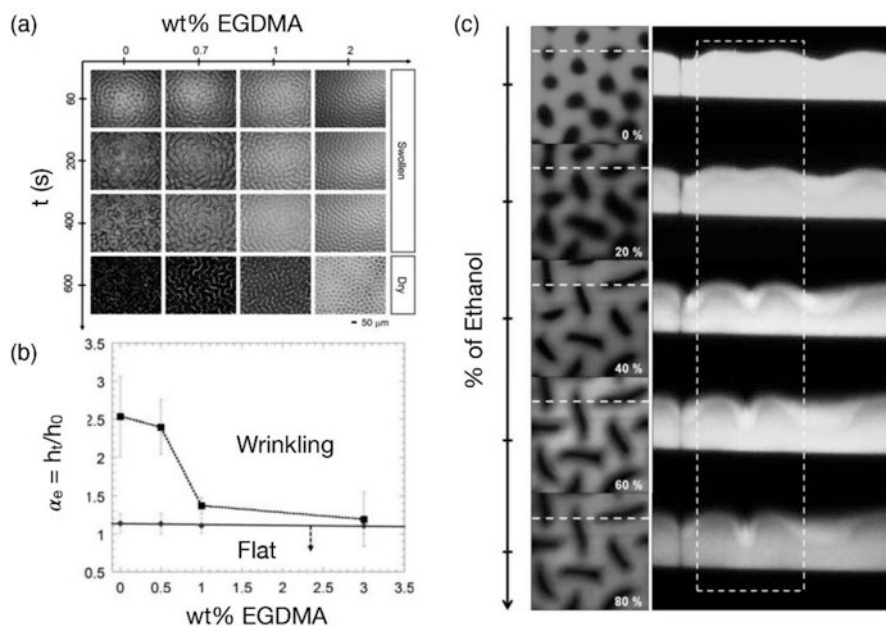


**Fig. 9.8** (a) Optical microscopy images showing the evolution of swelling patterns of polyHEMA hydrogels as a function of the degree of cross-linking. (b) The dependence of equilibrium expansion ratio ( $\alpha_e$ ) on cross-linkers concentration. The solid line shows the critical expansion ratio ( $\alpha_c$ ) for the onset of wrinkling. (c) Confocal microscopy images of the cross sections of polyHEMA films (3 wt.% EGDMA) showing the dynamic evolution from wrinkling to creasing instability when ethanol was gradually added to the system. (Reproduced with permission from Ref. [16] (a and b) and [17] (c))

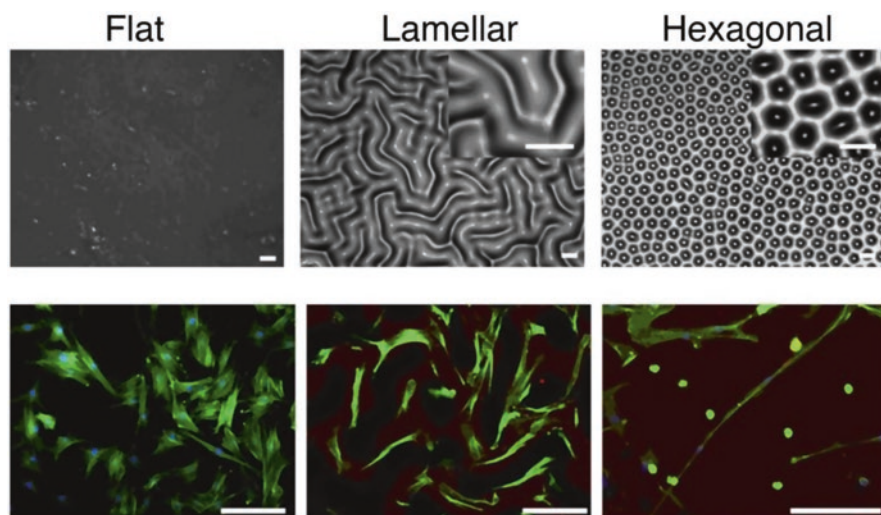


**Fig. 9.9** (Top panel) polyHEMA gels containing 1 wt.% EGDMA with different surface patterns. Scale bars are 50 mm (bottom panel). Fluorescent microscopy images of hMSCs seeded on the corresponding hydrogel patterns. Scale bars are 100 mm. (Reproduced with permission from Ref. [45])

were allowed for the high-throughput generation of multicellular spheroids [46]. Thousands of monodisperse spheroids could be easily produced within a single polyHEMA-coated well.

Recently, Gu et al. developed a simpler one-step UV curing method to fabricate the wrinkling patterns on the polyHEMA system [47]. The one-step method involved introducing linear polyHEMA directly into the solutions containing HEMA monomers, cross-linkers EGDMA, and photoinitiators Darocur 1173 and exposing the solution to UV light only one time. The addition of linear polyHEMA allowed for a 3D physical network to form in the solution which stabilized the skin layer and prevented the surface of the film from becoming corrugated after the UV curing process. With the non-corrugated, smooth PHEMA films, the group was able to generate various wrinkling patterns, including the types presented by Guvendiren et al., by changing both the linear polyHEMA and cross-linker concentrations. Li et al. demonstrated another method of creating a gradient of cross-linking density within the polymer films via reactive silane infusion into hydrogel films. During the infusion process, silane reacted with the hydroxyl groups of the polyHEMA polymer and condensed with itself, resulting in a gradient cross-linked top layer and a uniform uncross-linked bottom layer. Subsequent solvent swelling triggered the formation of nano- to micro-scale patterns [15].

### 9.3.1.3 Poly(Vinyl Alcohol) (PVA)

Inspired by the wrinkling behavior observed when human skin is exposed to water for prolonged periods of time, Zeng et al. created various moisture-sensitive film-substrate bilayer devices, composed of a UV-cross-linked poly(vinyl alcohol) PVA film attached to a soft polydimethylsiloxane (PDMS) substrate, to study and control the reversibility and stability of wrinkles [24]. By adjusting the thickness of the PVA film, PVA cross-linking gradient, PVA/PDMS thickness ratio, and PDMS modulus, three distinct types of moisture-induced wrinkling dynamics were obtained: (A) completely reversible wrinkles, (B) irreversible wrinkles, and (C) completely irreversible wrinkles. The film-substrate bilayer device capable of exhibiting completely reversible wrinkling dynamics used a thin and stiff PVA film that was uniformly cross-linked and a thick and soft PDMS. After exposing to a cool mist, wrinkles formed on the PVA film disappeared after drying and reappeared after moisturizing again. The irreversible wrinkling system used the same film and substrate properties used in system A but instead used an uncross-linked PVA film. Wrinkles were observed after the initial exposure to moisture but disappeared after drying and never returned after further exposure to moisture. As described by Zeng et al., the uncross-linked PVA film was able to induce wrinkles, but due to the film not being cross-linked, during the initial exposure to moisture, the modulus continued to decrease until the wrinkles disappeared. Additionally, the wrinkles could not form after further exposure to moisture due to the reduced swelling strain of the PVA and its inability to create the necessary critical compressive stress to induce wrinkles. Finally, the completely irreversible wrinkling system used a thick PVA

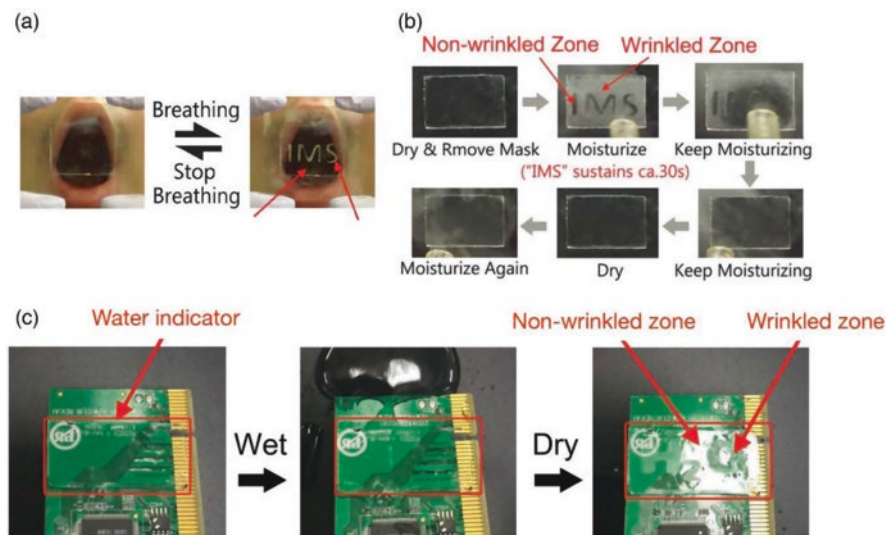


**Fig. 9.10** (a) The hidden pattern “IMS” was reversibly revealed by breathing on type-A sample. (b) The irreversible wrinkling response was demonstrated on type-B PVA films. (c) A type-C PVA film which acted as a water indicator was attached to a circuit board. After water exposure and drying the film, the hidden H<sub>2</sub>O pattern appeared. (Reproduced with permission from Ref. [24])

film with a cross-linking gradient caused by oxygen inhibition at the surface and a tougher PDMS substrate with a higher elastic modulus. The resulting dynamics consisted of wrinkles that remained even after drying or moisturizing again. The cross-linking gradient allowed the PVA film to exhibit a swelling gradient where the swelling degree gradually decreased along the film depth. When exposed to moisture, the less swollen bottom layers exerted compressive forces to the top layer that were enough to reach the critical stresses required to induce wrinkles. These moisture-responsive systems show many potential applications in optical devices, such as anti-counterfeit tabs, encryption devices, moisture indicators, light diffusers, and antiglare films (Fig. 9.10).

Huraux et al. demonstrated an example of drying-induced morphology on chemically cross-linked PVA gels drying with a free end or with the gels fixed at a constant length [19]. The surface formed wrinkles when drying quickly at low humidity, while the surface remained flat when drying at high humidity. The authors attributed these findings to the crossing of the glass transition temperature of the top hydrogel layer when the drying is fast enough. They proposed the wrinkling was formed following the mechanism that includes three successive steps. First, a concentration gradient was formed due to evaporation from the surface, and the outer skin layer was under stretching. Next, the rapid solvent evaporation caused the skin layer to cross the glass transition temperature, resulting in the formation of a glassy skin layer and the removal of the in-plane tensile tension within the layer. Subsequent solvent evaporation and contraction of the soft bulk layer compressed the glassy skin layer and triggered the formation of wrinkling.

### 9.3.1.4 Layer-By-Layer Assemblies

In recent years, many studies have focused on ultrathin hydrogel membranes using layer-by-layer (LBL) assembly approach. LBL hydrogel films have been employed for many applications, such as biosensors [48], biocoatings [49], and controlled release [50–51]. The films are fabricated by depositing alternating layers which are bonded through complementary interactions, such as electrostatic attraction, hydrogen bonding, and host-guest interactions [52]. The swelling properties, and thus the resulted surface patterns, can be adjusted by ion type, ionic strength, charge density, film thickness, and deposition method [53]. Swelling-induced surface instability has been observed for hydrogen-bonded LBL multilayer films based on poly(vinyl pyrrolidone) (PVP) and poly(acrylic acid) (PAA) in ethanol/water mixtures (Fig. 9.11) [33]. By changing the composition and pH of the solvent, wrinkles of small and shallow holes were developed via a nucleation-growth process. Unlike most other hydrogels, where critical swelling ratio  $\alpha_c$  is insensitive to film thickness [11–12], the critical swelling ratio increased as film thickness increased. It is interesting that in this system, the patterns formed on the constrained hydrogel films disappeared at equilibrium swelling. Normally the restoration of a flat surface when fully swollen is observed only for unconstrained hydrogels. This can be explained by the fact that the thickness of the swollen layer increases with the advancement of swelling, leading to the disappearance of swelling mismatch and thus the relief of compressive stress. The unusual phenomenon found in the constrained PVP/PAA hydrogel films was caused by a different way, in which the rearrangement of hydrogen bonding interactions was recovered between the PVP and PAA chains, leading to the relief of compressive stress. Another example that takes advantage of hydrogen bonding LBL

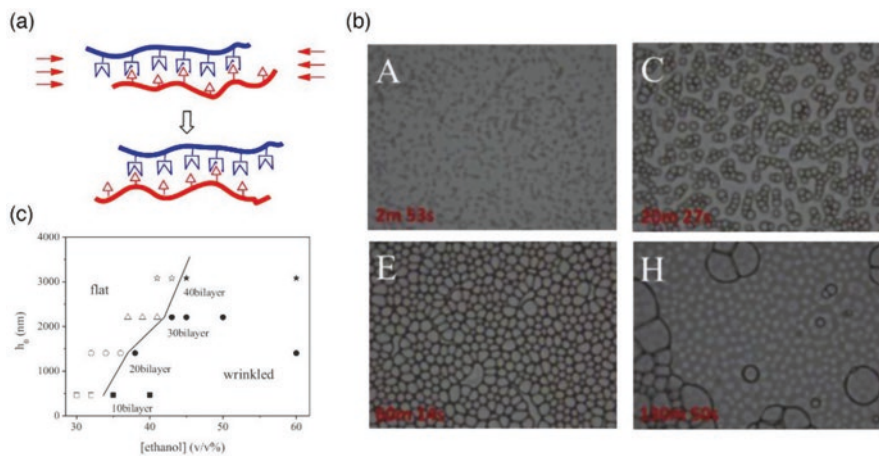


**Fig. 9.11** (a) Schematic diagram showing the relief of the compressive stress through the rearrangement of the dynamic network of PVP/PAA layers. (b) Time evolution of instability morphology of a PVP/PAA 20 bilayer films soaking in 40% ethanol/water mixture. (c) Phase diagram showing the transition between the flat and wrinkled surface with different film thickness and ethanol-water ratio. (Reproduced with permission from Ref. [33])

assembly to produce different wrinkling patterns is reported by Hou et al. [53]. Hou and coworkers fabricated (PAA/PEG) $n$  on the PDMS substrate, followed by covalently cross-linking with heat. During heating, the water molecules which act as plasticizers were removed, leading to a sharp increase of Young's modulus of (PAA/PEG) $n$  films. Wrinkles were formed upon cooling due to thermal expansion mismatch between the rigid cross-linked (PAA/PEG) $n$  and the soft PDMS substrate. A sequential and reversible evolution of surface patterns was observed during swelling and deswelling (drying at different elevated temperatures). When immersed into a pH 2.5 aqueous solution, the thermal-induced primary labyrinth wrinkles first disappeared, and then highly ordered hexagonal dimple array appeared. With longer swelling duration, segmented labyrinth patterns were formed. Different surface wrinkling patterns can be reversibly generated by drying, and the resulted deswelled patterns can be finely tuned depending on the swelling-induced patterns and the drying temperatures.

### 9.3.1.5 Poly(Ethylene Glycol)-Based

Taking advantage of swelling-induced wrinkling, Chan et al. developed a Responsive Surface-wrinkled Adhesive (RSA) using photopolymerized polyethylene glycol methyl acrylate hydrogels uniformly cross-linked with polyethylene glycol dimethacrylate (Fig. 9.12) [54]. The hydrogels were formed on a hemispherical-shaped

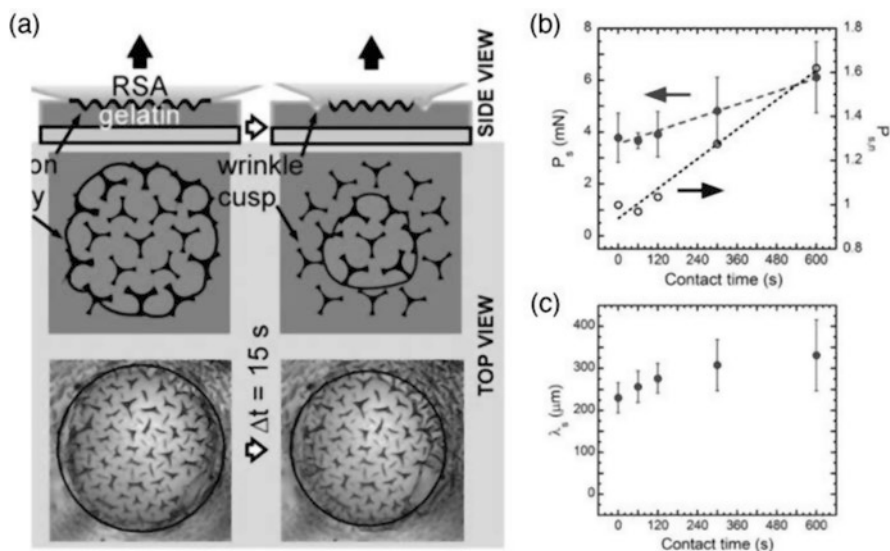


**Fig. 9.12** (a) Separation process of the RSA-gelatin surface. (b) Maximum separation force ( $P_s$ ) and the normalized separation force ( $P_{s,n}$ ) as a function of contact time for the RSA-gelatin surface. (c) Changes in wavelength ( $\lambda_s$ ) of wrinkles at  $P_s$  versus contact time. (Reproduced with permission from Ref. [54])

cross-linked PDMS mold and brought into contact with a gelatin hydrogel for different periods of time. Enhanced adhesion was observed as the contact time with the gelatin layer was increased. It is commonly known that the increase in adhesion with contact time for dry pressure-sensitive adhesives is due to interdiffusion of polymer chains at the interface, which is highly dependent on chain relaxation time [55]. However, this explanation did not satisfy their observation since the relaxation times of both the RSA and gelatin chains ( $\sim 1$  s for RSA and  $\sim 0.01$  s for gelatin) are much shorter than the investigated contact times (0, 60, 120, 300, and 600 s). Instead, the authors attributed the enhancement in adhesion to the disruption of crack propagation by locally pinning the crack front by the wrinkled topography. By controlling the time-dependent amplitude and wavelength of wrinkles, the interfacial adhesion can be controlled. This study provided an alternative adhesion mechanism, making it an excellent method for the future development of biomedical adhesives for soft tissues.

### 9.3.2 Temperature-Induced

#### 9.3.2.1 Poly(*N*-Isopropylacrylamide)(polyNIPAM)-Based

Poly(*N*-isopropylacrylamide) (polyNIPAM) is the most extensively studied thermo-responsive hydrogels for biomedical applications since its low critical solution temperature (LCST) in water is very close to body temperature [56]. In addition, these hydrogels exhibit fast swelling and deswelling in response to temperature change, which make them an ideal platform to study thermal-induced surface instability. The LCST of polyNIPAM in water is around 32 °C, below which, the polymers swell and above which, the polymers shrink. Copolymerization of polyNIPAM with a charged monomer, such as sodium acrylate (SA), is commonly used to increase polymer-water interactions and shift the LCST to a higher temperature, which allows for bringing the transition temperature closer to physiologically relevant temperatures. Earlier findings of constrained gels can be traced back to Li et al. [57], demonstrating the dependence of temperature, time, external constraint, and thermal path, on the shrinking patterns of polyNIPAM-SA gels. The mechanism of the formation and evolution of patterns in shrinking gels showed marked differences than in swelling gels. When gel shrinks, a dense skin layer is formed shielding a swollen gel core. The inhomogeneity in osmotic pressure and polymer concentration in the exterior and interior of the gel drives the formation of patterns. The results showed that the patterns evolved from hexagonal and grain to bubble patterns at temperatures below, near, and above the LCST (Fig. 9.13). Unlike swelling patterns, shrinking patterns are in general metastable or unstable and hard to preserve. The hexagonal, grain, and bubble patterns persisted only for weeks, around 5 h, and about 2 days, respectively. They further employed two different thermal paths: In the first approach (A), gels were abruptly heated from room temperature to

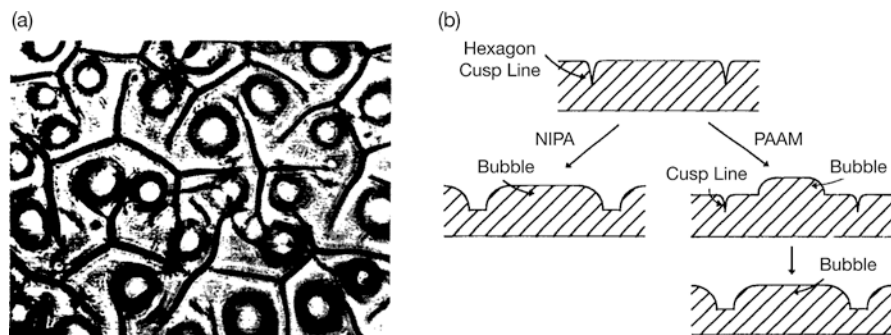


**Fig. 9.13** (a) The appearance of bubble patterns during thermal shrinkage in the polyNIPAM-SA gels. (b) Schematic diagram comparing the formation of bubble patterns in polyNIPAM and pAAM hydrogels. (Reproduced with permission from Ref. [57])

different temperatures (above  $T_c$ ) and equilibrated for 24 h; In the second approach (B), gels were heated in a stepwise manner at  $1\text{ }^\circ\text{C}$  per 24 h from room temperature to higher temperatures. Comparing patterns formed under these two routes revealed that the wavelength in A is smaller than that in B, no grain patterns were observed in B, and the wavelength of the hexagonal patterns remained the same in A, while the wavelength increased as the temperature was raised in B. They attributed the difference in the length scale of patterns to differences in shrinking kinetics. The authors also compared the results to the shrinking patterns formed in constrained pAAM gels in acetone/water mixtures [39].

To direct swell-induced crease locations, Kim et al. attached polyNIPAM-SA hydrogels on the substrates with predetermined topographic features [58]. The patterns on the underlying substrates translated into the crease patterns in the hydrogels. At room temperature, the gel swelled and formed self-contact creases, hiding certain areas within the folds. At  $\sim 37\text{ }^\circ\text{C}$ , the gel deswelled and surface unfolded, exposing the hidden areas and allowing for deposition of biochemically functionalized polyelectrolytes (e.g., poly(L-lysine), peptides, enzymes, and biomolecular ligands) (Fig. 9.14). The hydrogels able to form patterns at desired locations and reversibly hide and display chemical functionality in response to temperature changes show great potential for applications in dynamic cell culture systems. The same research group further investigated the effect of quench depth on the creasing behavior [12]. For shallow quench depth beyond critical strain for the onset of creasing, a crease formed through nucleation and growth, where heterogeneous defects served as nucleation sites. The presence of defects also restricted creases from rearranging and caused strong cycle-to-cycle memory for the crease locations. Precise measurements of critical strain for the onset of creasing  $\epsilon_M$  for different film thickness were achieved through measurement of isothermal crease growth velocities at different quench depths. Results showed that as film thickness was reduced, the  $\epsilon_M$  slightly increased since the energy barrier caused by gel/water interfacial tension was more pronounced. The transition from wrinkles to folds has been

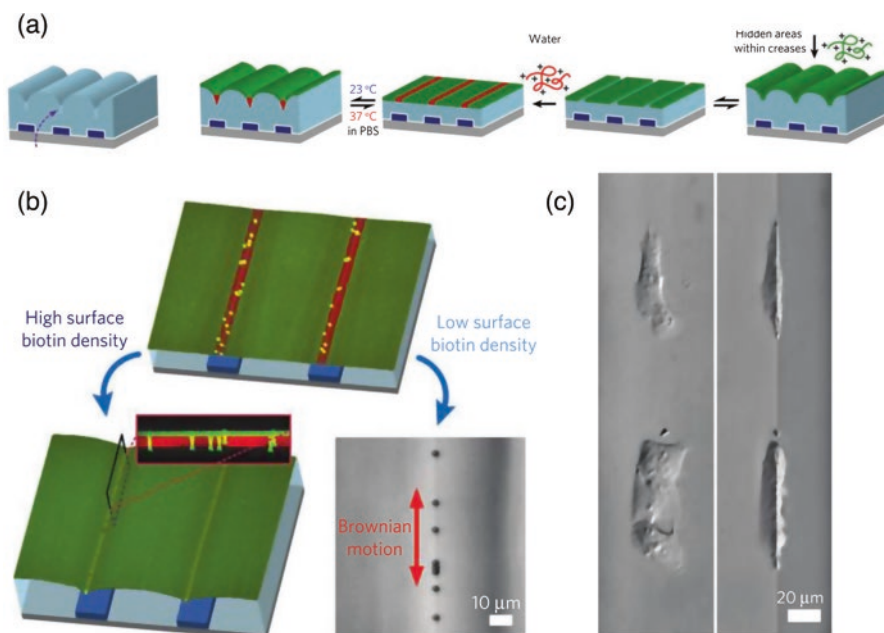


**Fig. 9.14** (a) Fabrication process of polyNIPAM scaffolds with dynamic display of patterns. (b) Streptavidin-coated beads selectively adhered to the biotin-functionalized region (top) at 37 °C. Depending on the biotin density, the beads are either encapsulated within creased (bottom left) or detached from the surface (bottom right) when the scaffold was cooled to 23 °C. (c) Optical microscopic images showing the epithelial cells selectively adhered to RGD-functionalized regions at 37 °C (left) and encapsulated within creases at 23 °C (right). (Reproduced with permission from Ref. [58])

reported on bilayer hydrogels composed of a thin crust of silica networks copolymerized with polyNIPAM and a soft bottom layer of polyNIPAM [14]. Reversible wrinkles appeared on cooling, and folding occurred at much lower temperatures. The bilayer hydrogels also showed the peristaltic motion of wrinkles. By controlling the shape of the hybrid silica layer (triangular shape) as well as the cooling rate and temperature, the speed and direction of the peristaltic motion can be modulated, which shows great potential as soft actuators.

### 9.3.3 Other Types of Stimuli

Other methods which have been reported recently include electric field- and light-induced instability. The use of light and electric field as an external stimulus has the advantages of being easy to employ and generating surface instabilities with

rapid stimuli responses. Xu and Hayward electrically actuated the formation of creases and craters in anionic polyNIPAM hydrogels using low voltages (2–4 V) [25]. The anionic polyNIPAM hydrogel was first deposited on micro-patterned gold electrodes and then swelled in the phosphate-buffered saline (PBS) solution at selective temperatures, to yield a swelling ratio slightly below the onset of creasing. The subsequent application of voltage to underlying electrodes generated creases above the anodes, but not on the cathodes. Observations showed that the electrically driven creases were deeper (crease depth reaches ~70% of the swelled gel thickness) and occurred substantially faster (within a few seconds) compared with the thermally induced patterns. However, the underlying mechanism for the rapid formation of deep electrically driven instability remains unclear, and thus further investigation is required. The same research group reported light-responsive creases based on hybrid gels of anionic polyNIPAM and iron oxide nanoparticles [59]. The authors followed the same approach used in the previous study [58] to create reversible hide and display stripe patterns first. Due to the incorporation of light-absorbance nanoparticles and their strong light-to-heat conversion properties, the heat was generated in hydrogels upon blue light exposure for 3 min. Gels were then deswelled, causing the surface to unfold and expose the hidden areas. After removal of the blue light, creases were reformed over approximately 3 min. The hybrid hydrogel system offers a novel approach to creating a reversible transition between flat states and crease patterns in selected regions by simply exposing light to the interested area.

## 9.4 Conclusion and Outlook

In summary, many interesting instability patterns and potential applications in hydrogel systems are discussed in this chapter, which are summarized in Table 9.1. A variety of patterns with a different shape, wavelength, and amplitude can be easily generated by manipulating the layer properties (uniform, bilayer, and gradient) and different external stimuli (solvent, thermal, electric field, or light). In particular, recent research has focused on the utilization of hydrogel instability patterns for applications in tissue engineering due to their unique characteristics similar to biological soft tissues. In spite of the extensive work that has been reported, however, many challenges still exist which need further investigation. Expected future studies include large-scale fabrication with precise control of surface patterns; hydrogel exhibiting faster response kinetics (especially for thick films); preparation of patterns at nanometer-scale size; development of “smart” hydrogels with switchable instability patterns; and last but not least, creating surface instability patterns in three-dimensional systems, which could potentially expand their applications.

**Table 9.1** Types of hydrogel, surface instability patterns, and potential applications reported in different hydrogel configurations

Layer structure	Top layer	Substrate	Patterns	Stimuli	Applications
<i>Uniform</i>	pAAM [5, 9–12, 15, 37, 39], polyNIPAM [25], [57–59], PVP/PAA LBL films [33], PAA/PEG LBL films [53], PEG-based [54]	Non-swelling PAAM [5], glass slide [10–12, 37, 54, 58–59], petri dish [9], cross-linked PDMS [53–54], silicon wafers [25, 33]	Creases [5, 9–12, 25, 37, 58–59], wrinkles [33, 53–54]	Solvent (swell-induced) [5, 9–12, 33, 37, 53–54], solvent (shrink-induced) [39], thermal (swell-induced) [25, 58–59], thermal (shrink-induced) [57], light [59], electrical field [25]	Artificial tumor models [5], biomedical adhesives [54], dynamic substrates for cellular biology [37, 58], voltage/light-switchable active surfaces [25, 59]
<i>Layered</i>	pAAM [29], hybrid silica/polyNIPAM gel [14], stiff PVA [24]	Soft/non-swelling pAAM [29], polyNIPAM [14], PDMS [24], glass slide [58],	Wrinkles [14, 24], folds [14, 29]	Solvent (swell-induced) [24, 29], thermal [14]	Soft actuators [14], optical devices triggered by moisture [24]
<i>Gradient</i>	polyHEMA [15–18, 45–47, 60], PVA [24], dried PVA [19],	Silicon wafers [15, 60], glass slides [17–18, 45–47, 61], PDMS [24], soft PVA [19]	Wrinkles [15, 16, 18, 19, 24, 45–47, 60], creases [17]	Solvent (swell-induced) [15–18, 24, 45–47, 60], solvent (shrink-induced) [19]	Cell culture substrates [45], optical devices triggered by moisture [24], high-throughput generation of cellular spheroids [46]

## References

1. A.E. Shyer, T. Tallinen, N.L. Nerurkar, Z. Wei, E.S. Gil, D.L. Kaplan, C.J. Tabin, L. Mahadevan, Villification: How the gut gets its villi. *Science* **342**(6155), 212 (2013)
2. G. Limbert, E. Kuhl, On skin microrelief and the emergence of expression micro-wrinkles. *Soft Matter* **14**(8), 1292–1300 (2018). <https://doi.org/10.1039/C7SM01969F>
3. T. Tallinen, J.Y. Chung, J.S. Biggins, L. Mahadevan, Gyrfication from constrained cortical expansion. *Proc. Natl. Acad. Sci.* **111**(35), 12667 (2014)
4. P. Ciarletta, Buckling instability in growing tumor spheroids. *Phys. Rev. Lett.* **110**(15), 158102 (2013)
5. J. Dervaux, Y. Couder, M.-A. Guedeau-Boudeville, M. Ben Amar, Shape transition in artificial tumors: From smooth buckles to singular creases. *Phys. Rev. Lett.* **107**(1), 018103 (2011)
6. J. Rodríguez-Hernández, Wrinkled interfaces: Taking advantage of surface instabilities to pattern polymer surfaces. *Prog. Polym. Sci.* **42**, 1–41 (2015). <https://doi.org/10.1016/j.progpolymsci.2014.07.008>
7. S.E. Sheppard, F.A. Elliott, The reticulation of Gelatine. *J. Ind. Eng. Chem.* **10**(9), 727–732 (1918). <https://doi.org/10.1021/ie50105a018>

8. P. Thirkell, S. Hoskins, *Continuous Tone Digital Output, Using Archival Proven Printing Methods and Materials* (Institute of Physics, London, 2003), p. 24
9. T. Tanaka, S.-T. Sun, Y. Hirokawa, S. Katayama, J. Kucera, Y. Hirose, T. Amiya, Mechanical instability of gels at the phase transition. *Nature* **325**, 796 (1987). <https://doi.org/10.1038/325796a0>
10. Q. Du, Y. Guan, X.X. Zhu, Y. Zhang, Swelling-induced surface instability patterns guided by pre-introduced structures. *Soft Matter* **11**(10), 1937–1944 (2015). <https://doi.org/10.1039/C4SM02584A>
11. V. Trujillo, J. Kim, R.C. Hayward, Creasing instability of surface-attached hydrogels. *Soft Matter* **4**(3), 564–569 (2008). <https://doi.org/10.1039/B713263H>
12. J. Yoon, J. Kim, R.C. Hayward, Nucleation, growth, and hysteresis of surface creases on swelled polymer gels. *Soft Matter* **6**(22), 5807–5816 (2010). <https://doi.org/10.1039/C0SM00372G>
13. J. Kim, Morphological analysis of crease patterns formed on surface-attached hydrogel with a gradient in thickness. *J. Appl. Polym. Sci.* **131**(13), 40482 (2014). <https://doi.org/10.1002/app.40482>
14. Y. Tokudome, H. Kuniwaki, K. Suzuki, D. Carboni, G. Poologasundarampillai, M. Takahashi, Thermoresponsive wrinkles on hydrogels for soft actuators. *Adv. Mater. Interfaces* **3**(12), 1500802 (2016). <https://doi.org/10.1002/admi.201500802>
15. Y. Li, J.J. Peterson, S.B. Jhaveri, K.R. Carter, Patterned polymer films via reactive silane infusion-induced wrinkling. *Langmuir* **29**(14), 4632–4639 (2013). <https://doi.org/10.1021/la400155d>
16. M. Guvendiren, J.A. Burdick, S. Yang, Kinetic study of swelling-induced surface pattern formation and ordering in hydrogel films with depth-wise crosslinking gradient. *Soft Matter* **6**(9), 2044–2049 (2010). <https://doi.org/10.1039/B927374C>
17. M. Guvendiren, J.A. Burdick, S. Yang, Solvent induced transition from wrinkles to creases in thin film gels with depth-wise crosslinking gradients. *Soft Matter* **6**(22), 5795–5801 (2010)
18. M. Guvendiren, S. Yang, J.A. Burdick, Swelling-induced surface patterns in hydrogels with gradient crosslinking density. *Adv. Funct. Mater.* **19**(19), 3038–3045 (2009). <https://doi.org/10.1002/adfm.200900622>
19. K. Huriaux, T. Narita, B. Bresson, C. Fretigny, F. Lequeux, Wrinkling of a nanometric glassy skin/crust induced by drying in poly(vinyl alcohol) gels. *Soft Matter* **8**(31), 8075–8081 (2012). <https://doi.org/10.1039/C2SM25480H>
20. S.K. Basu, L.E. Scriven, L.F. Francis, A.V. McCormick, Mechanism of wrinkle formation in curing coatings. *Prog. Org. Coat.* **53**(1), 1–16 (2005). <https://doi.org/10.1016/j.porgcoat.2004.08.007>
21. S. Yang, K. Khare, P.C. Lin, Harnessing surface wrinkle patterns in soft matter. *Adv. Funct. Mater.* **20**(16), 2550–2564 (2010). <https://doi.org/10.1002/adfm.201000034>
22. W.R. Drummond, M.L. Knight, M.L. Brannon, N.A. Peppas, Surface instabilities during swelling of pH-sensitive hydrogels. *J. Control. Release* **7**(2), 181–183 (1988). [https://doi.org/10.1016/0168-3659\(88\)90010-7](https://doi.org/10.1016/0168-3659(88)90010-7)
23. A. Ghatak, A.L. Das, Kink instability of a highly deformable elastic cylinder. *Phys. Rev. Lett.* **99**(7), 076101 (2007)
24. S. Zeng, R. Li, S.G. Freire, V.M.M. Garbellotto, E.Y. Huang, A.T. Smith, C. Hu, W.R.T. Tait, Z. Bian, G. Zheng, D. Zhang, L. Sun, Moisture-responsive wrinkling surfaces with tunable dynamics. *Adv. Mater.* **29**(24), 1700828 (2017). <https://doi.org/10.1002/adma.201700828>
25. B. Xu, C. Hayward Ryan, Low-voltage switching of crease patterns on hydrogel surfaces. *Adv. Mater.* **25**(39), 5555–5559 (2013). <https://doi.org/10.1002/adma.201300968>
26. M. Kato, Y. Tsuboi, A. Kikuchi, T.-A. Asoh, Hydrogel adhesion with wrinkle formation by spatial control of polymer networks. *J. Phys. Chem. B* **120**(22), 5042–5046 (2016). <https://doi.org/10.1021/acs.jpcc.6b01449>
27. B. Li, Y.-P. Cao, X.-Q. Feng, H. Gao, Surface wrinkling of mucosa induced by volumetric growth: Theory, simulation and experiment. *J. Mech. Phys. Solids* **59**(4), 758–774 (2011). <https://doi.org/10.1016/j.jmps.2011.01.010>

28. Y. Cao, Y. Jiang, B. Li, X. Feng, Biomechanical modeling of surface wrinkling of soft tissues with growth-dependent mechanical properties. *Acta Mech. Solida Sin.* **25**(5), 483–492 (2012). [https://doi.org/10.1016/S0894-9166\(12\)60043-3](https://doi.org/10.1016/S0894-9166(12)60043-3)
29. E. Sultan, A. Boudaoud, The buckling of a swollen thin gel layer bound to a compliant substrate. *J. Appl. Mech.* **75**(5), 051002 (2008). <https://doi.org/10.1115/1.2936922>
30. E.B. Hohlfield, *Creasing, Point-Bifurcations, and the Spontaneous Breakdown of Scale-Invariance* (Harvard University, Cambridge, MA, 2008)
31. A.N. Gent, I.S. Cho, Surface instabilities in compressed or bent rubber blocks. *Rubber Chem. Technol.* **72**(2), 253–262 (1999). <https://doi.org/10.5254/1.3538798>
32. M.K. Kang, R. Huang, Swell-induced surface instability of confined hydrogel layers on substrates. *J. Mech. Phys. Solids* **58**(10), 1582–1598 (2010). <https://doi.org/10.1016/j.jmps.2010.07.008>
33. Q. Han, C. Li, Y. Guan, X.X. Zhu, Y. Zhang, Swelling-induced surface instability of a hydrogen-bonded LBL film and its self-healing. *Polymer* **55**(9), 2197–2204 (2014). <https://doi.org/10.1016/j.polymer.2014.03.015>
34. Q. Wang, Zhao, X. A three-dimensional phase diagram of growth-induced surface instabilities. *Sci. Rep.* **5**, 8887 (2015). <https://doi.org/10.1038/srep08887> <https://www.nature.com/articles/srep08887#supplementary-information>
35. M.A. Biot, Surface instability of rubber in compression. *Appl. Sci. Res. Sect. A* **12**(2), 168–182 (1963). <https://doi.org/10.1007/BF03184638>
36. E. Southern, A.G. Thomas, Effect of constraints on the equilibrium swelling of rubber vulcanizates. *J. Polym. Sci. Part A Gen. Pap.* **3**(2), 641–646 (1965). <https://doi.org/10.1002/pol.1965.100030220>
37. K. Saha, J. Kim, E. Irwin, J. Yoon, F. Momin, V. Trujillo, D.V. Schaffer, K.E. Healy, R.C. Hayward, Surface creasing instability of soft polyacrylamide cell culture substrates. *Biophys. J.* **99**(12), L94–L96 (2010). <https://doi.org/10.1016/j.bpj.2010.09.045>
38. T. Mora, A. Boudaoud, Buckling of swelling gels. *Eur. Phys. J. E Soft Matter* **20**(2), 119–124 (2006). <https://doi.org/10.1140/epje/i2005-10124-5>
39. Y. Li, C. Li, Z. Hu, Pattern formation of constrained acrylamide/sodium acrylate copolymer gels in acetone/water mixture. *J. Chem. Phys.* **100**(6), 4637–4644 (1994). <https://doi.org/10.1063/1.466296>
40. A. Opdahl, H. Kim Seong, S. Koffas Telly, C. Marmo, A. Somorjai Gabor, Surface mechanical properties of pHEMA contact lenses: Viscoelastic and adhesive property changes on exposure to controlled humidity. *J. Biomed. Mater. Res. A* **67A**(1), 350–356 (2003). <https://doi.org/10.1002/jbm.a.10054>
41. G.A. Hutcheon, C. Messiou, R.M. Wyre, M.C. Davies, S. Downes, Water absorption and surface properties of novel poly(ethylmethacrylate) polymer systems for use in bone and cartilage repair. *Biomaterials* **22**(7), 667–676 (2001). [https://doi.org/10.1016/S0142-9612\(00\)00229-5](https://doi.org/10.1016/S0142-9612(00)00229-5)
42. R.W. Kormeyer, N.A. Peppas, Solute and penetrant diffusion in swellable polymers. III. Drug release from glassy poly(HEMA-co-NVP) copolymers. *J. Control. Release* **1**(2), 89–98 (1984). [https://doi.org/10.1016/0168-3659\(84\)90001-4](https://doi.org/10.1016/0168-3659(84)90001-4)
43. L. Ferreira, M.M. Vidal, M.H. Gil, Evaluation of poly(2-hydroxyethyl methacrylate) gels as drug delivery systems at different pH values. *Int. J. Pharm.* **194**(2), 169–180 (2000). [https://doi.org/10.1016/S0378-5173\(99\)00375-0](https://doi.org/10.1016/S0378-5173(99)00375-0)
44. J.D. Andrade, Hydrogels for medical and related applications. *Am. Chem. Soc.* **31**, 380 (1976)
45. M. Guvendiren, J.A. Burdick, The control of stem cell morphology and differentiation by hydrogel surface wrinkles. *Biomaterials* **31**(25), 6511–6518 (2010). <https://doi.org/10.1016/j.biomaterials.2010.05.037>
46. Z. Zhao, J. Gu, Y. Zhao, Y. Guan, X.X. Zhu, Y. Zhang, Hydrogel thin film with swelling-induced wrinkling patterns for high-throughput generation of multicellular spheroids. *Biomacromolecules* **15**(9), 3306–3312 (2014). <https://doi.org/10.1021/bm500722g>
47. J. Gu, X. Li, H. Ma, Y. Guan, Y. Zhang, One-step synthesis of PHEMA hydrogel films capable of generating highly ordered wrinkling patterns. *Polymer* **110**, 114–123 (2017). <https://doi.org/10.1016/j.polymer.2016.12.076>

48. M.M. Barsan, M. David, M. Florescu, L. Țugulea, C.M.A. Brett, A new self-assembled layer-by-layer glucose biosensor based on chitosan biopolymer entrapped enzyme with nitrogen doped graphene. *Bioelectrochemistry* **99**, 46–52 (2014). <https://doi.org/10.1016/j.bioelechem.2014.06.004>
49. M.M. de Villiers, D.P. Otto, S.J. Strydom, Y.M. Lvov, Introduction to nanocoatings produced by layer-by-layer (LbL) self-assembly. *Adv. Drug Deliv. Rev.* **63**(9), 701–715 (2011). <https://doi.org/10.1016/j.addr.2011.05.011>
50. P.T. Hammond, Building biomedical materials layer-by-layer. *Mater. Today* **15**(5), 196–206 (2012). [https://doi.org/10.1016/S1369-7021\(12\)70090-1](https://doi.org/10.1016/S1369-7021(12)70090-1)
51. S. Mehrotra, D. Lynam, R. Maloney, M. Pawelec, H. Tuszynski, I. Lee, C. Chan, J. Sakamoto, Time controlled protein release from layer-by-layer assembled multi-layer functionalized agarose hydrogels. *Adv. Funct. Mater.* **20**(2), 247–258 (2009). <https://doi.org/10.1002/adfm.200901172>
52. J. Borges, J.F. Mano, Molecular interactions driving the layer-by-layer assembly of multilayers. *Chem. Rev.* **114**(18), 8883–8942 (2014). <https://doi.org/10.1021/cr400531v>
53. J. Hou, Q. Li, X. Han, C. Lu, Swelling/deswelling-induced reversible surface wrinkling on layer-by-layer multilayers. *J. Phys. Chem. B* **118**(49), 14502–14509 (2014). <https://doi.org/10.1021/jp508724n>
54. E.P. Chan, J.M. Karp, R.S. Langer, A “Self-Pinning” adhesive based on responsive surface wrinkles. *J. Polym. Sci. B Polym. Phys.* **49**(1), 40–44 (2011). <https://doi.org/10.1002/polb.22165>
55. M.M. Feldstein, R.A. Siegel, Molecular and nanoscale factors governing pressure-sensitive adhesion strength of viscoelastic polymers. *J. Polym. Sci. B Polym. Phys.* **50**(11), 739–772 (2012). <https://doi.org/10.1002/polb.23065>
56. A. Gandhi, A. Paul, S.O. Sen, K.K. Sen, Studies on thermoresponsive polymers: Phase behaviour, drug delivery and biomedical applications. *Asian J Pharm Sci* **10**(2), 99–107 (2015). <https://doi.org/10.1016/j.ajps.2014.08.010>
57. C. Li, Z. Hu, Y. Li, Temperature and time dependencies of surface patterns in constrained ionic N-isopropylacrylamide gels. *J. Chem. Phys.* **100**(6), 4645–4652 (1994). <https://doi.org/10.1063/1.466247>
58. J. Kim, J. Yoon, R.C. Hayward, Dynamic display of biomolecular patterns through an elastic creasing instability of stimuli-responsive hydrogels. *Nat. Mater.* **9**, 159 (2009). <https://doi.org/10.1038/nmat2606> <https://www.nature.com/articles/nmat2606#supplementary-information>
59. J. Yoon, P. Bian, J. Kim, J. McCarthy Thomas, C. Hayward Ryan, Local switching of chemical patterns through light-triggered unfolding of creased hydrogel surfaces. *Angew. Chem.* **124**(29), 7258–7261 (2012). <https://doi.org/10.1002/ange.201202692>
60. C.M. González-Henríquez, D.H. Sagredo-Oyarce, M.A. Sarabia-Vallejos, J. Rodríguez-Hernández, Fabrication of micro and sub-micrometer wrinkled hydrogel surfaces through thermal and photocrosslinking processes. *Polymer* **101**, 24–33 (2016). <https://doi.org/10.1016/j.polymer.2016.08.051>
61. C. Robert, E. Kamal, W. Honglu, S. Wei, Biofabrication of a three-dimensional liver microorgan as an in vitro drug metabolism model. *Biofabrication* **2**(4), 045004 (2010)

# Chapter 10

## Ripples and Wrinkles in Graphene: Beyond Continuum Mechanics



Hervé Elettro and Francisco Melo

### 10.1 Introduction

Graphene, an atomically thin layer of carbon, was born from a casual Friday experiment in Manchester in 2004. The serendipitous discovery startled the whole scientific community: while carbon cages (0D fullerene), nanotubes (1D), and graphite/diamond (3D) have long been studied [1], several theoretical works predicted the lack of stability of (2D) graphene even at low temperatures [2, 3]. In 2017, the number of new scientific publications and newly filed patents related to graphene reached 70,000 and 20,000, respectively. The excitement stems from a range of astonishingly accessible characteristics such as ballistic fermion transport, quantum Hall effect at room temperature [4, 1], giant flow slippage [5], or record thermal and mechanical properties [6, 7]. Envisioned applications for 2D materials encompass novel healthcare solutions [8], high-frequency computing [9], flexible solar cells [10], and ultraefficient water filtration [11] among others (see Fig. 10.1b).

The European Council pledged one *billion* euros to the development of new graphene-based technologies. Its general assembly recently took place (April 2018) and describes the current state of industrial applications of graphene: “Ericsson spoke of its exciting 5G technology with photonics switching for datacom traffic. Emberion presented its mission to provide game-changing solutions for professional infrared imaging and photodetection and launched its first product to market, a single-pixel photodetector. GRAPHENE-XT announced the sale of the first 5 km roll of the graphene film. Thales discussed their roadmap to commercialize graphene-based supercapacitors in the next 2–3 years.” [12].

This chapter proposes to shed light on the peculiar mechanics of graphene and other 2D materials, in particular concerning the unique wrinkling processes

---

H. Elettro (✉) · F. Melo (✉)

Departamento de Física, Universidad de Santiago de Chile, Santiago, Chile  
e-mail: [herve.elettro@epfl.ch](mailto:herve.elettro@epfl.ch); [francisco.melo@usach.cl](mailto:francisco.melo@usach.cl)

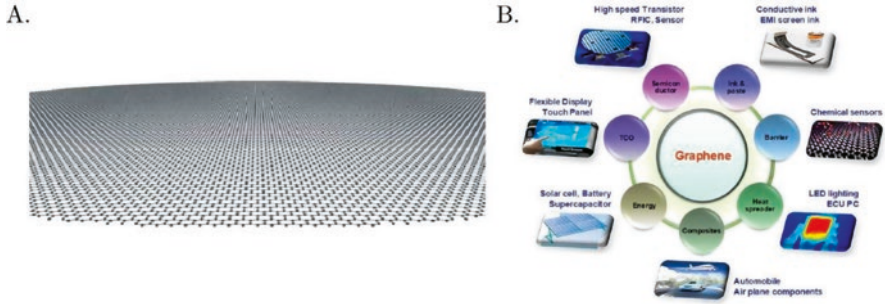


**Fig. 10.1** (a) Artistic view of graphene structure: a one atom thin allotrope of carbon with a perfect honeycomb lattice. (b) Overview of the predicted applications for graphene within the next 10 years. Reprinted with permission from (a) Meyer et al. [13], *Nature* 446 (2007) 60–63 (copyright 2007 Springer Nature) and (b) Ferrari et al. [14], *RSC Nanoscale* 446 (2015) 4598–4810 (open access)

occurring in supported and freestanding 2D membranes. Buckling, wrinkling, and folding are intrinsically controlled by the material mechanical properties and interactions with its potential substrate [15, 16]. The first section discusses the different physical parameters responsible for the effective elastic constants of monolayer and few-layer graphene, taking origin beyond the realm of continuum mechanics. The second part details the observation of induced wrinkles and ripples in graphene under different mechanisms. The third part describes applications of wrinkles in graphene, from enhanced water transport to hydrogen storage.

## 10.2 Mechanical Properties of Flat and Corrugated Graphene

### 10.2.1 Beyond Continuum Mechanics and the Plate Phenomenology

Theoretical, numerical and experimental works (truss-type analytical model, molecular dynamics simulations, Atomic Force Microscope (AFM) indentation) [17–19] showed that the intrinsic stretching (Young’s) modulus of monolayer graphene is on par with that of (bulk) graphite or diamond, at  $E = 1 \pm 0.2$  TPa. Classical mechanical engineering applied to monolayer graphene thus yields a realistic value for *in-plane* elasticity. However, the ultimate atomic thinness of monolayer graphene geometrically decouples the stretching (*in-plane*) and bending (*out-of-plane*) modes [20, 21]. This invalidates the fundamental assumptions of the Kirchhoff-Love plate theory, which links the resistance to (*out-of-plane*) bending loads per unit width  $\kappa_0$  with the *in-plane* Young’s modulus  $E$  through:

$$\kappa_0 = \frac{dM}{d\left(\frac{1}{R}\right)} = \frac{Eh^3}{12(1-\nu^2)} [22]$$

with  $M$  the bending moment,  $1/R$  the resulting curvature,  $h$  the plate thickness, and  $\nu$  the Poisson ratio of the material. Indeed, the Kirchhoff-Love plate theory assumes a linear evolution of strain and stress fields in the plate thickness, with reference to a neutral mid-surface. Monolayer graphene is nothing but the remaining neutral mid-surface, displaying pure bending curvature without extension or compression of the *in-plane* network [21].

Zhang et al. [21] describe the physical origin of bending stiffness in monolayer graphene with an orbital bond model, treated under an extended density functional-based tight-binding theory to describe realistic interatomic interactions [23]. They found that the nonvanishing bending stiffness of monolayer graphene emerges from the geometrical misalignment of the  $\pi$ -orbitals due to the breaking of symmetry during bending (see Fig. 10.2), in fundamental contrast with bulk materials.

The accepted theoretical value for the bending stiffness of monolayer graphene is  $\kappa_0 = 1.1\text{--}1.6$  eV, depending slightly on the considered method [20, 21, 25, 28]. This is an order of magnitude lower than the predictions of continuum mechanics  $\kappa_{\text{CM}} = 22$  eV with a Poisson ratio of  $\nu = 0.17$  [29]. This enabled Tapasztó et al. [30] to report experimental access to a new regime of subnanometer wrinkles, forbidden by continuum mechanics but allowed by the exotic mechanics of atomically thin structures. Furthermore, the mechanical constants of graphene are anisotropic [31, 32] on the scale of a single crystal (typically a few  $\mu\text{m}$ ), an indirect consequence of the honeycomb geometry of its lattice (see Fig. 10.2). For instance, Choi et al. [33] mapped graphene sheets using FFM (friction force microscopy), where the torsion of an AFM tip is recorded during lateral scanning. They found a clear

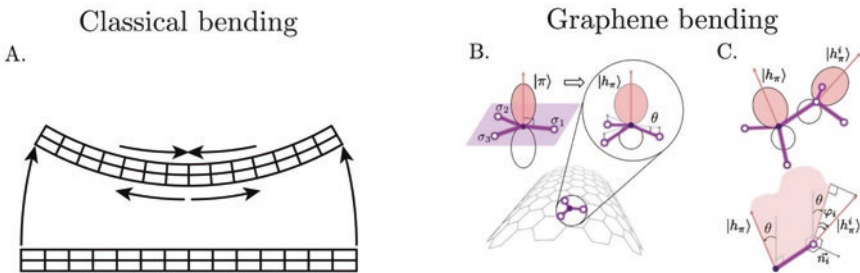


**Fig. 10.2** (a) In classical mechanical engineering, bending implies a strain profile over a reference mid-surface (bottom). As a result, the top interface is compressed, while the bottom interface is stretched (top). (b) In contrast, the finite bending rigidity of monolayer graphene takes origin in the curvature-induced misalignment of the  $\pi$ -orbitals. The  $\pi$ -orbital on a flat graphene deforms into an asymmetric  $h\pi$  orbital under bending. (c)  $h\pi$  orbitals of neighboring carbon atoms interact and produce resistance to bending. (Adapted with permission from (a) Audoly and Pomeau [24] (copyright 2010 Oxford University Press) and (b–c) Zhang et al. [21], PRL 106 (2011))

correspondence between the orthotropic dependence of the friction coefficient and the orientation of the atomic lattice. Nevertheless, many mechanical experiments are performed using large-scale polycrystalline and/or few-layer graphene. For a matter of simplicity, we will thus discuss averaged isotropic elastic constants for graphene in the following.

Partial or complete restoring of continuum mechanics validity for graphene is possible under certain conditions. In bulk graphite, the interlayer adhesion is controlled by weak van der Waals forces [34, 35], which typically allow efficient mechanical and chemical exfoliation [36]. These short-range forces are nevertheless sufficient to bear the load transfer between layers and induce compression or stretching of the  $\sigma$  (*in-plane*) orbitals, recovering the Kirchhoff-Love plate model within 6% of error for  $N > 3$  perfectly cohesive graphene layers [21]. However, the locking mechanism between graphene layers is still under debate [37], and critical layer shear stress for sliding onset varies widely between 40 kPa [38] and 10 GPa [39, 40]. A free-sliding model gives  $\kappa = N^* \kappa_0$  for a laminated plate with  $N$  layers, while a perfectly bonded interface yields  $\kappa = N^3 \kappa_0$  [39, 41]. The adhesion energy between graphene-graphene/graphene-substrate plays a crucial role in the production of graphene sheets and the transfer to determine substrates and will be discussed in further details in Sect. 10.3. In addition, the presence of ripples partially recouples the mechanical modes anharmonically and leads to renormalization of the elastic constants [42, 43]. This will be discussed in detail in the next section.

## 10.2.2 Thermally Activated Ripples

The possible existence of freestanding 2D materials has been discussed for more than 70 years [2, 3] until the experimental discovery of Novoselov et al. [44] definitely settled the theoretical debate in 2004. The main argument against 2D materials is their intrinsically high sensitivity to thermal fluctuations, which leads to dramatic *out-of-plane* deformations. This causes the effective melting temperature of thin films to decrease well below room temperature for thicknesses of less than a dozen atoms [45, 46]. Meyer et al. [13] first measured the structure of suspended graphene and found evidence of height fluctuations of amplitude 1 nm over length scales of 10–25 nm for monolayer and bilayer graphene (see Fig. 10.3). These fluctuations are undetectable as soon as the graphene sample becomes thicker than a few layers (see Fig. 10.3 right).

The observed fluctuations are predominantly thermally activated flexural phonons [13, 47] and may be accompanied by static wrinkles due to stress gradients at the boundaries [48]. They are critical to the extraordinary transport properties of monolayer graphene: they decrease electron mobility in suspended graphene [49] but provide the dominant mechanism for heat transport [6] and create polarized carrier puddles [50].

Phonons and ripples also have a dramatic influence on the effective mechanical properties of graphene, comparable to the crumpling of a paper sheet. Here the effects of bending and stretching are reversed at the microstructure scale: a flat

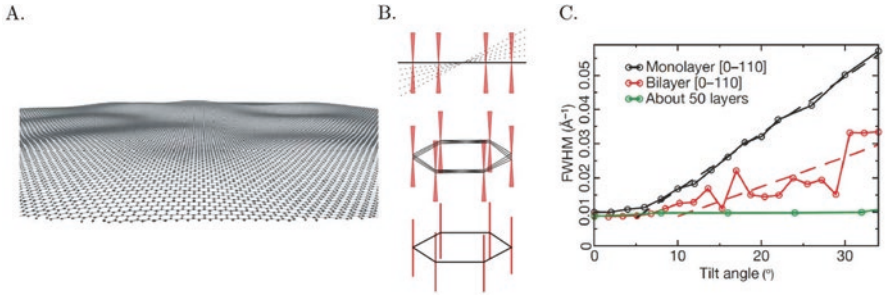


**Fig. 10.3** (a) Artistic view of thermal ripples on monolayer graphene. (b) Fluctuations of the local orientation of the lattice result in a blurred peak of electron diffraction. (c) Evolution of the height of the ripples as a function of the number of layers. The height fluctuation is measured as the full width at half maximum of the electron diffraction peaks of a tilted suspended graphene. (Adapted with permission from Meyer et al. [13], Nature 446 (2007) 60–63. Copyright 2007 Springer Nature)

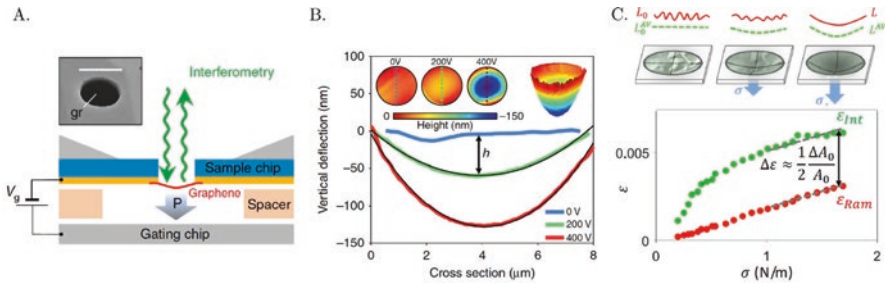


**Fig. 10.4** (a) Schematic of the experimental setup used to measure the deflection of suspended monolayer graphene under known electrostatic pressure. (b) Profiles of vertical deflection under increasing gate voltage. (c) Top: Thermal ripples crumple graphene and allow storage of a hidden area equivalent to an intrinsic extensibility. Bottom: Observed strain (green curve) and real strain of the lattice (red curve) measured by Raman spectroscopy versus applied 2D tension  $\sigma$  [36]. The maximum recorded value corresponds to a 3D tension of  $\approx 5$  GPa. Adapted with permission from (a–b) Nicholl et al. [48], Nature Communications 6 (2015) 8789 (copyright 2015 Springer Nature), and (c) Nicholl et al. [63], PRL 118 (2017) 266101 (copyright 2017 American Physical Society)

paper sheet is hard to stretch and easy to bend, while its crumpled version is easy to stretch and hard to bend [42, 51]. The mechanism of stretching a piece of crumpled paper is more similar to “dewrinkling” (see Fig. 10.4). The observed strain is simply due to the geometrical difference between curvilinear and projected area, producing a hidden area. This concept has been recently applied on a macroscopic scale to engineer conformable surfaces through capillary-induced folds [52]. Experimental access to the “real” strain of the graphene lattice is usually performed by Raman spectroscopy [36, 53, 54], where the inelastic scattering of a focused laser beam informs the internal structure of phonons and molecular vibrations [55]. This non-contact probing method has also been shown to be effective at measuring accurately the number of atomic layers, defect concentration, charge carrier concentration, and adsorbed molecules in graphene [56–60].

Applying further external strain then suppresses the effect of ripples and recovers the theoretical value of bending stiffness and 2D Young's modulus for as low as 0.25% [61, 62], leading to strong nonlinear tensile behavior with an anomalous Hooke's law exponent of 0.1 (see Fig. 10.4a and [63]). Strain-engineered graphene samples have no ripples and have such show a linear behavior, as shown in the inset of Fig. 10.4. The dewrinkling mechanism can also produce an effective negative Poisson ratio behavior for the sufficiently high hidden area, where graphene actually *expands* when stretched and loses its incompressibility. This is discussed in more details in Sect. 10.2.3.

On the other hand, bending a crumpled piece of paper induces local stretching due to the existence of Gaussian curvature [51]. This coupling between bending and stretching modes renormalizes the elastic constants and leads to an effective bending modulus  $\kappa_{\text{eff}}$  [42], with permission from (A–B) Nicholl et al. [48], Nature Communications 6 (2015) 8789 (copyright 2015 Springer Nature), and (C) Nicholl et al. [63], PRL 118 (2017) 266101 (copyright 2017 American Physical Society).

$$\kappa_{\text{eff}}/\kappa_0 = \sqrt{\frac{Y_0 h^2}{\kappa_0}} \quad \text{and} \quad E_{\text{eff}}/E = \sqrt{\frac{\kappa_0}{Y_0 h^2}} \quad (10.1)$$

where  $Y_0 = Et$  is the 2D Young's modulus,  $t = 3.35 \text{ \AA}$  is the van der Waals thickness of a graphene layer [17, 64],  $h$  is the amplitude of the ripples, and  $\langle \dots \rangle$  denotes the average operator. It is important to note that static and dynamic ripples have a similar influence on the effective bending rigidity [48]. For thermally activated ripples, this yields:

$$\kappa_{\text{eff}} = \kappa_0 \left( \frac{W}{l_G} \right)^\eta \quad \text{where} \quad l_G = 2\pi \sqrt{\frac{16\pi \kappa_0^2}{3Y_0 \kappa_B T}} \quad (10.2)$$

where  $W$  is the width of the graphene sample,  $l_G$  is the Ginzburg length [27, 47, 65], and  $\eta$  is a scaling exponent, found to be near 0.8 by self-consistent perturbation theory and confirmed by simulations [43, 66, 67]. The value of the Ginzburg length for graphene at room temperature is  $l_G \approx 40 \text{ \AA}$  and represents an intrinsic length for the thermally activated ripples as well as an upper limit for a perfectly flat graphene sheet [42]. It is also the 2D equivalent of the persistence length described in polymer physics [68, 69]. Eq. (10.2) represents a strong violation of the classical Hooke's law, where the stiffness of a material does not depend on its geometry [70]. The experimental work reported by Nicholl et al. [48] confirmed the predicted reduction of Young's modulus (see Eq. (10.1)) by recording the deflection of graphene blisters under known electrostatic pressures (see Fig. 10.4a). For micron-scale graphene sample at room temperature, the bending rigidity may increase 1000-fold. Blees et al. [71] measured the rigidity thermal enhancement by diverse methods (laser pressure and sample-scale thermal fluctuations) of a  $10 \text{ \mu m}$  graphene cantilever and found  $3000_{-200}^{+17000} \text{ eV}$ . The long-tail (lognormal) distribution is a sign of the strongly nonlinear process activated by random thermal fluctuations [72]. This effect can be

strongly suppressed and recover values slightly higher than the theoretical prediction ( $B \approx 1.1\text{--}1.6$  eV given in Sect. 10.2.1) by clamping or adhering to a substrate: Lindahl et al. [73] found  $7.1_{-3.0}^{+4.0}$  eV by the electrostatic snapping of a  $2.5\ \mu\text{m}$  suspended fully clamped single-layer graphene, and Scharfenberg et al. [74] measured  $10 \pm 5$  eV for a graphene monolayer flattening corrugated PDMS.

Higher temperatures intensify thermal crumpling and enhance the hidden area mechanism, by triggering low-energy *out-of-plane* vibration modes [56, 75, 76]. This yields a negative thermal expansion coefficient for monolayer graphene  $\alpha \approx \frac{1}{l} \frac{\partial L}{\partial T} -7 \times 10^{-6}$  up to  $-2 \times 10^{-5}$  K $^{-1}$  300 k at [76–78]. Given that thinner structures are more sensitive to thermally activated ripples, the value of the thermal expansion coefficient is amplified for 2D materials compared to its bulk counterpart [77, 78]. In Sect. 10.3.1, we examine the later stages of thermal crumpling and its consequences.

### 10.2.3 Effects of Physical Defects

Physical defects are naturally present in as-grown graphene, especially for large-scale growth methods (see further details in Sect. 10.3.2). The presence of defects is usually seen as a drawback and limits the electron mobility and transport properties of graphene [60]. Recently, Moreno et al. [79] successfully synthesized multifunctional nanoporous graphene with anisotropic bandgaps compatible with the semiconductor industry ( $\approx 1$  eV). From the mechanical point of view, removing native atoms from the lattice produces dislocations that usually result in softening [80]. Surprisingly, Style et al. [81] showed that very soft solids (with Young's moduli on the scale of kPa) with sufficiently small inclusions could be stiffer than the bulk matrix, due to the buildup of interfacial energy. Fracture toughness, long believed to be a material intrinsic property, has been found to depend on sample size, revealing an intrinsic length linked to the defect concentration [82, 83]. Furthermore, compressive stress and *out-of-plane* deformation induced by defects, physical or topological such as the connection points of wrinkles, smoothen the singularity at the crack tip [84–86] and increase the toughness of materials.

Lopéz-Polín et al. [19] irradiated pristine graphene with energetic Ar $^+$  ions to obtain a controlled density of defects, measured in situ by Raman spectroscopy [60]. They used AFM micromechanical indentation to assess the *in-plane* Young's moduli. They report the peculiar behavior of defective graphene that may become stiffer than its pristine counterpart at low defect concentrations (see Fig. 10.5a). At higher concentrations, the natural tendency to softening is recovered, attaining a maximum *in-plane* stiffness of 1.6 TPa at a defect concentration of  $1 \times 10^{13}$  cm $^{-2}$ .

The authors explain that the observed variation is a result of two competitive mechanisms: the quenching of long-wavelength fluctuations (dominant at low defect concentrations) and the classical softening by material removal [80]. Quenching results in stiffening because of the reduction of anharmonic renormalization as

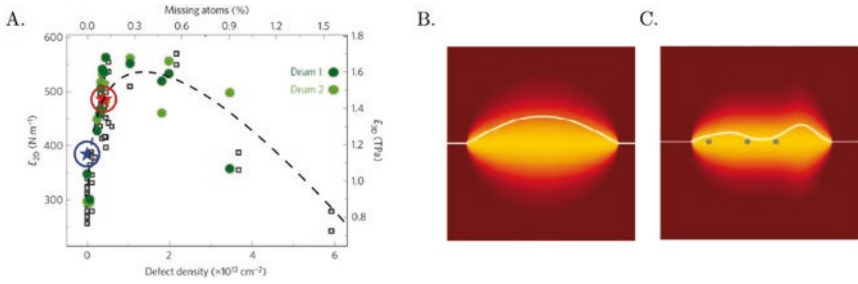


**Fig. 10.5** (a) Influence of the defect's concentration on the *in-plane* stretching modulus. Graphene with a relatively low defect concentration can be stiffer than their pristine counterpart. Classical softening is recovered at higher defect concentrations. (b and c) The presence of defects modifies the structure of thermally activated ripples in graphene. The quenching of long-wavelength fluctuations (c) explains the observed stiffening. (Reproduced with permission from López-Polín et al. [19], Nature Physics 11 (2015) 26–31. Copyright 2015 Springer Nature)

shown in Eq. (10.1). However, defects act as nucleation sites for cracks and provoke early brittle fracture in graphene by crack opening [7]. This is evidenced in the tensile test of a pristine graphene in which a crack has been precisely cut by focused ion beam (FIB) (see Fig. 10.6 right).

The fracture toughness of defective graphene is about 50% lower than the intrinsic strength of pristine graphene, where the catastrophic failure mode is a collective fracture of all C–C bonds, as shown in Fig. 10.6c, e. Defective graphene is bounded by the Griffith criterion under the classical theory of brittle fracture,  $\sigma_c = \sqrt{2\gamma E / \pi a_0}$ , where  $\sigma_c$  is the critical stress for the onset of fast fracture,  $\gamma$  is the crack interfacial energy,  $E$  is the Young's modulus, and  $a_0$  is the initial crack length [88]. López-Polín et al. [87] later found that defects confine the crack propagation (see Fig. 10.6e), maintaining defective graphene at a record fracture toughness of 50 GPa, much higher than any other materials. Defects also triggers short-wavelength fluctuations by releasing *in-plane* elastic energy into *out-of-plane* deformations [89, 90]. This amplifies the morphology of thermal ripples through localization at the defect site and allows the defect-based topological design of corrugation patterns in graphene (see Fig. 10.7d and [91, 92]). However, the overall wrinkling level is decreased [76], as shown on Fig. 10.7e. It lead López-Polín et al. [76] to discover that the thermal expansion coefficient of graphene can be tuned over almost an order of magnitude by introducing defects, from  $-7 \times 10^{-6} \text{ K}^{-1}$  for pristine graphene to  $-1 \times 10^{-6} \text{ K}^{-1}$  for a defect density  $6 \times 10^{12} \text{ cm}^{-2}$ , corresponding to 0.15% of missing atoms.

Qin et al. [90] found that for a wrinkle aspect ratio  $\eta > 0.066$ , graphene shows an effective negative Poisson ratio and becomes auxetic, expanding under stretch in the transverse direction instead of contracting. This reveals a competition between the intrinsically positive Poisson's ratio of the graphene lattice and the auxetic behavior associated with the dewrinkling mechanism. Grima et al. [89] observe a similar behavior when increasing the concentration of defects above 1%, which amplify thermal ripples above the auxetic threshold. In the following, we analyze the structure of the wrinkles induced by different mechanisms.

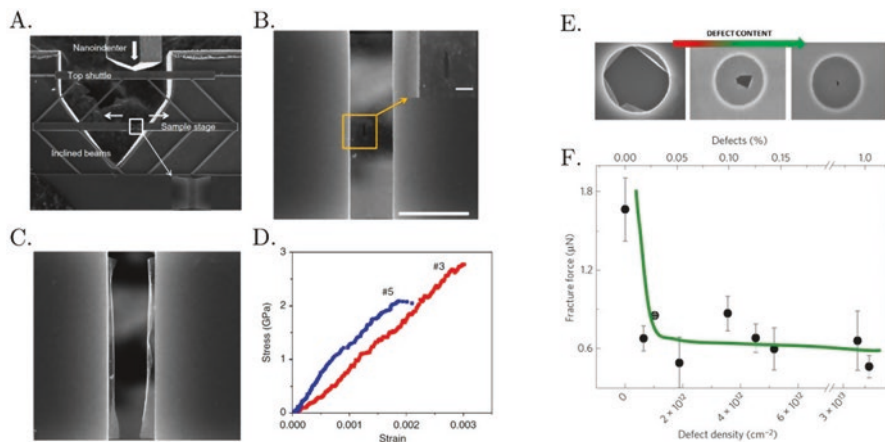


**Fig. 10.6** (a–d) Brittle fracture experiments in graphene with controlled initial crack. (a) SEM image of the microtensile machine. The nanoindenter pushes down on the top shuttle, applying pure tension on the graphene sample (white box) through the intermediate deflection of the inclined beams. (b) View of the graphene sample (scale bar 5  $\mu\text{m}$ ) and initial crack (yellow box inset, scale bar 500 nm). (c) View of the sample after fracture, showing rolled edges. (d) Strain-stress curves for selected samples. Note the high level of stress, on the scale of a few GPa. (e) Increasing defect density switches the fracture behavior of graphene from catastrophic failure (left) to confined crack (right). (f) The effective force to fracture a graphene sample plummets and then saturates at a final value for increasing defect density. Reproduced with permission from (a–d), Zhang et al. [7], Nature Communications 5 (2014) 3782 (copyright 2014 Springer Nature), (e) López-Polín et al. [19], Nature Physics 11 (2015) 26–31 (copyright 2015 Springer Nature), and (f) López-Polín et al. [87], ACS Nanoletters 15 (2015) 2050–2054 (copyright 2015 American Chemical Society)

## 10.3 Mechanisms of Induced Wrinkles

### 10.3.1 Self-Crumpling, Folding, and Tearing

In addition to the renormalization of the elastic constants, Kōsmrlj and Nelson [65] showed that for spherical thin shells, the coupling between undulations and the background curvature produces an effective negative surface tension that depends on the sphere radius. This drives instabilities in spherical thin shells at finite temperature and limits their size. At large radii or high temperatures, spheres collapse under the thermally induced inward pressure, as shown in Fig. 10.8. In flat graphene, the crumpling transition occurs at higher temperatures, induced by the disorder [93] stemming from the loss of directional memory. This is similar to how a polymer switches from a rigid rod to the path of a random 3D walk as it grows above its persistence length.

Due to large *out-of-plane* motion, graphene may present spontaneous tearing and peeling from its substrate, forming self-folding nanoribbons with a well-defined tapered geometry [94], as demonstrated by Fig. 10.9. The process is driven by the thermodynamic exchange of interfacial energy (graphene-substrate to

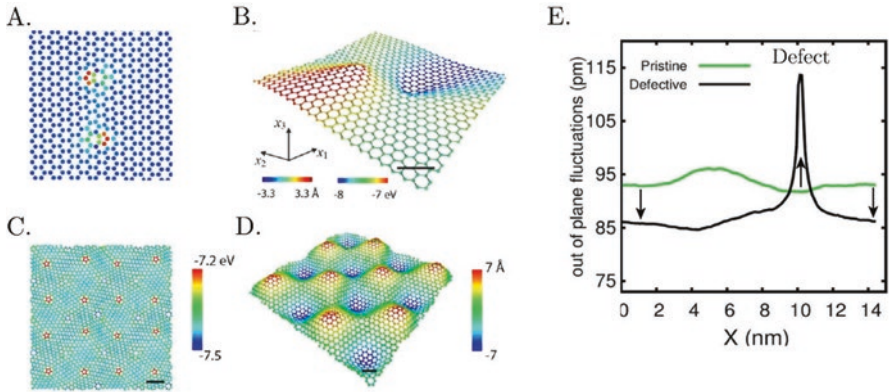


**Fig. 10.7** (a–b) Top view and perspective view of the atomic configuration and *out-of-plane* deformation of a dislocation dipole in a monolayer graphene sheet. (c) Potential energy contour of a periodic array of disclinations. (d) Atomistic simulations show the configuration of pattern engineered graphene ruga. Scale bars all represent 1 nm. (e) The amplitude of the *out-of-plane* fluctuations at  $T = 300$  K measured along a line across a defect. While the defect site localizes large wrinkles, its surroundings see lesser fluctuations. Adapted with permission from (a–d). Zhang et al. [92], *JMPS* 67 (2014) 2–13 (copyright 2014 Elsevier), and (e) López-Polín et al. [76], *Carbon* 116 (2017) 670–677 (copyright 2017 Elsevier)

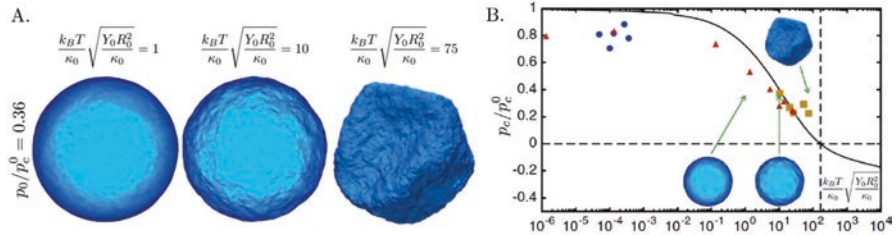


**Fig. 10.8** (a) View of thermally crumpled spherical thin shells of radius  $R_0$  under 36% external critical pressure for buckling. The level of thermal fluctuations  $\frac{\kappa_B T}{\kappa_0} \sqrt{\frac{Y_0 R_0^2}{\kappa_0}}$  increases from 1 (left) to 75 (right). (b) The critical buckling pressure  $p_c$  decreases with increasing thermal fluctuations and may become negative, indicating spontaneous thermal crumpling and collapse. (Adapted with permission from Kósmrlj and Nelson [65], *PRX* 7 (2017) 011002. Open access)

graphene-graphene) into tearing and peeling energy and is activated by thermal fluctuations. The final ribbon state is at equilibrium, with a final width such that the interfacial gain is not sufficient to tear the graphene lattice on the ribbon edges. The formation of graphene ribbons must overcome the substrate adhesion, graphene tearing resistance, and elastic strain energy present in the fold [94], all of which will dictate the final geometry (taper angle and end width) of the ribbon [95]. Chen et al. [96] discuss the inverse problem of the stability of a forced graphene fold against thermal fluctuations and find a minimum length of a few nanometers for a

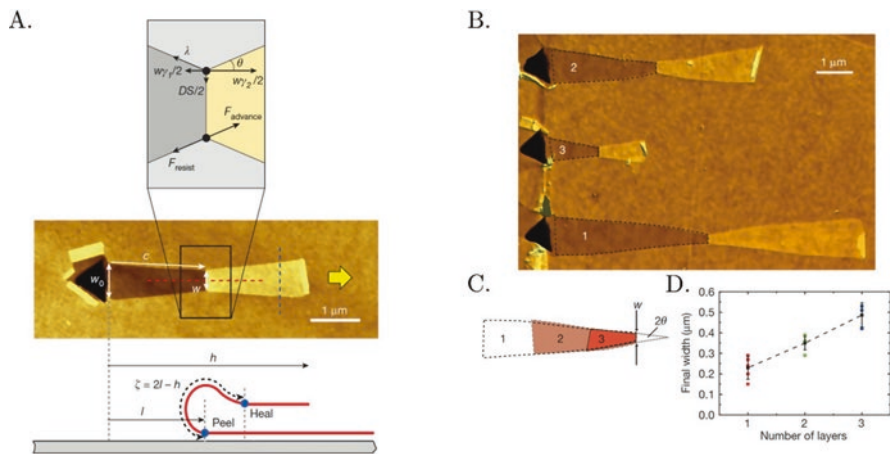


**Fig. 10.9** (a) The gain in interfacial energy (peeling versus healing) drives the self-folding mechanism in bilayer graphene. After initial release via indentation (the triangular black area on the left side of the central picture), thermal fluctuations set the growth rate of the ribbons by overcoming the threshold of substrate adhesion and tearing resistance of the graphene edges. (b) Atomic force microscopy (AFM) image of the spontaneous growth of three tapered ribbons observed in bilayer graphene. (c) Superposition of the three ribbon shapes depicted in B demonstrates a constant taper angle  $\theta \approx 12^\circ$ . (d) The final width of the tapered ribbon as a function of the number of layers of the graphene sheet. The trend indicates that the ribbon is finally arrested by tearing resistance and not interlayer friction. (Reproduced with permission from Annett and Cross [94], Nature 535 (2016) 271–275. Copyright 2016 Springer Nature)

stable fold. The thermally activated self-folding process modifies the morphology of graphene samples suspended over microtrenches formed by the roughness of the substrate. This implies that the effective contact area of graphene depends strongly on temperature. The unique sensitivity of 2D membranes to thermal fluctuations offers new strategies for strain engineering through self-tensioning [97, 98].

Annett and Cross [94] found that the main barrier to ribbon formation is the tearing resistance of graphene in the case of their experiments performed on bilayer graphene on a 300 nm thermal silicon oxide layer. From Fig. 10.9d, the bond rupture energy density is estimated to be  $30 \text{ eV nm}^{-1}$ , compatible with the view that C–C covalent atomic bonds are ruptured. The graphene-SiO<sub>2</sub> adhesion energy is in the range  $\approx 0.6$ – $2.8 \text{ eV nm}^{-2}$ , equivalent to  $0.1$ – $0.45 \text{ Jm}^{-2}$  [41, 99]), and strongly depends on the substrate surface conditions [37]. These values are reminiscent of solid-liquid adhesion energy, highlighting the effect of the extreme flexibility of graphene, which allows liquid-like conformable surface matching up to the delamination limit at  $N \approx 5$  layers [41], where graphene sits on the corrugation of its substrate. Given the intermediate range of values of the interlayer binding energy of graphene ( $1.45$ – $2.15 \text{ eV nm}^{-2}$  [39, 100]), this might favor stable attachment to the substrate or spontaneous ribbon growth. Engineering graphene nanoribbons with a controlled taper angle and length is thus possible by tuning the adhesion energy of graphene to its substrate, for instance, by functionalization, or adjusting substrate roughness or relative humidity [100].

### 10.3.2 Wrinkles Induced by the Fabrication Process

Monolayer and few-layer graphene can be synthesized by a variety of methods: mechanical exfoliation (adhesive tape) [44], graphite oxide reduction [101], and graphite intercalation with guest molecules [102]. Recent efforts have focused on the production of industrial quantities of graphene at low cost: Yi and Shen [103] successfully produced few-layer graphene sheets using the hydrodynamic shear stress of a kitchen blender, and Seo et al. [104] grew mono- to few-layer graphene by cooking soybean oil at 800 °C under ambient pressure. Today, the most common method to grow large-scale, high-quality monolayer graphene is still chemical vapor deposition (CVD). It consists of the thermal decomposition of high-purity methane in a hydrogen atmosphere under high vacuum and leads to atomic carbon being dissolved in the bulk metal foil. Upon cooling, 2D crystals of graphene precipitate, the *in-plane* growth mode being activated preferentially by highly efficient surface catalysis [105]. To date, copper is the most common substrate for graphene production due to its low cost, which is the main parameter of choice for industrial scales [14]. For precise condensed matter experiments, ultrahigh-quality single-crystal graphene is usually grown on substrates with weak interactions, such as hexagonal boron nitride [106, 107], iridium, or platinum [108].

Graphene may develop wrinkles due to its interactions with the substrate under different mechanisms: (i) natural roughness of the substrate (see Fig. 10.10a–d and [109]), (ii) thermal expansion coefficient mismatch (see Fig. 10.10e, f), (iii) strain

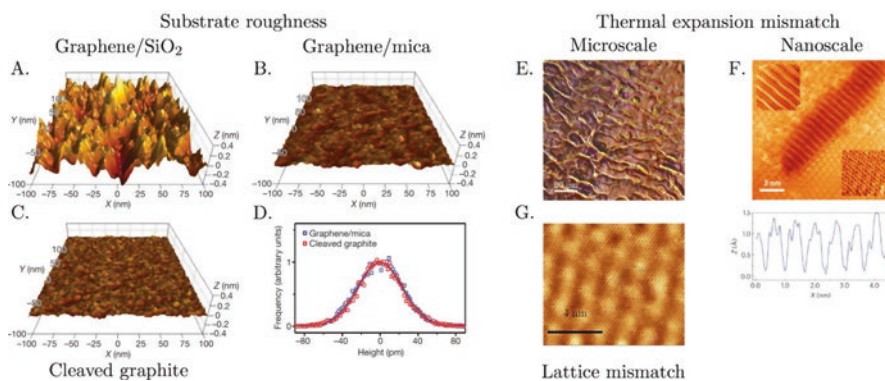


**Fig. 10.10** (a–d) Roughness of monolayer graphene deposited on SiO<sub>2</sub> (a) and mica (b). (c) Roughness of freshly cleaved graphite. (d) Graphene on mica and freshly cleaved graphite are both considered atomically flat, with a standard deviation of 24 pm in the roughness distribution, corresponding to 7% of the size of a carbon atom. (e) Optical image of wrinkles developing on the copper substrate as a result of thermal contraction. The typical wavelength is on the scale of tens of micrometers. (f) Atomic-resolution scanning tunneling microscope (STM) images (top) of graphene nanowrinkle islands developing over nanotrenches as a result of thermal strain engineering. Bottom: Nano-wrinkle profiles from STM intensity. Each wrinkle contains only 6 C–C bonds. (g) STM image of monolayer graphene on SiC. The lattice mismatch produces a superlattice of corrugations, producing contrasting spots from the tunneling current. Adapted with permission from (a–d), Lui et al. [109], Nature 462 (2009) 339 (copyright 2009 Springer Nature), (e) courtesy of Dr. Hervé Eletto, (f) Tapasztó et al. [30], Nature Physics 8 (2012) 739–742 (copyright 2012 Springer Nature), and (g) Goler et al. [111], JPCC 117 (2013) 11506–11513 (copyright 2013 by American Chemical Society)

due to lattice mismatch (see Fig. 10.10g. and [110, 111]), or (iv) nucleation of defect lines in the substrate [112].

The difference of thermal expansion coefficient between graphene and its substrate drives wrinkle formation [78] spanning four decades in size, from the micron-size wrinkle of the substrate surface to the nano-wrinkle that develops in graphene locally suspended over nanotrenches [30]. Thermal cycling is efficient and reliable to engineer reproducible wrinkle patterns [73]. Wrinkles may also form during substrate transfer [113], due to residual stresses during surface matching [114], solvent trapping during dip coating [115], or residues from the protective PMMA layer [116]. On yet a smaller scale, graphene nanobubbles often appear near flake boundaries and are typically 5 nm wide and 1 nm tall. Due to the symmetry of the honeycomb atomic lattice, they have a triangular shape and show some extremely high local curvature, leading Levy et al. [117] to report the measurement of pseudo-magnetic fields up to 300 T.

### 10.3.3 Structure Modification Due to Chemical Defects and Adsorbates

Monolayer graphene is a unique structure in the sense of adsorption: the whole material is nothing but surface, and no bulk atoms are shielded from the environment. As such, graphene is highly sensitive to adsorbates, which are known to potentially disrupt graphene's electronic structure by chemisorption (orbital mixing) [118]. Hydrogen-functionalized graphene sees its Young's modulus and tensile strength decreased by as much as 30% and 65%, respectively, with increased coverage [119]. Poulin et al. [120] showed that chemical defects can drastically decrease graphene bending stiffness. They measured the thermal fluctuations of a suspension of graphene oxide flakes by small-angle X-ray scattering under increasing shear rates in a Couette cell. From the flattening of the flakes, they could infer an effective bending stiffness of  $1 k_B T$ , almost 2 orders of magnitude lower than the theoretical prediction, while the *in-plane* Young's modulus of graphene oxide is close to that of pristine graphene [120]. This shows that a relatively small oxygen content ( $\approx 20\%$ ) disrupts the stretching and bending modes in a different fashion. Indeed, stretching only involves nearest-neighbor interactions, while bending affects much wider surroundings.

Svatek et al. [121] reported the appearance of spontaneous curvature and stiffening of graphene when the adsorbate is an alkane. Using TTC ( $C_{44}H_{90}$ ) adsorbed on a graphene sheet supported by an increasing number of water layers, they found that wrinkles develop. The lattice mismatch between the alkane and graphene produces a curvature-dependent adsorption energy [121], which compensates the cost of bending the graphene/alkane layer (see Fig. 10.11).

Interestingly, Lee et al. [122] have shown that the effective reactivity of graphene also depends on the van der Waals interactions with the substrate. Coupled with its natural low electronic noise, this enabled the detection of individual molecules, the ultimate goal of any chemical sensor ([123], and see Sect. 10.4.2 for more details).

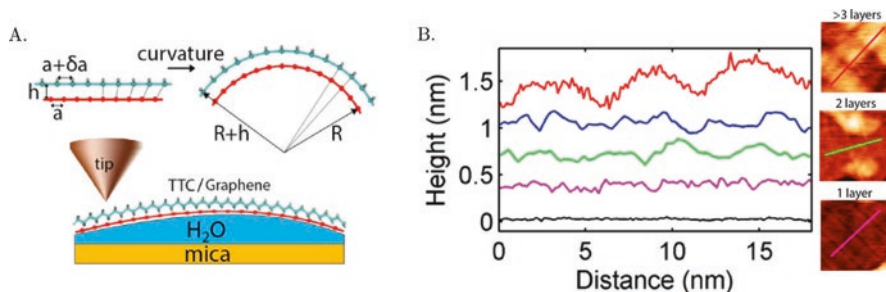


**Fig. 10.11** (a) Monolayer graphene develops spontaneous curvature under adsorption of alkane molecules, in order to geometrically compensate lattice mismatch. (b) Height profile of TTC on graphene supported by an increasing number of water layers (none (black), 1 (pink), 2 (green), 3 (blue), >3 (red)), releasing the elastic bonds with the mica substrate. Above 3 water layers, wrinkles are clearly visible, with a wavelength that roughly corresponds to one TTC molecule. (Adapted with permission from Svatek et al. [121], ACS Nanoletters 15 (2015) 159–164. Open access)

This is highly desired in medical applications, as higher sensitivity translates into earlier disease diagnostics. This motivated Gao et al. [124] to recently demonstrate a sub-femtomolar DNA detection on graphene biosensors.

## 10.4 Applications of Wrinkles in Graphene

### 10.4.1 Kirigami Nanomachines

Origami (*ori*, “fold”; *gami*, “paper”) and kirigami (*kiri*, “cut”; *gami*, “paper”) have been applied for centuries to skillfully turn two-dimensional sheets into three-dimensional objects. Capillary actuation [125], stress gradients in bilayers [126] or composites [127], and other 4D printing techniques [128] are also valuable assembly methods for 3D mesostructures. The scalable properties of these techniques have been recently explored with graphene, a well-suited fundamental brick for robust microscale structures and metamaterials with tunable mechanical properties [129] such as stretchable electrodes [130], springs, and hinges (Fig. 10.12 left).

These devices can be made through lithography from polycrystalline monolayer graphene grown on copper by chemical vapor deposition (CVD). After the transfer of graphene to fused silica wafer, previously covered with an aluminum release layer, optical lithography can be used to pattern both the graphene and gold pads that are designed to act as handles of graphene motifs. Etching of the aluminum layer allows for the release of graphene devices on the free surface of an aqueous solution. Adding salts or surfactants enables the control of surface and bulk properties of the solution, which ultimately governs the electrical and mechanical response of graphene devices (Fig. 10.12d). In addition, the devices can be remotely actuated *out-of-plane* by means of an infrared laser or an external magnetic field when the

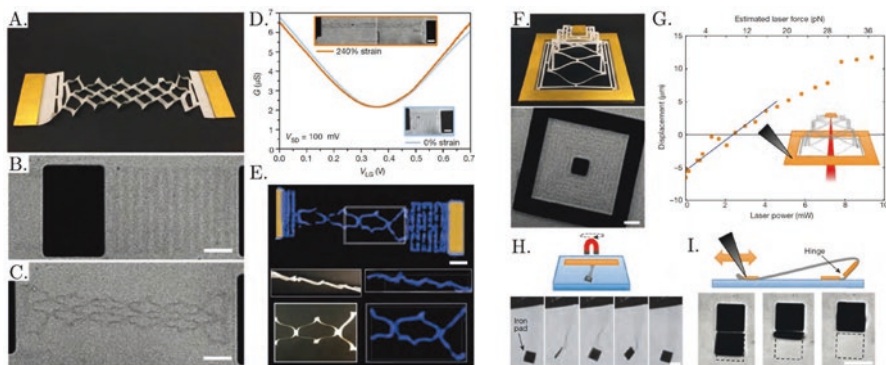


**Fig. 10.12** (a–e) Stretchable graphene transistor. (a–b) Paper and graphene *in-plane kirigami* springs, respectively (paper is shown for comparison). (c) Graphene spring stretched by about 70%. (d) The conductance of the graphene transistor, at 10 mmol KCl ionic strength, is plotted as a function of liquid-gate voltage VLG at source-drain bias VSD = 100 mV, for null (blue) and 240% (orange) stretching. (e) Three-dimensional reconstruction of a graphene spring. Insets show views of sections of the graphene (right) and paper models (left). Top images show side views; bottom images show top views. Scale bars are 10  $\mu m$ . (f–i) Remote actuation. (f) Paper model (top) graphene *kirigami* pyramid (bottom). Infrared laser produces *out-of-plane* stretching. (g) Schematic and force-distance curve for a pyramid spring. (h) A rotating magnetic field twists and untwists along graphene strip. The gold pad is replaced by iron. (i) A monolayer graphene hinge actuated by a graphene arm. Stills show the hinge closing. Scale bars are 10  $\mu m$ . (Reproduced with permission from Blees et al. [71], Nature 524 (2015) 204. Copyright 2015 Springer Nature)

gold pads are replaced by iron (Fig. 10.12 right). The use of atomically thin membranes highlights the potential of origami-inspired fabrication of miniaturized machines at its ultimate limit [71]. Environment-responsive metamaterials are also possible by adding sensing capabilities such as chemical tags to graphene kirigami [131]. Prototypes of ultrathin bimorph actuators able to bend in response to differential strain have been achieved by bonding graphene sheets to nanometer-thick layers of glass. These bimorphs produce numerous 3D microstructures, including tetrahedron, helices of the controllable pitch, high-angle folds and clasps, basic origami motifs with bidirectional folding, and boxes. In addition to thermal actuation, bimorphs can rapidly respond to the local electrolyte concentration due to ion exchange reaction that takes place within the glass.

These achievements led to envisage several applications. For example, force sensors with femtonewton force resolution and very high sensitivities can be easily designed as springs. Their stiffness is tunable over more than nine orders of magnitudes, covering the spectrum from atomic force microscopes to optical traps [71]. These techniques can be extended to a broad family of two-dimensional materials to integrate new optical, electronic, and mechanical properties with the final goal of developing functional devices that respond to light or magnetic field, temperature, or chemical signals. These devices represent exciting new opportunities for sensing, manipulation, and nanoscale robotics.

### 10.4.2 *Nano-electromechanical Resonators*

Recent advances point to graphene as the perfect candidate to reach the ultimate limit of miniaturization of NEMS. Due to its enormous stiffness and low density, nanodrums up to 10 GHz [132] and nanobeams in excess of 300 GHz [133] have been developed. Moreover, multilayer graphene enables variable frequency resonators, extending the frequency domain of these nanodevices [134]. Suspended graphene can be connected to electrodes, which makes graphene-based mechanical nanoresonators realistic candidates for sensing applications [123, 132, 133, 135]. Indeed, ultrasensitive mass and force sensors have been developed [136], and successful detection of an individual gas molecule that attaches and detaches from graphene surface has been achieved with unprecedented signal/noise ratio [123]. This impressive sensitivity is possible since graphene involves exceptionally low electronic noise [123]. Chemical detectors and probes that are sensitive to charges and magnetic fields or mechanical strain are also possible, setting graphene as the ultimate most sensitive material, able to convert minute deformations into detectable electrical signals.

### 10.4.3 *Bandgap Opening for Electronics*

Semiconductors are fundamental to the electronics industry because high-quality transistors rely on a large *on-off* current ratio [137]. In that view, graphene is “too good” of an electronic conductor and possesses a detrimental nonvanishing conductivity even at zero charge carrier density [4], with the consequence that it cannot be efficiently turned off. Strategies to engineer a controllable bandgap in graphene include adsorbates [58, 138], doping [139, 140], confinement in graphene nanoribbons [79, 141], or the use of graphene bilayers [137].

Electrons in graphene are unique in the sense that they undergo ballistic transport like massless Dirac fermions [4, 142]. They are thus very sensitive to any disturbance in interatomic distances. Strain engineering has been demonstrated to induce bandgaps up to 0.5 eV [143] and pseudo-magnetic fields in excess of 300 T [117, 144]. Interestingly, while curvature in atomically thin graphene does not produce *in-plane* strain (see Sect. 10.2.1), the *out-of-plane* distance between carbon atoms in the curved lattice is modified. This explains why flexural and planar deformations couple with electronic transport properties [145]. Partovi-Azar et al. [50] showed that ripples create a nonuniform distribution of interatomic distances, which leads to the formation of electron-hole puddles in graphene at finite temperature. The experimental observation and mapping of such structures have been successfully performed by Martin et al. [146] using a scanning single-electron transistor. Finally, Moreno et al. [79] showed that graphene with highly ordered rectangular nanopores has an anisotropic bandgap, with 1.2 eV in the direction of the pores and 0.4 eV perpendicular to them. The versatility and record properties of graphene can thus be applied to configurations currently unattainable due to the intrinsic limitations of silicone.

### 10.4.4 Curvature-Dependent Adsorption: Application to Hydrogen Storage

Hydrogen is considered one of the cleanest energy sources because its combustion releases an amount of energy that can triple that of petroleum and produces only water vapor [147]. However, the efficient storage of hydrogen is a challenging issue since common storage systems capable of withstanding the necessary high pressures (300–700 bar) are expensive and bulky. The preferential ability of atomic hydrogen to chemisorb on graphene at high densities makes graphene a perfect candidate for hydrogen storage. Fully hydrogenated graphene is an  $sp^3$  hybridized structure with a buckled honeycomb lattice called “graphene” and has been found experimentally to be stable at ambient conditions [139]. As such, a graphene sheet can accept up to one hydrogen atom per carbon site (maximum 1:1 stoichiometry), reaching densities that outperform other current storage solutions [147]. Strategies for realistic applications include engineering nanostructured graphene with low interlayer distance and chemical functionalization with alkali atoms (Li, Na, and K) [147–149]. However, the energy barriers for dihydrogen splitting and adsorption on graphene are high at normal conditions, and a reversible mechanism for hydrogen load/unload is required for realistic applications. Recently, Tozzini and Pellegrini [150] explored the effects of structural manipulations to lower the adsorption barriers. Using scanning tunneling microscopy on an intrinsically curved substrate (SiC(0001)) in a controlled atmosphere, hydrogen was found only on convex areas of the graphene lattice. This suggests that both the binding energy and the adsorption barrier can be controlled through the local curvature of the graphene lattice. A simple explanation of this effect is that the convex surface of graphene ( $sp^2$  graphite-like orbitals) is distorted toward  $sp^3$  orbitals (diamond-like). Thus, the protruding  $\pi$  orbitals become more reactive to bind hydrogen. Figure 10.13 depicts the controlled

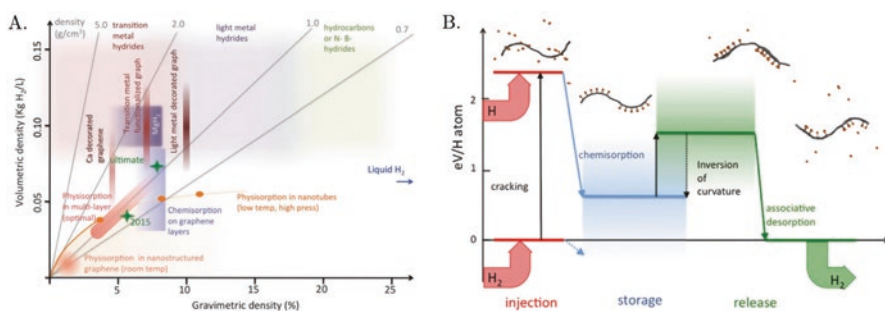


**Fig. 10.13** (a) Comparison of existing hydrogen storage systems. High volumetric hydrogen density (stored hydrogen mass per unit system volume) and high gravimetric density (total weight percentage of  $H_2$ ) are desirable. Green stars represent goals of the Department of Energy of the USA for realistic market applications. Reproduced from Tozzini and Pellegrini [147], PCCP 15 (2013) 80–89, by permission of the Royal Society of Chemistry. (b) Hydrogen storage and release by mechanical actuation of monolayer graphene. Reversible dissociative chemisorption is achieved under the control of graphene curvature field. Reproduced with permission from Tozzini and Pellegrini [150], JPCC 115 (2011) 25523–25528. Copyright 2011 American Chemical Society

adsorption and release of hydrogen through low power mechanical actuation [111, 150]. The use of traveling wave on graphene has been also suggested for fast and efficient desorption [147].

### 10.4.5 Enhanced Water Diffusion and Transport

Recent advances in nanoscale water transport in graphene-related materials open exciting avenues for ultrafast water filtration. Nair et al. [11] found that graphene oxide (GO) membranes allow quasi-unimpeded permeation of water, at least  $10^{10}$  times faster than helium, but are impermeable to liquids, vapors, and gases [11]. These membranes are made of GO flakes organized in a lamellar structure similar to nacre and exhibit great mechanical strength and flexibility, even for films with submicron thicknesses. It can thus be expected that GO membranes will be used as barrier films in the design of filtration and separation materials and for selective removal of water. Moreover, the observation that water moves through carbon nanotubes at extremely high rates has stimulated the idea of developing nanotube-based membranes for desalination and nano-filtration [151, 152]. Recently, accurate measurements of water flow in single carbon nanotubes [5] have measured unexpectedly large flow slippage, demonstrating that water experiences almost no friction in carbon nanotubes. However, in boron nitride nanotubes with similar radii, no slippage has been observed, recovering classical Poiseuille profiles. The latter are similar to carbon nanotubes, but electronically different, which indicates that the origin of such contrast is likely due to the details of the interaction of water with the solid surface. Despite these subtle disparities, the fast-evolving technology of graphene may provide carbon nanotube bundles or suitably folded graphene with enough flow capacity to make ultrafast water treatment a reality (Fig. 10.14).

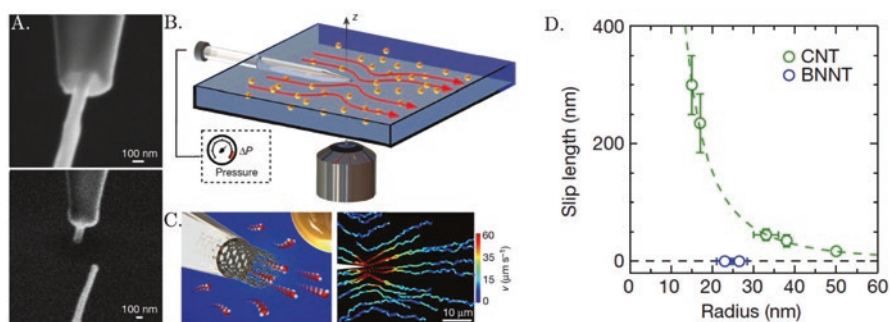


**Fig. 10.14** Flow slippage inside a carbon nanotube. (a) SEM image of a single carbon nanotube inserted into a nanocapillary (top) and after sealing (bottom) [5]. (b) Fluidic cell experimental setup presenting the flow profile around a nanojet from the nanotube (orange spheres are tracer particles). (c) Left—sketch of the nanotube attached to a nanocapillary tip with water molecules emerging from the jet and external flow. Right—measurement of the velocity field allows for the exact determination of water transport through the nanotube for a given pressure drop. (Reproduced with permission from Secchi et al. [5], *Nature* 537 (2016) 210–213. Copyright 2016 Springer Nature)

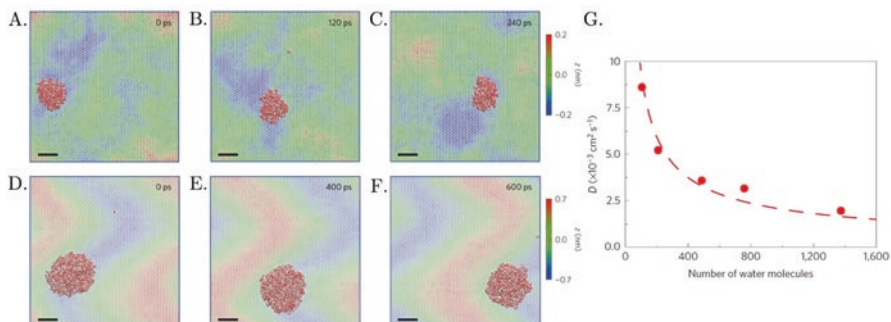


**Fig. 10.15** “Surfing” mechanism of water nanodroplets on thermally activated ripples on graphene. (a–f) Snapshots of MD simulations for (a–c). A 2 nm water nanodroplet diffusing on 0.2 nm ripples in graphene and (d–f). A 4.4 nm water nanodroplet diffusing on 0.7 nm ripples in graphene. Larger clusters preferentially sit at the bottom of the ripple and are thus dragged forward by the dynamic ripples. (g) Diffusion coefficient of water nanodroplets as a function of their size. (Reproduced with permission from Ma et al. [153], Nature Materials 15 (2016) 66–71. Copyright 2016 Springer Nature)

This spectacular phenomenon can be interpreted under the new perspective of the recent results of Ma et al. [153], showing ultrafast diffusion of nanosized water droplet over suspended graphene. They performed force field-based molecular dynamics (MD) simulations with clusters of a few hundred water molecules sitting on fluctuating graphene. Their results indicate that thermally activated ripples can promote dramatically nanodroplet diffusion, reaching values  $10^2$ – $10^3$  higher than in the case of self-diffusion of water molecules. The governing mechanism involves water nanodroplets hovering on the dynamic pattern of thermally activated phonons, as shown in Fig. 10.15.

## 10.5 Conclusion and Perspectives

Graphene is a versatile material: its ultimate thinness opens a realm of exciting opportunities for groundbreaking technologies. Its unique mechanical behavior derives from the breakdown of continuum mechanics and fuels new physics such as bending stiffness controlled by  $\pi$ -orbital misalignment, renormalization of elastic constants due to thermal fluctuations, self-tearing, or extreme sensitivity to adsorbates. Ripples and wrinkles develop in mono- and few-layer graphene under a variety of mechanisms, where stress gradients can originate from physical or chemical defects, thermal expansion mismatch, or unrelaxed interactions with the substrate. Feedback between graphene mechanical, electronic, and chemical properties have been discussed and open new fundamental questions and opportunities for breakthrough technologies. This includes nanomachines, chemical sensors with ultimate single-molecule sensibility, efficient hydrogen storage, and water filtration. The concepts discussed here are applicable to other 2D materials, paving the way for bottom-up laminated heterostructures made of atomic Lego blocks [34] with composite properties.

**Acknowledgment** We acknowledge the financial support from FONDECYT/CONICYT-Chile through the postdoctoral project N° 3160152 and from H2020 through the Marie Skłodowska-Curie Individual Fellowship N° 750802. F.M. is grateful to FONDECYT/Anillo Act-1410. We thank P. Reis, A. Kösmrlj, J-C. Géminard, J. Bico, B. Roman, E. Katifori, and L. Gordillo for enlightening discussions.

## References

1. A.K. Geim, K.S. Novoselov, *Nat. Mater.* **6**, 183–191 (2007)
2. R. Peierls, *Ann. IH Poincare* **5**, 177–222 (1935)
3. L.D. Landau, E.M. Lifshitz, L. Pitaevskii, *Statistical Physics, Part I* (Pergamon Press, Oxford/New York, 1980)
4. K. Novoselov, A.K. Geim, S. Morozov, D. Jiang, M. Katsnelson, I. Grigorieva, S. Dubonos, A. Firsov, *Nature* **438**, 197–200 (2005)
5. E. Secchi, S. Marbach, A. Niguès, D. Stein, A. Siria, L. Bocquet, *Nature* **537**, 210–213 (2016)
6. L. Lindsay, D. Broido, N. Mingo, *Phys. Rev. B* **82**, 115427 (2010)
7. P. Zhang, L. Ma, F. Fan, Z. Zeng, C. Peng, P.E. Loya, Z. Liu, Y. Gong, J. Zhang, X. Zhang, et al., *Nat. Commun.* **5**, 3782 (2014)
8. T.R. Nayak, H. Andersen, V.S. Makam, C. Khaw, S. Bae, X. Xu, P.-L.R. Ee, J.-H. Ahn, B.H. Hong, G. Pastorin, et al., *ACS Nano* **5**, 4670–4678 (2011)
9. Y.-M. Lin, C. Dimitrakopoulos, K.A. Jenkins, D.B. Farmer, H.-Y. Chiu, A. Grill, P. Avouris, *Science* **327**, 662–662 (2010)
10. T.-H. Han, H. Kim, S.-J. Kwon, T.-W. Lee, *Mater. Sci. Eng. R. Rep* **118**, 1–43 (2017)
11. R.R. Nair, H.A. Wu, P.N. Jayaram, I.V. Grigorieva, A.K. Geim, *Science* **335**, 442–444 (2012)
12. The Graphene Flagship General Assembly 2018. (2018). <https://graphene-flagship.eu/the-graphene-flagship-general-assembly-2018>
13. J.C. Meyer, A.K. Geim, M.I. Katsnelson, K.S. Novoselov, T.J. Booth, S. Roth, *Nature* **446**, 60–63 (2007)
14. A.C. Ferrari, F. Bonaccorso, V. Fal'Ko, K.S. Novoselov, S. Roche, P. Bøggild, S. Borini, F.H. Koppens, V. Palermo, N. Pugno, et al., *Nanoscale* **7**, 4598–4810 (2015)
15. F. Brau, P. Damman, H. Diamant, T.A. Witten, *Soft Matter* **9**, 8177–8186 (2013)
16. J.E. Gordon, *Structures: Or why Things don't Fall Down* (Da Capo Press, Cambridge, MA, 2003)
17. F. Scarpa, S. Adhikari, A.S. Phani, *Nanotechnology* **20**, 065709 (2009)
18. C. Lee, X. Wei, J.W. Kysar, J. Hone, *Science* **321**, 385–388 (2008)
19. G. López-Polín, C. Gómez-Navarro, V. Parente, F. Guinea, M.I. Katsnelson, F. Pérez-Murano, J. Gómez-Herrero, *Nat. Phys.* **11**, 26–31 (2015)
20. Q. Lu, M. Arroyo, R. Huang, *J. Phys. D. Appl. Phys.* **42**, 102002 (2009)
21. D.-B. Zhang, E. Akatyeva, T. Dumitrică, *Phys. Rev. Lett.* **106**, 255503 (2011)
22. A.E.H. Love, *Philos. Trans. R. Soc. Lond. A* **179**, 491–546 (1888)
23. A. Carlson, T. Dumitrică, *Nanotechnology* **18**, 065706 (2007)
24. B. Audoly, Y. Pomeau, *Elasticity and Geometry: From Hair Curls to the Nonlinear Response of Shells* (Oxford University Press, Oxford/New York, 2010)
25. Y. Wei, B. Wang, J. Wu, R. Yang, M.L. Dunn, *Nano Lett.* **13**, 26–30 (2013)
26. I. Nikiforov, E. Dontsova, R.D. James, T. Dumitrică, *Phys. Rev. B* **89**, 155437 (2014)
27. J.H. Los, A. Fasolino, M.I. Katsnelson, *npj 2D Mater. Appl.* **1**, 9 (2017)
28. J. Los, A. Fasolino, M. Katsnelson, *Phys. Rev. Lett.* **116**, 015901 (2006)
29. O. Blakslee, D. Proctor, E. Seldin, G. Spence, T. Weng, *J. Appl. Phys.* **41**, 3373–3382 (1970)
30. L. Tapasztó, T. Dumitrică, S.J. Kim, P. Nemes-Incze, C. Hwang, L.P. Biró, *Nat. Phys.* **8**, 739–742 (2012)

31. Z. Ni, H. Bu, M. Zou, H. Yi, K. Bi, Y. Chen, *Phys. B Condens. Matter* **405**, 1301–1306 (2010)
32. Y. Zhang, L. Liu, N. Xi, Y. Wang, Z. Dong, U.C. Wejinya, *Sci. China Phys. Mech. Astron.* **57**, 663–667 (2014)
33. J.S. Choi, J.-S. Kim, I.-S. Byun, D.H. Lee, M.J. Lee, B.H. Park, C. Lee, D. Yoon, H. Cheong, K.H. Lee, et al., *Science* **333**, 607–610 (2011)
34. A.K. Geim, I.V. Grigorieva, *Nature* **499**, 419–425 (2013)
35. K.S. Novoselov, A. Mishchenko, A. Carvalho, A.H. Castro Neto, *Science* **353**, aac9439 (2016)
36. C.N.R. Rao, A.K. Sood, *Graphene: Synthesis, Properties, and Phenomena* (Wiley, Weinheim, 2013)
37. D. Akinwande, C.J. Brennan, J.S. Bunch, P. Egberts, J.R. Felts, H. Gao, R. Huang, J.-S. Kim, T. Li, Y. Li, et al., *Extreme Mech. Lett.* **13**, 42–77 (2017)
38. G. Wang, Z. Dai, Y. Wang, P. Tan, L. Liu, Z. Xu, Y. Wei, R. Huang, Z. Zhang, *Phys. Rev. Lett.* **119**, 036101 (2017)
39. X. Chen, C. Yi, C. Ke, *Appl. Phys. Lett.* **106**, 101907 (2015)
40. L. Ruiz, W. Xia, Z. Meng, S. Keten, *Carbon* **82**, 103–115 (2015)
41. M. Yamamoto, O. Pierre-Louis, J. Huang, M.S. Fuhrer, T.L. Einstein, W.G. Cullen, *Phys. Rev. X* **2**, 041018 (2012)
42. A. Kösmrlj, D.R. Nelson, *Phys. Rev. E* **88**, 012136 (2013)
43. J.A. Aronovitz, T.C. Lubensky, *Phys. Rev. Lett.* **60**, 2634 (1988)
44. K. Novoselov, D. Jiang, F. Schedin, T. Booth, V. Khotkevich, S. Morozov, A. Geim, *Proc. Natl. Acad. Sci. U. S. A.* **102**, 10451–10453 (2005)
45. J. Venables, G. Spiller, M. Hanbucken, *Rep. Prog. Phys.* **47**, 399 (1984)
46. J. Evans, P. Thiel, M.C. Bartelt, *Surf. Sci. Rep.* **61**, 1–128 (2006)
47. A. Fasolino, J. Los, M.I. Katsnelson, *Nat. Mater.* **6**, 858–861 (2007)
48. R.J. Nicholl, H.J. Conley, N.V. Lavrik, I. Vlassioux, Y.S. Puzyrev, V.P. Sreenivas, S.T. Pantelides, K.I. Bolotin, *Nat. Commun.* **6**, 8789 (2015)
49. E.V. Castro, H. Ochoa, M.I. Katsnelson, R.V. Gorbachev, D.C. Elias, K.S. Novoselov, A.K. Geim, F. Guinea, *Phys. Rev. Lett.* **105**, 266601 (2010)
50. P. Partovi-Azar, N. Nafari, M.R.R. Tabar, *Phys. Rev. B* **83**, 165434 (2011)
51. M.B. Amar, Y. Pomeau, *Proc. Math. Phys. Eng. Sci.* **453**, 729–755 (1997)
52. P. Grandgeorge, N. Krins, A. Hourlier-Fargette, C. Laberty-Robert, S. Neukirch, A. Antkowiak, *Science* **360**, 296–299 (2018)
53. T.M.G. Mohiuddin, A. Lombardo, R.R. Nair, A. Bonetti, G. Savini, R. Jalil, N. Bonini, D.M. Basko, C. Galiotis, N. Marzari, et al. *Phys. Rev. B* **79**, 205433 (2009)
54. A.C. Ferrari, D.M. Basko, *Nat. Nanotechnol.* **8**, 235 (2013)
55. N. Colthup, *Introduction to Infrared and Raman Spectroscopy* (Elsevier, Burlington, 2012)
56. D. Yoon, Y.-W. Son, H. Cheong, *Nano Lett.* **11**, 3227–3231 (2011)
57. L. Malard, M. Pimenta, G. Dresselhaus, M. Dresselhaus, *Phys. Rep.* **473**, 51–87 (2009)
58. F. Yavari, C. Kritzing, C. Gaire, L. Song, H. Gulapalli, T. Borca-Tasciuc, P.M. Ajayan, N. Koratkar, *Small* **6**, 2535–2538 (2010)
59. Z.H. Ni, T. Yu, Z.Q. Luo, Y.Y. Wang, L. Liu, C.P. Wong, J. Miao, W. Huang, Z.X. Shen, *ACS Nano* **3**, 569–574 (2009)
60. L.G. Cançado, A. Jorio, E.M. Ferreira, F. Stavale, C. Achete, R. Capaz, M. Moutinho, A. Lombardo, T. Kulmala, A. Ferrari, *Nano Lett.* **11**, 3190–3196 (2011)
61. R. Roldán, A. Fasolino, K.V. Zakharchenko, M.I. Katsnelson, *Phys. Rev. B* **83**, 174104 (2011)
62. G. López-Polín, M. Jaafar, F. Guinea, R. Roldán, C. Gómez-Navarro, J. Gómez-Herrero, *Carbon* **124**, 42–48 (2017)
63. R.J.T. Nicholl, N.V. Lavrik, I. Vlassioux, B.R. Srijanto, K.I. Bolotin, *Phys. Rev. Lett.* **118**, 266101 (2017)
64. Y. Huang, J. Wu, K.-C. Hwang, *Phys. Rev. B* **74**, 245413 (2006)
65. A. Kösmrlj, D.R. Nelson, *Phys. Rev. X* **7**, 011002 (2017)

66. P. Le Doussal, L. Radzihovsky, Phys. Rev. Lett. **69**, 1209 (1992)
67. D. Nelson, L. Peliti, J. Phys. **48**, 1085–1092 (1987)
68. P. Flory, M. Volkenstein, et al., *Statistical Mechanics of Chain Molecules* (Hanser Publishers, Munich, 1969)
69. P.-G. De Gennes, P.-G. Gennes, *Scaling Concepts in Polymer Physics* (Cornell University Press, Ithaca/London, 1979)
70. M.J. Bowick, A. Kösmrlj, D.R. Nelson, R. Sknepnek, Phys. Rev. B **95**, 104109 (2017)
71. M.K. Bleses, A.W. Barnard, P.A. Rose, S.P. Roberts, K.L. McGill, P.Y. Huang, A.R. Ruyack, J.W. Kevek, B. Kobrin, D.A. Muller, et al., Nature **524**, 204 (2015)
72. W. CAN, O. LOG, Bioscience **51**, 341–352 (2001)
73. N. Lindahl, D. Midtvedt, J. Svensson, O.A. Nerushev, N. Lindvall, A. Isacsson, E.E. Campbell, Nano Lett. **12**, 3526–3531 (2012)
74. S. Scharfenberg, D. Rocklin, C. Chialvo, R.L. Weaver, P.M. Goldbart, N. Mason, Appl. Phys. Lett. **98**, 091908 (2011)
75. P.L. De Andres, F. Guinea, M.I. Katsnelson, Phys. Rev. B **86**, 144103 (2012)
76. G. López-Polín, M. Ortega, J. Vilhena, I. Alda, J. Gomez-Herrero, P.A. Serena, C. Gomez-Navarro, R. Pérez, Carbon **116**, 670–677 (2017)
77. X. Hu, P. Yasaei, J. Jokisaari, S. Ögüt, A. Salehi-Khojin, R.F. Klie, Phys. Rev. Lett. **120**, 055902 (2018)
78. W. Bao, F. Miao, Z. Chen, H. Zhang, W. Jang, C. Dames, C.N. Lau, Nat. Nanotechnol. **4**, 562–566 (2009)
79. C. Moreno, M. Vilas-Varela, B. Kretz, A. Garcia-Lekue, M.V. Costache, M. Paradinas, M. Panighel, G. Ceballos, S.O. Valenzuela, D. Peña, et al., Science **360**, 199–203 (2018)
80. J.D. Eshelby, Proc. R. Soc. Lond. A Math. Phys. Eng. Sci. **241**, 376–396 (1957)
81. R.W. Style, R. Boltyanskiy, B. Allen, K.E. Jensen, H.P. Foote, J.S. Wettlaufer, E.R. Dufresne, Nat. Phys. **11**, 82–87 (2015)
82. N. Fleck, G. Muller, M. Ashby, J. Hutchinson, Acta Metall. Mater. **42**, 475–487 (1994)
83. J. GREER, W. OLIVER, W. NIX, Acta Mater. **54**, 1705–1705 (2006)
84. T. Zhang, X. Li, H. Gao, Extreme Mech. Lett **1**, 3–8 (2014)
85. T. Zhang, H. Gao, J. Appl. Mech. **82**, 051001 (2015)
86. N.P. Mitchell, V. Koning, V. Vitelli, W.T.M. Irvine, Nat. Mater. **16**, 89–93 (2017)
87. G. López-Polín, J. Gómez-Herrero, C. Gómez-Navarro, Nano Lett. **15**, 2050–2054 (2015)
88. A.A. Griffith, M. Eng, Philos. Trans. R. Soc. Lond. A **221**, 163–198 (1921)
89. J.N. Grima, S. Winczewski, L. Mizzi, M.C. Grech, R. Cauchi, R. Gatt, D. Attard, K.W. Wojciechowski, J. Rybicki, Adv. Mater. **27**, 1455–1459 (2014)
90. H. Qin, Y. Sun, J.Z. Liu, M. Li, Y. Liu, Nanoscale **9**, 4135–4142 (2017)
91. C. Wang, L. Lan, Y. Liu, H. Tan, Comput. Mater. Sci. **77**, 250–253 (2013)
92. T. Zhang, X. Li, H. Gao, J. Mech. Phys. Solids **67**, 2–13 (2014)
93. I. Gornyi, V.Y. Kachorovskii, A. Mirlin, Phys. Rev. B **92**, 155428 (2015)
94. J. Annett, G.L. Cross, Nature **535**, 271–275 (2016)
95. E. Hamm, P. Reis, M. LeBlanc, B. Roman, E. Cerda, Nat. Mater. **7**, 386–390 (2008)
96. X. Chen, L. Zhang, Y. Zhao, X. Wang, C. Ke, J. Appl. Phys. **116**, 164301 (2014)
97. Z. Budrikis, S. Zapperi, Nano Lett. **16**, 387–391 (2015)
98. J. Bunch, M. Dunn, Solid State Commun. **152**, 1359–1364 (2012)
99. S.P. Koenig, N.G. Boddeti, M.L. Dunn, J.S. Bunch, Nat. Nanotechnol. **6**, 543–546 (2011)
100. D. Sen, K.S. Novoselov, P.M. Reis, M.J. Buehler, Small **6**, 1108–1116 (2010)
101. O.C. Compton, S.T. Nguyen, Small **6**, 711–723 (2010)
102. M.J. Allen, V.C. Tung, R.B. Kaner, Chem. Rev. **110**, 132–145 (2009)
103. M. Yi, Z. Shen, Carbon **78**, 622–626 (2014)
104. D.H. Seo, S. Pineda, J. Fang, Y. Gozukara, S. Yick, A. Bendavid, S.K.H. Lam, A.T. Murdock, A.B. Murphy, Z.J. Han, et al. Nat. Commun. **8**, 14217 (2017)
105. C. Mattevi, H. Kim, M. Chhowalla, J. Mater. Chem. **21**, 3324–3334 (2011)
106. D. Bandurin, I. Torre, R.K. Kumar, M.B. Shalom, A. Tomadin, A. Principi, G. Auton, E. Khestanova, K. Novoselov, I. Grigorieva, et al., Science **351**, 1055–1058 (2016)

107. W. Yang, G. Chen, Z. Shi, C.-C. Liu, L. Zhang, G. Xie, M. Cheng, D. Wang, R. Yang, D. Shi, et al. *Nat. Mater.* **12**, 792–797 (2013)
108. P. Sutter, J.T. Sadowski, E. Sutter, *Phys. Rev. B* **80**, 245411 (2009)
109. C.H. Lui, L. Liu, K.F. Mak, G.W. Flynn, T.F. Heinz, *Nature* **462**, 339 (2009)
110. A.L.V. de Parga, F. Calleja, B. Borca, M.C.G. Passeggi, J.J. Hinarejos, F. Guinea, R. Miranda, *Phys. Rev. Lett.* **100**, 056807 (2008)
111. S. Goler, C. Coletti, V. Tozzini, V. Piazza, T. Mashoff, F. Beltram, V. Pellegrini, S. Heun, *J. Phys. Chem. C* **117**, 11506–11513 (2013)
112. S.J. Chae, F. Güneş, K.K. Kim, E.S. Kim, G.H. Han, S.M. Kim, H.-J. Shin, S.-M. Yoon, J.-Y. Choi, M.H. Park, et al. *Adv. Mater.* **21**, 2328–2333 (2009)
113. N. Liu, Z. Pan, L. Fu, C. Zhang, B. Dai, Z. Liu, *Nano Res.* **4**, 996–1004 (2011)
114. C.T. Cherian, F. Giustiniiano, I. Martin-Fernandez, H. Andersen, J. Balakrishnan, B. Özyilmaz, *Small* **11**, 189–194 (2015)
115. L. Gao, G.-X. Ni, Y. Liu, B. Liu, A.H.C. Neto, K.P. Loh, *Nature* **505**, 190–194 (2014)
116. X. Liang, B.A. Sperling, I. Calizo, G. Cheng, C.A. Hacker, Q. Zhang, Y. Obeng, K. Yan, H. Peng, Q. Li, et al., *ACS Nano* **5**, 9144–9153 (2011)
117. N. Levy, S. Burke, K. Meaker, M. Panlasigui, A. Zettl, F. Guinea, A.C. Neto, M. Crommie, *Science* **329**, 544–547 (2010)
118. S. Böttcher, H. Vita, M. Weser, F. Bisti, Y.S. Dedkov, K. Horn, *J. Phys. Chem. Lett.* **8**, 3668–3672 (2017)
119. Q. Pei, Y. Zhang, V. Shenoy, *Carbon* **48**, 898–904 (2010)
120. P. Poulin, R. Jalili, W. Neri, F. Nallet, T. Divoux, A. Colin, S.H. Aboutalebi, G. Wallace, C. Zakri, *Proc. Natl. Acad. Sci.* 201605121 (2016)
121. S.A. Svatek, O.R. Scott, J.P. Rivett, K. Wright, M. Baldoni, E. Bichoutskaia, T. Taniguchi, K. Watanabe, A.J. Marsden, N.R. Wilson, et al., *Nano Lett.* **15**, 159–164 (2014)
122. J.H. Lee, A. Avsar, J. Jung, J.Y. Tan, K. Watanabe, T. Taniguchi, S. Natarajan, G. Eda, S. Adam, A.H. Castro Neto, et al., *Nano Lett.* **15**, 319–325 (2014)
123. F. Schedin, A.K. Geim, S.V. Morozov, E.W. Hill, P. Blake, M.I. Katsnelson, K.S. Novoselov, *Nat. Mater.* **6**, 652–655 (2007)
124. Z. Gao, H. Xia, J. Zauberman, M. Tomaiuolo, J. Ping, Q. Zhang, P. Ducos, H. Ye, S. Wang, X. Yang, et al., *Nano Lett.* **18**, 3509–3515 (2018)
125. C. Py, P. Reverdy, L. Doppler, J. Bico, B. Roman, C.N. Baroud, *Phys. Rev. Lett.* **98**, 156103 (2007)
126. M. Boudot, H. Elettro, D. Grosso, *ACS Nano* **10**, 10031–10040 (2016)
127. J. Kim, J.A. Hanna, M. Byun, C.D. Santangelo, R.C. Hayward, *Science* **335**, 1201–1205 (2012)
128. Y. Zhang, F. Zhang, Z. Yan, Q. Ma, X. Li, Y. Huang, J.A. Rogers, *Nature Reviews Materials* **2**, 17019 (2017)
129. B. Florijn, C. Coulais, M. van Hecke, *Phys. Rev. Lett.* **113**, 175503 (2014)
130. J. Zang, S. Ryu, N. Pugno, Q. Wang, Q. Tu, M.J. Buehler, X. Zhao, *Nat. Mater.* **12**, 321–325 (2013)
131. M.Z. Miskin, K.J. Dorsey, B. Bircan, Y. Han, D.A. Muller, P.L. McEuen, I. Cohen, *Proc. Natl. Acad. Sci.* **115**, 466–470 (2018)
132. M. Poot, H.S. van der Zant, *Appl. Phys. Lett.* **92**, 063111 (2008)
133. K.S. Novoselov, V.I. Falko, L. Colombo, P.R. Gellert, M.G. Schwab, K. Kim, *Nature* **490**, 192–200 (2012)
134. Y. Liu, Z. Xu, Q. Zheng, *J. Mech. Phys. Solids* **59**, 1613–1622 (2011)
135. C. Chen, S. Rosenblatt, K.I. Bolotin, W. Kalb, P. Kim, I. Kymissis, H.L. Stormer, T.F. Heinz, J. Hone, *Nat. Nanotechnol.* **4**, 861–867 (2009)
136. J.S. Bunch, A.M. van der Zande, S.S. Verbridge, I.W. Frank, D.M. Tanenbaum, J.M. Parpia, H.G. Craighead, P.L. McEuen, *Science* **315**, 490–493 (2007)
137. F. Xia, D.B. Farmer, Y.-m. Lin, P. Avouris, *Nano Lett.* **10**, 715–718 (2010)
138. J. Berashevich, T. Chakraborty, *Phys. Rev. B* **80**, 033404 (2009)

139. D.C. Elias, R.R. Nair, T. Mohiuddin, S. Morozov, P. Blake, M. Halsall, A. Ferrari, D. Boukhvalov, M. Katsnelson, A. Geim, et al., *Science* **323**, 610–613 (2009)
140. R. Phillipson, C.J. Lockhart de la Rosa, J. Teyssandier, P. Walke, D. Waghray, Y. Fujita, J. Adisoejoso, K.S. Mali, I. Asselberghs, C. Huyghebaert, et al. *Nanoscale* **8**, 20017–20026 (2016)
141. X. Wang, Y. Ouyang, X. Li, H. Wang, J. Guo, H. Dai, *Phys. Rev. Lett.* **100**, 206803 (2008)
142. M.I. Katsnelson, *Mater. Today* **10**, 20–27 (2007)
143. G. Gui, J. Li, J. Zhong, *Phys. Rev. B* **78**, 075435 (2008)
144. F. Guinea, M. Katsnelson, A. Geim, *Nat. Phys.* **6**, 30 (2010)
145. V.M. Pereira, A.H. Castro Neto, H.Y. Liang, L. Mahadevan, *Phys. Rev. Lett.* **105**, 156603 (2010)
146. J. Martin, N. Akerman, G. Ulbricht, T. Lohmann, J.v. Smet, K. Von Klitzing, A. Yacoby, *Nat. Phys.* **4**, 144 (2008)
147. V. Tozzini, V. Pellegrini, *Phys. Chem. Chem. Phys.* **15**, 80–89 (2013)
148. C. Ataca, E. Aktu'rk, S. Ciraci, H. Ustunel, *Appl. Phys. Lett.* **93**, 043123 (2008)
149. A. Tapia, C. Acosta, R. Medina-Esquivel, G. Canto, *Comput. Mater. Sci.* **50**, 2427–2432 (2011)
150. V. Tozzini, V. Pellegrini, *J. Phys. Chem. C* **115**, 25523–25528 (2011)
151. Y. Han, Z. Xu, C. Gao, *Adv. Funct. Mater.* **23**, 3693–3700 (2013)
152. R. Joshi, P. Carbone, F.-C. Wang, V.G. Kravets, Y. Su, I.V. Grigorieva, H. Wu, A.K. Geim, R.R. Nair, *Science* **343**, 752–754 (2014)
153. M. Ma, G. Tocci, A. Michaelides, G. Aeppli, *Nat. Mater.* **15**, 66–71 (2016)

# Chapter 11

## Wrinkling Labyrinth Patterns on Elastomeric Janus Particles



Ana Catarina Trindade, Pedro Patrício, Paulo Ivo Teixeira,  
and Maria Helena Godinho

### 11.1 Janus Particles

#### 11.1.1 Colloidal Particles

The significant advances in colloidal particles made in the last century produced a large number of studies, new applications, and products for beneficial uses.

The name “colloid” derives from the Greek word “*kolas*”, which means “the glue thing,” and was first popularized by the Scottish chemist Thomas Graham in 1870. Nowadays, the science of colloids covers a large number of sections of physical chemistry and technology [1].

Colloidal particles are fundamental to nature and technology. Colloids are heterogeneous mixtures where one of the substances is dispersed in another, in the

---

A. C. Trindade (✉)

Department of Physics, Norwegian University of Science and Technology (NTNU),  
Trondheim, Norway

i3N/CENIMAT, Faculdade de Ciências e Tecnologia, FCT, Universidade NOVA de Lisboa,  
Campus de Caparica, Caparica, Portugal

e-mail: [ana.c.trindade@ntnu.no](mailto:ana.c.trindade@ntnu.no)

P. Patrício · P. I. Teixeira

ISEL – Instituto Superior de Engenharia de Lisboa, Instituto Politécnico de Lisboa,  
Lisbon, Portugal

Centro de Física Teórica e Computacional, Faculdade de Ciências da Universidade de Lisboa,  
Lisboa, Portugal

M. H. Godinho

i3N/CENIMAT, Faculdade de Ciências e Tecnologia, FCT, Universidade NOVA de Lisboa,  
Campus de Caparica, Caparica, Portugal

Departamento de Ciência dos Materiais, Faculdade de Ciências e Tecnologia, FCT,  
Universidade NOVA de Lisboa, Campus de Caparica, Caparica, Portugal

form of small particles or aggregates of molecules. The discrete phase is known as the disperse medium, while the continuous phase is the dispersant medium. Colloids are particles that have a diameter of hundreds of nanometers to a few micrometers and that are evenly dispersed in fluids [2]. Colloids are also known as colloidal dispersions because the particles remain dispersed in the fluid, not settling down at the bottom, as happens in a suspension. Two typical phenomena that are exhibited in colloidal dispersions are Brownian motion (a random zigzag motion of particles that can be seen under a microscope) and the Tyndall effect (when a strong light is shone through a colloidal dispersion, the light beam becomes visible as a column of light) [3].

Colloids are ubiquitous in our everyday life, dating back to ancient times. They have a huge impact and influence and are used frequently in several processes of goods (included potable water), in separation processes in biotechnology, in wastewater treatment, and/or in orthomolecular therapy. Some useful examples include mayonnaise, colored glass, milk, butter, muddy water, gelatin, blood, hair spray, clouds, or paper. Other colloids can be undesirable, like soot or particle pollution, for example. From a scientific point of view, colloids are very interesting systems, as they combine the essence of both microscopic particles and macroscopic objects: they are small enough to be agitated by thermal energy yet large and slow enough in their Brownian diffusion to be observed by optical microscopy in real time. Dominant interactions in colloidal systems, such as electrostatic, van der Waals, and dipolar interactions, govern the system behavior in a similar manner, as in atomic and molecular systems [4].

Colloidal nanoparticles can become the “atoms” and “molecules” of tomorrow’s materials if they can be successfully assembled into useful structures.

It can be confusing to distinguish some colloidal suspensions from solutions, but an easy membrane test can be useful. If the “solution/suspension” passes through the membrane, it is a solution; if not, it is a colloidal solution or suspension.

### ***11.1.2 Janus Particles: A Special Class of Colloidal Particles***

In mythology, Janus is the god with two faces who represents dichotomy. Usually, he was placed in the doors of temples back to back, so he could look in opposite directions at the same time.

The first scientific work on Janus particles was presented in 1985 by Lee et al. on asymmetric poly(styrene)/poly(methyl methacrylate) (PMMA) lattices from seeded emulsion polymerization [5]. Later, Casagrande and Veyssié performed some investigations on glass spheres and described the preparation of nanobeads, which was made hydrophobic on only one hemisphere using octadecyltrichlorosilane, while the other hemisphere was protected with a cellulosic varnish [6, 7].

However, the concept of Janus particles was only popularized a few years later, in 1991, by de Gennes in his Nobel Lecture [8]. de Gennes proposed a new kind of surfactant, amphiphilic colloidal particles with one polar face and one nonpolar face [8]. Of all surfactants, this one would adsorb to a liquid interface, and the amphiphilicity would stabilize the interface but allow the “skin” to “breathe” through interstices between these Janus particles. Since then, there has been huge progress in exploiting this anisotropy for materials design and assembly.

The Janus god had two faces. Similarly, Janus asymmetric particles have two incompatible sides. Janus structures are objects on a micro- or nanometer scale that possess non-centrosymmetric architectures. Janus particles are a special class of colloidal particles with different chemical makeups on their two hemispheres. The terminology is based on the special architectural feature of having two sides or at least two surfaces of different chemistry and/or polarity [9]. The most common type of Janus particle is a nanosized sphere with hemispherical amphiphilicity, that is, one-half of the sphere is polar and, the other half is nonpolar.

As is often the case in modern materials research, it is possible to find an analog to Janus particles in nature (fungi, plants, viruses, etc.) [10].

The concept of Janus particles did not attract much attention until about 15 years later, but now this concept is widespread in the field of colloidal systems [11–13]. This original Janus concept has drawn in scientists and engineers, and different Janus particles of different sizes and shapes have been reported (Fig. 11.1). Inorganic materials [14–17], dendrimers [18–20], liquid crystalline compounds [21–23], and polymers [24–27] have been used to synthesize Janus-like asymmetric architectures.

**Fig. 11.1** Schematic illustration of the two-faced Roman god Janus (middle) and Janus particles of different morphologies and shapes



### 11.1.3 *Janus Particles: Synthesis and Applications*

Since the first synthesis of Janus particles in 1988 [6, 7], many useful and imaginative approaches and methods have been developed for the fabrication and development of Janus structures, not only in small amounts for academic study but also in large amounts suited for industrial use.

Powerful tools for engineering the production of particular target structures in Janus particles have been based on chemical methods (selective crystallization and deposition), physical methods (electrified jetting, microcontact printing, emulsion drying, selective deposition, surface templating, direct writing, or lithography), or biologically inspired methods (which include the use of plant extracts, fungi, or viruses to synthesize metal nanoparticles of various shapes). Different new approaches to particle synthesis can give a wide spectrum of particle anisotropies with many exotic structures and diverse peculiar properties (e.g., electronic and optical).

The various materials and techniques that can be employed to synthesize Janus particles can be classified into two different categories: surface modification (selectively modifying only one part of isotropic particles to make their surface anisotropic) and compartmentalization (building Janus particles from scratch so the synthesized particles are anisotropic in composition).

Nowadays surface modification is the most common and exploited method to synthesize Janus anisotropic particles. This is due to the fact that the synthesis of nano- and colloidal particles with isotropic surface chemistry is a very well-known and well-exploited field. Janus particles can be easily derived from surface modification schemes of isotropic particles. The main idea is to protect part of the initially homogeneous particle when modifying the unprotected part. This protection can be applied using masks, templates, and/or geometric constraints imposed by neighboring particles. Sometimes this procedure can also be combined with the development of physical vapor or lithography techniques.

Another alternative method of surface modification is physical deposition using electron beam evaporation or sputter coating. This allows the design of Janus particles with many new and elaborate geometries. Moreover, using directional coating by electron beam evaporation of a monolayer of colloidal particles, anisotropic particles can be produced that are coated with metals or other materials in a precise half-half geometry. Using sequential physical deposition and/or new masks, it is possible to obtain Janus anisotropic particles with more than one patch.

Especially if particular surface chemistry properties are desired, the coating can also enable the surface modification of colloidal particles.

The compartmentalization method allows obtaining anisotropic particles that are Janus not only on the surface but also in the bulk. Depending on the synthesis technique, a wide range of different compartments can be realized, thus expanding the potential functions and applications of these Janus particles.

Different methods to synthesize multiple separated compartments in a single Janus particle have been tested and developed, including microfluidics [29–32] and

electrodynamic cojetting [33, 34], chemical synthesis, and polymer self-assembly [35–37].

The appeal of the Janus concept goes far beyond synthesis, and Janus particles are very useful in self-assembly. The interactions between Janus particles are much more complex than for two isotropic particles and depend not only on particle separation but also on mutual concentration and relative orientations. The two different faces of a Janus particle respond to an external field (electric field, magnetic field, chemical gradient, temperature gradient, etc.) differently, which leads to the assembly of micelles and membranes that are vital to cells and other several biological functions. The versatility of these Janus particles allows the tuning of the properties and functions of self-assembled materials and offers new approaches to designing new materials with controlled and desirable properties.

Many fascinating potential applications for Janus anisotropic particles arise from the fact that they possess two distinguishable faces [38]. Janus particles can be used not only as solid surfactants, as predicted by de Gennes [8], but also in many other interesting and novel potential applications that include interfacial stabilizers [39–41], microprobes or biosensors [27, 42, 43], drug delivery [44–47], reconfigurable materials (electronic paper or displays) [48–50], nanoengines [51–53] or micromotors [54, 55], optical imaging [28, 56], diagnosis applications, [57–59] and catalysis [60–62]. Because of the broad definition of Janus particles, many micro- and nano-sized particles possessing anisotropic properties are classed as Janus [38]. Actually, the concept of Janus particles includes all colloidal-sized particles with two regions of different surface chemical composition, possessing interactions that depend not only on their separation but also on their orientation [63, 64].

## 11.2 Static and Dynamic Periodic Patterns: Wrinkling and Buckling

Static and dynamic periodic patterns, such as stripes and dots, are ubiquitous in nature and are present in different sizes and shapes, such as plant pollens and peppercorn seeds. These wrinkled patterns range from small wrinkles in soft materials such as the skin to much larger wavelength buckles in lava flows. This kind of wrinkles is frequently observed in pumpkins, melons, nuts, and dehydrated fruits or even in the skin of large animals (e.g., elephants, rhinos, and reptiles). Biological systems also show numerous self-organized periodic patterns, such as the stripe pattern of intestines and arteries, the surface pattern of the brain, and the microtopographical surface structures on lotus leaves. Even at the cellular scale, latitudinal undulations have been found in human neutrophil cells, mineralized yeast cells, fish spawns, and venom-infected sperm. Some of the patterns, present in such complex systems, have evolved by natural selection over millions of years and enhance survival and prosperity in nature. Some examples of how this periodicity can be useful to some biological systems are the reduction of turbulent drag/hydrodynamic

friction as found on sharkskin or dragonfly wings, special wetting/cleaning properties such as the celebrated lotus effect, and the skin surface of the so-called “sandfish” which reduces friction and abrasion dramatically by shrinking the specific friction surface (so, sandfish can even “swim” under the sand). Wrinkles and folds also play an important role in facilitating nutrient absorption in intestines. They are invaluable when attempting to improve or correct nature, e.g., by aiding cell adhesion at the interfaces of biomaterials and biological systems.

Given this amount and diversity of benefits, it is not surprising that a huge variety of approaches to the fabrication of such structures has been developed in recent years.

### 11.3 Wrinkling in Freestanding Flexible Elastomers

In this chapter, we will focus on different surface topographies of elastomeric particles. Most of the work done, so far, in this field is related to polydimethylsiloxane (PDMS) elastomers [65–68]. We will focus on polyurethane/urea elastomers because that is our field of expertise and because they are the precursor materials for the wrinkling labyrinthic Janus particles discussed in this chapter. However, qualitatively the same effects can be obtained with any other network-forming polymer.

In block copolymers containing stiff and soft groups, if one or more of the reactive blocks is multifunctional (functionality,  $f > 2$ ), chains can be cross-linked, and a polymeric network is obtained.

The polyurethane/urea elastomeric membranes prepared earlier [69, 70], from precursor solutions composed of a polyurethane prepolymer (PU,  $f = 3$ ) in the presence of hydroxyl terminated prepolymer (PBDO,  $f = 2$ ), exhibited quite uncommon behavior on stretching. Instead of becoming whitish during stretching and then clear again when the strain is removed, these polyurethane/urea films remained fairly clear on stretching and became translucent when released. This interesting mechanico-optical effect was found to be reversible and dependent on the preparation conditions and on the applied external stress. Detailed microscopic observation of the films revealed different surface properties and the existence of a texture of bands and wrinkles, arranged perpendicularly to the direction of stretching [69, 71].

It was also found that the morphological features of the freestanding urethane/urea elastomeric film surface can be tuned, in a reproducible and reversible way. Moreover, for the same elastomeric material, six pattern states were described, the relation between them and how they can be manipulated (Fig. 11.2).

The mechanism of how wrinkled patterns appear on elastomeric films can be interpreted in terms of a simple model proposed in 1998 by Bowden [72]. In this model, we consider that each film consists of two different parts: a stiff skin on top of a soft(er) bulk. In the case of urethane/urea films, the upper skin results from the more extensive cross-linking of the polyurethane promoted by ultraviolet (UV) irradiation. When the film is stretched, the skin and substrate deform in different ways: the stiff skin will deform plastically more than the substrate. After removing the

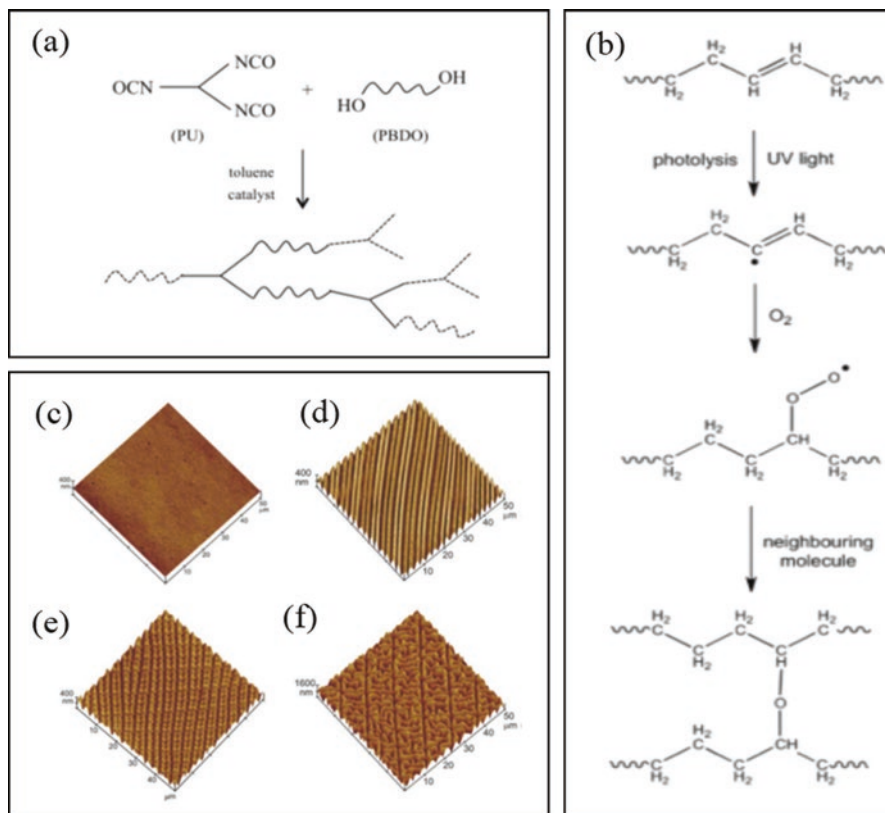


**Fig. 11.2** (a) Synthesis of bi-soft segment urethane/urea elastomers from poly (propylene oxide) (PU), with a degree of polymerization ( $DP$ ) equal to 20 and a functionality ( $f$ ) of 3 and polybutadiene diol (PBDO with  $DP = 50$  and  $f = 2$ ). (b) Schematic of PBDO double-bond opening, by UV in the presence of oxygen, which promotes the cross-linking reaction on the irradiated surface of the spheres. (c–f) AFM images of a polyurethane/polybutadiene diol (PU/PBDO) film: (c) Immediately after UV irradiation and before any mechanical stress has been applied, the film is smooth; (d) stretching the film along one direction induces a regular one-dimensional wrinkling. (e) Further stretching along a second direction perpendicular to the first induces a two-dimensional texture resulting from the superposition of the two one-dimensional waves of wrinkling. (f) Swelling the film in toluene imprints the texture permanently. (Adapted from Ref. [73] © 2017, Taylor and Francis Online and © 2006, Springer, reproduced with permission; and adapted from Ref. [69]. © EDP Sciences/Società Italiana di Fisica/Springer-Verlag 2007, reproduced with kind permission of The European Physical Journal (EPJ))

stress, the substrate will want to go back to its original (pre-deformation) dimensions, but the skin is now bigger than it was before. The result is a net compressive stress acting on the skin (due to the bulk) and a net extensional stress acting on the bulk (due to the skin) (Fig. 11.3).

In other words, the skin behaves as an elastic plate subjected to in-plane compression; hence it will buckle. The wrinkle wavelength,  $\lambda$ , will be determined by the

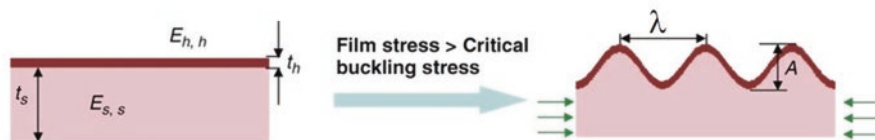


**Fig. 11.3** Wrinkle formation through buckling instabilities in various bilayer systems. Schematic for wrinkle formation in a “bilayer system.”  $E$  and  $t$  are the film elastic modulus and film thickness, respectively. The subscripts “ $h$ ” and “ $s$ ” denote the top (stiff) layer and bottom (soft) layer;  $\lambda$  and  $A$  are the wrinkle wavelength and amplitude. (Adapted from Ref. [72] by permission of Nature Publishing Group)

competition between the bending energy of the thin stiff skin (which penalizes short wavelengths) and the bulk elastic energy of the softcore (which penalizes long wavelengths). This yields that the flat state becomes linearly unstable with respect to a wrinkled state of wavelength given by:

$$\lambda \sim t_h (E_h / E_s)^{1/3} \quad (11.1)$$

where  $E_h$  and  $E_s$  are Young’s moduli of the stiff skin and the softcore, respectively, and  $t_h$  is the stiff skin thickness, assumed to be much smaller than that of the substrate. Thus, the wrinkle wavelength scales with the thickness of the stiff layer, which is the only relevant length scale in the problem.

## 11.4 Janus Wrinkled Spheres

Other Janus membranes and particles with other geometries may be more convenient for potential applications. Wrinkled spheres and colloids (based on PMDS, silica, or silicone rubbers) have been prepared by several different methods: directly from wrinkled templates [74], directional UV-induced reactions [75], selective contact thermodynamic reactions [76], stress-driven [77], photolithography [78], aerodynamic dry control [79], pickering emulsion [80], selective  $O_2$  plasma exposure [81], chemical oxidation [82], protecting masks [83], etc. Despite all this work, wrinkling labyrinth patterns on elastomeric Janus particles have only been exploited for spheres produced from polyurethane/urea systems mentioned in the previous paragraph.

Using the same chemistry as for films, a simple microfluidic device (adapted from Ref. [84]) can be employed to obtain spherical elastomeric polyurethane/urea particles with diameters, ranging from tenths of a micron to a few mm [85]. After being produced, washed, and isolated, one hemisphere of these spheres was modified, without altering the surface of the other, by temporarily masking the hemisphere to be left unmodified during UV irradiation. Masking can be achieved by depositing the precursor particles onto a solid opaque cellulosic film. The wrinkled surface of the Janus sphere will appear on the irradiated hemisphere after swelling

and de-swelling the whole sphere in an appropriate solvent. Thus, similar to the elastomeric urethane/urea films, these Janus spheres can also possess one wrinkled hemisphere, while the other hemisphere is smooth (Fig. 11.4).

During swelling in an appropriate solvent, both the inner (softer) core and the outer (stiffer) skin deform by the same amount, and the outer surface remains smooth. Upon drying (deswelling) all the elastomer network will contract, due to the loss of solvent and to the loss of the unreacted prepolymer blocks (“sol fraction”).

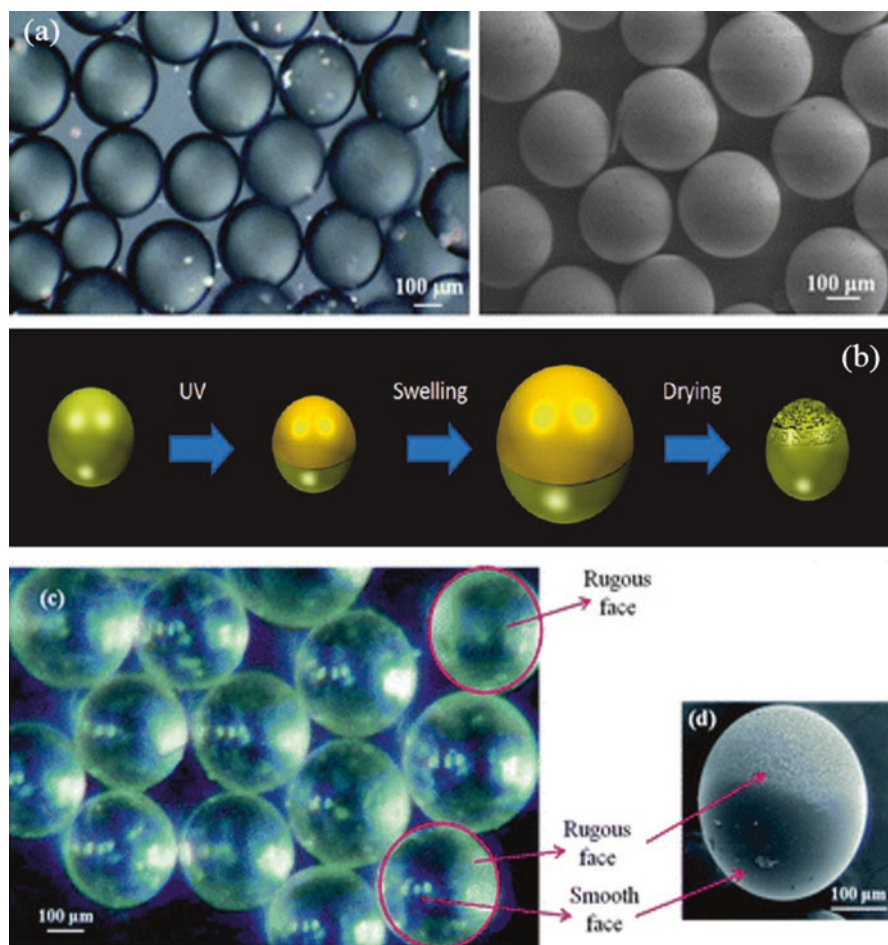


**Fig. 11.4** (a) Monodisperse micro-sized spheres can be produced using a simple fluidic device: POM and SEM images of spheres with a diameter of about 300 nm. (b) Schematic of the production of asymmetric elastomeric particles with wrinkling labyrinth patterns on one hemisphere: UV irradiation is followed by swelling the particles in toluene and drying them. (c–d) Photos of the spheres’ scattering wrinkled and shiny smooth hemispheres after UV irradiation. (Adapted from Ref. [85] with permission from The Royal Society of Chemistry) (Adapted with permission from *Macromolecules* **2011**, *44* (7), 2220–2228. © 2011, American Chemical Society)

The softer core has a lower cross-linking density and will recover its natural dimensions, whereas the stiff skin, being more densely cross-linked, will not. Consequently, this size mismatch gives rise to an internal stress, which triggers the buckling instability of the skin, resulting in an asymmetric Janus elastomeric sphere with two different hemispheres: one smooth and one wrinkly.

Taking into account the model proposed for the films [72], in these elastomeric spheres, the wavelength  $\lambda$  of the buckling linear instability will depend on the dimensionless ratio of the thickness of the outer skin ( $t_h$ ) and the radius of the sphere ( $R$ ).

The dependence of the wrinkle wavelength  $\lambda$  vs. the colatitude  $\theta$  (where  $\theta = 0^\circ$  corresponds to the point where the incident UV light was shone perpendicular to the sphere and  $\theta = 90^\circ$  to the boundary between the two half-hemispheres) is plotted in Fig. 11.5. The thickness of the stiff skin (shown in the inset) decreases from  $\theta = 0^\circ$  to  $\theta = 90^\circ$ , which clearly affects  $\lambda$ . For a cylindrical geometry, a generalization of Eq. (11.1) was derived from an analytical approach:

$$\lambda / R \sim (t_h / R)^{3/4} \quad (11.2)$$

valid for  $R/h < 50$  (above this value one essentially recovers Eq. (11.1)), whereas a fit to our experimental data (for Janus spheres) gave an exponent of 0.82 instead [86]. This is in reasonable agreement with numerical results by Cao et al. [87] for micron-sized particles consisting of a closed silica shell on a silver substrate, which suggests an exponent close to 0.8.

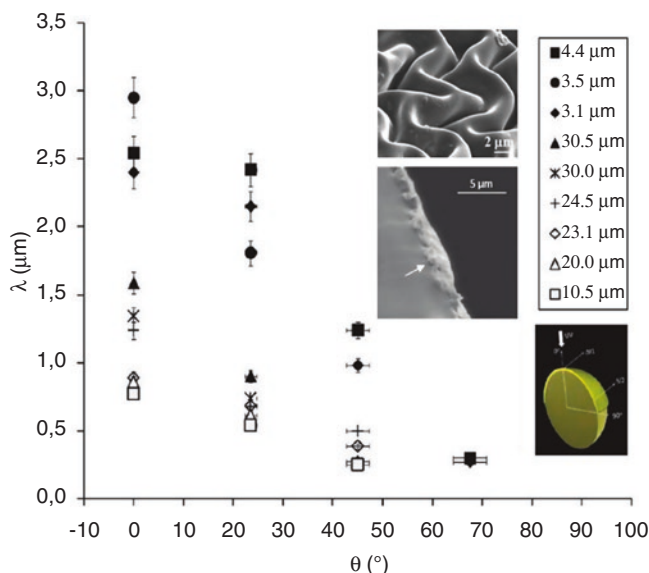


**Fig. 11.5** Dependence of  $\lambda$ , the wrinkle wavelength of linear instability, on the skin thickness and sphere diameter. (Adapted with permission from *Macromolecules* **2011**, *44* (7), 2220–2228. © 2011, American Chemical Society)

## 11.5 Janus Wrinkled Fibers

Using the same PU/PBDO system, as for films and spheres, we described the wrinkling instability produced in long and cylindrical elastomeric fibers with radii in the nano-/micron range. These fibers are synthesized via two chemical steps, adapted from the procedure and details described earlier: first, the reaction between PU and PBDO and the second step promoted by UV irradiation.

PU/PBDO fibers were produced by the electrospinning technique. This technique allows the production of continuous fibers, collected in an appropriate target. The term “electrospinning” derives from the fact that this technique is based on the use of an electric field for the production of fibers, and, so, the fiber deposition is based on the electrostatic repulsion of electric charges.

The typical configuration of an electrospinning deposition system comprises a syringe (containing the polymer solution from which the fibers are intended to be produced), a diffuser pump (which controls the flow rate of the solution through the needle of the syringe), a metallic target (where the deposited fibers are collected and the zero electrical potential is maintained), and a voltage source (to apply a potential difference between the needle tip and the target). A syringe is filled with the reacting PU/PBDO mixture, and a voltage is set up between the needle and a target. A rotating target mounted some distance from the syringe was used. As the viscous elastomeric solution exits the needle, it is accelerated by the voltage toward the target as a long thin fiber.

The fabrication process is shown schematically in Fig. 11.6. Due to the target geometry, the fibers remained taut.

After being collected in the target and dried, the fibers are UV-irradiated on only one side and swollen in toluene while still mounted on the target and under tension. At this stage, the fibers are smooth on both sides, although they are anisotropic: the irradiated side has a stiff skin, while the non-irradiated side has a soft skin. This anisotropy, combined with solvent evaporation, causes a size mismatch between skin and core. When the fibers are removed from the target, the tension is released, and they immediately start curling into helices. Still, the stiff skin remains smooth, and the wrinkled surface only shows up after the fiber attains a well-defined helical shape [88].

We proposed [88] a simple elastic model, predicting that, as the fibers deswell, they first curl, but remain smooth. Only at some curvature critical value, the fiber stops curling and wrinkles appear at the irradiated surface. As the de-swelling proceeds, these wrinkles grow in amplitude but retain a well-defined wavelength.

Once again, as it was predicted for the spheres, both curling and wrinkling are governed by the interplay of bending the skin and dilating the core. The elastic energy of the curled, non-wrinkled state is proportional to the square of the skin-core size mismatch ( $\epsilon^2$ ), while the elastic energy of the wrinkled state grows linearly with  $\epsilon$ . As the fiber dries,  $\epsilon$  increases, and the smooth fiber curls, with a radius that is proportional to  $\epsilon^{-1}$ . Only at some critical mismatch,  $\epsilon_c \sim (E_{sc}/E_{ss})^{2/3}$ , it becomes energetically favorable to stop curling and start wrinkling, with a wavelength given by Eq. (11.1).

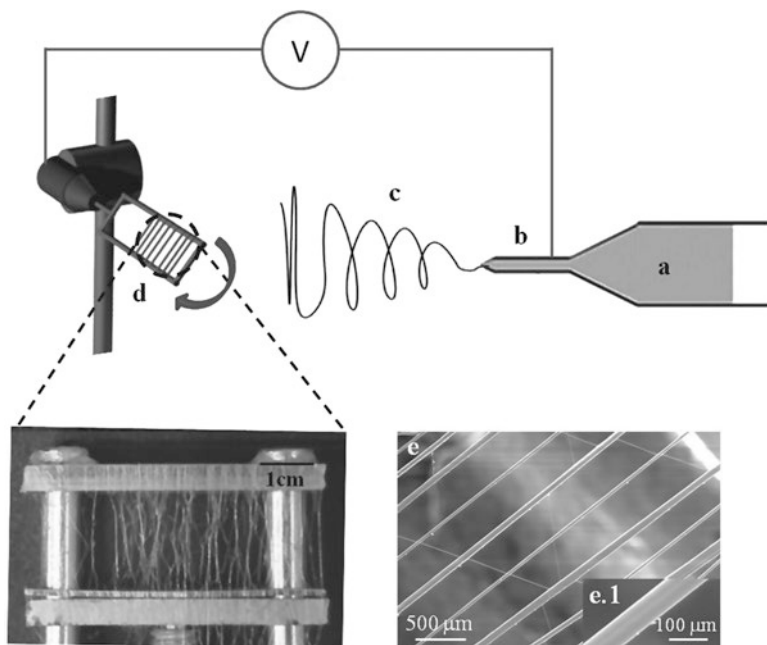


**Fig. 11.6** Schematics of fiber production by the electrospinning technique. (a) Syringe filled with elastomer PU/PBDO precursor solution; (b) syringe needle, connected to high-voltage supply; (c) elastomeric fiber accelerating toward the target; (d) rotating target used to obtain aligned and tautly suspended fibers; (e) SEM image of aligned fibers as electrospun, with a smooth surface (see inset (e.1)). (From Ref. [88], © WILEY-VCH Verlag GmbH & Co. KGaA, Weinheim, reproduced with permission)

The same qualitative behavior can be observed, on a vastly different length scale, in the tendrils of climbing plants, as they age and dry: first they curl, and then they wrinkle (Fig. 11.7).

## 11.6 Conclusions

Current research on colloids has enabled the preparation of Janus particles by a variety of techniques. It is now possible to produce significant quantities of well-defined Janus particles with different architectures. In addition, some of the developed preparation methods can be extended to industrial scale, making technological applications of Janus particles feasible. Along with the development of new methods to prepare Janus particles, possible applications are emerging, especially as highly specific sensors and self-motile particles and for the stabilization of interfaces. However, the high costs currently associated with the production of Janus particles will limit some technological applications.

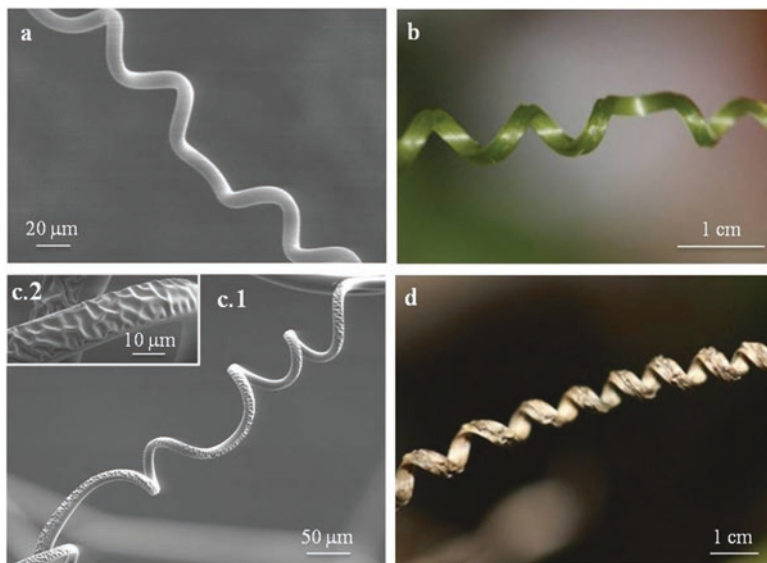


**Fig. 11.7** Electrospun PU/PBDO fibers mimicking young and old plant tendrils. A smooth fiber (a) mimics a young tendril (b); an asymmetrically wrinkled fiber (c.1) mimics an old tendril (d). (c.2) shows the detail of an asymmetrically wrinkled fiber in (c.1). Notice the wrinkling is on the outside of the helix, consistent with the assumption that the stiff skin contracts less than the soft core on drying. (From Ref. [88], © WILEY-VCH Verlag GmbH & Co. KGaA, Weinheim, reproduced with permission)

Exploiting the ability of elastomers to modify their surface through buckling and wrinkling, it was possible to develop a simple, low-cost, and low-tech method to fabricate Janus elastomeric particles with different geometries (planar films, spherical particles, and cylindrical fibers) from a single elastomeric material and use easily available chemicals. Different textures were induced through applied strains or promoted by swelling in an appropriate solvent. These textures have well-defined wavelengths, from below microns to mm, can be easily tuned, and have therefore been considered relevant for possible medical applications, in particular for bacterial adhesion. Preliminary results for *Staphylococcus epidermidis* adhesion at different modified polyurethane/urea elastomeric samples have already been reported [89] and demonstrated the interest in using these elastomers as model surfaces in bacterial adhesion studies.

This latter result opens up new perspectives on biomimetic materials, as functionalities can be added by having “young” (smooth, small surface area) and “old” (wrinkled, large surface area) regions coexist in the same material. For example, a Janus micromanipulator could conceivably be constructed, where a micro- or nano-sized object would be grabbed and carried by an array of wrinkled particles and then released at a very precise location simply by adjusting the pattern.

Looking to the future, a wide research field is opened, and we will certainly see a range of developments taking place based on the concept of Janus asymmetric colloids.

**Acknowledgments** This work is funded by FEDER through the COMPETE 2020 Program and National Funds through FCT – Portuguese Foundation for Science and Technology under project numbers POCI- 01-0145-FEDER-007688 (Reference UID/CTM/50025), UID/FIS/00618/2013, PTDC/FIS-NAN/01117/2014, PTDC/CTMBIO/6178/2014, and M-ERA-NET2/0007/2016 (CellColor).

## References

1. H.W. Melville, *Advances in colloid science*. *Nature* **151**, 5–6 (1943)
2. F. Schlesener, *Colloidal Particles in Critical Fluids* (Cuvillier Verlag Gottinger, Gottingen, 2004)
3. R.S. Krishnan, On the depolarisation of Tyndall scattering in colloids. *Proceedings of the Indian Academy of Sciences – Section A* **1**(10), 717–722 (1935)
4. G. Schmid, *Clusters and Colloids: From Theory to Applications* (VCH Verlagsgesellschaft mbH, Weinheim/New York, 2008)
5. I. Cho, K.W. Lee, Morphology of latex particles formed by poly(methyl methacrylate)-seeded emulsion polymerization of styrene. *J. Appl. Polym. Sci.* **30**(5), 1903–1926 (1985)
6. C. Casagrande, P. Fabre, E. Raphael, M. Veyssie, Janus Beads – Realization and Behavior at Water Oil Interfaces. *Europhys. Lett.* **9**, 251–255 (1989)
7. C. Casagrande, M.J. Veyssie, Beads – realization and 1st observation of interfacial properties. *C. R. Acad. Sci. (Paris)* **306**, 1423–1425 (1988)
8. P.G. de Gennes, *Soft matter*. *Rev. Mod. Phys.* **64**(3), 4 (1992)
9. A. Walther, A.H.E. Muller, Janus particles. *Soft Matter* **4**, 663–668 (2008)
10. H.J. Hektor, K. Scholtmeijer, Hydrophobins: Proteins with potential. *Curr. Opin. Biotechnol.* **16**(4), 434–439 (2005)
11. L. Hong, S. Jiang, S. Granick, Simple method to produce Janus colloidal particles in large quantity. *Langmuir* **22**(23), 9495–9499 (2006)
12. S. Jiang, Q. Chen, M. Tripathy, E. Luijten, K.S. Schweizer, S. Granick, Janus particle synthesis and assembly. *Adv. Mater.* **22**(10), 1060–1071 (2010)
13. F. Liang, B. Liu, Z. Cao, Z. Yang, Janus colloids toward interfacial engineering. *Langmuir* **34**(14), 4123–4131 (2018)
14. A.-H. Lu, E.L. Salabas, F. Schuth, Magnetic nanoparticles: Synthesis, protection, functionalization, and application. *Angew. Chem. Int. Ed. Engl.* **46**, 1222–1244 (2007)
15. J. Gao, H. Gu, B. Xu, Multifunctional magnetic nanoparticles: Design, synthesis, and biomedical applications. *Acc. Chem. Res.* **42**(8), 1097–1107 (2009)
16. U. Jeong, X. Teng, Y. Wang, H. Yang, Y. Xia, Superparamagnetic colloids: Controlled synthesis and niche applications. *Adv. Mater.* **19**(1), 33–60 (2006)
17. N. Zhao, M. Gao, Magnetic Janus particles prepared by a flame synthetic approach: Synthesis, characterizations and properties. *Adv. Mater.* **21**(2), 184–187 (2009)
18. Y. Li, W.-B. Zhang, I.F. Hsieh, G. Zhang, Y. Cao, X. Li, C. Wesdemiotis, B. Lotz, H. Xiong, S.Z.D. Cheng, Breaking symmetry toward nonspherical Janus particles based on polyhedral oligomeric silsesquioxanes: Molecular design, “Click” synthesis, and hierarchical structure. *J. Am. Chem. Soc.* **133**(28), 10712–10715 (2011)
19. X. Feng, R. Zhang, Y. Li, Y.-I. Hong, D. Guo, K. Lang, K.-Y. Wu, M. Huang, J. Mao, C. Wesdemiotis, Y. Nishiyama, W.-B. Zhang, T. Miyoshi, T. Li, S.Z.D. Cheng, Hierarchical self-organization of AB<sub>n</sub> Dendron-like molecules into a supramolecular lattice sequence. *ACS Cent. Sci.* **3**(8), 860–867 (2017)

20. H. Wu, Y.-Q. Zhang, M.-B. Hu, L.-J. Ren, Y. Lin, W. Wang, Creating quasi two-dimensional cluster-assembled materials through self-assembly of a Janus Polyoxometalate-Silsesquioxane co-cluster. *Langmuir* **33**(21), 5283–5290 (2017)
21. C. Ohm, N. Kapernaum, D. Nonnenmacher, F. Giesselmann, C. Serra, R. Zentel, Microfluidic synthesis of highly shape-anisotropic particles from liquid crystalline elastomers with defined director field configurations. *J. Am. Chem. Soc.* **133**(14), 5305–5311 (2011)
22. T. Hessberger, L.B. Braun, F. Henrich, C. Muller, F. Giesselmann, C. Serra, R. Zentel, Co-flow microfluidic synthesis of liquid crystalline actuating Janus particles. *J. Mater. Chem. C* **4**, 8778–8786 (2016)
23. V.B. Varma, R.G. Wu, Z.P. Wang, R.V. Ramanujan, Magnetic Janus particles synthesized using droplet micro-magnetofluidic techniques for protein detection. *Lab Chip* **17**(20), 3514–3525 (2017)
24. P.-F. Jin, Y. Shao, G.-Z. Yin, S. Yang, J. He, P. Ni, W.-B. Zhang, Janus Polystyrene–Polydimethylsiloxane star polymers with a cubic core. *Macromolecules* **51**(2), 419–427 (2018)
25. F. Wurm, A.F.M. Kilbinger, Polymeric Janus particles. *Angew. Chem. Int. Ed.* **48**(45), 8412–8421 (2009)
26. S. Lone, I.W. Cheong, Fabrication of polymeric Janus particles by droplet microfluidics. *RSC Adv.* **4**(26), 13322–13333 (2014)
27. H. Yabu, M. Kanahara, M. Shimomura, T. Arita, K. Harano, E. Nakamura, T. Higuchi, H. Jinnai, Polymer Janus particles containing block-copolymer stabilized magnetic nanoparticles. *ACS Appl. Mater. Interfaces* **5**(8), 3262–3266 (2013)
28. Y. Yi, L. Sanchez, Y. Gao, Y. Yu, Janus particles for biological imaging and sensing. *Analyst* **141**(12), 3526–3539 (2016)
29. G. Luo, L. Du, Y. Wang, Y. Lu, J. Xu, Controllable preparation of particles with microfluidics. *Particuology* **9**(6), 545–558 (2011)
30. X.-T. Sun, M. Liu, Z.-R. Xu, Microfluidic fabrication of multifunctional particles and their analytical applications. *Talanta* **121**, 163–177 (2014)
31. T. Nisisako, Recent advances in microfluidic production of Janus droplets and particles. *Curr. Opin. Colloid Interface Sci.* **25**, 1–12 (2016)
32. Z. Nie, W. Li, M. Seo, S. Xu, E. Kumacheva, Janus and ternary particles generated by microfluidic synthesis: Design, synthesis, and self-assembly. *J. Am. Chem. Soc.* **128**(29), 9408–9412 (2006)
33. K.-H. Roh, D.C. Martin, J. Lahann, Biphasic Janus particles with nanoscale anisotropy. *Nat. Mater.* **4**, 759–763 (2005)
34. S. Rahmani, C.H. Villa, A.F. Dishman, M.E. Grabowski, D.C. Pan, H. Durmaz, A.C. Misra, L. Colón-Meléndez, M.J. Solomon, V.R. Muzykantov, J. Lahann, Long-circulating Janus nanoparticles made by electrohydrodynamic co-jetting for systemic drug delivery applications. *J. Drug Target.* **23**(7–8), 750–758 (2015)
35. Z. Cao, Q. Bian, Y. Chen, F. Liang, G. Wang, Light-responsive janus-particle-based coatings for cell capture and release. *ACS Macro Lett.* **6**(10), 1124–1128 (2017)
36. A. Walther, A.H.E. Müller, Janus particles: Synthesis, self-assembly, physical properties, and applications. *Chem. Rev.* **113**(7), 5194–5261 (2013)
37. S. Sacanna, M. Korpics, K. Rodriguez, L. Colón-Meléndez, S.-H. Kim, D.J. Pine, G.-R. Yi, Shaping colloids for self-assembly. *Nat. Commun.* **4**(1688), 1–6 (2013)
38. J. Zhang, B.A. Grzybowski, S. Granick, Janus particle synthesis, assembly, and application. *Langmuir* **33**, 6964–6977 (2017)
39. A. Walther, M. Hoffmann, H.E. Müller Axel, Emulsion polymerization using Janus particles as stabilizers. *Angew. Chem.* **120**(4), 723–726 (2007)
40. X. Pei, Y. Tan, K. Xu, C. Liu, C. Lu, P. Wang, Pickering polymerization of styrene stabilized by starch-based nanospheres. *Polym. Chem.* **7**(19), 3325–3333 (2016)
41. J. Tang, P.J. Quinlan, K.C. Tam, Stimuli-responsive Pickering emulsions: Recent advances and potential applications. *Soft Matter* **11**(18), 3512–3529 (2015)
42. Y. Gao, Y. Yu, How half-coated Janus particles enter cells. *J. Am. Chem. Soc.* **135**(51), 19091–19094 (2013)

43. F. Khan, M. Tanaka, Designing smart biomaterials for tissue engineering. *Int. J. Mol. Sci.* **19**, 17 (2018)
44. J.A. Champion, Y.K. Katare, S. Mitragotri, Particle shape: A new design parameter for micro- and nanoscale drug delivery carriers. *J. Control. Release* **121**(1), 3–9 (2007)
45. Y. Zhang, H.F. Chan, K.W. Leong, Advanced materials and processing for drug delivery: The past and the future. *Adv. Drug Deliv. Rev.* **65**(1), 104–120 (2013)
46. H. Xie, Z.-G. She, S. Wang, G. Sharma, J.W. Smith, One-step fabrication of polymeric Janus nanoparticles for drug delivery. *Langmuir* **28**(9), 4459–4463 (2012)
47. S. Hwang, J. Lahann, Differentially degradable Janus particles for controlled release applications. *Macromol. Rapid Commun.* **33**(14), 1178–1183 (2012)
48. P. Johal, S. Chaudhary, Electronic paper technology. *Int. J. Adv. Res. Sci. Eng.* **2**(9), 106–110 (2013)
49. Y. Komazakia, H. Hirama, T. Torii, Electrically and magnetically dual-driven Janus particles for handwriting-enabled electronic paper. *J. Appl. Phys.* **117**, 154506 (2015)
50. Y. Komazaki, T. Torii, Memory effect canceling and novel driving scheme of twisting-ball display via space-charge polarization. *J. Soc. Inf. Disp.* **25**(5), 295–301 (2017)
51. X. Ma, A. Jannasch, U.-R. Albrecht, K. Hahn, A. Miguel-López, E. Schäffer, S. Sánchez, Enzyme-powered hollow mesoporous Janus nanomotors. *Nano Lett.* **15**(10), 7043–7050 (2015)
52. P.S. Schattling, M.A. Ramos-Docampo, V. Salgueiriño, B. Städler, Double-fueled Janus swimmers with magnetotactic behavior. *ACS Nano* **11**(4), 3973–3983 (2017)
53. M. Guix, S.M. Weiz, O.G. Schmidt, M. Medina-Sánchez, Self-propelled micro/nanoparticle motors. *Part. Part. Syst. Character.* **35**(2), 1700382 (2018)
54. J. Zhang, J. Yan, S. Granick, Directed self-assembly pathways of active colloidal clusters. *Angew. Chem. Int. Ed.* **55**(17), 5166–5169 (2016)
55. J. Yan, M. Han, J. Zhang, C. Xu, E. Luijten, S. Granick, Reconfiguring active particles by electrostatic imbalance. *Nat. Mater.* **15**, 1095–1099 (2016)
56. K.-H. Roh, M. Yoshida, J. Lahann, Water-stable biphasic nanocolloids with potential use as anisotropic imaging probes. *Langmuir* **23**(10), 5683–5688 (2007)
57. J. Jiang, H. Gu, H. Shao, E. Devlin, G.C. Papaefthymiou, J.Y. Ying, Bifunctional Fe<sub>3</sub>O<sub>4</sub>-Ag heterodimer nanoparticles for two-photon fluorescence imaging and magnetic manipulation. *Adv. Mater.* **20**, 4403–4407 (2008)
58. S.H. Hu, X. Gao, Nanocomposites with spatially separated functionalities for combined imaging and magnetolytic therapy. *J. Am. Chem. Soc.* **132**, 7234–7237 (2010)
59. L.Y. Wu, B.M. Ross, S. Hong, L.P. Lee, Bioinspired nanocorals with decoupled cellular targeting and sensing functionality. *Small* **6**, 503–507 (2010)
60. A. Kirillova, C. Schliebe, G. Stoychev, A. Jakob, H. Lang, A. Synytska, Hybrid hairy Janus particles decorated with metallic nanoparticles for catalytic applications. *ACS Appl. Mater. Interfaces* **7**(38), 21218–21225 (2015)
61. J. Faria, M.P. Ruiz, D.E. Resasco, Phase-selective catalysis in emulsions stabilized by Janus silica-nanoparticles. *Adv. Synth. Catal.* **352**(14–15), 2359–2364 (2010)
62. L. Baraban, D. Makarov, R. Streubel, I. Mönch, D. Grimm, S. Sanchez, O.G. Schmidt, Catalytic Janus motors on microfluidic chip: Deterministic motion for targeted cargo delivery. *ACS Nano* **6**(4), 3383–3389 (2012)
63. S. Jiang, Q. Chen, M. Tripathy, E. Luijten, K.S. Schweizer, S. Steve Granick, Janus particle synthesis and assembly. *Adv. Mater.* **22**, 1060–1071 (2010)
64. J.-W. Kim, R.J. Larsen, D.A. Weitz, Synthesis of nonspherical colloidal particles with anisotropic properties. *J. Am. Chem. Soc.* **128**(44), 14374–14377 (2006)
65. J. Genzer, J. Groenewold, Soft matter with hard skin: From skin wrinkles to templating and material characterization. *Soft Matter* **2**(4), 310–323 (2006)
66. Y. Xuan, X. Guo, Y. Cui, Crack-free controlled wrinkling of a bilayer film with a gradient interface. *Soft Matter* **8**(37), 9603–9609 (2012)
67. T. Okayasu, H.L. Zhang, D.G. Bucknall, Spontaneous formation of ordered lateral patterns in polymer thin-film structures. *Adv. Funct. Mater.* **14**(11), 1081–1088 (2004)

68. A.F. Miller, Materials science: Exploiting wrinkle formation. *Science* **317**(5838), 605–606 (2007)
69. M.H. Godinho, A.C. Trindade, J.L. Figueirinhas, L.V. Melo, P. Brogueira, A.M. Deus, P.I.C. Teixeira, Tuneable micro-and nano-periodic structures in a free-standing flexible urethane/urea elastomer film. *Eur. Phys. J. E Soft Matter* **21**, 319–330 (2006)
70. C. Zhao, M.N. de Pinho, Design of polypropylene oxide/polybutadiene bi-soft segment urethane/urea polymer for pervaporation membranes. *Polymer* **40**(22), 6089–6097 (1999)
71. A.C. Trindade, M.H. Godinho, J.L. Figueirinhas, Shear induced finite orientational order in urethane/urea elastomers. *Polymer* **45**(16), 5551–5555 (2004)
72. N. Bowden, S. Briittain, A.G. Evans, J.W. Hutchinson, G.M. Whitesides, Spontaneous formation of ordered structures in thin films of metals supported on an elastomeric polymer. *Nature* **393**, 146–149 (1998)
73. A.C. Trindade, A.P.C. Almeida, J.P. Canejo, P. Patrício, P. Pieranski, M.H. Godinho, Elastomeric patterns probed by a nematic liquid crystal. *Mol. Cryst. Liq. Cryst.* **657**(11), 136–146 (2017)
74. J. Yin, C. Lu, Hierarchical surface wrinkles directed by wrinkled templates. *Soft Matter* **8**(24), 6528–6534 (2012)
75. L. Liu, M. Ren, W. Yang, Preparation of polymeric Janus particles by directional UV-directed reactions. *Langmuir* **25**, 11048–11053 (2009)
76. X. Cai, Y. Wang, X. Wang, J. Ji, J. Hong, H. Pan, J. Chen, M. Xue, Fabrication of ultrafine soft-matter arrays by selective contact thermochemical reaction. *Sci. Rep.* **3**, 1780 (2013)
77. J. Yin, Z. Cao, I. Sheinman, X. Chen, Stress-driven buckling patterns in spheroidal core/shell structures. *Proc. Natl. Acad. Sci.* **105**(49), 19132–19135 (2008)
78. M. Li, N. Hakimi, R. Perez, S. Waldman, A. Kozinski Janusz, K. Hwang Dae, Microarchitecture for a three-dimensional wrinkled surface platform. *Adv. Mater.* **27**(11), 1880–1886 (2015)
79. D. Terwagne, M. Brojan, M. Reis Pedro, Smart morphable surfaces for aerodynamic drag control. *Adv. Mater.* **26**(38), 6608–6611 (2014)
80. B. Liu, W. Wei, X. Qu, Z. Yang, Janus colloids formed by biphasic grafting at a pickering emulsion interface. *Angew. Chem.* **120**(21), 4037–4039 (2008)
81. Y. Yang, X. Han, W. Ding, S. Jiang, Y. Cao, C. Lu, Controlled free edge effects in surface wrinkling via combination of external straining and selective O<sub>2</sub> plasma exposure. *Langmuir* **29**(23), 7170–7177 (2013)
82. M. Watanabe, K. Mizukami, Well-ordered wrinkling patterns on chemically oxidized poly(dimethylsiloxane) surfaces. *Macromolecules* **45**(17), 7128–7134 (2012)
83. J. Ji, M. Fuji, H. Watanabe, T. Shirai, Partially functionalized Janus ZnO spheres prepared by protecting mask techniques. *Colloids Surf. A Physicochem. Eng. Asp.* **393**, 6–10 (2012)
84. S.-W. Choi, I.W. Cheong, J.-H. Kim, Y. Xia, Preparation of uniform microspheres using a simple fluidic device and their crystallization into close-packed lattices. *Small* **5**, 454–459 (2009)
85. A.C. Trindade, J.P. Canejo, P. Patrício, P. Brogueira, P.I.C. Teixeira, M.H. Godinho, Hierarchical wrinkling on elastomeric Janus spheres. *J. Mater. Chem.* **22**, 22044 (2012)
86. A.C. Trindade, J.P. Canejo, L.F.V. Pinto, P. Patrício, P. Brogueira, P.I.C. Teixeira, M.H. Godinho, Wrinkling labyrinth patterns on elastomeric janus particles. *Macromolecules* **44**(7), 2220–2228 (2011)
87. G. Cao, X. Chen, C. Li, Z. Cao, If- assembled gular and labyrinth buckling patterns of thin films on spherical subtes. *Phys. Rev. Let.* **100**, 036102 (2008)
88. A.C. Trindade, J.P. Canejo, P.I.C. Teixeira, P. Patrício, M.H. Godinho, First curl, then wrinkle. *Macromol. Rapid Commun.* **34**(20), 1618–1622 (2013)
89. P. Teixeira, A.C. Trindade, M.H. Godinho, J. Azeredo, R. Oliveira, J.G. Fonseca, Staphylococcus epidermidis adhesion on modified urea/urethane elastomers. *J. Biomater. Sci. Polym. Ed.* **17**(1-2), 239-246 (2006)

# **Part IV**

## **Applications**

# Chapter 12

## Wrinkled Surfaces Designed for Biorelated Applications



C. M. González-Henríquez, M. A. Sarabia Vallejos,  
and Juan Rodríguez-Hernández

### 12.1 Background

To take advantage of surface instabilities is a common way to generate micro-patterned structures on the top of soft materials; this methodology permits to create a wide size range of different morphologies such as wrinkles, creases, and folds.

Surface morphological instabilities on soft materials with a stiff thin surface layer have raised considerable research interest in the last years. These surface patterns occur in nature with growth, development, and aging of biological systems. For example, surface patterns favor organs to grow in extended surface areas to facilitate mass exchange in blood cells and intestinal villi and to enhance intellectual capacity of the brain. Furrows form on animal skins or plant surfaces to adapt to the aging process; biofilm form channels within structures to aid the transport of nutrients and water critical for biofilm growth, and epithelial cells delaminate to avoid tissue overcrowding. Although these surface patterns are believed to be the

---

C. M. González-Henríquez (✉)

Departamento de Química, Facultad de Ciencias Naturales, Matemáticas y del Medio Ambiente, Universidad Tecnológica Metropolitana, Santiago, Chile

Programa Institucional de Fomento a la Investigación, Desarrollo e Innovación, Universidad Tecnológica Metropolitana, Santiago, Chile

e-mail: [carmen.gonzalez@utem.cl](mailto:carmen.gonzalez@utem.cl)

M. A. Sarabia Vallejos

Departamento de Ingeniería Estructural y Geotecnia, Pontificia Universidad Católica de Chile, Escuela de Ingeniería, Santiago, Chile

Instituto de Ingeniería Biológica y Médica, Santiago, Chile

J. Rodríguez-Hernández (✉)

Departamento de Química Macromolecular Aplicada, Polymer Functionalization Group, Instituto de Ciencia y Tecnología de Polímeros-Consejo Superior de Investigaciones Científicas (ICTP-CSIC), Madrid, Spain

e-mail: [jrodriguez@ictp.csic.es](mailto:jrodriguez@ictp.csic.es)

result of complex interactions between genetic, biochemical, and biological processes, accumulating evidence has shown that mechanical forces play a critical role in controlling their formation.

Advances in material chemistry can enable different strategies to impart reversible patterned topographies and surface characteristics which can mimic or resemble biological environments. Accordingly, wrinkled patterns have been widely used in the biomedical area for different applications such as cell culture scaffolds, cell proliferation, biofouling strategies, tissue engineering applications, controlled drug delivery, biomedical implants, super-hydrophilic/super-hydrophobic coatings [1], cellular alignment, cellular differentiation [2–4], and multicellular spheroids generation [5, 6]. Extensive studies have also revealed that topography plays an important role in cell adhesion, proliferation, differentiation, and migration and has been considered as an essential parameter for design biomaterials which resemble the extracellular matrix [7, 8].

In this chapter, we will be focused on revised innovative biomedical systems, and also several examples which use wrinkled patterns supported on different substrates are reviewed.

## 12.2 Cell Proliferation

Cellular behavior can be highly influenced by the chemical and physical surface characteristics of biomaterial used as substrate. Accordingly, materials topography has been long considered as a crucial feature for cell-cell interactions and also between cell-extracellular matrices (environment). There exist a close relationship between the topographical features of the medium and the cellular activity occurring in their surface. The biomaterial community performs important advances in the last years by producing various types of pattern models which have been developed and examined in a range of sizes (micro- or nanoscales, including hierarchical structures consisting of both) and shapes (pillars, holes, grooves, folds, creases, grids, wrinkles, ripples, and islands, among others). According to this, the chemical and physical properties of the cell-substrate surface significantly influence cell growth, differentiation, and morphology and also could allow or avoid cell death. This fact is particularly important during cell scaffold fabrication because patterning could facilitate the attachment or induction of the cellular activities required to develop useful cell-based devices, and it could be also an important feature to improve the biocompatibility of the biomaterials intended to be used for tissue engineering applications [9].

An interesting example is reported by Isawa et al. [10] which developed a potential fabrication methodology for tissue engineering applications, specifically for wound healing treatment. The methodology reported in this article is based on the formation of a thin polymerized layer over a chitosan (CS) film via their immersion in a methanol solution which contains a phenolic acid (ferulic acid, FE). The subsequent surface reaction with horseradish peroxidase (HRP) is used to mimicking the

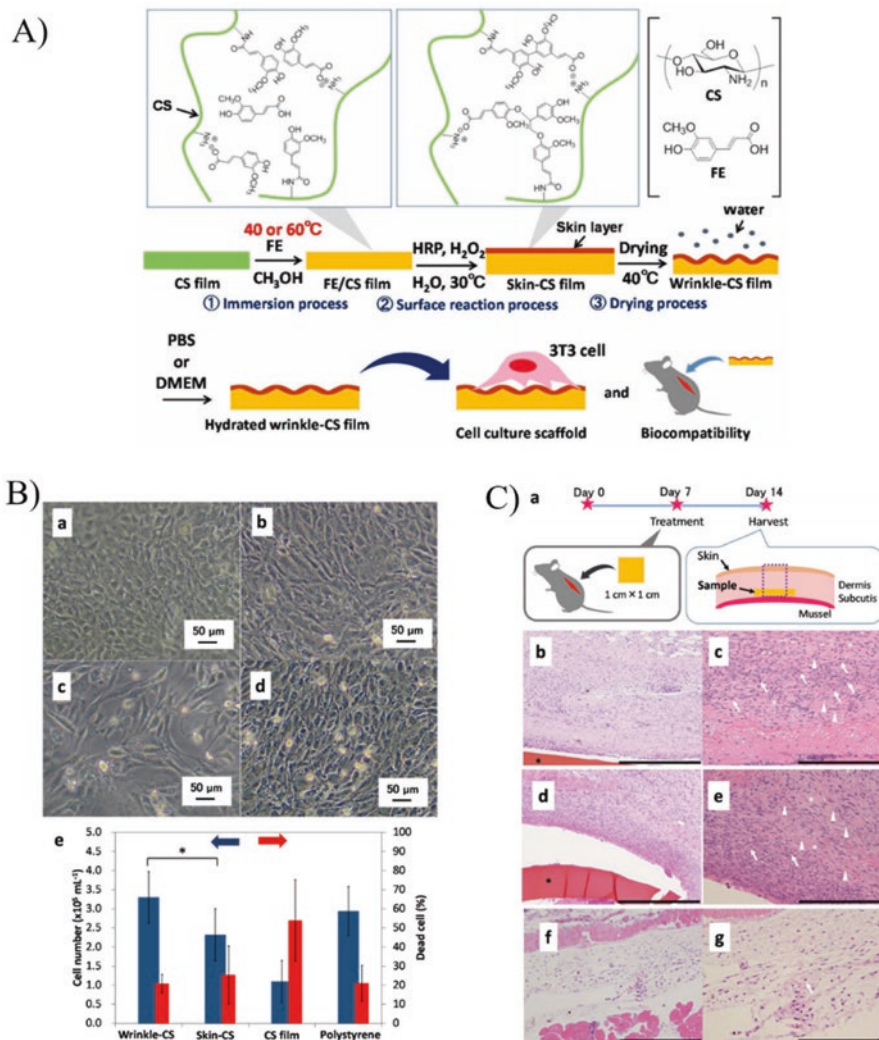


**Fig. 12.1** (a) Schematic description of the methodology employed in this study. (b) Optical microscopy images of the cells cultured adhered to the wrinkled-CS films. Also, analytical results of cell number and dead cells are depicted. (c) Material biocompatibility evaluation. Scheme of the animal experiment and histopathological properties of the wrinkled-CS films. (Reproduced with permission from Ref. [10])

wood lignification process. This procedure generates covalent bonds between the CS substrate and the phenolic acid. A surface relief produces micron-scale wrinkles upon substrate drying as a result of inhomogeneous shrinkage of the material (Fig. 12.1a). While the material is maintained on water, it is possible to use it as cell culture scaffold. The most relevant results showed in this article demonstrate that

wavelength/amplitude (aspect ratio), roughness, and Young's moduli of the wrinkled surface decrease with temperature increase (from 40 °C to 60 °C). Detailed characterization of the wrinkled structures in phosphate-buffered saline (PBS) was performed by using atomic force microscopy (AFM). In parallel, cell culture was developed over the wrinkled surface in order to confirm the potential applicability of these synthesized surfaces which present mechano-structural cues. To corroborate the biocompatibility of the wrinkled hydrogel films, implant replacement studies in mice were carried out.

In order to evaluate the effect of the wrinkled surface composed by CS and oligomeric FE side chains on cellular behavior, fibroblasts were cultured on the films prepared via an immersion treatment at 40 °C. This procedure was carried out in high glucose medium (DMEM). Figure 12.1b shows optical microscopy images of the cells adhered to the substrate after 2 days. Additionally, cell counts and frequencies of the dead cells are shown in the same figure. For the wrinkled-CS film, cell numbers and the frequency of dead cells were  $3.20 \pm 0.87 \times 10^5 \text{ mL}^{-1}$  and  $20.8 \pm 4.8\%$ , respectively; these were higher and lower, respectively, than those of the skin-CS film with a flat surface, indicating that the wrinkle morphology had some positive effects on cell proliferation compared to the skin-CS and CS films. The results also clearly indicate that the skin layer composed of the ionic cross-linking of CS and oligomeric FE side chains has higher compatibility with cells than the CS film surface. As a control, a polystyrene plate (cell culture dish) was used. Cell number and frequency of dead cells were  $2.82 \pm 0.68 \times 10^5 \text{ mL}^{-1}$  and  $21.1 \pm 9.4\%$ , in this case, which were comparable to those obtained from the wrinkle-CS film, indicating that the wrinkle-CS film is suitable as a cell culture substrate.

Figure 12.1c shows a schematic illustration of the *in vivo* experiments performed with mice. In the evaluation of biocompatibility in animals of the wrinkle-CS film and skin-CS film, the negative control is presented also. In the wrinkle-CS film, many neutrophils, fibroblasts, and collagens were observed. Additionally, few neutrophils in the skin-CS film were found. The negative control shows few neutrophils, fibroblasts, and collagens. These results indicate that the 3D structure of the wrinkle-CS films induces neutrophils to the films. The migrations of fibroblasts were observed in the wrinkle-CS and skin-CS film. CS has high migration activities *in vivo*. The results of the present study indicate that the wrinkle-CS film induces neutrophil infiltration and the migration of fibroblasts, which might indicate that the wrinkle-CS films are effective in enhancing wound healing processes.

Similarly, Peng et al. [11] focused their attention on a simple, low-cost, and effective alternative to fabricating poly(dimethylsiloxane) (PDMS) films which present a dual-structured hierarchical topography on the surface via a chemical modification using dopamine-glycopolymer composites to enhance the biocompatibility and adhesion of cells on the films. The influence of physicochemical properties of the surface PDMS film on cell growth and morphologies were deeply studied. Experimentally, the group of Peng et al. firstly fabricated porous polymers films by using breath figure (BF) patterns on the surface of the PDMS films using polystyrene (PS) solution at a humidity of 60%. This process allows creating hexagonally

packed pore patterns. Next, a liquid prepolymer mixture of PDMS was poured over the PS film with BF figures on the surface, and then the prepolymer was heated in an oven at 70 °C for 1 h. Finally, PDMS replica was peeled off from the master (PS film) resulting in hexagonally packed sphere-like structures. Posteriorly, the films are subjected to a mechanical pre-stretching and then to a UVO treatment for 10 min to induce the cross-linking on the PDMS top layer. By following these procedures, aligned wrinkled structures were obtained by releasing the UVO-treated pre-stretched PDMS films (Fig. 12.2a).

In Fig. 12.2a, the chemical modification of PDMS (PDMS-T) consisted in the dopamine-carbohydrate anchorage on the surface is also showed. The PDMS-T copolymer, which presents an Mw of 700, was also studied by contact angle, FT-IT, XPS, and AFM (Fig. 12.2b). In Fig. 12.2c is possible to observe that on smooth PDMS surface without a chemical modification, cells adhering to the substrate randomly grow over the substrates. Cells on the wrinkled surface without a chemical modification show a large impact on cell morphology. In the case of hierarchical topography surface without a chemical modification, a large number of cells are round, indicating an effect produced by the topographic variation. After the chemical modification, the hierarchical topography shows less round cells; in fact, the majority of cells adhering to the substrate are elongated along the ridge/groove of wrinkled structures. The inclusion of dopamine-glycopolymer increases the adhesion between cells and hierarchical topography surface, inducing the alignment of cells adhering to the substrate via the coupling or synergism of the hierarchical topography and chemical modification which both, in conjunction, promote the orientation of cells.

On the other hand, the group of Li et al. [12] in the year 2016 reported a methodology which includes stop-flow lithography (SFL) in combination with a rapid wrinkling post-process to generate wrinkled non-spherical particles, which permit not only designed particles with particular size and shape but also with a hierarchy and tunable wrinkle morphology. Experimentally, a photo-curable monomer flow, consisting of 95% poly(ethylene glycol diacrylate) (PEGDA) with a molecular weight of 700 g/mol and 5% of 2-hydroxy-2-methylpropiophenone (Darocur 1173), is stopped in a microfluidic channel. This mixture of PDMS and a curing agent at a ratio of 10:1 was subsequently polymerized by using a controllable UV beam mounted on a microscope frame; in parallel, a photomask is put in between to polymerize the monomer into defined shapes while the PDMS is flowing, thus producing particles of defined shapes and sizes according to the photomask and the flow used to fabricate it (Fig. 12.3a).

Posteriorly, these particles were exposed to plasma to generate surface instabilities which after PDMS natural oxidation produce a wrinkled pattern on top. The morphologies can be controlled by tuning the concentration of monomer used. By using various concentrations, different morphologies of wrinkled patterns after plasma treatment can be obtained (Fig. 12.3b–c). The results demonstrated that cells tend to attach on wrinkled zones; in general, the cells climbed and conformed onto the particles, occupying a large surface area of this pattern, which is not observed on the smooth particles (Fig. 12.3d). These results were also confirmed by using a

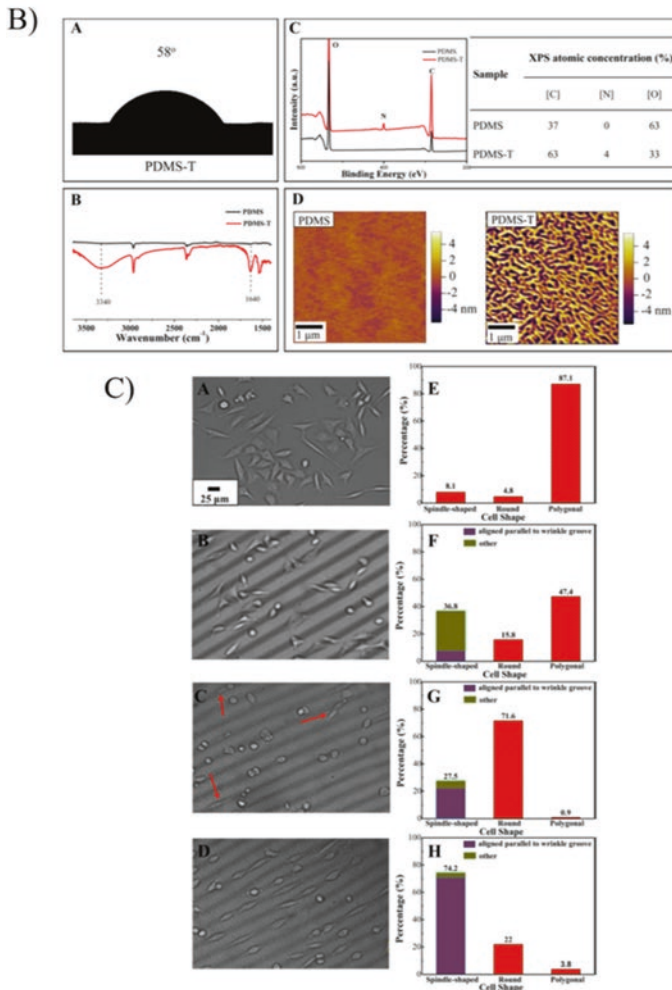
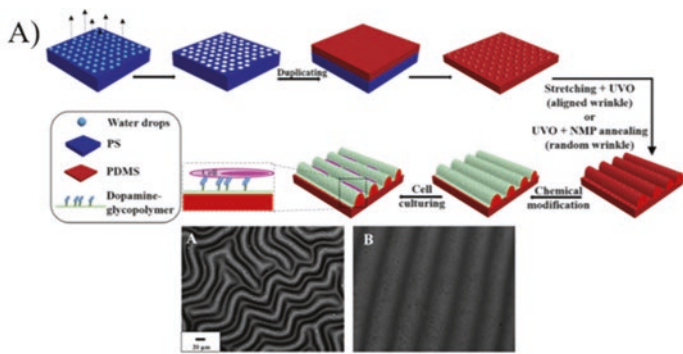


**Fig. 12.2** (a) Schematic of the preparation of modified dual-structured hierarchical topography surface and cell behavior on the surface; (b) characterization using contact angle, FT-IR, XPS spectra, and AFM; and (c) optical microscope images and quantitative data of cell morphologies on different substrates (A, E) flat surface, (B, F) aligned wrinkle surface, (C, G) dual-structured hierarchical topography surface, and (D, H) glycopolymers. (Reproduced with permission from Ref. [11])

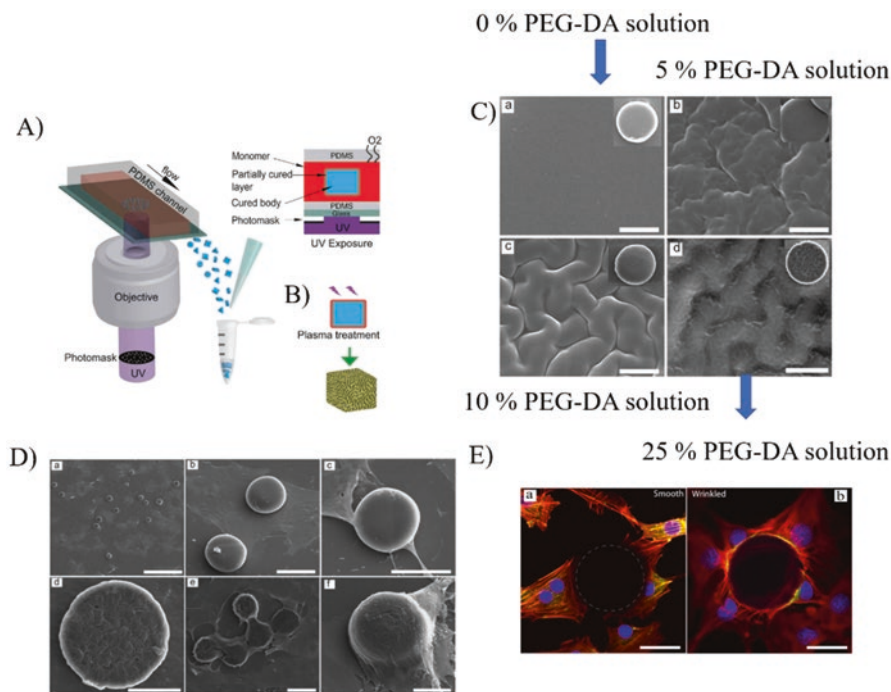


**Fig. 12.3** (a) Schematic illustration of the particle generation using a stop-flow lithography technique. (b) After washing away the uncured monomers on the particle surface, the surface of the particles turned into wrinkled patterns after the plasma is treated. (c) Wrinkled morphologies using different concentrations of PEGDA. (d) SEM images show cells spread on the substrate and ignore the smooth particles. (e) Confocal fluorescence microscopy images of cells around smooth and wrinkled particles. (Reproduced with permission from Ref. [12])

fluorescence confocal microscope. For the smooth particles, the cells appeared to ignore the smooth particles and attached only to the substrate, indicated by actin networks appearing only on the substrate. In contrast, on the wrinkled particles, the cell attachment to the surface of the particles was observed with actin networks appearing to extend predominantly outward from the top edge of the particle and focal adhesions at the particle edges (Fig. 12.3e). These results may be beneficial to many biomedical applications where cell attachment to a surface or particle is desired, such as cell micro-carriers, cell physiological study, and tissue engineering.

Another interesting example was reported by the group of Van Rijn et al. [13], which developed a multiscale topographical gradient approach with different inorganic biomaterials prepared by following a masked plasma-oxidation procedure with subsequent overoxidation to obtain a  $\text{SiO}_2$ -like surface or metal evaporation, resulting in metal oxides ( $\text{TiO}_2$ ,  $\text{CrO}_3$ , and  $\text{Al}_2\text{O}_3$ ) upon air exposure, two oxidation times (100 and 650 s) were carried out (Fig. 12.4). The wrinkle dimensions and surface chemistry were examined by AFM and XPS, respectively. The wrinkle size

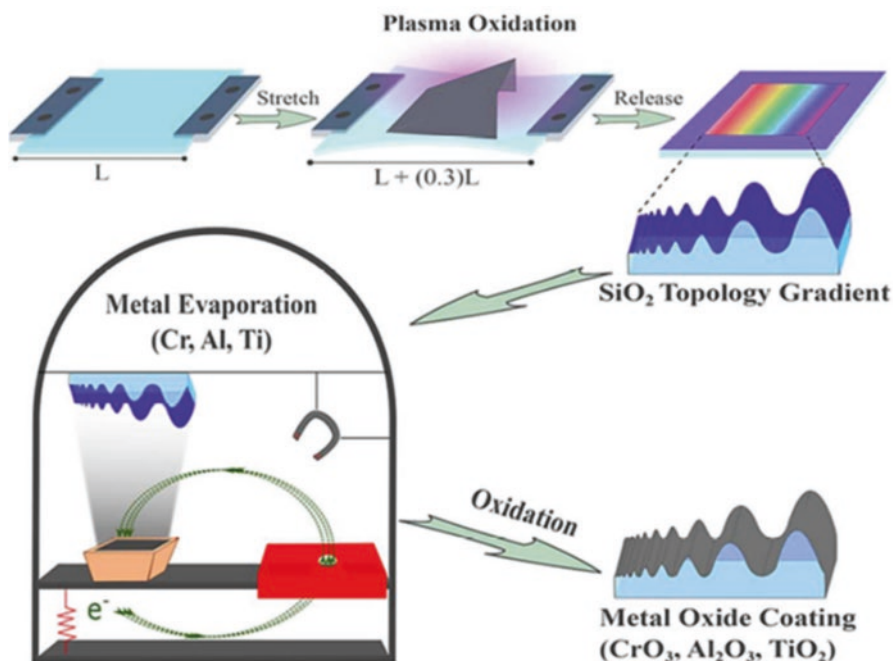


**Fig. 12.4** Schematic illustration of the process used to prepare wrinkled gradients with  $\text{SiO}_2$  via prolonged plasma oxidation and different metal oxide coatings by metal evaporation and exposure to air under ambient conditions. (Reproduced with permission from Ref. [13])

increases from the least exposed side to the most exposed side (open side of the mask) for both oxidation times.

The topographical gradients were seeded with human bone marrow-derived mesenchymal stem cells (hBM-MSCs) to study the effects of wrinkle dimensions and biomaterial composition on cellular responses, including cell adhesion, spreading, morphology changes (e.g., elongation and orientation), cytoskeleton, and filopodia as well as the formation and orientation of focal adhesion contacts. Figure 12.5 (top) shows AFM micrographies of the wrinkled patterns obtained by using this methodology at different positions. As is possible to observe, the spacing between grooves tends to increase with the plasma exposure time. Figure 12.5 (bottom) revealed that many cells on the microtopography that had high elongation and alignment contained elongated and uniformly oriented focal adhesion. This observation raises the notion that focal adhesion alignment may precede cell elongation and determine the direction of the future elongation axis. These data also indicate that topographical dimension and materials chemistry can provide synergistic stimulation to effect the formation and organization of focal adhesion complexes. Notably, it was found an apparent correlation between focal adhesion orientation and cell alignment. Also, FA (area/cell) and orientation were determined by a quantitative analysis of the positively stained focal adhesion. As a summary, optimal substratum conditions

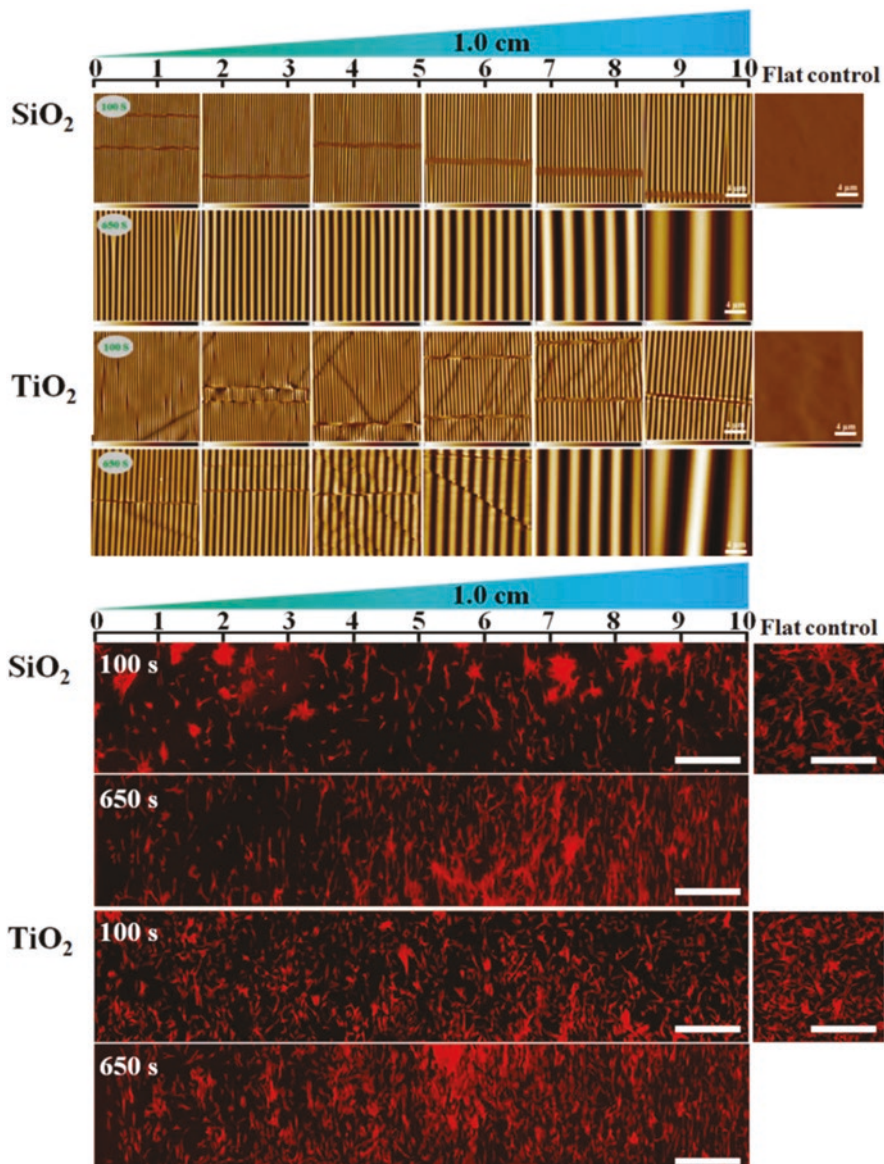


**Fig. 12.5** (top) AFM images of topography (wrinkle) gradients with SiO<sub>2</sub> along the 1.0 cm PDMS substrate. (bottom) Fluorescence microscopy images of the gradients representing the full length of the samples. (Reproduced with permission from Ref. [13])

promoted hBM-MSC alignment and elongation, cytoskeleton arrangement, filopodia development, as well as cell adhesion *in vitro*, which depended both on topography and interface material.

### 12.3 Control of Cellular Alignment/Differentiation

In the year 2015, Aufan et al. [1] fabricate both topographically and electrically active flexible biomaterials by using a simple and affordable method. Experimentally, the authors create wrinkled topographies of conductive polypyrrole (wPPy) on a PDMS surface by deposition of a PPy thin layer under swelling-induced strained conditions. Different patterns were produced by varying the PDMS swelling strains and the PPy layer thickness (Fig. 12.6a). Morphological structures of the wPPy/PDMS samples were analyzed via FE-SEM and AFM. Additionally, surface resistance and water contact angle were measured in the mentioned study. Finally,

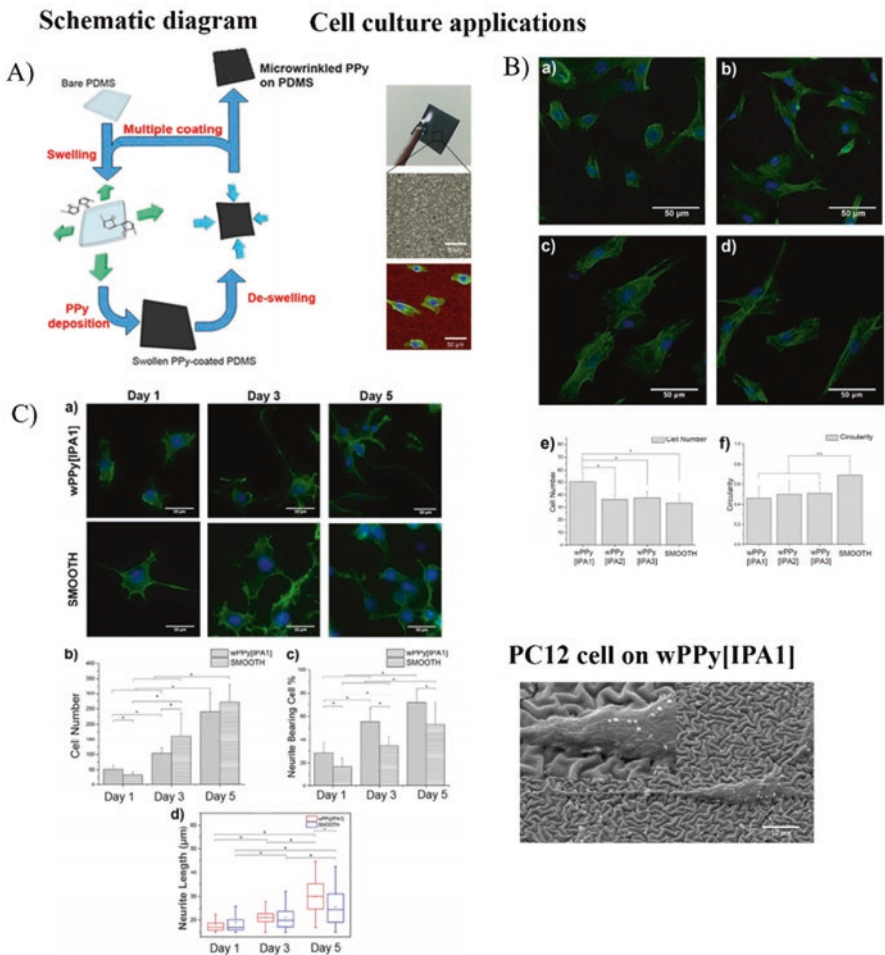


**Fig. 12.6** (a) Schematic diagram of wPPy on PDMS and results of cell growth. (b) Immunostaining images of fibroblasts cells on wPPy/PDMS surfaces. (c) Effect of conductive wrinkled substrates on neuronal cells. (Reproduced with permission from Ref. [1])

biocompatibility tests were carried out by culturing fibroblast and neuronal cells on the material surface. These tests were performed with the finality to explore the effect of the conductive wrinkled topographies on cell behavior and the feasibility of potential tissue engineering applications.

Figure 12.6b shows some representative images of fibroblasts cultured on smooth PPy and wPPy surfaces. In this study, a major amount of cells are founded adhered over wPPy, which also displayed more elongated shape compared to the cells on the smooth PPy controls. In both cases, wPPy and smooth PPy were used as controls for comparison. In the case of neuronal cells, their number increased during the incubation. Interestingly, more cells were observed on the smooth PPy than on the wPPy after 3 days. Additionally, wPPy surfaces promoted neurite formation, resulting in more neurite-bearing cells than on its smooth counterparts, after 5 days of incubation (Fig. 12.6c). In summary, the obtained results indicate that wrinkled topographies – wPPy substrates – promote cell adhesion and neurite outgrowth of both fibroblasts and neuronal cells.

Similar studies were performed by Greco et al. [3], who employed conducting polymers (PEDOT:PSS) as soft, biocompatible, and conductive interfaces or as part of bioelectronic devices. These surfaces acted as smart scaffolds which allow the spontaneous cell alignment, envisioning their electrical stimulation; thus, cell adhesion and proliferation were evaluated by using C2C12 murine skeletal muscle cells. On the other hand, Chen et al. [2] introduce an ultra-rapid, tunable, robust, facile, and inexpensive fabrication method to create multiscale self-similar alignment grooves ranging from nano- to microscales as biomimetic cell culture devices based on mechanical pre-stretching of polyethylene (PE) substrates which were then exposed to plasma etching procedures and then released from stretch. This procedure generates controllable scale uniaxially aligned wrinkles.

## 12.4 Spheroid Generation

Three-dimensional multicellular spheroids (MCSs) have a complex architecture, and also their dynamic cell-cell/cell-matrix interactions and bio-mimicking in vivo microenvironment become a highly difficult to reproduce natural structure. The MCSs are the fundamental building blocks for tissue reconstruction; these spheroid structures have emerged as a powerful tool to narrow down the gap between the in vitro and in vivo models [14]. For this motive, the MCSs can be used in various important applications in the biomedical area including drug screening and tumor studies, being a promise to be used as building block in organ printing for the construction of hybrid artificial organs.

Different conventional methods are intended to form multicellular structures, such as suspension culture in nonadhesive surfaces [15, 16], hanging drops [17], spinner flasks, rotational bioreactors [18], external force-driven MCS aggregations [19], or natural polymers for microfluidic platform [20, 21]. The problem with these

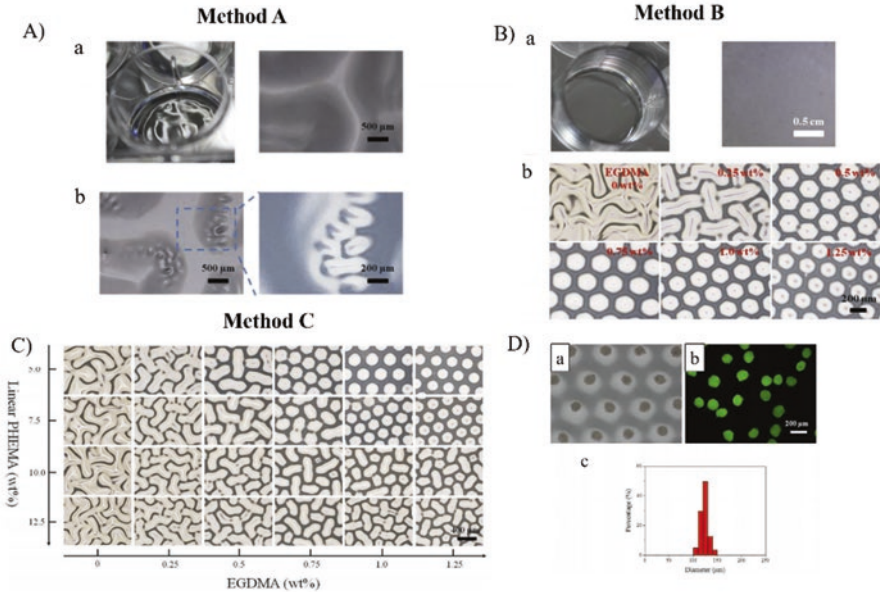


**Fig. 12.7** (a) Photograph and micrograph image of a PHEMA film synthesized by one-step UV curing of HEMA liquid (method A). (b) PHEMA film synthesized using method B. Also, micrographs of wrinkling patterns developed on the PHEMA films with various contents of cross-linker. (c) Swelling-induced wrinkling patterns on PHEMA films synthesized by method C. (d) Fluorescence and optical microscopy image of the multicellular spheroids stained with AO/EB. (Reproduced with permission from Ref. [5])

conventional methods relies in the fact that biorelated applications need uniform MCS, both in shape and size, in order to be useful for developing tissue engineering devices, a characteristic that these methodologies can't afford.

Accordingly, revolutionary methods that can generate MCSs with more control on these features (size and shape) need to be designed. To take advantage of microstructured patterns to generating highly controlled MCSs is the aim of some research groups. As an example, poly(hydroxyethyl methyl acrylate) (PHEMA films) with highly ordered wrinkling patterns are expected to have many remarkable applications, such as drug screening [22, 23] or tumor evolution studies [2, 24], among others. Zhang et al. [5] developed three different methods for PHEMA film synthesis (Fig. 12.7). In method A, the prepolymer solution was prepared by adding the HEMA monomer, a cross-linker agent, ethylene glycol dimethylacrylate (EGDMA), and a photoinitiator Darocur 1173. The prepolymeric solution was then added to the wells of cell culture plates and then irradiated for 180 s with UV light – curing system. This procedure generates a corrugated surface (irregular) on the surfaces instead of a smooth one (Fig. 12.7a). In method B, the same prepolymeric solution was first UV-irradiated for 20 s. After standing for 5 h, the resulting polymer chains diffuse throughout the remaining prepolymeric liquid solution, producing a physical and intrigued 3D network. Later, this system was irradiated

again for 180 s to fully cure the solution, obtaining polymeric films with a smooth surface (Fig. 12.7b). In method C, besides the cross-linker EGDMA and the photoinitiator Darocur 1173, various amounts of linear PHEMA were dissolved into HEMA. The prepolymer solution was then cured by 180 s utilizing UV irradiation. According to these experiments, samples with a low content of linear PHEMA (from 0 to 2.5%) result in films which still have a corrugated surface. In contrast, for samples with a high linear PHEMA content ( $\geq 5\%$ ), the resulting films exhibit a smooth surface (Fig. 12.7c).

To generate multicellular spheroids, the PHEMA films were first swelled in water to produce highly ordered, honeycomb-like wrinkling patterns. Cell suspensions were then added to the surface, which under the influence of gravity settled down and accumulated in the microcaves in several minutes. These cells gradually aggregated into cellular spheroids. The relatively weak cell-substrate interaction facilitates the formation of multicellular aggregates (Fig. 12.7d). Due to the high regularity of the patterns, the number of cells accumulated in each microcave is almost the same in all the cases. Therefore, the resulting spheroids displayed a narrow size distribution. In addition, the multicellular spheroids exhibit a high viability as shown in Fig. 12.7d when almost all cells are stained green (live) instead of red (dead).

Similar studies were carried out by Zhao et al. [6], in the year 2014, which utilize a swelling method to fabricate microstructures intended to create MCSs by gravity in aqueous environments, which can be used in cell biology and drug screening and help reduce the use of animals in research.

## 12.5 Antifouling Behavior

Marine biofouling is a costly, complex, and environmentally harmful phenomenon caused by the adhesion and accumulation of marine organism on a surface immersed in seawater. Ye et al. [20] reported a model for marine antibiofouling surface based on polymer brushes of wrinkled silicon elastomer (wPDMS). Polymer brushes (POEGMA and PSPMA) were grafted via surface-initiated atom transfer radical polymerization (Si-ATRP). FT-IR, XPS, and contact angle measurements were carried out for these samples. Finally, a series of laboratory static and dynamic bioassays, as well as field immersion tests, were performed to systematically study the relationship between surface chemistry, topography, and their inherent antifouling properties. The results indicated that the marine organism's adhesion was strongly influenced by the surface chemical composition and surface microtopography of the material. The synergistic effect of surface chemistry, surface topography, and bulk properties of the substrates endowed the new marine coatings with excellent antifouling properties [20].

Figure 12.8a shows the schematic approach used to fabricate polymer brushes via the functionalization of PDMS micropatterns via Si-ATRP. Additionally, static water contact angle measurement confirmed the hydrophilicity of the polymer

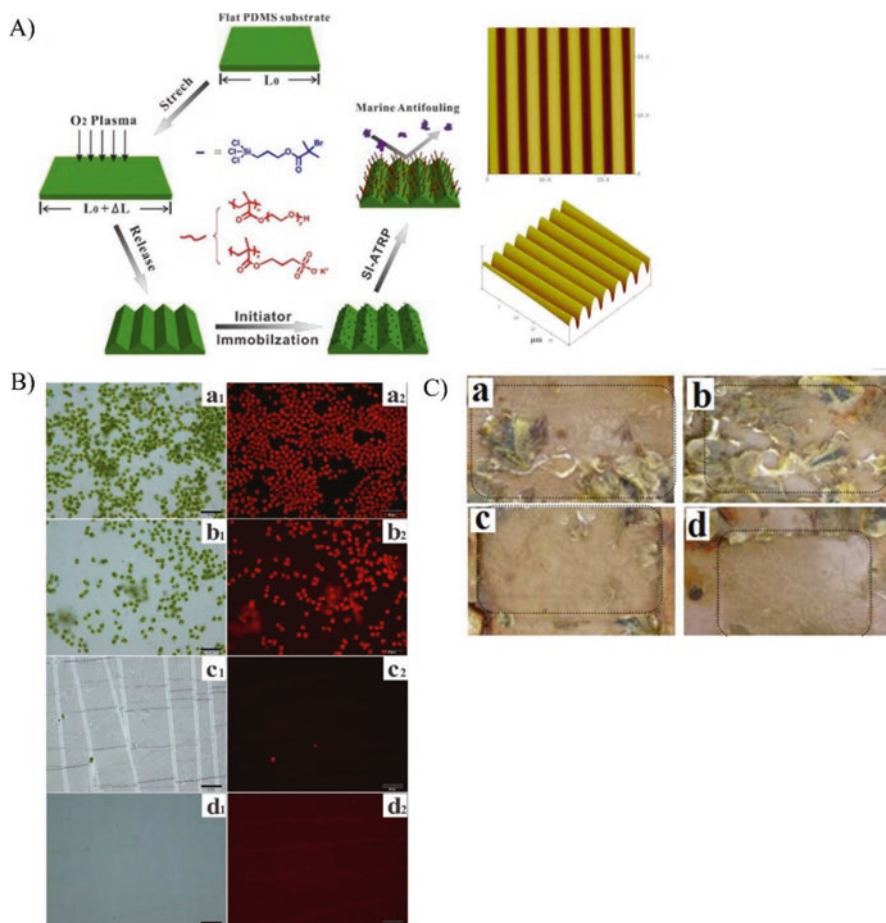


**Fig. 12.8** (a) Scheme illustration of the polymer brushes formation via the functionalization of PDMS micropatterns via SI-ATRP. (b) Optical microscope and fluorescence microscopy images of *Chlorella* settled on various samples. (c) Images of PDMS samples after immersion in seawater (July 2011–August 2011, Yellow Sea, Qingdao, +36°05'N, +120°31'E) for 40 days. (Reproduced with permission from Ref. [20])

brushes. Figure 12.8b showed representative optical and fluorescence microscopy images of the settled *Chlorella* spp. on different surfaces. The bare PDMS was almost fully covered with *Chlorella* (Fig. 12.8a<sub>1</sub>, a<sub>2</sub>). It showed the characteristics of “gregariousness”; the attachment of one microalga tends to promote the attachment of additional microalgae in the same vicinity, resulting in large clusters attached to the surface. The wPDMS was only partially covered with *Chlorella* (Fig. 12.8b<sub>1</sub>, b<sub>2</sub>); it was evident that the reduction of *Chlorella* attachment can be attributed to the wrinkled topologies. However, there was almost no *Chlorella* attached to the POEGMA and PSPMA modified surfaces (Fig. 12.8c<sub>1</sub>, c<sub>2</sub>, d<sub>1</sub>, d<sub>2</sub>). The sample mounted on stainless steel supported was immersed in seawater at a

depth of about 1 m. As shown in Fig. 12.8c, after 40 days of seawater immersion, the flat PDMS substrate was fouled considerably, and a similar result occurred in wPDMS substrate. Interestingly, POEGMA and PSPMA brushes grafted wPDMS remained relatively clean after the same period.

Another example of this application was carried out by Neto et al. [25]. The aim of this study was to mimic the lubricating mechanism of the pitcher plant using nanostructured wrinkled surface. The wrinkled surfaces are shown to be slippery and on underwater environments inhibit the attachment bacteria and algae. This kind of structures was fabricated using three different polymers (Teflon AF 1600, polystyrene (PS), and poly(4-vinyl pyridine) (P4VP) on top of two shrinkable substrates (polyshrink and shrink wrap) through spin-coating method. SEM, AFM images, and contact angle images are shown in Fig. 12.9a. The volume of trapped lubricant was quantified by adding Nile red to the silicone oil before infusion, then extracting the oil and the Nile red from the surfaces in heptane, and measuring by fluorimeter. Higher volumes of lubricant induced lower roll-off angles for water droplets and in turn induced better antifouling performance. It is known that the wrinkled surfaces scatter incident light, reducing the transparency of the substrate; therefore, by infusing the wrinkled substrates with silicone oil, the transparency increased from 85% to 90% throughout the visible range in water and from around 60 to 85% in air (Fig. 12.9b). This behavior makes these surfaces ideally suited to protect underwater sensor and cameras from fouling. Finally, results of the marine test are observed in Fig. 12.9b. The infused surfaces displayed stability in seawater and inhibited the growth of *Pseudoalteromonas* spp. bacteria. Field tests in the waters of Sydney Harbour over 7 weeks showed that silicone oil infusion inhibited the attachment of algae, but as the silicone oil was slowly depleted over time, algal attachment increased.

## 12.6 Conclusions and Remarks

In this chapter were reviewed the most innovative and recent examples of biorelated applications in which wrinkled patterns over polymer surfaces are used. The effect that causes the surface micromorphology variation on material biocompatibility, cell proliferation, cellular alignment, or differentiation is some of the topics briefly discussed in this chapter. Different applications such as the creation of antibiofouling or tissue engineering devices were also detailed. Various kinds of materials and methodologies used to form wrinkled patterns were mentioned and explained in this chapter. There are several research groups interested in generating micro-patterned surfaces on biocompatible materials at these days, particularly by taking advantage of surface instabilities, which is an easy and affordable method to create these micro-cues. These patterns are incredibly interesting mainly because this kind of structures resembles the natural architecture of most of the surfaces present in nature, making it suitable for biorelated applications.

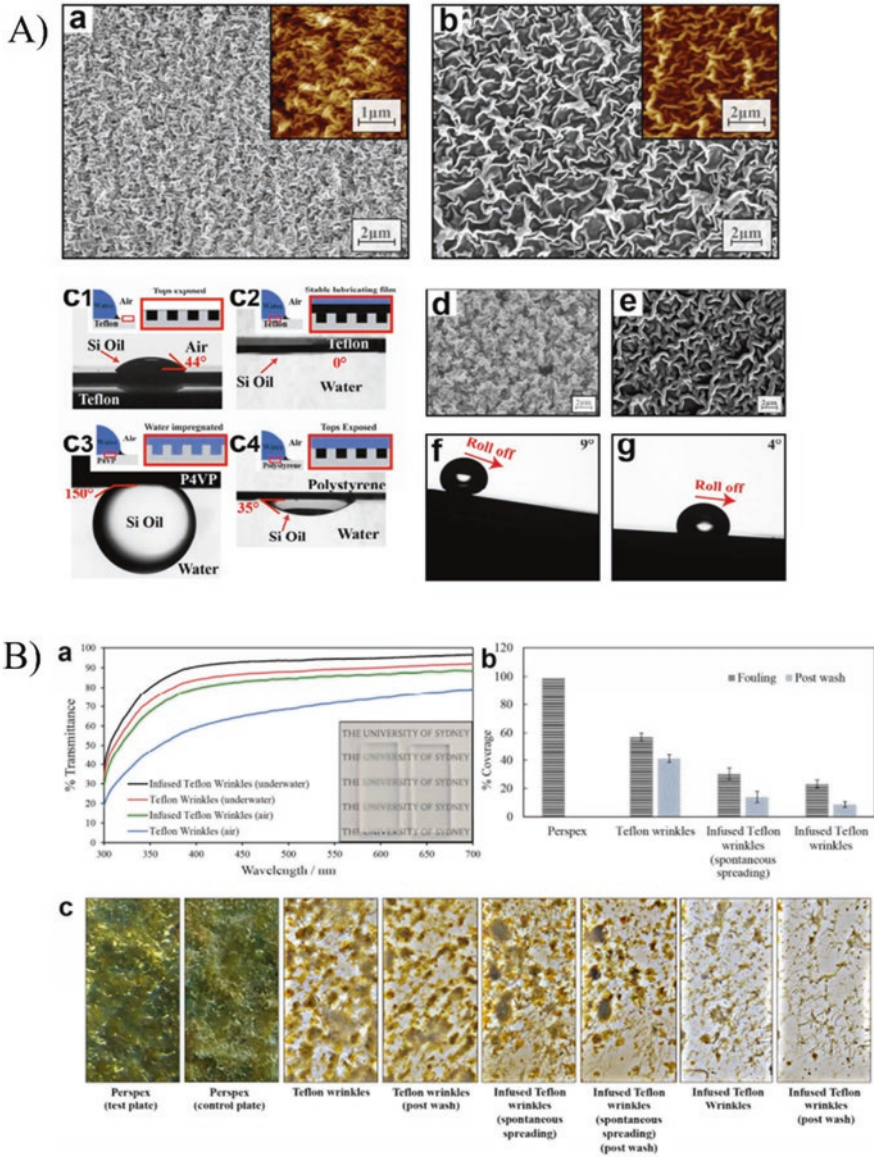


**Fig. 12.9** (a) SEM micrograph of Tefflon wrinkles on Polyshrink and Tefflon wrinkles on shrink wrap. Also contact angle images of silicone oil droplets on flat Tefflon in air, underwater, on wrinkled P4VP and PS in water are depicted. Images of roll-off at different angles are also showed. (b) Transmission spectra for Tefflon wrinkles and infused Tefflon wrinkles in both air and water. Also, the average percentage coverage of fouling on surfaces tested in the ocean for 7 weeks and after washing with water. Finally, optical images of fouled surfaces, after 7 weeks of testing in the ocean and after being washed. (Reproduced with permission from Ref. [25])

**Acknowledgments** The authors acknowledge financial support given by FONDECYT Grant N° 1170209. M.A. Sarabia acknowledges the financial support given by CONICYT through the doctoral program Scholarship Grant. J. Rodriguez-Hernandez acknowledges financial support from Ministerio de Economía y Competitividad (MINECO) (Project MAT2016-78437-R, FEDER-EU) and, finally, VRAC Grant Number L216-04 of Universidad Tecnológica Metropolitana.

## References

1. M.R. Aufan, Y. Sumi, S. Kim, et al., Facile synthesis of conductive polypyrrole wrinkle topographies on polydimethylsiloxane via a swelling-deswelling process and their potential uses in tissue engineering. *ACS Appl. Mater. Interfaces* **7**, 23454–23463 (2015)
2. A. Chen, D.K. Lieu, L. Freschauf, et al., Shrink-film configurable multiscale wrinkles for functional alignment of human embryonic stem cells and their cardiac derivatives. *Adv. Mater.* **23**, 5785–5791 (2011)
3. F. Greco, T. Fujie, L. Ricotti, et al., Microwrinkled conducting polymer Interface for anisotropic multicellular alignment. *ACS Appl. Mater. Interfaces* **5**, 573–584 (2013)
4. M. Guvendiren, J.A. Burdick, The control of stem cell morphology and differentiation by hydrogel surface wrinkles. *Biomaterials* **31**, 6511–6518 (2010)
5. J. Gu, X. Li, H. Ma, et al., One-step synthesis of PHEMA hydrogel films capable of generating highly ordered wrinkling patterns. *Polymer (Guildf)* **110**, 114–123 (2017)
6. Z. Zhao, J. Gu, Y. Zhao, et al., Hydrogel thin film with swelling-induced wrinkling patterns for high-throughput generation of multicellular spheroids. *Biomacromolecules* **15**, 3306–3312 (2014)
7. M. Nikkhah, F. Edalat, S. Manoucheri, et al., Engineering microscale topographies to control the cell-substrate Interface. *Biomaterials* **33**, 5230–5246 (2012)
8. D. Hoffman-kim, J.A. Mitchel, R.V. Bellamkonda, NIH Public Access. *Annu. Rev. Biomed. Eng* **12**, 203–231 (2010)
9. H.J. Jeon, C.G. Simon, G.H. Kim, A mini-review: Cell response to microscale, nanoscale, and hierarchical patterning of surface structure. *J. Biomed. Mater. Res. B Appl. Biomater.* **102**, 1580–1594 (2014)
10. H. Izawa, N. Okuda, T. Yonemura, et al., Application of bio-based wrinkled surfaces as cell culture scaffolds. *Colloid. Interface.* **2**, 15 (2018)
11. L. Peng, S. Zhou, B. Yang, et al., Chemically modified surface having a dual-structured hierarchical topography for controlled cell growth. *ACS Appl. Mater. Interfaces* **9**, 24339–24347 (2017)
12. M. Li, D. Joung, B. Hughes, et al., Wrinkling non-spherical particles and its application in cell attachment promotion. *Sci. Rep.* **6**, 30463 (2016)
13. Q. Zhou, O. Castañeda Ocampo, C.F. Guimarães, et al., Screening platform for cell contact guidance based on inorganic biomaterial micro/nanotopographical gradients. *ACS Appl. Mater. Interfaces* **9**, 31433–31445 (2017)
14. X. Cui, Y. Hartanto, H. Zhang, Advances in multicellular spheroids formation. *J. R. Soc. Interface* **14**, 20160877 (2017)
15. A. Ivascu, M. Kubbies, Rapid generation of single-tumor spheroids for high-throughput cell function and toxicity analysis. *J. Biomol. Screen.* **11**, 922–932 (2006)
16. X. Cui, S. Dini, S. Dai, et al., A mechanistic study on tumour spheroid formation in thermosensitive hydrogels: Experiments and mathematical modelling. *RSC Adv.* **6**, 73282–73291 (2016)
17. M.B. Oliveira, A.I. Neto, C.R. Correia, et al., Superhydrophobic chips for cell spheroids high-throughput generation and drug screening. *ACS Appl. Mater. Interfaces* **6**, 9488–9495 (2014)

18. M. Ingram, G.B. Techy, R. Saroufeem, et al., Three-dimensional growth patterns of various human tumor cell lines in simulated microgravity of a NASA bioreactor. *In Vitro Cell. Dev. Biol. Anim.* **33**, 459–466 (1997)
19. K. Chen, M. Wu, F. Guo, et al., Rapid formation of size-controllable multicellular spheroids: Via 3D acoustic tweezers. *Lab Chip* **16**, 2636–2643 (2016)
20. Y. Zhang, H. Hu, X. Pei, et al., Polymer brushes on structural surfaces: A novel synergistic strategy for perfectly resisting algae settlement. *Biomater. Sci.* **5**, 2493–2500 (2017)
21. J.Z. Wang, Y.X. Zhu, H.C. Ma, et al., Developing Multi-Cellular Tumor Spheroid Model (MCTS) in the Chitosan/Collagen/Alginate (CCA) fibrous scaffold for anticancer drug screening. *Mater. Sci. Eng. C* **62**, 215–225 (2016)
22. V.H.B. Ho, N.K.H. Slater, R. Chen, PH-responsive Endosomolytic pseudo-peptides for drug delivery to multicellular spheroids tumour models. *Biomaterials* **32**, 2953–2958 (2011)
23. L. Xia, R.B. Sakban, Y. Qu, et al., Tethered spheroids as an in vitro hepatocyte model for drug safety screening. *Biomaterials* **33**, 2165–2176 (2012)
24. J. Zhang, S. Zhao, Y. Zhu, et al., Three-dimensional printing of strontium-containing mesoporous bioactive glass scaffolds for bone regeneration. *Acta Biomater.* **10**, 2269–2281 (2014)
25. C.S. Ware, T. Smith-Palmer, S. Peppou-Chapman, et al., Marine antifouling behavior of lubricant-infused nanowrinkled polymeric surfaces. *ACS Appl. Mater. Interfaces* **10**, 4173–4182 (2018)

# Chapter 13

## Tuning Surface Morphology of Polymer Films Through Bilayered Structures, Mechanical Forces, and External Stimuli



Ying Li and Shan Tang

### 13.1 Introduction

When a semi-infinite hyperelastic polymer material is under compression, its free surface would become unstable and form sinusoidal waves (wrinkles) upon a critical strain  $\epsilon_{\text{Biot}} = 0.46$  [1], according to Biot's linear perturbation analysis with plane-strain conditions. However, experimental [2–4], theoretical [4, 5], and computational [6, 7] studies reveal that sharp creases occurred on the surface at the critical strain  $\epsilon_{\text{crease}} = 0.35$ . The creases, other than wrinkles, are usually observed when a block of an elastomer is bent since  $\epsilon_{\text{crease}} < \epsilon_{\text{Biot}}$ . However, when a stiff thin film attached on a compliant thick substrate is under compression, wrinkles are usually occurred to release the stress [8, 9], as shown in Fig. 13.1. Wrinkles are surface undulations in the space with infinitesimal strain, while creases are localized self-contacted regions with large strain relative to their initial homogeneous state. Therefore, the cross section of a crease has a very sharp tip, which is distinct from that of a wrinkle. These surface instabilities have been widely applied to control biomolecular patterns and enzymatic activity [10], biofouling [11], interfacial adhesion [12], and cellular behavior [13]. Nevertheless, these instabilities may also lead to failure of materials, such as buckling of microelectromechanical systems [14–16] and composite materials [17, 18]. Therefore, it raises a critical question: How these surface instabilities can be controlled and suppressed?

As an attempt to answer the above question, Cao and Hutchinson have computationally and theoretically studied a bilayered structure with a stiff elastomer film on

---

Y. Li (✉)

Department of Mechanical Engineering and Institute of Materials Science,  
University of Connecticut, Storrs, CT, USA  
e-mail: [ying.3.li@uconn.edu](mailto:ying.3.li@uconn.edu)

S. Tang

Department of Engineering Mechanics, Dalian University of Technology, Dalian, China

© Springer Nature Switzerland AG 2019

C. M. González-Henríquez, J. Rodríguez-Hernández (eds.), *Wrinkled Polymer Surfaces*, [https://doi.org/10.1007/978-3-030-05123-5\\_13](https://doi.org/10.1007/978-3-030-05123-5_13)

291

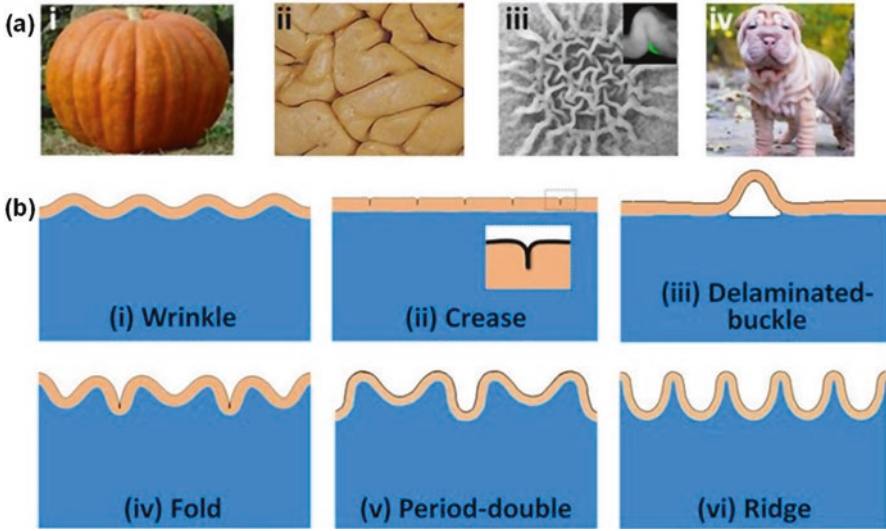


**Fig. 13.1** Illustrations of examples and schematics different surface instabilities. (a) Examples of growth-induced surface instabilities on (i) the pumpkin skin, (ii) the cerebral cortex, (iii) the biofilm, and (iv) the dog skin. (b) Schematics of surface instabilities for bilayered structure: (i) wrinkle, (ii) crease, (iii) delaminated-buckle, (iv) fold, (v) period-double, and (vi) ridge. (Adapted from Ref. [19])

a polymeric substrate [20]. Their results demonstrate that the critical strain for the onset of wrinkles  $\epsilon_{\text{wrinkle}}$  can be easily tuned via the Young's modulus ratio between the film and the substrate  $E_f/E_s$ , where  $E_f$  and  $E_s$  are the moduli for the film and the substrate, respectively. For instance, when  $E_f/E_s = 20$ ,  $\epsilon_{\text{wrinkle}} = 0.07$  (refer to Fig. 9 therein) [20]. However,  $\epsilon_{\text{wrinkle}}$  has been dramatically increased to 0.3 for  $E_f/E_s = 2$ , which is much smaller than  $\epsilon_{\text{Biot}}$  and  $\epsilon_{\text{crease}}$  (refer to Fig. 2 therein) [20]. A unified phase diagram for different surface instabilities of compressed film/substrate systems has been obtained by Wang and Zhao [21], by considering the moduli of the film and the substrate, the interfacial adhesion strength, the film thickness, and the pre-stretch of the substrate. Although these studies can be used to control the different surface instabilities, the related material failure still cannot be prevented. Very recently, Jin and Suo have shown that the surface creases can be suppressed by the strain-stiffening materials [22]. When the material stiffens deeply at large strains, its surface is initially smooth, then forms creases, and finally becomes smooth as the compressive strain increases. If the material stiffens deeply at small strains, the creases will never occur and be completely suppressed [22]. According to the authors' knowledge, the work of Jin and Suo [22] is the first, which attempted to suppress surface instabilities of materials under large compression, although it relies on the intrinsic mechanical properties of materials, indicating that it may not be applicable to many other materials without strain-stiffening.

Growth-induced surface instabilities of layered soft solids have been attracting great interest recently. For a bilayered system with a thin stiff layer and a thick compliant substrate, the mismatch of the volume expansion between these two layers

can lead to compressive stress in a layer, and then the free surface of the system is wrinkled to minimize the system energy. For instance, Yin et al. [23, 24] simplified the natural fruits and vegetables as a core/shell system with a stiff exocarp (shell) and a compliant carcocarp (core). The different undulating morphologies found in a variety of fruits and vegetables are explained by the volume growth of the inner core. Li et al. [7, 25] studied the volumetric growth of mucosal layers in the inner layer of soft tissues such as the esophagus, pulmonary airway, and many animal lumens. The folding or wrinkling of mucosal layers is explained through the buckling analysis, accounting for the volumetric growth of mucosal layers. The folding or wrinkling patterns may serve as the clinical symptoms of diseases in these organs. Ciarletta et al. [26] further established morphological phase diagrams for the pattern selection of tubular tissues due to the growth process initiated by epithelial differentiation or pathological conditions. In these studies, the volumetric change of a layer is described by an extra growth tensor  $F_g$ , induced by the molecular diffusion during this process. Then, the total deformation gradient is formulated as  $F = F_e F_g$ , with  $F_e$  representing the elastic deformation without volumetric change [27].

In this chapter, we try to highlight our recent studies on the surface instabilities of polymer thin films, under the influence of bilayered structures, mechanical forces, and external stimuli. Section 13.2 will demonstrate how the compressibility of the substrate can influence the buckling and post-buckling behaviors of a perfectly bonded hard thin film [28]. We find that Poisson's ratio cannot only shift the critical strain for the onset of buckling but also affect the buckling modes. Section 13.3 explores the surface instability of bilayered hydrogel subjected to both compression and solvent absorption [29]. Our results show that when the thickness of the upper layer is very large, surface wrinkles can exist without transforming into period doublings. The pre-absorption of the water can result in folds or unexpected hierarchical wrinkles, which can be realized in experiments through further efforts. Section 13.4 discusses the transition of surface–interface creasing in bilayered hydrogels [30]. The surface or interface crease of the bilayered hydrogels under swelling is found to be governed by both the modulus ratio and the height ratio between the thin film and substrate. Section 13.5 studies surface instability of monolayer graphene supported by a soft (polymer) substrate under equal-biaxial compression [31]. Regardless of the interfacial adhesion strength between the graphene and the substrate, herringbone wrinkles have always been observed due to their lowest energy status, compared with the checkerboard, hexagonal, triangular, and one-dimensional sinusoidal modes. Note that there are many excellent reviews about the surface instabilities of thin film/substrate systems [7, 32–35]. Due to the space limit, we do not cover these topics in this book chapter.

## 13.2 Effect of Poisson's Ratio of the Substrate on Surface Instability Patterns of Bilayered Polymers

Here, we discuss another mechanism of volumetric change in the surface instabilities of a bilayered system under compression, which originates from the compressibility of polymeric materials. For isotropic materials, Poisson's ratio ranges from  $-1$  to  $0.5$ .

Polymeric materials are usually assumed to be incompressible with a Poisson's ratio of 0.5. Thus, its volume is conserved under external loadings. However, it is well-known that the soft polymeric materials can be compressible, the extent of which depends on the temperature  $T$  or its microstructure. For instance, polymers at a temperature  $T$  above their glass transition temperature  $T_g$  behave like incompressible materials, while they act compressible when  $T < T_g$ , as elaborated in a recent review by Greaves et al. [36]. The temperature-dependent Poisson's ratio for polymeric materials has also been recently confirmed by our molecular simulations [37]. Besides, many polymeric materials with negative Poisson's ratio are designed and invented recently [36, 38–40]. Polymer gels such as hydrogels can absorb or discharge water molecules, resulting in dramatic volumetric changes. A previous study also demonstrated that gels can exhibit negative Poisson's ratio close to  $-1$  near the phase transition [41]. Inspired by these phenomena, we can roughly simplify these materials as hyperelastic soft solids with compressibility. To consider the volumetric changes of these soft solids, the deformation energy of the material is decomposed into the deviatoric and volumetric strain energy parts, which have been discussed in the previous study [42]. Here we should emphasize that all the previous theoretical [1, 2, 4, 8] and computational [6, 19–21, 43] studies assume that the elastomer is incompressible with Poisson's ratio fixed to be 0.5 for simplifying the surface instability problem.

Therefore, we provide a new way to tune the surface instability of a bilayered structure under large compression by changing the compressibility of the substrate. A thin stiff film is coated on a thick compliant substrate for the bilayered structure. Through theoretical analysis, we find that the surface wrinkles can be delayed to a large compressive strain ( $\epsilon_{\text{Biot}}$ ), if the substrate has a negative Poisson's ratio. Inspired by the theoretical results, we develop a finite element analysis (FEA) model to quantitatively study the surface instability of the thin film/substrate system under compression, with related morphological transition during this process. The FEA results further confirm that creases, wrinkles, period doubling and folds (secondary bifurcations after the initial instability, cf. Fig. 13.1), and other surface instability forms can be suppressed and delayed to a very large compressive strain  $\epsilon_{\text{Biot}}$ . However, these instabilities cannot be delayed when Poisson's ratio of the substrate is positive. Therefore, Poisson's ratio of the substrate is identified as the key to tune and suppress the surface instabilities of materials during compression. It also opens up a new way to understand the surface instability behaviors of the thin film/substrate systems, which can be utilized to design stretchable electronics and laminates of packaging materials.

We first set the modulus ratio  $E_f/E_s = 5$ , where  $E_f$  and  $E_s$  are Young's moduli of the film and substrate, respectively. The theoretical solution is obtained by the recently proposed semi-theoretical algorithm [44] to solve the incremental equilibrium equations with appropriate boundary conditions. The theoretically predicted critical strain for the onset of instability is presented in Fig. 13.2 as a solid line. Here the critical strain is defined as  $\epsilon_{\text{crit}} = 1 - \lambda_{\text{crit}}$ , which is consistent with the previous study reported by Biot [1] and Cao and Hutchinson [20]. The critical strain obtained from FEA is also given in Fig. 13.2, denoted by star symbols, which is consistent with our theoretical prediction. It is clearly shown that the critical strain monotonically decreases with  $\nu_s$  (Poisson's ratio of the substrate) increasing from  $-1$  to 0.5, signaling

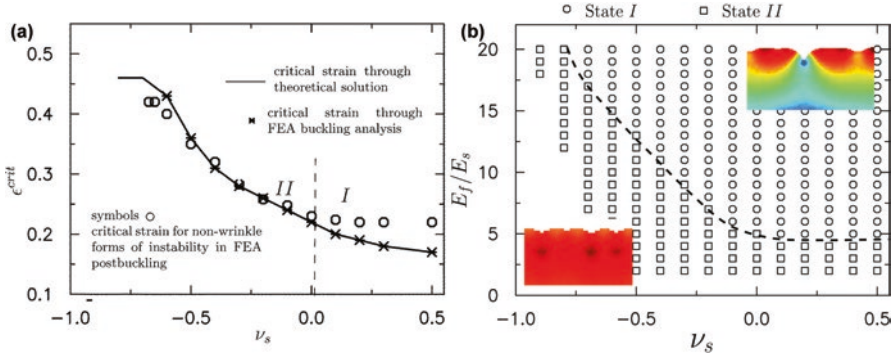


**Fig. 13.2** (a) Critical strain  $\epsilon_{crit}$  versus Poisson’s ratio of substrate  $\nu_s$  for the fixed modulus ratio  $E_f/E_s = 5$ . (b) Phase diagram for a hard thin film on a soft substrate under compression. According to different modulus ratio  $E_f/E_s$  and substrate Poisson’s ratio  $\nu_s$ , two different regimes have been identified (cf. (a)), which are separated by the dashed line

that the substrate with negative Poisson’s ratio can dramatically delay the surface instability. When Poisson’s ratio of the substrate is positive, Poisson’s ratio effect on the critical strain is not pronounced, while the critical strain has been dramatically increased from 0.23 to 0.46 when  $\nu_s$  is reduced from 0.0 to  $-1$ . If Poisson’s ratio of the substrate approaches  $-1$ , the limitation for the isotropic materials, the critical strain will also reach the limit  $\epsilon_{Biot} = 0.46$ . Although we only show the results for  $E_f/E_s = 5$ , other cases with different modulus ratios still follow the same trend. All these theoretical results demonstrate that the substrate with a negative Poisson’s ratio can help to suppress and delay the surface instability of the attached thin film during compression. However, it is impossible to pass the critical strain  $\epsilon_{Biot} = 0.46$  without instability. Although we do not have an exact physical explanation on this phenomenon, we suspect that the reduced Poisson’s ratio is equivalent to the increased effective modulus  $E/(1 - \nu^2)$  under plane-strain conditions. The effective modulus will be extremely large as Poisson’s ratio of the substrate is approaching  $-1$ . When the modulus of the substrate is equal or larger than the thin film, the critical strain will be Biot’s solution [20].

The effect of substrate Poisson’s ratio  $\nu_s$  can be qualitatively understood in the following way. When  $\nu_s > 0$ , both the thin film and substrate are compressed along the  $X_1$  direction while stretched along the  $X_2$  direction due to Poisson’s effect. Up to a certain value of the compressive strain, the surface of the thin film undulates to minimize the free energy of the system [15, 16]. However, if the substrate has a negative Poisson’s ratio with  $\nu_s < 0$ , the thin film and substrate will be stretched and compressed along the  $X_2$  direction, respectively. In this way, the undulation of the thin film will be canceled out due to the compression of the substrate and compatibility between the film and the substrate (assuming that the thin film is perfectly bound to the substrate). Therefore, the surface instability can be dramatically suppressed and delayed, when Poisson’s ratio of the substrate is close to  $-1$ , as observed by our above theoretical and numerical analysis.

We then illustrate the typical instability patterns with different Poisson’s ratio of the substrate under a fixed modulus ratio  $E_f/E_s = 5$ . The evolution of surface mor-

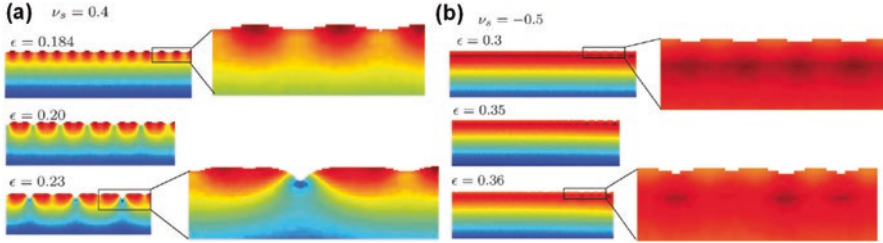


**Fig. 13.3** Evolution of surface morphologies for the thin film/substrate system under compression. The modulus ratio  $E_f/E_s$  is fixed to be 5. Two different values for Poisson's ratio of the substrate are considered, 0.4 and  $-0.5$ , corresponding to the regimes I and II in Fig. 13.2a, respectively

phologies with two different Poisson's ratios  $\nu_s = 0.4$  (regime I) and  $-0.5$  (regime II) is given in Fig. 13.2. For  $\nu_s = 0.4$ , the periodic wrinkles occur around 0.18, which is consistent with above the theoretical and FEA prediction through linear perturbation analysis (cf. Fig. 13.2). The periodic wrinkles evolve into the doubling period and fold afterward. The observed trend is similar to that given by Cao and Hutchinson [20] for a thin stiff film on a thick compliant substrate, while both the thin film and the substrate are incompressible. However, when  $\nu_s = -0.5$ , the surface still maintains flat under large compressive strain. When the compressive strain is close to the critical strain for periodic wrinkles (0.36), the surface wrinkles with very small amplitude have been observed. Note that 0.36 is comparable with the critical strain  $\epsilon_{\text{crease}} = 0.35$  for a homogeneous neo-Hookean solid under compression [4, 5]. This is greatly different from what has been observed for the case with  $\nu_s = 0.4$  (Fig. 13.3).

According to the above simulation results, we notice that two dimensionless parameters, modulus ratio  $E_f/E_s$  and the substrate Poisson's ratio  $\nu_s$ , primarily affect the instability patterns. To explore how the instability pattern varies with these two parameters  $E_f/E_s$  and  $\nu_s$ , a phase diagram is given in Fig. 13.2b. Two different regimes (regimes I and II shown in Fig. 13.2a) have been identified and marked as the circles and squares, respectively. The phase boundary between these two regimes is denoted by a dashed line. When the modulus ratio  $E_f/E_s$  is fixed, with the increasing  $\nu_s$ , the periodic doublings and folds are more pronounced after initial periodic wrinkles. When  $E_f/E_s$  is less than 5, the instability pattern within regime II is always observed. Similar to Baru et al. [45] and Auguste et al. [46], the modulus ratio in their theoretical analysis and experiments is larger than 5 to observe the evident periodic doublings and folds.

### 13.3 Surface Instability of Bilayered Hydrogel Subjected to Both Compression and Solvent Absorption

For bilayered hydrogels, the surface morphology caused by the instability is usually controlled by the solvent-induced swelling/shrinking and mechanical force. Here, two important issues on the instability of bilayered hydrogels, which were not

considered in the previous studies, are considered in this section. First, the upper layer of a hydrogel is not necessarily too thin. Thus we investigated how the thickness of the upper layer can affect the surface morphology of bilayered hydrogels under compression through both FEA simulation and theoretical analysis. Second, a hydrogel can absorb water molecules before the mechanical compression. The effect of the pre-absorption of water before the mechanical compression was studied through FEA simulations and theoretical analysis. Our results show that when the thickness of the upper layer is very large, surface wrinkles can exist without transforming into period doublings. The pre-absorption of the water can result in folds or unexpected hierarchical wrinkles, which can be realized in experiments through further efforts.

Here we first show the effect of the upper layer thickness through FEA simulations. The displacement in the  $y$ -direction of the bottom edge and the left boundary in the  $x$ -direction was fixed. The uniform displacement in the  $x$ -direction was set as zero in the expansion stage and imposed monotonically on the right edge in the compression process. Figure 13.4a shows deformation configurations for three different thickness ratios  $h^t/h^b$  of 1/17, 1/30, and 1/50 under plane-strain conditions at different levels of compression in our post-buckling analysis. Here, the superscripts  $t$  and  $b$  represent the upper and lower layers, respectively. The compressive strain is marked below each figure. These strain levels were chosen because the typical instability patterns are shown clearly. The initial volume fraction of the polymer for the bottom layer was  $\phi_0^b = 0.1$ , while the top layer was  $\phi_0^t = 0.22$  or 0.3. When  $h^t/h^b = 1/50$ , the thickness of the top layer was much smaller compared with the substrate, which was consistent with the bilayered system studied by many previous researchers [20, 45]. For both cases ( $\phi_0^b = 0.1$ ,  $\phi_0^t = 0.22$ ) and ( $\phi_0^b = 0.1$ ,  $\phi_0^t = 0.3$ ), we can see that as the compressive deformation increased, wrinkles formed on the flat surface first and evolved into the pattern of period doublings later. This period doubling was first reported by compression on the bilayered structure of the hard thin film (PDMS) on soft substrate (PDMS) through experiments [45]. Later, the FEA simulations by Cao and Hutchinson [6] further confirmed this interesting phenomenon. Their work also shows that when the modulus ratio between the thin film and substrate is greater than 5, the wrinkles change into period doubling (see Fig. 13.9 therein). When the modulus ratio between the thin film and substrate is less than 5, the initial wrinkles transform into a local fold and creasing (see Fig. 13.10 therein). When the thickness of the thin film was larger ( $h^t/h^b = 1/30$ ), we observed that the wrinkles appeared first but periodic doubling could not be observed for the ( $\phi_0^b = 0.1$ ,  $\phi_0^t = 0.22$ ) case, even when the imposed compressive strain was around 26%. For ( $\phi_0^b = 0.1$ ,  $\phi_0^t = 0.3$ ), the wrinkles transformed into tripling. Such tripling is reported by Auguste et al. [46] for a soft bilayer with a pre-stretched substrate. When the thickness of the thin film is much larger ( $h^t/h^b = 1/17$ ), we can see that wrinkles appeared first but periodic doubling could not be observed for ( $\phi_0^b = 0.1$ ,  $\phi_0^t = 0.22$ ). For ( $\phi_0^b = 0.1$ ,  $\phi_0^t = 0.3$ ), the tripling did not appear, but folds were observed.

Summarizing the results in Fig. 13.4a, we can conclude that when the thickness of the upper layer is increasing and is a little stiffer than the substrate ( $\phi_0^t$  is a little

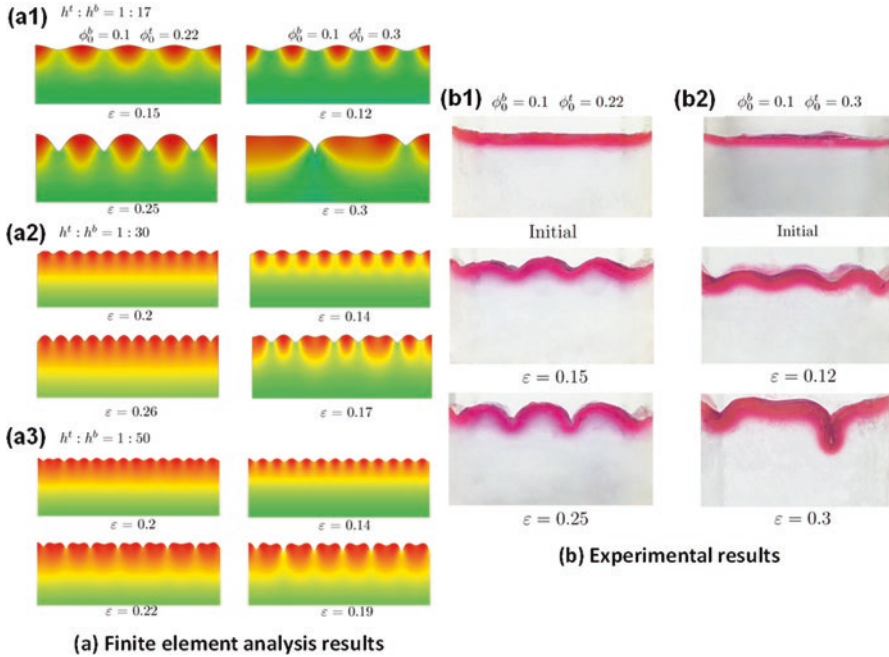


**Fig. 13.4** (a) Finite element simulation results on surface morphologies of bilayered hydrogels under different levels of compressive strain for different thickness ratios of upper and lower layers: (a1)  $h^t/h^b = 1/17$ ; (a2)  $h^t/h^b = 1/30$ ; and (a3)  $h^t/h^b = 1/50$ . The initial volume fraction of polymer chain in the lower layer was  $\phi_0^b = 0.1$ . Two initial volume fractions of the polymer chain in the upper layer were considered:  $\phi_0^t = 0.22$  or  $0.3$ , shown in the left and right columns, respectively. (b) Experimental observations on surface morphologies of bilayered hydrogels under different levels of compressive strain for the thickness ratio of the upper and lower layers  $h^t/h^b = 1/17$ . The initial volume fraction of polymer chain in the lower layer is  $\phi_0^b = 0.1$ . Two initial volume fractions of the polymer chain in the upper layer are considered: (b1)  $\phi_0^t = 0.22$ ; (b2)  $\phi_0^t = 0.3$

greater than  $\phi_0^b$ ), the periodic doublings cannot appear and only surface wrinkles can exist. When the thickness of the upper layer is increasing and is much stiffer than the substrate ( $\phi_0^t$  is much larger than  $\phi_0^b$ ), periodic doubling can evolve into folds. In fact, the theoretical prediction given by Brau et al. [45] on the basis of bilayered PDMS/PDMS experimental data shows that the critical compression is not related to the thickness of the upper layer ( $\epsilon^{crit} = 0.02(1 - \nu)^2 / (1 - 2\nu)^2$ , where  $\nu$  is Poisson's ratio), because their work assumed that the top layer was very thin compared with the substrate and plate theory was employed to describe the deformation of the upper layer.

Here we also show the experimental results to confirm the above simulation results. A bilayered hydrogel was fabricated with  $\phi_0^b = 0.1$  and  $\phi_0^t = 0.22$  or  $0.3$ . The thickness ratio between the top layer and the bottom layer was  $1/17$ . Figure 13.4b shows the deformation configurations under different levels of compressive strain in

the experiments. The cases ( $\phi_0^b = 0.1$ ,  $\phi_0^t = 0.22$ ) and ( $\phi_0^b = 0.1$ ,  $\phi_0^t = 0.3$ ) are shown in Figure 13.4b1 and b2, respectively. For the case ( $\phi_0^b = 0.1$ ,  $\phi_0^t = 0.22$ ), only wrinkles on the surface were observed, consistent with our numerical predictions. Further increments in the compressive strain could cause fracture of the hydrogel. For the case ( $\phi_0^b = 0.1$ ,  $\phi_0^t = 0.3$ ), the wrinkles transformed into folds directly without periodic doubling. The experimental observations showed good agreement with the simulation results given in Fig. 13.4a.

The surface instability of a bilayered structure can be affected by the absorption of water in the top layer, the mechanical compression, or both. The surface instability under the pure mechanical compression has been discussed in the above sections. We now discuss the absorption of water and the combined absorption of water and mechanical compression on the surface instability of bilayered hydrogels. The post-buckling analysis on bilayered hydrogels through ABAQUS was performed and is given in this section. The top layer absorbed water first, followed by the mechanical compression. This study shows the deformation configuration at a compressive strain of 0.4 for ( $\phi_0^b = 0.1$ ,  $\phi_0^t = 0.12$ ) and  $\mu^t / \mu_0^t = 0.7$  in Fig. 13.5a. In this case, the wrinkles with small amplitude transform into multiple localizations. With the slight increment in compression, the localization continued to develop into the form of an incipient fold. This configuration was very similar to that shown in Figure 10 of Ref. [20] for bilayered neo-Hookean solids with a modulus ratio between the top and bottom layers of less than 10. In Fig. 13.5b, the deformation configurations at compressive strains of 0.14 and 0.2 for the ( $\phi_0^b = 0.1$ ,  $\phi_0^t = 0.22$ ) and  $\mu^t / \mu_0^t = 0.5$  cases are shown. We can see in Fig. 13.5b that the sinusoidal wrinkles were stable prior to the onset of period doublings. This configuration was very similar to that shown in Figure 9 of Ref. [20] for bilayered neo-Hookean solids with a modulus ratio between the upper and lower layers of greater than 10.

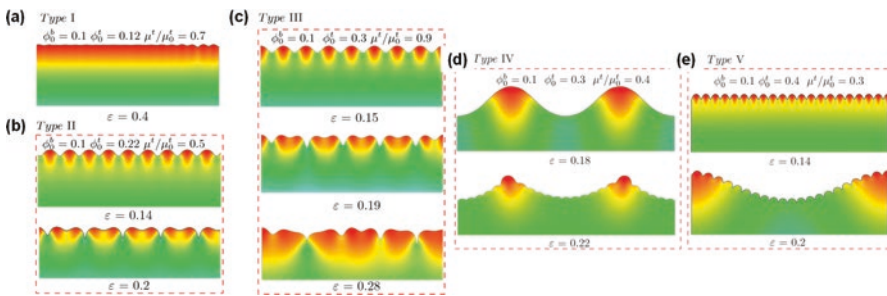


**Fig. 13.5** Surface morphologies of bilayered hydrogel modeled by the finite element analysis simulations under different levels of compressive strain with the pre-absorption of water in the upper layer, when the initial volume fraction of polymer chain  $\phi_0^t$  varied and the lower layer was fixed as  $\phi_0^b = 0.1$ : (a)  $\phi_0^t = 0.12$ , (b)  $\phi_0^t = 0.22$ , and (c)  $\phi_0^t = 0.3$ . These are typical surface instability patterns, named types I, II, and III, respectively. The initial volume fraction of polymer chain in the upper layer  $\phi_0^t$  was much larger with (c)  $\phi_0^t = 0.3$  and (d)  $\phi_0^t = 0.4$ . These are typical surface instability patterns, named types IV and V, respectively

The present work shows that these two behaviors are also representative of bilayered hydrogels.

When we further increased the volume fraction of polymer chains in the top layer, ( $\phi_0^b = 0.1$ ,  $\phi_0^t = 0.3$ ) and  $\mu^t / \mu_0^t = 0.9$ , the deformation configurations were as presented in Fig. 13.5c. It can be seen that wrinkles evolved into period doublings and transformed into folds at larger compressive deformations. This behavior was qualitatively different from what is given in Ref. [20] for bilayered neo-Hookean solids. However, it is similar to Figure 12 shown in Ref. [20] with a small pre-stretch in the complainant substrate. This demonstrates the importance of the initial absorption of water in the upper layer on the surface instability of bilayered hydrogels.

When the volume fraction of the polymer chains in the upper layer was much larger than that in the lower layer, with more absorption of water in the upper layer, the representative deformation configurations under different imposed compressive strains were as shown in Fig. 13.5d, e. The material constants were  $\phi_0^b = 0.1$  and  $\phi_0^t = 0.3$  with the pre-absorption of water characterized by  $\mu^t / \mu_0^t = 0.4$  for Fig. 13.5d, while they were  $\phi_0^b = 0.1$  and  $\phi_0^t = 0.4$  with  $\mu^t / \mu_0^t = 0.3$  for Fig. 13.5e. In the case shown in Fig. 13.5d, wrinkles with a large wavelength appeared first. With the increment in compressive deformation, the appearance of secondary wrinkles with a smaller wavelength on the wrinkles with a large wavelength led to a hierarchical wavy structure. Different approaches for soft material systems such as PDMS are proposed [47, 48]. Shao et al. [47] used the surface wrinkles to fabricate a surface with a periodic variation in curvature. The formation of a hierarchical wrinkling pattern could be controlled by regulating the curvature of the surface. Wang et al. [49] recently proposed an approach to utilize a three-layer system (an aluminum thin film deposited on a hard PDMS, attached to a pre-stretched soft PDMS substrate) to form a wrinkling pattern with three orders. In the case shown in Fig. 13.5e, the wrinkles with a small wavelength appeared first. With the further increment in compressive strain, wrinkles with a larger wavelength occurred. These also formed a hierarchical pattern of wrinkles on the surface.

According to the above computational observations, extensive FEA simulations were performed for wide ranges of the initial absorption of water value ( $\alpha^t / \alpha_0^t$ ) and initial volume fraction of the polymer chains in the top layer ( $\phi_0^t$ ). The initial volume fraction of the polymer chains in the bottom layer was fixed as  $\phi_0^b = 0.1$ . Figure 13.6 presents our numerical findings in a form analogous to a phase diagram, wherein the abscissa denotes  $\phi_0^t$  and the ordinate is  $\alpha^t / \alpha_0^t$ . The discrete points shown correspond to the discrete levels of  $\alpha^t / \alpha_0^t$  and  $\phi_0^t$  analyzed, where black-filled quadrangles, purple-filled triangles, and yellow-filled inverted triangles represent the formation of surface patterns of types I, II, and III, respectively, in Fig. 13.5a–c. Blue full circles and red full squares in Fig. 13.5d, e denote types IV and V, respectively. With this phase diagram at hand, it will be possible for us to tune the absorption of the water and initial volume fraction of polymer chains of the upper layer to control the surface morphology.

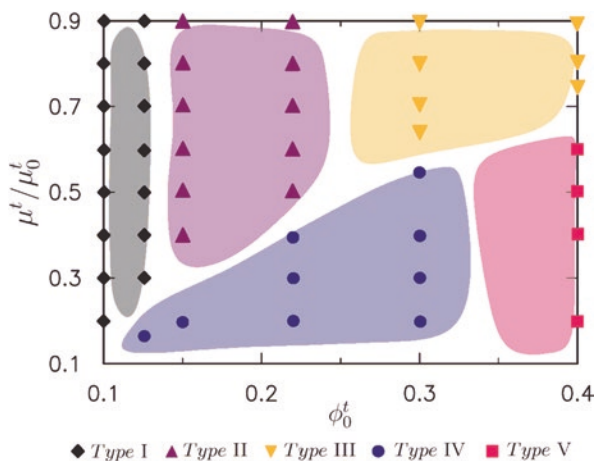


**Fig. 13.6** Predicted phase diagram by finite element simulations for the occurrence of typical surface morphologies (types I, II, III, IV, and V) shown in Fig. 13.5. The phase diagram was constructed as a function of the initial absorption of water  $\alpha^t / \alpha_0^t$  and initial volume fraction of polymer chain  $\phi_0^t$  of the bilayered hydrogel under both the pre-absorption of water in the upper layer and mechanical compression. The initial volume fraction of polymer chain in the bottom layer was fixed as  $\phi_0^b = 0.1$

### 13.4 Transition of Surface–Interface Creasing in Bilayered Hydrogels

While extensive works have been devoted to understand surface instabilities (wrinkles or creases) and explore their applications in responsive materials and soft actuators, the phenomenon of interface instability has received relatively less attention. As the name implies, this kind of instability is confined to the interface of the bilayered structure, wherein the top layer (or film) buckles into the substrate and forms a V shape. Notably, Jin et al. [50] have shown the existence of interface creases for a bilayered hydrogel under swelling. Similar to their surface counterparts, interface creases form at lower compressive strain than interface wrinkles, while such a critical strain is higher than that of surface creases [50]. On the other hand, Xu et al. [51] have studied a two-stage electrochemically driven delamination and formation of blisters of a hydrogel thin film supported using a micro-patterned interdigitated electrode. In their study, the thermally induced deswelling of gels can allow the delaminated film to return to its original flat state, demonstrating the ability to create locally controllable interface topographies, thereby enabling many potential applications. For instance, the interface crease in a bilayered soft material with an ion-flowing electrolyte hydrogel as the upper layer can retard the ion flow in the electrolyte hydrogel. However, it is not clear under which conditions the interface creases can occur, other than surface creases. To overcome the above issue,

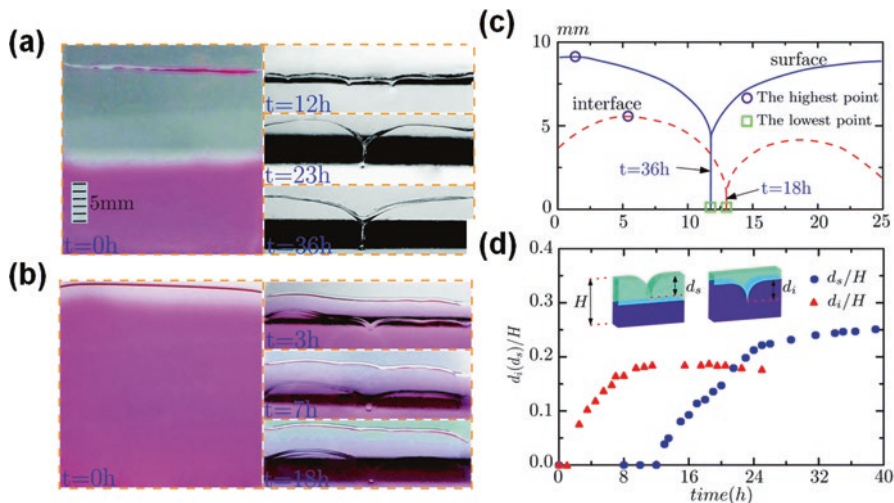


**Fig. 13.7** (a) Surface crease initiates at  $t = 12$  h, continues to grow at  $t = 23$  h, and finally saturates at  $t = 36$  h. (b) The interface crease demonstrates similar characteristics to the surface crease, where initiation begins at  $t = 3$  h and saturates at  $t = 18$  h. (c) Quantification of the morphology of the surface crease (solid line) and the interface crease (dotted line) at equilibrium, with the self-contacting region indicated by arrows. The axes represent the dimensions of the window in which measurements are taken; the x-axis denotes the horizontal distance, and the y-axis denotes the vertical distance between the crease tip and the surface/interface. (d) The normalized crease depth  $d_i/H$  (or  $d_s/H$ ) as a function of time, where the subscripts  $i$  and  $s$  refer to the interface and the surface, respectively. The height ratios of lower to upper layers are 1 and 10 for the bilayered hydrogels in (a) and (b), respectively. The modulus ratio of lower to upper layers is approximately 56 for both cases

we combine numerical simulations and experimental studies to understand the surface and interface creases of bilayered hydrogels.

We begin by showing the observed surface and interface creases of the bilayered hydrogels under swelling. Figure 13.7a, b presents the profiles of surface and interface creases, respectively, from their initial flat states to the final equilibrium states wherein swelling no longer takes place. Both figures refer to two separate experiments in which the initial height ratios of the lower to upper layers are set as 1 and 10 in Fig. 13.7a, b, respectively. For both creases, the surface or interface self-contacts and folds onto itself and continues to “grow” downward during the swelling process. The growth of these creases ceases once swelling equilibrium is attained. The profiles of these creases at equilibrium are quantified by direct measurement through the glass over a lateral region of 25 mm as depicted in Fig. 13.7c. The vertical measurements are taken from the tip of the crease to the respective flat surface or interface. Here,  $d_i$  and  $d_s$  refer to the depths of interface and surface creases, respectively. In practice, when we measure the depth of the crease, we find the lowest point of the crease first and locate the highest point mostly close to the lowest one. The vertical distance between these two points is defined as the depth of the crease, which is shown in Fig. 13.7c. Compared to the surface crease, the observed smaller interface crease

depth can be attributed to the increased difficulty in pulling material from the upper layer toward the lower one during the formation and growth of the interface crease.

The presence of the upper layer and its associated constraint also results in the increased curvature of the interface crease. The initiation and evolution of interface and surface creases can be characterized by plotting the normalized interface crease depth ( $d_i/H$ ) and surface crease depth ( $d_s/H$ ) as a function of time, as shown in Fig. 13.7d. The plot essentially shows the time evolution of the creases of Fig. 13.7a, b, where  $H$  denotes the initial height of the bilayered hydrogel. The sharp increases of  $d_i/H$  and  $d_s/H$  correspond to the nucleation of interface and surface creases, respectively. Focusing on the interface crease, a shallow interface crease first nucleates in the swelling bilayered hydrogel after about 3 h and grows rapidly in depth with increasing time (Fig. 13.7a, b), with the interface crease reaching approximately the initial thickness of the upper layer after about 7 h. The interface crease depth saturates after approximately 18 h. The surface crease demonstrates similar characteristics: the crease forms after around 10 h and saturates at approximately 24 h later (Fig. 13.7a, b). Unlike the low-voltage-driven crease formation on the surface of polyelectrolyte gels [52], the crease in our experiments does not evolve into a crater, where the self-contact region of the crease opens up and is progressively widened. While the experimental data suggest that surface creases occur later than the interface creases, this observation may not be universal. As is well-known, the diffusion of water molecules into a hydrogel is the dominant factor for swelling and the formation of creases. It can also be influenced by the modulus and height of both layers. Further detailed studies will be carried out to understand this phenomenon.

With the above experimental observations, we are now positioned to examine the onset and subsequent evolution of surface or interface creases through FEA simulations. In this regard, the bilayered hydrogel is modeled under plane-strain conditions where the heights of the upper and lower layers are denoted by  $H_1$  and  $H_2$ , respectively. We assume that only a single crease forms on the surface or the interface at the center of the specimen, so that only half of it needs to be modeled. Here we should emphasize that multiple creases can be formed on the surface or the interface in our experiments. But the assumption of a single crease can greatly simplify the problem and provide detailed insights into the formation of these creases. As such a symmetric boundary condition is applied along the line of symmetry (right edges in the top panel of Fig. 13.8a, b). Roller boundary conditions are also applied on the left and bottom edges to reflect the constraints imposed by a glass container. The top surface remains traction free. The lower layer is taken to be much stiffer than the upper one. As discussed in Cai et al. [53], a small perturbation is introduced by placing an imperfection, in the form of a quarter circle of radius  $R = 0.005 H$  (convergence study with different sizes of imperfection  $R$  is also investigated; see Fig. 13.8d), on the surface or interface to trigger the crease initiation, as shown in the insets of Fig. 13.8a, b. Swelling and deswelling of the hydrogel are numerically accomplished by the loading parameter  $\Delta\mu$ : the swelling process is mimicked by reducing  $\Delta\mu$  and vice versa. During the course of the swelling, the surface or interface crease forms at a critical value of  $\Delta\mu$ , where compressive stresses resulting from the transverse expansion of the bilayer lead to buckling of

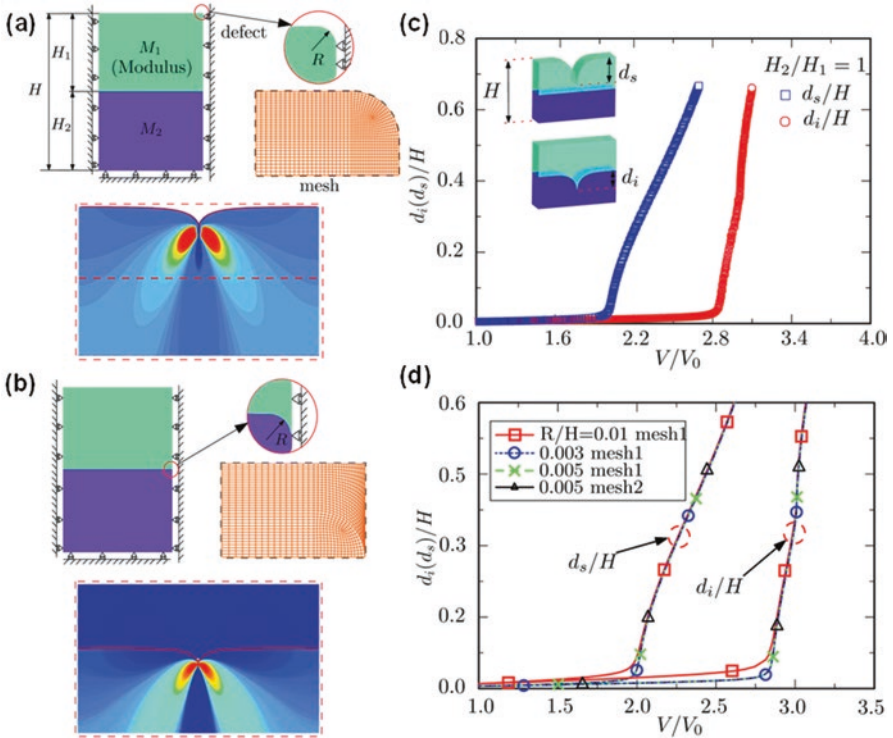


**Fig. 13.8** Finite element models to simulate (a) surface and (b) interface creases. For subfigures, the top panel shows the schematic of the plane-strain condition of the bilayered hydrogel employed to analyze the surface crease and the interface crease. Only half of the specimen needs to be modeled due to symmetric conditions, and hence the roller boundary conditions are imposed on the left edges of the two models. (c) Normalized crease depths  $d_s/H$  (interface crease) and  $d_i/H$  (surface crease) are plotted as a function of the volumetric increase. (d) The normalized depth of the crease is given as a function of volume expansion with different imperfection and mesh sizes. The crease is seeded with different defect radius  $R$ . Meshes 1 and 2 use 20 and 40 elements along the defect, respectively

the bilayered structures, as shown in the bottom panel in Fig. 13.8a, b. The FEA mesh around the initial imperfection is also given. The plane-strain element CPE4H is used in all these simulations. The total number of elements for the FEA model is around 20,000, following the mesh convergence study.

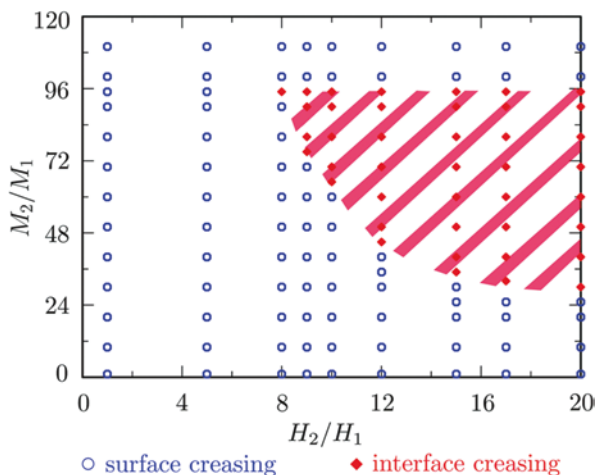
Through simulated swelling, we are able to correlate  $\Delta\mu$  with the normalized volumetric increment of the bilayered hydrogel  $V/V_0$ , where  $V$  and  $V_0$  denote the volumes in the current deformed and initial undeformed states, respectively. Figure 13.8c plots the normalized crease depths  $d_s/H$  and  $d_i/H$  of surface and interface creases, respectively, against the normalized volume  $V/V_0$  of the bilayered hydrogel during the swelling process, where the heights of the two layers are identical as  $H_2/H_1 = 1$ . Displaying similar qualitative characteristics to that of Figs. 13.7c and 13.8c indicates that the initiation of the crease occurs at a critical volume  $V/V_0$  corresponding to a sharp

increase of crease depth  $d_i/H$  (or  $d_s/H$ ). The critical volume, therefore, establishes the criterion for the onset of surface and interface creases. It also forms the basis of our subsequent numerical analyses on the switching of surface to interface creases under the effects of geometrical and material variations. At this juncture, it is worth noting that the FEA model does not take into account the water absorption limit of the hydrogels, which is not true in reality (the water absorption will stop when the water absorbed by the hydrogel is in chemical equilibrium with the external water). As such, the crease depth does not saturate and will continue to grow as long as swelling is taking place, unlike that observed experimentally.

We further explore the influences of the initial size of defects and the finite element mesh on the critical volume expansion to trigger the formation of surface–interface creases. The crease is seeded with defects of different depths. Meshes with different sizes are used: meshes 1 and 2 use 20 and 40 elements along the defect, respectively. The depth of the crease as a function of volume expansion with different sizes of defect and mesh is given in Fig. 13.8d. According to Fig. 13.8d, as long as the defect is small in comparison with the thickness of each layer but larger than the surrounding mesh size, the defect depth and the mesh size have negligible effects on the critical volume expansion for the onset of the surface–interface crease within the studied range. A similar phenomenon has been observed by Jin et al. [50] for rubbery materials under compression.

According to the above experimental and computational observations, we then perform extensive FEA simulations for wide ranges of height ratios ( $1 \leq H_2/H_1 \leq 20$ ) and modulus ratios ( $1 \leq M_2/M_1 \leq 110$ ). Figure 13.9 presents our numerical findings in a form analogous to a phase diagram wherein the abscissa denotes  $H_2/H_1$  and the ordinate denotes  $M_2/M_1$ . The discrete points shown as marked correspond to the discrete levels of  $H_2/H_1$  and  $M_2/M_1$  analyzed, where blue open circles and red full circles represent formations of surface and interface creases, respectively. It should be emphasized that in FEA simulations, we have assumed that the two layers are perfectly bonded together such that delamination and barreling instability are excluded.

**Fig. 13.9** Numerically predicted phase diagram for the first nucleation of the interface or surface crease. The phase diagram is constructed as a function of the height ratio  $H_2/H_1$  and modulus ratio  $M_2/M_1$  of bilayered hydrogels



With this phase diagram at hand, we can tune the modulus and height ratios to control the occurrence of surface or interface creases. According to the phase diagram given in Fig. 13.9, we find that the interface crease of the bilayered hydrogels can only occur at a moderate modulus ratio ( $24 < M_2/M_1 < 96$ ) and a large height ratio ( $H_2/H_1 \geq 8$ ). Such an observation is in good agreement with our previous experimental results shown in Fig. 13.7. The surface and interface creases have been observed for  $H_2/H_1 = 1$  and 10, respectively, although the modulus ratio,  $M_2/M_1$ , is not explicitly given.

### 13.5 Reversible Wrinkles of Monolayer Graphene on a Polymer Substrate

In this section, the surface instability of monolayer graphene supported by a soft (polymer) substrate under equal-biaxial compression has been explored through large-scale coarse-grained molecular simulations [31]. Regardless of the interfacial adhesion strength between the graphene and the substrate, herringbone wrinkles have always been observed due to their lowest energy status, compared with the checkerboard, hexagonal, triangular, and one-dimensional sinusoidal modes. Moreover, the graphene–polymer substrate interaction energy has a negligible effect on the critical strain for the onset of these wrinkles. Yet, if the graphene is bonded to a rigid (non-deformable) substrate, the critical strain increases with increasing graphene–substrate interfacial strength. The surface wrinkles of graphene are delayed and suppressed by the strong bonding of graphene to the rigid substrate. Besides, only localized folds and crumples have been observed on the surface of graphene, when graphene–substrate interaction energy is strong enough. All these observations signal that the deformability (stiffness) of the substrate plays an essential role in determining the morphology of supported graphene under compression. In addition, when a flat graphene is attached on a highly pre-strained (50%) polymer substrate, wrinkles will be formed on its surface during the relaxation of pre-strain within the polymer substrate. The wrinkled graphene could be stretched up to 50% without fracture, accompanied by the diminishing of surface wrinkles. Therefore, it opens a new avenue to enhance the stretchability of graphene materials and enables the future applications of graphene and other 2D materials in stretchable and flexible electronics.

To understand these behaviors of monolayer graphene on a rigid substrate under equal-biaxial compression, the snapshots of graphene at different strain levels are given in Fig. 13.10. The instability of monolayer graphene occurs at strains of 2.2% and 5.3% for  $\epsilon_{\text{wall}} = 0.1$  and 30, respectively. Another compelling observation is that the instability morphologies of graphene are different according to the value of  $\epsilon_{\text{wall}}$  or graphene–substrate adhesion energy. For instance, when  $\epsilon_{\text{wall}} = 0.1$ , wrinkles are formed on the surface of graphene with a herringbone pattern, while localized folds are formed when the interaction between graphene and the substrate is very strong, such as  $\epsilon_{\text{wall}} = 5$  and 30. Here the graphene delaminated from the rigid substrate

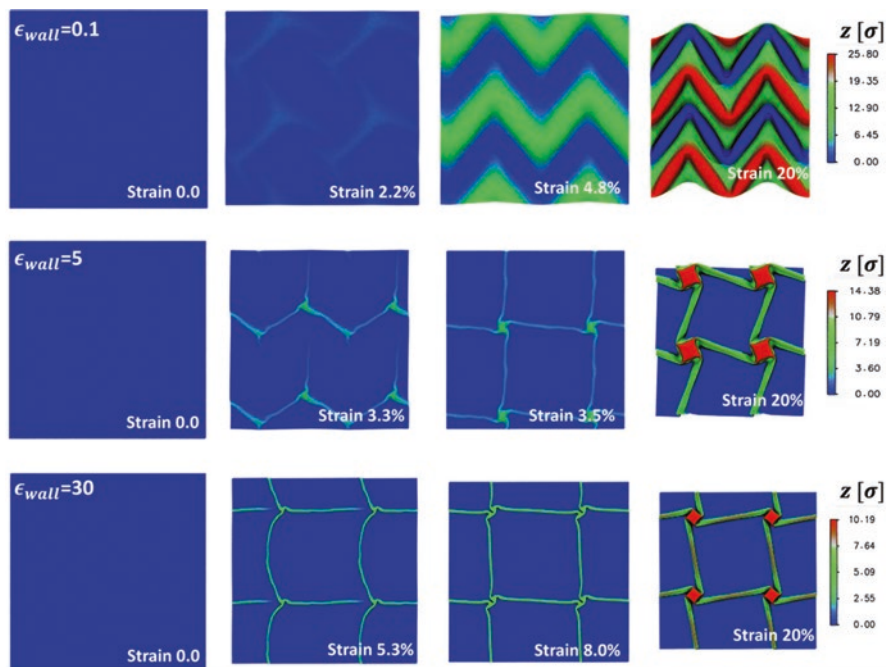


**Fig. 13.10** Snapshots of monolayer graphene supported by a rigid substrate under equal-biaxial compression. The coarse-grained carbon atoms are colored according to their out-of-plane ( $z$  direction) displacements

during the compression for  $\epsilon_{\text{wall}} = 0.1$ . Therefore, wrinkles are formed to release the stretching energy of graphene during the compression, while, under the strong interfacial adhesion with the rigid substrate ( $\epsilon_{\text{wall}} = 5$  or  $30$ ), the localized folds and crumples are formed to accommodate in-plane stretching energy and maintain the bonding between graphene and the substrate.

From the above results, the interfacial adhesion energy between the graphene and the rigid substrate controls the onset of surface instability and its morphology, which is in good agreement with previous molecular simulation and continuum modeling [54–57]. When  $\epsilon_{\text{wall}}$  is large enough, the graphene sheet is fully bonded with the rigid substrate. During equal-biaxial compression, only localized folds are allowed to minimize the stretching energy within the monolayer graphene [57], while maintaining the adhesion energy of the graphene–substrate system. In addition, the buckling of the graphene is delayed and suppressed by its strong adhesion to the rigid substrate. Therefore, the critical strain for the onset of buckling increases with the adhesion energy increasing, in agreement with the previous continuum modeling [56]. While for the extremely small adhesion energy  $\epsilon_{\text{wall}} = 0.1$ , the graphene sheet will be fully delaminated from the rigid substrate during the compression, forming herringbone wrinkles.

In contrast to the rigid (non-deformable) substrate, the monolayer graphene supported by a soft (polymer) substrate shows distinct behaviors. The snapshots of monolayer graphene on a polymer substrate during equal-biaxial compression are presented in Fig. 13.11. From these snapshots, it has been further confirmed that the onset of the surface instability of monolayer graphene occurs at a compressive strain of 2%, regardless of the pair potential parameter  $\epsilon_{GS}$ . Only the herringbone wrinkles have been observed for all these cases, signaling that localized folds exclusively occur for the graphene supported by a rigid substrate. When the monolayer graphene is supported by a soft (polymer) substrate, the substrate will be deformed with attached graphene during the compression. Thus, the surface morphology is not only determined by the strain energy of graphene and graphene–substrate interfacial energy but also by the strain energy of the polymer substrate. More importantly, changes of the graphene–substrate interfacial energy are negligible, within studied ranges of the adhesion energy. Thus, the system needs to overcome the energy barriers introduced by the graphene-bending energy and polymer substrate strain energy, driven by the cutdown of graphene-stretching energy. This situation is very similar to a stiff thin film bonded on a compliant thick substrate under equal-biaxial compression [58–60]. Both theoretical and finite element simulations reveal that the herringbone wrinkles have the lowest energy, followed by the checkerboard,

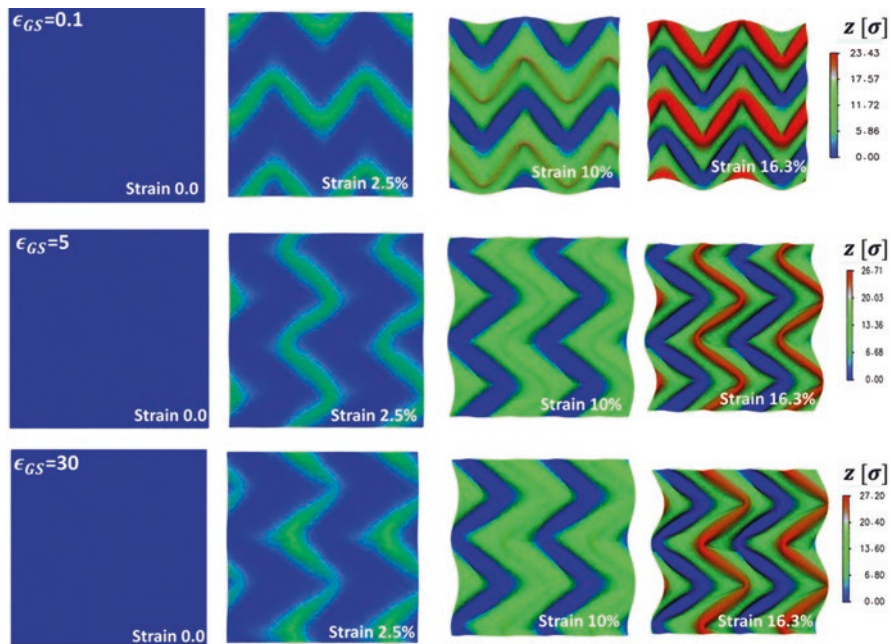


**Fig. 13.11** Snapshots of monolayer graphene supported by a soft (polymer) substrate under equal-biaxial compression. The coarse-grained carbon atoms are colored according to their out-of-plane ( $z$  direction) displacements

with hexagonal, triangular, and one-dimensional sinusoidal modes. Therefore, the thin film/substrate always displays the herringbone pattern on its surface under a large compressive strain, which has also been confirmed in experiments [58, 59, 61]. From our coarse-grained molecular simulations, it seems that the above results at the continuum level still hold for a thin film with atomic scale thickness, such as monolayer graphene. Thus, the graphene bonded to a soft (polymer) substrate still exhibits herringbone wrinkles under equal-biaxial compression, as it is the only mode among others that relaxes in-plane stress in all directions without incurring significant stretching energy [60, 61].

In the above cases, the polymer substrate does not have any pre-strain. To further explore the pre-strain effect, the polymer substrate has been equal-biaxial stretched to about 50%. Then, a monolayer graphene sheet with a size of  $135 \times 135 \sigma$  (the total number of atoms is about 43,608) is attached on the surface of the pre-stretched polymer substrate. Afterward, the graphene–substrate system has been allowed to be systematically relaxed, until the strain within the polymer substrate has been reduced to zero. Thereafter, the system has been equal-biaxial stretched again, up to 50% strain. During the release stage, the monolayer graphene is under compression, induced by the shrinkage of the bonded polymer substrate. Thus, the force within the graphene rapidly increases with the shrinking of the polymer substrate, accompanied by the increasing of stretching energy of graphene. Then, wrinkles are formed on the surface of graphene to release the stretching energy. Later, the force is maintained as a constant value or slightly reduced, according to the interfacial strength between the graphene and the polymer substrate ( $\epsilon_{GS} = 1.0$  or 10). Under equal-biaxial tension, the force within graphene will return to its original value along the path generated during the release stage. The interfacial adhesion between graphene and the polymer substrate is not affected by the strains within graphene or the polymer substrate. These simulation results also reveal that this process is fully reversible, evidenced by the facts that [31] (1) the force-strain curves are collapsed together during the releasing and stretching process and (2) the change of interfacial adhesion energy between the graphene and the pre-stretched polymer substrate is negligible. The snapshots of monolayer graphene during the releasing and stretching further confirm our above discussion, as given in Fig. 13.12. During the relaxation of pre-strain within the polymer substrate, the surface of graphene forms wrinkles with a herringbone pattern, accompanied by large out-of-plane deflection. Then, during the equal-biaxial stretching stage, these wrinkles will be gradually diminished with the applied tensile strain. Until the strain reaches 50%, the graphene sheet returns to its original flat state. In this way, the surface wrinkles of graphene are reversible, determined by the internal strain status of the bonded polymer substrate. In particular, the wrinkled graphene supported by the polymer substrate could be initially stretched up to 50%, without introducing the failure and damage of graphene. Therefore, such a pre-stretched graphene–polymer substrate system can be used in the design of stretchable and flexible electronics [54, 62–66].

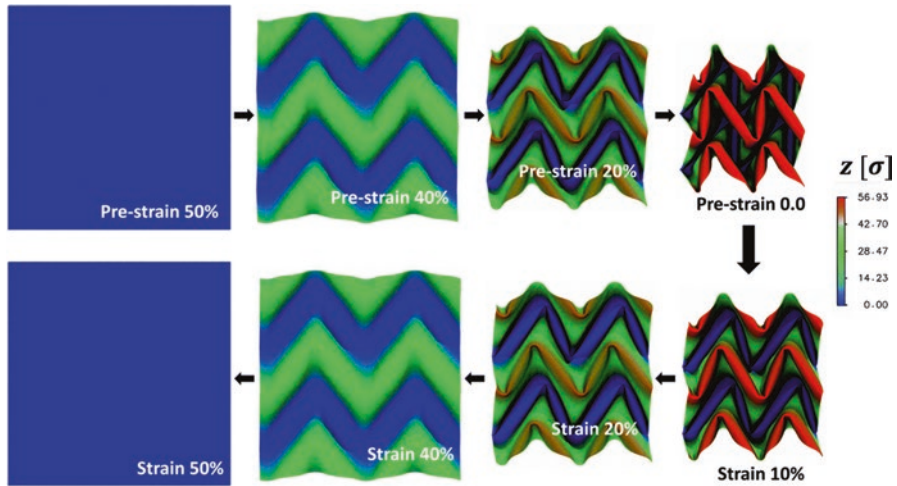


**Fig. 13.12** Snapshots of monolayer graphene supported by a pre-strained soft (polymer) substrate. The marked strain represents the strain level within the polymer substrate. The coarse-grained carbon atoms are colored according to their out-of-plane ( $z$  direction) displacements. Interaction between graphene and the polymer substrate is determined by the pair parameter  $\epsilon_{GS} = 10$

## 13.6 Conclusion

In this chapter, we have given an overview of the surface instability of polymer thin films through theoretical analysis, finite element simulations, and experimental studies. The different surface morphologies of these thin films can be designed and achieved by using the bilayered structures, mechanical forces, and external stimuli. Although these different surface morphologies have been intensively studied in the physics and mechanics field with many applications in engineering and biology, there are still many questions remain to be answered. From the fundamental point of view, a systematic understanding of the formation conditions and geometric characteristics of complex instabilities of polymer thin films and their layered structures remains a critical challenge. For instance, many other complex surface instability patterns have been recently observed, such as hierarchical wrinkles [67–70], period triples [9, 19, 71], and period quadruples [45, 72, 73]. Understanding and predicting these complex instability patterns require new theoretical, computational, and experimental studies. In addition, most of the current studies focus on the isotropic and homogeneous structures and materials, the instability formation of polymer thin films and layered structures can be dramatically affected by their intrinsic curvatures [23, 24, 74], anisotropy, and inhomogeneous properties [16, 25, 37, 75–82]. These issues offer many intriguing problems and interesting opportunities for future studies.

## References

1. M.A. Biot, Surface instability of rubber in compression. *Appl. Sci. Res. Sect. A* **12**, 168–182 (1963)
2. A. Gent, I. Cho, Surface instabilities in compressed or bent rubber blocks. *Rubber Chem. Technol.* **72**, 253–262 (1999)
3. A. Ghatak, A.L. Das, Kink instability of a highly deformable elastic cylinder. *Phys. Rev. Lett.* **99**, 076101 (2007)
4. W. Hong, X. Zhao, Z. Suo, Formation of creases on the surfaces of elastomers and gels. *Appl. Phys. Lett.* **95**, 111901 (2009)
5. E. Hohlfield, L. Mahadevan, Unfolding the sulcus. *Phys. Rev. Lett.* **106**, 105702 (2011)
6. Y. Cao, J.W. Hutchinson, From wrinkles to creases in elastomers: the instability and imperfection-sensitivity of wrinkling, in *Proceedings of the Royal Society of London A: Mathematical, Physical and Engineering Sciences*, The Royal Society: 2011; p rspa20110384
7. B. Li, Y.-P. Cao, X.-Q. Feng, H. Gao, Mechanics of morphological instabilities and surface wrinkling in soft materials: A review. *Soft Matter* **8**, 5728–5745 (2012)
8. H. Mei, R. Huang, J.Y. Chung, C.M. Stafford, H.-H. Yu, Buckling modes of elastic thin films on elastic substrates. *Appl. Phys. Lett.* **90**, 151902 (2007)
9. J.-Y. Sun, S. Xia, M.-W. Mon, K. H. Oh, K.-S. Kim, Folding wrinkles of a thin stiff layer on a soft substrate, in *Proceedings of Royal Society A* 2011, rspa20110567
10. J. Kim, J. Yoon, R.C. Hayward, Dynamic display of biomolecular patterns through an elastic creasing instability of stimuli-responsive hydrogels. *Nat. Mater.* **9**, 159 (2010)
11. P. Shivapooja, Q. Wang, B. Orihuela, D. Rittschof, G.P. López, X. Zhao, Bioinspired surfaces with dynamic topography for active control of biofouling. *Adv. Mater.* **25**, 1430–1434 (2013)
12. E.P. Chan, J.M. Karp, R.S. Langer, A “self-pinning” adhesive based on responsive surface wrinkles. *J. Polym. Sci. B Polym. Phys.* **49**, 40–44 (2011)
13. K. Saha, J. Kim, E. Irwin, J. Yoon, F. Momin, V. Trujillo, D.V. Schaffer, K.E. Healy, R.C. Hayward, Surface creasing instability of soft polyacrylamide cell culture substrates. *Biophys. J.* **99**, L94–L96 (2010)
14. S. Krylov, B.R. Ilic, D. Schreiber, S. Seretensky, H. Craighead, The pull-in behavior of electrostatically actuated bistable microstructures. *J. Micromech. Microeng.* **18**, 055026 (2008)
15. Y. Li, X.-S. Wang, X.-K. Meng, Buckling behavior of metal film/substrate structure under pure bending. *Appl. Phys. Lett.* **92**, 131902 (2008)
16. Y. Li, X.-S. Wang, Q. Fan, Effects of elastic anisotropy on the surface stability of thin film/substrate system. *Int. J. Eng. Sci.* **46**, 1325–1333 (2008)
17. V.V. Bolotin, Delaminations in composite structures: Its origin, buckling, growth and stability. *Compos. Part B Eng.* **27**, 129–145 (1996)
18. Y. Hu, A. Hiltner, E. Baer, Buckling in elastomer/plastic/elastomer 3-layer films. *Polym. Compos.* **25**, 653–661 (2004)
19. Q. Wang, X. Zhao, A three-dimensional phase diagram of growth-induced surface instabilities. *Sci. Rep.* **5**, 8887 (2015)
20. Y. Cao, J.W. Hutchinson, Wrinkling phenomena in neo-Hookean film/substrate bilayers. *J. Appl. Mech.* **79**, 031019 (2012)
21. Q. Wang, X. Zhao, Phase diagrams of instabilities in compressed film-substrate systems. *J. Appl. Mech.* **81**, 051004 (2014)
22. L. Jin, Z. Suo, Smoothing creases on surfaces of strain-stiffening materials. *J. Mech. Phys. Solids* **74**, 68–79 (2015)
23. J. Yin, Z. Cao, C. Li, I. Sheinman, X. Chen, Stress-driven buckling patterns in spheroidal core/shell structures. *Proc Natl Acad Sci* **105**, 19132–19135 (2008)
24. J. Yin, X. Chen, I. Sheinman, Anisotropic buckling patterns in spheroidal film/substrate systems and their implications in some natural and biological systems. *J. Mech. Phys. Solids* **57**, 1470–1484 (2009)

25. B. Li, F. Jia, Y.-P. Cao, X.-Q. Feng, H. Gao, Surface wrinkling patterns on a core-shell soft sphere. *Phys. Rev. Lett.* **106**, 234301 (2011)
26. P. Ciarletta, V. Balbi, E. Kuhl, Pattern selection in growing tubular tissues. *Phys. Rev. Lett.* **113**, 248101 (2014)
27. D. Ambrosi, G. Ateshian, E. Arruda, S. Cowin, J. Dumais, A. Goriely, G.A. Holzapfel, J.D. Humphrey, R. Kemkemer, E. Kuhl, Perspectives on biological growth and remodeling. *J. Mech. Phys. Solids* **59**, 863–883 (2011)
28. S. Tang, Y. Li, Y. Yang, Z. Guo, The effect of mechanical-driven volumetric change on instability patterns of bilayered soft solids. *Soft Matter* **11**, 7911–7919 (2015)
29. Z. Zhou, Y. Li, T. Guo, X. Guo, S. Tang, Surface instability of bilayer hydrogel subjected to both compression and solvent absorption. *Polymers* **10**, 624 (2018)
30. Z. Zhou, Y. Li, W. Wong, T. Guo, S. Tang, J. Luo, Transition of surface–interface creasing in bilayer hydrogels. *Soft Matter* **13**, 6011–6020 (2017)
31. Y. Li, Reversible wrinkles of monolayer graphene on a polymer substrate: Toward stretchable and flexible electronics. *Soft Matter* **12**, 3202–3213 (2016)
32. X. Chen, J. Yin, Buckling patterns of thin films on curved compliant substrates with applications to morphogenesis and three-dimensional micro-fabrication. *Soft Matter* **6**, 5667–5680 (2010)
33. M. Diab, T. Zhang, R. Zhao, H. Gao, K.-S. Kim, Ruga mechanics of creasing: From instantaneous to setback creases. *Proc. R. Soc. A* **469**, 20120753 (2013)
34. Q. Wang, X. Zhao, Beyond wrinkles: Multimodal surface instabilities for multifunctional patterning. *MRS Bull.* **41**, 115–122 (2016)
35. S. Deng, V. Berry, Wrinkled, rippled and crumpled graphene: An overview of formation mechanism, electronic properties, and applications. *Mater. Today* **19**, 197–212 (2016)
36. G.N. Greaves, A. Greer, R. Lakes, T. Rouxel, Poisson’s ratio and modern materials. *Nat. Mater.* **10**, 823 (2011)
37. S. Tang, Y. Li, W.K. Liu, X.X. Huang, Surface ripples of polymeric nanofibers under tension: The crucial role of Poisson’s ratio. *Macromolecules* **47**, 6503–6514 (2014)
38. G.W. Milton, Composite materials with Poisson’s ratios close to—1. *J. Mech. Phys. Solids* **40**, 1105–1137 (1992)
39. J.N. Grima, A. Alderson, K. Evans, Auxetic behaviour from rotating rigid units. *Phys. Status Solidi B* **242**, 561–575 (2005)
40. S. Babae, J. Shim, J.C. Weaver, E.R. Chen, N. Patel, K. Bertoldi, 3D soft metamaterials with negative Poisson’s ratio. *Adv. Mater.* **25**, 5044–5049 (2013)
41. S. Hirotsu, Softening of bulk modulus and negative Poisson’s ratio near the volume phase transition of polymer gels. *J. Chem. Phys.* **94**, 3949–3957 (1991)
42. E.M. Arruda, M.C. Boyce, A three-dimensional constitutive model for the large stretch behavior of rubber elastic materials. *J. Mech. Phys. Solids* **41**, 389–412 (1993)
43. W. Wong, T. Guo, Y. Zhang, L. Cheng, Surface instability maps for soft materials. *Soft Matter* **6**, 5743–5750 (2010)
44. S. Tang, Y. Yang, X.H. Peng, W.K. Liu, X.X. Huang, K. Elkhodary, A semi-numerical algorithm for instability of compressible multilayered structures. *Comput. Mech.* **56**, 63–75 (2015)
45. F. Brau, H. Vandeparre, A. Sabbah, C. Poulard, A. Boudaoud, P. Damman, Multiple-length-scale elastic instability mimics parametric resonance of nonlinear oscillators. *Nat. Phys.* **7**, 56 (2011)
46. A. Auguste, L. Jin, Z. Suo, R.C. Hayward, The role of substrate pre-stretch in post-wrinkling bifurcations. *Soft Matter* **10**, 6520–6529 (2014)
47. Z.-C. Shao, Y. Zhao, W. Zhang, Y. Cao, X.-Q. Feng, Curvature induced hierarchical wrinkling patterns in soft bilayers. *Soft Matter* **12**, 7977–7982 (2016)
48. W.-K. Lee, C.J. Engel, M.D. Huntington, J. Hu, T.W. Odom, Controlled three-dimensional hierarchical structuring by memory-based, sequential wrinkling. *Nano Lett.* **15**, 5624–5629 (2015)
49. Y. Wang, Q. Sun, J. Xiao, Simultaneous formation of multiscale hierarchical surface morphologies through sequential wrinkling and folding. *Appl. Phys. Lett.* **112**, 081602 (2018)

50. L. Jin, D. Chen, R.C. Hayward, Z. Suo, Creases on the interface between two soft materials. *Soft Matter* **10**, 303–311 (2014)
51. B.B. Xu, Q. Liu, Z. Suo, R.C. Hayward, Reversible electrochemically triggered delamination blistering of hydrogel films on micropatterned electrodes. *Adv. Funct. Mater.* **26**, 3218–3225 (2016)
52. B. Xu, R.C. Hayward, Low-voltage switching of crease patterns on hydrogel surfaces. *Adv. Mater.* **25**, 5555–5559 (2013)
53. S. Cai, D. Chen, Z. Suo, R.C. Hayward, Creasing instability of elastomer films. *Soft Matter* **8**, 1301–1304 (2012)
54. J. Zang, S. Ryu, N. Pugno, Q. Wang, Q. Tu, M.J. Buehler, X. Zhao, Multifunctionality and control of the crumpling and unfolding of large-area graphene. *Nat. Mater.* **12**, 321 (2013)
55. T. Al-Mulla, Z. Qin, M.J. Buehler, Crumpling deformation regimes of monolayer graphene on substrate: A molecular mechanics study. *J. Phys. Condens. Matter* **27**, 345401 (2015)
56. K. Zhang, M. Arroyo, Adhesion and friction control localized folding in supported graphene. *J. Appl. Phys.* **113**, 193501 (2013)
57. K. Zhang, M. Arroyo, Understanding and strain-engineering wrinkle networks in supported graphene through simulations. *J. Mech. Phys. Solids* **72**, 61–74 (2014)
58. X. Chen, J.W. Hutchinson, Herringbone buckling patterns of compressed thin films on compliant substrates. *J. Appl. Mech.* **71**, 597–603 (2004)
59. S. Cai, D. Breid, A.J. Crosby, Z. Suo, J.W. Hutchinson, Periodic patterns and energy states of buckled films on compliant substrates. *J. Mech. Phys. Solids* **59**, 1094–1114 (2011)
60. J. Song, H. Jiang, W. Choi, D. Khang, Y. Huang, J. Rogers, An analytical study of two-dimensional buckling of thin films on compliant substrates. *J. Appl. Phys.* **103**, 014303 (2008)
61. W.M. Choi, J. Song, D.-Y. Khang, H. Jiang, Y.Y. Huang, J.A. Rogers, Biaxially stretchable “wavy” silicon nanomembranes. *Nano Lett.* **7**, 1655–1663 (2007)
62. S.-K. Lee, B.J. Kim, H. Jang, S.C. Yoon, C. Lee, B.H. Hong, J.A. Rogers, J.H. Cho, J.-H. Ahn, Stretchable graphene transistors with printed dielectrics and gate electrodes. *Nano Lett.* **11**, 4642–4646 (2011)
63. Y. Wang, L. Wang, T. Yang, X. Li, X. Zang, M. Zhu, K. Wang, D. Wu, H. Zhu, Wearable and highly sensitive graphene strain sensors for human motion monitoring. *Adv. Funct. Mater.* **24**, 4666–4670 (2014)
64. J. Bai, Y. Huang, Fabrication and electrical properties of graphene nanoribbons. *Mater. Sci. Eng. R Rep.* **70**, 341–353 (2010)
65. S. Kabiri Ameri, R. Ho, H. Jang, L. Tao, Y. Wang, L. Wang, D.M. Schnyer, D. Akinwande, N. Lu, Graphene electronic tattoo sensors. *ACS Nano* **11**, 7634–7641 (2017)
66. D. Song, A. Mahajan, E.B. Secor, M.C. Hersam, L.F. Francis, C.D. Frisbie, High-resolution transfer printing of graphene lines for fully printed, flexible electronics. *ACS Nano* **11**, 7431–7439 (2017)
67. K. Efimenko, M. Rackaitis, E. Manias, A. Vaziri, L. Mahadevan, J. Genzer, Nested self-similar wrinkling patterns in skins. *Nat. Mater.* **4**, 293 (2005)
68. W.-K. Lee, W.-B. Jung, S.R. Nagel, T.W. Odom, Stretchable superhydrophobicity from monolithic, three-dimensional hierarchical wrinkles. *Nano Lett.* **16**, 3774–3779 (2016)
69. G. Lin, P. Chandrasekaran, C. Lv, Q. Zhang, Y. Tang, L. Han, J. Yin, Self-similar hierarchical wrinkles as a potential multifunctional smart window with simultaneously tunable transparency, structural color, and droplet transport. *ACS Appl. Mater. Interfaces* **9**, 26510–26517 (2017)
70. J. Yin, C. Lu, Hierarchical surface wrinkles directed by wrinkled templates. *Soft Matter* **8**, 6528–6534 (2012)
71. S. Budday, E. Kuhl, J.W. Hutchinson, Period-doubling and period-tripling in growing bilayered systems. *Philos. Mag.* **95**, 3208–3224 (2015)
72. R. Zhao, T. Zhang, M. Diab, H. Gao, K.-S. Kim, The primary bilayer ruga-phase diagram I: Localizations in ruga evolution. *Extreme Mech. Lett.* **4**, 76–82 (2015)
73. A. Haji Hosseinloo, K. Turitsyn, Energy harvesting via wrinkling instabilities. *Appl. Phys. Lett.* **110**, 013901 (2017)

74. T. Tallinen, J.Y. Chung, J.S. Biggins, L. Mahadevan, Gyrfication from constrained cortical expansion. *Proc. Natl. Acad. Sci.* **111**, 12667–12672 (2014)
75. Q.-D. To, Stress concentration and surface instability of anisotropic solids with slightly wavy boundary. *Int. J. Solids Struct.* **49**, 151–160 (2012)
76. A.E. Shyer, T. Tallinen, N.L. Nerurkar, Z. Wei, E.S. Gil, D.L. Kaplan, C.J. Tabin, L. Mahadevan, Villification: How the gut gets its villi. *Science* **342**, 212–218 (2013)
77. M.B. Amar, F. Jia, Anisotropic growth shapes intestinal tissues during embryogenesis. *Proc. Natl. Acad. Sci.* **110**, 10525–10530 (2013)
78. G.M. Grason, B. Davidovitch, Universal collapse of stress and wrinkle-to-scar transition in spherically confined crystalline sheets. *Proc. Natl. Acad. Sci.* **110**, 12893–12898 (2013)
79. H. Qiu, Y. Li, T.F. Guo, X. Guo, S. Tang, Deformation and pattern transformation of porous soft solids under biaxial loading: Experiments and simulations. *Extreme Mech. Lett.* **20**, 81–90 (2018)
80. Z. Li, Z. Zhou, Y. Li, S. Tang, Effect of cyclic loading on surface instability of silicone rubber under compression. *Polymers* **9**, 148 (2017)
81. S. Tang, Y. Li, W.K. Liu, N. Hu, X.H. Peng, Z. Guo, Tensile stress-driven surface wrinkles on cylindrical core-shell soft solids. *J. Appl. Mech.* **82**, 121002 (2015)
82. D. Peng, Z. Zhou, Y. Liu, T. Guo, Y. Li, S. Tang, Computational modeling of the effect of sulci during tumor growth and cerebral edema. *J. Nanomater.* **2016**, 3038790 (2016)

# Chapter 14

## Other Applications of Wrinkled Polymer Surfaces



C. M. González-Henríquez, M. A. Sarabia Vallejos,  
and Juan Rodríguez-Hernández

### 14.1 Background

Surface wrinkling is a spontaneous physical process that creates naturally unique and complex topographies on the surface of materials [1, 2]. These morphologies are suitable for the design of intelligent materials, due to their interesting and useful characteristics in variable fields like optical [3] and electronic devices [4], surface-enhanced Raman spectroscopy substrates [5], tunable wettability substrates [6], adhesion [7], and antifouling and cell culture, among other possible applications [8–13].

In this chapter, some of the most relevant applications, which were not mentioned in the previous chapters, will be reviewed, for example, conducting shrinkable devices, shape memory polymers, electrochromic devices, organic photovoltaic cells and organic light-emitting diodes, smart displays, anti-counterfeiting, photo-modulation of surface wrinkles, solar cells, smart windows, and light controllable sensors.

---

C. M. González-Henríquez (✉)

Departamento de Química, Facultad de Ciencias Naturales, Matemáticas y del Medio Ambiente, Universidad Tecnológica Metropolitana, Santiago, Chile

Programa Institucional de Fomento a la Investigación, Desarrollo e Innovación, Universidad Tecnológica Metropolitana, Santiago, Chile

e-mail: [carmen.gonzalez@utem.cl](mailto:carmen.gonzalez@utem.cl)

M. A. Sarabia Vallejos

Departamento de Ingeniería Estructural y Geotecnia, Pontificia Universidad Católica de Chile, Escuela de Ingeniería, Santiago, Chile

Instituto de Ingeniería Biológica y Médica, Santiago, Chile

J. Rodríguez-Hernández (✉)

Departamento de Química Macromolecular Aplicada, Polymer Functionalization Group, Instituto de Ciencia y Tecnología de Polímeros-Consejo Superior de Investigaciones Científicas (ICTP-CSIC), Madrid, Spain

e-mail: [jrodriguez@ictp.csic.es](mailto:jrodriguez@ictp.csic.es)

## 14.2 Conducting Shrinkable Devices

By controlling the dimensions of micro-/nano-patterns, it is possible to improve some relevant characteristics of smart scaffolds and biointerfaces useful for cell culture and other bio-related applications. According to this, there is an increasing interest in employing conducting polymers as soft, biocompatible, conductive bio-interfaces or as parts of bioelectronic devices [10].

Greco et al. in the year 2015 reported the fabrication and characterization of a metal-polymer nanocomposite (AuNPs/PS). This system was developed via the implantation of neutral Au nanoparticles by using supersonic cluster beam implantation (SCBI) technique over a commercial shrinkable thermoplastic material (polyshrink®) mainly composed of polystyrene (PS). Experimentally, SCBI neutral metallic cluster is supersonically accelerated toward the surface of a target polymer film (Fig. 14.1a). The results showed that the isotropic surface wrinkling (biaxial 2D) was obtained on samples by inducing thermal shrinking at  $T = 160\text{ }^{\circ}\text{C}$  for 6 min. By mechanically confining the shrinking of the material, the alignment of wrinkles along a given direction was imposed, creating anisotropic (uniaxially aligned, 1D) surface patterns (Fig. 14.1a). The average surface roughness of flat (not shrunk) samples, as measured by AFM, was almost unaffected by increasing the implantation dose (equivalent thickness) in the case of shrunk nanocomposites, as a result of surface wrinkling (Fig. 14.1b). On the other hand, the sharp augmentation (five-six orders of magnitude) by increasing the implantation dose is related to a connectivity rise of implanted conductive particles (Fig. 14.1b). In summary, by varying the nanoparticle implantation dose, it was possible to tune the surface topographical patterns as well as to modulate the electrical conductance ( $G$ ) of the systems. These results are relevant in comparison to a typical wrinkled bilayer of metal/polymers, being a way to follow and to control the corresponding evolution of wrinkling, as well as the electrical conductivity of the nanocomposites. This methodology could open the way to several applications requiring multiscale integration and organization of periodic structures in the field of optics, biointerfacing, sensing, and microfabrication.

Another possible application of wrinkled patterns is as heat transfer enhancement or catalysis. For example, through a surface modification of a metallic structure, the group of Yang et al. in the year 2017 [15] suggested an experimental technique to fabricate microscale metallic wrinkles on a curved surface using a contact and electro-replication process. As the first step, a UV-curable adhesive (NOA68T resin) was deposited on a substrate with  $180\text{ }\mu\text{m}$  thickness, and then the film was weakly polymerized by short UV exposure of 5 s ( $400\text{ mW/cm}^2$ ). Posteriorly, wrinkles were generated on the skin of the weakly polymerized layer by compressive forces that occurred during the thermal post-process. Then, the master was replicated using a poly(dimethylsiloxane) (PDMS) mold, and the metallic wrinkles were reproduced on a curved metallic surface using the replicated mold in a nickel-based electroforming system (Fig. 14.2a).

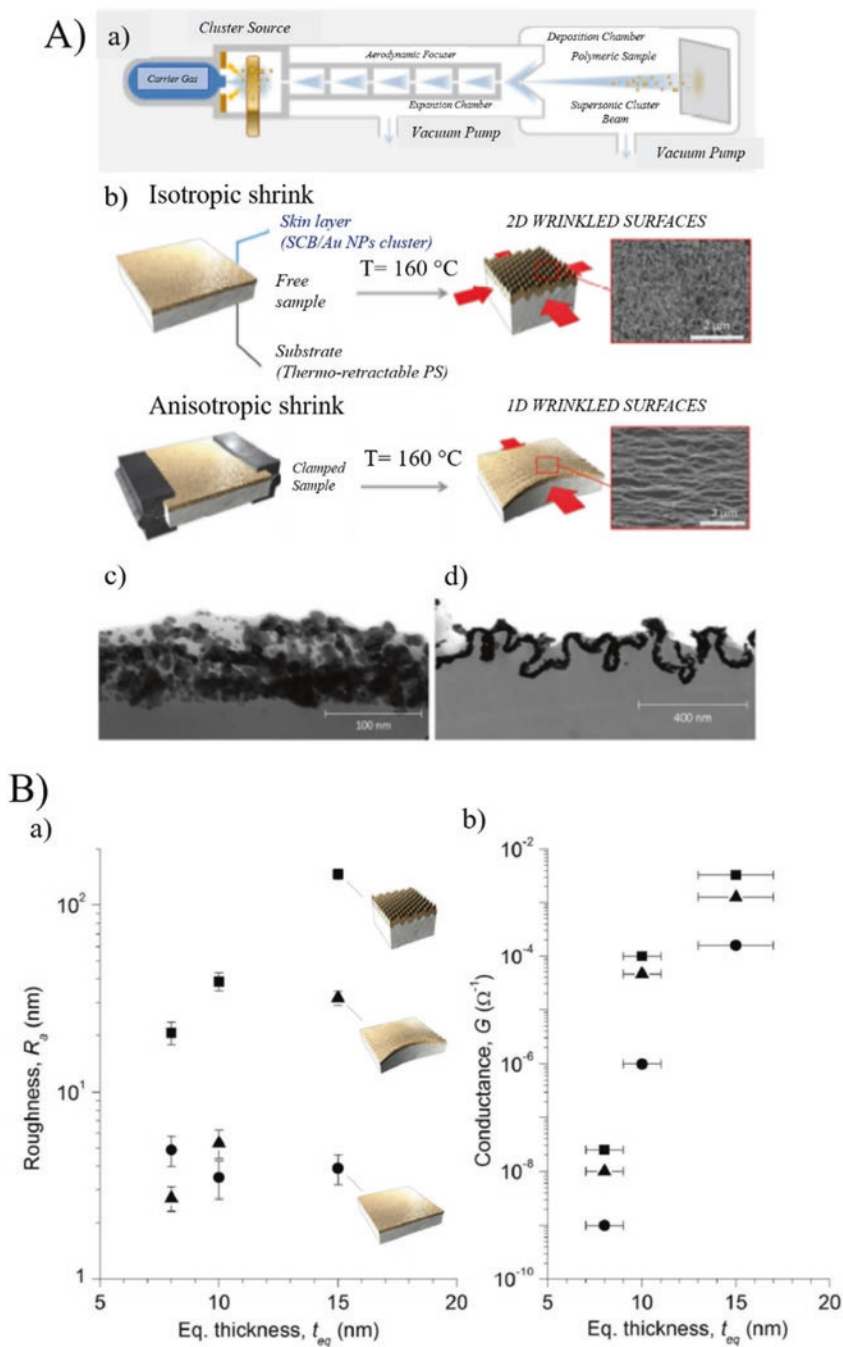


**Fig. 14.1** (a) Schematic view of AuNPs implantation process with SCBI apparatus. Also, thermally induced shrink processes to obtain 1D and 2D wrinkling are shown together with TEM images of cross-sections of AuNPs/PS composites. (b) Surface roughness  $R_s$  (a) and conductance  $G$  of SCBI-implanted nanocomposites. (Reproduced with permission from Ref. [14])

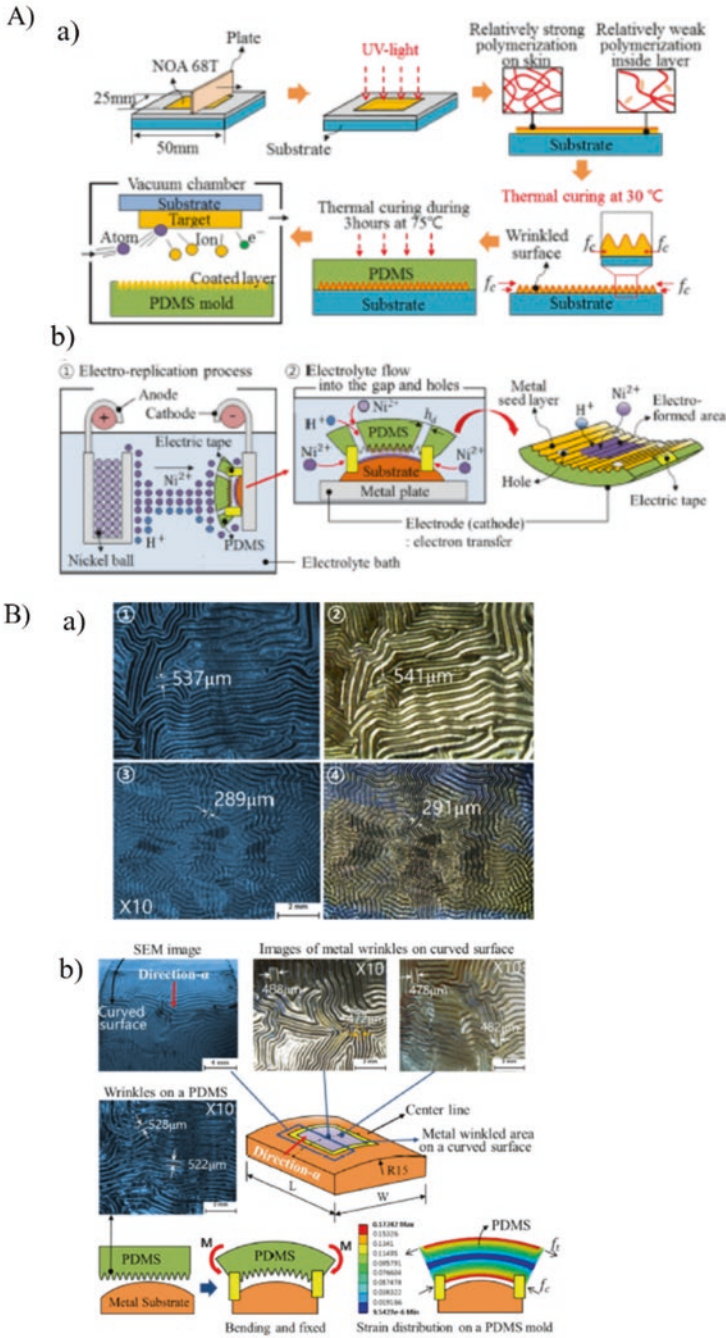


**Fig. 14.2** (a) Schematic diagram of the fabrication process and wrinkle generation. The fabrication process of master patterns, PDMS molding, and seeding of a metal layer on the mold are also shown. Schematics of electroforming process are also depicted. (b) Stereomicroscopy images of fabricated wrinkles and their replicas. (Reproduced with permission from Ref. [15])

The fabrication results of metallic wrinkles are shown in Fig. 14.2b, in which wrinkle dimensions were measured at six different positions and averaged. In this article, Yang et al. used two different kinds of master wrinkle patterns having an average width of 281 and 525  $\mu\text{m}$ , which were electro-replicated on flat plates. The results demonstrated that the replicas on the flat metal plate did not show any significant size difference from the master wrinkle pattern. However, when the master wrinkle pattern, with an average width of 525  $\mu\text{m}$ , was replicated on a curved metal surface, the width of the wrinkles decreased nearly 8.6%, attributed to the PDMS mold.

### 14.3 Shape Memory Polymers

Shape memory polymers (SMPs) are a particular type of smart materials that can recover their original shapes after severe deformations in the presence of external stimuli, such as temperature, light, magnetic field, or humidity [16]. Due to their unique properties, SMPs have shown to have promising applications in the fields of microelectromechanical systems, biomedical devices, and active surface patterning.

Accordingly, Wang and Xiao [17] in the year 2017 published a method to generate heat responsive SMPs. One thin film is bonded to PDMS substrate, forming a bilayered system. By taking advantage of the shape memory effect, the formation and disappearance of surface wrinkling can be reversibly achieved. Experimentally, *tert*-butyl acrylate (*t*BA) as monomer and poly(ethylene glycol) dimethacrylate (PEGDMA) as a cross-linking agent were used, which were mixed in a weight ratio of 4:1. 2,2-Dimethoxy-2-phenylacetophenone was added to the reaction mixture as photo-initiator. Posteriorly, the polymeric solution is injected into a mold, made of two glass slides with a spacer between them to control the thickness. The mold with polymer solution is then placed under a UV lamp for 5 min, followed by a post-curing process in the oven at 80  $^{\circ}\text{C}$  for 1 h. The PDMS was made from an elastomer using a ratio of 20:1. In Fig. 14.3a, the reversible process used to generate programmable wrinkles is schematically shown, demonstrating that smart surface adhesion can be enabled through this method.

Figure 14.3b shows a schematic diagram of the experimental setup used to measure surface adhesion by force-displacement of a single sample in two programming cycles with different program strains. The authors demonstrated that an initially flat SMP film on PDMS can provide a maximum pull-off force of 3.3 mN. In order to reduce the surface adhesion, a 5% program strain can be used to induce wrinkling of the SMP film, leading to the reduction of the pull-off force to 2.1 mN, corresponding to 36.4% reduction; these results are shown in Fig. 14.3b. Additionally, the reduced surface adhesion can be recovered to 3.3 mN by simply heating up the bilayer system to 60  $^{\circ}\text{C}$ . If further reduction in surface adhesion is desired, a larger program strain can be used to induce SMP film wrinkling. For example, if 20% of strain is used, the pull-off force provided by the wrinkled SMP film is reduced to 0.22 mN, corresponding to 93.3% reduction. The surface adhesion can be recovered

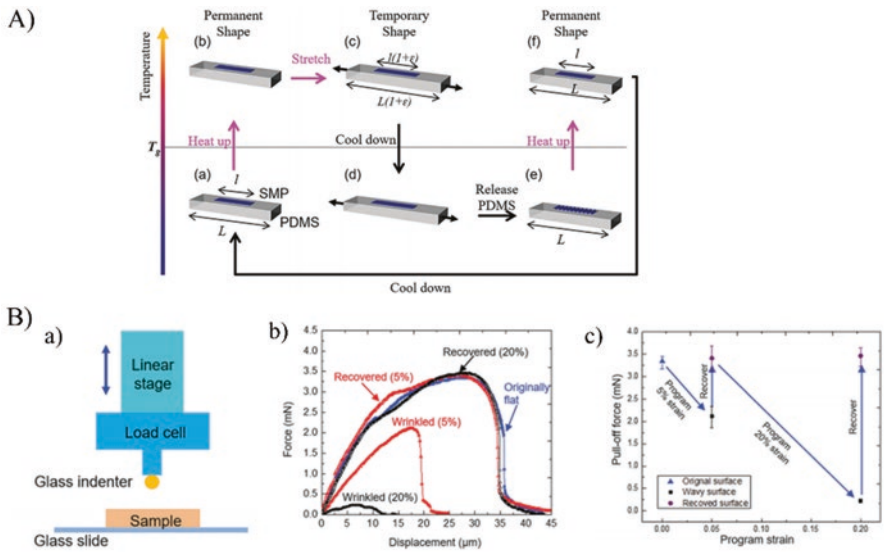


**Fig. 14.3** (a) Schematic illustration of the cycles of the programmable, reversible, and repeatable wrinkling of an SMP thin film on a PDMS substrate. (b) Experimental setup of the adhesion test. Adhesion force versus displacement at different stages in programming cycles with different program strains. (Reproduced with permission from Ref. [17])

to the maximum pull-off force of 3.3 mN again by heating. This process of programming the surface adhesion can be repeated several times, and the surface adhesion is completely reversible. This study can be useful for applications in different areas such as surface engineering, tunable optical grating, smart adhesion, and soft robotic, among others.

A similar example was studied by Pei-Chun et al., who reported a PDMS-SMP composite whose surface micro-wrinkles can be dynamically programmed by an electrical current supplied. The composite can be applied in the programmable modulation of surface adhesion, friction, wettability, etc. [18].

Recently, Gomard et al. (2018) introduced a new SMP fabrication method. This method seems to be highly versatile, which was demonstrated by fabricating disordered transmission grating with various tailorable mean periodicities. Their transmissive and reflective properties were then analyzed angle-dependently and with respect to the direction of the incident light. Besides, it was demonstrated that the surface wrinkles can be employed as a light-harvesting coating, and therefore relevant for photovoltaic (PV) applications. As a proof of concept, the authors evaluate the optoelectronic properties of the composite by using solar cells. Figure 14.4a shows that the stretched samples serve as substrates, which were then subsequently covered with a thin film of a different polymer, polymethylmethacrylate (PMMA), using the spin-coating method. When shape memory effect is triggered by rising the sample's temperature above the SMP's switching temperature, the substrates contract to their original size. This causes the PMMA coating to wrinkle in order to

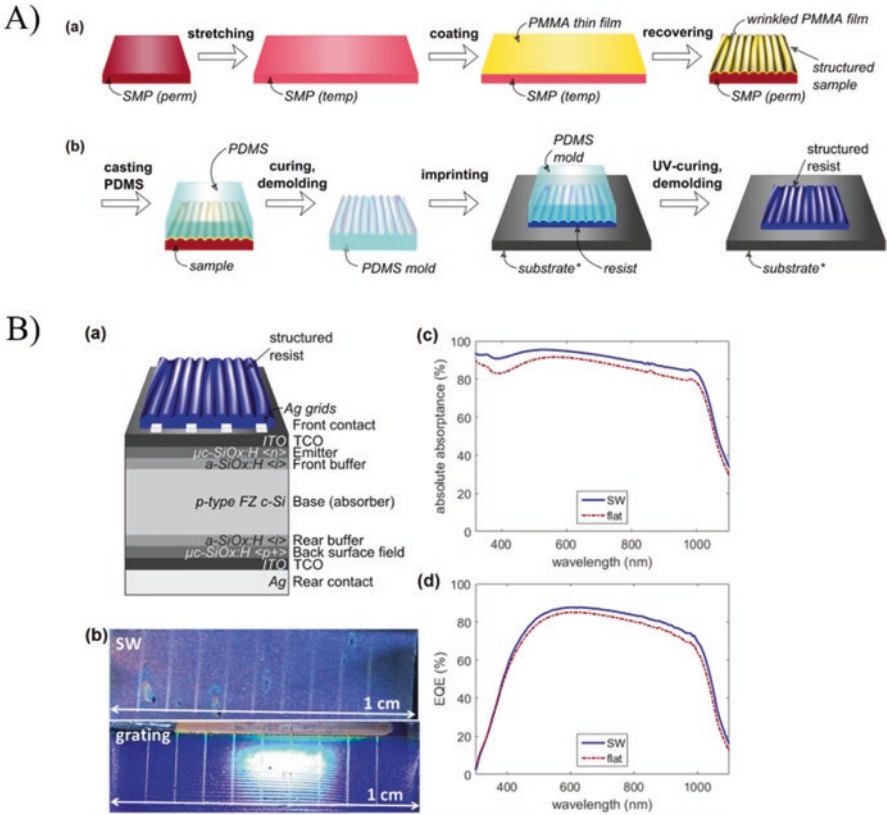


**Fig. 14.4** (a) Schematic illustration of the fabrication and replication routes of disordered diffraction gratings using SPM and PDMS molds. (b) Anti-glaring effect and enhanced light-harvesting properties in c-Si solar cells covered with wrinkled coatings. (Reproduced with permission from Ref. [19])

compensate for the compressive stresses, resulting in 1D disordered gratings. In order to replicate the surface wrinkles, they were covered by a thick PDMS layer as shown in Fig. 14.4a.

In Fig. 14.4b, a scheme of the corresponding PV devices is shown, where the p-type absorber has a thickness of 250  $\mu\text{m}$  and the planar indium tin oxide (ITO) layer serves as a transparent and conductive front side electrode. In the same figure, the results obtained from the solar cell, thus, a short-circuit current density increase reaching 4.8% under normal incidence due to the combined light in-coupling and retro-reflection effects, are also depicted. Considering the superior light in-coupling capability of the wrinkles over planar coatings or periodic gratings at high angles of incidence, greater photocurrent enhancements are anticipated using oblique illumination.

Possible improvements in smart windows were performed by Lau et al. [20], which used transparent elastomer-based substrates with a surface electrode that pro-

vides electrically controlled micro-wrinkling. The theoretical base of this behavior is related to the fact that the diffusely scattered transmitted light appears opaque when the surface is micro-wrinkled. When the material is electrically activated, the wrinkles are flattened, thus making the windows transparent like window blinds. However, the initial prototypes of these electrically tunable windows showed limited transparency tuning because their transparent electrodes cannot be completely flattened.

Other modifications of the SPMs were developed by Soleymani et al. [21], who carefully examined the structural evolution and tuning of poly(styrene) (PS)-based wrinkled surfaces through the variation of nanoparticle parameters attached to the substrate via silane bonding. Some of the parameters varied were the diameter, number of layer, and density of Au nanoparticles and also some substrate parameters like number of constrained axes during the wrinkling process. In this article, a preliminary application of these wrinkled films as SERS-active substrates for the molecular detection of analytes was shown. These wrinkled metal nanoparticle films or polymer composites could be applied to a number of applications including chemical sensors, biosensors, and optoelectronics.

On the other hand, Odom et al. [22] presented a memory-based polymer with hierarchical wrinkling approach where both the wavelength and the orientation of previous-generation wrinkles can be preserved as the next generation of wrinkles is formed. Multigenerational wrinkles were produced in prestrained, thermoplastic PS sheets by carrying out sequential cycles of plasma-mediated skin layer formation followed by global strain relief. According to this study, the memory-based hierarchical nano-wrinkling provides a general approach to construct polymeric, 3D patterns that have potential in unidirectional liquid transport, anti-biofouling substrates, and omniphobic surfaces.

## 14.4 Electrochromic Devices

The electrochromic devices (ECD) have attracted growing attention in the last years due to their potential application in displays and smart systems, including windows, rearview mirrors, and helmet visors [23].

Sojoudi et al. fabricated a flexible and transparent ECD, using (poly(3,4-ethylene dioxythiophene) poly(styrene sulfonate) (PEDOT/PSS) and graphene as active conductive electrode films, and a flexible and compliant polyurethane substrate with 1-ethyl-3-methylimidazolium bis(trifluoromethyl sulfonyl)imide (EMI-TSFI) additive as an ionic liquid (Fig. 14.5a). Figure 14.5b qualitatively shows the functionality and the transmittance variation while the device was flexed. The device was then

---

**Fig. 14.5** (continued) in reduced (blue) and oxidized (bleached) states while it is being flexed under an applied voltage of  $\pm 15$  V and their change in transmittance percentage with uniaxial strains. (c) Water contact angle measurements on polyurethane, pristine graphene, and wrinkled graphene, also a water droplet placed on the device, exhibiting a contact angle of  $110^\circ \pm 2^\circ$  in oxidized (bleached) and reduced (blue) states. (Reproduced with permission from Ref. [24])

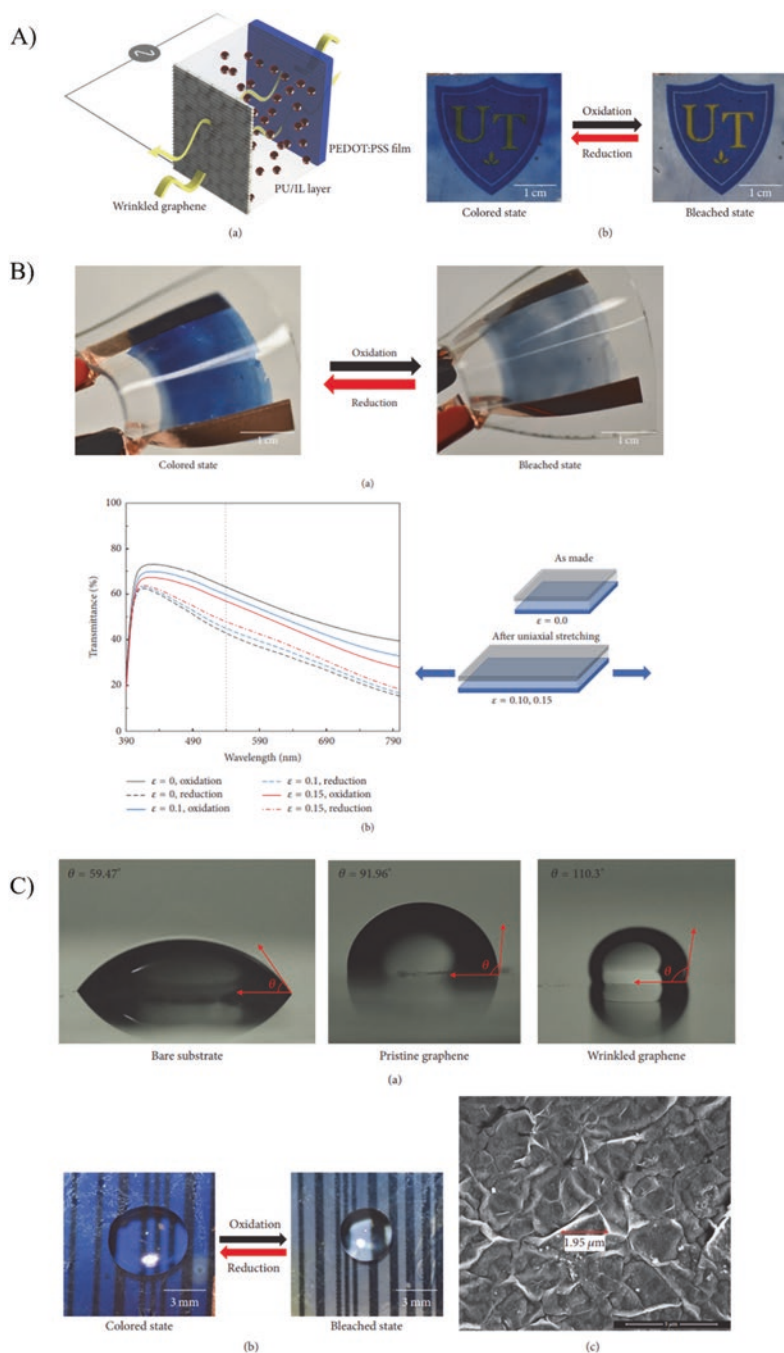


**Fig. 14.5** (a) Schematic illustration of an ECD showing wrinkled graphene and PEDOT/PSS as transparent conductive electrodes. Also, photographs of the ECD at reduced (blue) state and oxidized (bleached) state under an applied potential of  $\pm 12$  V. (b) Photographs of the flexible ECD

stretched uniaxially at strain rates of  $\epsilon = 0.10$  and  $\epsilon = 0.15$ . Figure 14.5b also shows the transmittance response in oxidation and reduction states at different strain rates. Figure 14.5c shows the water contact angle of polyurethane substrate ( $59.47 \pm 3^\circ$ ), pristine multilayered graphene ( $91.96 \pm 3^\circ$ ), and wrinkled graphene with an induced prestrain of 0.3 ( $110 \pm 2^\circ$ ), indicating an increase in anti-wetting nature of the graphene films. Figure 14.5c also shows the hydrophobic nature of the devices with color contrast in the reduced and oxidized states. The authors showed that the contact angle increased with higher prestrains. Additionally, Fig. 14.5c reports that the wrinkles have a periodicity of  $1.95 \mu\text{m}$ , which was observed by SEM.

## 14.5 Organic Photovoltaic Cells and Organic Light-Emitting Diodes

Yan et al. [25] reported the experimental efforts to fabricate geometrically tunable and spontaneously formed nano-wrinkled structures. These surface textures could be used as means for photon management, which becomes an attractive route for manufacturing large-area and low-cost efficient organic photovoltaic (OPV) cells and organic light-emitting diode (OLED) devices. Therefore, this article shows the experimental and theoretical efforts to incorporate the spontaneously formed regular and periodic nano-wrinkled structures into these devices, aiming to develop a low-cost and large-area fabrication method to increase the light absorption of the active layer in OPV devices and the light extraction efficiencies of OLED devices. Figure 14.6 shows the formation of wrinkled patterns at different fabrication stages using PDMS on a chromium-copper sputtered silicon wafer. Oxygen plasma was used to create a surface oxide layer, whose period and amplitude of the wrinkles increase as the plasma treating time increases. The wrinkled patterns are transferred to a rigid substrate for the fabrication of organic optoelectronic devices (Fig. 14.6b). Additionally, numerical studies were carried out, thus showing the band diagram for a planar and wrinkled OLED device (Fig. 14.6c). In this spectrum, the four straight and bright line segments are the air light line folded into the first Brillouin zone, and the other bent lines are the photonic-plasmonic bands in this periodic structure. Figure 14.6d shows the electric field intensity distribution at its two band edges. This work serves as a base for future experimental studies of large-area low-cost organic optoelectronic devices using wrinkles to achieve photon management.

## 14.6 Smart Displays/Anti-counterfeiting and Photo-Modulation of Surface Wrinkles

The group of Zong et al. [26] design light-erasable wrinkles over PDMS substrates using an azobenzene-containing polymer as the top layer. The compressive stress could be released by the trans/cis photoisomerization of azobenzene moieties upon illumination.

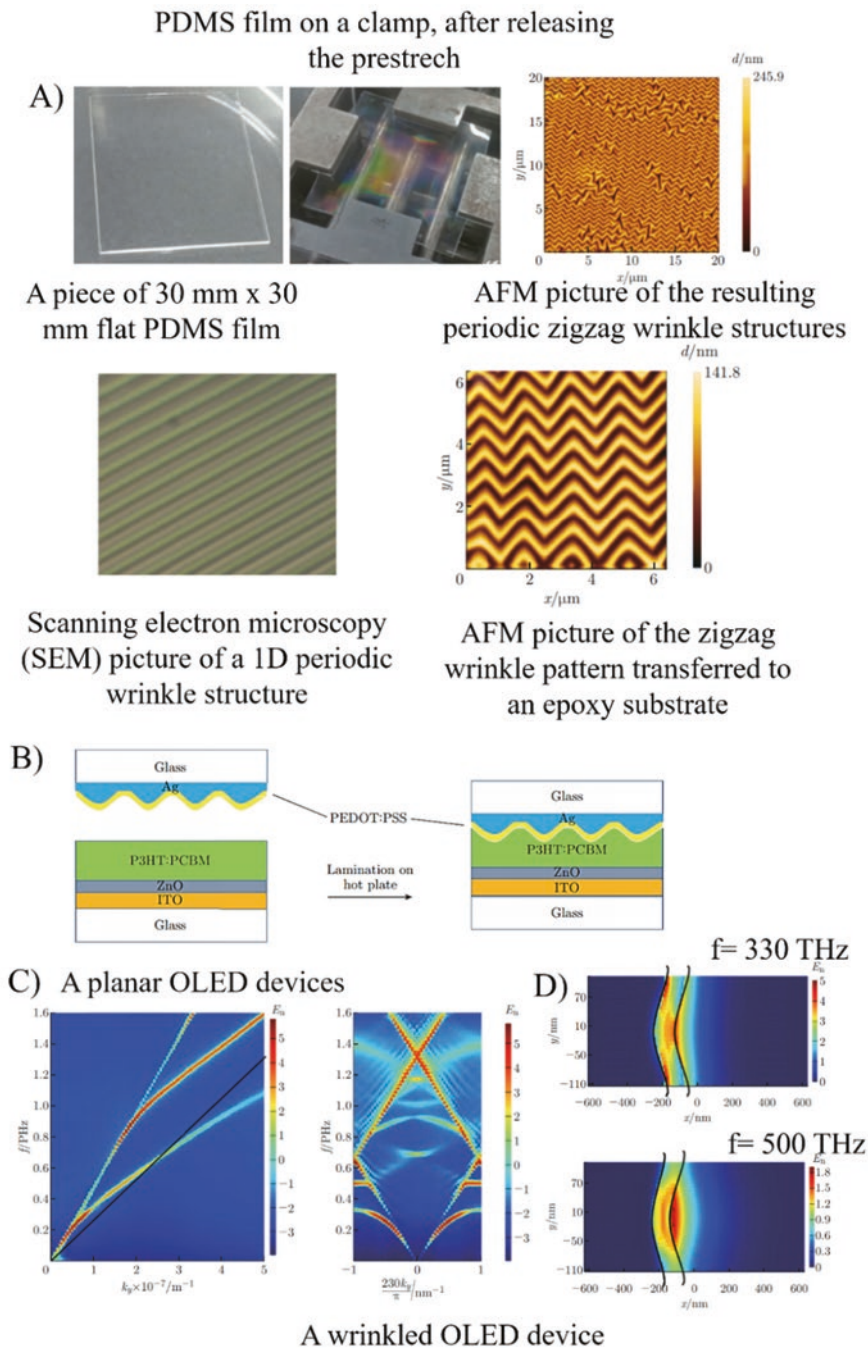


**Fig. 14.6** (a) Wrinkles at different fabrication stages. (b) Wrinkle structures incorporated into the inverted OPV structures through lamination. (c) Band structures and (d) electric field intensity distribution at band edges. (Reproduced with permission from Ref. [25])

Similarly, Sun et al. [27] reported three different types of moisture-responsive wrinkling dynamics in polyvinyl alcohol (PVA) films over PDMS substrate. The wrinkled topography depends on the mechanical and structural properties of the film and substrate. The moisture-dependent responsive properties of the PVA thin film can be varied by controlling the thickness and cross-linking degree/gradient, as well as the film-to-substrate thickness ratio.

Jiang et al. developed a facile strategy to fabricate multiresponsive dynamic wrinkling patterns by regulating Young's modulus and cross-linking density of the skin layers via dynamic chemistry [28–30]. In these reversible patterns, only one parameter for the recording and reading of information, fluorescence or topography, can be controlled dynamically by external stimuli, probably reducing the information capacity and security. A reversible pattern with both fluorescence and topography responses to a single stimulus will undoubtedly increase the information capacity and security but has rarely been reported so far.

The same group mentioned above fabricates a reversible dynamic dual-pattern based on a bilayer system whose fluorescence and wrinkled topography are controlled simultaneously by incident light. Anthracene (AN,  $\pi$ -electron rich) and naphthalene diimide (NDI,  $\pi$ -electron poor) were used as a top layer with a PDMS layer as a substrate. The charge transfer interaction leads to red fluorescence of the top copolymer material, while both AN and NDI units emit a blue-green fluorescence. Figure 14.7a shows the reversible dynamic dual-pattern with wrinkled topography and fluorescence in response to light stimuli. In Fig. 14.7b a sequence of AFM images is shown, which corresponds to fluorescence photographs under UV light providing visualization of the irradiation time-dependent growth of the dual-patterns of random wrinkles and fluorescence induced by the dimerization reaction. An increase in the wavelength and amplitude of the wrinkles could be observed from a flat state to the random wrinkles upon 365 nm UV irradiation. Additionally, when the samples are exposed to 254 nm or 150 °C, the reversible photodimerization of the skin layer enabled the feasible erasure of the wrinkle morphology via modulus decreasing of the top layer and the release of the compressive stress caused by the photocleavage of the AN dimer. Figure 14.7c shows the positive images with a green fluorescence pattern of the annulus and stripes or “SJTU” within the red fluorescence background. This reversible dual-patterned surface with dynamic fluorescence and wrinkles can serve well for the development of a new type of smart material surface (smart displays and message storage) as shown in Fig. 14.7d.

On the other hand, Zeng et al. use a series of moisture-sensitive film-substrate bilayer systems to achieve unique moisture-activated wrinkling dynamics [27]. In parallel, Jiang and co-workers could be able to fabricate temperature-controlled wrinkling patterns with reversible morphology and multifunctional properties via dynamic Diels-Alder chemical reaction [30]. Similarly, Yoon et al. reported light-induced switching surface creases based on a photothermal effect caused by iron oxide nanoparticles embedded in poly(N-isopropylacrylamide) (PIPA Am) gels [31]. Recently, several groups have harnessed some azobenzene-containing polymers to develop dynamic wrinkling systems by taking advantage of the photo-softening and/or stress release/reorganization arising from the trans/cis photoisomerization of azo-components [26, 30, 32, 33].

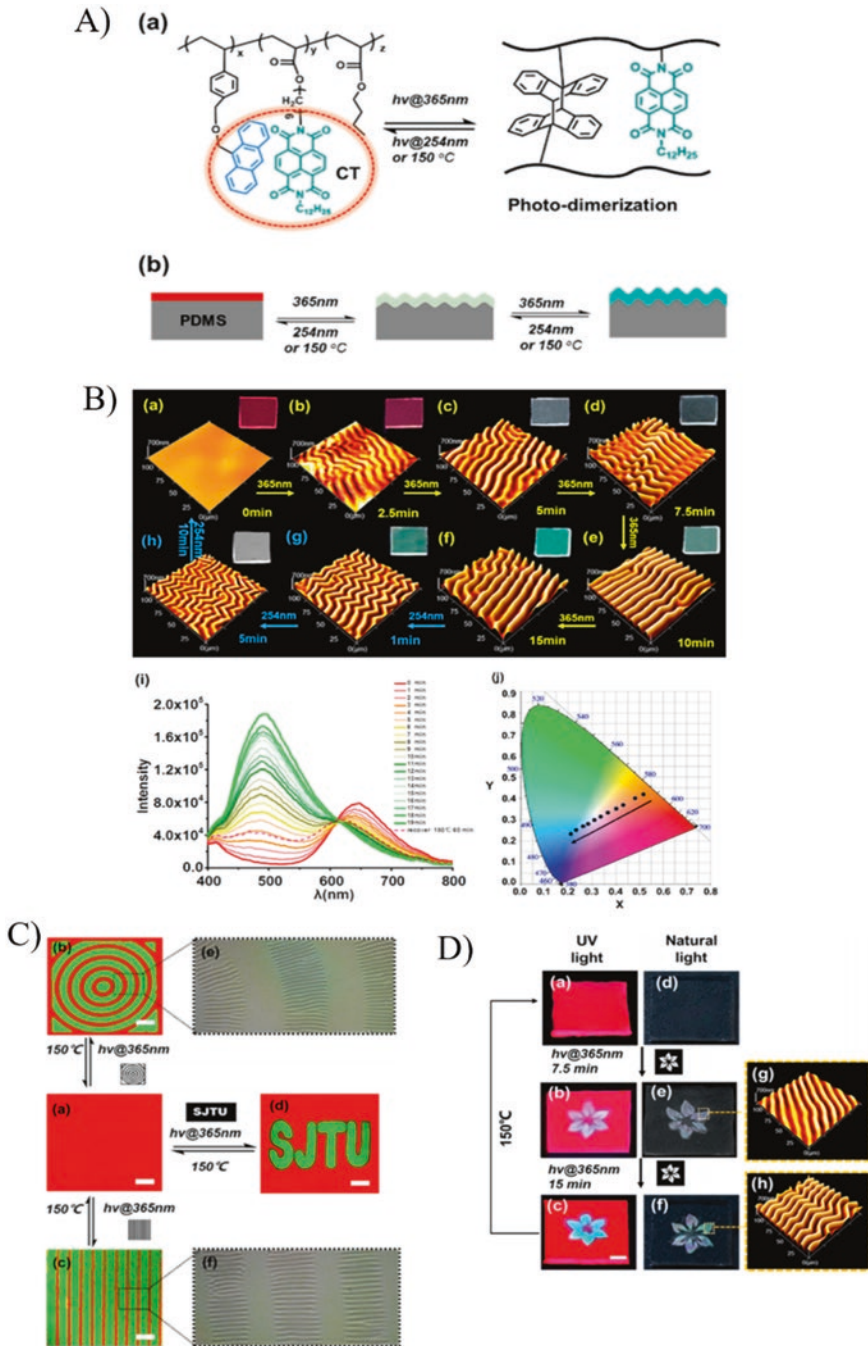


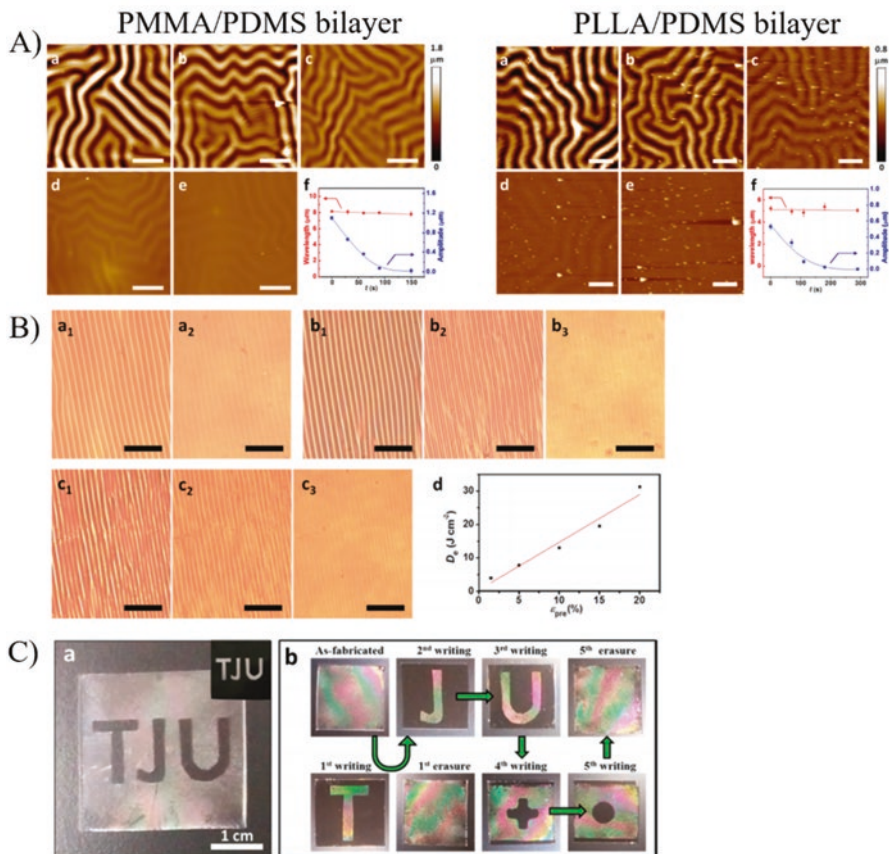
**Fig. 14.7** (a) Chemical structure of the composites used and its reversible photodimerization. Also, the fabrication process of the reversible dual-pattern based on bilayer system is shown. (b) AFM microographies of the reversible morphology when the sample is subjected to UV irradiation at different wavelengths. (c) Reversible dual-patterns with fluorescence and hierarchical wrinkles obtained through a photomask. (d) Reversible dual-pattern with fluorescence and hierarchical wrinkles obtained through a macro-mask. Photographs of “flower” macro-patterns with reversible fluorescence and wrinkles. (Reproduced with permission from Ref. [19])

Lu et al. reported a green and effective strategy to fabricate light-responsive (phototunable) micropatterns by taking advantage of photodegradation chemistry. This method paves the way for diverse applications such as optical information display or storage and fabrication of smart multifunctional surfaces, among others. According to the findings of Lu et al., two kinds of typical commercial available photodegradable polymers, PMMA and poly(lactic acid) (PLA), were used as representative models. When UV light irradiation is applied, a chain breakage is produced during the photolysis process, and the stress field of photodegradable polymer-based wrinkling systems undergoes a continuous disturbance, leading to the release or reorganization of the internal stress.

In Fig. 14.8a, a thermal-induced wrinkling system of PMMA/PDMS and PLLA/PDMS bilayer is shown, which were heated up to 100 °C or 90 °C. Upon cooling to room temperature, labyrinth wrinkles are generated on the surface. When these samples are exposed to UV light, the wrinkling patterns were gradually erased (the wrinkle amplitude progressively decreases with the exposure time). Figure 14.8b shows the effect that produces the application of the optical erasure dose ( $D_e$ ), which is roughly independent of the initial wrinkle wavelength. The  $D_e$  increases with  $\epsilon_{pre}$ ; this connection between both parameters verifies that the phototunable evolution of surface wrinkles is intimately related to the photodegradation-induced stress/strain release in the wrinkled film. Finally, as is presented in Fig. 14.8c, the “TJU” logo is written through selective UV exposure with the corresponding photomask. This selective wrinkling effect has a remarkable stability and can be maintained in the daylight for 3 months approximately. Notably, the PMMA/PDMS bilayer has a good durability in the cycling of the thermal-induced wrinkling/UV-exposed dewrinkling.

Following the same scientific interest, Li et al. reported a simple method to generate reversible wrinkling patterns whose morphology possesses a fast response to multi-stimuli such as light and acid/base gases. The supramolecular polymer network is composed of a pyridine-containing copolymer, namely, P4VP-PS-PnBA, and an anthracene-containing carboxylic acid (AN-COOH), which can be cross-linked dynamically through reversible photodimerization of AN and the hydrogen bond between carboxyl and pyridine groups. The generation and elimination processes of wrinkled patterns were performed by photodimerization reaction. The wrinkled pattern could be erased by hydrogen chloride and ammonia and then regenerated by heating, allowing the evaporation of these components (Fig. 14.9a). As shown in Fig. 14.9b, a sequence of AFM images depicts the irradiation-time dependence growth of wrinkled patterns induced by the dimerization reaction. Additionally, the cross-linked network in the top layer could be broken, leading to a decrease in Young's moduli of the surface and, therefore, a release of the compressive stress generating an erasure of the surface wrinkling patterns. On the other hand, Fig. 14.9c indicates that the wrinkled patterns are very sensitive to HCl gas. Figure 14.9d shows the versatility of the technique, which could be used in non-ink printing for smart display or security purposes.

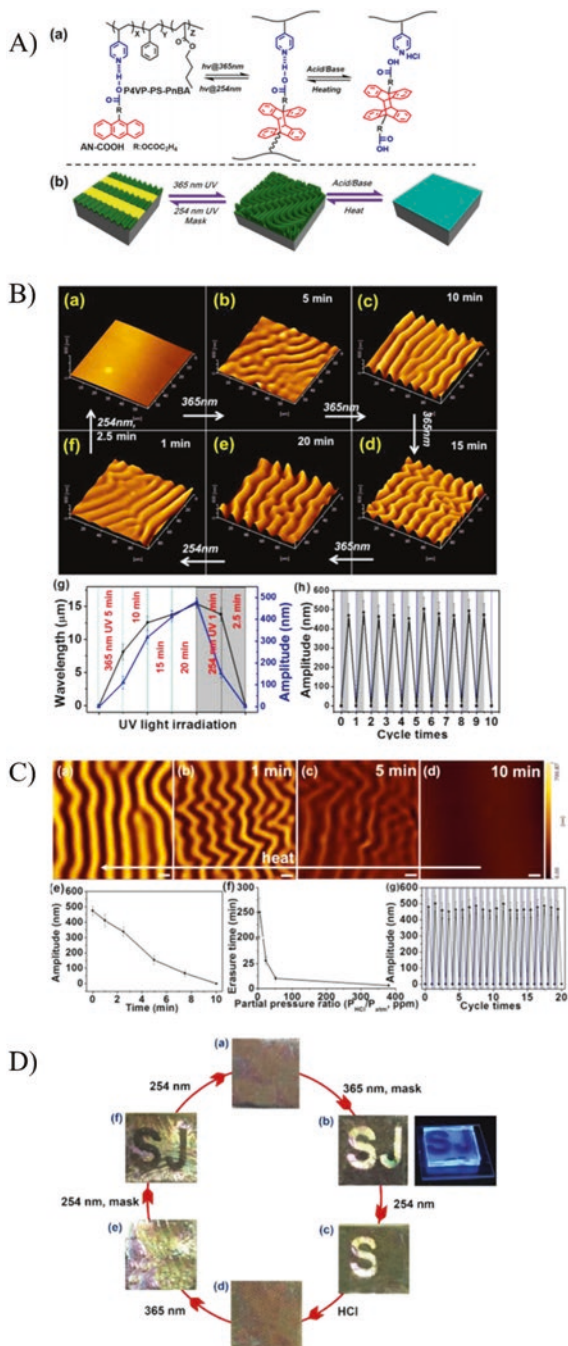
As was previously mentioned, the surface wrinkle formation has attracted much attention due to their facile fabrication. Seki et al., in the year 2017, created a new



**Fig. 14.8** (a) AFM images and dependence of the wrinkling pattern with respect to exposure time: 0 s, 70 s, 110 s, 180 s, and 290 s. (b) In situ optical observations of the wrinkle evolution on the PLLA/PDMS bilayer during UV light irradiation with variable exposure dose. (c) Photographs which show the repetitive writing/erasure of information by multiple cycling of selective UV exposure/thermal-induced wrinkling. (Reproduced with permission from Ref. [34])

methodology whose wrinkle formation and features are controlled by light irradiation [35]. This research group introduces results on tunable surface wrinkle formation in response to light using azobenzene-containing liquid crystalline polymers (Fig. 14.10a). In this study two strategies were proposed: (1) anisotropic wrinkle formation using a photo-alignable radical initiator in UV-curable liquid crystal films and (2) modulation of wrinkle formation using a series of azobenzene liquid crystalline polymers. Figure 14.10b shows optical microscopic and white light interferometric images of the wrinkled films. The observed averaged wrinkle wavelengths in the higher and lower regions were 1.9 and 1.7  $\mu\text{m}$ , respectively. These values agree well with calculated values, 1.8 and 1.6  $\mu\text{m}$ , respectively, based on Young's modulus data.

**Fig. 14.9** (a) Schematic illustration of the formation/erasure of wrinkles with UV and acid-base solution exposure. (b) AFM micrographies of the evolution process of generation/erasure of wrinkling patterns exposed to UV light. (c) Dynamic wrinkle response to hydrogen chloride exposure for different times: 0, 1, 5, 10 min. (d) Schematic representation of multiresponsive wrinkling patterns in smart display or storage information devices. (Reproduced with permission from Ref. [28])



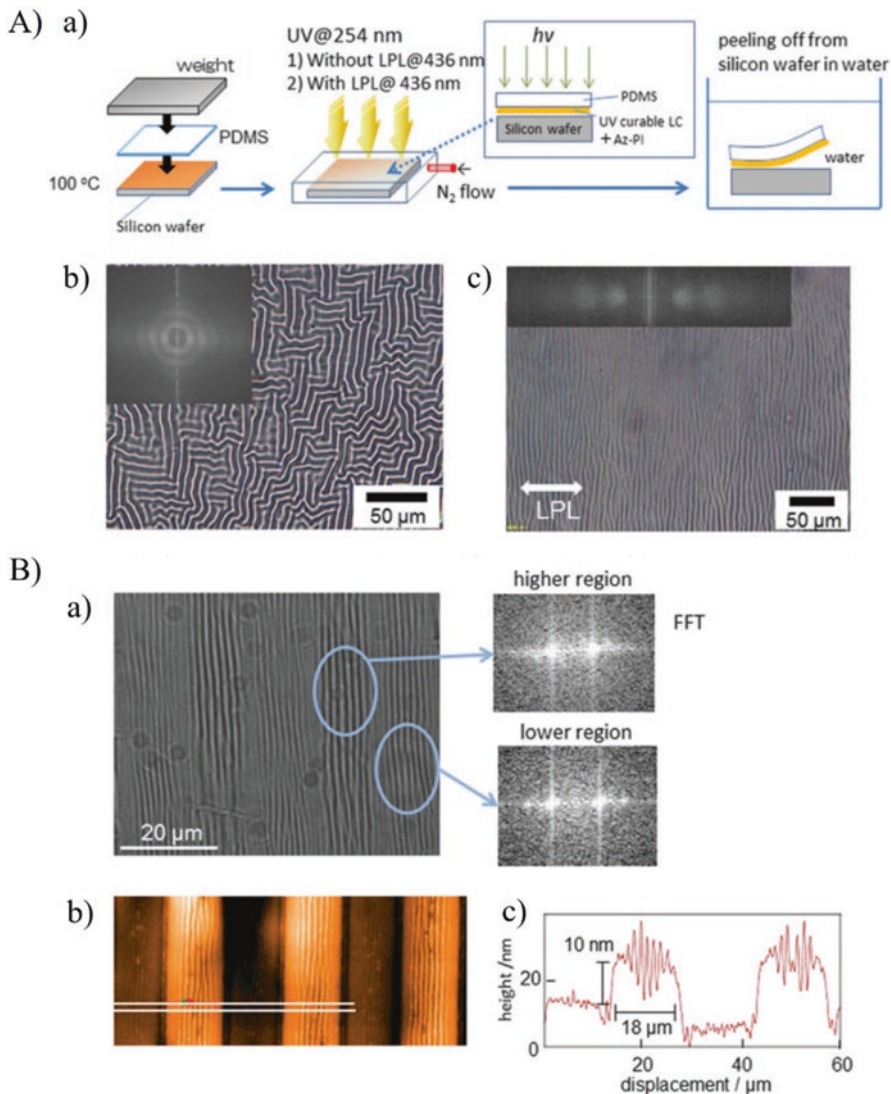


**Fig. 14.10** (a) Schematic representation of the wrinkle formation on an LC-PDMS laminated film. (b) Optical microscopic image and white light interferometric image after 10% uniaxial compression perpendicular to a line pattern. (Reproduced with permission from Ref. [32, 36])

## 14.7 Solar Cells

The organic-inorganic perovskite is a highly crystallographic material used as a base for several optoelectronic devices, such as photovoltaics, photodetectors, light-emitting diodes, transistors, and memory storage devices. Abate et al. presented the formation of wrinkles in thin PEGDA films induced by a cross-linking gradient

formed during an O<sub>2</sub> plasma treatment. In Fig. 14.11a some SEM images of the structures formed on top by using this methodology are depicted. In parallel, a change of the film appearance from transparent to whitish, caused by the increased light scattering from the wrinkles, was observed. By taking advantage of this effect, the stable perovskite microcrystals were dispersed in a polymer matrix in toluene and stabilized by alkyl ammonium chains at the crystal surface. Optical micrographs in transmission mode, fluorescence micrographs, AFM, SEM, DLS, X-ray diffraction, and fluorescence spectroscopy were carried out to the samples [37].

Figure 14.11b proves that the perovskite crystals were preferably located at the bottom of the ridges. This was further confirmed by fluorescence microscopy upon UV excitation, where the areas of the green emission of the perovskite crystals were found to coincide with the location of the wrinkles. In this same figure (right hand) transmittance and photoluminescence (PL) spectra of wrinkled perovskite-containing films are shown.

On the other hand, inverted polymer solar cells (IPSCs) have been fabricated by using different processing methods and layer combinations in order to achieve the above desired properties. Thus, zinc oxide (ZnO) is one of the most promising candidates for an electron transport material for IPSCs due to its good environmental stability, high transparency in the visible and near-infrared regions, and high electron mobility [38].

The group of Ryu et al. [39] fabricated amorphous ZnO wrinkled structures using low-temperature static annealing (SA). The wrinkled structures were obtained at 150 °C and flat structures were created at 200 °C using the SA process. The surface morphology of the deposited ZnO layers and their surface roughness at the different annealing temperatures were characterized using AFM, as shown in Fig. 14.12a.

Active solar cell layers were deposited on the ZnO layers annealed at different temperatures. This blend has shown to improve the efficiency of optical photovoltaic devices due to its rapid intramolecular charge separation and high photovoltaic activity. After deposition of this layer, the surface and cross-sectional morphologies of the obtained structures were studied using AFM and Cs-corrected STEM analysis (Fig. 14.12b). These analyses confirmed that the process of depositing the active layer did not change the wrinkled surface morphology and the flat morphology obtained for ZnO deposition, due to its low film thickness. The transmission efficiency of the structure after deposition of the active layer was analyzed, and the results showed that the absorbance of the device in both cases was compromised despite the active layer being thin. This research has a high potential for flexible electronics, such as plastic substrates and polymer gas barriers.

## 14.8 Smart Windows and Light Controllable Electronics

Over the past few years, there has been an increasing demand for stretchable electrodes for flexible and soft electronic devices which have gained tremendous attention as future electronics due to its flexibility and lightweight, especially for

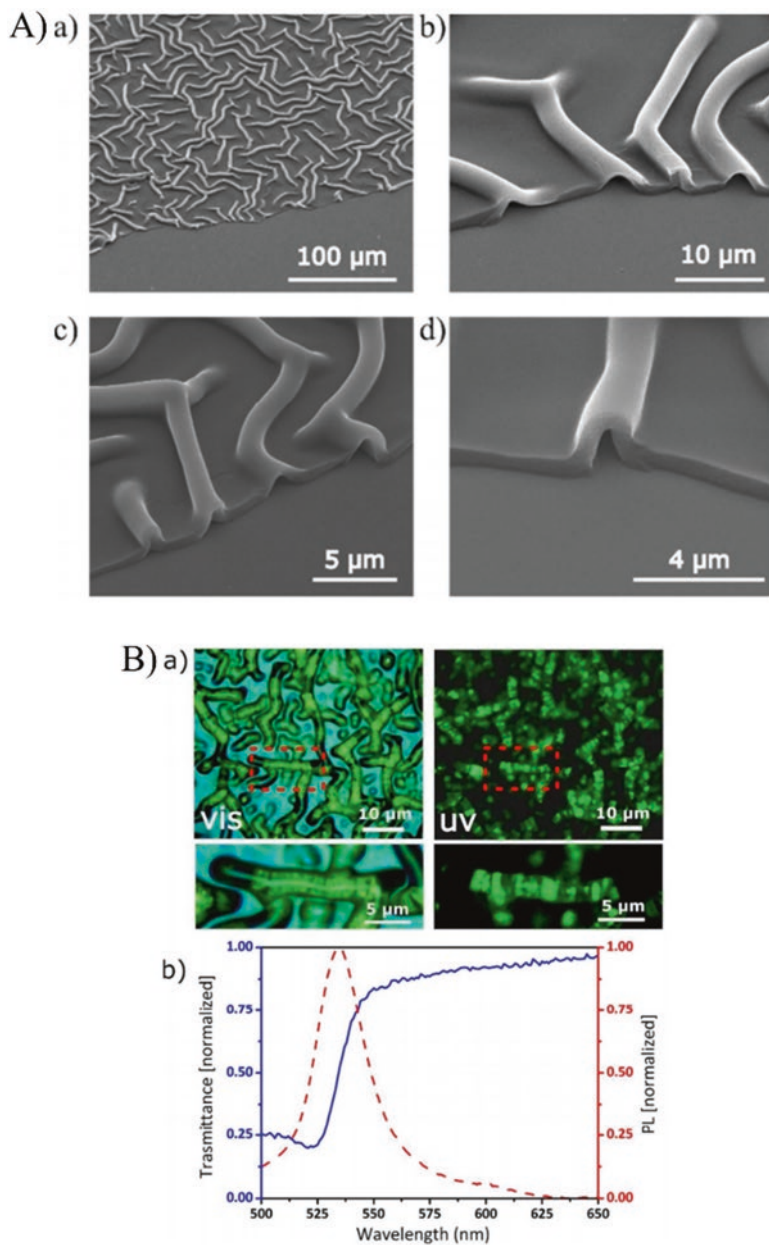


**Fig. 14.11** (a) SEM images of a section of PEGDA wrinkle film. (b) Microscopy images of wrinkled patterns filled with perovskite crystals. (Reproduced with permission from Ref. [37])

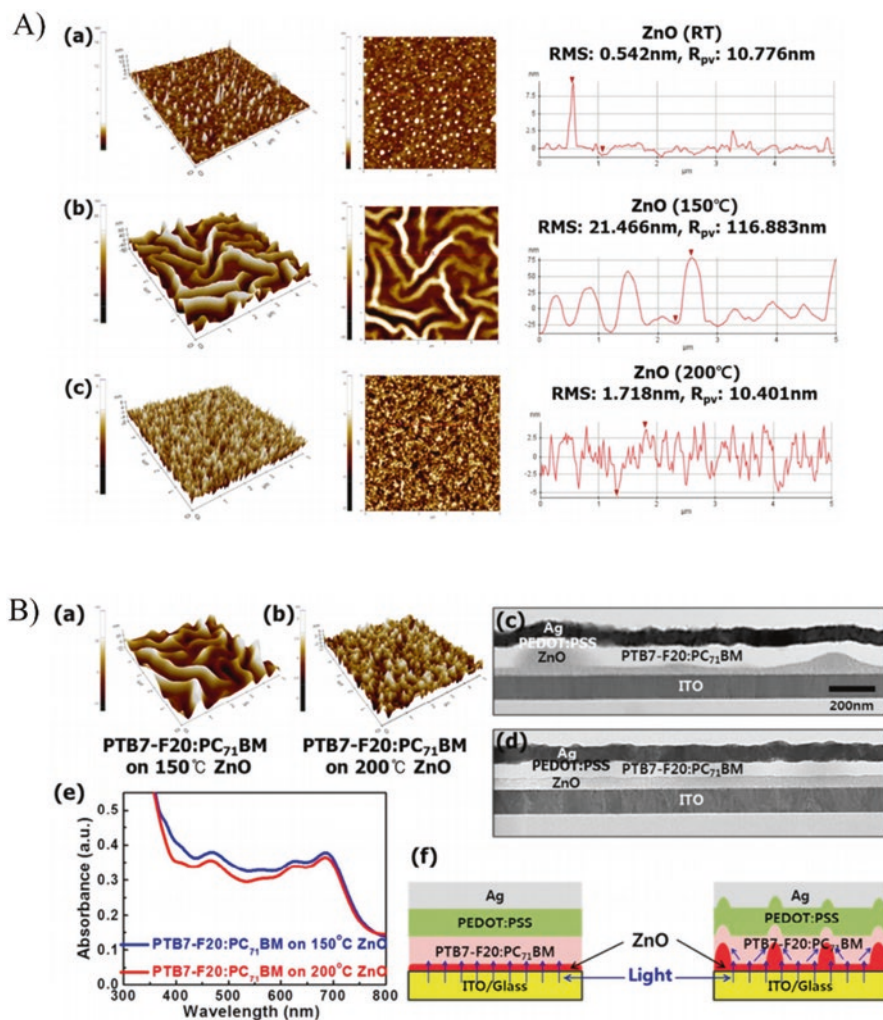


**Fig. 14.12** (a) AFM analysis of the surface morphology and roughness of ZnO deposited at RT, 150 °C, and 200 °C. (b) AFM surface morphologies of the device structure after deposition of the active layer on the ZnO annealed layer (wrinkled and flat). Also, a cross-sectional FE-SEM analysis is observed. The visible light absorbance of the ZnO layer is depicted in the plot together with a schema comparing the light scattering and diffraction mechanisms. (Reproduced with permission from Ref. [39])

applications in wearable electronics. An electrode in such devices requires special functionalities to be twisted, bent, stretched, and deformed into variable shapes. Also, it needs to have the capacity to be restored to their original state. According to this, Oh et al. [40] described an elastomer actuator with wrinkled hybrid electrodes which may be a candidate to tune the transmittance of smart window systems. Specifically, they reported uni- or biaxially wrinkled graphene-silver nanowire

hybrid electrodes. The system consists of graphene layers fabricated via chemical vapor deposition (CVD) and silver nanowires interpenetrated in the structure. A monolayer of graphene grown by CVD on a Cu foil was transferred onto a biaxially prestrained elastomer substrate, and silver nanowires were sprayed on the transferred graphene surface. The prestrained film was released to develop a wrinkled structure (Fig. 14.13a, b). Their morphological and electrical properties were deeply studied. Figure 14.13c is a graphical representation of the relationship between the rate of the area change and the transmittance obtained when a voltage is applied to the actuator. Using a sample without the wrinkled electrodes, experimental results confirmed that the area change rate was about 27% and the transmittance at 550 nm was changed by 8%. Additionally, for the wrinkle-free sample, the change in the active area of the dielectric elastomer actuator with graphene-AgNWs hybrid electrodes also was measured with respect to the applied voltages. The wrinkled electrode structure exhibited about a 33% change in area ratio and a transmittance change of about 15%. It can be confirmed that the transmittance was about twice as large as that in the case of the wrinkle-free sample.

The biaxially wrinkled graphene and silver nanowires hybrid electrodes were very suitable for high actuating performance of electroactive dielectric elastomers compared with the wrinkle-free case. These results showed that the optical transparency of the highly stretchable electrode can be successfully tuned by modulating input voltages.

Similar studies and applications were developed by Ying et al., who explored the harnessing of dynamically tunable hierarchical wrinkles for the design of a potential multifunctional smart window with combined structural color and water droplet transport control. The self-similar hierarchical wrinkles with both nanoscale and microscale features were generated on a prestrained PDMS elastomer through sequential strain release and multistep oxygen plasma treatment [41]. Another example of this application was developed by Ge et al., which prepared a composite film consisting of a thin layer of a quasi-amorphous array of silica nanoparticles (NPs) embedded in bulk elastomeric PDMS [42].

On the other hand, Li et al. reported a simple and versatile strategy for the fabrication of near-infrared (NIR) light-responsive dynamic wrinkle by using a carbon nanotube (CNT) containing PDMS elastomer as a substrate, with various functional polymers serving as the top stiff layers. This type of NIR-driven dynamic wrinkle patterns could be applied eventually in smart displays, dynamic gratings, and light control electronics [43].

Similarly, the group of Cheng et al. reported a novel nanoscale wrinkled structure fabrication process using fluorocarbon plasma on PDMS and Solaris membranes. By varying the plasma treatment time, the wavelength of the wrinkled structures could be controlled. Thus, the high electron affinity and high transparency enabled the membrane to improve the performance of a triboelectric nanogenerator, being an attractive potential for future applications in micro- and nano-devices, especially in transparent energy harvesters [44].

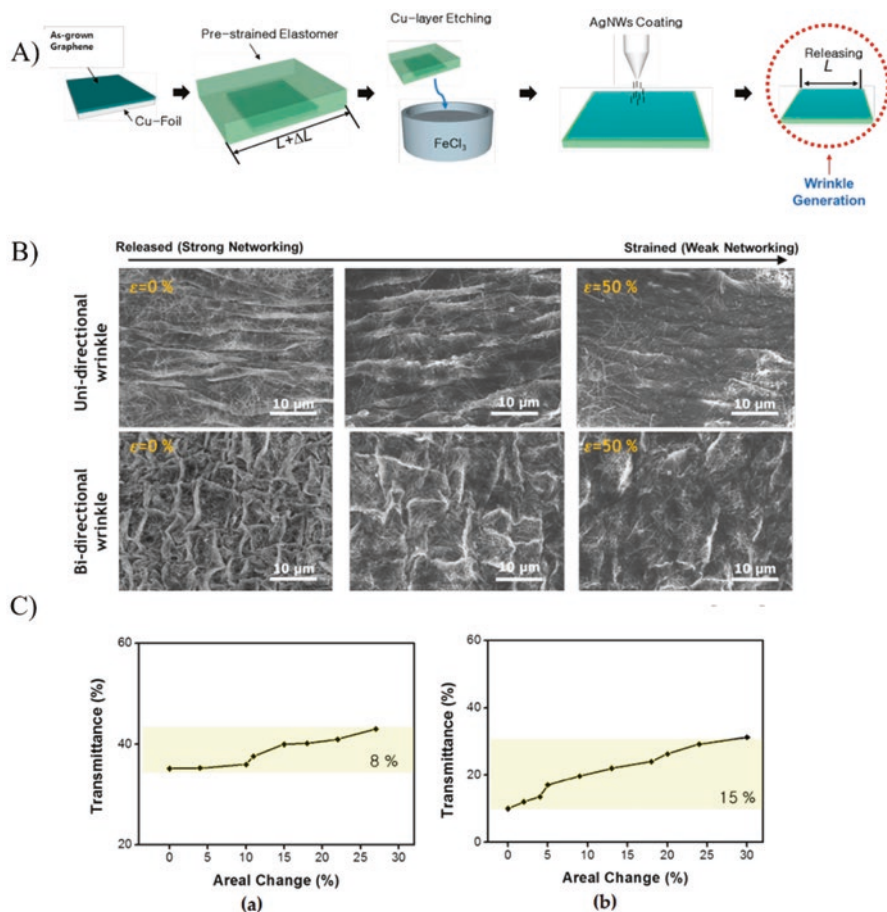


**Fig. 14.13** (a) Schematic representation of the fabrication process of the wrinkled graphene-AgNWs hybrid electrode. (b) SEM images of the morphology changes in the electrode surface with mechanical tensile strains. (c) Optical transmittance control of wrinkle-free and wrinkled elastomer actuator with electrical input. (Reproduced with permission from Ref. [40])

## 14.9 Sensors and Actuators

Electronic skins refer to electronic devices that mimic the flexible and sensory performance of human skin by transducing various external stimuli into electrical signals. Particularly, skin-like pressure sensors, which can detect electrical changes upon mechanical deformation, are intensively investigated due to the simple device configuration, low power consumption, and easy transduction mechanism. Particularly, if micropatterns are generated in their surfaces, the devices could incredibly increase the contact area, thus improving the pressure sensor sensitivity in several orders of magnitude.

An example of this was reported by the group of Zhang et al. [45] who fabricated force-sensitive hydrogels with ultra-stretchable capacity. To achieve this, dried chitosan microspheres (CSM) were immersed into acrylamide/acetic acid aqueous solution, which rapidly swell large amounts of pre-polymerized solution. Then, the polymerization reaction was carried out in the CSM colloid to obtain transparent chitosan/polyacrylamide (PAAm) hydrogels. Different pre-polymer solutions were tested, resulting in homogeneous or inhomogeneous swelling (Fig. 14.14a–c). The swelling capacity is directly related to the mechanical properties which present the material, as is possible to observe in Fig. 14.14d–e.

Then, these stretchable materials were tested as pressure sensor devices. Their electrical response to tension and compression were measured, showing interesting results (Fig. 14.15a, b). Accordingly, forefinger pressure sensor devices were fabricated using this material. In Fig. 14.15c, d, photographs of the hand monitor for different grasping motions and their corresponding resistance variations are shown.

A similar application was tested by the group of Huang and Dong et al. [46], using acrylamide and polyvinyl alcohol hydrogels. The particularity of this material is that its pressure-sensing performance has an incredibly high resolution ( $0.05 \text{ kPa}^{-1}$  for  $0 - 3.27 \text{ kPa}$ ) and fast response (150 ms) in a wide range of dynamic tests ( $0-6.67 \text{ kPa}$ ). Its high sensitivity allows detecting both tiny (phonation, air flowing, and saliva swallowing) and robust (finger and limb motions) physiological activities. The synthesis of the material involves a UV exposure process, which generates surface instabilities in the material. After strain release, hierarchy-nested micro-wrinkled patterns are formed on top. These self-patterned architectures are responsible for increasing the contact area significantly, which endows the pressure sensor with high sensitivity, as it was explained previously. Some images of the hierarchy-nested patterns are depicted in Fig. 14.16 (top). Finally, pressure sensor device tests are shown in Fig. 14.16 (bottom) (fist making, forefinger bending, elbow motion, and knee motion).

In the year 2016, Wang et al. [47] synthesize a hydrogel composite based on PDMS and silver layers. The PDMS substrate was immersed in bovine serum albumin (BSA), followed by an adequate swelling in chloroform. The silver film was successfully grown after a short-term electroless deposition in a mixture of Tollens' reagent. Then, the PDMS slice started to shrink due to chloroform evaporation. The Ag film undulates forming wrinkles as a result of out-of-plane stresses between the layers. Figure 14.17 (top) shows a schematic description of the wrinkling formation methodology. The size of the wrinkled pattern can be modulated via the modification of parameters like PDMS cross-linking degree, swelling time, or metal layer thickness. These pressure sensors, conveniently sandwiched between two wrinkled layers, are capable of transforming mechanical motions into electrical signals. Wrinkled patterns formed on top have a remarkably deformable ability, satisfying the demands for ultrasensitive detection of external pressure (below 1 Pa). Accordingly, Fig. 14.17 (bottom) shows some of the results obtained from sensing sound tests. Four different sounds were tested in this study, the words China, Chemistry, and Renmin University and a piece of music. The photographs and the diagram show the switching of LED when the sensor is exposed to voice.

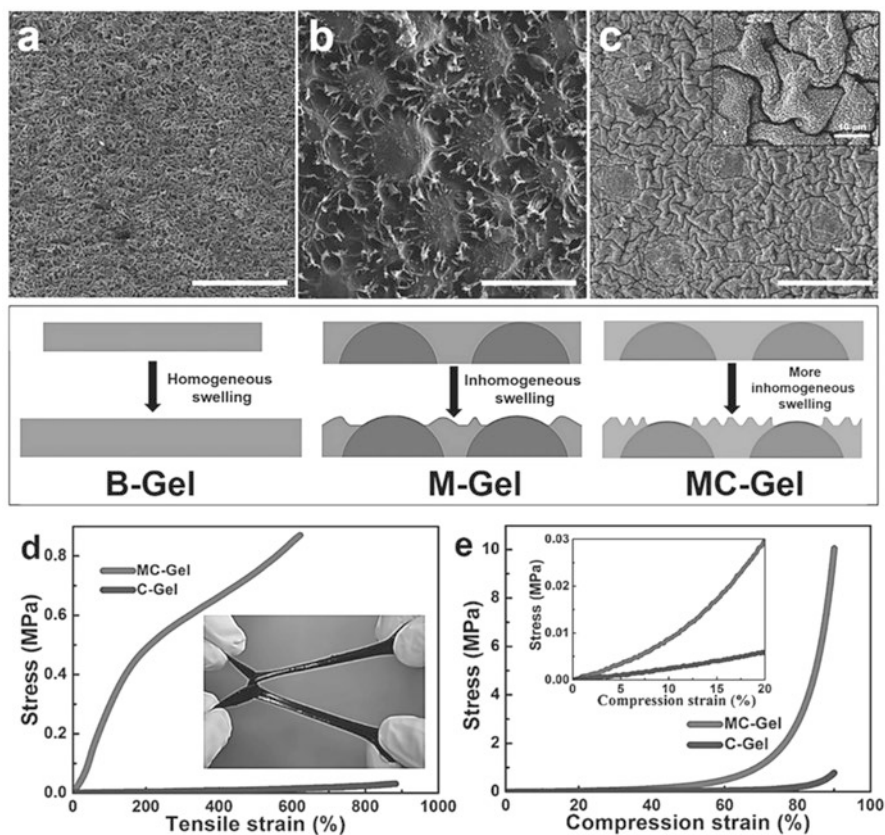


**Fig. 14.14** SEM micrographs of (a) bare gel, (b) CSM-gel composite with partial acrylamide polymerization, and (c) CSM-gel with acrylamide and aniline full polymerization. Mechanical performance of the materials under (d) tensile and (e) compressive tests. (Reproduced with permission from Ref. [45])

Soft microactuators with stimuli-responsive tunable chemistries are highly demanded in complex multifunctional and biocompatible microdevices. Multifunctional actuators are especially significant for nano-/micro-artificial anatomies, which perform particular and specific functions such as transportation, selection, recognition, and others. Particularly, the group of Takahashi et al. [48] in the year 2016 demonstrated an adaptive use of surface wrinkled patterns which exhibit a peristaltic motion allowing to selectively transport micro-objects on bilayered soft materials under the thermal stimulus. The bilayered materials made of thermoresponsive poly(*N*-iso-propyl acrylamide) (PNIPAM) and hybrid silica form wrinkled patterns of submillimeter dimensions which react to temperature variation. Figure 14.18 shows some of the more interesting results obtained by changing the ambient temperature. As is possible to observe, the peristaltic motion generates the

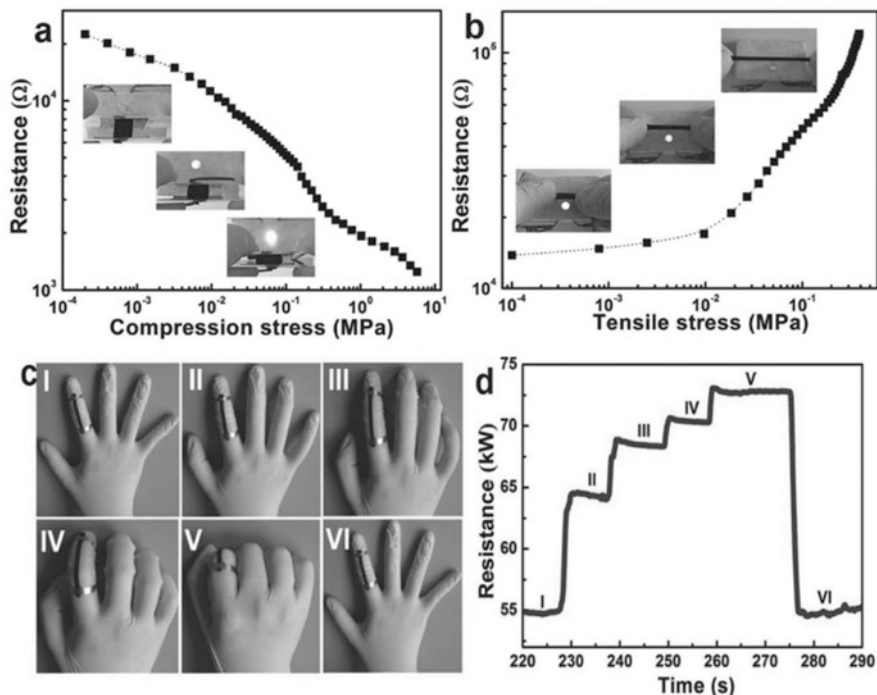


**Fig. 14.15** Electrical response of the material coined as MC-gel for (a) tensile and (b) compressive tests. Their performance as a hand gesture monitor is tested using a forefinger device for (c) different grasping motions by measuring (d) its resistive response in each case. (Reproduced with permission from Ref. [45])

movement of big particles (red dashed circle), while the smaller ones (yellow dashed circle) remain almost in the same place.

## 14.10 Conclusion

In this chapter, various novel applications, involving the use of wrinkled patterns, were mentioned and explained. The control of wrinkle morphology and dimensions is a crucial factor for developing several kinds of applications. According to the literature, the wrinkle wavelength is related to the film thickness, and the amplitude depends on the applied stresses and the magnitude of induced strain mismatch. In summary, the wrinkled pattern fabrication method is fundamental to create devices with a desirable functionality. One of the most relevant applications revised in this chapter is, for example, the AuNPs implantation process on the surface of a PDMS substrate which favors the electrical conductivity of the nanocomposite, being a relevant material in the optics field, biointerfacing, sensing, and microfabrication.

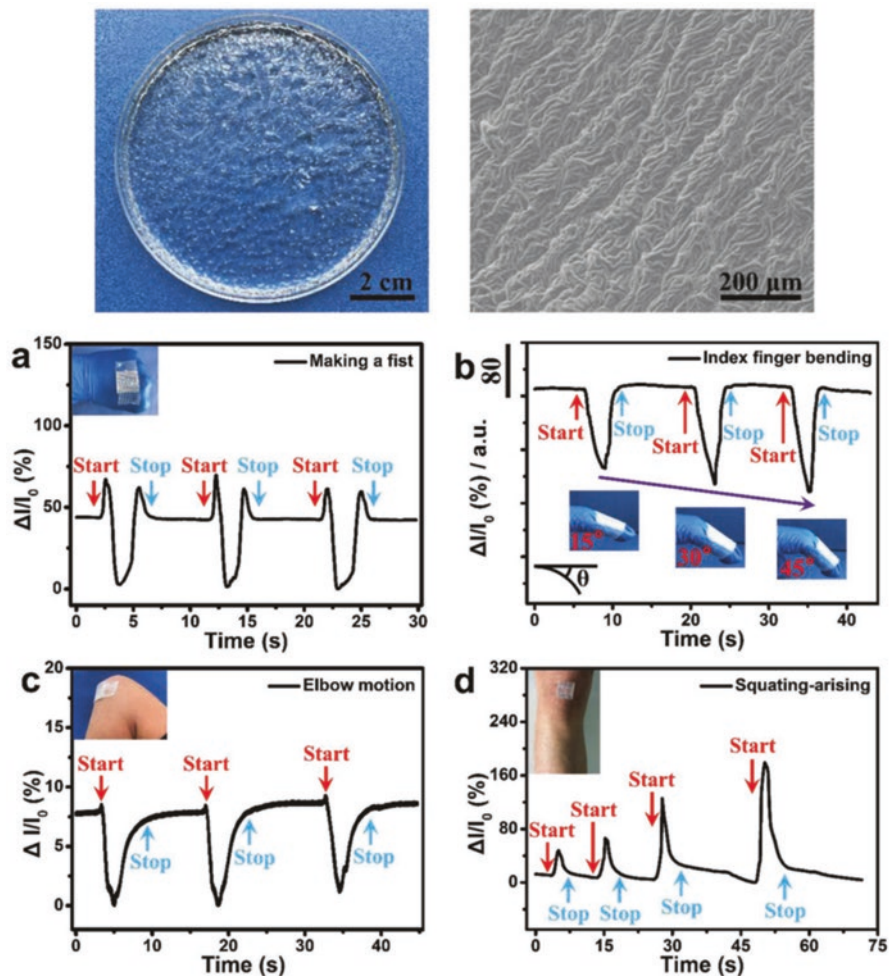


**Fig. 14.16** (top) Photograph of a large-area hydrogel film and SEM image of the binary hierarchy-nested wrinkled hydrogel surface. (bottom) The electric response of fist making, forefinger bending, elbow motion, and knee motion. (Reproduced with permission from Ref. [46])

Other interesting applications revised in this chapter are light tunable materials based on azobenzene polymers which possess surface wrinkled patterns and liquid crystalline composites, the formation of ZnO layers over wrinkled surfaces which could produce multiple diffractions at various angles being potentially useful for flexible electrodes or pressure sensors whose electrical response is related to the tension and compression exerted on the material. Additionally, technological devices for solar cells, smart windows, stretchable electronics, smart displays, and anti-counterfeiting devices, among others, were also mentioned.

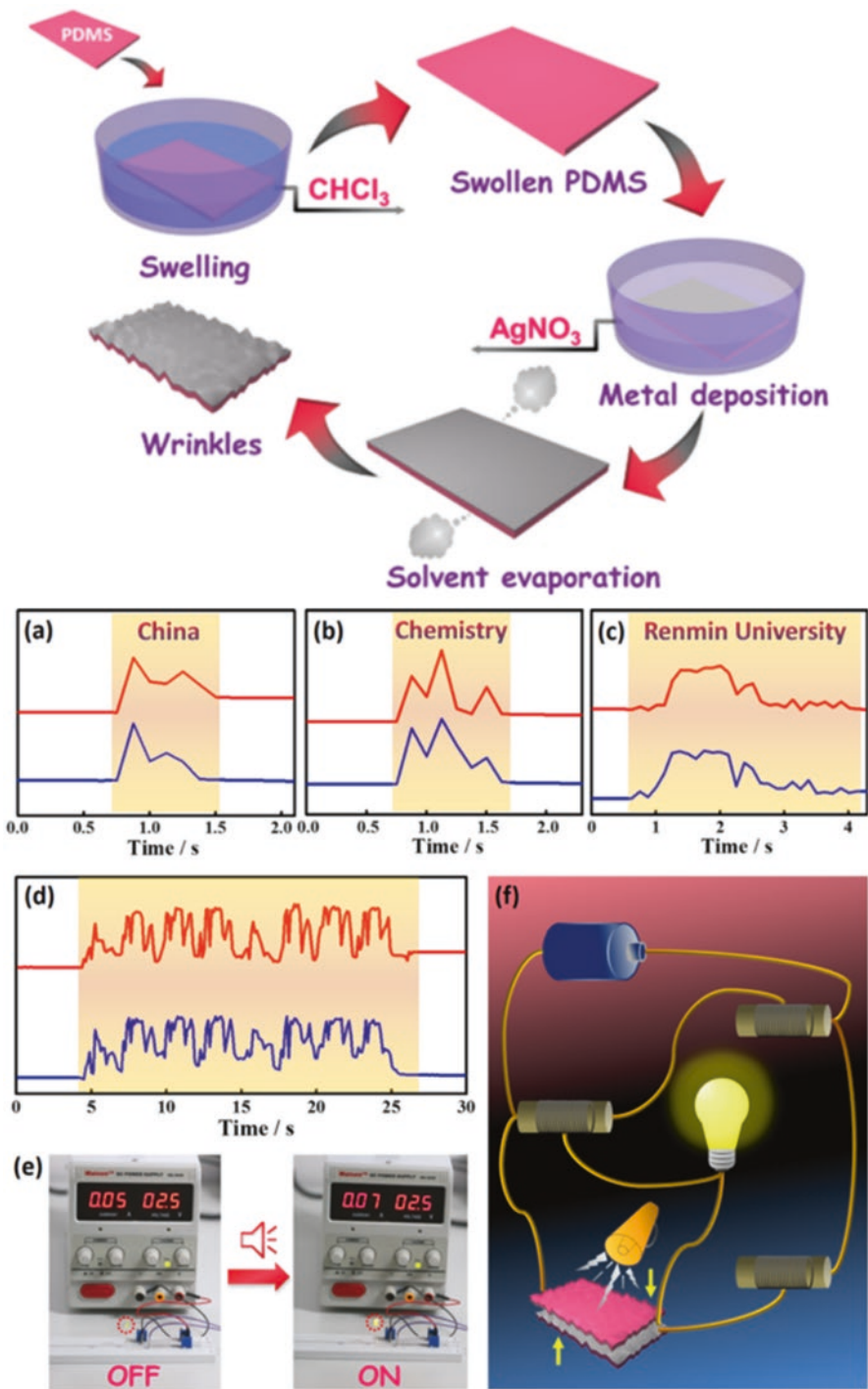


**Fig. 14.17** (top) Schematic illustration of the deposition of Ag wrinkles on PDMS via polymer swelling and electroless deposition. (bottom) Sensing tests of external sounds by the pressure sensor, photographs and a diagram of switching LED on/off by exposing the pressure sensor to voice. (Reproduced with permission from Ref. [47])

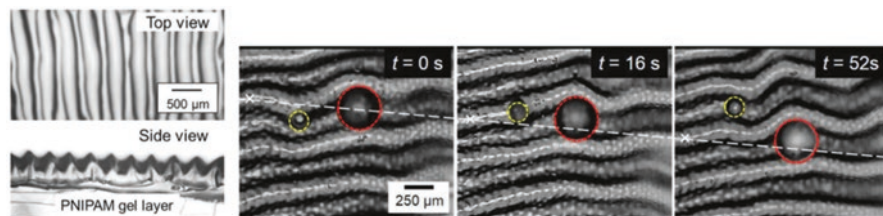


**Fig. 14.18** Optical microscope images (top and side views) of the anisotropic micro-wrinkled pattern. Snapshots showing the anisotropic wrinkles during the cooling process. The sub-500  $\mu\text{m}$  waves with long-range order move in one direction to carry the larger particle, whereas the smaller particle stays at the original position. (Reproduced with permission from Ref. [48])

**Acknowledgments** The authors acknowledge the financial support given by FONDECYT Grant N° 1170209. M.A. Sarabia acknowledges the financial support given by CONICYT through the doctoral program scholarship grant. J. Rodríguez-Hernández acknowledges the financial support from Ministerio de Economía y Competitividad (MINECO) (Project MAT2016-78437-R, FEDER-EU). Finally, we acknowledge VRAC Grant Number L216-04 of Universidad Tecnológica Metropolitana.

## References

1. L. Ionov, Biomimetic 3D self-assembling biomicroconstructs by spontaneous deformation of thin polymer films. *J. Mater. Chem.* **22**, 19366–19375 (2012)
2. J. Genzer, J. Groenewold, Soft matter with hard skin: From skin wrinkles to templating and material characterization. *Soft Matter* **2**, 310–323 (2006)
3. T. Ohzono, K. Suzuki, T. Yamaguchi, et al., Tunable optical diffuser based on deformable wrinkles. *Adv. Opt. Mater.* **1**, 374–380 (2013)
4. S.G. Lee, H. Kim, H.H. Choi, et al., Evaporation-induced self-alignment and transfer of semiconductor nanowires by wrinkled elastomeric templates. *Adv. Mater.* **25**, 2162–2166 (2013)
5. H. Stenberg, A. Matikainen, S. Daniel, et al., Self-organized polymer wrinkles: A lithography-free pathway for Surface-Enhanced Raman Scattering (SERS) substrates. *Macromol. Mater. Eng.* **300**, 386–390 (2015)
6. Y. Li, S. Dai, J. John, et al., Superhydrophobic surfaces from hierarchically structured wrinkled polymers. *ACS Appl. Mater. Interfaces* **5**, 11066–11073 (2013)
7. C.S. Davis, D. Martina, C. Creton, et al., Enhanced adhesion of elastic materials to small-scale wrinkles. *Langmuir* **28**, 14899–14908 (2012)
8. M.R. Aufan, Y. Sumi, S. Kim, et al., Facile synthesis of conductive polypyrrole wrinkle topographies on polydimethylsiloxane via a swelling-deswelling process and their potential uses in tissue engineering. *ACS Appl. Mater. Interfaces* **7**, 23454–23463 (2015)
9. A. Chen, D.K. Lieu, L. Freschauf, et al., Shrink-film configurable multiscale wrinkles for functional alignment of human embryonic stem cells and their cardiac derivatives. *Adv. Mater.* **23**, 5785–5791 (2011)
10. F. Greco, T. Fujie, L. Ricotti, et al., Microwrinkled conducting polymer interface for anisotropic multicellular alignment. *ACS Appl. Mater. Interfaces* **5**, 573–584 (2013)
11. J. Gu, X. Li, H. Ma, et al., One-step synthesis of PHEMA hydrogel films capable of generating highly ordered wrinkling patterns. *Polymer (Guildf)* **110**, 114–123 (2017)
12. M. Guvendiren, J.A. Burdick, The control of stem cell morphology and differentiation by hydrogel surface wrinkles. *Biomaterials* **31**, 6511–6518 (2010)

13. Z. Zhao, J. Gu, Y. Zhao, et al., Hydrogel thin film with swelling-induced wrinkling patterns for high-throughput generation of multicellular spheroids. *Biomacromolecules* **15**, 3306–3312 (2014)
14. F. Greco, A. Bellacicca, M. Gemmi, et al., Conducting shrinkable nanocomposite based on nanoparticle implanted plastic sheet: Tunable thermally induced surface wrinkling. *ACS Appl. Mater. Interfaces* **7**, 7060–7065 (2015)
15. J.H. Yang, Z.j. Zhao, B.S. Shin, et al., Metallization of microscale wrinkles on a curved surface by contact and electro-replication method. *Int. J. Adv. Manuf. Technol.* **92**, 1165–1172 (2017)
16. W.M. Huang, Z. Ding, C.C. Wang, et al., Shape memory materials. *Mater. Today* **13**, 54–61 (2010)
17. Y. Wang, J. Xiao, Programmable, reversible and repeatable wrinkling of shape memory polymer thin films on elastomeric substrates for smart adhesion. *Soft Matter* **13**, 5317–5323 (2017)
18. P.-L. Ko, F.-L. Chang, C.-H. Li, et al., Dynamically programmable surface micro-wrinkles on PDMS-SMA composite. *Smart Mater. Struct* **23**(1–9), 115007 (2014)
19. S. Schauer, R. Schmager, R. Hünig, et al., Disordered diffraction gratings tailored by shape-memory based wrinkling and their application to photovoltaics. *Opt. Mater. Express* **8**, 184 (2018)
20. D. Wei, M. Shrestha, A. Asundi, et al., Controlled micro-wrinkling of ultrathin indium-tin-oxide films for transparency tuning. *Proc. SPIE – Int. Soc. Opt. Eng.* **10449**, 1–9 (2017)
21. C.M. Gabardo, J. Yang, N.J. Smith, et al., Programmable wrinkling of self-assembled nanoparticle films on shape memory polymers. *ACS Nano* **10**, 8829–8836 (2016)
22. W.K. Lee, C.J. Engel, M.D. Huntington, et al., Controlled three-dimensional hierarchical structuring by memory-based, sequential wrinkling. *Nano Lett.* **15**, 5624–5629 (2015)
23. Y. Alesanco, P. Miram, D. Sebastian, All-in-one gel-based electrochromic devices: Strengths and recent developments. *Materials* **11**, 1–27 (2018)
24. S.K. Nemani, D. Chen, M.H. Mohamed, et al., Stretchable and hydrophobic electrochromic devices using wrinkled graphene and PEDOT:PSS. *J. Nanomater.* **2018**, 1–10 (2018)
25. Q. Ji, C. Zhang, X. Qi, et al., Enhancing the efficiencies of organic photovoltaic and organic light-emitting diode devices by regular nano-wrinkle patterns. *J. Shanghai Jiaotong Univ.* **23**, 45–51 (2018)
26. C. Zong, Y. Zhao, H. Ji, et al., Tuning and erasing surface wrinkles by reversible visible-light-induced photoisomerization. *Angew. Chemie – Int. Ed.* **55**, 3931–3935 (2016)
27. S. Zeng, R. Li, S.G. Freire, et al., Moisture-responsive wrinkling surfaces with tunable dynamics. *Adv. Mater.* **29**, 1700828 (2017)
28. F. Li, H. Hou, J. Yin, et al., Multi-responsive wrinkling patterns by the photoswitchable supramolecular network. *ACS Macro Lett.* **6**, 848–853 (2017)
29. H. Hou, F. Li, Z. Su, et al., Light-reversible hierarchical patterns by dynamic photo-dimerization induced wrinkling. *J. Mater. Chem. C* **5**, 8765–8773 (2017)
30. H. Hou, J. Yin, X. Jiang, Reversible Diels–Alder reaction to control wrinkle patterns: From dynamic chemistry to dynamic patterns. *Adv. Mater.* **28**, 9126–9132 (2016)
31. J. Yoon, P. Bian, J. Kim, et al., Local switching of chemical patterns through light-triggered unfolding of creased hydrogel surfaces. *Angew. Chemie – Int. Ed.* **51**, 7146–7149 (2012)
32. T. Takeshima, W.Y. Liao, Y. Nagashima, et al., Photoresponsive surface wrinkle morphologies in liquid crystalline polymer films. *Macromolecules* **48**, 6378–6384 (2015)
33. H. Ji, Y. Zhao, C. Zong, et al., Simple and versatile strategy to prevent surface wrinkling by visible light irradiation. *ACS Appl. Mater. Interfaces* **8**, 19127–19134 (2016)
34. J. Wang, J. Xie, C. Zong, et al., Light-modulated surface micropatterns with multifunctional surface properties on photodegradable polymer films. *ACS Appl. Mater. Interfaces* **9**, 37402–37410 (2017)
35. T. Seki, D. Yamaoka, T. Takeshima, et al., Photo-modulations of surface wrinkles formed on elastomer sheets. *Mol. Cryst. Liq. Cryst.* **644**, 52–60 (2017)
36. D. Yamaoka, M. Hara, S. Nagano, et al., Photoalignable radical initiator for anisotropic polymerization in liquid crystalline media. *Macromolecules* **48**, 908–914 (2015)

37. G. Nasti, S. Sanchez, I. Gunkel, et al., Patterning of perovskite-polymer films by wrinkling instabilities. *Soft Matter* **13**, 1654–1659 (2017)
38. Y. Sun, J.H. Seo, C.J. Takacs, et al., Inverted polymer solar cells integrated with a low-temperature-annealed sol-gel-derived ZnO film as an electron transport layer. *Adv. Mater.* **23**, 1679–1683 (2011)
39. S.Y. Ryu, J.H. Seo, H. Hafeez, et al., Effects of the wrinkle structure and flat structure formed during static low-temperature annealing of ZnO on the performance of inverted polymer solar cells. *J. Phys. Chem. C* **121**, 9191–9201 (2017)
40. K.-W. Jun, J.-N. Kim, J.-Y. Jung, et al., Wrinkled graphene–AgNWs hybrid electrodes for smart window. *Micromachines* **8**, 43 (2017)
41. G. Lin, P. Chandrasekaran, C. Lv, et al., Self-similar hierarchical wrinkles as a potential multi-functional smart window with simultaneously tunable transparency, structural color, and drop-let transport. *ACS Appl. Mater. Interfaces* **9**, 26510–26517 (2017)
42. D. Ge, E. Lee, L. Yang, et al., A robust smart window: Reversibly switching from high transparency to angle-independent structural color display. *Adv. Mater.* **27**, 2489–2495 (2015)
43. F. Li, H. Hou, J. Yin, et al., Near-infrared light – Responsive dynamic wrinkle patterns. *Sci. Adv.* **4**(4), 1–9 (2018)
44. X. Cheng, L. Miao, Z. Su, et al., Controlled fabrication of nanoscale wrinkle structure by fluorocarbon plasma for highly transparent triboelectric nanogenerator. *Microsyst. Nanoeng.* **3**, 16074 (2017)
45. J. Duan, X. Liang, J. Guo, et al., Ultra-stretchable and force-sensitive hydrogels reinforced with chitosan microspheres embedded in polymer networks. *Adv. Mater.* **28**, 8037–8044 (2016)
46. G. Ge, Y. Zhang, J. Shao, et al., Stretchable, transparent, and self-patterned hydrogel-based pressure sensor for human motions detection. *Adv. Funct. Mater.* **28**, 1–8 (2018)
47. N. Gao, X. Zhang, S. Liao, et al., Polymer swelling induced conductive wrinkles for an ultra-sensitive pressure sensor. *ACS Macro Lett.* **5**, 823–827 (2016)
48. Y. Tokudome, H. Kuniwaki, K. Suzuki, et al., Thermoresponsive wrinkles on hydrogels for soft actuators. *Adv. Mater. Interfaces* **3**, 1–5 (2016)

# Chapter 15

## Summary and Future Outlooks



C. M. González-Henríquez, M. A. Sarabia Vallejos,  
and Juan Rodríguez-Hernández

### 15.1 Book Summary

The aim of this book is to introduce to the reader the main and basic knowledge about the strategies and methodologies used to form wrinkled patterns on polymer surfaces. Also, the most recent applications in which these patterns are used are listed and explained.

Firstly, a general description of the conventional techniques to generate different structures at the surface in a controlled manner is revised. Then, novel alternatives for polymer wrinkling are mentioned and explained. Accordingly, some of the methodologies explained to form surface instabilities involves frontal polymerization/vitrification, ion-beam bombardment, interfacial swelling, laser-induced periodic surface structures, and direct laser interference patterning.

Additionally, different materials employed to generate the wrinkles are described. The choice of material is intimately related to the application for which the device

---

C. M. González-Henríquez (✉)

Departamento de Química, Facultad de Ciencias Naturales, Matemáticas y del Medio Ambiente, Universidad Tecnológica Metropolitana, Santiago, Chile

Programa Institucional de Fomento a la Investigación, Desarrollo e Innovación,  
Universidad Tecnológica Metropolitana, Santiago, Chile  
e-mail: [carmen.gonzalez@utem.cl](mailto:carmen.gonzalez@utem.cl)

M. A. Sarabia Vallejos

Departamento de Ingeniería Estructural y Geotecnia, Pontificia Universidad Católica de Chile, Escuela de Ingeniería, Santiago, Chile

Instituto de Ingeniería Biológica y Médica, Santiago, Chile

J. Rodríguez-Hernández (✉)

Departamento de Química Macromolecular Aplicada, Polymer Functionalization Group,  
Instituto de Ciencia y Tecnología de Polímeros-Consejo Superior de Investigaciones Científicas (ICTP-CSIC), Madrid, Spain  
e-mail: [jrodriguez@ictp.csic.es](mailto:jrodriguez@ictp.csic.es)

is intended, such as hydrogels in the biomedical area, graphene as flexible electronic devices, and nanoparticle embedded in poly(dimethylsiloxane) (PDMS) substrates for photo-modulation or smart displays, among others.

In the next paragraphs, a summary of the sections included in this book are described.

## 15.2 Section 1: Generalities on Surface Instabilities

In the first and second chapter, we perform a brief summary of the theoretical basis of how surface instabilities are generated. Most of the recent works in the area have been focused on developing methodologies to control pattern dimensions, such as wavelength and amplitude. Thus, two alternative strategies have been carried out: on one hand, through the use of sophisticated tools or expensive and time-consuming methodologies which manipulate the surface morphology in a highly controlled manner and, on the other hand, the studies which take advantage of the surface instabilities induced in soft materials, such as polymer surfaces, to spontaneously produce the wrinkled patterns. In the case of the last methodology, the instabilities can be created in metastable films by applying external stimuli such as mechanical stretching, electrical field, or thermal gradients. Afterward, upon the remotion of the stimuli applied, the relaxation of the material is produced, thus generating different surface morphologies due to the mismatch between the top layer and the foundation. In Chap. 2, the most relevant techniques to generate this pattern are mentioned. Also, the most influencing technique parameters are listed, and their effect on surface morphology is mentioned.

As a summary, the fabrication process of wrinkled patterns could be separated into three different groups:

- Close to equilibrium, whose structuration is driven by thermodynamics (dewetting, direct convection, self-assembly, and microphase separation, surface aggregation, and template-guided structuration).
- Far from equilibrium, which requires a field-induced and dynamic control of surface structuration (electrohydrodynamic, thermal-gradient, surface wrinkling, creasing and folding, and reaction-diffusion).
- Waterborne methods, where the polymer is altered by a changing environment (breath figures, water-ion-induced nanostructuration, and nanobubble-assisted nano-patterning).

## 15.3 Section 2: Novel Approach for Wrinkle Pattern Formation

This section is divided into five chapters, which covers different novel methodologies used to generate surface instabilities. The methods to produce functionalized and topographically controlled polymer surfaces are of great interest in different

research fields ranging from biomedical or engineering to basic research (like physics, biology, and chemistry). Some of the methodologies explained in this section are frontal polymerization (FP), ion beam (IB), interfacial swelling on the thermoplastic surface, laser-induced periodic surface structures (LIPSS), and direct laser interference patterning.

FP is based on the generation of thin layers of a polymerized material over unpolymerized composites. The technique consists in the formation of a frontal reaction in a localized zone of the material; the polymerization travels in only a unique direction, thus producing a polymerization front.

On the other hand, the IB technique has been mainly used to produce a surface oxidation of the material (e.g., PDMS), thus producing a change in the mechanical properties of the top material, inducing variations in contact angle and aspect ratio of the wrinkled formed, among others.

Another listed method in this chapter is the interfacial swelling on a thermoplastic surface which is based on a photosensitive mixture that remains in contact with the substrate and is then irradiated with UV-vis to assure complete monomer conversion. Subsequently, the cover is removed, and the material formed is submerged in an absorbing solution. At this point, two different scenarios are possible. On the one hand, some photosensitive mixtures clearly detached from the surface and, interestingly, produced both a wrinkled hydrogel surface and a wrinkled thermoplastic counterpart. On the other hand, using other photosensitive mixtures, the hydrogel remains anchored at the surface.

Finally, the LIPSS methodology is also explained; in this case, the polymer surface is exposed to a given number of pulses of a linearly polarized laser within a narrow fluence range well below the ablation threshold. The absorption of polymer, thermal conductivity, and diffusivity are important on tuning the obtained periodic structures.

## 15.4 Section 3: Material Employed in Wrinkles Formation

In this section, the main, most relevant, and useful materials used to generating wrinkled patterns are listed; all of them are polymeric surfaces that have particular characteristics which make them appropriate for one application in particular.

For example, hydrogels were used mainly as biocompatible scaffolds or substrates for different biorelated applications, like biosensor stabilization (humecting cushion for lipid bilayers), for generating bioselective antibiofouling surfaces, or as supports for generating multicellular spheroid structures, for example. An entire chapter is related to smart responsive structures, mainly based on hydrogel materials. In this section, several applications such as the creation of dynamical substrates for cellular biology, cell culture substrates, soft actuators, and moisture triggered devices for optical applications.

Some elastomeric materials, such as PDMS and PMMA, are also mentioned as materials to generate wrinkled patterns on their surface which could be useful in

several applications. In particular, one chapter is focused on the formation of Janus particles with wrinkled surfaces and variable chemistry in one of the hemispheres or Janus fibers which present similar structure than plant tendrils. Also, a mixture of polymers with different materials are mentioned in this section, for example, graphene layers embedded on different materials are used with different applications like flexible/wearable electronic devices, Kirigami nanomachines, nano-electro mechanical resonators, bandgap opening electronics, hydrogen storage, water diffusion, and transport, among others.

## 15.5 Section 4: Applications

Finally, the last section was focused on the applications in which these devices that possess wrinkled patterns on their surface can be applied. Specifically, the first chapter of this section is particularly focused on biorelated applications, which includes topics like cell proliferation substrates, platforms which induce cell differentiation, scaffolds for generating multicellular spheroid structures, or surfaces which present antibiofouling behavior.

In a different chapter of this section, we briefly resume some of the most interesting, relevant, and high-impact applications which take advantage of wrinkled patterns that are not related to biological systems. Among the applications exposed in this chapter, we could highlight some examples like conducting shrinkable devices, shape memory, wrinkled surfaces, electrochromic and solar cell devices, OLEDs, light-controllable electronics, sensors, and actuators, among others. Some particularly interesting applications are, for example, tunable wrinkled surfaces which after a photomask UV exposure or heating processes could generate specially controlled wrinkled patterns which can be erased under certain conditions like environmental pH. Other interesting ones are the pressure sensors that can take advantage of the contact area increase generated by wrinkling surfaces for increasing their sensibility or peristaltic wrinkled patterns which could selectively move particles of a specific size while leaving the rest in the same place.

## 15.6 Audience and Future Outlooks

The methodologies, strategies, and applications are only some of the most relevant examples listed in this book. We consider that wrinkled surface patterns, particularly the generated over polymer films, could be specially interesting for chemists involved in the modification of the surface chemistry, physicists interested in the control of the surface properties including wettability and adhesion/friction, and biochemists focused in the design of materials for biorelated applications in which the functionality and surface topography have been demonstrated to be crucial. The engineering of platforms, with particularly desired surface properties, is also a current topic of industrial interest for actual and future applications.

Since its inception, wrinkled micro- and nano-pattern generation over the material surface has been used to create a variety of devices with highly interesting and specific applications in several research fields. Particularly, the creation of these patterns over polymeric surfaces has been very useful due to their remarkable characteristic to possessing an easy tunable chemistry with a positive outlook for the future due to prior limitations on common patterning methodologies. One future direction of research into the principles of micro- and nano-patterning relays in the biomedical field, mainly because surface properties are of key importance in this topic due to surface direct interaction with the biological systems. As it was fully revised in this book, wrinkled surfaces, by its own, possess an enhanced ability for cell attachment, which, in conjunction with chemical surface modifications, could generate highly specific and efficient platforms for biocompatible devices, biomolecular sensing, bioselective transport, diffusion of some biological entities, anti-biofouling surfaces, cell proliferation devices, or living tissue scaffolds, among others. Future biomedical devices are expected to take advantage of these technological improvements along with other key features from each particular research field, thus making possible to create biocompatible materials which also preserve its particular designed function under rough biological environments.

**Acknowledgments** The authors acknowledge the financial support given by FONDECYT Grant N° 1170209. M.A. Sarabia acknowledges the financial support given by CONICYT through the doctoral program Scholarship Grant. J. Rodriguez-Hernandez acknowledges the financial support from Ministerio de Economía y Competitividad (MINECO) (Project MAT2016-78437-R, FEDER-EU) and, finally, VRAC Grant Number L216-04 of Universidad Tecnológica Metropolitana.

# Index

## A

Aging process, 273  
Air plasma, 66, 67, 77, 81, 82  
Alamar Blue assay, 133  
Amphiphilic gels, 66  
Annealing temperature, 24  
Anthracene, 326  
Antibiofouling, 285, 287  
Anti-counterfeiting devices, *see* Smart windows/displays  
Antifouling behavior, 285, 287  
Argon plasma, 78  
Asymmetrically localized folds, 93  
Attenuated total reflectance FT-IR (ATR FT-IR), 66  
Azobenzene-based polymer layers, 71  
Azobenzene liquid crystalline polymers, 329

## B

Beer-Lambert law, 150  
Bi-axially wrinkled graphene, 335  
Bilayered systems  
  elastic substrates, 21  
  liquid substrates, 21–23  
  rigid top layer  
    metallic/polymeric thin film deposition, 27, 28  
    surface treatments, 27  
  viscoelastic substrates, 23–25  
  viscous liquids, 23  
  yielding/softening, 26, 27  
Biocompatibility model, 132  
Biocompatible devices, 283  
Biocompatible materials, 198

Biological and engineering applications, 348, 349  
Biomedical applications, 274, 279, 283  
Biorelated applications, 348  
Biosensor stabilization, 347  
Blade casting method, 76, 77  
Bovine serum albumin (BSA), 337  
Breath-figure method, 186

## C

Capillary forces, 48, 49  
Carbon nanotube (CNT), 246, 335  
Cell behavior  
  microwrinkled surfaces, 116, 118, 119  
Cell culture  
  microwrinkled surfaces, 116, 118, 119  
Cell proliferation, 274  
  biomaterial community, 274  
  biomedical applications, 279  
  cell culture, 276  
  chitosan (CS) film, 274–276  
  hBM-MSCs, 280  
  materials topography, 274  
  morphologies, 277  
  multiscale topographical gradient approach, 279, 280  
  PDMS films, 276–278  
  PDMS-T copolymer, 277  
  potential fabrication methodology, 274  
  stop-flow lithography (SFL), 277, 279  
Cellular alignment/differentiation, 282, 283  
Chemical vapor deposition (CVD), 240, 242, 335  
China wood oil, 6

- Chitosan microspheres (CSM), 337  
*Chlorella* spp., 286  
 Classical mechanical engineering, 230, 231  
 CO<sub>2</sub> laser oxidation method, 73, 75  
 Conducting shrinkable devices  
   AFM, 316  
   AuNPs/PS, 316, 317  
   fabrication process, 318  
   heat transfer enhancement/catalysis, 316  
   metallic wrinkles, 319  
   metal/polymers, 316  
   PDMS, 316, 321  
   SCBI, 316, 317  
   smart scaffolds and biointerfaces, 316  
   SPM molds, 321  
   surface wrinkling, 316  
   thermal post-process, 316  
   wrinkle generation, 318  
 Contact angle, 127, 129, 130  
 Continuum mechanics, 230–232, 247  
 Creasing, 210, 212, 214, 215, 221, 223  
   in bilayer hydrogels, 301–305  
   thin film and substrate, 297
- D**
- Deposition time, 90, 92, 93  
 Depth-wise gradient films, 37–39  
 Diamond-like carbon (DLC), 78, 97, 99, 101  
 9,10-Dibromo-anthracene (DBA), 44  
 Dielectric elastomers, 115  
 Direct laser interference patterning (DLIP),  
   49–51  
   laser systems, 158  
   metallurgical processes, 158  
   modelling, in polymers  
     (see Modelling, DLIP)  
   multiple-scale interference patterning, 163,  
     165–170  
   principle of interference, 158–160  
   single-scale interference patterning,  
     160–164  
 Direct oxidation, 27
- E**
- Elastic–damage response, 26  
 Elastic energy, 263  
 Elasticity, 259, 263  
 Elastomer, 68  
 Electric field-induced instabilities, 6  
 Electric fields, 144
- Electrochromic devices (ECD)  
   PEDOT:PSS, 322–323  
   smart windows/displays, 322  
 Electrohydrodynamic lithography, 144  
 Electronic skins, 336  
 Electrospinning, 263  
 Electro-wrinkling deformation, 116  
 Embryonic stem (ES) cells, 121  
 Energy dependence, IB, 102, 104–106  
 Ethylene glycol dimethylacrylate (EGDMA),  
   284, 285  
 1-Ethyl-3-methylimidazolium  
   bis(trifluoromethyl sulfonyl)imide  
   (EMI-TSFI), 322
- F**
- Fabrication  
   facilities, 3  
   films structures (see Films structures)  
   stages, 325  
   wrinkled formation (see Wrinkled  
     formation)
- Far-ranging applications, 79  
 FE-SEM images, 96, 98  
 Field-induced assembly, 8  
 Field tests, 287  
 Film dewetting, 4  
 Films structures  
   categories, 20  
   depth-wise gradient films, 37–39  
   forming wrinkles, 20  
   homogeneous films  
     (see Homogeneous films)  
   layered (see Layered films)
- Finite element analysis (FEA), 294, 296, 297,  
   300, 303–305  
 Finite element models, 304  
 Finite element simulation, 298, 299, 301,  
   308, 310  
 5G technology, 229  
 Fluorescent brightener, 65  
 Focused ion beam (FIB), 86, 89, 94, 102,  
   104–106  
 Folding, 209, 210, 213, 222  
 Folds, 292–294, 296–298, 306–308  
 Free radical photopolymerization, 65  
 Frontal polymerization (FP), 347  
   adiabatic system, MMA, 63  
   definition, 67  
   exothermic reaction, 64  
   mechanical/thermal behavior, 67

- photoactivated cationic ring-opening, 64
  - photofrontal polymerizations (*see* Photofrontal polymerizations)
  - plasma-ignited (*see* Plasma-ignited FP)
  - polymerization front, 63
  - thermopolymerization, 64
  - types, 63
  - Frontal vitrification, 63, 77
- G**
- Glancing angle deposition (GLAD), 90
  - Glass transition temperature, 26
  - Gradient film
    - anisotropic swelling, 112
    - fabricate reversible wrinkled planar surfaces, 114, 115
    - functionalization, solid substrate, 114
    - in-plane compressive stress, 112
    - morphological changes, 113
    - PHEMA, 113, 114
    - photosensitive mixture, 113, 114
    - structures, 112
    - surface layer, 113
    - swelling-induced wrinkling, 112, 113
    - thermal pre-polymerization, 114
    - thickness and crosslinker concentration, 113
    - UV photopolymerization, 114
  - Graphene
    - applications, wrinkles
      - band gap opening, for electronics, 244
      - curvature-dependent adsorption, 245, 246
      - enhanced water diffusion and transport, 245–247
      - kirigami nanomachines, 242, 243
      - nano-electromechanical resonators, 244
      - NEMS, 244
    - buckling, wrinkling and folding, 230
    - characteristics, 229
    - induced wrinkles, mechanisms of
      - chemical defects and adsorbates, structure modification, 241, 242
      - by fabrication process, 240, 241
      - self-crumpling, folding and tearing, 237–239
    - industrial applications, 229
    - mechanical properties
      - continuum mechanics and plate phenomenology, 230–232
      - physical defects, 235, 236
    - serendipitous discovery, 229
    - structure, 230
    - thermally-activated ripples
      - dewrinkling mechanism, 234
      - experimental setup, 233
      - extraordinary transport properties, 232
      - Ginzburg length, 234
      - phonons and ripples, 232
      - temperatures, 235
      - 2D materials, 229
- H**
- Hexamethyldisiloxane (HMDSO), 99
  - 1,6-Hexanediol diacrylate (HDDA), 65
  - High-throughput processing, polycarbonate (PC)
    - exemplary confocal microscopic images, 171
    - fabrication, 171
    - foils, 170
    - patterning performance, 173
    - pattern periodicity, 171
    - processing speeds, 171
    - process parameters, 171
    - q-switched high power Nd:YAG laser, 170
    - two-beam laser interference setup, 170
  - Homogeneous films
    - capillary forces, 48, 49
    - DLIP, 49–51
    - drying films, 41, 43–45
    - elastoplastic polymer, 40
    - LIPPS, 51–53
    - Marangoni convection (*see* Marangoni convection)
    - mechanical instability, 41
    - phase diagram, 41, 42
    - solvent casting, 41, 43, 45
    - solvent swelling, 40, 41
    - surface morphology, PVA gels dried, 41, 44, 45
  - Homogeneously crosslinked hydrogels, 114–117
  - Honeycomb pattern, 186
  - Horseradish peroxidase (HRP), 274
  - Hot embossing/molding, 4
  - Human and murine pluripotent stem cells, 121
  - Human bone marrow-derived mesenchymal stem cells (hBM-MSC), 280, 281
  - Human embryonic stem cells (hESCs), 121
  - Human mesenchymal stem cells (hMSCs), 118–120
  - Human umbilical vein endothelial cells (HUVECs), 121
  - Hydrogels
    - applications, wrinkled patterns, 183
    - bioengineering 3D culture system, 200
    - biomimetic artificial bilayers, 198
    - contact angle, 195, 196

Hydrogels (*cont.*)

- DMAEMA, 196
  - electrospinning technique, 198
  - film, as a “lubricant cushion”, 198
  - on HEMA, 196
  - HEMA:PEGDA hydrogels, 195
  - micro-hydrogel shapes, 201
  - spin-coating technique, 198
  - stem cells, 199
  - TFMA, 196–198
  - biological and physical attributes, 184
  - buckling, 184
  - characteristics, 183
  - electric field and light-induced instability, 222
  - micro-hydrogel shapes, 202
  - osmotic pressure, 211
  - physical and chemical properties, 205
  - solvent-induced systems
    - LBL assemblies, 218, 219
    - pAAM-based hydrogels, 211
    - polyacrylamide/pAAM-based hydrogels, 211–213
    - poly(ethylene-glycol)-based, 219, 220
    - polyHEMA, 214, 216
    - PVA, 216, 217
  - temperature-induced (*see* Poly(N-isopropylacrylamide) (polyNIPAM))
    - wrinkle formation, 184
    - wrinkling process, in bilayered system, 184
- Hydrogen, 245
- Hydrogen storage systems, 245
- 2-Hydroxypropyl acrylate (HPA), 66

**I**

- IB deposition, 88, 89
- IB incidence angle, 94, 95
- Indirect laser interference writing, 144
- Indium tin oxide (ITO), 321
- Instabilities, 143
- Interfacial diffusion, 111, 123, 124
- Interfacial swelling, 347
- Interference patterning methods
  - DLIP, 158 (*see also* Direct laser interference patterning (DLIP))
  - laser-based technologies, 157
  - LIL, 157
  - ordered topographies, 157
- In-volume laser surface treatment
  - argon ion, 174
  - characteristics, 173
  - cross-section polisher, 173

- diffraction efficiency, PMMA/PC foils, 175
- in-volume DLIP concept, 175
- line-like interference distribution, 173
- PMMA/PC foil, 173
- temperature distribution, 173, 174
- zero-order intensity, 175

- Ion accelerator, 88
- Ion beam (IB), 347
- Ion beam (IB) bombardment
  - advantages, 85
  - deposition, 88, 89
  - FIB, 86
  - induce structural modifications, 85
  - micro- and nano-patterned surfaces, 85
  - micro- and nano-scale features, 86
  - modifiable and cheap materials, 86
  - PDMS, 86
  - wrinkling, 86–88
- Ion-beam (IB)-induced surface patterns
  - aspect ratio
    - deposition time, 90, 92, 93
    - incidence angle, 94, 95
    - ion beam voltages, 93, 94
    - metal ion implantation, 95, 96
    - temperature variations, 89–91
    - energy dependence, 102, 104–106
- Ion beam (IB) voltages, 93, 94
- Ion milling, 89
- IR laser ignited FP, 66
- Irradiation, 146
- Isobornyl acrylate (IBOA), 65

**J**

- Janus fibers, 263, 348
- Janus films, 258, 260, 261
- Janus particles
  - asymmetric particles, 255
  - colloidal particles, 253, 254
  - compartmentalization method, 256
  - developed preparation methods, 264
  - dichotomy, 254
  - on glass spheres, 254
  - liquid interface and amphiphilicity, 255
  - modern materials research, 255
  - morphologies and shapes, 255
  - original Janus concept, 255
  - physical deposition, 256
  - in self-assembly, 257
  - static and dynamic periodic patterns, 257, 258
  - surface modification, 256

- synthesis and applications, 256, 257
  - terminology, 255
  - wrinkled fibres, 263–265
  - wrinkled spheres, 260–262
- K**
- Kirchhoff-Love plate theory, 230
  - Kirigami nanomachines, 242, 243
- L**
- Laser ablation, 4
  - Laser-induced periodic surface structures (LIPPS), 51–53, 347
    - accumulation, laser pulses, 147
    - AFM topography, 144
    - Beer-Lambert law, 150
    - blends, 152
    - composites, 152
    - experimental setup, 145, 146
    - features, 146
    - ferroelectric properties, 153
    - fluence and temperatures, 151
    - frozen surface inhomogeneities, 148
    - illumination conditions, 151
    - irradiation conditions, 148
    - modified Gaussian beam, 147
    - nanostructures, 149
      - on PET, 152
      - polymer film, 147
      - on PS films, 148
      - on quartz, 149
      - stainless steel and biomaterials, 152
      - temperature, 147
  - Laser scanning, 4
  - Layer-by-layer (LBL)
    - assemblies, 218, 219
    - methodology, 28
  - Layered films
    - bilayered systems (*see* Bilayered systems)
    - description, 20
    - elastic foundation, 20
  - Light-emitting diode (LED), 66
  - Light focusing plastic rod, 64
  - Linear stability analysis, 23
  - Liquid crystals (LCs), 101
  - Liquid substrates, 21–23
- NUV–vis light exposure, 46, 48
  - optical micrographs, patterned samples, 46, 48
  - photosensitizers, 44
  - polymer patterning methodology, 44, 47
  - principles, 44
  - PS thin film, 43, 46
  - thermal annealing, 44, 46, 48
  - three-dimensional topography, 44
- Marine biofouling, 285
  - Metacrylic acid (MAA), 67
  - Metal ion implantation, 95, 96
  - Metallic/polymeric thin film deposition, 27, 28
  - Metallic wrinkles, 319
  - Metal-polymer nanocomposite (AuNPs/PS), 316
  - Methyl methacrylate (MMA), 63
  - Microchips, 3
  - Microelectromechanical (MEM) devices, 3
  - Microlens arrays, 35, 36
  - Micrometer-size structures, 114
  - Micro-/nanoimprinting, 4
  - Micro-/nanostructured polymer surfaces, 3, 4, 12
  - Microstructured wrinkled hydrogels, 118, 120, 121
  - Microwrinkled surfaces, 11
    - cell behavior, 116, 118, 119
  - Millipore water, 22
  - Modelling, DLIP
    - ablation coefficients, 178
    - ablation process, 176
    - experimental vs. calculated profiles, 178
    - geometry and characteristic pitch, 176
    - PC substrates, 177
    - periodic modulation, 177
    - structuring behavior, 176
    - structuring coefficients, 178
    - structuring processes, 177
    - UV laser interference irradiation, 176
  - Monolayer graphene, 306–310
  - Multicellular spheroids (MCSs), 283–285
  - Multifunctional actuators, 338
  - Multiple-scale interference patterning
    - multiple-pulse strategy, 167–169
    - single-pulse strategy, 163, 165, 166
  - Multi-walled carbon nanotubes/PDMS (MWCNT/PDMS), 96–98
- N**
- Nano- and micro-patterned hydrogels
    - breath-figure method, 186
    - honeycomb pattern, 186
    - indentation parameters, 185

- Nano- and micro-patterned hydrogels (*cont.*)  
 micro-honeycomb patterns, 185  
 normal mechanical force, 185  
 on polymer surfaces, 185  
 simple and cost-effective approach, 185  
 stereo-lithography principles, 185  
 viscoelastic lithography, 185
- Nano-electromechanical resonators, 244
- Nanoengineering, 239, 240
- Nanomechanics, 242–244
- Nanostructures, 149
- n-Butyl acrylate (nBA), 35
- Near-infrared (NIR), 335
- Near UV–visible light (NUV–vis)  
 photosensitizer, 44
- Negative-charged surfaces, wrinkle periods,  
 134–136
- N-methylolacrylamide (NMA), 66
- N,N-Dimethylaminoethyl methacrylate  
 (DMAEMA), 195
- N-vinylimidazole (VI), 66
- N-vinylpyrrolidone (NVP), 66
- O**
- Optical erasure dose ( $D_c$ ), 328
- Ordered pores, 143
- Organic light-emitting diodes (OLEDs),  
 324, 348
- Organic photovoltaic (OPV), 324
- O/Si ratios, 90
- P**
- Pancreatic islet cells, 121
- Patterned-hydrogel fabrication process, 116
- Period doubling, 297
- Periodical intensity field, 159
- Perovskite crystals, 332, 333
- Phase separation, 4
- PHEMA films, 113–115, 117, 121–123
- PHEMA wrinkled substrates, 199
- Phosphate buffered saline (PBS), 223
- Photoactivated cationic ring-opening FP, 64
- Photobleaching initiator, 65
- Photocaged superbase (QA-DBU), 65
- Photodimerization reaction, 328
- Photofrontal polymerizations  
 azobenzene-based polymer layers, 71  
 chemical structure, UV liquid resin, 72  
 CO<sub>2</sub> laser oxidation method, 73, 75  
 contact angles, 70  
 elastomer, 68  
 fluorescent brightener, 65  
 front speed, 65  
 generation, 68, 69  
 IR laser ignited, 66  
 light focusing plastic rod, 64  
 methodology, 64  
 one-pot approach, 70  
 one-step protocol, 71  
 PDMS layers, 72  
 photobleaching initiator, 65  
 photocaged superbase (QA-DBU), 65  
 photoinitiator, 64  
 photolithography, UV masks, 68, 69  
 photomasks during UV exposure, 68, 69  
 photopolymerization, 68  
 photo-triggered ascending redox FP, 65  
 photo-triggered method, 65  
 physicochemical process, 65  
 and plasma-ignited FP, 81, 82  
 prepolymer solution, 72  
 procedure, 68, 69  
 quenching, free radicals, 71  
 radiation input, 64  
 synthesis method, 64  
 thermally sensitive polymer  
 synthesized, 65  
 and thermo (*see* Thermo/photofrontal  
 polymerization)  
 2,3,5,6-tetrafluorostyrene and backbone  
 structures, 72, 73  
 3D optical profilometer, 71  
 TMPTA, 65  
 UV gradient photopolymerization  
 methods, 68  
 UV irradiation, 71, 72  
 UVO, 72–74  
 wrinkling formation mechanism, 71  
 wrinkling formation protocol, 70
- Photoinitiator, 64
- Photomask, 44
- Photopolymerizable vinylic hydrogels, 187
- Photopolymerization, 68
- Photosensitive mixture, 114
- Photosensitizers, 44
- Photo-triggered method, 65
- Photovoltaic (PV), 320
- Photovoltaic/solar cells  
 AFM analysis, 332, 334  
 alkyl ammonium chains, 332  
 Cs-corrected STEM analysis, 332  
 IPSCs, 332  
 PEGDA, 331, 333  
 perovskite crystals, 332  
 SA process, 332  
 ZnO layers, 332

- Physicochemical process, 65
- Piezoresistive tactile sensors, 96
- Plasma-ignited FP
- advantages, 67
  - air plasma, 66, 67, 77
  - amphiphilic gels, 66
  - argon plasma, 78
  - Ar plasma exposure on PDMS substrates, 78–80
  - biaxial stretching conditions, 79, 80
  - electron energy, 66
  - experiments, 66
  - far-ranging applications, 79
  - frontal vitrification, 77
  - layer thicknesses, 77
  - LED, 66
  - MAA, 67
  - methodology, 67, 77, 78
  - micrograph, wrinkled pattern, 77
  - NMA, 66
  - N-vinylimidazole (VI), 66
  - NVP, 66
  - one-dimensional, two-dimensional/nested hierarchical wrinkling patterns, 79
  - O<sub>2</sub> plasma exposure/stretching, 78, 79
  - PDMS microspheres, 81
  - and photofrontal polymerizations, 81, 82
  - pre-stretched PDMS substrates, 78
  - QD, 66
  - spatioselective method, 78
  - time-saving and convenient, 66
- Poisson's ratio, 10
- Polyacrylamide (pAAM)-based hydrogels
- copolymer hydrogels, 212
  - folding, 213
  - as a model system, 211
  - osmotic pressure and swelling, 211
  - pattern formation and evolution, 213
  - rubber with moduli, 212
  - strip geometry, 213
- Poly(caprolactone) (PCL) nanofibrous, 200, 201
- Polydimethylsiloxane (PDMS), 21, 27, 28, 30, 32–36, 86–97, 100–106, 216, 217, 316, 346, 347
- Polyelectrolyte multilayers (PEM), 28
- Polyester, 22
- Poly(3,4- ethylene dioxythiophene)
- polystyrene sulfonate (PEDOT:PSS), 322
- Poly(ethylene-glycol)-based hydrogels, 219, 220
- Poly(ethylene glycol diacrylate) (PEGDA), 277, 279
- Polyethylene terephthalate (PET), 152, 153
- Poly(hydroxyethyl methacrylate) (polyHEMA), 39, 284, 285
- alcohol and alcohol/water mixture, 214
  - in biomedical fields, 214
  - infusion process, 216
  - instability patterns, 214
  - swelling patterns, 215
  - wrinkle evolution, 214
  - wrinkling patterns, 216
- Polyimide (PI) layer, 101
- Poly(isobutyl methacrylate) (PiBMA), 74
- Poly(isobutyl methacrylate) (PiBMA) film, 44
- Poly(lactic acid) (PLA), 328
- Polymer films
- SIs (*see* Surface instabilities (SIs))
  - surface–interface, transition, 301–306
- Polymer solar cells (IPSCs), 332
- Polymer surfaces
- IB (*see* Ion-beam (IB) bombardment)
- Polymerization front, 63
- Poly(methyl methacrylate) (PMMA), 90, 92, 93, 185, 320, 347
- Poly(n-butyl acrylate) (PnBA) film, 36
- Poly(N-isopropylacrylamide) (polyNIPAM), 220
- copolymerization, 220
  - dynamic cell culture systems, 221
  - fabrication process, 222
  - reversible wrinkles, 222
  - shrinking patterns, 220
  - surface-instability patterns and potential applications, 223, 224
  - swelling patterns, 220
  - in water, LCST, 220
  - wavelength, 221
- Polystyrene (PS), 21, 316, 322
- Polyurethane/polybutadiene diol (PU/PBDO), 259
- Polyurethane/urea elastomers, 258
- Poly(vinyl alcohol) (PVA), 326
- crosslinking gradient, 217
  - drying-induced morphology, 217
  - film-substrate bilayer device, 216
  - irreversible wrinkling response, 217
  - irreversible wrinkling system, 216
  - moisture-induced wrinkling dynamics, 216
  - moisture-responsive systems, 217
  - solvent evaporation, 217
- Power-law dependence, 81
- Pre-stretched rubber sheet, 23
- Principle of interference, 158
- Printing plate, 205
- Profilometer images, 131
- Pseudoalteromonas* spp., 287

Pulsed lasers, 144, 153  
 PU/PBDO fibers, 263, 265

## Q

Q-switched Nd:YAG laser, 146  
 Quantum dot (QD), 66

## R

Raman confocal, 127, 129, 130  
 Reactive ion etching (RIE), 27, 89  
 Responsive Surface-wrinkled Adhesive (RSA), 219  
 Ripples, in graphene, 232–234, 236, 247

## S

Self-assembly, 4, 7  
 Self-organized surface patterns, 348  
 Semi-periodically distributed ridges, 93  
 Shape memory polymers (SMPs)  
   fabrication method, 320  
   ITO, 321  
   PDMS, 319  
   plasma-mediated skin layer formation, 322  
   PMMA, 320  
   post-curing process, 319  
   PS, 322  
   SERS-active substrates, 322  
   smart windows, 321  
   solar cells, 320  
 Shedding angle, 102  
 Shrinkable controllable electronics  
   bi-axially wrinkled graphene, 335  
   CDV, 335  
   CNT, 335  
   oxygen plasma treatment, 335  
   PDMS, 335  
   silver nanowires hybrid electrodes, 335  
   wearable electronics, 334  
   wrinkled graphene-AgNWs hybrid electrode, 335, 336  
   wrinkled-structure fabrication process, 335  
   wrinkle-free sample, 335  
 Silica nanoparticles (NPs), 335  
 Silicone oil, 287, 288  
 Silicon-on-insulator (SOI) wafers, 34  
 Silver nanowires hybrid electrodes, 335  
 Single-scale interference patterning, 160–164  
 Skin-like pressure sensors, 336  
 Smart polymers, 348, 349  
 Smart windows/displays, surface wrinkles  
   AN dimer, 326, 327

azobenzene-containing polymer, 324  
 azobenzene liquid crystalline polymers, 329  
 bilayer system, 326  
 crosslinked network, 328  
 D<sub>e</sub>, 328  
 dynamic wrinkling systems, 326  
 facile fabrication, 328  
 facile strategy, 326  
 generation/erasure, wrinkling, 328, 330  
 green and effective strategy, 328  
 LC-PDMS, 331  
 moisture-sensitive film-substrate bilayer systems, 326  
 photodimerization, 326, 328  
 PIPA Am, 326  
 PLA, 328  
 PLLA/PDMS, 328, 329  
 PMMA/PDMS, 328  
 PVA, 326  
 pyridine-containing copolymer, 328  
 Soft gel, 22  
 Soft lithography, 4  
 Spheroid generation  
   conventional methods, 283  
   EGDMA, 285  
   MCSs, 283, 285  
   PHEMA film synthesis, 284  
   revolutionary methods, 284  
 Spin-coating method, 320  
 Spin-coating technique, 74  
 Spinodal wrinkling, 29  
 Static annealing (SA), 332  
 Stiff skin, 93  
 Strain engineering, 240, 244  
 Superhydrophobicity, 102  
 Supersonic cluster beam implantation (SCBI), 316  
 Surface chemical composition, 129, 136  
 Surface cracking, 104  
 Surface instabilities (SIs)  
   advantages, 4, 64  
   bilayer hydrogels  
     compressive strain, 297, 298  
     configurations, 299  
     hierarchical wrinkling pattern, 300  
     periodic doublings, 298  
     post-buckling analysis, 299  
     pre-absorption, water, 297  
     surface morphologies, 296, 299  
     thickness ratio, 298  
     thin film and substrate, 297  
   characteristics, 6  
   classification, 4  
   compressed film/substrate systems, 292

- compressive strain, 206
  - confined systems, 4
  - confinement, generation, 206
  - conventional patterning, 4
  - cost reduction, 4
  - creases, 209
  - depth-wise gradient, in hydrogels, 208
  - development, 207
  - dimensionless parameters, 209
  - examples and schematics, 292
  - external stimuli, 4
  - fabrication facilities, 3
  - fabrication of surface patterns, 19
  - field-induced assembly, 8
  - film dewetting, 4
  - film structure systems, 206
  - formation of wrinkles, 53
  - generation, on hydrogels
    - by cooling and heating steps, 191
    - by electrophoresis, 187, 190, 191
    - by heating and UV exposure steps, 192, 193
    - by swelling/drying processes, 187–189
  - growth-induced, 292
  - hot embossing/molding, 4
  - hydrogel films, 208
  - hydrogel systems, 206
  - irreversible patterns, 209
  - MEM devices, 3
  - metastable films, 4
  - microchips, 3
  - micro-/nanoimprinting, 4
  - micro-/nanostructured polymer surfaces, 3
  - modes, 209
  - mucosae, 210
  - numerically-simulated phase diagram, 210
  - pattern formation, 206
  - phase separation, 4
  - Poisson's ratio
    - dimensionless parameters, 296
    - FEA model, 294
    - polymer gels, 294
    - polymeric materials, 294
    - substrate, 294
    - substrate Poisson's ratio, 295
    - surface instability, 295
    - surface morphologies, 295–296
    - thin stiff film, 294
  - structuration driven by thermodynamics, 4, 7
  - support layer, 206
  - surface patterns, 5
  - surface-attached hydrogels, 211
    - uniform soft gel layer, 207
    - waterborne methods, 9
  - Surface instabilities patterns, 346
  - Surface laser-light scattering (SLS), 24
  - Surface morphological instabilities, 273
  - Surface patterns
    - hydrogels, 205
      - as mucosal folds, 205
      - in soft hydrogels, 205
  - Surface structuring, 157, 176
  - Surfing mechanism, water nanodroplets, 247
  - Swelling
    - anisotropic, 207, 208
    - creasing, 210
    - critical swelling ratio, 218
    - and deswelling, 219, 220
    - hydrogen-bonded LBL multilayer films, 218
    - and mechanical properties, 207
    - pAAM hydrogels, 211
    - PVA, 216
    - ratio, 211
    - swelling ratio, 214
    - for unconstrained hydrogels, 211
  - Swelling-induced wrinkles
    - atactic PS solutions, 36
    - buckling process, microlens formation, 36
    - characteristics, 35
    - diffusion process, 37
    - microlens arrays, 35, 36
    - moduli-mismatch oxidized PDMS
      - regions, 36
    - monomer solution, 35
    - preparation of bilayers, 36
    - titanium (Ti) layer, 36
  - Swelling ratio, 211
  - Swollen gel, 110
- T**
- Temperature variations, 89–91
  - Templates, 143
  - Tert*-butyl acrylate (*t*BA), 319
  - Thermal fluctuations, 232, 234, 238, 239, 247
  - Thermal gradients, 6
  - Thermal properties, 148, 151
  - Thermodynamics, 4, 7, 346
  - Thermo/photofrontal polymerizations
    - annealing cycle, 74
    - blade casting method, 76, 77
    - formation of coatings, 74
    - heating process, 76
    - light/thermo-reversible wrinkled patterns, 76
    - photomasks, 76

- Thermo/photofrontal polymerizations (*cont.*)  
 photopatterning and transferring method,  
 76, 77  
 PiBMA, 74  
 self-healing capacity, 76  
 spin-coating technique, 74  
 UVB/UVC irradiation, 74  
 wrinkling/unwrinkling processes, 76
- Thermoplastics, 123–126
- Thermosensitive polymers, 65
- Thiol-ene polymers, 76
- 3D dual scale surface structures method,  
 97, 100
- Three-dimensional (3D) multicellular  
 spheroids (MCSs), 121–123
- 3D optical profiler images, 131
- Tinuvin 328, 68
- Tissue engineering applications, 274, 279, 283
- Treated culture plates (TCP), 132, 133
- 2,2,2-Trifluoroethyl methacrylate (TFMA), 196
- Tri(propylene glycol) diacrylate (TPGDA), 65
- Trimethylolpropane triacrylate (TMPTA), 65
- 2D FFT patterns, 90, 91
- 2D materials, 229, 232, 235
- Two-dimensional (2D) wavy structures,  
 34, 35
- U**
- Ultrasensitive sensors/actuators  
 acrylamide, 337  
 ambient temperature, 338, 342  
 CSM, 337, 338  
 electronic devices, 336  
 external pressure, 337, 341  
 multifunctional actuators, 338  
 PDMS, 337  
 polyvinyl alcohol hydrogels, 337  
 pressure sensor device, 337, 339, 340  
 silver layers, 337  
 skin-like pressure sensors, 336  
 swelling capacity, 337  
 UV exposure process, 337  
 wrinkling formation, 337, 341
- Ultraviolet light, 27
- Ultraviolet ozone (UVO), 72–74, 82
- UV irradiation, 71, 72
- V**
- Vinylpyrrolidone (VP), 123
- Vinyl versatate (VeoVa 10), 66
- Virtual mask, 104
- Viscoelastic lithography, 185, 186
- Viscoelastic substrates  
 annealing temperatures, 24  
 elastic layer, 24  
 SLS, 24  
 stress-driven surface wavy patterns,  
 24, 25  
 theoretical and experimental studies, 23  
 thermal-induced surface wrinkling, 24  
 wrinkle morphologies, 24
- Viscous liquids, 23
- Voltage-induced wrinkles, 115
- von Karman plate theory, 24
- VP-based hydrogel wrinkled surfaces,  
 132, 133
- VP-based network, 129
- W**
- Waterborne methods, 9
- Wrinkled hydrogels  
 advantages, 111  
 applications, 111  
 characteristics, 110  
 characteristics (period and amplitude),  
 126–128  
 chemical actuators, 111  
 chemical composition, 131, 132  
 chemical design, 111  
 confocal Raman, 127, 129, 130  
 contact angle measurements, 127, 129, 130  
 definition, 111  
 development, soft actuation devices, 111  
 equilibrium, 111  
 film configurations, 112  
 film foundation, 109  
 gradient film (*see* Gradient film)  
 homogeneous/gradient film, 112  
 homogeneously crosslinked, 114–117  
 hydration, 111  
 microstructured, 118, 120, 121  
 negative-charged surfaces, 134–136  
 residual stress, 110  
 substrates on thermoplastic polymers,  
 123–126  
 surface coatings, 111  
 surface structuration, 112  
 surface structures, 109, 110  
 swelling, 109, 110  
 3D MCSs, 121–123  
 VP-based, 132, 133

- Wrinkled patterns
  - aspect ratio
    - deposition time, 90, 92, 93
    - incidence angle, 94, 95
    - ion beam voltages, 93, 94
    - metal ion implantation, 95, 96
    - temperature variations, 89–91
  - configuring, by templates, 96–102
    - AFM and 2D-FFT images, 97, 99
    - characteristics, localized irradiation-induced wrinkle, 97
    - chemical analysis and mechanical properties, 102
    - DLC, 97, 99, 101
    - FE-SEM images, 96, 98
    - HMDSO, 99
    - IB irradiation-induced wrinkle formation mechanism, 97
    - LCs, 101
    - manufacturing process, 102
    - maze structures, 101, 102
    - microstructures with periodic and ordered directionalities, 101
    - MWCNT/PDMS, 96–98
    - nanostructured superhydrophobic silk, 101
    - PDMS film, 101, 103
    - ridge-guiding structures, 102
    - 3-D dual scale surface structures method, 97, 100
    - wrinkled walls, 101
  - FP (*see* Frontal polymerization (FP))
    - generation, 67, 68
  - Wrinkled walls, 101
- Wrinkle formation
  - mechanical stretching/compression
    - advantages, 32
    - heating, 34
    - homogeneity, 32
    - 1D ripples to 2D herringbone structures, 33, 34
    - one-dimensional wrinkles, 33
    - optical microscopy images, transmission mode, 32
    - stress relaxation, 32, 33
    - stripe patterns, 33
    - 2D buckled structures, 34
    - 2D wavy structures, 34, 35
    - wrinkle patterns, 33
    - Young's modulus, 32
  - thermal variations
    - anisotropic wrinkling, 30, 31
    - heating, 28, 29
    - microstructured molds, 30
    - microstructured PS layer, 30
    - morphologies, 29, 30
    - PDMS, 30
    - polymer/metal bilayer systems, 30
    - principle, 28
    - spinodal wrinkling, 29
    - temperature, 29
    - types, 29
- Wrinkles
  - buckling patterns, 86, 87
  - creases, 291
  - folding/wrinkling patterns, 293
  - geometries, 88
  - graphene (*see* Graphene)
  - herringbone, 308
  - herringbone pattern, 87
  - hierarchical wrinkling pattern, 300
  - instability, 86
  - metal film, 86
  - period doubling, 297
  - periodic, 296
  - pre-absorption, water, 297
  - semi-regular pattern, buckles, 88
  - sinusoidal, 299
  - surface instabilities, 291, 292
  - surface mechanical instabilities, 88
  - Young's modulus ratio, 292
- Wrinkles patterns formation, 346, 347
- Wrinkle wavelength, 339
- Wrinkle wavenumbers, 90
- Wrinkling
  - amplitude, 11
  - appear, 6
  - applications, 11
  - bilayer systems, 10, 11
  - and buckling, 7
  - on covalently-anchored hydrogels (*see* Hydrogels)
  - elastomeric PDMS, 6
  - environmental gases, 7
  - fabrication, elements, 6
  - folded structures, 11
  - formation, 6
  - in free-standing flexible elastomers, 258–260
  - human/fruit skin, 6
  - instability, 6, 9
  - intestine/mammalian brain, 6
  - mechanical stress force, 10
  - mechanically induced surface instabilities, 6
  - mechanisms, 10

- Wrinkling (*cont.*)  
  parameters, 10  
  sandwich, 6  
  UV light, 7  
  wavelength, 11
- Wrinkling mechanisms  
  formation  
    mechanical stretching/compression,  
      32–34  
    thermal variations, 28–31
- Swelling-induced wrinkles, 35–37
- Wrinkling under capillary forces, 48, 49
- Wrinkling-unwrinkling approach, 26
- Y**  
Young's modulus, 32, 106, 292
- Z**  
Zinc oxide (ZnO), 332